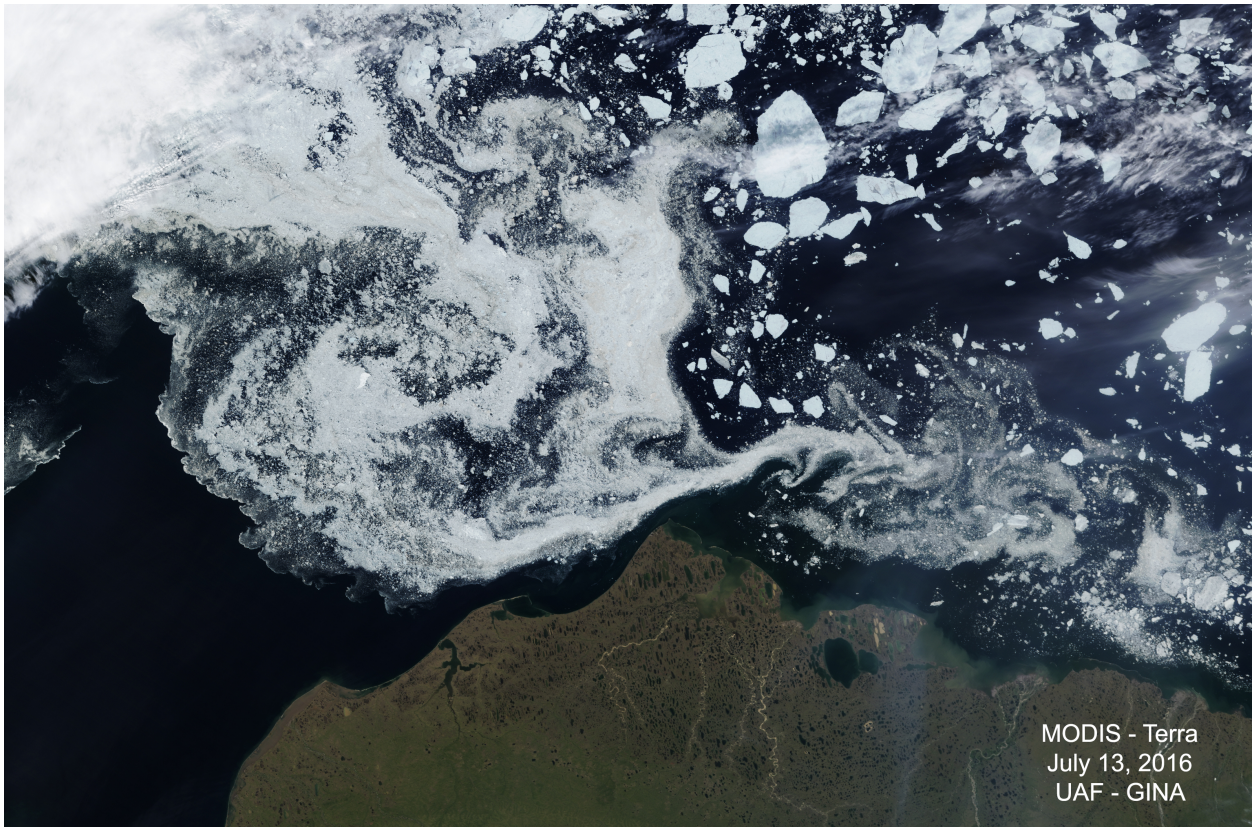


# Characterization of the Circulation on the Continental Shelf Areas of the Northeastern Chukchi and Western Beaufort Seas





# Characterization of the Circulation on the Continental Shelf Areas of the Northeastern Chukchi and Western Beaufort Seas

December 2017

Authors:

Thomas J. Weingartner<sup>1</sup>, PI; Robert Pickart<sup>2</sup>, Co-PI; and Peter Winsor<sup>1</sup>, Co-PI

Co-Authors:

W. Bryce Corlett<sup>2</sup>, Elizabeth L. Dobbins<sup>1</sup>, Ying-Chih Fang<sup>1</sup>, Cayman Irvine<sup>1</sup>, Brita Irving<sup>1</sup>, Min Li<sup>2</sup>, Kofan Lu<sup>1</sup>, Rachel Potter<sup>1</sup>, Hank Stascewich<sup>1</sup>, and Chase Stoudt<sup>1</sup>

Prepared under BOEM Agreement M12AC00008 by:

<sup>1</sup>University of Alaska Fairbanks  
College of Fisheries and Ocean Sciences  
Fairbanks, AK 99775-7220

<sup>2</sup>Woods Hole Oceanographic Institution  
Department of Physical Oceanography  
Woods Hole, MA 02543



## **DISCLAIMER**

Study collaboration and funding were provided by the US Department of the Interior, Bureau of Ocean Energy Management (BOEM), Environmental Studies Program, Washington, DC, under Agreement Number M12AC00008. This report has been technically reviewed by BOEM, and it has been approved for publication. The views and conclusions contained in this document are those of the authors and should not be interpreted as representing the opinions or policies of the US Government, nor does mention of trade names or commercial products constitute endorsement or recommendation for use.

## **REPORT AVAILABILITY**

To download a PDF file of this report, go to the US Department of the Interior, Bureau of Ocean Energy Management [Data and Information Systems webpage \(http://www.boem.gov/Environmental-Studies-EnvData/\)](http://www.boem.gov/Environmental-Studies-EnvData/), click on the link for the Environmental Studies Program Information System (ESPIS), and search on 2017-065. The report is also available at the National Technical Reports Library at <https://ntrl.ntis.gov/NTRL/>.

## **CITATION**

Weingartner TJ, Pickart R, Winsor P, et al. 2017. Characterization of the Circulation on the Continental Shelf Areas of the Northeast Chukchi and Western Beaufort Seas. Fairbanks, AK: US Department of the Interior, Bureau of Ocean Energy Management. OCS Study BOEM 2017-065. 221 p.

## **ABOUT THE COVER**

Visible MODIS Terra image from July 13, 2016, acquired from the University of Alaska Fairbanks Geographic Information Network of Alaska.

## ACKNOWLEDGMENTS

In addition to those mentioned in partnerships (Section A3.0), there are many people who played a role in the success of this endeavor. Additional partner funding was provided by Shell, ConocoPhillips Alaska, the Alaska Ocean Observing System, and the State of Alaska Coastal Impact Assistance Program. Special thanks goes to Molly McCammon (AOOS), John Cologgi, Caryn Rea, and Chris Yetsko (CPAI), A. Michael Macrander and Robert Raye (SEPI), Steinar Elroy (Statoil), and Sheyna Wisdom (Olgoonik Fairweather) for partner program management efforts.

We thank Warren Horowitz (BOEM) for his keen interest and advice throughout this program and for his assistance in procuring several partners that participated in the project

We also thank the officers and crews of the R/V *Norseman II*, R/V *Westward Wind*, and USCGC *Healy* for their skill and efficiency in conducting work safely at sea. John Kemp, Frank Bahr, David Leech, and Peter Shipton conducted the WHOI and UAF mooring operations. Leandra de Sousa, Billy Adams, Willard Neakok, and Robert Suydam deployed drifters under the sponsorship of the North Slope Borough–Shell Baseline Studies Program. James Kelly, Kim Martini, and Steve Sweet provided HFR field assistance, and logistical support was appreciated from UIC Science. We are grateful to the Ukpeagvik Iñupiat, Olgoonik, and Cully Corporations for the use of their lands and the villages of Barrow, Wainwright, and Point Lay, Alaska, for their cooperation and support.

Frank Bahr and Dan Torres processed all of the WHOI data, while Carolina Nobre, Peigen Lin, and Yiquan Qi assisted in the scientific analysis. Todd Mudge (ASL) oversaw the industry mooring operations and the processing of the industry mooring data with assistance from Keith Borg and Dawn Sadowy (ASL).

We thank Steve Okkonen and Carin Ashjian for sharing Barrow Canyon mooring data, as well as the sea ice remote sensing group at the University of Bremen, the National Snow and Ice Data Center, and the US National Ice Center for providing access to sea ice data sets and NOAA/OAR/ESRL PSD for NARR wind data access. Additional data utilized herein was collected under previous BOEM efforts involving Chukchi deployments of HFR and moorings (OCS Study 2012-079), CTD casts and moorings in the Hanna Shoal region (OCS Study 2016-047), and drifters in the Chukchi and Beaufort (OCS Study 2015-022). Industry, Shell/NSB baseline studies, and CSESP also provided program data for synthesis.

# Contents

List of Figures .....	v
List of Tables .....	xvii
List of Abbreviations and Acronyms .....	xviii
Abstract.....	xx
A. Introduction, Objectives, and Partnerships .....	A1
A.1 Introduction .....	A1
A.2 Objectives .....	A3
A.3 Partnerships .....	A4
B. The Chukchi Slope Current.....	B1
Abstract.....	B1
B.1 Introduction .....	B1
B.2 Data.....	B3
B.2.1 Shipboard Hydrographic and Velocity Data .....	B3
B.2.2 Surface Winds.....	B4
B.3 Methods .....	B5
B.3.1 Gridding and Averaging .....	B5
B.3.2 Defining the Currents .....	B6
B.3.3 Calculating Fluxes.....	B6
B.4 Mean Conditions .....	B7
B.4.1 Structure.....	B7
B.4.2 Transport.....	B11
B.5 Variability.....	B12
B.5.1 Seasonality.....	B12
B.5.2 Interannual Variability.....	B13
B.6 Nature of the Chukchi Slope Current .....	B14
B.6.1 Wind Influence .....	B14
B.6.2 Path and Downstream Evolution.....	B15
B.7 Pacific Water Mass Budget of the Chukchi Shelf.....	B17
B.8 Summary and Discussion .....	B19
C. Surface Current Patterns in the Northeastern Chukchi Sea and Their Response to Wind Forcing... C1	
Abstract.....	C1
C.1 Introduction .....	C1

C.2	Data and Methods.....	C3
C.2.1	Surface Currents.....	C3
C.2.2	Winds.....	C4
C.2.3	SOM Analysis.....	C4
C.2.4	EOF Analysis.....	C5
C.2.5	Hydrography.....	C5
C.2.6	Subsurface Currents.....	C5
C.3	Results.....	C5
C.3.1	SOM-derived Patterns.....	C5
C.3.2	The Role of Winds: SOM Perspective.....	C8
C.3.3	The Role of Winds: EOF Perspective.....	C11
C.3.4	Mean Circulation Patterns.....	C14
C.3.5	Spatial Correlation Structure.....	C16
C.4	Discussion.....	C16
C.5	Summary.....	C20
D.	Transport and Thermohaline Variability in Barrow Canyon on the Northeastern Chukchi Sea Shelf D1	
	Abstract.....	D1
D.1	Introduction.....	D1
D.2	Methods.....	D3
D.2.1	Moorings.....	D3
D.2.2	High-Frequency Radars (HFR).....	D3
D.2.3	Winds.....	D4
D.3	Results.....	D4
D.3.1	Kinematic Description.....	D4
D.3.2	Transport: Observations.....	D7
D.3.3	Transport: Hindcast and Climatology.....	D11
D.3.4	Thermohaline Variability.....	D15
D.4	Discussion.....	D18
D.4.1	Transport Comparisons.....	D18
D.4.2	Consequences of Transport Seasonality.....	D21
D.4.3	Hydrographic Implications.....	D22
D.4.4	Shelf Response to Wind-Forcing.....	D22
D.4.5	Transport Intermittency.....	D23
D.5	Summary.....	D24
E.	A Quasi-Lagrangian Perspective on the Surface Circulation of the Chukchi Sea.....	E1
E.1	Introduction.....	E1

E.2	Methods .....	E2
E.2.1	Drifter Deployments .....	E2
E.2.2	Momentum Balance Terms .....	E3
E.2.3	Wind and Current Variability .....	E5
E.3	Results .....	E6
E.3.1	Hydrographic Background.....	E6
E.3.2	Surface Circulation.....	E10
E.3.3	Dispersion .....	E24
E.3.4	Barrow Canyon Mesoscale Analyses.....	E26
E.4	Discussion and Summary .....	E30
F.	The Summer Hydrographic Structure of the Hanna Shoal Region on the Northeastern Chukchi Sea Shelf: 2011 – 2013.....	F1
	Abstract.....	F1
F.1	Introduction.....	F1
F.2	Data and Methods .....	F3
F.2.1	Hydrography.....	F3
F.2.2	Meteorology; Sea Ice Concentration, Drift, and Thickness; and Satellite-Tracked Drifters... F3	
F.3	Results .....	F4
F.3.1	Sea Ice Conditions .....	F4
F.3.2	Hydrography: Broad-Scale Perspective .....	F5
F.3.3	Hydrography: Hanna Shoal.....	F11
F.3.4	The North Side of Hanna Shoal .....	F14
F.4	Discussion .....	F17
F.5	Conclusion.....	F20
G.	Circulation of the Chukchi Sea Shelfbreak and Slope from Moored Timeseries .....	G1
	Abstract.....	G1
G.1	Introduction .....	G1
G.2	Data and Methods .....	G3
G.2.1	Mooring Data .....	G4
G.2.2	Wind Data .....	G6
G.2.3	Atmospheric Reanalysis Fields.....	G6
G.2.4	Ice Concentration Data .....	G6
G.3	Mean and Seasonality of the Circulation and Hydrography of the Shelfbreak and Slope .....	G7
G.4	Volume Transport of the Slope Current and Shelfbreak Jet .....	G12
G.5	Extreme States of the Slope Current and Shelfbreak Jet .....	G12
G.5.1	Strong Slope Current and Reversed Shelfbreak Jet.....	G13

G.5.2	Strong Shelfbreak Jet and Weak Slope Current.....	G16
G.6	Upwelling .....	G17
G.7	Propagation of Water Mass Signals from Barrow Canyon to the Chukchi Slope .....	G20
H.	Physical Oceanography of the Northeastern Chukchi Sea: A Synthesis.....	H1
H.1	Introduction .....	H1
H.2	Sea Ice .....	H1
H.3	Winter Sea Ice Statistical Properties.....	H5
H.4	Hydrography .....	H10
H.5	Circulation Connections .....	H21
H.5.1	Chukchi Sea Shelf .....	H21
H.5.2	Chukchi Sea Shelf and Alaskan Beaufort Sea Shelfbreak .....	H33
H.6	Summary.....	H40
I.	Recommendations for Future Study.....	I1
J.	References .....	J1
Appendix A: Surface Current Patterns in the Northeastern Chukchi Sea and Their Response to Wind Forcing.....		Appendix A -1
Appendix B: Tidal Ellipse Properties for the Chukchi Sea Shelf.....		Appendix B -1

## List of Figures

- Figure A1. Mean depth-integrated streamlines (white lines) in the Chukchi Sea, after Spall (2007; left). The bathymetry is colored and major bathymetric features are labeled. Bathymetric map of the northeastern Chukchi Sea, with place names included (right)..... A2
- Figure B1. Revised schematic of the circulation of the Chukchi Sea and western Beaufort Sea from Brugler et al. (2014), including an extended Chukchi shelfbreak jet and the newly described Chukchi slope current based on the results of this study. .... B2
- Figure B2. Locations of the 46 shipboard sections used in the study, color coded by cruise (see the legend and Table B1). The symbols denote the CTD stations comprising each section. The 90 m isobath is highlighted bold. .... B5
- Figure B3. Temperature-Salinity diagram of all of the hydrographic data offshore of the 90 m isobath and above 300 m depth. Each point denotes a single measurement, and the color represents the percentage of data within each grid cell of 0.1°C temperature by 0.1 salinity. The red lines indicate the different water mass boundaries. ACW = Alaskan coastal water; BSSW = Bering summer water; WW = newly-ventilated Pacific winter water; RWW = remnant Pacific winter water; MW = meltwater; AW = Atlantic water..... B8
- Figure B4. Mean vertical sections constructed from the 46 shipboard transects. (a) Potential temperature, and (b) Absolute geostrophic velocity overlain by potential density (contours,  $\text{kg m}^{-3}$ ). The black dashed lines denote the  $5 \text{ cm s}^{-1}$  velocity anomaly contour outlining the shelfbreak jet and slope current (see text). Positive velocities are eastward (the viewer is looking westward). The number of sections contributing to the mean at each cross-slope location is plotted in the top panel. .... B9
- Figure B5. Relative occurrence of the different water masses in the mean hydrographic section. The black dashed lines denote the outline the shelfbreak jet and slope current as in Figure B4..... B10
- Figure B6. Transport of the Chukchi slope current broken down by water mass (see Figure B3 for the water masses). Standard errors are indicated by the lines. (a) Volume transport; (b) Heat transport; (c) Freshwater transport..... B11
- Figure B7. Mean monthly occurrence of water masses on the Chukchi slope offshore of the 90 m isobath and shallower than 300 m. Standard errors are indicated. (See Figure B3 for the water masses.) ..... B12
- Figure B8. Mean monthly Pacific water transport of the Chukchi slope current with standard errors; N = 11 for July, 10 for August, 5 for September, and 8 for October. (a) Volume transport; (b) Heat transport; (c) Freshwater transport..... B13
- Figure B9. Interannual change in occurrence of water masses on the Chukchi slope from the early regime to the recent regime, offshore of the 90 m isobath and shallower than 300 m. Standard errors are indicated. (See Figure B3 for the water masses.)..... B14
- Figure B10. Interannual change in Pacific water transport of the Chukchi slope current from the early regime to the recent regime, with standard errors; N = 18 for the early regime, and 16 for the recent regime. (a) Volume transport; (b) Heat transport; (c) Freshwater transport. .... B14
- Figure B11. Mean along-shelfbreak 10 m wind speed from July – August each year, averaged over the Chukchi slope region ( $155 - 162^\circ\text{W}$  and  $72 - 74^\circ\text{N}$ ). The standard errors are indicated. Negative wind speeds are easterly. .... B15
- Figure B12. Composite vertical sections of absolute geostrophic velocity (color) and potential density (contours,  $\text{kg m}^{-3}$ ) during (a) calm wind conditions; and (b) times when the easterly winds exceeded  $4 \text{ m s}^{-1}$  prior to and during the occupation of the transect..... B16

Figure B13. (a) Map showing the position and strength of the Chukchi slope current for each of the transects that measured the current. The width of the arrows denotes the lateral scale of the current, and the length of the arrows denotes the mean speed of the current averaged over its width and depth. The shipboard transects are indicated by the dashed lines. (b) Same as (a) except for the Chukchi shelfbreak jet. .... B17

Figure B14. Mass budget of the Chukchi shelf inflows and outflows as discussed in the text, including the residual. Positive transports are inflows and negative transports are outflows. Standard errors are indicated. .... B19

Figure C1. (a) Map of the Chukchi Sea with place names. Blue dots indicate 2012 HFR network grid points with more than 60% temporal coverage. Red squares show locations of HFR field sites. The red outlined area represents the NARR wind domain used in the SOM and EOF analyses, with the red triangle the location representative of the shelf wind time series. Legs 1 and 2 are hydrographic transects conducted in September 2013. Black dot north of Wainwright denotes the BC2 mooring. Gray arrows show schematic pathways of Pacific waters. Bathymetric contours are drawn from 10 – 100 m at 10 m intervals. Place names include HV = Hope Valley, HC = Herald Canyon, HeS = Herald Shoal, CC = Central Channel, and HaS = Hanna Shoal. (b) Grid points within the red rectangle are used to determine upcanyon and downcanyon flow conditions. .... C2

Figure C2. Representative circulation regimes categorized from twelve SOM-derived patterns of surface currents (blue vectors) for 2012: (a) northeastward-flowing regime and (b) reversal regime. The frequency of regime occurrence is included in each panel, and the 80 m isobath is thicker to define Barrow Canyon. The inserted scatter plot denotes vertically-averaged velocities from mooring BC2 (black dot) when the flow regime occurred. Polar histograms on the right denote wind velocities associated with the flow regime (red triangle). The direction follows oceanographic convention and speed is shaded. The percentage indicates frequencies of winds blowing toward that direction. .... C6

Figure C2. (continued) (c) northwesterly wind regime and (d) divergent mode. Note that the scales of current vectors in (c) and (d) are different than those in (a) and (b). .... C7

Figure C3. Monthly occurrences of SOM-derived circulation regimes for 2010 – 2014 with different hatching denoting different years. (a)-(c) Northeastward-flowing regime (NE). (d)-(f) Reversal regime (R). (g)-(i) Divergent mode (D). (j)-(l) Northwesterly wind regime (NW). A 15-day data gap in August 2013 is the reason for few regime estimates in that month. .... C9

Figure C4. (a) Upper panel: time series of wind vectors in August 2012. The vector direction follows oceanographic convention. Lower panel: SOM-derived circulation regimes (black dots) in August 2012 and normalized data returns (gray line). The abbreviations are: R, reversal regime; D, divergent mode; G, pattern G; NW, northwesterly wind regime; NE, northeastward-flowing regime. (b) As in (a), but for September 2012. (c) As in (a), but for October 2012. .... C10

Figure C5. (a) EOF Mode 1 of 2012 reconstructed HFR data (blue vectors) and its explained variance. For clarity, only subsampled vectors are shown. (b) As in (a), but for Mode 2. (c) EOF Mode 1 of 2012 NARR winds (black vectors), also subsampled. (d) As in (c), but for Mode 2. .... C12

Figure C6. (a) Time series of wind speed with wind speeds  $\geq 6 \text{ m s}^{-1}$  highlighted in gray. (b) Time series of wind direction with gray shading corresponding to winds blowing from the northeast quadrant. (c) Time series of PC1 of surface currents (black) and PC1 of winds (gray) with gray shaded areas highlighting positive PC1 values. PC1 values approaching one indicate currents or winds approximating the Mode 1 structure. (d) Time series of representative circulation regimes derived from SOM (black dots): R, reversal (highlighted in gray); D, divergent mode; G, pattern G; NW, northwesterly wind; NE, northeastward-flowing. The gray shaded area highlights the reversal regime. Vertical red lines in each panel denote periods of selected reversal regimes (T1, T2, T3, and T4). Red arrow and bar denote a northeasterly wind event described in the text. .... C13

Figure C7. Mean (a) downcanyon and (b) upcanyon surface currents (blue vectors) for 2010 – 2014. Bathymetric contours (gray lines) are drawn within 200 m at 40 m intervals, with depths less than 40 m drawn at 10 m intervals. The black vector denotes the mean winds, and the polar histogram along 72°N denotes wind velocities. Areas circumscribed by dashed lines denote regions (labeled 1 – 4) of distinct flow behaviors (see text). For clarity, the vectors were subsampled. .... C15

Figure C8. Spatial distribution of complex correlations of surface currents with respect to a reference grid point (large black dot) for (a, c) downcanyon and (b, d) upcanyon flow. Black contour denotes the 0.8 correlation level. Correlation below the e-folding scale is shaded in cool colors. The 95% significance level is estimated from the effective number of degrees of freedom using the integral time scale..... C17

Figure C9. Vertical sections from September 2013 of potential temperature and salinity overlain with isopycnals (white contours) for (a, c) Leg 1 and (b, d) Leg 2. Black arrow denotes the location of 71.5°N. Note that the shading scales in (a) and (b) and the horizontal scales for Legs 1 and 2 are different. .... C18

Figure C10. HFR observations (blue vectors) during 12 – 19 September 2011 at indicated UTC time. The black vector denotes the wind at the cardinal hour of the snapshot, with the magnitude and direction shown in the legend, and the gray shaded vectors are winds for the preceding 12 and 24 hours. Bathymetric contours (gray lines) are drawn within 80 m at 10 m intervals. For clarity, the current vectors were subsampled..... C19

Figure D1. Bathymetric map of the northeastern Chukchi Sea showing mooring locations. The 2010 – 2012 arrays of 6 moorings are shown with black dots and consist of moorings BC1 (closest to the coast) through BC6. Additional moorings, summarized in the discussion, are shown using colored symbols. HFRs were located in Point Lay, Wainwright, and Barrow. The striped regions encapsulate that portion of the HFR mask containing 50% or more good data. .... D2

Figure D2. A) Vertically-averaged velocity vectors and variance ellipses for the moorings at the head of Barrow Canyon. Note the velocity scale change between the mean vector and the variance ellipse. B) Time series of the along-canyon currents at 20 m depth at mooring BC2. Both figures are based on the August 2010 – August 2011 mooring records. .... D5

Figure D3. Vertical sections of the mean annual: a) along-canyon,  $u_r$  and b) cross-canyon,  $v_r$  velocities. Mean sections of c)  $u_r$  and d)  $v_r$  for the downcanyon case, and mean sections of e)  $u_r$  and f)  $v_r$  for the upcanyon case. Vertical sections of the first EOF eigenvector for g)  $u_r$  and h)  $v_r$ . All figures are based on the August 2010 – August 2011 period. .... D6

Figure D4. Mean daily along-canyon winds (top) and transport (bottom). The dashed red line on the wind and transport time series denotes the record length means of  $-1.7 \text{ m s}^{-1}$  and  $0.19 \text{ Sv}$ , respectively. .... D8

Figure D5. Mean monthly along-canyon winds (top) and transport (bottom) are denoted by black lines and dots. Crosses and gray lines delineate the 95% confidence limits. Dashed red lines on show the record-length means in transport ( $0.19 \text{ Sv}$ ) and along-canyon wind velocity ( $1.7 \text{ m s}^{-1}$ ). .... D10

Figure D6. Panels A and B are the means (filled circles) and standard deviations (error bars) of the monthly transport and along-canyon wind velocity, respectively, for 2010 – 2015. Panel C is the mean monthly transport (black line and circles) and 95% confidence limits (error bars) based on the January 1979 – July 2015 GLM hindcast. The gray lines and circles indicate the maximum and minimum values in each month. Panel D displays the monthly means (circles) and standard deviations (squares) of the pseudostress for the January 1979 – July 2015 period at the three locations used in the GLM. .... D10

Figure D7. Probability density functions of the mean daily transport in Barrow Canyon for winter (October – April; top) and summer (May – September; bottom). Each panel includes the value of the mean, sample variance ( $s^2$ ), and the skewness (Skw) and kurtosis (Kur) coefficients, computed per King and Julstrom (1982). The vertical dashed line delineates the upcanyon from the downcanyon class intervals. .... D11

Figure D8. Mean monthly maps of sea level pressure (contours), wind speed (color), and direction (arrows) over the northern Bering and Chukchi seas. The 2011 maps are for: A) June, B) July, C) August, and D) September and the 2012 – 2013 maps are for: E) December, F) January, G) February, and H) March. ....	D12
Figure D9. Monthly transport anomalies (gray) for the 1979 – 2015 period based on the GLM hindcast. The thick red curve is the 13-month running mean of the anomalies. ....	D14
Figure D10. Sea level pressure (contours), surface wind vectors (arrows), and wind speeds (colors) for Marches (left) and Octobers (right) in which there was anomalously large upcanyon (top row; contour interval of 5 mb) and downcanyon transports (bottom row; contour interval of 2 mb). The maps are composites based on the month and years shown to the right of each map, which includes the mean monthly transport for those years. ....	D14
Figure D11. The seasonal cumulative probabilities for a) upcanyon and b) downcanyon events based on the hindcast transport record. The numbers associated with the seasons in the legend on each graph refer to the number of events over the 37-year record. ....	D15
Figure D12. Time series of salinity (top) and potential temperature, $\theta$ , (bottom) at moorings BC1 (black), BC2 (blue), and BC5 (red) for the August 2010 – August 2012 period. ....	D16
Figure D13. Time series of temperature (bottom) and salinity (middle) from mooring BC2 and the along-canyon transport (smoothed with a 7-day running mean; top). The horizontal line on the salinity plot delineates the 33.1 value. The light grey shading encompasses the periods of upcanyon transports that contained lower halocline and Atlantic Water signatures (e.g., $S > 33.1$ and $\theta > -1.6^\circ\text{C}$ ). The light yellow shading captures periods of dense water ( $S > 33.1$ and $\theta = \text{freezing point}$ ). ....	D17
Figure D14. Vertically-averaged mean velocity vectors and variance ellipses for currents and winds in A) 2010 – 2011, B) 2011 – 2012, and C) 2012 – 2013. Red symbols and text are for winds, black are for currents outside of the blue box, and blue are for currents within the blue boxes. Gray (black) vectors and ellipses in each figure denote record lengths of from 6 to 10 (11 to 12) months duration. ....	D19
Figure D15. Mean September – October 2013 surface current map of the western Beaufort Sea shelf and the northern end of Barrow Canyon. The mean winds at Barrow were from the east-northeast (as indicated by the arrow) at $3 \text{ m s}^{-1}$ . The red squares at the mouth of Barrow Canyon are the locations of the moorings discussed by Itoh et al. (2013). ....	D21
Figure E1. Bathymetric map of the Chukchi Sea showing the drifter deployment locations (triangles) in 2012 (magenta), 2013 (green), and 2014 (blue). The 2014 and 2013 deployments are used in evaluating the momentum balances and the 2014 deployments were used to update relative dispersion estimates presented by Weingartner et al. (2015). The villages of Point Hope (PH), Point Lay (PL), Wainwright (W), and Barrow (B) are indicated. The black horizontal line offshore of Point Lay shows the August 2013 trajectory of a glider and the red horizontal line shows the September 2013 location of the Acrobat CTD section northeast of Hanna Shoal. ....	E3
Figure E2. Delineation of the five different classification groups used to examine the fates of drifters moving northeastward through Barrow Canyon. A drifter must pass northeastward across the “Start Line” in order to be considered in the analysis. The yellow star indicates the location of the point of interest (POI) on the 100 m isobath. ....	E5
Figure E3. Map showing the shelfbreak and slope “boxes” used to evaluate mean and eddy kinetic energies. These regions are the Chukchi (blue), Barrow Canyon (green), and Beaufort (yellow). ....	E6

Figure E4. Top panel: map showing location (indicated by red line) of the west-to-east transect of glider 191 from 10 to 14 August 2013. The bottom three panels are the vertical sections of temperature (top), salinity (middle), and density (expressed as  $\sigma_t$ ; bottom) along the transect. The westernmost end of the transect is on the left of the figure. .... E7

Figure E5. Vertical sections of temperature, salinity, and  $\sigma_t$  from an Acrobat transect along the northeastern side of Hanna Shoal on 11 September 2013. The western part of the section is on the left-hand side of the figure. .... E8

Figure E6. Vertical sections of temperature, salinity, and  $\sigma_t$  from an Acrobat transect across the top of Hanna Shoal on 10 September 2013. The northern part of the section is on the left-hand side of the figure. .... E9

Figure E7. Vertical sections of temperature, salinity, and  $\sigma_t$  from an Acrobat transect on the northwest side of Hanna Shoal on 10 September 2013. The southeast end of the section is on the left-hand side of the figure. .... E9

Figure E8. Trajectory of the Point Lay 2013 cluster centroid (color-coded by SST) and the 13 individual drifters within this cluster (top panel). Additional plots are the time series of the centroid (2<sup>nd</sup> from top) and wind (3<sup>rd</sup> from top) velocities and SST (bottom). The colored symbols along each trajectory are at 5-day intervals and correspond to the date axis on the SST time series plot. Events A, B, and CC1 – 4 are discussed in the text. .... E11

Figure E9. Time series of the zonal (top) and meridional (bottom) velocity components associated with the Stokes (blue), Ekman (red), and geostrophic (yellow) contributions to the surface velocity. The letters and vertical lines correspond to the periods in Figure E8 and discussed in the text. .... E12

Figure E10. As in Figure E8 but for the Point Lay 2014 cluster. Segments D, E, and F are discussed in the text. .... E13

Figure E11. Time series of the zonal (top) and meridional (bottom) velocity components associated with the Stokes (blue), Ekman (red), and geostrophic (yellow) contributions to the surface velocity for the Point Lay 2014 deployment. The letters and vertical lines correspond to the periods in Figure E10 and are discussed in the text. .... E14

Figure E12. As in Figure E8 but for the Point Hope 2014 northerly cluster. Segments G, H, and I are discussed in the text. .... E15

Figure E13. As in Figure E8 but for the Point Hope 2014 southerly cluster. Segments J, K, L, and M are discussed in the text. .... E16

Figure E14. Time series of the four terms comprising the deformation tensor (div = divergence, RV = relative vorticity, STR DEF = stretching deformation, and SHR DEF = shearing deformation. The Point Hope North cluster terms are in blue and those for the Point Hope South cluster are red. Units are  $10^{-5} \text{ s}^{-1}$ . .... E18

Figure E15. Time series of the terms comprising the absolute vorticity tendencies for the Point Hope North (blue) and Point Hope South (red) clusters. From top to bottom these are the rate of change of absolute vorticity, stretching vorticity, and the sum of the first two terms. Units are  $10^{-9} \text{ s}^{-2}$ . .... E18

Figure E16. Time series of the zonal (top) and meridional (bottom) velocity components associated with the Stokes (blue), Ekman (red), and geostrophic (yellow) contributions to the surface velocity for the Point Hope North deployment. The letters and vertical lines correspond to the periods in Figure E12 and are discussed in the text. .... E19

Figure E17. Time series of the zonal (top) and meridional (bottom) velocity components associated with the Stokes (blue), Ekman (red), and geostrophic (yellow) contributions to the surface velocity for the Point Hope South deployment. The letters and vertical lines correspond to the periods in Figure E13 and are discussed in the text. .... E20

Figure E18. As in Figure E8 but for the NE Hanna Shoal cluster. Segments N and O are discussed in the text. .... E21

Figure E19. Time series of the zonal (top) and meridional (bottom) velocity components associated with the Stokes (blue), Ekman (red), and geostrophic (yellow) contributions to the surface velocity for the NE Hanna Shoal deployment. The letters and vertical lines correspond to the periods in Figure E18 and are discussed in the text. .... E22

Figure E20. As in Figure E8 but for the NW Hanna Shoal cluster. Segments P, Q, and R are discussed in the text. .... E23

Figure E21. Time series of the zonal (top) and meridional (bottom) velocity components associated with the Stokes (blue), Ekman (red), and geostrophic (yellow) contributions to the surface velocity for the NW Hanna Shoal 2013 deployment. The letters and vertical lines correspond to the periods in Figure E20 and are discussed in the text. .... E24

Figure E22. Time series of relative zonal ( $D_x^2$ ; top left) and meridional ( $D_y^2$ ; top right) dispersion, the cross-correlation term ( $D_{xy}$ ; bottom left), and the relative dispersion ( $D^2$ ; bottom right) for the Point Lay 2014 cluster. As indicated in the upper left, each panel includes the mean ( $\mu$ ) value and the mean value  $\pm$  one standard deviation (s). .... E25

Figure E23. Time series of relative zonal ( $D_x^2$ ; top left) and meridional ( $D_y^2$ ; top right) dispersion, the cross-correlation term ( $D_{xy}$ ; bottom left), and the relative dispersion ( $D^2$ ; bottom right) for the Point Hope northern cluster. Each panel includes the mean ( $\mu$ ) value and the mean value  $\pm$  one standard deviation (s) per Figure E22. .... E25

Figure E24. Time series of relative zonal ( $D_x^2$ ; top left) and meridional ( $D_y^2$ ; top right) dispersion, the cross-correlation term ( $D_{xy}$ ; bottom left), and the relative dispersion ( $D^2$ ; bottom right) for the Point Hope southern cluster. Each panel includes the mean ( $\mu$ ) value and the mean value  $\pm$  one standard deviation (s) per Figure E22. .... E26

Figure E25. Time series of relative zonal ( $D_x^2$ ; top left) and meridional ( $D_y^2$ ; top right) dispersion, the cross-correlation term ( $D_{xy}$ ; bottom left), and the relative dispersion ( $D^2$ ; bottom right) for the entire Point Hope cluster. Each panel includes the mean ( $\mu$ ) value and the mean value  $\pm$  one standard deviation (s) per Figure E22. .... E27

Figure E26. Trajectories and summary statistics for all 1 m drogued drifters according to their turning classification. .... E29

Figure E27. Log-log plots of the relative meridional ( $D_y^2$ ; top), zonal ( $D_x^2$ ; middle), and horizontal ( $D^2$ ; bottom) dispersion based on the 2012, 2013, and 2014 clusters. The black dashed lines are the 95% confidence interval on the mean (blue curve). On the bottom plot, the Lagrangian time scale ( $T_L$ ) is  $\leq 2$  days and denoted by the red, dotted line and the red solid line denotes a dispersion growth rate proportional to  $t^2$ . .... E31

Figure F1. A) Bathymetric map of the Chukchi Sea showing principal flow pathways northward from Bering Strait. The pathway denoted by the red arrow denotes the Alaskan Coastal Current, which carries the freshest and warmest fraction of the Bering Strait outflow and the blue arrows denote the pathways for the cooler and saltier fractions. B) Map of Hanna Shoal and the surrounding shelf showing locations of 2012 (blue) and 2013 (red) CTD stations. C) Location of various current meter and ice profiling sonar (IPS) moorings (symbols) and Acrobat towed-CTD transects (blue lines). .... F2

Figure F2. Sea ice concentration maps on 15 June (top) 15 July (middle) and mean daily wind vectors (bottom). Panels a, b and c are for 2011, d, e, and f are for 2012, and g, h, and i are for 2013. The features labeled in map E are: Herald Valley (HV), Herald Shoal (HeS), Central Channel (CC), Hanna Shoal (HaS), and Barrow Canyon (BC). Wind vector plots include mean monthly wind velocity and wind speed in parentheses. .... F4

Figure F3. Maps of the 15% ice concentration isopleth at biweekly intervals for the August – September period (top row) and mean daily wind vectors (bottom row). Panels a and b are for 2011, c and d are for 2012, and e and f are for 2013. The mean monthly wind velocity and wind speed (in parentheses) are listed below the x-axis for each year..... F6

Figure F4. Plan views of temperature (left) and salinity (right) in August and September of 2012 based on averages of the upper and bottom 10 m of the water column. The village of Wainwright is designated with a “W”. Filled circles show CTD station locations..... F7

Figure F5. Plan views of temperature (left) and salinity (right) from August and September 2011 based on averages of the upper and bottom 10 m of the water column. The village of Wainwright is designated with a “W”. Filled circles show CTD station locations. The black line in panel c shows the location of the vertical sections from 2011 and 2102 shown in Figure F6. .... F8

Figure F6. Vertical sections of potential temperature (top row) and salinity (bottom row) collected from early to late of September 2011 (a, b) and 2012 (c, d), respectively. The location of both sections is shown in Figure F5c. Hanna Shoal is denoted as “HS”. Inverted triangles indicate station locations. .... F9

Figure F7. Vertical sections of potential temperature (a, b), salinity (c, d), and fluorescence expressed as  $\mu\text{g l}^{-1}$  of chlorophyll a (e, f) in September 2012 along Leg M (left) and Leg Q (right). The white contours indicate  $\sigma_t$  isolines. The arrows at the top of each figure indicate latitude  $71.5^\circ\text{N}$ . The locations of these transects are shown in Figure F1c. The front along Leg M is located at  $71.2^\circ\text{N}$  as indicated. .... F10

Figure F8. Histograms of density variance at 10 m depth as a function of horizontal length scale based on 2013 Acrobat CTD tows collected north of the front (gray stippled bars) and south (black bars) of the front. The horizontal bars denote the mean density variance in each band for the gray bars. .... F11

Figure F9. Vertical sections of potential temperature ( $\theta$ ; top) and salinity (S; bottom) along transects 1-12 (a, b), 2-12 (c, d), and 3-12 (e, f) on the northwestern, northern, and northeastern sides of Hanna Shoal, respectively. Figure F1 shows transect locations. Hanna Shoal is on the left of each panel. .... F12

Figure F10. As in Figure F9 but for transects 1-13 (a, b), 2-13 (c, d), and 3-13 (e, f) on the northwestern, northern, and northeastern sides of Hanna Shoal, respectively. Figure F1 shows transect locations. Hanna Shoal is on the left of each panel. .... F12

Figure F11. As in Figure F9 but for transects 4-12 (a, b), 5-12 (c, d), and 4-13 (e, f). Panels a, b, e, and f are on the southern side of Hanna Shoal, and panels c and d are on the southeastern side. Figure F1 shows transect locations. Hanna Shoal is on the left of each panel. Note the temperature scale differs from that of Figures F9 and F10. .... F13

Figure F12. The trajectories of 6 satellite-tracked drifters (1 m drogue depth) deployed offshore of Icy Cape on 12 August 2012. One of the trajectories is color-coded according to measured SST. The various symbols along each trajectory are at 7-day intervals with the dates given on the wind vector time series (bottom plot). The 20, 40, 50, 100, and 1,000 m isobaths are labeled. Green triangles signify the deployment position and red stars the last good transmission from each drifter..... F15

Figure F13. Scatterplots of potential temperature versus salinity over the upper 30 m of the water column for sections 1, 2, and 3 in 2012 (left) and 2013 (right). Only stations along the first 65 km of the transect are included. Note the scales change between 2012 and 2013. The black slanted line denotes the freezing point curve. The larger symbols outlined in yellow depict the mean values along each section in the upper 15 m..... F16

Figure F14. Baroclinic, geostrophic velocity field for transects a) 3-12, b) 2-13, and c) 3-13. The corresponding temperature and salinity sections are shown in Figures F9 e, f; F10 b, d; and F10 e, f, respectively. Positive velocities are north-northwestward and negative values are south-southeastward. .... F16

Figure F15. Each row shows the mean January – March ice and wind velocities (left panels) and regional wind vectors and sea level pressure (right side) over the northern Bering and Chukchi seas for 2011 (top row), 2012 (middle row), and 2013 (bottom row). Black arrows and ellipses denote the mean ice velocity and the corresponding velocity variance ellipses, while the red arrows and ellipses are for the winds... F19

Figure G1. Schematic circulation in the Chukchi Sea (from Corlett and Pickart 2017), showing the three pathways by which Pacific water flows poleward through the Chukchi Sea.....G2

Figure G2. (a) Bathymetric map of the northeastern Chukchi Sea showing mooring locations used in the study. The six moorings comprising the shelfbreak/slope array are shown by the yellow stars. The three additional moorings east of Hanna Shoal and the mooring at the head of Barrow Canyon are shown by the red and blue stars, respectively. The red line and black coordinate frame indicate the rotated coordinate system. The bathymetry is from IBCAO v3. (b) Large-scale map showing the entire Chukchi Sea. The region in (a) is indicated by the dashed box. The magenta and cyan boxes delineate the domain over which the ice concentration is calculated for the shelfbreak/slope array and for the coastal polynya region south of Barrow Canyon, respectively. The mooring sites are shown by the black dots. (c) Configuration of shelfbreak/slope moorings in the vertical plane. The origin of the x-axis is Hanna Shoal. ....G4

Figure G3. Year-long, depth-mean velocity vectors (blue) at the mooring sites and mean 10 m wind vector (black) at the Barrow, AK meteorological station. The standard error ellipses are shown (see the scales at the lower left). The red line indicates the along-stream direction (see Figure G2). ....G7

Figure G4. (a) Year-long mean along-stream velocity section (positive is southeastward). The thick black line is the zero velocity contour. The dashed black line shows the boundary of shelfbreak and slope. The grey shading denotes regions of no data coverage. The mooring sites are shown at the top. (b) Potential temperature-Salinity diagram for all of the hydrographic data. The color represents the percentage of data within a 0.1°C by 0.1°C grid. The black lines delimit the different water masses: MW = meltwater; ACW = Alaskan Coastal Water; BSSW = Bering Sea Summer Water; RWW = Remnant Winter Water; WW = newly-ventilated Winter Water; AW = Atlantic Water.....G8

Figure G5. Vertical sections of the seasonally averaged along-stream velocity. The presentation is the same as in Figure G4a. ....G9

Figure G6. Depth-time plot of potential temperature and salinity at CS4 (a, c) and CS5 (b, d), overlain by potential density (contours).....G10

Figure G7. Wind rose showing wind speed and direction at Barrow for the duration of the deployment.G11

Figure G8. (a) Daily-mean wind velocity at the Barrow meteorological station (blue vectors). The gray shading and red vectors denote periods of northeasterly wind, and the corresponding mean wind velocity, preceding the three major occurrences of reduced ice cover at the mooring array site and south of Barrow Canyon. (b) Ice concentration timeseries at the array site (cyan curve) and at the location of the polynya south of Barrow Canyon (magenta curve). The gray shading indicates the three periods of reduced ice concentration. ....G11

Figure G9. Volume transport timeseries of (a) the Chukchi slope current (blue curve), and (b) the Chukchi shelfbreak jet (yellow curve is the full transport and green dashed curve is the positive transport). (c) Monthly-averaged slope current transport with standard errors. (d) Monthly-averaged transport and standard errors for the full shelfbreak jet (yellow curve) and for times when the jet transport is positive (green dashed curve).....G13

Figure G10. Composite velocity sections during (a, b) calm wind conditions and (c, d) times when the easterly winds exceeded  $4 \text{ m s}^{-1}$  for the months of July – October. (a) and (c) are reconstructed sections of absolute geostrophic velocities (color) from Corlett and Pickart (2017). (b) and (d) are velocity sections (color) from mooring data. The thin black lines are velocity contours.....G14

Figure G11. Composite average fields for the strong slope current and reversed shelfbreak jet events with southwesterly wind. (a) Vertical section of alongstream velocity. The number of events and their total duration is marked on the lower left. (b) Vertical section of alongstream velocity anomaly (composite minus the year-long mean). (c) Sea level pressure (color) and 10 m wind vectors from NARR, along with the measured wind from the Barrow meteorological station (purple vector). The location of the shelfbreak/slope mooring array is indicated by the purple star. (d) Wind stress curl (color). .....G15

Figure G12. Same as Figure G11, except the strong slope current and reversed shelfbreak jet events with northeasterly wind.....G16

Figure G13. Same as Figure G11, except the strong shelfbreak jet and weak slope current events with northeasterly wind.....G17

Figure G14. Composite average fields prior to the strongest upwelling event (event 9, May 2014). (a) Sea level pressure (color) and 10 m wind vectors from NARR, along with the measured wind from the Barrow meteorological station (blue vector). The location of the shelfbreak/slope mooring array is indicated by the purple star. (b) Along-stream velocity section. (c) Density timeseries at mooring CS2 and FM1 from 3 days before the event to 3 days after the event, where the bold indicates the time period before the upwelling. The dashed lines are the 20-day low-passed curves. (d) Wind stress curl (color). (e) Cross-stream velocity section (positive is northeastward). (f) Depth-averaged (0 – 250 m) velocity vectors at the mooring sites (blue arrows) and the mean velocity vector of all moorings (large arrow). .....G19

Figure G15. Same as Figure G14, except for the time period during the upwelling. ....G19

Figure G16. Same as Figure G14, except for the time period after the upwelling. ....G20

Figure G17. Timeseries of water mass occurrence at the Chukchi shelfbreak/slope moorings (CS2, CS4) and the mooring at the head of Barrow Canyon (BC2). See Figures G2 and G3 for mooring locations. Note that there is no depth scale for moorings CS2 and BC2 since these sites have a single sensor near the bottom. The gray shading indicates times when the flow is in the opposite direction of the predominant current (southwestward, southeastward, and northwestward in the three panels, respectively). The black triangles denote the time periods when the bulk of Winter Water was present. ....G21

Figure G18. Potential temperature of the Winter Water at (a) mooring BC2 at head of Barrow Canyon (near the bottom) and CS4 on the Chukchi slope. The light gray shading means that there is no WW present. The dark gray shading indicates when the flow is in the opposite direction of the primary current (southwestward and southeastward in (a) and (b), respectively). The black triangles denote the time periods when the bulk of WW appeared. ....G22

Figure H1. Map showing the locations of moorings used in this section of the report as a function of year. Moorings Cj (Crackerjack), Bu (Burger), Site1 & 2, CPAI 01 & 02, Statoi 3 & 4, and HS 01-06 were all deployed and processed under industry support. HSNE and HSNW moorings were supported by the BOEM-COMIDA program. WBC and EBC were supported by NSF. Barrow Canyon moorings (BC 1 – 6) were supported by BOEM Study 2012-079, and BC2 from 2012 – 2016 was supported by this project. .H2

Figure H2. The spatial structure of the most significant EOFs of ice concentration for May (top row), June (middle row), July (bottom left), and August (bottom right). Where sketched, the white dotted lines outline the region of maximum spatial variability in EOF1.....H3

Figure H3. The evolution of sea ice concentrations as seen on 30 October (top row), 15 November (middle row), and 30 November (bottom row) for 2011 (left column), 2012 (middle column), and 2013 (right column).....H6

Figure H4. Ice displacement as a function of time for the Burger deployments from 2010 – 2011 (top), 2011 – 2012 (middle), and 2012 – 2013 IPS and ADCP deployments. The stars indicate the starting position and correspond to the first 50 km segment in which any ice was recorded. Red dots indicate the mid-point of each 50 km segment and every other segment is labeled by date.....H7

Figure H5. Mean ice thickness and statistical fits as a function of time (50 km segment) for the Burger deployments from 2010 – 2011 (top), 2011 – 2012 (middle), and 2012 – 2013 (bottom). Means encircled by a red ellipse suggest periods of new, thinner ice formation, and those with a blue ellipse suggest periods when thicker ice was advected over the site.....H8

Figure H6. Probability density functions (pdfs) for selected dates from the Burger 2010 – 2011 (left), Burger 2011 – 2012 (middle), and Burger 2012 – 2013 (right) IPS deployments. The y-axes represent the percentage of time a particular ice thickness interval (x-axis) occurred over the 50 km long sampling interval. Numbers in parentheses in legend indicate the percentage of all observations less than or equal to the maximum value of the ice thickness on the x-axis. Note that the x-axis maximum is 2 m for the top row and 4 m for the bottom two rows.....H10

Figure H7. Time series of the primary (blue) and secondary (red) mode ice thickness modes along with logarithmic statistical through time. The modes are determined from each 50 km segment for the Burger deployments from 2010 – 2011 (top), 2011 – 2012 (middle), and 2012 – 2013 (bottom). .....H11

Figure H8. Potential temperature-salinity ( $\theta/S$ ) diagram illustrating various water masses found on the northeastern Chukchi Sea shelf in summer and early fall. ....H12

Figure H9. Summary figures for Acrobat Leg Y. The left hand side consists of vertical sections of temperature (top), salinity (middle), and chlorophyll (bottom). The black contours on each section are isolines of potential density plotted at a contour interval of 2. The right hand sides of each figure contain a transect location map (top right) and a  $\theta/S$  plot based on the data from that section. The view is toward the southwest with land to the left of each panel. ....H13

Figure H10. As in Figure H6 but for Acrobat Leg E. ....H13

Figure H11. As in Figure H6 but for Acrobat Leg BB.....H14

Figure H12. As in Figure H6 but for Acrobat Leg Q.....H14

Figure H13. As in Figure H6 but for Acrobat Leg S. ....H15

Figure H14. As in Figure H6 but for Acrobat Leg U. ....H15

Figure H15. Mean surface current vectors for the week of 5 September 2012, as estimated from HFRs. ....H16

Figure H16. Color-coded (by SST) trajectory of a satellite-tracked drifter released at the location of the green triangle on 13 August 2012. The drifter's last reported position was on 15 November 2012 at the location of the red star. ....H17

Figure H17. Time series of vertically averaged current vectors (top), temperature (middle) and salinity (bottom) at 47 m depth from mooring HSNW50-12. The timing of the temperature maximum ( $T_{max}$ ) and the descent to the freezing point ( $T_f$ ) are noted. .... H18

Figure H18. Time series of vertically averaged current vectors (top), temperature (middle) and salinity (bottom) at 23 m (red) and 47 m (blue) depth from mooring HSNE50-12. The timing of the temperature maximum ( $T_{max}$ ) and the descent to the freezing point ( $T_f$ ) are noted..... H18

Figure H19. Time series of bottom temperature and salinity from the COMIDA 2013 – 2014 mooring array..... H20

Figure H20. Mean vectors and variance ellipses for the 2010 – 2011 moorings. Full-length records are in black, partial-length records are in gray, and NARR wind records are in red. .... H21

Figure H21. Mean vectors and variance ellipses for the 2011 – 2012 moorings. Full-length records are in black, partial-length records are in gray, and NARR wind records are in red. .... H22

Figure H22. Mean vectors and variance ellipses for the 2012 – 2013 moorings. Full-length records are in black, partial-length records are in gray, and NARR wind records are in red. .... H23

Figure H23. Mean vectors and variance ellipses for the 2013 – 2014 moorings. Full-length records are in black, partial-length records are in gray, and NARR wind records are in red. .... H24

Figure H24. Mean monthly vectors and current ellipses (black) in the topmost ADCP bin (~7 m depth) for the months of May, June, July, and August 2011. Comparable quantities are shown for the winds in red. Mooring WBC is highlighted by the orange box in each figure. Gray ellipses and vectors indicate less than a full month's worth of data was available. .... H25

Figure H25. The first three EOF modes of the principal axis velocity component for the 2011 – 2012 mooring array..... H26

Figure H26. The first three EOF modes of the principal axis velocity component for the 2012 – 2013 mooring array..... H27

Figure H27. The first three EOF modes of the principal axis velocity component for the 2013 – 2014 mooring array..... H27

Figure H28. The first three EOF modes of the principal axis velocity component for the 2011 – 2012 mooring array, which includes Bering Strait. .... H29

Figure H29. The first three EOF modes of the principal axis velocity component for the 2012 – 2013 mooring array, which includes Bering Strait. .... H29

Figure H30. The first three EOF modes of the principal axis velocity component for the 2013 – 2014 mooring array, which includes Bering Strait. .... H30

Figure H31. Cross-spectral results between vertically averaged currents in Bering Strait and the Central Channel for the entire 2008 – 2014 record (left), the individual May – September periods (middle), and the October – April periods (right). Top panel is coherence-squared and bottom panel is the phase. .... H30

Figure H32. Cross-spectral results between vertically averaged currents in Bering Strait and the Burger for the entire 2010 – 2013 record (left), the individual May – September periods (middle), and the October – April periods (right). Top panel is coherence-squared and bottom panel is the phase..... H31

Figure H33. Cross-spectral results between vertically averaged currents in Bering Strait and Barrow Canyon for the entire 2011 – 2013 record (left), the individual May – September periods (middle), and the October – April periods (right). Top panel is coherence-squared and bottom panel is the phase. .... H32

Figure H34. Climatological annual cycle based on mean monthly values of Barrow Canyon transport (top left) and vertically-averaged velocities projected along the principal axis at moorings over the central shelf: Burger (Bu), CPAI01 (previously called Site 1), and in the Central Channel at mooring Crackerjack (Cj). Dotted horizontal lines on the velocity figures denote the annual mean. .... H32

Figure H35. Mean monthly transports at BC2 (blue) and BS3 (red) in Sverdrups. .... H33

Figure H36. Coherence squared and phase spectra of mean daily transports at Barrow Canyon and along the Beaufort shelfbreak for the entire record (left), May – September (middle) and October – April (right). .... H34

Figure H37. Linear regressions of BS3 against BC2 mean monthly transports for all months (upper left), January – April (upper right), May – September (lower left), and October –December (lower right). .... H34

Figure H38. Linear regressions of BS3 against BC2 daily mean transport for all months (upper left), January – April (upper right), May – September (lower left), and October – December (lower right). .... H35

Figure H39. Monthly distribution of flow regimes. .... H37

Figure H40. Annual cycle of the four flow regimes characterizing transports in Barrow Canyon and the Beaufort shelfbreak. .... H37

Figure H41. Frequency of occurrence of regimes as a function of the direction toward which the wind at Barrow (PABR) is blowing. .... H38

Figure H42. Mean surface currents estimated from the Point Barrow and Cape Simpson HFR systems under different wind conditions in 2013. The number of hours under which a given wind condition prevailed is indicated in the upper right hand corner of each map. .... H39

Figure H43. Coherence squared and phase spectra of mean daily transports at Bering Strait and along the Beaufort shelfbreak for the entire record (left), May – September (middle), and October – April (right). .... H40

Figure H44. Tidal ellipses for the principal semi-diurnal (upper four panels) and diurnal tides on the Chukchi Sea shelf. .... H41

Figure H45. Schematic of the mean circulation of the northeastern Chukchi Sea. The red line denotes the Alaskan Coastal Water (ACW) front bordering the offshore side of the Alaskan Coastal Current. The blue line indicates the meltwater/Bering Sea Summer Water (MW/BSSW) front surrounding Hanna Shoal. Black arrows indicate regions where the surface and sub-surface currents are similar in direction and magnitude. Green arrows indicate near-bottom currents, and purple arrows indicate near-surface currents. .... H42

Figure A-1. (a)-(h), SOM-derived patterns No. 1–8 of surface currents (blue vectors) and paired winds (black vectors) for 2012 data. Pattern number and its relative frequency of occurrence are shown in the lower right corner. The 80 m isobath is thicker to define Barrow Canyon. Note that the scales of current vectors in Patterns No. 3–8 are different. .... Appendix A - 2

Figure A-1. (continued) (i)-(l), SOM-derived patterns No. 9–12 of surface currents (blue vectors) and paired winds (black vectors) for 2012 data. .... Appendix A - 3

Figure A-2. (a) Upper panel: time series of wind vectors in August 2012. The vector direction follows oceanographic convention. Lower panel: SOM-derived patterns (black dots) in August 2012 and normalized data returns (gray line). Pattern numbers correspond to Figure A-1. Pattern 0 denotes times when data return is zero. (b) As in (a), but for September 2012. (c) As in (a), but for October 2012. .... Appendix A - 4

## List of Tables

Table B1. Hydrographic and velocity data sources, delineated between cruise (by row) and section (by semicolons). VMADCP = vessel-mounted ADCP; LADCP = lowered ADCP. ....	B4
Table C1. Summary of the EOF correlation analysis from the reconstructed fields. The correlations are all significant at the 95% significance level using the effective number of degrees of freedom derived from the integral time scale. ....	C11
Table D1. Mooring positions and depths for the Barrow Canyon (BC) array and locations of NARR wind gridpoints. ....	D4
Table D2. Row 1 is the linear regression model used to compute Barrow Canyon transports (T) from mooring BC2. Rows 2 and 3 are the winter and summer generalized linear models (GLM) used to hindcast Barrow Canyon transport based on winds listed in Table D1 over the Bering Sea shelf (C40), Bering Strait (A3) and Barrow Canyon (BC2). Terms in parentheses are the 95% confidence limits on the model coefficients using an integral time scale of 4 days. The wind components ( $V$ , $U$ ) and lags at each site are defined in the footnote. ....	D8
Table E1. Mean and Eddy Kinetic Energy comparisons for 1 m drogued Microstar drifters. ....	E28
Table E2. Mean and Eddy Kinetic Energy comparisons for 10 m drogued SVP drifters. ....	E28
Table G1. Mooring information ....	G5
Table G2. Statistics for the two types of extreme events considered in the text: (i) strong slope current and reversed shelfbreak jet; (ii) strong shelfbreak jet and weak slope current. The first column indicates the quadrant from which the wind was blowing. The percentage in parentheses means the fraction of the event length relative to the total length in the last row. The underlined percentages represent the fraction of total length relative to the entire year-long duration of the record. ....	G15
Table G3. Statistics of all upwelling events. The rows show the event number, length (in days) of each event, value of the upwelling index (UI, unit: $\text{kg m}^{-3} \text{h}$ ), mean wind direction, and sign of the mean wind stress curl condition (+ and – mean positive and negative curl, respectively) in the vicinity of mooring array (cyan box in Figure G2b) for the day before each event. ....	G18
Table H1. Number of days observed and the frequency of occurrence of different flow regimes in Barrow Canyon (BC2) and the Beaufort shelfbreak (BS3). ....	H36
Table A-1. A summary of the original SOM patterns and how they are grouped as circulation regimes in the main manuscript. ....	Appendix A - 1
Table B-1. M2 Tidal Ellipse Parameters ....	Appendix B - 1
Table B-2. S2 Tidal Ellipse Parameters ....	Appendix B - 2
Table B-3. N2 Tidal Ellipse Parameters ....	Appendix B - 3
Table B-4. K2 Tidal Ellipse Parameters ....	Appendix B - 4
Table B-5. O1 Tidal Ellipse Parameters ....	Appendix B - 5
Table B-6. P1 Tidal Ellipse Parameters ....	Appendix B - 6
Table B-7. K1 Tidal Ellipse Parameters ....	Appendix B - 7
Table B-8. Q1 Tidal Ellipse Parameters ....	Appendix B - 8

## List of Abbreviations and Acronyms

ACC	Alaskan Coastal Current
ACW	Alaska Coastal Water
ADCP	Acoustic Doppler Current Profiler
AON	Arctic Observing Network
AOOS	Alaska Ocean Observing System
AMSR	Advanced Microwave Scanning Radiometer
AVHRR	Advanced Very High Resolution Radiometer
AW	Atlantic Water
BC	Barrow Canyon
BOEM	Bureau of Ocean Energy Management
BSEE	Bureau of Safety and Environmental Enforcement
BSSW	Bering Sea Summer Water
BSW	Bering Sea Water
CCW	Counterclockwise
CIAP	Coastal Impact Assistance Program
CMP	Coastal Moored Profiler
CODE	Coastal Ocean Dynamics Experiment
COMIDA	Chukchi Sea Offshore Monitoring in Drilling Area
CSESP	Chukchi Sea Environmental Studies Program
CSW	Chukchi Summer Water
CTD	Conductivity-Temperature-Depth
CW	Clockwise
CWP	Coastal Winched Profiler
DBO	Distributed Biological Observatory
DINEOF	Data Interpolating Empirical Orthogonal Functions
EBC	Eastern Barrow Canyon
EHSS	East Hanna Shoal Shelf
EKE	Eddy Kinetic Energy
EOF	Empirical Orthogonal Function
ETOPO	Earth Topography
GLM	Generalized Linear Model
HFR	High-Frequency Radar
IOOS	Integrated Ocean Observing System
IPS	Ice Profiling Sonar
ISCAT	Inductive Sacrificial MicroCat
MKE	Mean Kinetic Energy
MW	Meltwater
NARR	North American Regional Reanalysis
NASA	National Aeronautics and Space Administration
NCEP	National Centers for Environmental Prediction
NIC	National Ice Center
NOAA	National Oceanic and Atmospheric Administration

NODC	National Oceanographic Data Center
NSB	North Slope Borough
NSF	National Science Foundation
OI	Optimal Interpolation
PABR	Barrow Wiley Post-Will Rogers Memorial Airport
PC	Principal Component
PI	Principal Investigator
POI	Point of Interest
PV	Potential Vorticity
R/V	Research Vessel
ROR	Ratio of Overlapping Radials
RPM	Remote Power Module
RWW	Remnant Winter Water
SLP	Sea Level Pressure
SOM	Self-Organizing Map
SMMR	Scanning Multichannel Microwave Radiometer
SSM/I	Special Sensor Microwave/Imager
SSMIS	Special Sensor Microwave Imager/Sounder
SST	Sea Surface Temperature
SVP	Surface Velocity Program
T/C/P	Temperature/Conductivity/Pressure
T/S	Temperature/Salinity
UAF	University of Alaska Fairbanks
USCGC	United States Coast Guard Cutter
VMADCP	Vessel-Mounted Acoustic Doppler Current Profiler
WBC	Western Barrow Canyon
WHOI	Woods Hole Oceanographic Institution
WW	Winter Water

## Abstract

This program utilized a wide variety of observations obtained from moored oceanographic instruments, satellite-tracked drifters, hydrography (both recent, from towed-CTD and autonomous underwater vehicles, and historic, from ship measurements), high-frequency radars (HFR), meteorological buoys, and satellite imagery to develop an improved understanding of the physical oceanography of the northeastern Chukchi shelf, as well as exchanges between the Chukchi/Beaufort shelves and the adjacent basin. Our measurements spanned the shelf region from Point Hope northward to the Chukchi and Beaufort continental slopes and from the Alaskan coast to the US-Russian Convention Line. Our primary focus area was the shelf and shelfbreak region between the Central Channel and the western Beaufort Sea and north to the shelfbreak.

Throughout the year and over most of the shelf south of  $71.5^{\circ}\text{N}$ , including within the Central Channel and along the northwest side of Hanna Shoal (as far north as the 50 m isobath), the flow is weakly sheared vertically, such that the surface and sub-surface flows coincide with respect to flow direction, if not magnitude. Exceptions to this may involve large shears between drifting ice and the sub-surface flow and/or large shears during the melt season. During melt, the near-surface stratification is very strong (similar to the stratification found on the shelf east of Hanna Shoal), such that the sub-surface and surface circulations are uncoupled from one another. This is the situation encountered on the East Hanna Shoal Shelf (EHSS) where vertical shears are large year-round. Other regions of strong vertical shear include the Beaufort and Chukchi shelfbreaks and slopes and portions of Barrow Canyon in summer and fall.

We have examined the strength, persistence, and variability of the model-predicted (Winsor and Chapman 2004; Spall 2007) clockwise circulation around Hanna Shoal, including southwestward flow over the shelf between the Barrow Canyon and Hanna Shoal. Substantial elements of the models are largely correct, but there are important differences between the models and observations. We found that the component of the clockwise circulation on the northwest side of Hanna Shoal extends through the water column as predicted by the models and includes cold Bering Sea Water (BSW) and Winter Water (WW) along the bottom. Both of these water masses are transported from the Central Channel and Herald Canyon. However, on the EHSS, only the bottom waters, consisting of BSW and WW, engage in the clockwise circulation. The upper layer flows westward and/or northwestward over the EHSS. This flow is a consequence of density gradients that extend northeastward and eastward from Hanna Shoal, which drive a counterclockwise baroclinic, geostrophic circulation in the upper layer that transports meltwater (MW) and/or modified Alaskan Coastal Water. The latter is transported onto the EHSS via Ekman transport from Barrow Canyon and/or by onshelf transport from the Chukchi shelfbreak. The different flow regimes on either side of Hanna Shoal have two effects. First, these result in a zonal exchange of water masses that maintains the strong stratification year-round on the EHSS. Second, we infer that the shelf north of Hanna Shoal is a region of zonal flow convergence wherein waters must be transported toward the shelfbreak. This transport, which certainly involves the surface layers and possibly also bottom waters, should affect the magnitude and structure of the flow over the Chukchi shelfbreak.

Models also suggest that the clockwise flow around Hanna Shoal extends south of Hanna Shoal in the form of a southwestward drift that eventually turns eastward across the central shelf and continues toward the head of Barrow Canyon. The observations indicate that this is not the case. Indeed, we found that there was no net transport between the EHSS and the central shelf. Instead there is a southeastward flow along the south side of Hanna Shoal that transports water (usually WW) toward the head of Barrow Canyon. This flow essentially represents a dynamic boundary that blocks communication between the EHSS and the central shelf. As a consequence of this boundary and the weak mean flow on the northern side of the Shoal, the residence time of bottom waters on the shelf east of the Shoal is  $\sim 9$  months, much longer than elsewhere in the Chukchi Sea.

As noted, the inferred zonal convergence north of the Shoal provides a possible mechanism for shelf/slope exchange in which MW, WW, and BSW are transported offshelf in this area. There are however other mechanisms that foster exchange. Our retrospective analysis of hydrographic data from the Chukchi shelfbreak indicates that this consists of a surface flow that carries Chukchi Sea water masses (the Pacific-derived summer waters, WW, and MW) westward and an eastward sub-surface flow that is confined to the shelfbreak and which transports WW eastward. The waters flowing westward are largely derived from the Barrow Canyon outflow. The WW that comprises the eastward subsurface flow are mainly derived from northward flows through the Central Channel and Herald Canyon, although some probably form in winter around the periphery of Hanna Shoal. The potential vorticity structure of the shelfbreak circulation satisfies the conditions for baroclinic instability, which should lead to eddy-driven exchanges between the shelfbreak and basin as is known to occur frequently along the Beaufort Sea shelfbreak.

Our results suggest that most of the Chukchi shelf water masses that enter the head of Barrow Canyon are drawn from the shelf south of Hanna Shoal. Of the 0.2 Sv average transport we estimate to be flowing into the head of the canyon, at least  $\sim 0.1$  Sv flows eastward across the central shelf from the Central Channel. The remainder presumably flows northeastward along the coast. Although we are unable to estimate the transports involved, we infer that additional waters enter the canyon along its length (downcanyon from the head) due to spillage of bottom waters from the EHSS or from westward-flowing waters from the Beaufort Sea. There also appears to be, on average, an upcanyon flow along the west side of the canyon. This flow probably transports waters from the subsurface shelfbreak current flowing eastward along the Chukchi slope. Most likely this inflow proceeds only part way up the canyon because it continuously loses mass to the downcanyon transport along the east side of the canyon. WW comprise the bulk of the water masses spilling into the canyon and/or transported upcanyon from the shelfbreak.

The circulation and transports in the Central Channel, across the central shelf, and in Barrow Canyon vary annually and are (mostly) in-phase with the annual transport cycle in Bering Strait. For the 2010 – 2015 period, we found that the downcanyon transport is large (0.4 – 0.6 Sv) from May through August, weak ( $\leq 0.2$  Sv) from September through November and from February through April, and reversed (e.g., upcanyon at  $\sim 0.1$  Sv) in December and January. The annual cycle over the central shelf is in-phase with that in Barrow Canyon and includes a reversed (westward) flow in December and January. In contrast, the flow in the Central Channel is northward in all months. These results suggest that in early winter the circulation over the northeastern Chukchi Sea shelf undergoes a major reorganization: waters transported upcanyon may extend onto the central shelf, and nearshore waters are transported westward into the Central Channel and even the western Chukchi Sea. Once in the Central Channel, these nearshore waters would be transported northward. This reorganization provides a means by which WW, formed in the latent heat polynyas along the northwest coast of Alaska in December and January, can be carried far offshore and eventually to Hanna Shoal.

This seasonal reorganization of the flow was likely reflected during synoptic coastal upwelling events such as the one captured by satellite-tracked drifters August 2014. During that event, the cross-shelf transport of surface coastal waters was a response to various competing mechanisms including the geostrophic transport associated with the mean Pacific-Arctic pressure gradient and, in response to the winds, surface Ekman drift, shelf-wide pressure gradient adjustments, and Stokes' drift, which although small, is not negligible. The drifter observations showed that surface nearshore waters can be transported from the coast to either the Central Channel and/or the head of Herald Canyon in less than a month. Similarly, self-organized mapping analytics applied to the HFR observations clearly indicate that waters transported up Barrow Canyon can easily be carried westward onto the central shelf and/or southward along the Alaskan coast. In fall, the coastal upwelling events and Barrow Canyon reversals likely lead to cooling of nearshore waters and thus enhance ice formation.

The shelf circulation also includes a complex variety of mesoscale circulations. One example (observed about 10% of the time) is the “divergent” mode, which occurs during transitions from northeasterly to southeasterly winds. In such events, a pair of counter-rotating vortices form in which the eastward onshore flow from the central shelf splits upon approaching the coast; some water enters a cyclonic vortex to the north of Wainwright and some enters an anticyclonic vortex offshore of Point Lay. The water entering the anticyclonic vortex recirculates over the central shelf. Two other examples are the inferred shedding or generation of eddies as the Alaskan Coastal Current rounds Point Hope and the collision of the westward-flowing Beaufort shelf waters with the along-canyon flow in Barrow Canyon. There are also numerous MW fronts that occur on this shelf, which we suggest are of two types (at least). The first type consists of what appears to be numerous small sub-mesoscale ( $\leq 6$  km) fronts that are shallow (10 – 15 m thick) and found over Hanna Shoal and the EHSS. There is another, more prominent, type of mesoscale front, which in August and September extends from the western end of Hanna Shoal eastward to the head of Barrow Canyon along the south side of the Shoal and then northward along the western half of Barrow Canyon. These fronts separate moderately-stratified Bering Sea Summer Waters to the south (and east in Barrow Canyon) from the strongly-stratified, two-layered MW/WW structure to the north. The fronts are  $\sim 15$  km wide, baroclinically unstable, and generate both anticyclonic and cyclonic eddies at the surface and anticyclonic eddies primarily within the pycnocline north of the front.

These mesoscale and sub-mesoscale motions play an important role in the lateral and vertical mixing of water masses and in the dispersion of dissolved and suspended materials. To a large degree, the mesoscale phenomena that we have identified on the shelf are linked to the distribution of MW. Over the northeastern shelf, the summer MW pool is tied to ice conditions over Hanna Shoal, which can vary considerably from year-to-year. We suggest that the rate of ice retreat over the Shoal in summer depends less on summer winds and the shelf circulation than it does on winter conditions that affect the grounding of thick ice on the Shoal.

## A. Introduction, Objectives, and Partnerships

### A.1 Introduction

This report provides a summary and synthesis of data collected over the shelf and shelfbreak of the northeastern Chukchi and western Beaufort seas from 2012 through 2014. The study was an expansion of an earlier effort, “Application of High Frequency Radar to Potential Hydrocarbon Development Areas in the Northeast Chukchi Sea” that was jointly supported by BOEM, ConocoPhillips, and Shell between 2009 and 2011. As described below, the present study was also made possible through a variety of partnerships. The field components of both this and the earlier study included gliders (autonomous underwater vehicles), high frequency radars (HFRs), shipboard measurements of the hydrographic and velocity fields, satellite imagery, satellite-tracked drifters, and year-round moorings.

The Chukchi and Beaufort seas are the northernmost shelves bordering Alaska. Although properly a part of the western Arctic Ocean, the Chukchi shelf is atmospherically and oceanographically linked to the Pacific Ocean. These connections influence the wind and wave regimes, ice distribution, and the water masses and circulation characteristics of both seas. The atmospheric connection is primarily via two centers of action: the Aleutian Low and Beaufort High. Both of these features vary in time, position, strength, and interact with polar air masses that affect regional meteorological conditions. The oceanographic link is via the mean northward flow through Bering Strait, which is sustained by the large-scale pressure gradient between the Pacific and Atlantic Oceans (Coachman et al. 1975; Aagaard et al. 2006).

The northward transport of mass, heat, nutrients, carbon, and organisms through the Strait bequeath this region with biophysical characteristics unique among arctic shelves. For example, in comparison to most other arctic shelves, the spring retreat of ice occurs earlier and fall ice formation is delayed in the Chukchi Sea because of the northward heat flux through the strait. Woodgate et al. (2006). Shimada et al. (2006), and Steele et al. (2010) contend that this heat flux may be an important source of interannual variability in the ice cover over the western Beaufort Sea. Similarly, the enormous biological productivity of the region (Walsh et al. 1989; Grebmeier and McRoy 1989; Springer and McRoy 1993; Arrigo and van Dijken 2015), including its ability to support large and diverse marine mammal populations (Citta et al. 2015), is attributed to the carbon and nutrient loads carried through Bering Strait.

The shallow (~50 m) Chukchi shelf extends ~800 km northward from Bering Strait to the shelfbreak along the 200 m isobath. Figure A1a (from Spall 2007) is a model-based depiction of the mean circulation over the shelf and suggests that the northward flow through Bering Strait proceeds along three principal pathways (Figure A1b) with each pathway associated with a distinct bathymetric feature: Herald Canyon, the Central Channel, and Barrow Canyon. The troughs are separated from one another by shoals. Herald Shoal separates Herald Canyon from the Central Channel and Hanna Shoal lies between Barrow Canyon and the Central Channel.

The westernmost branch enters Herald Canyon (Coachman et al. 1975; Walsh et al. 1989; Hansell et al. 1993; Pickart et al. 2010) and while some of it appears to spread eastward across the northern shelf, a significant portion of the water exiting Herald Canyon forms an eastward-flowing shelfbreak jet along the edge of the Chukchi Sea (e.g., Mathis et al. 2007; Pickart et al. 2010). Existing observations, although limited in time and space, suggest that the flow passing through the Central Channel is steered eastward towards Hanna Shoal (Johnson 1989; Münchow and Carmack 1997; Gong and Pickart 2015). Upon reaching the Shoal a portion of the water appears to flow anti-cyclonically around the Shoal, consistent

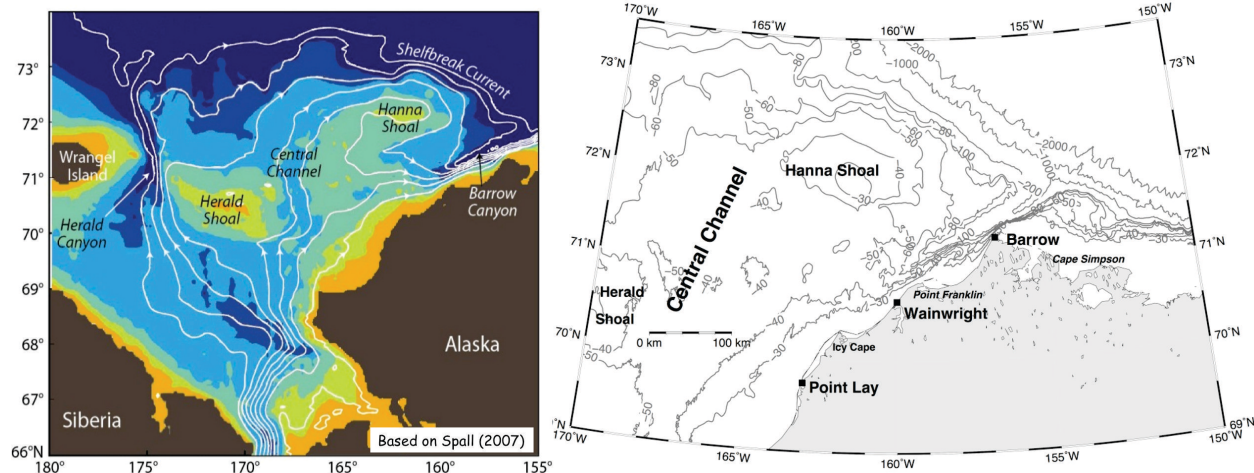


**Figure A1.** Mean depth-integrated streamlines (white lines) in the Chukchi Sea, after Spall (2007; left). The bathymetry is colored and major bathymetric features are labeled. Bathymetric map of the northeastern Chukchi Sea, with place names included (right).

with the numerical models of Winsor and Chapman (2004) and Spall (2007). Recent evidence suggests, however, that part of the water passes to the south of the Shoal (Pickart et al. 2016). Ultimately all of the water is believed to enter the head of Barrow Canyon. Upon exiting the canyon – in the absence of winds – some of the water turns eastward again and forms a shelfbreak jet along the edge of the Beaufort Sea (Nikolopoulos et al. 2009; von Appen and Pickart 2012). New evidence from the present study indicates, however, that a significant portion of the water exiting Barrow Canyon turns westward and forms a jet over the Chukchi continental slope (see below). In the presence of easterly winds, models suggest that much of the water entering the Pacific sector of the Arctic Ocean ultimately ends up exiting the Chukchi shelf via Herald Canyon.

According to the models and observations a portion of the water that enters the Central Channel flows eastward toward the Alaskan coast across the central shelf, i.e., before reaching the latitude of Hanna Shoal (Paquette and Bourke 1974; Weingartner et al. 2005). Limited hydrography led Weingartner et al. (2013a) to suggest that, in summer, some of the water flowing northward in the Central Channel spreads eastward along its length as far north as the southwest side of Hanna Shoal. As these waters flow eastward they encounter dense (cold, salty) bottom waters along the south and southeast sides of Hanna Shoal. These dense waters were formed the previous winter either locally or elsewhere on the Chukchi shelf or in the northern Bering Sea. Model results (Figure A1) suggest that the source of this dense water is from the east side of Hanna Shoal, but Pickart et al. (2016) suggest that some of this dense water is transported eastward along the south side of Hanna Shoal.

At this point, several questions arise with respect to a number of the inferences drawn from the models and the limited observations pertaining to the shelf circulation in the vicinity of Hanna Shoal. For example, to what extent is the eastward flow partitioned between the shelf and shelfbreak? What are the downstream (e.g., eastward) fates of these flows; does all of the water enter Barrow Canyon, and, if so, where and how is this accomplished? How do the magnitudes and the horizontal and vertical structure of these flows vary in time? And finally, how do they vary with respect to winds and circulation elsewhere on the shelf?

The third branch of Bering Sea water flows northeastward along the Alaskan coast towards Barrow Canyon at the junction of the Chukchi and Beaufort shelves (Mountain et al. 1976; Paquette and Bourke

1981). In summer, this flow includes the northward extension of the Alaskan Coastal Current (ACC) that originates south of Bering Strait (Aagaard et al. 1985; Aagaard 1988; Münchow et al. 2000). At the head of Barrow Canyon, the ACC is joined by waters flowing eastward from the central shelf and, as suggested by the model streamlines, with water flowing southward from the east side of Hanna Shoal. The merged flow then continues downcanyon as a narrow, but strong, coastal jet (Aagaard and Roach 1990; Pickart et al. 2005). Hence in summer and fall, the canyon outflow contains a horizontally- and vertically-structured complex of water masses (Pickart et al. 2005; Shroyer and Plueddemann 2012) that includes warm, dilute Alaskan Coastal Water (carried by the ACC); cold, dilute waters due to melting sea ice; dense winter waters; relatively warm and salty Bering Sea Water, and mixtures of each. Although the importance of Barrow Canyon as a potential drain for a broad portion of the Chukchi Sea shelf has long been recognized, there were no comprehensive efforts to measure the transport that enters the head of the canyon.

The flow field described above is substantially influenced by winds, which on average blow from the east-northeast. Consequently the mean flow tends to oppose the mean winds. Earlier work (Weingartner et al. 2005) suggested that flow variations tended to be coherent with wind variations on synoptic time scales. Those observations, however, were based on a limited number of moorings, with most measurements made near the seabed. Thus, there was concern that the measurements may not reflect the near-surface currents. We expect there may be a thin, wind-forced layer across which the currents are sheared. Presumably, the thickness of this layer (and the dynamics that govern the motion in this layer) varies spatially over the shelf and throughout the year with seasonal changes in stratification, ice cover, wave climate, and wind velocity. This last point is crucial in considering the ultimate development of oil spill trajectory models for the Chukchi shelf. Models that incorporate only wind-forcing to compute surface drift could produce serious discrepancies, where the surface currents arise in response to forcing by both the winds and the large-scale (and opposing) pressure field.

## **A.2 Objectives**

The overall goal of this program, as defined in the original BOEM statement of work, is to provide an improved understanding of the physical oceanography of the northeastern Chukchi shelf and exchanges between the Chukchi/Beaufort shelves and the adjacent basin. The questions outlined above guided the development of several specific objectives designed to meet the overall goal of the study. These include:

1. Conditions, locations, and frequency under which the surface (upper 1 m) circulation does/does not coincide with the sub-surface flow as measured by moored current meters;
2. Strength, persistence, and variability of the model-predicted clockwise circulation around Hanna Shoal, including the southwestward flow over the shelf between the Barrow Canyon and Hanna Shoal (Winsor and Chapman 2004; Spall 2007);
3. Conditions that govern, and the frequency of occurrence of, the along-shore and divergent modes that occur in the Wainwright-Point Lay region;
4. Mass transport contributions of the flow around Hanna Shoal and the eastward (shoreward) flow from the central Chukchi Sea shelf to the Barrow Canyon transport;
5. Mesoscale dynamics driving the shelf-basin exchange of heat, salt, momentum, and nitrate, and quantify the magnitude of the exchange;
6. Spatial and temporal variability in the shelf-basin exchange processes (including eddies) and isolate the causes of this variability in terms of local wind forcing, boundary current stability, and/or shelf wave phenomena.
7. Connections between the circulation on the northeast Chukchi shelf, the flow of water into/out of Barrow Canyon, and the shelf-basin exchange processes on either side of the canyon.

8. Local momentum balances, and, where and when possible, how the pressure field adjusts for given wind conditions and/or mesoscale flows.

In aggregate, the results can be used to guide the development and evaluation of oil spill trajectory models likely to be used for this region and can provide insights on processes relevant to the functioning of this marine ecosystem.

The project included three field years (2012 – 2014) and involved measurements along the Chukchi and Beaufort shelfbreaks, around Hanna Shoal, and over the northeast Chukchi Sea including Barrow Canyon. The field program involved high-frequency, shore-based, surface current mapping radars (HFR), autonomous underwater vehicles (gliders), satellite-tracked drifters, year-round moored oceanographic instruments, and shipboard measurements of hydrography (standard Conductivity-Temperature-Depth (CTD) profiles and/or towed CTD packages) and, in some cases, the current structure based on vessel-mounted acoustic Doppler current profilers (VMADCP).

### A.3 Partnerships

A unique aspect of this program is that it involved a very extensive set of partnerships with industry, other agencies, and our own academic institutions. These partnerships included both direct and/or in-kind support. The following partners were involved in this program:

1. The State of Alaska's Coastal Impact Assistance Program (CIAP) provided support for a HFR site at Cape Simpson in the western Beaufort Sea. This support enabled purchase of an HFR system, a remote power module (RPM) (Statscewich et al. 2011), and the logistics to operate the site for the measurement years of 2013 – 2014. The Cape Simpson site was paired with a similar HFR-RPM installation at Point Barrow to enable HFR measurements over the western Beaufort Sea and the mouth of Barrow Canyon.
2. The autonomous underwater vehicle glider program was augmented with a Teledyne Webb glider purchased with AOOS funding. This enabled us to carry out additional glider surveys and collect extensive sections over the ice-free season in the northeastern Chukchi Sea.
3. Pickart maintained a subsurface mooring in the western Beaufort Sea, as part of the Arctic Observing Network (AON) funded by the National Science Foundation (NSF). The mooring was in place during the BOEM fieldwork and the data made available to the project. In addition, shipboard CTD/ADCP surveys were carried out in October 2013 (13 transects) and July 2014 (10 transects) on the USCGC *Healy*. This included occupations along the Chukchi slope mooring line as well as transects to the west and east (extending into the Beaufort Sea).
4. Japanese colleagues, funded by the Japan Agency for Marine Earth Science and Technology maintained moorings at the mouth of Barrow Canyon during the study period.
5. The BOEM-funded Chukchi Sea Offshore Monitoring in Drilling Area (COMIDA) Hanna Shoal Ecosystem Study commenced in August 2012 and concluded fieldwork in September 2014. This was an interdisciplinary program that included hydrographic surveys over and around Hanna Shoal and the deployment of 6 oceanographic, subsurface moorings per year northwest and northeast of the Shoal.
6. The industry-sponsored Chukchi Sea Environmental Studies Program (CSESP) provided extensive hydrographic data from 2008 – 2014 over the northeastern Chukchi shelf. These data are used in the synthesis component of this project.
7. The Alaska Ocean Observing System (AOOS) as a part of the NOAA-supported Integrated Ocean Observing System (IOOS) program has provided support for the operations and maintenance of the HFR network involved in this program.

8. NSF supported S. Okkonen (UAF) and C. Ashjian (WHOI) in a biophysical process study relevant to marine mammal foraging in the Point Barrow region. As part of this effort Okkonen deployed two oceanographic moorings midway along the western and eastern walls of Barrow Canyon in 2011 – 2012. Drs. Okkonen and Ashjian have shared these data with us.
9. Industry (Conoco-Phillips, Shell, and Statoil) have recently provided their ADCP and IPS (ice-profiling sonar) data from oceanographic moorings deployed in the Chukchi Sea since 2008.
10. This BOEM program has supported Lagrangian surface current measurements using satellite-tracked drifters. This sampling effort was substantially augmented from 2012 – 2014 by the North Slope Borough (NSB)/Shell Baseline Studies Program. This program supports research efforts that address concerns raised by NSB residents. In collaboration with residents from the communities of Point Hope, Point Lay, Wainwright, Barrow, and Kaktovik, the NSB executed an extensive set of near-shore drifter deployments in collaboration with this BOEM study.
11. Pickart was a PI in the NASA-supported program “Impacts of Climate on EcoSystems and Chemistry of the Arctic Pacific Environment” (ICESCAPE). This entailed two extensive physical/biological summertime shipboard surveys of the Chukchi Sea in 2010 and 2011, including vessel-mounted ADCP data. These data were provided to the synthesis component of this report.
12. Pickart is a Co-PI in the NSF-funded program “Study of Under Ice Blooms in the Chukchi Ecosystem” (SUBICE). This included an extensive shipboard hydrographic survey on *Healy* in May to June 2014, from which the data were made available to the project. In addition, a mooring was deployed from Oct 2013 to July 2014 north of the Central Channel to augment the BOEM array. The data from the mooring were provided to the project.
13. Pickart is a Co-PI of the Russian-American Long Term Census of the Arctic (RUSALCA) program, funded by NOAA. In summer 2012 a physical/biological survey was carried out in the western Chukchi Sea in Russian waters aboard the *Professor Khromov*. This also included direct velocity measurements from the ship using a lowered ADCP, as well as a detailed survey of Herald Canyon. These data are available to the synthesis component of this report.
14. The University of Alaska School of Fisheries and Ocean Sciences provided support for the continuation of oceanographic measurements in Barrow Canyon from August 2014 – August 2015. This extra year has permitted the establishment of a 5-year transport time series in Barrow Canyon.
15. The Woods Hole Oceanographic Institution provided funding for four additional moorings to augment the BOEM-funded moorings on the Chukchi slope. These were in place from October 2013 to September 2014, and consisted of profiling CTD measurements and ADCP measurements. The shiptime to deploy and recover these moorings (and the BOEM moorings) was provided by NSF. The additional mooring data will be available to the synthesis component of this report.
16. Pickart is a Co-PI of the Distributed Biological Observatory (DBO) project funded by NSF as part of AON. This is an ongoing program that includes a collection of opportunistic measurements at critical locations in the Chukchi Sea (depending on ship schedules and availability). The DBO data are available to the synthesis component of this report.
17. Each HFR field site was made possible due to partnerships with several villages (Point Lay, Wainwright, and Barrow) as well as the Cully, Olgoonik, and Ukpeagvik Iñupiat Corporations, who allowed use of their lands and often provided logistic support.
18. Winsor is the Co-PI of the BOEM sponsored program "Arctic Tracer Release Experiment (ARCTREX): Applications for Mapping Spilled Oil in Arctic Waters" conducted Autonomous Underwater Vehicle (AUV) and Acrobat surveys in the northeastern Chukchi Sea.
19. Industry provided shiptime support for the summer deployment and fall recovery of the meteorological buoy and shared the data from their additional buoys in the Chukchi and Beaufort Seas.

20. Winsor is a Co-PI on the AOOS funded project “Autonomous real-time detection of marine mammals in the Arctic” which utilizes glider technologies developed within the project reported on here. We used data from those surveys in this report.

The report proceeds through a number of sections which have been and/or are being prepared for submission in peer-reviewed journals. Section B consists of a retrospective analysis of the hydrographic and velocity structure of the shelfbreak in the northeastern Chukchi Sea published in *Progress in Oceanography*. Section C outlines the main findings from the HFR measurements, in press with the *Journal of Geophysical Research-Oceans*. Section D examines transport variability at the head of Barrow Canyon based on data obtained from five years of oceanographic moorings, published in the *Journal of Geophysical Research-Oceans*. Section E augments previous analyses (Weingartner et al. 2015) of the surface circulation as captured by satellite-tracked drifters. Section F provides a description of the hydrography of the Hanna Shoal region. Section G addresses the Chukchi Sea shelfbreak and slope, and Section H consists of a preliminary synthesis of these and other data sets from the Chukchi Sea. (Please note that the circulation maps given in each section vary slightly from each other to better address their subject matter, with the overall average circulation derived from measurements in this study given in Section H.) The last two sections consist of a suite of recommended future studies and references, respectively.

## B. The Chukchi Slope Current

### Abstract

Using a collection of 46 shipboard hydrographic/velocity transects occupied across the shelfbreak and slope of the Chukchi Sea between 2002 – 2014, we have quantified the existence of a current transporting Pacific-origin water westward over the upper continental slope. It has been named the Chukchi slope current, which is believed to emanate from Barrow Canyon. The current is surface-intensified, order 50 km wide, and advects both summer and winter waters. It is not trapped to a particular isobath, but instead is reminiscent of a free jet. There is no significant variation in Pacific water transport with distance from Barrow Canyon. A potential vorticity analysis suggests that the flow is baroclinically unstable, consistent with the notion that it meanders. The current is present during all synoptic wind conditions, but increases in strength from summer to fall presumably due to the seasonal enhancement of the easterly winds in the region. Its transport increased over the 12-year period of data coverage, also likely in response to wind forcing. In the mean, the slope current transports  $0.50 \pm 0.07$  Sv of Pacific water. This estimate allows us to construct a balanced mass budget of the Chukchi shelf inflows and outflows. Our study also confirms the existence of an eastward-flowing Chukchi shelfbreak jet transporting  $0.10 \pm 0.03$  Sv of Pacific water towards Barrow Canyon.

### B.1 Introduction

The means by which Pacific water crosses the Chukchi Sea, and the locations where the water exits the shelf into the interior Arctic Ocean, directly impacts various aspects of the Arctic ecosystem. The three main pathways of Pacific water on the shelf are the western branch into Herald Canyon, the Central Channel branch which flows northward between Herald and Hanna Shoals, and the coastal pathway (known as the Alaskan coastal current in summer and fall, Figure B1). During winter and spring, cold Pacific water flows through Bering Strait into the Chukchi Sea (Woodgate et al. 2005). This water is high in nutrients (Lowry et al. 2015), and consequently helps spur primary production on the shelf (Hill et al. 2005; Arrigo et al. 2014). In late spring and summer, warmer and fresher Pacific waters enter the Chukchi Sea, which are believed to play a significant role in both melting and delaying the formation of pack-ice both on the shelf (e.g., Weingartner et al. 2005) and in the basin (Steele et al. 2010; Woodgate et al. 2012; Brugler et al. 2014). The Pacific water transported across the shelf is also believed to contribute significantly to the reservoir of freshwater offshore in the Beaufort Gyre (e.g., Pickart et al. 2013).

The coldest type of Pacific water is known as newly-ventilated winter water (WW), which is near the freezing point. This originates from the northern Bering Sea (e.g., Muench et al. 1988) but can also be formed, or further transformed, locally on the Chukchi shelf in polynyas and leads (e.g., Weingartner et al. 1998; Itoh et al. 2012; Pickart et al. 2016; Pacini et al. submitted). As the season progresses, the temperature of this water moderates via solar heating and/or mixing with warmer ambient waters, at which point it is referred to as remnant winter water (RWW). (In the case of extreme warming, the WW can be converted to a weakly stratified summer water mass; Gong and Pickart 2016.) During summer and early fall, the Chukchi Sea contains two different types of warm Pacific water masses. The first is Alaskan coastal water (ACW) which stems largely from fluvial runoff in the Gulf of Alaska. The second is a combination of Anadyr water and central Bering shelf water, which mix north of Bering Strait (Coachman et al. 1975) to form a water mass known as Bering Sea summer water (BSSW).

Recent studies have revised our understanding of the circulation of Pacific-origin water on the Chukchi shelf, including the partitioning of transport between the different flow pathways. While the notion of

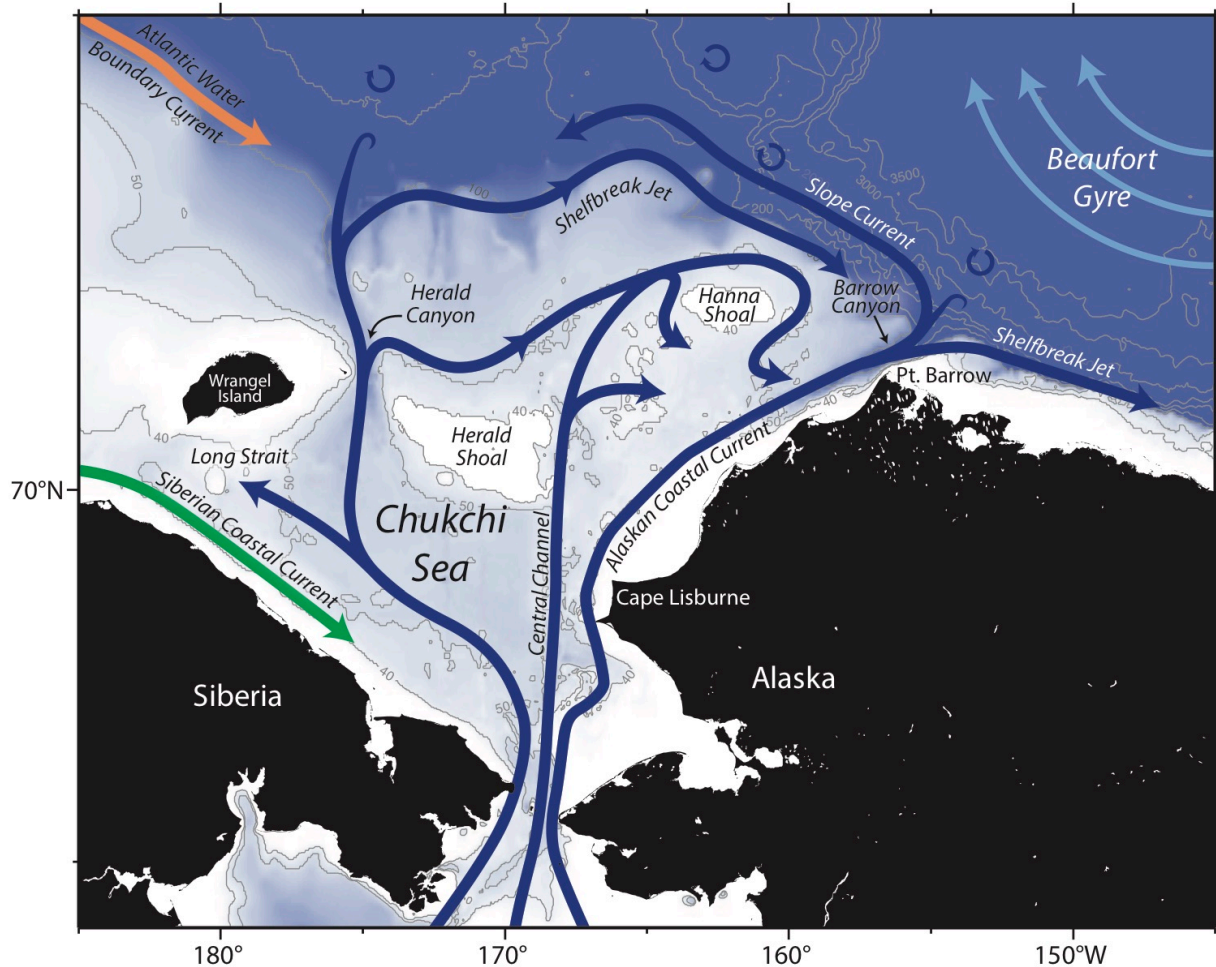


**Figure B1.** Revised schematic of the circulation of the Chukchi Sea and western Beaufort Sea from Brugler et al. (2014), including an extended Chukchi shelfbreak jet and the newly described Chukchi slope current based on the results of this study.

three main branches remains intact, it is now believed that, as the Pacific water progresses across the shelf, it divides into a number of smaller branches or filaments on the northeast part of the shelf (Pickart et al. 2016). Among other things, this impacts the timing of the advection of the high-nutrient WW across the shelf, which in turn has ramifications for the primary production (Lowry et al. 2015). With regard to transport, the yearly averaged volume flux in each of the three main flow branches is thought to be comparable (Woodgate et al. 2005). However, recent data suggest that, at least during the summer months, much of the Pacific water entering Bering Strait drains into Barrow Canyon in the northeast part of the shelf (Itoh et al. 2013; Gong and Pickart 2016; Pickart et al. 2016).

Presently, the mechanisms by which Pacific water exits the Chukchi shelf into the Canada basin — and the geographical locations where this occurs — are not fully understood. It is known that some portion of the outflowing Pacific water ends up as a shelfbreak jet that, in the mean, flows eastward along the edge of the Beaufort Sea (Nikolopoulos et al. 2009). While the configuration of this jet changes seasonally (surface-intensified during late-summer/early-fall, bottom-intensified over the remainder of the year), the current is a year-round feature. There is also evidence of a shelfbreak jet along the edge of the Chukchi Sea that, in the absence of wind forcing, flows to the east (Pickart et al. 2005; Mathis et al. 2007; Llinás et al. 2009; Pickart et al. 2016). The source of this is believed to be the outflow from Herald Canyon

(Pickart et al. 2010). However, the data are largely anecdotal, and there are no published estimates of the transport of this shelfbreak flow.

Notably, the volume transport of Pacific water in the Beaufort shelfbreak jet is only a small fraction of what enters the Chukchi Sea through Bering Strait. Using data from seven moorings deployed across the current from 2002 – 2003, Nikolopoulos et al. (2009) calculated the mean volume flux of Pacific water to be  $0.13 \pm 0.08$  Sv, which is only about 15% of the long-term transport through Bering Strait (0.83 Sv; Roach et al. 1995). Furthermore, while the northward volume flux through Bering Strait has increased in recent years to just over 1 Sv (Woodgate et al. 2012), the eastward transport of Pacific water in the Beaufort shelfbreak jet has decreased to 0.021 – 0.041 Sv (Brugler et al. 2014). This implies that the jet now only accounts for less than 5% of the Pacific water that enters the Chukchi Sea. (The summertime transport of the Beaufort shelfbreak jet increases to approximately 0.25 Sv (Brugler et al. 2014), still far less than the transport through Bering Strait.)

This begs the question, where and how does the bulk of the Pacific water exit the Chukchi Shelf? As noted above, Woodgate et al. (2005) argued that each of the three main branches transports a similar amount of Pacific water. However, a significant portion of the water in the western branch is diverted to the east just north of Herald Shoal (Pickart et al. 2010), progressing along the northern Chukchi shelf and joining the central branch (Spall 2007; Pickart et al. 2016) (Figure B1). This combined central/western branch is then believed to flow into Barrow Canyon, adding to the puzzle regarding the small transport of the Beaufort shelfbreak jet. Brugler et al. (2014) attributed the recent decrease in strength of the Beaufort shelfbreak jet to enhanced easterly winds. This is consistent with the larger number of wind-driven upwelling events over the last decade noted by Pickart et al. (2013), during which the flow of the jet is reversed to the west (Schulze and Pickart 2012). Brugler et al. (2014) presented data from a shipboard section occupied across the Chukchi slope just west of Barrow Canyon, which, together with a series of satellite images, revealed that the outflow from the canyon veered westward during such an event. This may provide a clue as to the fate of the Pacific water exiting the canyon and hence the “missing” transport in the Beaufort shelfbreak jet, but it should be remembered that this was only a synoptic occurrence.

Unlike the Beaufort Sea, where the shelfbreak jet is robustly documented using both mooring and shipboard data, the circulation along the Chukchi shelfbreak and slope has yet to be quantified. In light of the unaccounted transport leaving Barrow Canyon, and the observation of a jet of water veering to the west out of the canyon during a wind event, this motivates a study of the flow along the outer edge of the Chukchi Sea. Here we use a collection of historical shipboard sections occupied across the Chukchi shelfbreak/slope to investigate the circulation during the warm months of the year. The data reveal the existence of a heretofore unquantified current over the Chukchi slope that advects a significant amount of Pacific-origin water westward. The data also robustly document the presence of an eastward-flowing shelfbreak jet transporting a small amount of Pacific water toward Barrow Canyon. The paper is organized as follows. We start with a presentation of the shipboard data and an explanation of the technique used to create a mean section. We then describe the mean characteristics of the Chukchi slope current and shelfbreak jet, including the water masses they advect. This is followed by an investigation of the seasonal and interannual variation of the slope current. Next we explore the nature of the slope current and some aspects of its dynamics. Finally, we discuss the ramifications of these new components of the circulation in light of the mass budget of the Chukchi shelf.

## **B.2 Data**

### **B.2.1 Shipboard Hydrographic and Velocity Data**

We have compiled all publicly available shipboard sections occupied across the Chukchi shelfbreak/slope with the criteria that (1) they have high spatial resolution (typical station spacing of approximately 10

km), and (2) direct velocity measurements were made in addition to the hydrographic measurements. This resulted in 46 sections carried out during the period 2002 – 2014 (Table B1), spanning geographically from west of Barrow Canyon to 168°W (Figure B2). All but two of the cruises were done on the USCGC *Healy*. The exceptions were the July – August 2002 cruise on the USCGC *Polar Star* and the July – August 2003 cruise on the R/V *Nathaniel B. Palmer*. In each case a Sea-Bird 911+ conductivity-temperature-depth (CTD) instrument was used, with dual T/C sensors that were calibrated pre- and post-cruise. Most of the velocity measurements were made with a hull-mounted acoustic Doppler current profiler (ADCP), except the *Polar Star* cruise which used a lowered ADCP.

The data extend seasonally from May through October, although all of the May and June occupations occurred during 2002 – 2004. Therefore, the seasonal analysis is restricted to the months of July through October. In addition, there were no sections occupied between 2005 and 2008, so for the interannual analysis we consider two time periods: 2002 – 2004, which is referred to as the early regime, and 2009 – 2014, which is referred to as the recent regime. All of the cruises in the early time period were conducted as part of the Western Arctic Shelf-Basin Interactions (SBI) program. To avoid confounding spatial and interannual trends, both the spatial and interannual analyses have been restricted to a region within 300 km of Barrow Canyon.

### B.2.2 Surface Winds

To assess the impact of winds on the hydrographic and velocity structure in our domain, we used the North American Regional Reanalysis (NARR) 10 m wind field (Mesinger et al. 2006), which has a spatial and temporal resolution of 32 km and 6 hours, respectively. The wind conditions for each shipboard transect were characterized by averaging over the 36 hours prior to the midpoint time of the section. We considered the along-shelfbreak component of the wind, where the orientation of the shelfbreak (119.6°T) was determined using a linear regression of the 90 m isobath between 166°W and the mouth of Barrow Canyon. Along-shelfbreak winds are hereafter referred to as easterly (negative) and westerly (positive) winds.

**Table B1.** Hydrographic and velocity data sources, delineated between cruise (by row) and section (by semicolons). VMADCP = vessel-mounted ADCP; LADCP = lowered ADCP.

Cruise	Ship	Year	Month	Dates	Velocity
HLY02	USCGC <i>Healy</i>	2002	May	17–22; 23–30	VMADCP
PLS0201	USCGC <i>Polar Star</i>	2002	Jul./Aug.	21–22; 4–6	LADCP
HLY0203	USCGC <i>Healy</i>	2002	Aug.	6–12; 13–18	VMADCP
NBP03	R/V <i>N.B. Palmer</i>	2003	Jul./Aug.	23–26; 27–31; 3–4; 5–7; 7–8; 8–9; 10–11	VMADCP
HLY0303	USCGC <i>Healy</i>	2003	Sep./Oct.	16–17; 17–19; 11–14; 15–16	VMADCP
HLY0402	USCGC <i>Healy</i>	2004	May/Jun.	24–4	VMADCP
HLY0403	USCGC <i>Healy</i>	2004	Aug.	10–17; 18–24	VMADCP
HLY0404	USCGC <i>Healy</i>	2004	Sep.	15–16; 17–19	VMADCP
HLY09	USCGC <i>Healy</i>	2009	Aug.	6	VMADCP
HLY10	USCGC <i>Healy</i>	2010	Jul.	11; 13–14; 14–15	VMADCP
HLY1003	USCGC <i>Healy</i>	2010	Sep.	11; 12	VMADCP
HLY11	USCGC <i>Healy</i>	2011	Jul.	7–8; 9–10; 10–12; 14–15	VMADCP
HLY1103	USCGC <i>Healy</i>	2011	Oct.	8–9; 22	VMADCP
HLY12	USCGC <i>Healy</i>	2012	Oct.	9–11	VMADCP
HLY1301	USCGC <i>Healy</i>	2013	Aug.	13–14	VMADCP
HLY 1303	USCGC <i>Healy</i>	2013	Oct.	10–11; 13; 13–14; 15	VMADCP
HLY 1402	USCGC <i>Healy</i>	2014	Jul.	10–11; 13; 13–14; 20–22; 22–23; 24–25	VMADCP

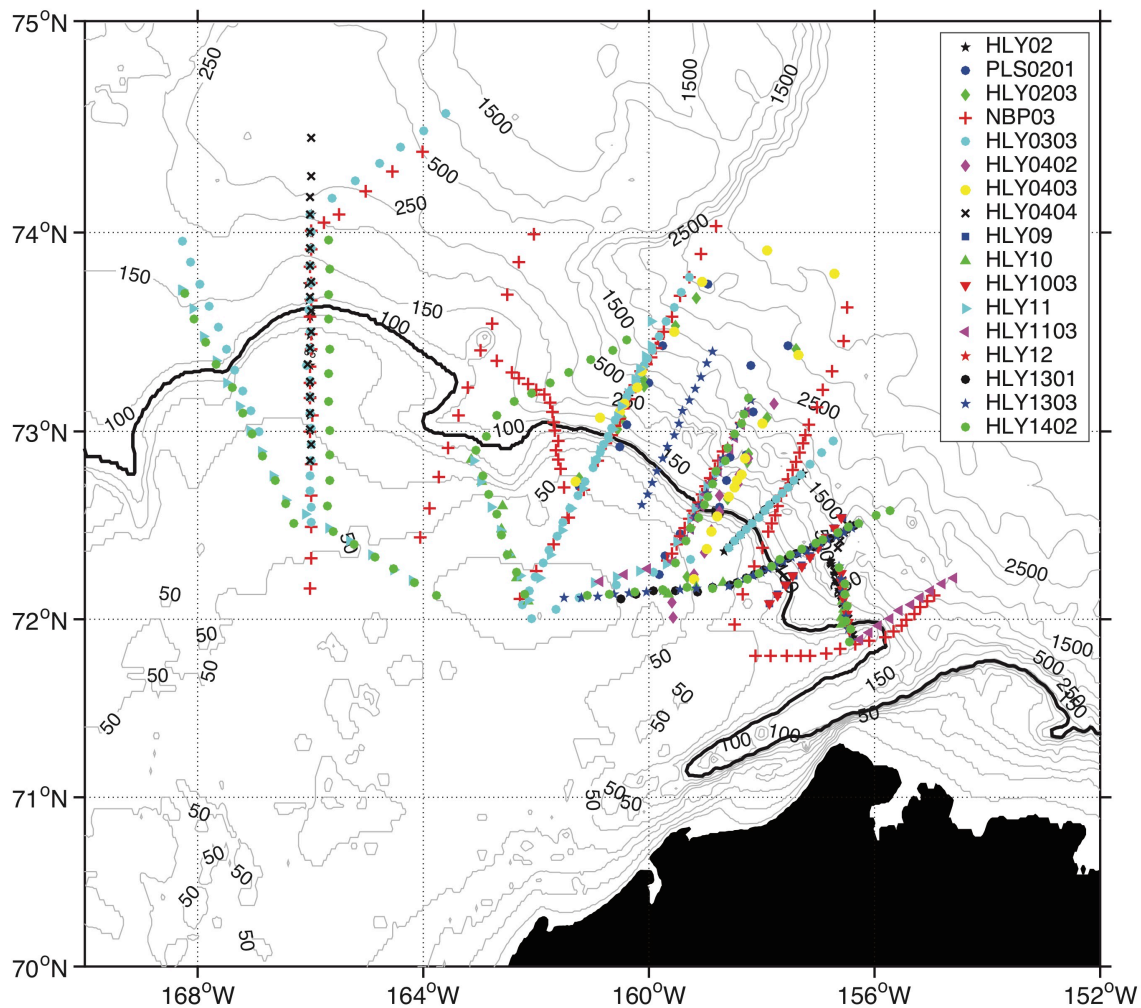


**Figure B2.** Locations of the 46 shipboard sections used in the study, color coded by cruise (see the legend and Table B1). The symbols denote the CTD stations comprising each section. The 90 m isobath is highlighted bold.

## B.3 Methods

### B.3.1 Gridding and Averaging

Vertical sections of hydrographic variables (potential temperature, salinity, and potential density) were constructed for each transect using a Laplacian-spline interpolator. This was also done for the cross-transect component of the ADCP velocity. The gridded velocity was then used to reference the gridded sections of thermal wind shear to compute sections of absolute geostrophic velocity, where the matching was done at each grid point over the common depth range of the thermal wind shear and directly-measured velocity.

It is of interest to compute mean vertical sections of the various properties. In order to do this, it was necessary to construct an average cross-slope bottom profile and to locate each CTD station along this

profile. As a first step, we followed the methodology of Pickart (2004) by constructing a Cartesian coordinate system aligned with the 90 m isobath over our domain of interest (the topography was smoothed first). Then a cross-slope bottom profile was created for each section (bottom depth versus cross-stream distance in the Cartesian frame). The value of bottom depth was the echosounder depth associated with the station (for those stations with no recorded echosounder value we used an interpolated value from ETOPO2, which was less than 10% of the time).

After each of the bottom profiles was made, we aligned them at the shelfbreak, where the shelfbreak was defined as the location of the greatest change in bathymetric slope along the section. Then the mean bottom was computed at each cross-slope location ( $x = 0$  corresponds to the shelfbreak). Next, every station was assigned a cross-stream location along the mean profile according to its bottom depth. This resulted in some distortion in the station spacing for the sections. However, the largest distortions of the along-section distance between stations occurred at the inshore and offshore ends of the sections, and, overall, the majority of between-station spacings were changed by a factor less than three (most cases corresponded to reduced spacing). The mean vertical property sections were then computed using the Laplacian-spline interpolator, with a grid spacing of 3 km in  $x$  and 5 m in depth ( $z$ ).

For completeness we tried two other techniques for computing the mean bottom profile: (1) aligning the sections at a given isobath (90 m), and (2) doing the same except that the bottom depths along each section were computed using ETOPO2 at the resolution of the digital product (i.e., to obtain higher cross-stream resolution of the bottom). Reassuringly, these other two techniques produced comparable results.

### B.3.2 Defining the Currents

As noted in the introduction, our collection of shipboard sections revealed the presence of a westward-flowing current over the Chukchi slope. Such a feature was observed in 37 of the 46 transects (80% of the occupations); all but two of the transects in which the feature did not occur are limited in their off-shelf extent (less than 30 km off-shelf). In order to quantify the characteristics of the current we needed to objectively define its width and vertical scale in each of the vertical sections (in addition to the mean section). We did this using the  $5 \text{ cm s}^{-1}$  velocity anomaly contour, where the anomaly was relative to the mean velocity across the entire section (i.e., the full lateral and vertical extent of the section). We note that in some instances there was an additional region of enhanced westward flow at the offshore end of the section (discussed below). In the cases when the  $5 \text{ cm s}^{-1}$  anomaly contour did not reach the surface on either side of the slope current, we used the locations where this contour reached its minimum depth to delineate the width of the current.

The location and dimensions of the shelfbreak jet were also defined by the  $5 \text{ cm s}^{-1}$  anomaly contour, but in this case the flow could be either eastward or westward. This feature was present in 30 of the 46 transects (65% of the occupations; in the remaining occupations the flow near the shelfbreak was very weak). As an added constraint we limited the offshore extent of the jet to be within the vicinity of the shelfbreak to avoid the contamination of shelfbreak jet estimates by the slope current.

### B.3.3 Calculating Fluxes

Following Woodgate et al. (2010), we calculate heat fluxes relative to the freezing point of seawater in Bering Strait:

$$HF = \int (\rho(\theta - \theta_0)C_p U_g) \partial A \quad (1)$$

where  $\theta$  is the potential temperature,  $C_p$  is the specific heat of seawater,  $U_g$  is the absolute geostrophic velocity, and  $\theta_0$  is the reference temperature ( $-1.91^\circ\text{C}$ ). The integral is taken over the cross-sectional area

of the section (A). While there are issues interpreting the heat flux across a section when there is a non-zero net mass flux, Woodgate, et al. (2010) and others argue that it is meaningful in this regional context because the Pacific water exiting the Arctic Ocean is close to the freezing point (Steele et al. 2004). Hence the heat flux calculated as such sheds light on the ability of this water to melt sea ice in the Arctic domain.

Freshwater fluxes are determined relative to the mean Arctic salinity reported by Aagaard and Carmack (1989):

$$FWF = \int \left(1 - \frac{S}{S_0}\right) U_g \partial A \quad (2)$$

where  $S$  is the salinity and  $S_0$  is the reference salinity (34.8).

Fluxes are calculated for both the Pacific water and Atlantic water. Following Nikolopoulos et al. (2009), we take the boundary between these two water masses to be the depth of maximum Ertel potential vorticity across the section. This corresponds to the base of the Pacific WW layer and is generally near  $-1.3^\circ\text{C}$  (see Nikolopoulos et al. 2009 for details).

## B.4 Mean Conditions

### B.4.1 Structure

Using the technique described in Section B3.1, we created mean vertical sections of hydrographic variables and velocity. Before presenting these, however, it is informative to quantify the different water masses observed on the Chukchi slope. This was done by constructing a volumetric temperature/salinity (T/S) diagram (Figure B3) for all of the data seaward of the 90 m isobath. The four Pacific water masses described in the introduction are labeled in the figure. Our analysis also includes a fresher water mass that is composed of fluvial, precipitation, and ice melt contributions; this water mass is labeled “meltwater” to be consistent with the literature (e.g., Gong and Pickart 2016; Lin et al. 2016). We note that these water mass boundaries are not precise and should be considered as guidelines, since the characteristics of the Pacific water change from year-to-year (e.g., Pisareva et al. 2015). Nonetheless the core T/S values of the different water masses are robust and distinct.

By far, the most common type of Pacific water measured on the Chukchi slope, for the months of May to October, is RWW (46.2%). This is true as well for the Beaufort slope (over the full seasonal cycle; Brugler et al. 2014). Although much less common, there were appreciable amounts of WW measured in the surveys (3.3%). Regarding the two summer Pacific water masses, BSSW was present to a moderate degree (5.2%), while there was only a small amount of ACW (less than 1%, although seasonally the amount was larger, see Section B5.1). The presence of these warm Pacific waters is addressed below. The final two water masses in Figure B3 are the Atlantic water (AW) at depth (33.6%) and meltwater (MW) in the surface layer (11.6%).

Returning now to the mean vertical sections, the average potential temperature section (Figure B4a) shows a warm surface layer, cold intermediate layer, and a warm deep layer below about 150 m. The cold layer is a combination of WW and RWW, while the deep layer is AW. While this thermal structure is to be expected, of note is the fact that the warmest part of the surface layer resides over the continental slope, not the shelf. The isopycnals generally slope downward progressing offshore, although they tend to flatten out at the seaward end of the section. There is also a region of enhanced isopycnal slope over the upper continental slope in the AW.

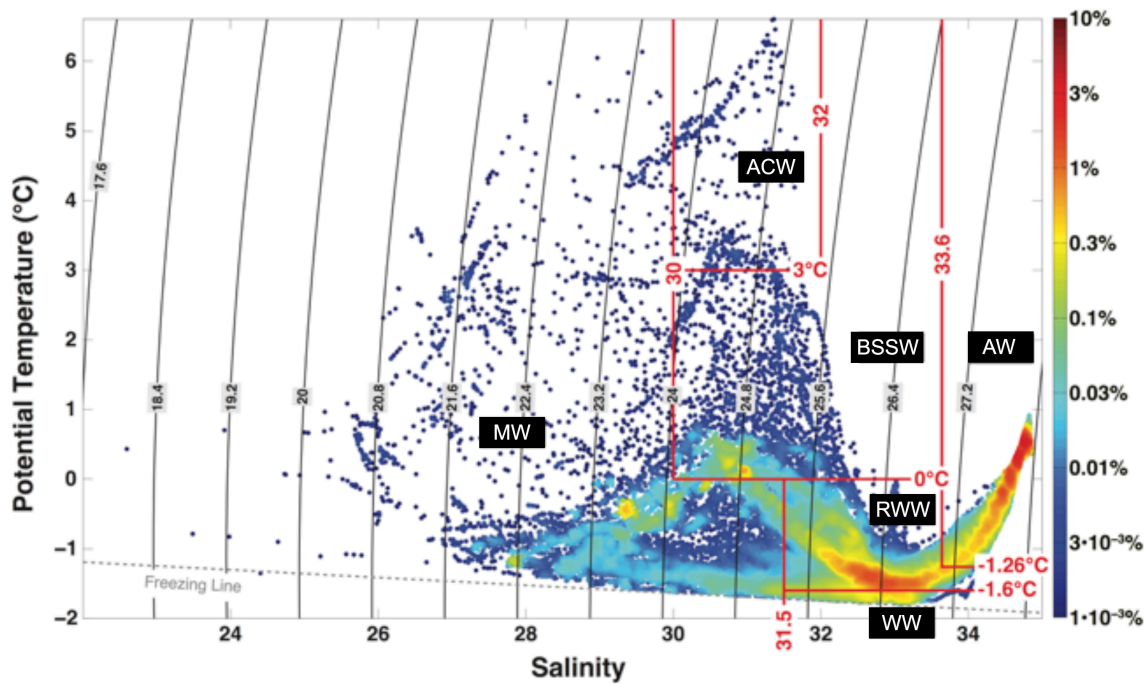


**Figure B3.** Temperature-Salinity diagram of all of the hydrographic data offshore of the 90 m isobath and above 300 m depth. Each point denotes a single measurement, and the color represents the percentage of data within each grid cell of 0.1°C temperature by 0.1 salinity. The red lines indicate the different water mass boundaries. ACW = Alaskan coastal water; BSSW = Bering summer water; WW = newly-ventilated Pacific winter water; RWW = remnant Pacific winter water; MW = meltwater; AW = Atlantic water.

The mean section of absolute geostrophic velocity (Figure B4b) reveals two distinct circulation components. The first is a bottom-intensified, eastward-flowing shelfbreak jet. While previous studies have suggested the existence of this current using synoptic data (e.g., Pickart et al. 2005; Mathis et al. 2007), our mean section robustly documents that such a feature exists along the edge of the Chukchi Sea. Dynamically this makes sense, as there is northward flow of Pacific water along the eastern flank of Herald Canyon (Woodgate et al. 2005; Pickart et al. 2010) some of which should turn eastward, following isobaths, to form a shelfbreak jet. This is analogous to the formation of the Beaufort shelfbreak jet via the outflow from Barrow Canyon (Pickart et al. 2005). A notable feature of the shelfbreak jet in Figure B4b is the enhanced near-bottom flow of AW associated with the strong isopycnal tilt noted above. Interestingly, the Beaufort shelfbreak jet also has a deep tail of eastward-flowing AW (Nikolopoulos et al. 2009; Brugler et al. 2014), which is believed to be associated with the spin-down phase of upwelling events that are common throughout the year (see Pickart et al. 2011). Further investigation is necessary to determine if the same mechanism is at work on the Chukchi slope.

While the existence of an eastward-flowing shelfbreak jet was anticipated, it was less clear what to expect on the continental slope. Our mean velocity section reveals the presence of a surface-intensified westward current seaward of the shelfbreak that is O(50 km) wide (Figure B4b), significantly broader than the shelfbreak jet. The strongest velocities are in the upper 150 m (i.e., in the Pacific layer), although the current extends deeper than this into the Atlantic layer. Laterally, the strongest mean flow is within 25 km of the shelfbreak, although there is significant flow out to 60 km (the mean section suggests a double core structure, but this is due to the relatively small sample size as the synoptic realizations generally do not indicate such a feature).

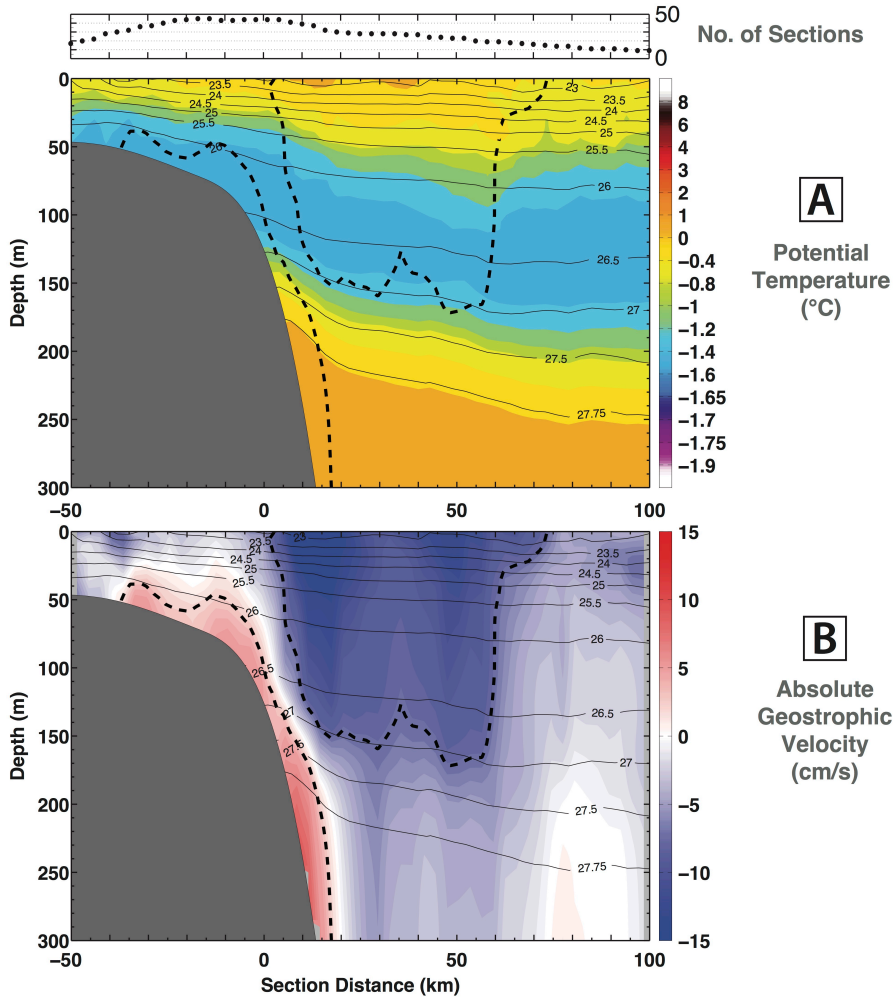


**Figure B4.** Mean vertical sections constructed from the 46 shipboard transects. (a) Potential temperature, and (b) Absolute geostrophic velocity overlain by potential density (contours,  $\text{kg m}^{-3}$ ). The black dashed lines denote the  $5 \text{ cm s}^{-1}$  velocity anomaly contour outlining the shelfbreak jet and slope current (see text). Positive velocities are eastward (the viewer is looking westward). The number of sections contributing to the mean at each cross-slope location is plotted in the top panel.

We refer to this current as the Chukchi slope current. To our knowledge this is the first robust documentation of the current, which we believe emanates (at least in part) from the outflow from Barrow Canyon. As noted in the introduction, the synoptic measurements reported in Brugler et al. (2014) are consistent with this notion, as are the sea surface temperature data and water column velocity measurements reported by Okkonen et al. (2009). Notably, the largest signature of Pacific summer water in the mean section of Figure B4a occurs within the current. The mass budget constructed below (Section B7) also suggests that the Chukchi slope current is fed by outflow from Barrow Canyon. Seaward of the slope current, near the offshore end of the mean section, there is another region of surface-intensified westward flow. This is weaker and less baroclinic and is presumed to be the southward edge of the Beaufort Gyre. Such an interpretation is in line with unpublished data from the Beaufort Sea, which indicates that the edge of the gyre is roughly 100 km offshore of the shelfbreak. This is considered below in more detail in the Discussion section.

The distribution of water masses associated with the mean hydrographic sections supports our claim that the Chukchi slope current advects Pacific water out of Barrow Canyon. In particular, we computed the percent occurrence across the shelf/slope of each of the water masses present in the T/S diagram of Figure B3. These are shown in the different panels of Figure B5. (Note that there is a steady decrease in occurrence near the seaward edge of the section due to data coverage, but this has been accounted for by normalizing by the number of realizations available at each given location.) MW is present across the entire section in the surface layer, though most prevalent on the outer shelf, while AW is found across the entire section in the deep layer. Notably, the highest percentages of BSSW, ACW, and RWW are found within the slope current. By contrast, the largest amount of WW occurs within the shelfbreak jet. These results suggest that the slope current is a fast-track for advecting Pacific water out of Barrow Canyon (in

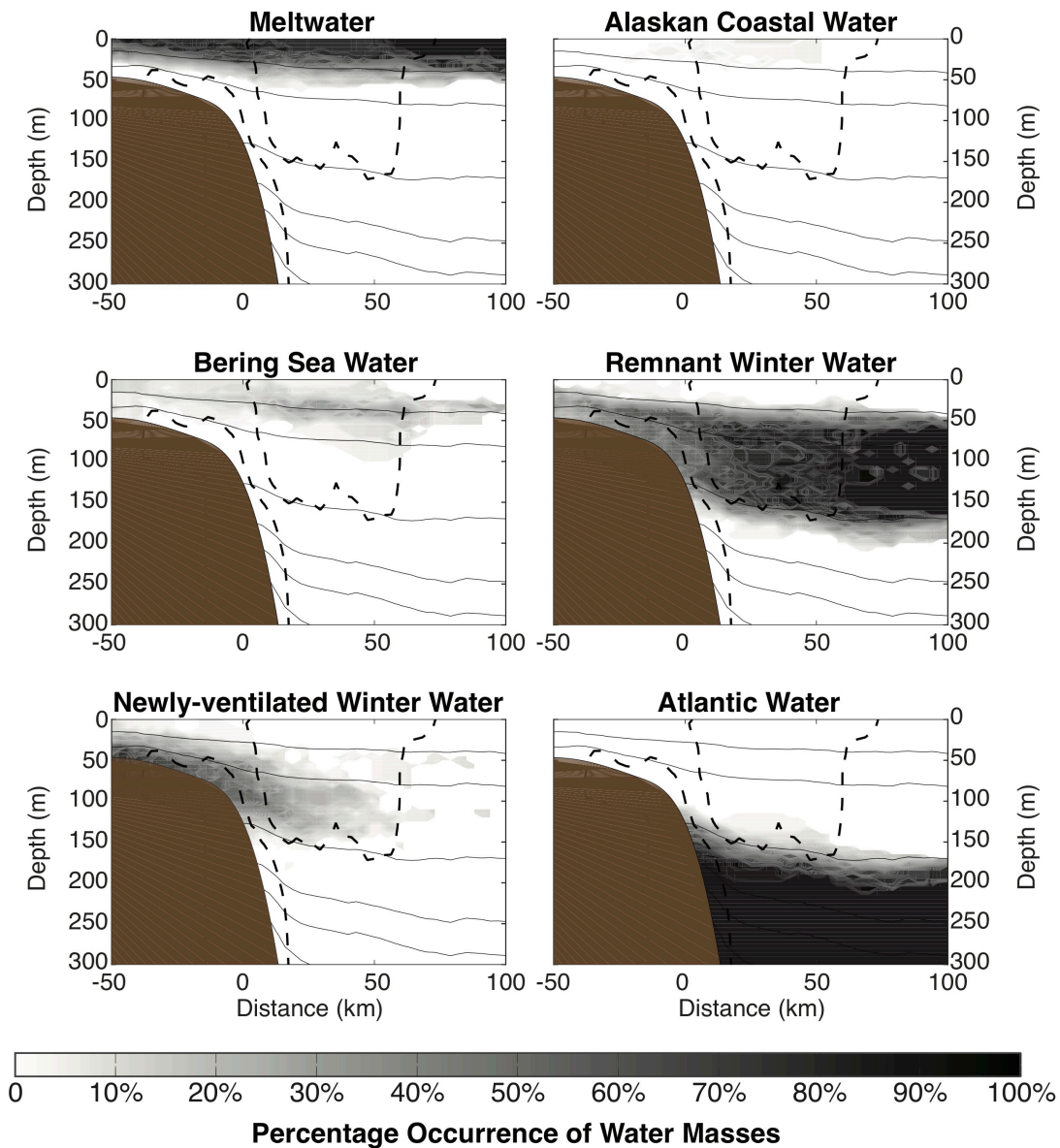


**Figure B5.** Relative occurrence of the different water masses in the mean hydrographic section. The black dashed lines denote the outline the shelfbreak jet and slope current as in Figure B4.

the warm months this would consist of RWW, BSSW, and ACW), while the shelfbreak jet is a slower, longer route for Pacific water emanating from Herald Canyon (hence WW is only showing up along the Chukchi shelfbreak at this time of year).

### B.4.2 Transport

Based on the average absolute geostrophic velocity section (Figure B4b), the mean westward volume transport of Pacific water in the Chukchi slope current, for the months of July – October, is  $-0.50 \pm 0.07$  Sv (all error estimates in the paper are standard errors). This excludes MW (see Section B3.3 for how we distinguished between Pacific water and Atlantic water). The corresponding eastward transport of the shelfbreak jet is much smaller than this,  $0.10 \pm 0.03$  Sv. These values are put into context of the mass budget of the Chukchi shelf in Section B7. The mean heat flux of the Pacific water in the slope current is  $-1.4$  TW, which is roughly half of the summertime estimate of Brugler et al. (2014) for the Beaufort shelfbreak jet ( $\sim 3$  TW). The mean Pacific freshwater transport of the slope current is  $-33$  mSv, which is roughly 50% greater than the summertime value of the Beaufort shelfbreak jet ( $\sim 20$  mSv). Both the corresponding heat and freshwater transports of the Chukchi shelfbreak jet are far smaller than these values ( $0.18$  TW and  $5.3$  mSv, respectively).

The volume, heat, and freshwater transports of the Chukchi slope current are broken down by water masses in Figure B6. For this calculation we computed the transports for each realization that measured the slope current and then computed the mean, in order to circumvent the smoothing out of individual water masses in the mean section. (Note that this results in a 2% increase in volume flux, 22% increase in heat flux, and 3% increase in freshwater flux because of the selective sampling.) The largest volume transport component is associated with the RWW, followed by the MW contribution. The other components are comparable with the exception of the ACW, which is quite small. As is true for the volume flux, the heat flux is dominated by RWW and MW. However, the two Pacific summer waters (particularly BSSW) have fractionally greater contributions due to their warm temperatures, as does the AW. Finally, the same two water masses dominate the freshwater flux of the slope current — RWW and MW — but the latter contribution is greater due to its lower salinity.

It is worth noting that AW contributes to the full volume transport and heat transport of the slope current by roughly the same amount as BSSW (roughly 10% and 16% for volume transport and heat transport, respectively; Fig B6a, b). The fact that AW is flowing westward on the Chukchi slope is curious — this is

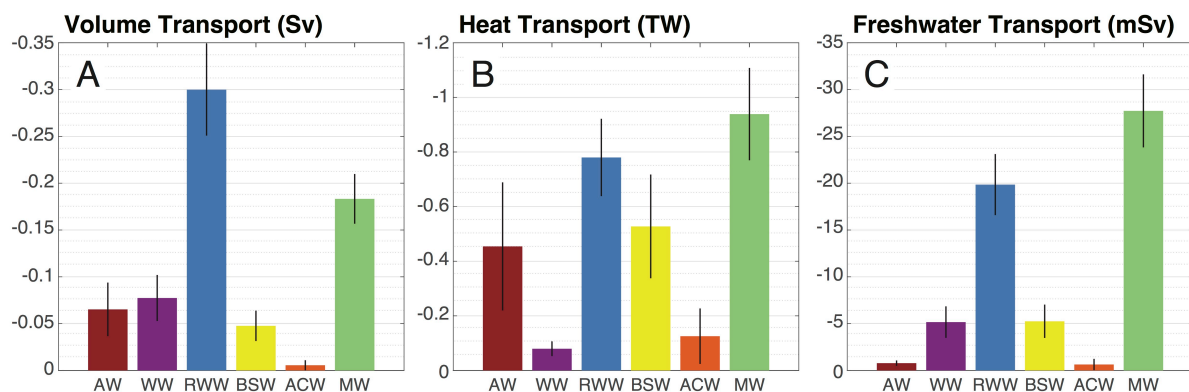


**Figure B6.** Transport of the Chukchi slope current broken down by water mass (see Figure B3 for the water masses). Standard errors are indicated by the lines. (a) Volume transport; (b) Heat transport; (c) Freshwater transport.

the opposite direction of the circumpolar boundary current that transports this water mass cyclonically around the sub-basins of the Arctic Ocean (e.g., Rudels et al. 1994; Aksenov et al. 2011). We have no explanation for this, and it warrants further investigation (beyond the scope of the present study).

## B.5 Variability

### B.5.1 Seasonality

There are pronounced seasonal changes in the presence of the different water masses on the Chukchi slope, as well as variations in the fluxes of mass, heat, and freshwater, from July to October. Starting with the water masses, we quantified the percent occurrence of each water type for each month seaward of the 90 m isobath (Figure B7). Both of the Pacific summer waters, BSSW and ACW, were barely present (or completely absent) in July and August, but increased in abundance in September. This trend continued for the BSSW in October, but the ACW content dropped again that month. Appen and Pickart (2012) noted that BSSW also remained on the Beaufort slope later in the warm season than ACW. The Pacific winter waters, RWW, and WW varied out of phase with each other on the Chukchi slope, with RWW increasing in October and WW decreasing markedly at that time. This is not surprising, since heating/mixing through the summer transforms WW into RWW. Finally, the AW content remained steady from July–September and then increased in October, while the amount of MW decreased steadily through the four-month period.

The most conspicuous seasonal change in Pacific water volume flux of the Chukchi slope current is the increase in westward transport in October (Figure B8). A possible explanation for this is the seasonality of the winds. We computed the monthly climatological along-shelfbreak 10 m wind speed over the Chukchi slope for the period 2002 – 2014. October has the strongest easterly winds during any month of the year, which would enhance the westward flow of the slope jet. A similar increase in heat flux and freshwater flux occurs during October as well. This is related not only to the wind, but is due in part to a substantial increase in the heat content and freshwater content of the water column (not shown). We note that the freshwater increase in October is not in line with the MW percentage (which is a minimum that month, Figure B7); it is related instead to the increase in the percentage of the RWW and the relatively

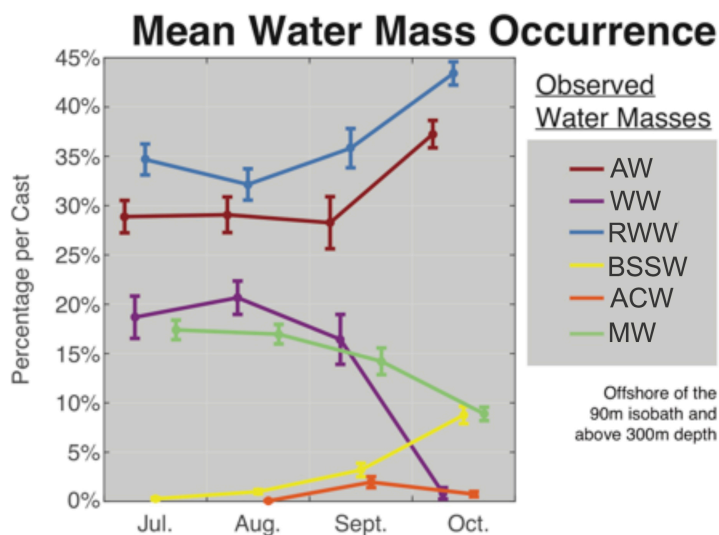


**Figure B7.** Mean monthly occurrence of water masses on the Chukchi slope offshore of the 90 m isobath and shallower than 300 m. Standard errors are indicated. (See Figure B3 for the water masses.)

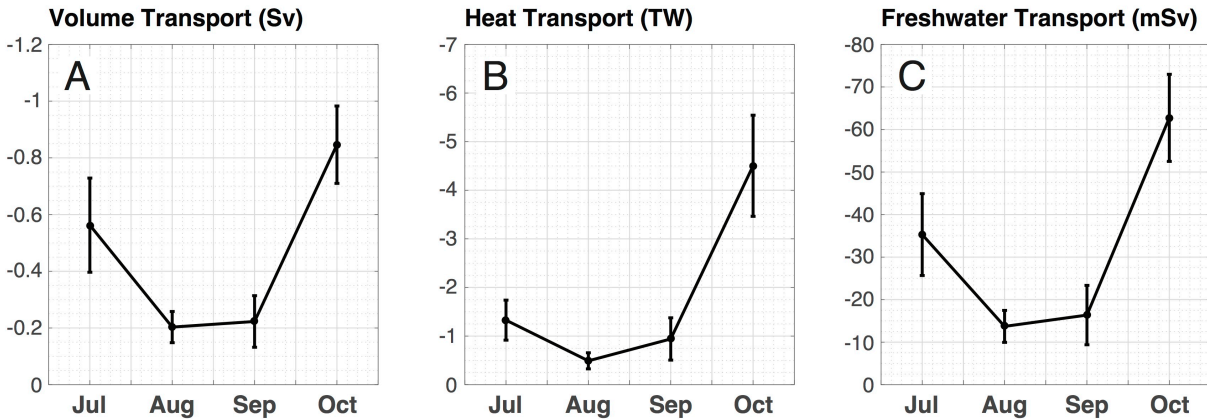


**Figure B8.** Mean monthly Pacific water transport of the Chukchi slope current with standard errors;  $N = 11$  for July, 10 for August, 5 for September, and 8 for October. (a) Volume transport; (b) Heat transport; (c) Freshwater transport.

fresh BSSW (note in Figure B3 that most of the BSSW is on the fresh end of that water mass range). In contrast to the Chukchi slope current, there is no pronounced seasonal variation in volume flux and freshwater flux of the Chukchi shelfbreak jet. While the shelfbreak jet reverses direction from eastward to westward in October — likely due to the increased easterly winds that month — the change is not statistically significant.

### B.5.2 Interannual Variability

As noted in Section B2.1, the temporal coverage of shipboard sections is such that we can only contrast the early regime (2002 – 2004) versus the recent regime (2009 – 2014) for July through October. In addition, to avoid aliasing spatial trends into interannual variability, we have restricted the spatial extent for interannual analyses to be within 300 km of Barrow Canyon. In terms of the water masses on the slope, there was no significant change in the three most prevalent water masses, the RWW, AW, and MW (Figure B9). However, the percent contribution of all of the other water masses did change significantly. Both of the Pacific summer waters increased in occurrence, particularly the BSSW, while the WW contribution decreased.

The volume, heat, and freshwater transport of Pacific water in the Chukchi slope current all increased significantly from the early regime to the recent regime (Figure B10). As was the case with the seasonal changes in the fluxes of the current, it seems likely that this was the result of the wind. We calculated the mean along-shelfbreak 10 m wind speed for July – October for each year that we have data. This reveals a noticeable change between the two regimes (Figure B11). In the early regime, two out of the three years had very weak average winds during this four-month period. By contrast, in the recent regime five out of the six years were characterized by easterly winds. This would favor a stronger westward-flowing slope current in the latter period. This is consistent the results of Brugler et al. (2014), who demonstrated that the eastward-flowing Beaufort shelfbreak jet was retarded by the enhanced easterly winds along the north slope of Alaska over a similar time period. It is also in line with the observed increase in the presence of ACW and BSSW on the Chukchi slope during the later regime (Figure B9). (Our data indicate a decreased transport of the Chukchi shelfbreak jet from the early regime to the later regime, but the change is not statistically meaningful.)

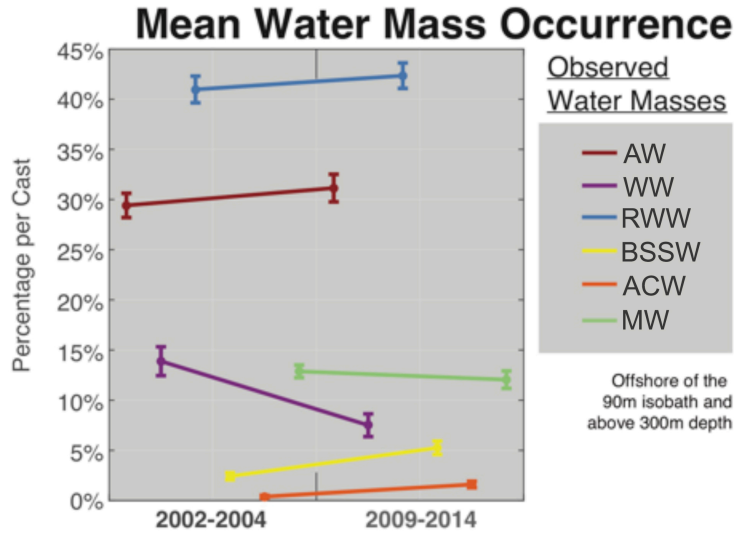


**Figure B9.** Interannual change in occurrence of water masses on the Chukchi slope from the early regime to the recent regime, offshore of the 90 m isobath and shallower than 300 m. Standard errors are indicated. (See Figure B3 for the water masses.)

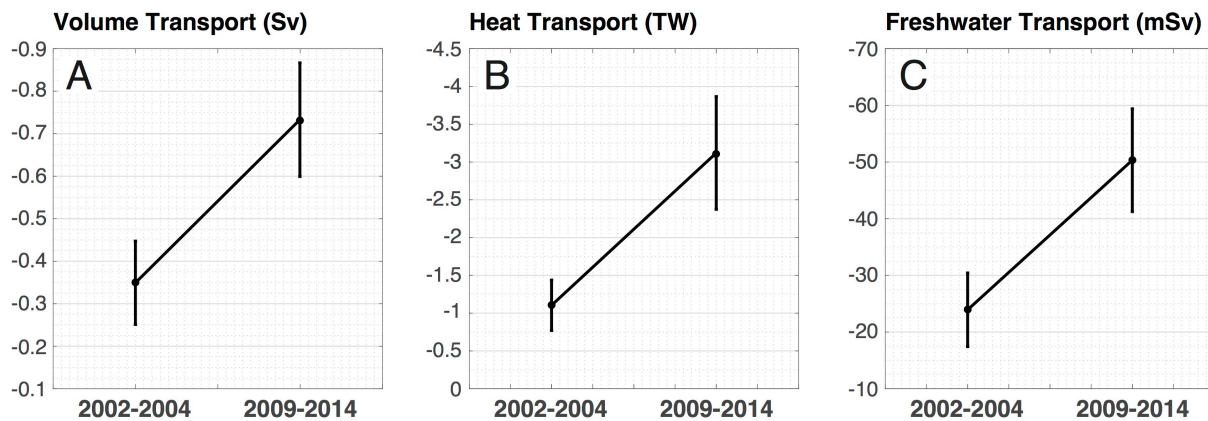


**Figure B10.** Interannual change in Pacific water transport of the Chukchi slope current from the early regime to the recent regime, with standard errors; N = 18 for the early regime, and 16 for the recent regime. (a) Volume transport; (b) Heat transport; (c) Freshwater transport.

## B.6 Nature of the Chukchi Slope Current

### B.6.1 Wind Influence

The apparent sensitivity of the Chukchi slope current to easterly winds on seasonal to interannual timescales makes one wonder if the current is present only during periods of substantial winds. For instance, it might be analogous to the Beaufort shelfbreak jet, which only flows to the west during upwelling-favorable winds. To investigate this, for each of the synoptic realizations we compared the transport of the current with the strength of the along-shelfbreak 10 m wind speed during/prior to the occupation of the transect (see Section B2.2). This reveals that, while the slope current is enhanced under synoptic wind forcing, it also exists when the winds are weak or even westerly. This relationship is

### Mean Jul.-Oct. Along-Shelfbreak Wind Speed

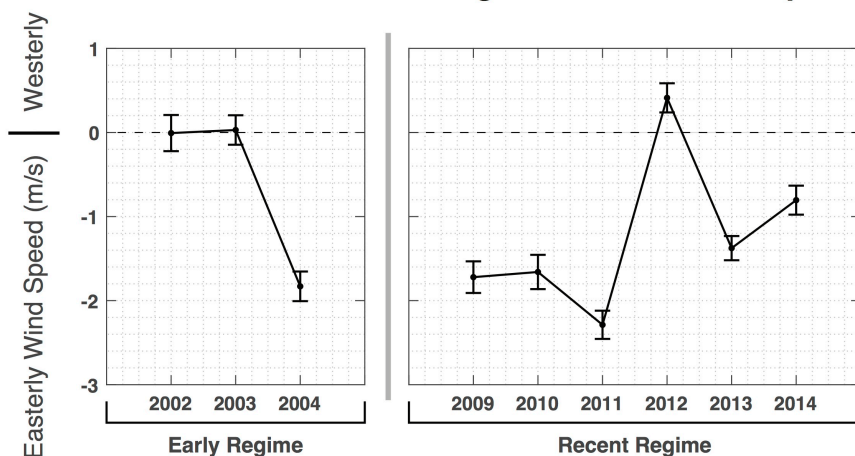


**Figure B11.** Mean along-shelfbreak 10 m wind speed from July – August each year, averaged over the Chukchi slope region (155 – 162°W and 72 – 74°N). The standard errors are indicated. Negative wind speeds are easterly.

significant at the 90% confidence interval and reveals a wind-dependent trend of  $-0.04 \text{ Sv per m s}^{-1}$  of easterly wind speed with a no-wind volume transport of  $-0.45 \text{ Sv}$ .

The influence of the wind on the Chukchi slope current is nicely visualized by constructing composite mean vertical sections under calm conditions versus times when there are moderate-to-strong easterly winds (Figure B12). In the weak wind composite the slope current is clearly evident, but it is relatively weak and the largest velocities are confined to the upper 40 m. By contrast, in the strong easterly wind composite the current is substantially stronger and the large velocities extend to 125 m. One also sees that the shelfbreak jet is considerably weakened under these latter conditions (the shelfbreak jet is reversed to the west in some of the synoptic easterly wind realizations). The overall conclusion is that, while the Chukchi slope current is sensitive to wind forcing, it still transports a notable amount of Pacific water to the west regardless of the synoptic winds.

#### B.6.2 Path and Downstream Evolution

Additional questions regarding the slope current are: What is the path of the current? How does it evolve going downstream? What is its ultimate fate? While definitive answers to these questions will require further observations and modeling, we can address some aspects here with the data in hand. As noted above, 37 of the 46 transects measured the presence of the slope current, and these realizations are depicted on a lateral map in Figure B13a. In the figure, the width of the arrows indicates the lateral scale of the current for the realization in question, while the length of the arrows denotes the mean speed of the current averaged over its width and depth (keep in mind that these are not true vectors; they are constrained to be normal to the sections).

One sees that the current is consistently located over the Chukchi continental slope throughout the entire domain, a distance of approximately 500 km westward from the mouth of Barrow Canyon. The median isobath over which the current resides (i.e., the region of strongest flow) is 238 m. In all but two of the realizations the current was shoreward of the 800 m isobath, and in 70% of the realizations it was inshore of the 400 m isobath. This implies that the current mainly resides on the upper continental slope but is not

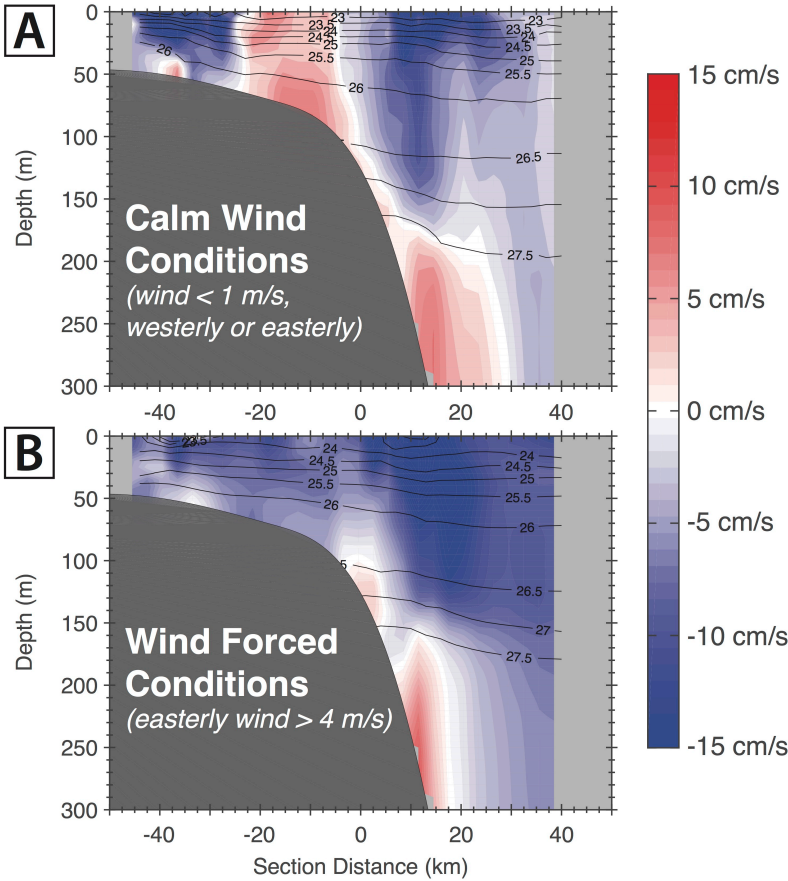


**Figure B12.** Composite vertical sections of absolute geostrophic velocity (color) and potential density (contours,  $\text{kg m}^{-3}$ ) during (a) calm wind conditions; and (b) times when the easterly winds exceeded  $4 \text{ m s}^{-1}$  prior to and during the occupation of the transect.

trapped to a particular isobath; it is instead more reminiscent of a free jet. In addition, we do not observe a statistically significant alongstream trend in transport for either the early regime or the recent regime. In Figure B13b we also show the analogous lateral map for the shelfbreak jet. It is evident that the shelfbreak jet is weaker and more narrow than the slope current, and at times it reverses to the west (in response to easterly winds, as noted earlier). The shelfbreak jet also does not exhibit any alongstream trend in volume transport.

The notion that the slope current is a meandering free jet suggests that it is baroclinically unstable. This was assessed by computing the Ertel potential vorticity ( $\Pi$ ) for each section,

$$\Pi = \underbrace{\frac{-f}{\rho} \frac{\partial \rho}{\partial z}}_1 + \underbrace{\frac{1}{\rho} \frac{\partial U_g}{\partial y} \frac{\partial \rho}{\partial z}}_2 - \underbrace{\frac{1}{\rho} \frac{\partial U_g}{\partial z} \frac{\partial \rho}{\partial y}}_3 \quad (3)$$

where  $f$  is the Coriolis parameter,  $\rho$  is density, and  $U_g$  is the cross-track absolute geostrophic velocity (see Pickart et al. 2005). Term 1 is the stretching vorticity, term 2 is the relative vorticity, and term 3 is the tilting vorticity. In general, the relative vorticity of the slope current is small (roughly 10 – 15% of  $f$ ), and the tilting component is negligible. As such,  $\Pi$  is dominated by the stretching term. A necessary condition

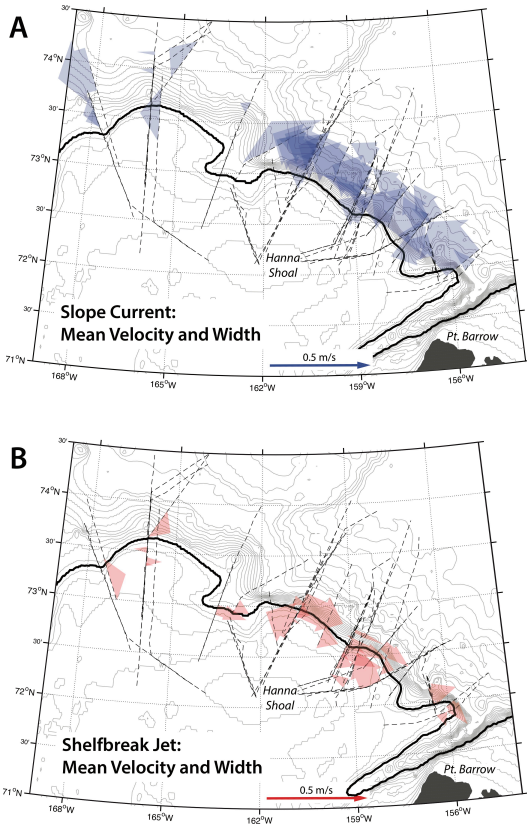


**Figure B13.** (a) Map showing the position and strength of the Chukchi slope current for each of the transects that measured the current. The width of the arrows denotes the lateral scale of the current, and the length of the arrows denotes the mean speed of the current averaged over its width and depth. The shipboard transects are indicated by the dashed lines. (b) Same as (a) except for the Chukchi shelfbreak jet.

for baroclinic instability is that the cross-stream gradient of  $\Pi$  change sign within the current. This was evaluated two ways. First we computed an average vertical profile of  $\partial\Pi/\partial y$  for each section and took the mean of this. Then we calculated  $\partial\Pi/\partial y$  from the mean vertical sections of Section B4 and computed an average vertical profile. Both techniques indicated that from roughly 30 – 50 m depth the cross-stream gradient of  $\Pi$  was negative, compared to everywhere else in the water column where it was positive. Hence the necessary condition for baroclinic instability is satisfied.

## B.7 Pacific Water Mass Budget of the Chukchi Shelf

The idea that a significant amount of Pacific-origin water exits Barrow Canyon as a westward-flowing current over the Chukchi slope motivates us to attempt a mass budget where we account for the different inflows and outflows associated with the Chukchi shelf. In this balance, it is assumed that there is no significant mass loss across the Chukchi shelfbreak between Herald and Barrow Canyons. While Timmermans et al. (2014) argue that subduction of Pacific water occurs from the shelf to the basin, our results imply that any associated volume transport would get entrained into the eastward-flowing shelfbreak jet or westward-flowing slope current. Since there is no significant alongstream trend in the volume flux of the shelfbreak jet, and the Pacific water transport of the slope current remains constant as

it flows westward from Barrow Canyon, this suggests that cross-shelfbreak subduction of mass is minimal.

An updated version of the Chukchi Sea circulation diagram shown by Brugler et al. (2014) is displayed in Figure B1, based on the new information presented in this study. In particular, it depicts Pacific water leaving Barrow Canyon in the slope current, as well as Pacific water flowing towards Barrow Canyon in the shelfbreak jet (where it is assumed to enter the western side of the canyon, then recirculate and exit the canyon). Using the known entrances and exits of Pacific water, a mass budget for the Chukchi shelf can be written as follows:

$$\begin{aligned}
 0 &= [\text{Bering Strait Inflow}] - [\text{Barrow Canyon Outflow}] \\
 &\quad - [\text{Long Strait Outflow}] - [\text{Herald Canyon Outflow}] \\
 \text{Barrow Canyon Outflow} &= [\text{Beaufort Shelfbreak Jet}] + [\text{Chukchi Slope Current}] \\
 &\quad - [\text{Chukchi Shelfbreak Jet}] \\
 \text{Herald Canyon Outflow} &= [\text{Chukchi Shelfbreak Jet}] + [\text{HCwest}]
 \end{aligned} \tag{4}$$

As a simplification, we assume that any mass loss directly north into the basin from Barrow Canyon or Herald Canyon is minimal. The idea here is that such a flux should occur via turbulent processes (e.g., eddy formation as depicted in Figure B1), which are sporadic. We assume instead that the main transport occurs via the major advective outflows. For Herald Canyon it is unknown if a portion of the outflow veers to the west (akin the Chukchi slope current), so we include an unknown contribution from such a current which is referred to in (4) as HCwest. The mean transport in the Beaufort shelfbreak jet is taken from Nikolopoulos et al. (2009), and the mean transports through Bering Strait and Long Strait are taken from Woodgate et al. (2005). The other two transport values — the Chukchi slope current and Chukchi shelfbreak jet — come from the present study.

The magnitudes of the known terms in (4) are shown graphically in Figure B14. One sees that the residual is very small, implying that mass is balanced on the Chukchi shelf within the accuracy of the different transport estimates. It further suggests that the outflow from Herald Canyon is small and that most/all of it feeds the Chukchi shelfbreak jet (i.e., HCwest is essentially zero). This seems to be at odds with the results of Woodgate et al. (2005) who presented a year-long transport value in Herald Canyon of 0.2 – 0.3 Sv, based mainly on a mooring on the eastern side of the canyon. However, the mooring in question was situated at the head of the canyon, and Pickart et al. (2010) present evidence, both from observations and numerical modeling, that most of the inflow on the eastern side of the canyon gets diverted to the east on the Chukchi shelf just north of Herald Shoal. This water then joins the Central Channel pathway and flows into Barrow Canyon (Pickart et al. 2016; Figure B1). In addition, data from multiple cruises suggest that there is no outflow from the western side of the mouth of Herald Canyon (Pickart et al. 2010; Linders et al. 2017).

Recently it has been argued that the transport of Pacific water through Bering Strait has increased over the past decade to 1.1 Sv (Woodgate et al. 2012). The interannual increase in transport of the Chukchi slope current, discussed in Section B5.2, could account for most of this increase. However, some of the enhancement of the slope current could also be due to diversion of Pacific water away from the Beaufort shelfbreak jet due to the stronger easterly winds of late (Brugler et al. 2014). The balance in Figure B14 implies that the mean outflow from Barrow Canyon is  $0.53 \pm 0.11$  Sv. Using 9 years of mooring data from the mouth of Barrow Canyon, Itoh et al. (2013) calculate a mean transport of  $0.45 \pm 0.07$  Sv. The two values agree with each other within the error bars, although it should be kept in mind that the former estimate does not include the cold season for the Chukchi slope current and Chukchi shelfbreak jet portions.

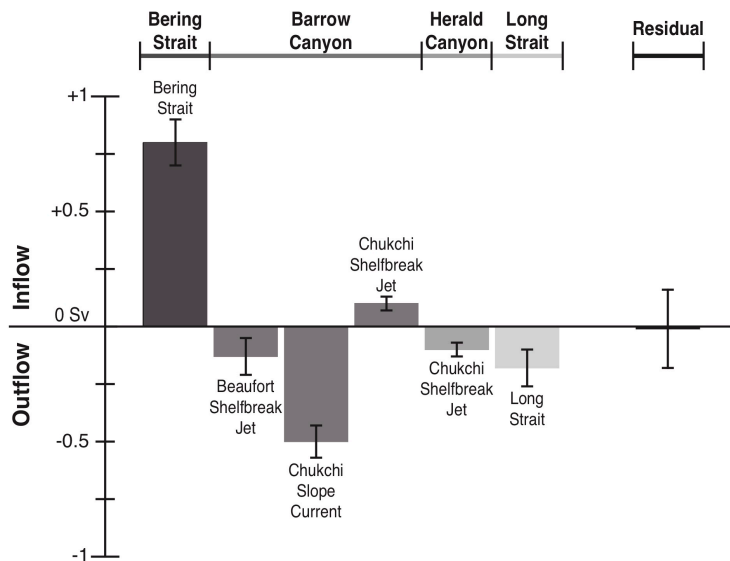


**Figure B14.** Mass budget of the Chukchi shelf inflows and outflows as discussed in the text, including the residual. Positive transports are inflows and negative transports are outflows. Standard errors are indicated.

Despite the uncertainty in the transport estimates of Figure B14, and keeping in mind the disparity in measurement techniques and spatial and temporal coverage of the different studies, the small residual nonetheless suggests that we have accurately accounted for most of the transport of Pacific water onto and off of the Chukchi shelf.

## B.8 Summary and Discussion

The analysis presented here has elucidated our understanding of the water masses and circulation along the shelfbreak and continental slope of the Chukchi Sea. The collection of historical shipboard transects confirmed the existence of a shelfbreak jet during the warm season that, in the mean, flows to the east as a bottom-intensified current. The jet is weakened under easterly wind forcing, and, synoptically, it can reverse and flow towards the west. Interestingly, the eastward mean flow extends into the Atlantic layer, associated with strongly sloped isopycnals becoming shallower onshore. Such a deep tail of the shelfbreak jet transporting Atlantic water is also observed in the Beaufort shelfbreak jet, but the mechanism for this in the Chukchi domain remains unexplored.

Offshore of the shelfbreak our data indicated the presence of a current flowing to the west, which we have named the Chukchi slope current. The current is surface-intensified,  $O(50 \text{ km})$  wide, located mainly on the upper continental slope, and extends into the Atlantic layer (although the flow at depth is weak). In the mean (July – October) it transports  $0.50 \pm 0.07 \text{ Sv}$  of Pacific water westward. In October, the Pacific water transport increases likely due to the stronger autumn easterly winds. The transport increased from the early regime (2002 – 2004) to the recent regime (2009 – 2014) presumably due to the enhanced zonal winds over this time frame. There is no alongstream trend in the cross-slope position of the current nor in the volume flux of the current. However, the current appears to meander, which implies that it is hydrodynamically unstable. Indeed, the cross-stream gradient of the Ertel potential vorticity changes sign with depth, which satisfies the necessary condition for baroclinic instability.

We believe that the slope current emanates from Barrow Canyon. This is consistent with the fact that the highest concentrations of the Pacific summer waters and remnant Pacific winter water were found in the current (the highest concentrations of newly ventilated Pacific winter water were observed in the shelfbreak jet, which is expected based on the seasonal timing of water exiting the Chukchi shelf). Furthermore, taking into account the transport of the Chukchi slope current and the Chukchi shelfbreak jet, we were able to construct a balanced mass budget for the different Chukchi shelf inflows and outflows. We note that several recent studies present schematic representations of the regional circulation that indicate flow emanating from Barrow Canyon and turning westward (e.g., Day et al. 2013; Dunton et al. 2014; Wood et al. 2015; Moore et al. 2016). However, none of these studies invoke data to support this notion.

It remains to be determined why such a large portion of the Pacific water exiting Barrow Canyon turns to the left instead of the right. Pickart et al. (2005) observed that newly ventilated Pacific winter water flowing northward through Barrow Canyon transposed from the western side of the canyon to the eastern side, suggesting that most of the flow should progress eastward in the Beaufort shelfbreak jet. However, this was a synoptic survey which may not be representative of the mean, or it may be that the densest Pacific water does in fact progress eastward out of the canyon. Keep in mind that most of the newly ventilated Pacific winter water in our mean section was found flowing eastward in the Chukchi shelfbreak jet. It also should be stressed that our data were confined to the warm season; the situation could be different during the other months of the year, although the mass balance in Figure B14 suggests that this is not generally the case.

It also needs to be explored what role the Beaufort Gyre might play in the existence and path of the Chukchi slope current. We have argued here that the slope current is not the southern arm of the gyre. In addition to the above evidence that the slope current originates from Barrow Canyon, it is difficult to believe that the gyre would be situated at such a shallow isobath on the Chukchi slope (the median isobath corresponding to the center of the slope current is 238 m). If this were the case, then one would think the same should be true on the Beaufort slope. A mooring array deployed across the Beaufort shelfbreak and slope from 2002 – 2004 at 152°W showed no evidence of this (Nikolopoulos et al. 2009). In particular, the flow is eastward over this part of the continental slope. We note however, that the bathymetry of the Beaufort slope is different than that of the Chukchi Slope, and the presence of the Northwind Ridge could influence the location of the gyre west of Barrow Canyon.

On the other hand, it is quite possible that the presence of the Beaufort Gyre is dynamically tied to the existence of the slope current such that the two features are not entirely distinct. For instance, ice velocity maps show westward flow at the outskirts of the Beaufort Gyre near the edge of the Chukchi Sea. This is shown clearly in Steele et al. (2004), who argue that, under negative Arctic Oscillation conditions, the gyre expands towards the Beaufort and Chukchi shelves (although Steele et al. (2004) state that ACW emanates from Barrow Canyon as eddies that subsequently get entrained into the gyre under these conditions). The winter mean sea surface height and surface geostrophic velocity maps of Mizobata et al. (2016) show evidence of a westward flow over the Chukchi slope that at times appears to be a separate current and at other times seems to be part of the gyre (see their Figure 4). Furthermore, a 10 year mean model simulation presented by Zhang et al. (2016) shows water exiting Barrow Canyon and turning westward along the southern edge of the Beaufort Gyre. Neither of these studies discuss this aspect of their results.

The role of wind in the formation of the Chukchi slope current needs to be investigated further as well. Okkonen et al. (2009) noted that, when the winds are out of the east, the Alaska coastal current can be displaced to the western side of Barrow Canyon. They also presented a sea surface temperature map during such conditions that showed a plume of warm water extending to the west out of the canyon. This is consistent with Brugler et al. (2014) who showed similar satellite evidence, along with velocity data

revealing the beginnings of the slope current. Surface drifters also depict flow heading west out of the canyon in response to wind events (Weingartner et al. 2015). Using a Pacific water tracer in a model simulation, Watanabe and Hasumi (2009) demonstrated that much of the water veers westward from Barrow Canyon during periods of strong easterly winds. It must be remembered, however, that while the Chukchi slope current is enhanced due to wind forcing, it is also present outside of such events, as demonstrated in the present study.

There are numerous ramifications associated with the notion that most of the Pacific water exiting Barrow Canyon progresses westward instead of eastward. Based on our data, the current has the potential to melt approximately 64,000 km<sup>2</sup> of 1 m thick ice over the period July – October, which is equivalent to a region extending 170 km seaward from the shelf edge between the mouth of Barrow Canyon and 166°W. The freshwater transport of the slope current is also substantial and could contribute to the freshwater reservoir of the Beaufort Gyre. The Pacific water needs to be fluxed offshore for this to happen, and it is unknown by what means this might occur, e.g., via eddy formation and/or wind-driven exchange (both of which occur in the Beaufort shelfbreak jet). It also remains to be determined what the ultimate fate of the Chukchi slope current is. Perhaps the current becomes ill-defined farther to the west or becomes entrained into the Beaufort Gyre. Further investigation is necessary to explore these and other aspects of the current, including its role in the regional ecosystem.

## C. Surface Current Patterns in the Northeastern Chukchi Sea and Their Response to Wind Forcing

### Abstract

We measured northeastern Chukchi Sea surface currents using high-frequency radar systems (HFR) during the ice-free periods of August to October from 2010 – 2014. We analyzed these data, along with regional winds, using Self-Organizing Maps (SOM) to develop a set of surface current-wind patterns. Temporal changes in the SOM patterns consist predominantly of two patterns comprising northeastward and southwestward surface currents. A third pattern represents a transitional stage established during the onset of strong northeasterly winds. These patterns are analogous to the first two eigenmodes of an empirical orthogonal function analysis of the HFR data. The first principal component (PC1) is significantly correlated ( $\sim 0.8$ ) to that of the winds and is directly related to the time series of SOM-derived patterns. The sign of PC1 changes when the speed of local northeasterly winds exceeds  $\sim 6 \text{ m s}^{-1}$ , at which point the northeastward surface currents reverse to the southwest. This finding agrees with previous models and observations that suggest this wind threshold is needed to overcome the pressure gradient between the Pacific and Arctic Oceans. The transitional stage is characterized by alongshore currents bifurcating in the vicinity of Icy Cape and wind-driven Ekman currents north of  $71.5^\circ\text{N}$ . Its development is a manifestation of interactions amongst the poleward pressure gradient, wind stress, and geostrophic flow due to the coastal setdown.

### C.1 Introduction

The Chukchi Sea is the gateway between the Pacific and Arctic Oceans. This vast marginal sea, though shallow in depth ( $\sim 50 \text{ m}$ ), is prominent in shaping the thermohaline structure and freshwater budget of the western Arctic Ocean. The annual mean transport of Pacific water into the Chukchi Sea through Bering Strait is  $\sim 0.8 \text{ Sv}$  (Roach et al. 1995; Woodgate et al. 2005) and was more recently reported as  $\sim 1.1 \text{ Sv}$  (Woodgate et al. 2012), resulting in a poleward flux of heat and freshwater that affects sea ice distributions (Shimada et al. 2006; Woodgate et al. 2006; Steele et al. 2008; Wood et al. 2015) and supplies  $\sim 30\%$  of the freshwater input to the Arctic Ocean (Serreze et al. 2006). Although the northward transport is forced by the steric height difference between the Bering Sea and Arctic Ocean due to interbasin salinity differences (Stigebrandt 1984; Aagaard et al. 2006), the flow field varies due to atmospheric forcing (Woodgate et al. 2012; Danielson et al. 2014).

As Pacific waters flow northward through Bering Strait and across the Chukchi Sea, observations (Paquette and Bourke 1981; Weingartner et al. 1998, 2005, 2013a; Woodgate et al. 2005; Pickart et al. 2010, 2016) and numerical models (Winsor and Chapman 2004; Spall 2007) indicate that the throughflow is bathymetrically steered along three major pathways (Figure C1). One branch follows Hope Valley and flows northward through Herald Canyon; another flows through the Central Channel between Herald and Hanna Shoals; and the third flows along the Alaskan coast and into Barrow Canyon where it becomes swift ( $\sim 50 \text{ cm s}^{-1}$ ) and narrow ( $\sim 40 \text{ km}$ ) (Winsor and Chapman 2004; Spall 2007; Itoh et al. 2013; Gong and Pickart 2015; Weingartner et al. 2017a). During summer and early fall, the coastal branch includes buoyant, nutrient poor Alaskan Coastal Water, carried by the Alaskan Coastal Current (ACC) (Paquette and Bourke 1974). Itoh et al. (2013) used long-term mooring observations at the mouth of Barrow Canyon and found the greatest heat and freshwater fluxes occur from August to October.

Owing to the shallowness of the Chukchi shelf, wind forcing substantially influences the circulation pathways. On average, each branch flows poleward, whereas the mean wind field over the Chukchi shelf

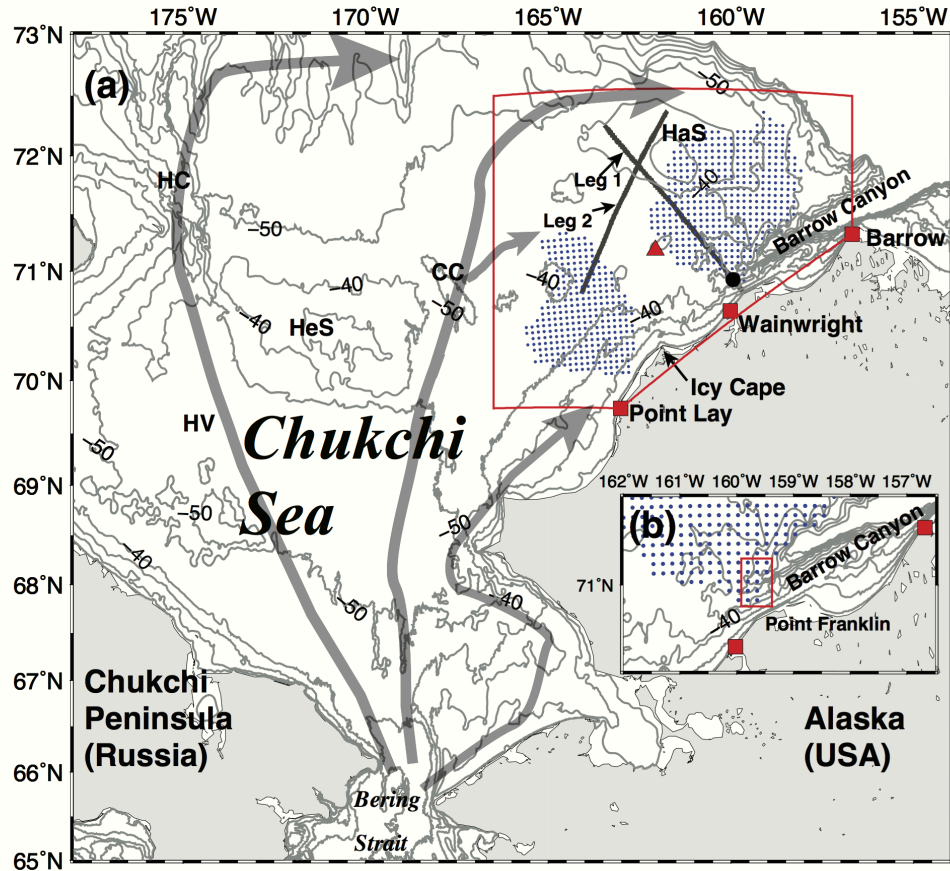


**Figure C1.** (a) Map of the Chukchi Sea with place names. Blue dots indicate 2012 HFR network grid points with more than 60% temporal coverage. Red squares show locations of HFR field sites. The red outlined area represents the NARR wind domain used in the SOM and EOF analyses, with the red triangle the location representative of the shelf wind time series. Legs 1 and 2 are hydrographic transects conducted in September 2013. Black dot north of Wainwright denotes the BC2 mooring. Gray arrows show schematic pathways of Pacific waters. Bathymetric contours are drawn from 10 – 100 m at 10 m intervals. Place names include HV = Hope Valley, HC = Herald Canyon, HeS = Herald Shoal, CC = Central Channel, and HaS = Hanna Shoal. (b) Grid points within the red rectangle are used to determine upcanyon and downcanyon flow conditions.

is from the east-northeast (Weingartner et al. 2013a) and opposes the mean flow. Local winds are highly correlated with the flow field on the Chukchi shelf (Weingartner et al. 2005; Itoh et al. 2013), except in Herald Canyon (Woodgate et al. 2005). Winsor and Chapman (2004) used a barotropic model to examine the sensitivity of shelf flow under changing winds and found that when northeasterly winds exceeded  $\sim 6 \text{ m s}^{-1}$ , the coastal current near Barrow reversed to the southwest. Similar reversals were observed using subsurface moorings and ship-borne surveys (Mountain et al. 1976; Johnson 1989; Aagaard and Roach 1990; Weingartner et al. 1998; Okkonen et al. 2009; Hirano et al. 2016); however subsurface measurements do not capture the upper few meters and so may not be representative of the surface current field. Therefore, surface current observations are essential to evaluate the flow imposed by wind forcing, especially when considering the potential transport of surface-trapped dissolved and suspended materials. In particular, surface currents may be important in the distribution of fish larvae (Wyllie-Echeverria et al. 1992; Geoffroy et al. 2016) and zooplankton (Questel et al. 2013).

This study focuses on synoptic surface current measurements collected in the northeastern Chukchi Sea using shore-based high-frequency radar systems (HFR) deployed along the Alaskan coast in the villages of Barrow, Wainwright, and Point Lay during the open water seasons of 2010 – 2014 (Figure C1). The HFR measurements have a resolution of 6 km and a range of ~150 km from the coast. We investigate the relationship between surface currents and winds using Self-Organizing Maps (SOM) (Kohonen 2001) to extract surface current patterns paired with wind fields.

The paper is arranged as follows. The HFR and North American Regional Reanalysis (NARR) data acquisition and processing are discussed in Section C2, followed by an overview and methodology of the SOM analysis. Section C3 presents the SOM-derived patterns, including their temporal evolutions in response to the winds. Surface current patterns from conventional empirical orthogonal function (EOF) analysis are also discussed. These results, along with mean circulation patterns, spatial correlations, and hydrographic observations, suggest differing dynamical environments north and south of ~71.5°N. Section C4 discusses the results with the aid of the regional hydrographic setting, and Section C5 summarizes the paper.

## C.2 Data and Methods

### C.2.1 Surface Currents

A three-HFR network monitored surface currents (~2 m depth, Stewart and Joy 1974) in the northeastern Chukchi Sea (Figure C1a) using 5 MHz SeaSonde systems. This frequency requires the presence of surface gravity waves with wavelengths of ~30 m (Barrick 1978; Paduan and Washburn 2013) and thus sufficient ice-free waters and winds to generate such waves. The SeaSonde records the reflected Bragg scatter from the waves, after which, assuming deep-water wave theory, one uses the Doppler-shifted radar return to calculate surface current speeds advancing toward or retreating from the radar. The HFR network presented herein is unique in that it is operated in a polar environment where waters are ice-covered ~8 months of the year. Sea ice presence varies from year-to-year and contaminates the radar signals. Therefore, we only considered the time period from 1 August to 31 October of each year, when little or no sea ice was present within the radar mask. The HFR site locations were dictated by grid power availability, which necessitated that our sites be more broadly separated (~150 km) than optimal (~75 km). Thus, the resultant radar coverage comprises two domains: a southern mask (Point Lay and Wainwright overlap) and a northern mask (Barrow and Wainwright overlap). The coverage leaves a persistent gap along ~162.5°W (Figure C1a). Although data from 2010 – 2014 were analyzed, we primarily present results from 2012 when spatial coverage was most extensive.

One-dimensional radial surface currents,  $\vec{r}$ , from each HFR were used to estimate two-dimensional surface currents,  $\vec{u}$ , following the optimal interpolation (OI) scheme of Kim et al. (2007, 2008). Fang et al. (2015) investigated the performance of the OI method applied to the Chukchi HFR network. They used analytical streamfunctions to simulate spatially and temporally varying currents and found that for derived  $\vec{u}$  with a normalized skill  $\geq 0.7$  (0 – 1 scale), errors were ~2° angle shift and <0.1% magnitude variation. They found that the most important quality control factor for the estimated  $\vec{u}$  is the contribution of radial velocities from different HFR, which is defined as the ratio of overlapping  $\vec{r}$  (ROR). The higher the ROR, the more biased the estimate of  $\vec{u}$ , by as much as ~20° in angle shift with a corresponding ~6% change in magnitude.

The  $\vec{u}$  were computed every cardinal hour, and the ROR at each grid point was determined. Fang et al. (2015) show that areas with  $\geq 0.7$  skill closely coincide to those with  $\text{ROR} < 5$ , thus grid points with  $\text{ROR} \geq 5$  were discarded. In addition, if the number of contributing  $\vec{r}$  in the search radius (35 km) of the grid point was <20, the OI-output  $\vec{u}$  at the grid point was flagged. The threshold 20 was used to prevent  $\vec{u}$

from being calculated using a small number of  $\vec{r}$ , which can result in erroneous current estimates. For the OI scheme we employed criterion based on the cosine angle of paired  $\vec{r}$  (Chavanne et al. 2007) to avoid estimates along the radar baseline where  $\vec{u}$  cannot be properly resolved. If the angle between paired  $\vec{r}$  was not between  $30 - 120^\circ$ , the grid point was excluded from the analysis. This range was chosen in conjunction with other quality control factors reported in Fang et al. (2015) to allow optimal determination of  $\vec{u}$ .

Data gaps can degrade filtering quality and cause spectral leakage that dampens filtered results, so after some experimentation, gaps in the  $\vec{u}$  time series for each year were filled with zeros following Chavanne et al. (2007). Grid points containing  $\geq 60\%$  temporal coverage (Figure C1a) were then filtered with a 9th order 40-hour cutoff low-pass Butterworth filter to remove high frequency signals (tidal and inertial motions).

## C.2.2 Winds

Wind velocities were extracted from the NARR 10 m surface field (Mesinger et al. 2006), at  $\sim 35$  km grid-spacing every 3 hours, for the same period as the HFR data and then linearly interpolated to hourly intervals and filtered as described above. Quantitative comparisons between the NARR winds and those measured at the Barrow and Wainwright airports were conducted in Weingartner et al. (2013b), who determined that NARR winds are a reliable proxy for observed winds. A domain covering the radar mask (Figure C1a) is used for the SOM and EOF analyses with  $162.1^\circ\text{W}$ ,  $71.2^\circ\text{N}$  (red triangle in Figure C1a) chosen as representative of winds in the study area.

## C.2.3 SOM Analysis

SOM is a tool capable of capturing detailed synoptic variability in a data set through time with multiple variables. Richardson et al. (2003) and Liu and Weisberg (2005) provide excellent background on the application of SOM to oceanographic data. Liu et al. (2006) investigated SOM sensitivities to varying parameter choices and discussed its performance compared with EOF analysis. Ideally, the major circulation features derived from both methods should be consistent with one another. However, Liu et al. (2006) showed that EOFs failed to extract pre-defined patterns from synthetic data, whereas SOM completed the task perfectly. The advantage of using SOM, a nonlinear approach, compared with EOFs for HFR currents is the capability to extract detailed patterns from synoptic data sets (Mau et al. 2007) and to identify when they occur in time. As will be shown, higher order EOF eigenmodes may not correctly capture complicated patterns.

We used the SOM Toolbox for our analysis (<http://www.cis.hut.fi/somtoolbox/>; v. 2.0) and followed the parameters discussed in Liu et al. (2006). As shown by Liu et al. (2007), Mihanović et al. (2011), and Vilibić et al. (2016), SOM is capable of incorporating two different data sets (e.g., HFR and wind data) to resolve associated patterns. Gap-filling approaches have been developed for HFR data (Kaplan and Lekien 2007; Fredj et al. 2016), but these tend to produce spurious results during periods of sparse data returns. Therefore, we replace HFR data gaps with zeros rather than using gap-filling approaches. This procedure makes the linear initialization of SOM numerically valid, so that the first two eigenmodes of the data matrix can be determined (Kohonen 2001). Beckers and Rixen (2003) found that introducing zeros into the raw data matrix can increase the variance of dominant modes and reduce errant interpolations.

The resultant number of patterns produced by SOM has to be chosen *a priori* and is subjective. The larger this number, the more temporal variability will be extracted from the data, while a smaller number of patterns tends to compress information yielding less temporal variability (Liu et al. 2006). After

experimentation, we found that twelve patterns are optimal for our data in that unique circulation features and data gaps can be isolated.

Twelve patterns were derived each year for 2010 – 2014. Although winds, radar coverage, and data gaps differed from year-to-year, we were able to categorize similar patterns into four major flow regimes (see Section C3.1). SOM patterns were visually confirmed with the data time series in each year to verify SOM performance. There was a pattern in all years made up of weak or negligible currents. We show that this weak current pattern correlates with a decrease in data returns (see Section C3.2) and can be treated as an error analog that facilitates our interpretation of resultant time series.

#### **C.2.4 EOF Analysis**

EOF analysis provides another perspective of surface current responses to winds. We will show that the first eigenmode and its principal component (PC1) corroborate the SOM-derived patterns. Due to data gaps, a direct EOF computation for  $\vec{u}$  was not possible; therefore, a field reconstructed approach called data interpolating empirical orthogonal functions (DINEOF) (Beckers and Rixen 2003; Taylor et al. 2013) was used to fill data gaps. (In August 2010 and 2013, there were too many  $\vec{u}$  gaps for effective use of the DINEOF approach, so the 1 September to 31 October period was used.) Reconstructed  $\vec{u}$  and wind time series for each year were then used individually for the EOF analysis following Kaihatu et al. (1998), resulting in two covariance matrices per year. Each EOF analysis yielded a corresponding PC, which we used to diagnose the flow fields. The resultant eigenvalue spectrum was evaluated according to North's significance test (North et al. 1982).

#### **C.2.5 Hydrography**

We used temperature and salinity data collected by a Sea-Bird 49 FastCAT CTD housed in a towed Acrobat system to highlight different hydrographic environments north and south of  $\sim 71.5^\circ\text{N}$ . One transect started from the western flank of Hanna Shoal and ran southeastward for  $\sim 200$  km to offshore Point Franklin, while a second began west of Wainwright near  $\sim 164^\circ\text{W}$  and ran  $\sim 200$  km northeastward to the northern edge of Hanna Shoal (Figure C1a). The Acrobat CTD sampled water depths of up to  $\sim 45$  m with horizontal and vertical resolutions of  $\sim 250$  m and  $\sim 0.5$  m, respectively. Details on instrumentation, data acquisition, and processing are given by Martini et al. (2016).

#### **C.2.6 Subsurface Currents**

An ADCP mooring near the head of Barrow Canyon (BC2; nominal 52.3 m depth) monitored transport through Barrow Canyon and was maintained from 2010 – 2015 (Figure C1a). These data allow us to compare flow behaviors throughout the water column. We used hourly time series of estimated alongcanyon transports following Weingartner et al. (2017a) and vertically averaged velocities to examine subsurface to surface current variations. Data processing of BC2 is found in Weingartner et al. (2017a).

### **C.3 Results**

#### **C.3.1 SOM-derived Patterns**

All twelve SOM-derived patterns for 2012 data with paired wind conditions are presented in Appendix A (Figure A-1). To simplify the presentation, we condense the twelve into four representative flow regimes (Figure C2a-d), along with polar histograms of accompanying wind conditions. The northeastward-flowing regime is the most common pattern (Figure C2a) and defined on the basis of northeastward flow inshore or near the 40 m isobath in the southern mask and in Barrow Canyon in the northern mask. For

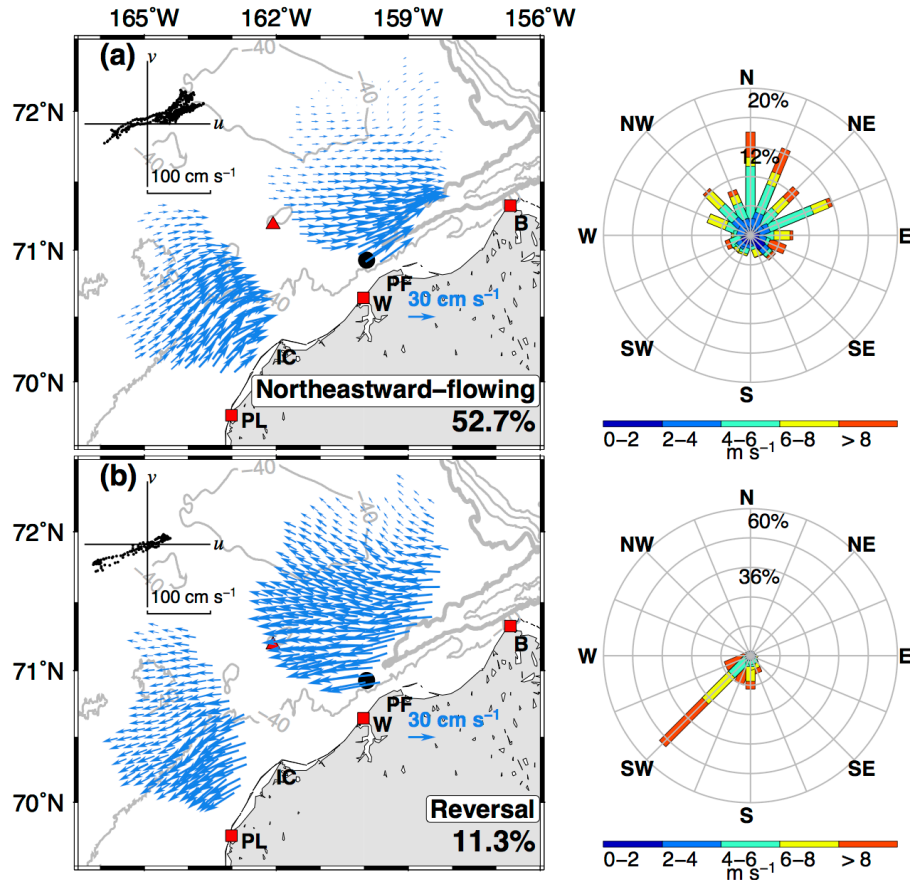


**Figure C2.** Representative circulation regimes categorized from twelve SOM-derived patterns of surface currents (blue vectors) for 2012: (a) northeastward-flowing regime and (b) reversal regime. The frequency of regime occurrence is included in each panel, and the 80 m isobath is thicker to define Barrow Canyon. The inserted scatter plot denotes vertically-averaged velocities from mooring BC2 (black dot) when the flow regime occurred. Polar histograms on the right denote wind velocities associated with the flow regime (red triangle). The direction follows oceanographic convention and speed is shaded. The percentage indicates frequencies of winds blowing toward that direction.

this regime the flow is coastally intensified with speeds  $>30 \text{ cm s}^{-1}$  in the canyon and within  $\sim 70 \text{ km}$  of the coast in the southern mask. Currents are weak over the central shelf ( $<20 \text{ cm s}^{-1}$ ) and even weaker ( $\sim 5 \text{ cm s}^{-1}$ ) north of  $71.5^\circ\text{N}$ . The northeastward-flowing regime occurred  $\sim 53\%$  of the time, and  $\sim 76\%$  of the winds associated with this pattern have a southerly component. Less than 10% of the winds are northeasterly with wind speeds  $<\sim 6 \text{ m s}^{-1}$ , suggesting that under these wind conditions the flow is forced primarily by the poleward pressure gradient. Velocity measurements from the BC2 mooring indicate the subsurface flow is also northeastward under these conditions. Coincident southwestward subsurface currents are remnant from flow transitions that have not been fully completed and lag the surface flow. Weingartner et al. (2017a) suggest an adjustment time scale of  $\sim 1$  day for the vertically-averaged flow in Barrow Canyon.

The second most common circulation feature is the reversal regime (Figure C2b), which occurred  $\sim 11\%$  of the time and whose structure is nearly opposite the northeastward-flowing regime. It consists of southwestward flow nearshore and westward flow farther offshore. The wind histogram shows  $\sim 60\%$  of the associated winds are northeasterly at  $>6 \text{ m s}^{-1}$  with  $\sim 10\%$  of occurrences associated with northerly

winds with speeds  $>6 \text{ m s}^{-1}$ . Reversal regime currents are stronger than those for the other circulation patterns, with current speeds  $>30 \text{ cm s}^{-1}$  in Barrow Canyon and inshore of the 40 m isobath offshore of Point Lay. Currents north of  $71.5^\circ\text{N}$  and east of Hanna Shoal are also swifter ( $\sim 15 \text{ cm s}^{-1}$ ) for this regime compared to the northeastward-flowing regime. Southwestward surface flow at BC2 predominates during the reversal regime. The occurrence of subsurface northeastward currents during the reversal regime is again due to the adjustment time from surface to depth. This result indicates that, at the head of Barrow Canyon, the flow structure is coherent vertically during the two most common surface circulation patterns but that the vertical shear may be substantial during flow transitions.

The third regime occurred  $\sim 16\%$  of the time and is denoted as the northwesterly wind regime (Figure C2c). For this pattern  $\sim 90\%$  of the winds are northwesterly, with more than half of the wind events having speeds  $>6 \text{ m s}^{-1}$ . This regime appears to result from interactions between the poleward pressure gradient (northeastward flow) and wind-induced Ekman transport (southward flow). The flow field appears to be spatially variable depending on which driving force dominates. For example, when winds initially shift to the northwesterly quadrant, the resultant Ekman transport may not be large enough to overcome the background pressure gradient. We have found cases where the currents south of  $71.5^\circ\text{N}$  are east-northeastward (similar to those seen in the northeastward-flowing regime), but southward north of  $71.5^\circ\text{N}$ . This flow pattern develops under evolving northwesterly winds and may last longer than a day. As northwesterly winds persist, the Ekman currents gradually overwhelm the poleward pressure gradient, so that currents are southward at  $\sim 10 - 15 \text{ cm s}^{-1}$  over much of the radar mask, with stronger flows ( $\sim 20 \text{ cm s}^{-1}$ ) inshore of the 40 m isobath and southeast of Hanna Shoal.

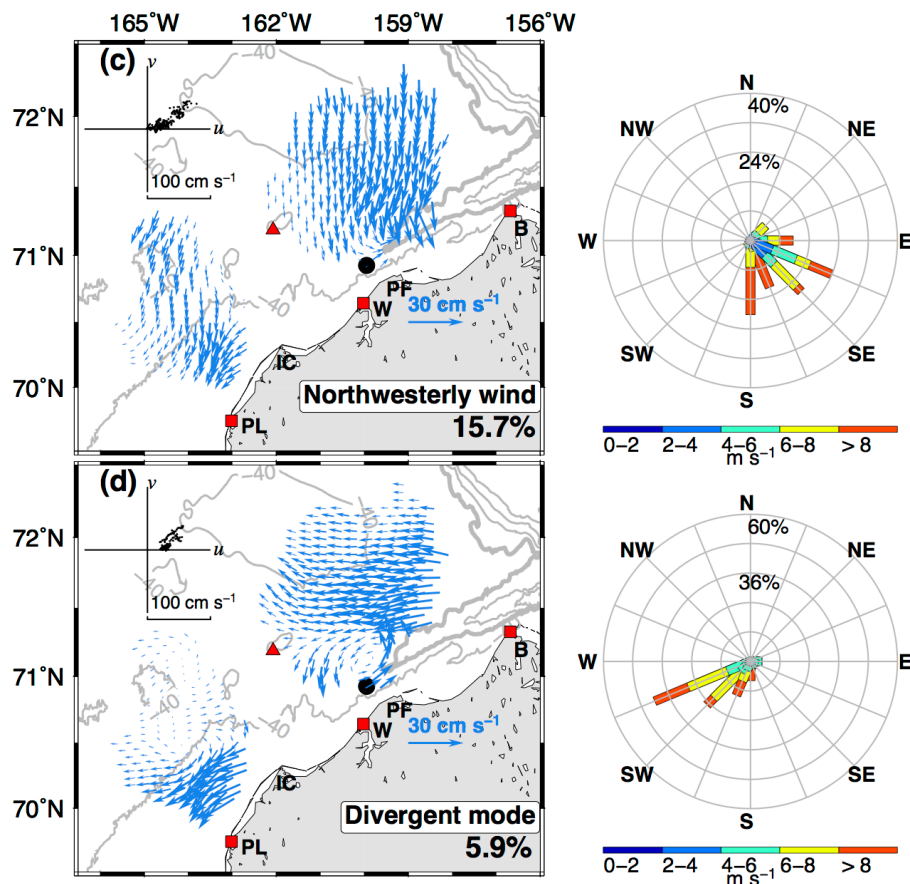


**Figure C2.** (continued) (c) northwesterly wind regime and (d) divergent mode. Note that the scales of current vectors in (c) and (d) are different than those in (a) and (b).

Subsurface flows observed at BC2 indicate predominately northeastward currents, indicating that the flow was vertically sheared over much of the canyon, except near Point Franklin where the surface flow was still northeastward. This finding implies that the subsurface flow over the central shelf must have been onshore in order to feed the transport in Barrow Canyon. This current pattern differs from the reversal regime, during which both the subsurface and surface flows were southwestward.

The fourth regime is the divergent mode (Figure C2d). North of 71.5°N, currents are ~10 cm s<sup>-1</sup> and westward. South of this latitude, a recirculation is suggested, which includes cyclonic flow near the head of Barrow Canyon and an anticyclonic circulation at ~164°W, 70.5°N. The recirculation includes northeastward currents in Barrow Canyon and southwestward currents in the southern mask between Icy Cape and Point Lay. Approximately 80% of the winds concurrent with the divergent mode are northeasterly, and ~70% of these winds have speeds >6 m s<sup>-1</sup>, similar to those of the reversal regime; however, the subsurface and surface flow at BC2 is still northeastward, in contrast to the reversal regime. We will demonstrate that the divergent mode is a transitional stage between the northeastward-flowing and reversal regimes, as northeasterly winds begin to overcome the poleward pressure gradient.

As previously mentioned in Section C2.3, SOM patterns vary slightly over the years; however, the regime descriptions above apply to all years. For example, the reversal regimes of 2010, 2011, 2013, and 2014 are all analogous to our description for the reversal regime in 2012. We find that the location of southwestward flow, offshore westward flow, and subsurface currents observed at BC2 approximate to the 2012 results. Similar agreements apply to the other three flow regimes.

Histograms show the monthly distribution of the four flow regimes for all years (Figure C3). The results indicate that the northwesterly wind regime was rare, consistent with the regional mean winds being predominantly from the east-northeast. The northeastward-flowing and reversal regimes occurred ~43% and ~27% of the time, respectively. In general, as the frequency of the northeastward-flowing regime increases the frequency of the reversal pattern decreases, and vice-versa. The divergent mode appeared ~7% of the time overall with durations varying from several hours to a maximum of ~5 days.

The remaining pattern, not included in our categorization, consists of variable and weak (~1 cm s<sup>-1</sup>) currents which are unreliable and occurred during periods of sparse data returns due to equipment maintenance, ice, ionospheric interference, and/or low winds. Collectively these conditions occurred ~14% of the time during 2012 and were aggregated into a pattern for data gaps referred to as G (see Appendix A Figure A-1e).

### **C.3.2 The Role of Winds: SOM Perspective**

To illustrate how surface currents change under varying wind conditions, time series of the SOM regimes from August through October 2012, along with wind vectors, are presented in Figure C4. The gray line in Figure C4 tracks the normalized data return and facilitates interpretation of regimes associated with data gaps. For example, Pattern G occurred from 11 to 14 August when data returns were very low. Low data returns also occurred from 10 to 14 October due to diurnal ionospheric interference (Teague 2001).

The wind field from 4 – 28 August was mainly southwesterly-southerly, and the northeastward-flowing regime persisted through most of the month. It was also present during the southerly wind events of 1 – 3, 6 – 7, and 20 – 28 October and occurred from 1 – 3 August and from 18 – 22 September when weak ( $\leq 4$  m s<sup>-1</sup>) winds from varying directions prevailed, consistent with our notion that weak winds are insufficient to overcome the poleward pressure gradient force.

After 28 August, southerly winds relaxed, and the winds became northeasterly and increased to a maximum of 10 m s<sup>-1</sup> on 31 August. During this wind transition, the circulation shifted briefly into the

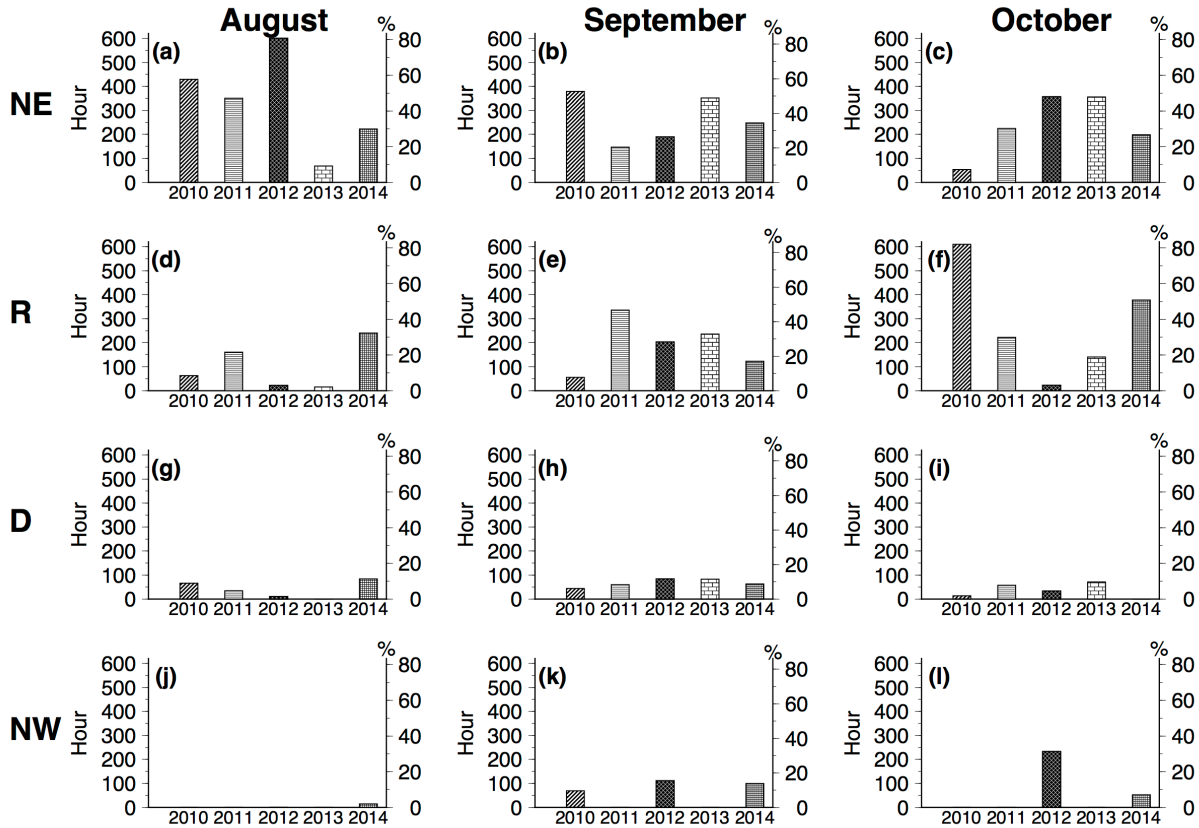


**Figure C3.** Monthly occurrences of SOM-derived circulation regimes for 2010 – 2014 with different hatching denoting different years. (a)-(c) Northeastward-flowing regime (NE). (d)-(f) Reversal regime (R). (g)-(i) Divergent mode (D). (j)-(l) Northwesterly wind regime (NW). A 15-day data gap in August 2013 is the reason for few regime estimates in that month.

divergent mode before the reversal regime was established. Reversal regimes consistently occurred during and/or shortly after pulses of strong ( $\sim 10 \text{ m s}^{-1}$ ) northerly and/or northeasterly winds (e.g., 16 – 17, 22 – 23, and 27 – 29 September and 30 – 31 October). The divergent mode accompanied each transition from the northeastward-flowing regime to the reversal pattern, appearing as the northeasterly winds increased to relatively high magnitudes. Based on the wind time series and the EOF analysis of Section C3.3, we find that the divergent mode occurred when northeasterly winds reached  $\sim 6 \text{ m s}^{-1}$ . Hence, the divergent mode appears to be a transition between these two regimes; a point we will return to in Section C4.

The northwesterly wind regime (Figure C2c) occurs primarily during periods when winds are veering from northwesterly to westerly or vice versa (e.g., 8 – 18 October) and/or during wind transitions involving westerlies (14 – 15 September). These results suggest that strong ( $>6 \text{ m s}^{-1}$ ) and sustained northwesterly winds ( $>1$  day) are required to initiate this regime. We did not observe this pattern in 2011 and 2013, however, because northwesterly winds seldom occurred. When present, these events were short-lived ( $<1$  day) in comparison to the  $>3$  day events registered in 2012.

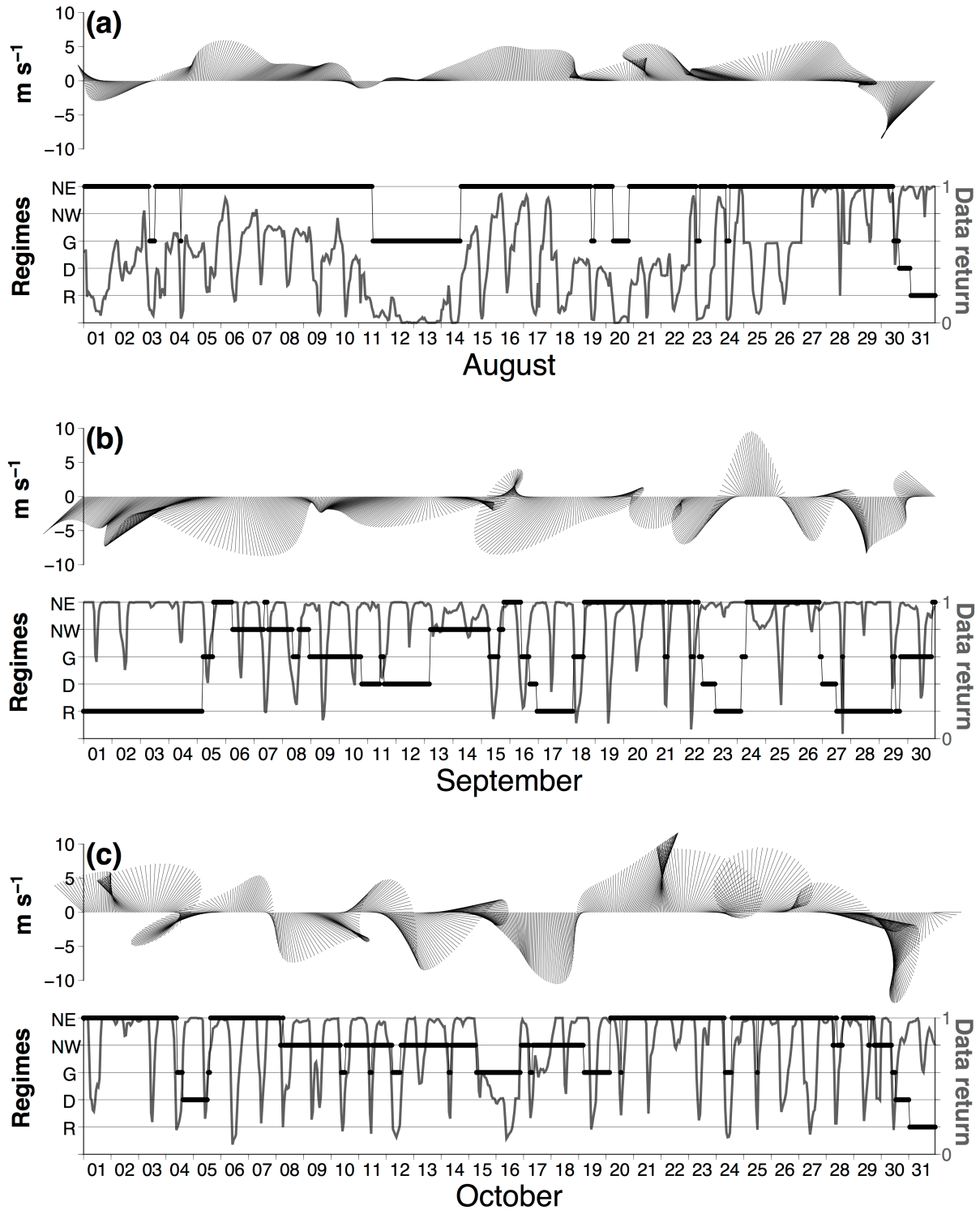


**Figure C4.** (a) Upper panel: time series of wind vectors in August 2012. The vector direction follows oceanographic convention. Lower panel: SOM-derived circulation regimes (black dots) in August 2012 and normalized data returns (gray line). The abbreviations are: R, reversal regime; D, divergent mode; G, pattern G; NW, northwesterly wind regime; NE, northeastward-flowing regime. (b) As in (a), but for September 2012. (c) As in (a), but for October 2012.

### C.3.3 The Role of Winds: EOF Perspective

The bulk of the SOM patterns are the northeastward-flowing and reversal regimes, which suggests that these should be linked to the leading EOFs (Mau et al. 2007). In this section, we use EOFs and SOM patterns to corroborate one another. Table C1 summarizes the EOF results in terms of the variance explained by the first (Mode 1) and second eigenmodes (Mode 2), the number of significant eigenmodes, and the correlation between PC1 of the currents and the winds. Mode 1 of the currents and winds account for at least 50% of the total variance, and the correlation between each variable's PC1 is significant. Mode 1 of the 2012 surface currents (Figure C5a) shows a pattern similar to the reversal regime derived from SOM (Figure C2b), which, when multiplied by its negative weight in the time domain, is analogous to the northeastward-flowing regime (Figure C2a). Mode 1 of the winds depicts northeasterlies (Figure C5c), and its negative weight describes southwesterly winds. The structures of Mode 1 in other years were similar to those in 2012, except in 2010 when Mode 1 for the winds was aligned in the east-west direction.

Mode 2 of the currents, which accounts for 9% to 17% (depending upon year) of the surface current variance, is characterized by southward flows and onshore currents that appear to bifurcate somewhere between Icy Cape and Wainwright (Figure C5b). Meanwhile, Mode 2 of the winds portrays northwesterlies (Figure C5d) and explains 19% to 34% of the variance across years. The structure of Mode 2 of the currents and winds in other years is comparable to those from 2012. The correlation between the principal components of Mode 2 (PC2) of the currents and the winds is only statistically significant for 2012 and 2014; however, as discussed later, we suspect that this relationship may not be meaningful.

Figure C6 shows the relationship between currents and winds in terms of wind speed and direction, PC1 of currents and winds, and the circulation regimes for the 2012 data. PC1 of currents and winds are normalized individually, and both are referenced to the reversal regime and northeasterly winds. PC1 values for the currents (winds) approaching unity indicate a flow field similar to that of Mode 1 (Figure C5a). In August, PC1 of the currents and winds were both generally negative (i.e., northeastward flow), consistent with the SOM results.

Northeasterly and northerly winds, as well as the divergent mode and reversal regime, were more frequent in September and October than in August. As a consequence positive PC1 values for both the currents and winds were also more frequent. For example, the winds were northeasterly at  $\sim 6 \text{ m s}^{-1}$  throughout 10

**Table C1.** Summary of the EOF correlation analysis from the reconstructed fields. The correlations are all significant at the 95% significance level using the effective number of degrees of freedom derived from the integral time scale.

Year	Months	Correlation coefficient between PC1 of currents and winds	# of significant eigenmodes (currents)	% variance explained by Mode 1 (currents, winds)	% variance explained by Mode 2 (currents, winds)
2010	9 – 10	0.36 <sup>a</sup>	2	50, 63	17, 30
2011	8 – 10	0.56	1	65, 65	9, 27
2012	8 – 10	0.74	2	57, 57	11, 34
2013	9 – 10	0.75	3	66, 60	15, 29
2014	8 – 10	0.83	3	64, 75	14, 19

<sup>a</sup>Low correlation coefficient is because wind Mode 1 in 2010 aligns nearly east-west, but Mode 1 of the currents is in the northeast-southwest direction.

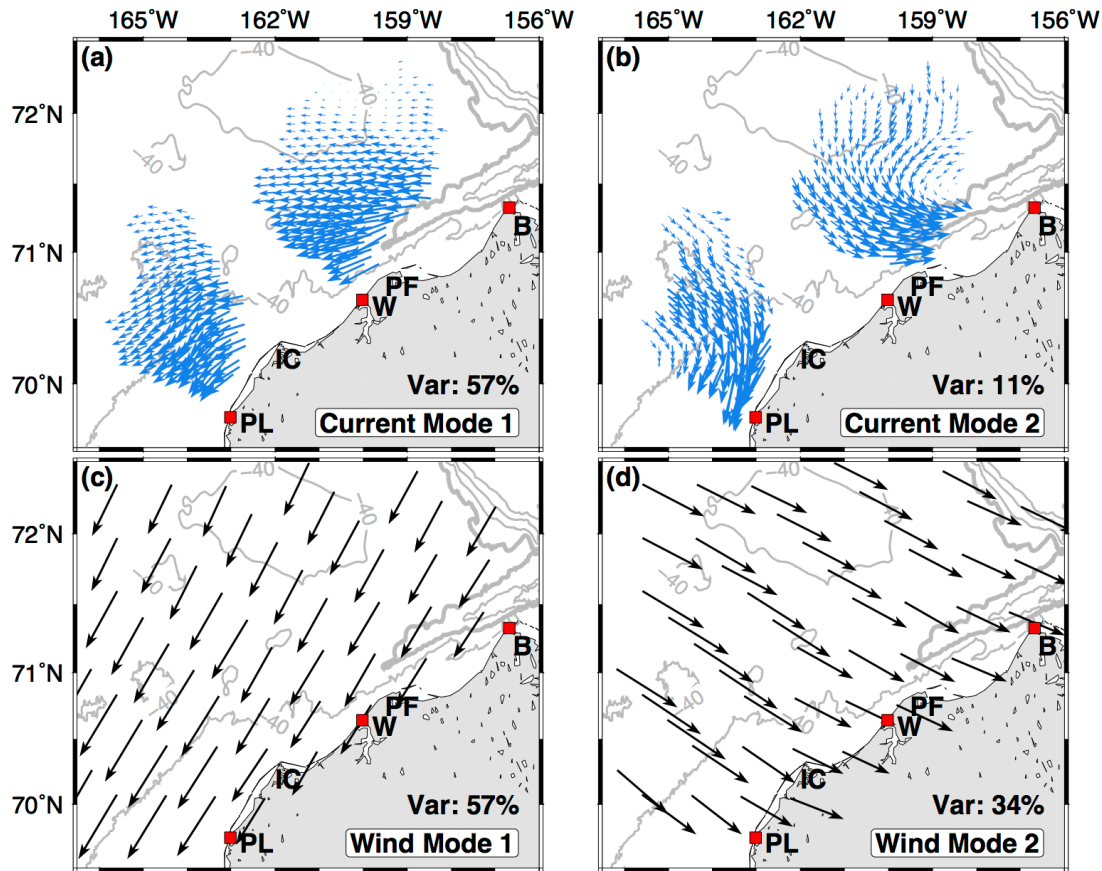


**Figure C5.** (a) EOF Mode 1 of 2012 reconstructed HFR data (blue vectors) and its explained variance. For clarity, only subsampled vectors are shown. (b) As in (a), but for Mode 2. (c) EOF Mode 1 of 2012 NARR winds (black vectors), also subsampled. (d) As in (c), but for Mode 2.

– 13 September, when the pattern corresponded to the divergent mode (indicated by a red arrow, Figure C6). During this period, the current PC1 was  $\sim 0.1$ , indicating the flow field had not yet fully reversed, consistent with the SOM analysis. Therefore, the EOF analysis corroborates the SOM conclusion that northeasterly winds  $\geq 6 \text{ m s}^{-1}$  are critical in shifting the surface circulation through the divergent mode and toward the reversal regime.

We examined four selected periods (labeled T1 – T4, Figure C6) in September that consisted of reversal regimes. Periods T1 – T3 had northeasterly winds  $> 6 \text{ m s}^{-1}$  (i.e., the wind PC1 had values  $> 0.5$ ). Each event was preceded by periods of weaker winds from varying directions. The current PC1 evolved similarly as its values changed from negative to positive. The temporal evolution of PC1 during each of these periods suggests that the reversals lagged the winds by 6 – 9 hours. Period T4 also corresponded to the reversal regime, when winds were northerly with speeds  $> 6 \text{ m s}^{-1}$ . Each of these reversals coincided with southwestward or upcanyon transports of  $\sim 1 \text{ Sv}$  as measured by BC2 (Weingartner et al. 2017a).

The PC1 values for the currents fluctuate when the northwesterly wind regime is present (e.g., 9 – 18 October) but are comparatively small ( $\leq \pm 0.2$ ). The northwesterly wind regime events are not described well by the evolution of PC1 because their overall flow behaviors are different from those associated with Mode 1. Unlike the good correspondence between the evolution of PC1 and the SOM-flow regimes, we do not find a direct relationship between PC2 and the flow regimes. For example, high positive PC2

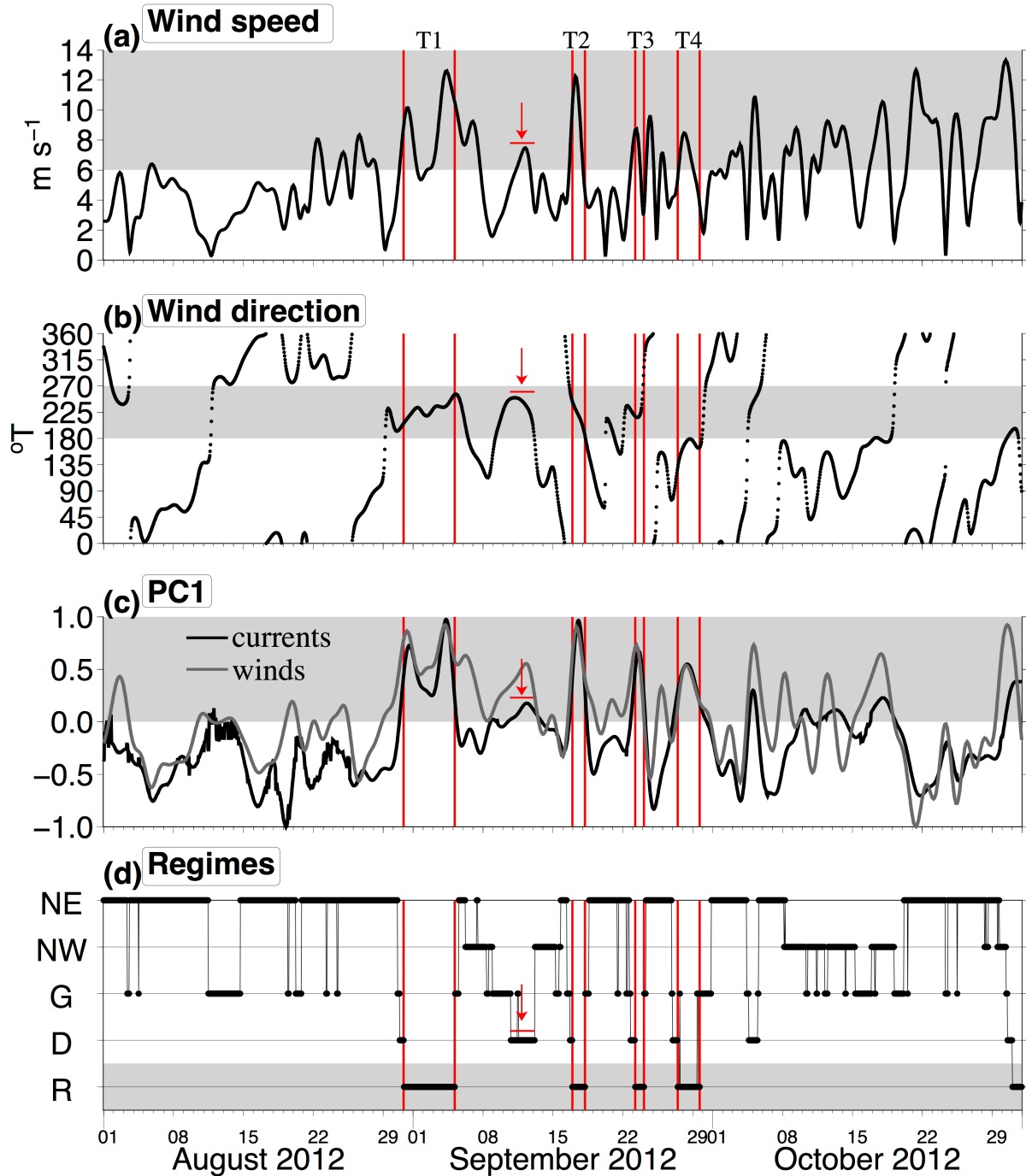


**Figure C6.** (a) Time series of wind speed with wind speeds  $\geq 6 \text{ m s}^{-1}$  highlighted in gray. (b) Time series of wind direction with gray shading corresponding to winds blowing from the northeast quadrant. (c) Time series of PC1 of surface currents (black) and PC1 of winds (gray) with gray shaded areas highlighting positive PC1 values. PC1 values approaching one indicate currents or winds approximating the Mode 1 structure. (d) Time series of representative circulation regimes derived from SOM (black dots): R, reversal (highlighted in gray); D, divergent mode; G, pattern G; NW, northwesterly wind; NE, northeastward-flowing. The gray shaded area highlights the reversal regime. Vertical red lines in each panel denote periods of selected reversal regimes (T1, T2, T3, and T4). Red arrow and bar denote a northeasterly wind event described in the text.

(~0.8) for winds and currents were found in August, but the observed winds and flow fields were predominately southerly and northeastward, respectively. We suspect that EOF Mode 2 of winds and currents is a consequence of the orthogonality requirement of the EOFs computation and thus a limitation of EOFs. Our results suggest that higher order eigenmodes should be interpreted cautiously for data sets containing large variability.

### C.3.4 Mean Circulation Patterns

We formed composite circulation maps for periods when the HFR data recorded downcanyon (northeastward) and upcanyon (southwestward) flow events for 2010 – 2014 (Figure C7). The classifications were defined by average flow conditions derived from twelve HFR grids (Figure C1b) near the head of Barrow Canyon. For the downcanyon condition flow is defined to be toward  $56^\circ\text{T} \pm 4^\circ$ , while for the upcanyon condition it is toward  $236^\circ\text{T} \pm 4^\circ$ , with  $56^\circ\text{T}$  the approximate axis of Barrow Canyon. Mean downcanyon and upcanyon patterns observed by HFR are comparable with the SOM-derived northeastward-flowing and reversal regimes, respectively.

For the 5-year period, we found 868 hourly surface current observations satisfying our downcanyon criterion. The polar histogram indicates that ~75% of the time the downcanyon pattern occurs under variable wind directions at moderate wind speeds ( $\leq 6 \text{ m s}^{-1}$ ). Approximately 25% of the winds were northeasterly ( $203 - 246^\circ\text{T}$ ), with only 5% of those  $> 6 \text{ m s}^{-1}$ . These strong northeasterlies are the catalyst for a reversal to upcanyon flow, and thus indicate when the flow field lagged the wind. The downcanyon average suggests four distinct flow regions (Figure C7a; labeled 1 – 4) under mean winds of  $\sim 1 \text{ m s}^{-1}$  westward ( $\sim 264^\circ\text{T}$ ). Region 1 lies north of  $71.5^\circ\text{N}$  on the eastern flank of Hanna Shoal, and here the mean currents are weak (a few  $\text{cm s}^{-1}$ ) and directionally variable. The flow in Region 2 is generally eastward with mean currents  $5 - 10 \text{ cm s}^{-1}$ , consistent with results from moorings, ship-borne surveys, and models (Winsor and Chapman 2004; Weingartner et al. 2005; Spall 2007; Gong and Pickart 2015). In the northwestern part of Region 2 the flow is southeastward, suggestive of flow moving eastward from the Central Channel across the shelf south of Hanna Shoal. Region 3 encompasses the head of Barrow Canyon, where mean currents are northeastward and swift ( $\sim 30 \text{ cm s}^{-1}$ ). The mean currents in Region 4, which covers the southern portion of the southern radar mask, are northeastward at  $\sim 10 \text{ cm s}^{-1}$ . The downcanyon average suggests convergence of the nearshore flow with that from the central shelf near  $70.8^\circ\text{N}$ ,  $162.5^\circ\text{W}$ , with current speeds increasing as these flows converge.

Observations consistent with the upcanyon criterion were fewer, with only 368 hourly values. Mean winds for the upcanyon composite (Figure C7b) were  $\sim 7 \text{ m s}^{-1}$  toward  $\sim 236^\circ\text{T}$ , consistent with the reversal regime. Winds were ~70% northeasterly, ~6% northerly, and ~11% easterly. Overall the currents are stronger than those of the downcanyon average. Surface currents in Region 1 are westward at  $\sim 9 \text{ cm s}^{-1}$ , diminishing northward, while currents in Region 2 are westward or northwestward at  $15 - 20 \text{ cm s}^{-1}$ , which could carry canyon waters toward the south side of Hanna Shoal and across the central shelf. Currents near Barrow Canyon (Region 3) are particularly strong, with a mean of  $\sim 50 \text{ cm s}^{-1}$  to the southwest ( $\sim 240^\circ\text{T}$ ). The flow in Region 4 is also southwestward ( $\sim 240^\circ\text{T}$ ) but with speeds of  $\sim 20 \text{ cm s}^{-1}$ .

The composites indicate that the down- and upcanyon flow structures in Regions 2 and 3 are mirror images of each other; however, Regions 1 and 4 are quite different from one another. For the upcanyon case, in Region 1 the flow is westward and oriented  $\sim 35^\circ$  to the right of the wind. For the downcanyon case the surface currents are weak and variable. We show later that the surface flow in Region 1 is consistent with Ekman dynamics.

For the Region 4 downcanyon case, the mean current speed is maximum ( $\sim 25 \text{ cm s}^{-1}$ ) over the 40 m isobath and not statistically different ( $p < 0.05$ ) from the speed over the 30 m isobaths, but in the upcanyon case, the mean speeds along these isobaths are significantly different from one another. It is maximum

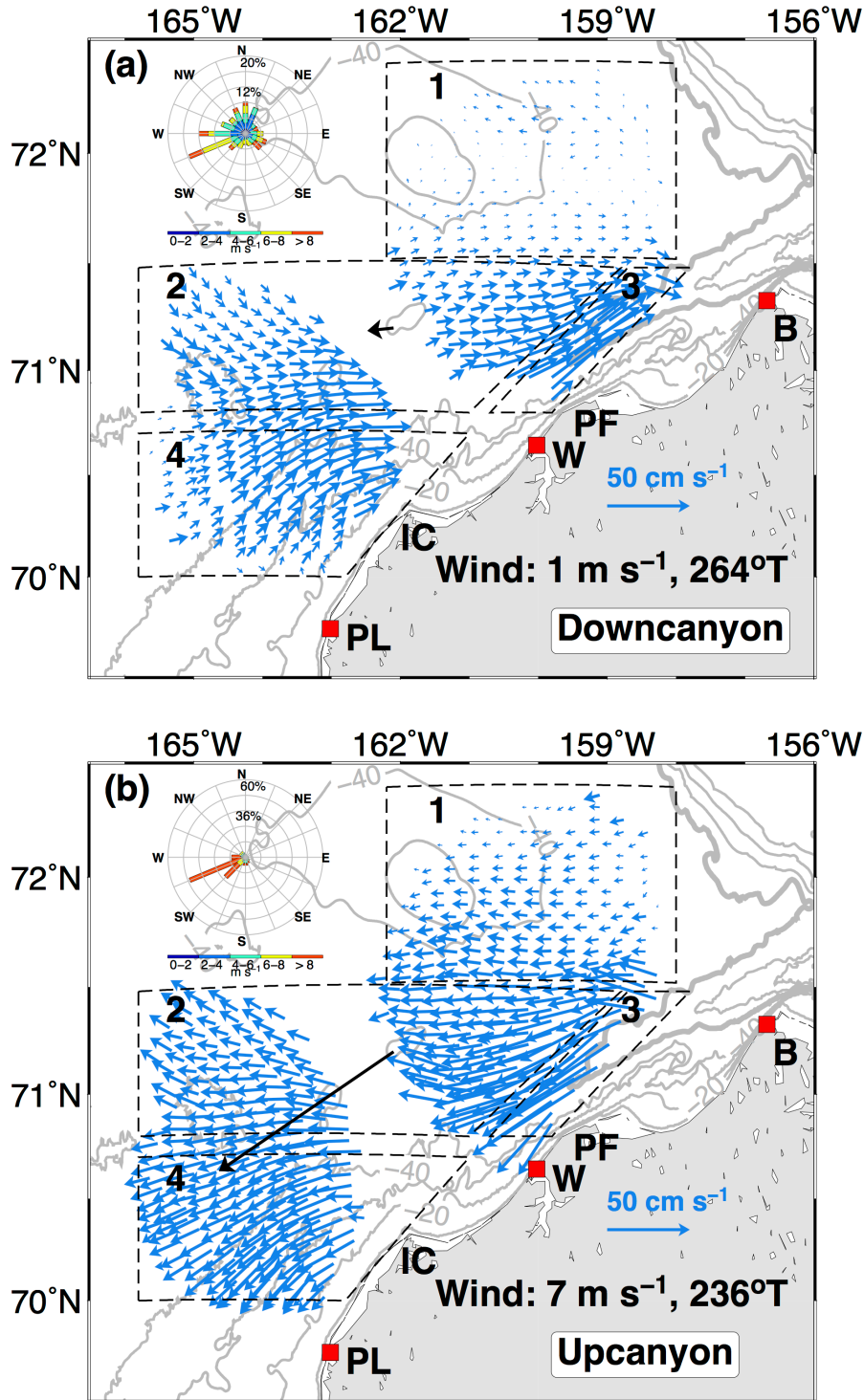


**Figure C7.** Mean (a) downcanyon and (b) upcanyon surface currents (blue vectors) for 2010 – 2014. Bathymetric contours (gray lines) are drawn within 200 m at 40 m intervals, with depths less than 40 m drawn at 10 m intervals. The black vector denotes the mean winds, and the polar histogram along 72°N denotes wind velocities. Areas circumscribed by dashed lines denote regions (labeled 1 – 4) of distinct flow behaviors (see text). For clarity, the vectors were subsampled.

( $\sim 38 \text{ cm s}^{-1}$ ) over the 30 m isobath and monotonically decreases offshore with the flow being  $\sim 32 \text{ cm s}^{-1}$  over the 40 m isobath. These differences imply an asymmetry in the alongshore transport, with more transport carried by the inner shelf flow during upcanyon events compared to downcanyon cases. In the upcanyon case, the alongshore winds cause a sea level setdown and an alongshore southwestward flow established by the cross-shore pressure gradient. This gradient should be greatest within  $\sim 50 \text{ km}$  of the coast, which is the e-folding scale for the 140 km barotropic radius of deformation (for a shelf depth of 40 m). In the downcanyon mean the winds are weak and directed offshore, in which case the mean flow is largely forced by the poleward pressure field and appears strongest over the 40 m isobath. This suggestion is consistent with the convergence in modeled streamlines shown by Winsor and Chapman (2004) and Spall (2007) for the same region.

### C.3.5 Spatial Correlation Structure

In this section we use the complex correlation function (Kundu and Allen 1976) to examine the spatial correlation structure of the down- and upcanyon flows using the DINEOF reconstructed data. The calculations use two reference grid points. The first, at  $71.2^\circ\text{N}$ ,  $160^\circ\text{W}$ , is chosen to examine relationships between flow near Barrow Canyon and those elsewhere. The second grid point, at  $72^\circ\text{N}$ ,  $160^\circ\text{W}$ , is over Hanna Shoal.

Based on the sample number (1148 for downcanyon; 249 for upcanyon) and estimated integral time scale ( $\sim 40$  hour) from the 2012 DINEOF field, the 95% significance levels for the down- and upcanyon correlations are 0.36 and 0.71, respectively. The correlation field using the Barrow Canyon grid point is similar for both flows (Figures C8a-b), with correlations high in the canyon and across the southern mask but much smaller north of  $71.5^\circ\text{N}$ . The correlated regions are quite large. For example, the largest distance between grid points with correlations  $\geq 0.8$  is  $\sim 170 \text{ km}$  for the downcanyon case and  $\sim 300 \text{ km}$  for the upcanyon.

Using the Hanna Shoal grid point, the well-correlated region is limited to the area north of  $71.5^\circ\text{N}$  for the downcanyon case (Figure C8c). The length scale of the strongest correlation is only  $\sim 30 \text{ km}$ , as expected given that the contributing currents are weak and variable in this region (Figure C7a). For the upcanyon case (Figure C8d), the spatial correlation structure is again significant and mainly confined to the region north of  $71.5^\circ\text{N}$  over a length scale of  $\sim 120 \text{ km}$ . In aggregate, the SOM and the mean and correlation fields indicate that the shelf circulation north of  $71.5^\circ\text{N}$  is dynamically different from the shelf to the south.

## C.4 Discussion

Our analyses have revealed two major surface circulation regimes related to the local winds. The northeastward-flowing regime transports water from along the coast and the central shelf into Barrow Canyon and toward the Arctic Ocean. During summer and early fall, this surface transport involves warm, low-salinity coastal waters and somewhat more saline waters from the central shelf. The reversal regime transports waters up the canyon and across the Chukchi shelf, suggesting upwelling within the canyon and along the west coast of Alaska. We also identified the divergent mode, a transitional flow field established as northeasterly winds intensify, which eventually evolves into the reversal regime. This mode includes divergence in the nearshore currents between Icy Cape and Wainwright, with one branch leading into Barrow Canyon and the other proceeding southwestward. In addition, we found that the currents north of  $71.5^\circ\text{N}$  (Region 1 in Figure C7) are distinctly different from the currents south of this latitude. We explore these findings in greater detail in the following paragraphs.

In summer and fall, a portion of the Bering Strait inflow is carried eastward from the Central Channel and merges with ACC waters as they approach Barrow Canyon. This eastward flow is represented in

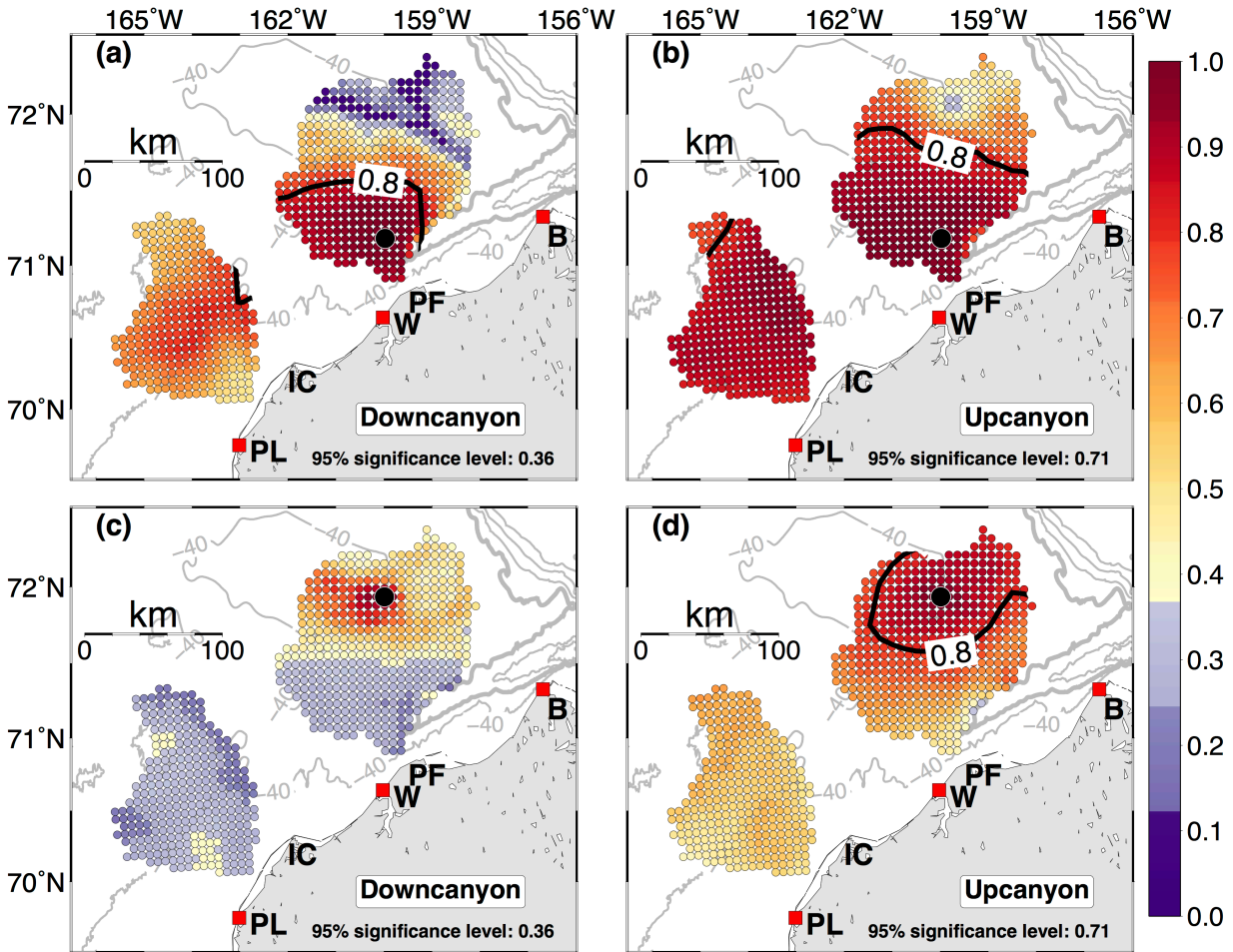


**Figure C8.** Spatial distribution of complex correlations of surface currents with respect to a reference grid point (large black dot) for (a, c) downcanyon and (b, d) upcanyon flow. Black contour denotes the 0.8 correlation level. Correlation below the e-folding scale is shaded in cool colors. The 95% significance level is estimated from the effective number of degrees of freedom using the integral time scale.

circulation models forced solely by the poleward pressure gradient (Winsor and Chapman 2004; Spall 2007), in prior observations (Weingartner et al. 2005, 2013a), and is largely consistent with the northeastward-flowing regime (Figure C2a) and observed downcanyon mean (Figure C7a). The models also indicate that some of the Central Channel transport flows geostrophically around the north side of Hanna Shoal. Along the east side of the Shoal the modeled flow is southward before turning eastward into the head of Barrow Canyon. This southward flow is much weaker than that on the western side because the isobaths diverge on the northeast side of the Shoal. However, the modeled southward flow is not captured by the SOM, nor is it evident in the vertically-averaged mean flows estimated from moorings on the shelf east of Hanna Shoal (Weingartner et al. 2017a).

We believe that one cause in the differences in surface circulation north and south of 71.5°N lies with the shelf hydrographic structure. Figure C9 shows vertical sections of potential temperature ( $\theta$ ) and salinity ( $S$ ) along Legs 1 and 2 (Figure C1) from September 2013. In both sections waters deeper than ~20 m were cold ( $<-1^{\circ}\text{C}$ ) and salty ( $\geq 32.5$ ) winter waters. North of 71.5°N a ~15 m deep surface layer contained

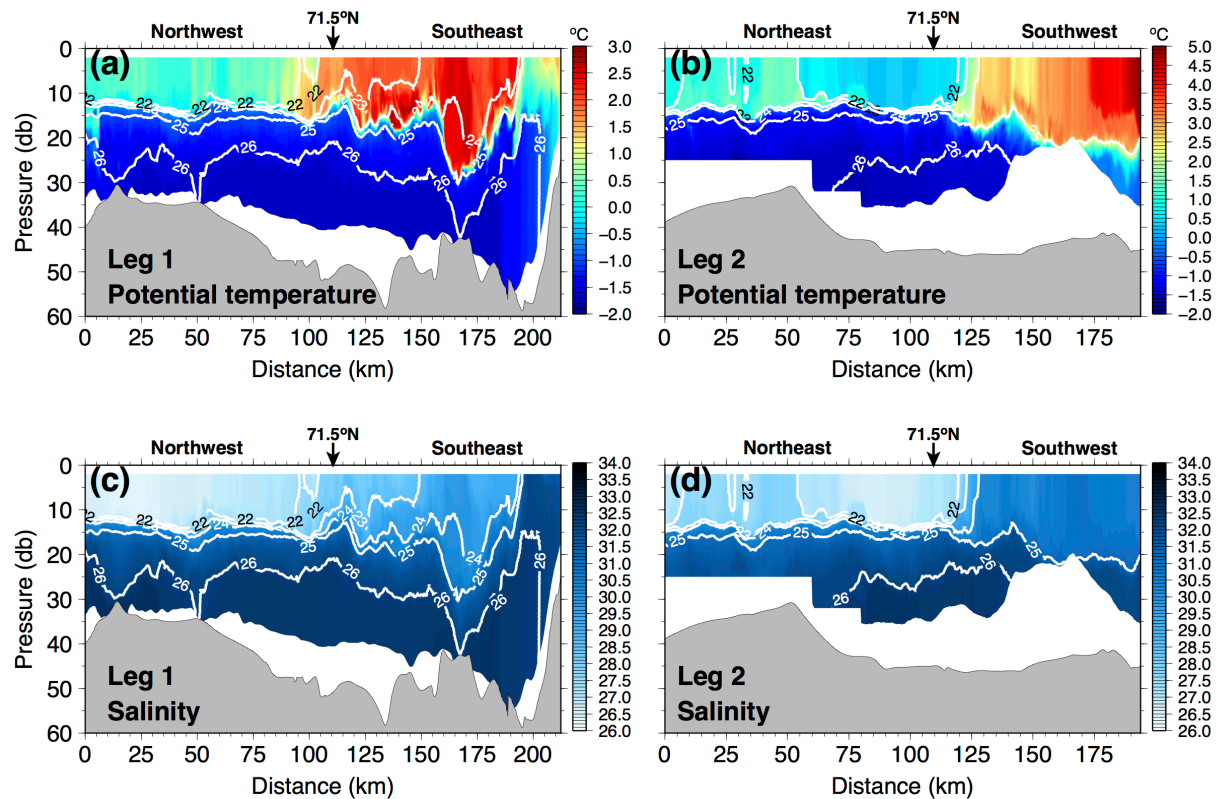


**Figure C9.** Vertical sections from September 2013 of potential temperature and salinity overlain with isopycnals (white contours) for (a, c) Leg 1 and (b, d) Leg 2. Black arrow denotes the location of 71.5°N. Note that the shading scales in (a) and (b) and the horizontal scales for Legs 1 and 2 are different.

cool (0°C) and fresh (salinity ~26 – 29) meltwaters (MW) underlain by a thin but strong pycnocline. South of 71.5°N the stratification was weaker and the surface waters were warmer (3 – 5°C), moderately salty (salinity ~31), and derived from Bering Sea summer waters. The front delineating these surface water masses was centered near 71.5°N. Similar fronts around this latitude are apparent in sections shown by Lu et al. (2015) and Weingartner et al. (2017b). The latter find that the shelf north of 71.5°N and east of Hanna Shoal supports a counterclockwise baroclinic geostrophic flow component that opposes the modeled barotropic flow around the Shoal. These opposing pressure tendencies result in weak geostrophic flow.

We suggest that the strong stratification north of 71.5°N in conjunction with weak geostrophic flow suggests that the surface currents in this region are largely governed by Ekman dynamics, with the Ekman layer presumably confined to the upper 15 m. For the upcanyon case, the mean winds were  $\sim 7 \text{ m s}^{-1}$  toward  $\sim 236^\circ\text{T}$ , which would impel a mean flow in the upper 15 m of  $\sim 6 \text{ cm s}^{-1}$  toward  $326^\circ\text{T}$ . The observed flow (within the upper 2 m) averaged  $9 \text{ cm s}^{-1}$  toward  $270^\circ\text{T}$  (i.e.,  $\sim 34^\circ$  to the right of the wind). As discussed in Dzwonkowski et al. (2011), baroclinic shear and stratification inhibit deepening of the surface boundary layer and reduce its interaction with the bottom boundary layer, resulting in enhancement of surface transport. South of 71.5°N the stratification is weaker and the flow is primarily barotropic and geostrophic (Weingartner et al. 2013a), so that wind momentum is diffused over much of the water column.

We next examine the dynamics associated with the divergent mode aided by snapshots of wind and surface current maps (Figure C10) from September 2011. The maps encompass a period when the winds transitioned from southerly (12 September; Figure C10a) to strong northeasterly (15 – 19 September; Figure C10b-d). Each map includes a vector showing the wind at the measurement time (black) along with the wind vectors for the preceding 12 (dark gray) and 24 hours (light gray).

Prior to 12 September the winds were southwesterly, and the northeastward-flowing regime held. At this time both the poleward pressure gradient and the coastal sea level setup acted in concert to propel the flow. On 13 September (not shown), the winds became east- northeasterly, and the divergent mode appeared for the next few days (Figure C10b). This transitional mode consisted of westward Ekman drift north of  $\sim 71.5^\circ\text{N}$  and southwestward alongshore flow inshore of the 30 m isobath offshore of Point Lay. The time scale for the appearance of these two circulation features is plausible. The Ekman adjustment time scale is only a few hours (Allen 1973), whereas the spinup time scale for the alongshore flow is proportional to  $h/r$ , where  $h$  is the water depth and  $r$  is the linear bottom friction coefficient. The adjustment to southwestward flow in the shallow ( $<30$  m) nearshore waters should be  $\leq 0.5$  day for

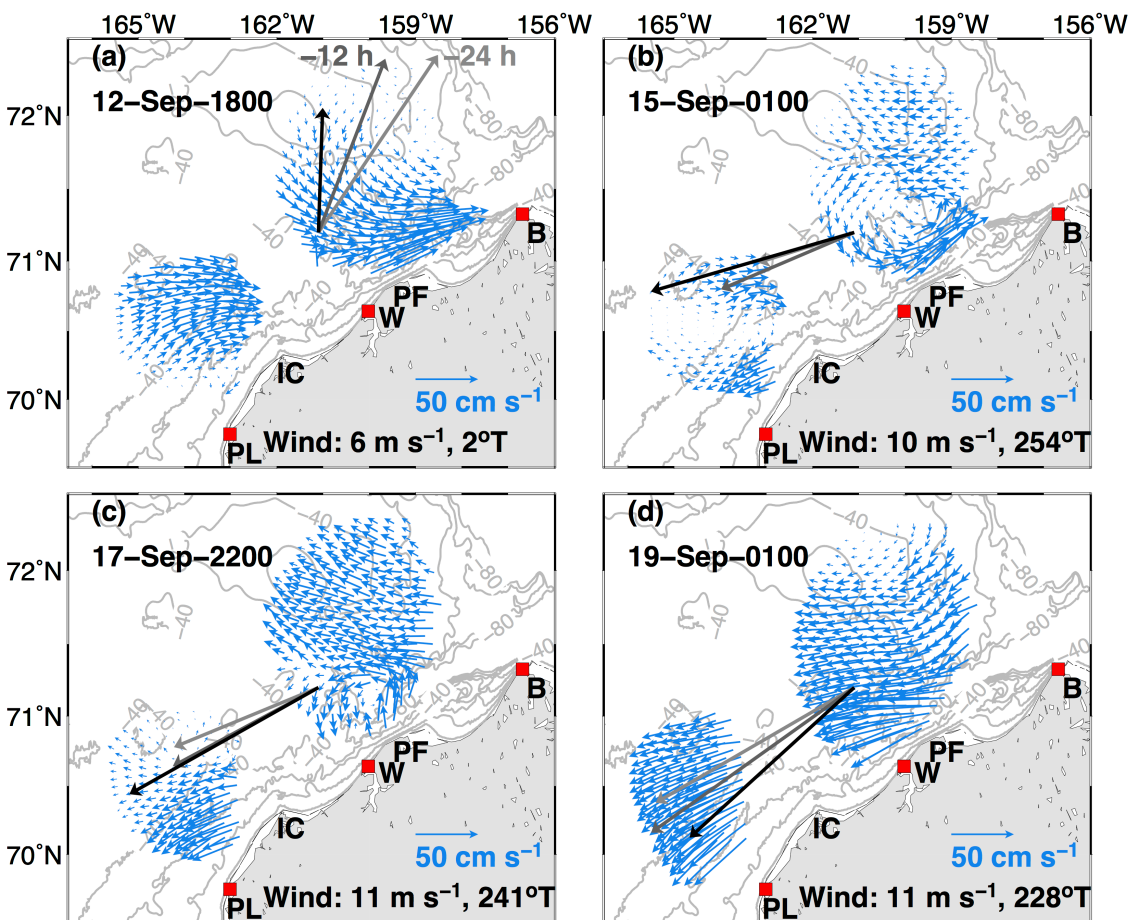


**Figure C10.** HFR observations (blue vectors) during 12 – 19 September 2011 at indicated UTC time. The black vector denotes the wind at the cardinal hour of the snapshot, with the magnitude and direction shown in the legend, and the gray shaded vectors are winds for the preceding 12 and 24 hours. Bathymetric contours (gray lines) are drawn within 80 m at 10 m intervals. For clarity, the current vectors were subsampled.

$r \sim 5 \times 10^{-4} \text{ m s}^{-1}$  (e.g., Brink 1998) but longer in deeper waters. Apparently there is a ridge in the cross-shore pressure gradient northwest of Icy Cape near  $\sim 70.5^\circ\text{N}$ , manifested in the velocity field as the region of negligible flow along  $\sim 70.5^\circ\text{N}$  on 15 September (Figures C10b). Note that the width of the southwestward flow is  $\sim 90 \text{ km}$  and less than the local barotropic radius of deformation ( $\sim 130 \text{ km}$ ). The implication is that although the cross-shore sea level gradient sloped downward onshore, it was of insufficient magnitude to reverse the pressure gradient farther offshore or in Barrow Canyon. By 17 September (Figure C10c) the winds had veered more towards the southwest. In response, canyon waters offshore of Point Franklin began veering northward, while the area of southwestward flow between Icy Cape and Point Lay expanded offshore. The winds continued to veer toward the southwest and intensified such that by 19 September the reversal regime was fully established, with the swiftest flows in the canyon and along the coast (Figure C10d). The divergent mode, although generally short-lived, thus has the potential to disperse materials advected from the central shelf along the coast of western Alaska and into Barrow Canyon.

We expect that the SOM-derived surface circulation patterns occur throughout the year and that the divergent mode should occur more frequently through late fall and winter when transitions between downcanyon and upcanyon flow events are more common (Weingartner et al. 2017a). However, threshold wind speeds that catalyze the changes amongst the various modes may differ given that the surface stress will be modulated by sea ice.

## C.5 Summary

We used SOM and EOFs in an examination of HFR-derived surface current patterns in the northeastern Chukchi Sea during the open-water seasons (nominally August – October) from 2010 – 2014. We identified major surface current circulation patterns and their dynamics in conjunction with regional winds and showed how this portion of the shelf surface circulation responds to the wind field and a background poleward pressure gradient.

We found that surface currents south of  $\sim 71.5^\circ\text{N}$  and in Barrow Canyon flow northeastward except when northeasterly winds exceed  $\sim 6 \text{ m s}^{-1}$ . The northeastward flow is primarily a manifestation of the large-scale pressure gradient between the Pacific and Arctic Oceans. When northeasterly wind speeds are  $>6 \text{ m s}^{-1}$ , the coastal sea level setdown is large enough to cause southwestward surface flow inshore and westward flow over the central shelf. Less frequently southward surface currents occur over portions of the domain in response to northwesterly or westerly winds exceeding  $\sim 6 \text{ m s}^{-1}$ .

We also detected the divergent mode, a transitional circulation feature of 1 to 5 days duration, which develops as the flow field adjusts from northeastward to southwestward in response to intensifying northeasterly winds. The divergent mode is characterized by eastward (onshore) flow across the central shelf, which diverges upon approaching the coast. A portion of this onshore flow continues into the head of Barrow Canyon while the remainder turns southwestward inshore of the 40 m isobath; however, sampling constraints prevented us from a precise determination of the nature of the divergence between these two regions. The divergent mode is a consequence of interaction amongst the poleward pressure gradient, increasing northeasterly winds ( $>\sim 6 \text{ m s}^{-1}$ ), local bathymetry, and the regional hydrographic structure.

Along  $\sim 71.5^\circ\text{N}$  there is an extensive zonally-oriented front. North of this front, surface pressure gradients are weak, and the surface currents are Ekman-like. The strong Ekman response occurs because the water column is strongly stratified; fresh, cool MW occupies the upper 15 m, and cold, salty winter waters occupy the bottom layer. South of the front the manifestation of the poleward pressure gradient is stronger, and the water column is less stratified, with the surface layer containing moderately salty and warmer Bering Sea summer waters.

## D. Transport and Thermohaline Variability in Barrow Canyon on the Northeastern Chukchi Sea Shelf

### Abstract

We used a 5-year time series of transport, temperature, and salinity from moorings at the head of Barrow Canyon to describe seasonal variations and construct a 37-year transport hindcast. The latter was developed from summer/winter regressions of transport against Bering-Chukchi winds. Seasonally, the regressions differ due to baroclinicity, stratification, spatial and seasonal variations in winds and/or the surface drag coefficients. The climatological annual cycle consists of summer downcanyon (toward the Arctic Ocean) transport of  $\sim 0.45$  Sv of warm, fresh waters; fall (October – December) upcanyon transport of  $\sim 0.1$  Sv of cooler, saltier waters; and negligible net winter (January – April) mass transport when shelf waters are saline and near-freezing. Fall upcanyon transports may modulate shelf freeze-up, and negligible winter transports could influence winter water properties. Transport variability is largest in fall and winter. Daily transport probability density functions are negatively skewed in all seasons, leptokurtic in summer and platykurtic in fall/winter. Kurtosis differences are manifested by transport intermittency with possible consequences for shelf-basin exchanges. The climatology implies that the Chukchi shelf circulation reorganizes annually: in summer  $\sim 40\%$  of the summer Bering Strait inflow leaves the shelf via Barrow Canyon, but from fall through winter all of it exits via the western Chukchi or Central Channel. We estimate a mean transport of  $\sim 0.2$  Sv;  $\sim 50\%$  less than estimates at the mouth of the canyon. Transport discrepancies may be due to inflows from the Beaufort shelf and from the Chukchi shelfbreak, with the latter entering the western side of the canyon.

### D.1 Introduction

Pacific-derived waters flowing northward through Bering Strait cross the Chukchi Sea along three principal pathways: Barrow Canyon on the northeastern shelf, Herald Valley in the west, and the Central Channel over the central shelf. The Pacific inflow is a substantial source of nutrients and carbon (Walsh et al. 1989; Codispoti et al. 2005; Nishino et al. 2011), heat (Steele et al. 2004; Shimada et al. 2006; Woodgate et al. 2010; Corlett and Pickart 2017), and freshwater (Yamamoto-Kawai et al. 2008) to the polar basin. The partitioning of the inflow amongst these channels is poorly understood, although it is clear that the transport variations are largely associated with winds over the Pacific sector of the Arctic (Winsor and Chapman 2004; Spall 2007; Danielson et al. 2014). Changes in Pacific water fluxes through these channels can affect rates and patterns of ice processes, biological production, and the potential vorticity (PV) structure of the adjacent shelfbreak and slope. The latter has consequences on shelf-basin exchange processes (Spall et al. 2008) and the circumpolar slope circulation (Spall 2013). Herein, we use a 5-year time series of moored measurements to examine hydrographic and transport variability at the head of Barrow Canyon and to construct a transport climatology using 37 years of regional winds.

Barrow Canyon extends  $\sim 220$  km from its head, north of Wainwright, to its mouth on the continental slope (Figure D1). Bottom depths increase linearly along its length from 50 m to 300 m. Between Wainwright and Barrow ( $\sim 140$  km) the canyon is bounded by the Alaskan coast; whereas north of Point Barrow, the canyon delimits the western end of the Beaufort Sea shelf. The western wall of the canyon adjoins a broad, shallow (40 – 60 m) bench that extends  $\sim 80$  km westward to Hanna Shoal. In cross-section, the canyon is nearly U-shaped, with the width varying from  $\sim 40$  km at its head to  $\sim 60$  km at its mouth (based on the distance between the 70 m isobaths on either side of the canyon mouth). The aspect ratio ( $d$ ), the ratio of the cross- to along-canyon length scales, is  $\sim 0.3$ .

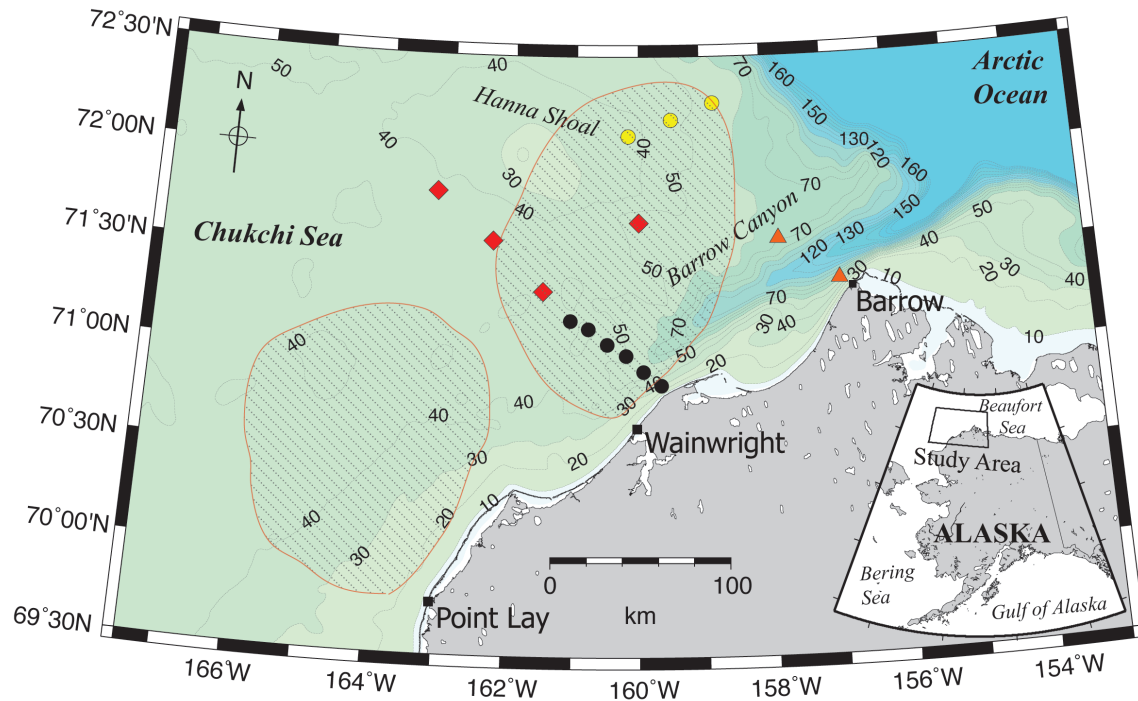


**Figure D1.** Bathymetric map of the northeastern Chukchi Sea showing mooring locations. The 2010 – 2012 arrays of 6 moorings are shown with black dots and consist of moorings BC1 (closest to the coast) through BC6. Additional moorings, summarized in the discussion, are shown using colored symbols. HFRs were located in Point Lay, Wainwright, and Barrow. The striped regions encapsulate that portion of the HFR mask containing 50% or more good data.

Most submarine canyons that incise shelfbreaks lie athwart the prevailing along-shelf currents that control the canyon circulation (e.g., Allen and Durrieu de Madron 2009). Barrow Canyon shares this feature insofar as the flow over the Chukchi/Beaufort shelfbreak is transverse to the canyon axis (e.g., Mountain et al. 1976; Pickart 2004; Nikolopoulos et al. 2009). In contrast to most canyons, currents along the longitudinal axis of Barrow Canyon are swifter than the transverse flows nearer its mouth and are strongly influenced by Bering and Chukchi shelf processes operating to the south. These shelf regions are also the source of summer and fall waters comprising the horizontally- and vertically-structured along-canyon flow (Pickart et al. 2005; Shroyer and Plueddemann 2012). The contributing water masses include moderately salty Bering Sea Water, fresh, warm Alaskan Coastal Water (ACW; Coachman, et al. 1975), near-freezing, saline winter-formed waters (WW) derived from ice production, and cool, dilute ice-meltwaters (MW).

The most comprehensive set of long-term transport measurements in Barrow Canyon is by Itoh et al. (2012) and Itoh et al. (2013). They used 3 moorings at the mouth of the canyon to estimate seasonal and interannual variations in canyon transports of mass, heat, and freshwater from 2000 – 2008. Their moorings were deployed at 10 km intervals, from east to west, on the 80, 250, and 150 m isobaths, respectively. They estimated a mean average transport of 0.45 Sv northeastward (which with the convention adopted in this paper is the downcanyon or positive flow direction) and into the Arctic Ocean. This flow opposes the mean northeasterly winds and is a consequence of the Pacific-Arctic pressure gradient that is also responsible for the mean northward transport in Bering Strait. Itoh et al. (2013) find that the flow varies seasonally and in-phase with the annual cycle of Bering Strait transport; i.e., maximum downcanyon transport occurs in summer, and minimum transport occurs in winter. In

accordance with previous studies (Aagaard and Roach 1990; Münchow and Carmack 1997; Weingartner et al. 1998; Pickart et al. 2005; Woodgate et al. 2005a; Itoh et al. 2012), they find that transport variations are primarily wind-forced, include reversals, have magnitudes of  $\sim 0.5 - 1.0$  Sv, and durations of one to many days.

Our measurements, made at the head of Barrow Canyon  $\sim 190$  km southwest (upcanyon) of the arrays discussed by Itoh et al. (2013), were part of a larger program to examine connections between Barrow Canyon, the northeastern Chukchi shelf, and the western Beaufort shelf in a region contemplated for offshore oil development. Section 2 describes the data sets. Section 3 examines kinematic features and transport variability derived from the observations. These data and regional winds are used to hindcast a 37-year (1979 – 2015) transport record. This section also examines the hydrographic properties in relation to circulation variability. Section 4 examines why our transports differ from Itoh et al.'s (2013) values and discusses potential implications of our findings on the Chukchi and Beaufort shelves and slopes. Section 5 summarizes the paper.

## **D.2 Methods**

### **D.2.1 Moorings**

From August 2010 – September 2012, six moorings (BC1 inshore to BC6 offshore), spaced  $\sim 13$  km apart, spanned the head of Barrow Canyon (Figure D1). Each mooring contained an upward looking 300 or 600 kHz Teledyne ADCP and a temperature/conductivity/pressure (TCP) recorder (Sea-Bird 37 or Sea-Bird 19). Moorings BC2 – BC5 included bottom-tracking for measuring ice keel depths and ice drift. Bottom-tracking was inactive on BC1 and BC6 because these included directional wave firmware (wave data are not discussed here). The TCP and ADCP were housed in a float situated  $\sim 4$  m above bottom and sampled hourly. BC1, nearest the coast, was deployed in a water depth of 31 m with its instruments mounted 1 m above the bottom in a Sea Spider frame. This design minimized damage from nearshore ice keels that can exceed 25 m depth. After recovering the array in September 2012, we deployed a single mooring (BC2) in succeeding years. We will show that BC2 provides statistically valid estimates of along-canyon transport, so BC2 data served as a proxy for transport from September 2012 to early August 2015. Table D1 lists positions, depths, and period of record for each mooring. There were several gaps in the mooring data due to premature failure of the ADCP on mooring BC2. As explained below, we filled some of these gaps with other data.

To provide context over a wider area of the shelf, we obtained mooring data supported by other programs. The red diamonds in Figure D1 indicate the locations of oil industry-sponsored moorings described by Mudge et al. (2015). The yellow circles are three moorings deployed northeast of Hanna Shoal (supported by the Bureau of Ocean Energy Management), and the two orange triangles are moorings (courtesy of S. Okkonen) spanning the canyon east of Barrow.

### **D.2.2 High-Frequency Radars (HFR)**

During the open water seasons of 2010 – 2014 we measured hourly surface currents (upper 2 m) at 6 km horizontal resolution in the northeast Chukchi Sea using  $\sim 5$  MHz HFRs (CODAR Ocean Sensors). Subsets of these data fill gaps in the transport time series. Field sites were located in the villages of Point Lay, Barrow, and Wainwright (Figure D1), which allowed collecting surface current data nominally within 180 km of the coast. An additional system was deployed at Cape Simpson (Figure D15) in 2013 and paired with the Barrow system to map currents in the western Beaufort Sea and over the mouth of the canyon. HFR calibrations were applied following (Barrick and Lipa 1986; Kohut and Glenn 2003), and HFR data were processed according to Weingartner et al. (2013a).

**Table D1.** Mooring positions and depths for the Barrow Canyon (BC) array and locations of NARR wind gridpoints.

2010 – 2011					
Mooring Name	Latitude (°N)	Longitude (°W)	Bottom Depth (m)	ADCP Depth (m)	ADCP Period of Record
BC1	70.85	-159.67	30.1	29	18 Aug. – 26 Aug.
BC2	70.92	-159.94	52.3	49	17 Aug. – 20 Aug.
BC3	71.00	-160.21	53.3	48.5	17 Aug. – 26 Aug.
BC4	71.06	-160.49	49.3	45	17 Aug. – 26 Aug.
BC5	71.13	-160.79	49.5	45.5	17 Aug. – 26 Aug.
BC6	71.17	-161.07	46.6	43	18 Aug. – 26 Aug.
2011 – 2012					
BC1	70.85	-159.67	30.1	29	30 Aug. – 7 Jul.
BC2	70.92	-159.94	52.3	49	30 Aug. – 4 May
BC3	71.00	-160.21	53.3	48.5	30 Aug. – 4 Jul.
BC4	71.06	-160.49	49.3	45	30 Aug. – 19 Jul.
BC5	71.13	-160.79	49.5	45.5	30 Aug. – 3 May
BC6	71.17	-161.07	46.6	43	30 Aug. – 31 Oct. (2011)
2012 – 2013					
BC2	70.92	159.94	52.3	49	9 Sep. – 13 Aug.
2013 – 2014					
BC2	70.92	159.94	52.3	49	11 Sep. – 24 Sep.
2014 – 2015					
BC2	70.92	159.94	52.3	49	24 Sep. – 10 Aug.
NARR Wind Gridpoints					
Geographic Area		Latitude (°N)		Longitude (°W)	
Barrow Canyon (BC2)		70.92		159.94	
Bering Strait (A3)		66.33		168.97	
Northern Bering Sea (C40)		60.34		169.02	

### D.2.3 Winds

Wind and sea level pressure (SLP) estimates were obtained from NOAA’s North American Regional Reanalysis (NARR) models (Mesinger et al. 2006) at gridpoints near the Barrow Canyon mooring array (BC2), Bering Strait, and the northern Bering Sea (Table D1). Both variables have space and time resolutions of 32 km and 3 hours, respectively.

## D.3 Results

### D.3.1 Kinematic Description

All six moorings from the 2010 – 2011 array provided year-long data sets. These data, lowpass-filtered to remove diurnal and shorter period fluctuations, are used to describe kinematic features of the flow at the head of the canyon. The record-length mean vertically-averaged velocity vectors and variance ellipses (Figure D2a) show that between moorings BC1 and BC3, the mean flow was northeastward at between 0.1 and 0.2 m s<sup>-1</sup>, with maximum values at BC2. Farther offshore (moorings BC4 – BC6), the mean

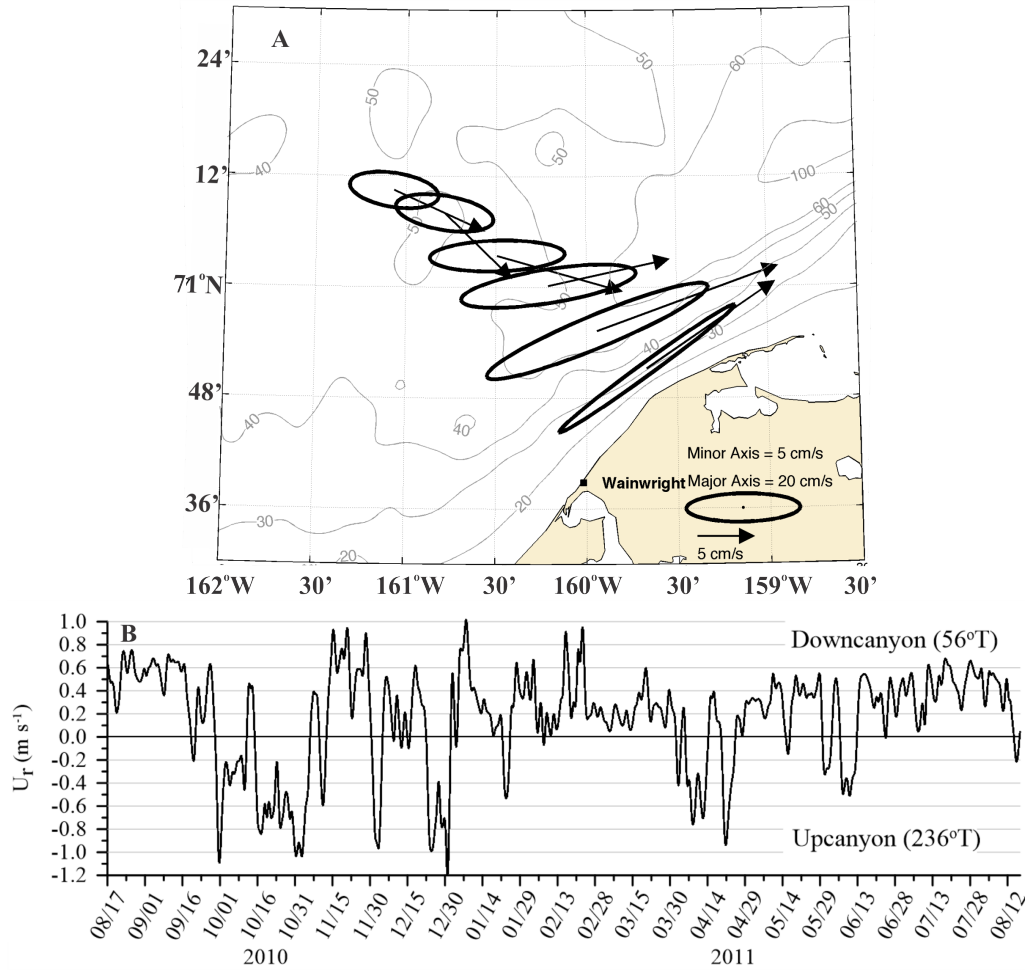


**Figure D2.** A) Vertically-averaged velocity vectors and variance ellipses for the moorings at the head of Barrow Canyon. Note the velocity scale change between the mean vector and the variance ellipse. B) Time series of the along-canyon currents at 20 m depth at mooring BC2. Both figures are based on the August 2010 – August 2011 mooring records.

vectors were east-southeastward and onshore at  $\sim 0.1 \text{ m s}^{-1}$ . The vectors imply that upon entering the western side of the canyon head the mean flow veered counterclockwise by  $\sim 25^\circ$  over a radius of 13 km (between BC4 and BC3), so the bulk of the along-shore flow occurred within  $\sim 35$  km of the coast. Ellipse orientations were along-shore polarized at the four inshore moorings (BC1 – BC4; where the topographic slopes are greatest) and cross-shore polarized at the two outer moorings (BC5 and BC6). Standard deviations of the along-shore flow were three times the mean values at BC1 – BC3 and twice the means at BC4 – BC6. On a monthly basis, the principal axes at each site varied by less than  $15^\circ$ . Currents along these axes explained  $>95\%$  of the current variance at moorings BC1 – BC3,  $>90\%$  at BC4, and  $>75\%$  at mooring BC5 and BC6.

Another perspective on the velocity structure is provided by vertical sections of velocity using an along- and cross-shore coordinate system based on the approximate orientation of the coast between Wainwright and Barrow. In this system, positive along-shore or downcanyon velocities,  $u_r$ , are toward  $56^\circ\text{T}$ , and  $u_r < 0$  is upcanyon toward  $236^\circ\text{T}$ . Positive cross-shore velocities,  $v_r$ , are offshore toward  $326^\circ\text{T}$ , and  $v_r < 0$  is onshore toward  $146^\circ\text{T}$ . We classified the flow as being down- or upcanyon according to the sign of  $u_r$  at

~20 m depth at BC2. (This classification scheme is satisfied by virtually any choice of depth or mooring position.) From 2010 – 2011 the  $u_r$  record (Figure D2b) indicated that the flow was generally downcanyon. Speeds were typically between 0.2 and 0.5 m s<sup>-1</sup>, but  $u_r$  often exceeded 0.5 m s<sup>-1</sup>, and its maximum was ~1.0 m s<sup>-1</sup>. Upcanyon currents occurred ~30% of the time, were generally swifter than downcanyon currents, and had a maximum speed of 1.2 m s<sup>-1</sup>. From mid-August – September 2010 and from May – August 2011 the flow was primarily downcanyon and steady compared to the period of October 2010 – April 2011, when current speeds and variations were greater. As determined from adjacent moorings, the mean cross-canyon Rossby number ( $Ro_y = \partial u_r / f \partial y$ , where  $y$  is the cross-shore coordinate and  $f$  is the Coriolis parameter) was  $\ll 1$ , but ~20% of  $Ro_y$  magnitudes were between 0.2 and 0.4 and highest on either side of BC2. The majority of the larger values were associated with upcanyon flows in fall indicating that, at times, the cross-shore advection of along-canyon momentum can be significant.

Figures D3a and b show the year-long mean vertical sections of  $u_r$  and  $v_r$ . On average, the flow was downcanyon everywhere despite the fact that the mean winds were ~2.4 m s<sup>-1</sup> towards 255°T, i.e., opposite the mean downcanyon flow. The  $u_r$  composite indicates an along-shore jet centered at BC2 with

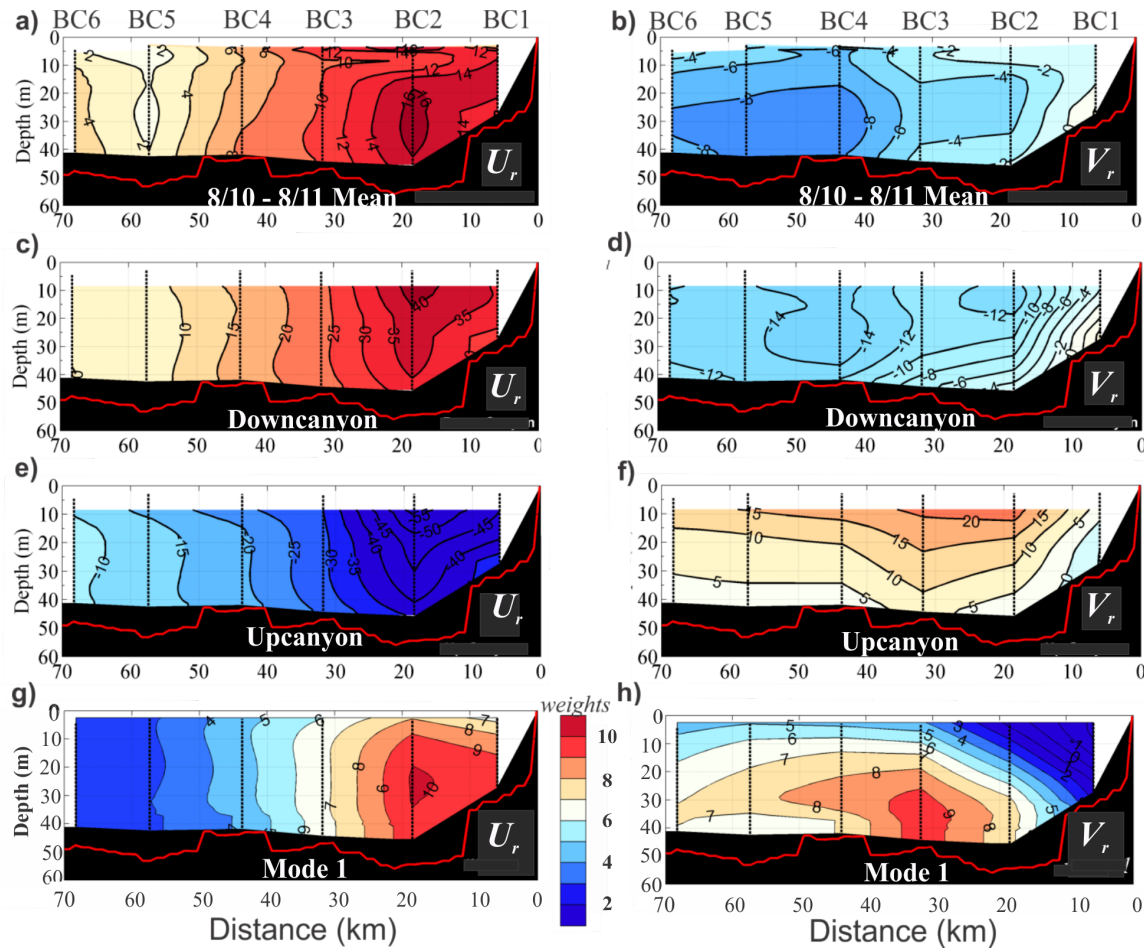


**Figure D3.** Vertical sections of the mean annual: a) along-canyon,  $u_r$  and b) cross-canyon,  $v_r$  velocities. Mean sections of c)  $u_r$  and d)  $v_r$  for the downcanyon case, and mean sections of e)  $u_r$  and f)  $v_r$  for the upcanyon case. Vertical sections of the first EOF eigenvector for g)  $u_r$  and h)  $v_r$ . All figures are based on the August 2010 – August 2011 period.

a maximum speed of  $0.16 \text{ m s}^{-1}$  between 20 and 40 m depth. The cross-shore flow was onshore everywhere, with the largest onshore velocities observed below 20 m depth at moorings BC4 – BC6. There were two regions of onshore convergence. The first was between BC3 and BC4 where, as noted (Figure D2a), the mean onshore flow veered counterclockwise into the canyon. The second was between BC1 and BC2 and likely reflects the coastal boundary constraint.

Figures D3c and d (D3e and f) are the  $u_r$  and  $v_r$  sections composited from all downcanyon (upcanyon) flow events, respectively. For both flow regimes the along-canyon structure had three features in common. First, each included an along-canyon jet, centered at BC2, which maximum speeds in the uppermost 20 m. Second, the jets are somewhat asymmetrical with the horizontal shear slightly larger on the offshore side of the jet (between BC2 and BC3) than on the inshore side. Third,  $v_r \sim \partial u_r$  in all sections, consistent with the aspect ratio. In the downcanyon case, there was little vertical shear in  $u_r$ , but considerable shear in  $v_r$  at BC1 and BC2. The  $v_r$ -distribution indicates onshore convergence between BC4 and BC1 with maximum convergence within  $\sim 20 \text{ km}$  of the coast. The mean  $u_r$  speeds for the upcanyon-flow composite (Figure D3e) were larger than those for the downcanyon case. The vertical shear in  $u_r$  was weak ( $\leq 10^{-3} \text{ s}^{-1}$ ) seaward of about 25 km, but substantial ( $\sim 5 \times 10^{-3} \text{ s}^{-1}$ ) within the core of the jet. For upcanyon flow  $v_r$  (Figure D3f) consisted of offshore, vertically-sheared flow everywhere, divergent between BC1 and BC2 but weakly convergent seaward of BC2.

Empirical orthogonal function (EOF) calculations indicate that the velocity fluctuations were highly coherent over the mooring array. The first EOF mode (Figures D3g and h) captures more than 90% of the variance in the velocity components. Mode weights for  $u_r$  were vertically uniform, greatest within 20 km of the coast, and much smaller seaward of BC4. For  $v_r$ , the amplitudes increased with depth, were greatest below 20 m at BC3, and smallest at the surface near the coast. (EOF results from 2011 – 2012 were similar.)

### D.3.2 Transport: Observations

We computed daily- and vertically-averaged transports assuming uniform velocity between the topmost bin and the surface. We also estimated transports by extrapolating to the surface either the upper ocean shear and/or interpolations between the uppermost measured velocity and the ice velocity. The different approaches yielded no significant differences in the transport estimates. Daily transports for 2010 – 2011 were then regressed against the mean daily vertically-averaged  $u_r$  at BC2 and BC4. Both regressions were statistically significant at the 95% confidence level. The BC2 (BC4) regression accounted for 96% (93%) of the variance. The BC2 regression (Table D2) was used to estimate mean daily transports for the August 2011 – August 2015 period. There were several gaps due to premature ADCP failure at BC2. The BC4 regression filled the gap from 4 May – 19 July 2012 (when BC4 died). Remaining gaps were 21 – 29 August 2011, 19 July – 9 September 2012, and 13 August – 10 September 2013. We filled most of these gaps by regressing the vertically-averaged velocity at BC2 in each year against the mean daily HFR surface velocity at grids surrounding the BC2 location. These regressions accounted for 80 – 90% of the BC2 transport variance in each case. Poor quality HFR returns due to drifting sea ice prevented interpolating transports during the 15-day period of 19 July – 2 August 2012. Errors in the transport estimates arise from the regressions procedures, the along-shore coordinate choice, and the neglect of transport between the coast and mooring. In aggregate we consider the uncertainty in these estimates to be between 15 and 20%.

The mean daily along-canyon winds and transport for the August 2011 – July 2015 period (Figure D4) are enormously variable. For transport, the coefficient of variation (the ratio of the standard deviation to the mean) is  $\sim 4$ , based on the record-length mean transport of 0.19 Sv. Mean daily values ranged from a maximum of  $\sim 1.6 \text{ Sv}$  (11 November 2013) to a minimum of  $-2.6 \text{ Sv}$  (19 January 2014). Transport event

**Table D2.** Row 1 is the linear regression model used to compute Barrow Canyon transports (T) from mooring BC2. Rows 2 and 3 are the winter and summer generalized linear models (GLM) used to hindcast Barrow Canyon transport based on winds listed in Table D1 over the Bering Sea shelf (C40), Bering Strait (A3) and Barrow Canyon (BC2). Terms in parentheses are the 95% confidence limits on the model coefficients using an integral time scale of 4 days. The wind components (V, U) and lags at each site are defined in the footnote.

	$r^2$
<p><i>Linear regression: transport vs. vertically-averaged along-canyon current at BC2</i>  <math>T(\text{Sv}) = 0.019(\pm 0.001) \cdot \text{BC2}(\text{cm s}^{-1}) - 0.007(\pm 0.04)</math></p>	0.96
<p><i>GLM: Mean daily winter (October – April) transport from along- and cross-shore winds<sup>1</sup></i>  <math>T = 0.04(\pm 0.038) + 0.021(\pm 0.007) \cdot \text{C40V} + 0.067(\pm 0.011) \cdot \text{A3V}</math>  <math>+ 0.084(\pm 0.015) \cdot \text{BC2U} - 0.038(\pm 0.013) \cdot \text{BC2V}</math></p>	0.59
<p><i>GLM: Mean daily summer (May – September) transports from winds<sup>1</sup></i>  <math>T = 0.56(\pm 0.031) + 0.025(\pm 0.007) \cdot \text{C40V} + 0.029(\pm 0.007) \cdot \text{A3V}</math>  <math>+ 0.062(\pm 0.013) \cdot \text{BC2U} - 0.018(\pm 0.013) \cdot \text{BC2V}</math></p>	0.55

<sup>1</sup>BC2U: 67°T; BC2V: 157°T both lead transport by 1 day; A3V: 15°T leads transport by 1.5 days; C40V: 315°T leads transport by 2.5 days.

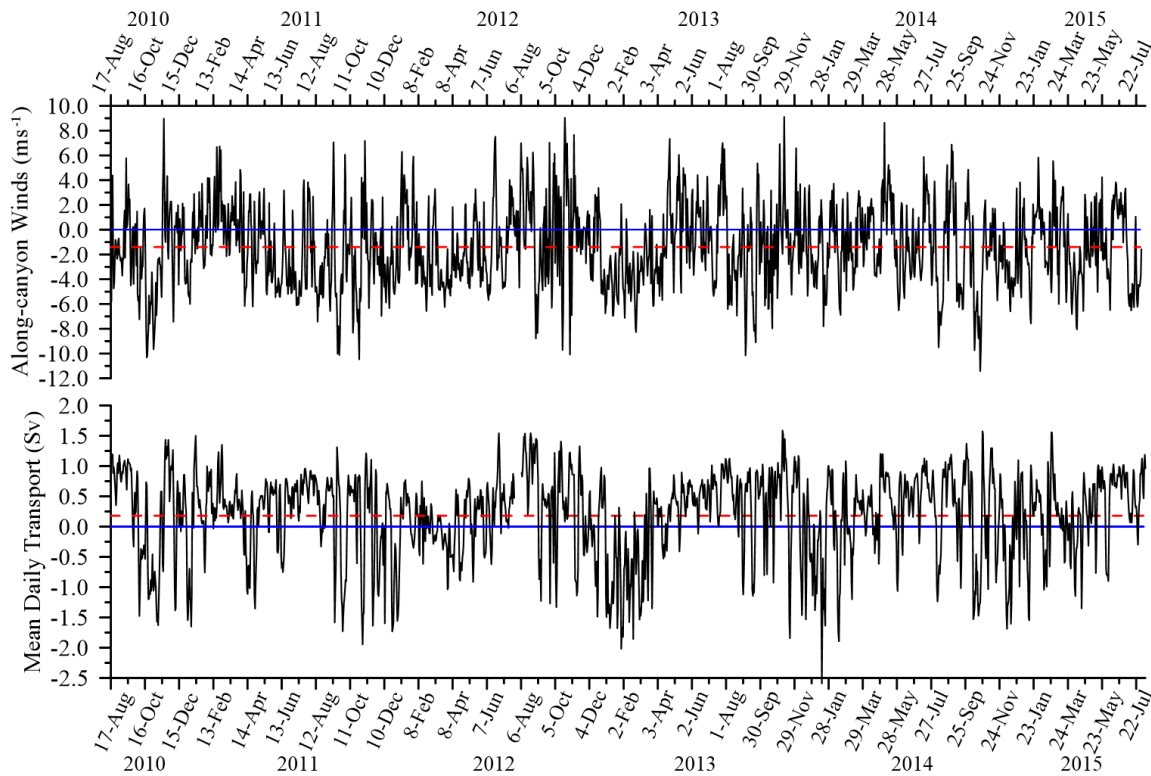


**Figure D4.** Mean daily along-canyon winds (top) and transport (bottom). The dashed red line on the wind and transport time series denotes the record length means of  $-1.7 \text{ m s}^{-1}$  and  $0.19 \text{ Sv}$ , respectively.

durations varied from 1 – 5 days, in which fluctuation amplitudes were frequently 0.5 Sv or greater, to episodes lasting a week or more.

Transport and along-canyon wind variations at monthly and longer timescales are shown with mean monthly values (Figure D5) along with their 95% confidence limits. (For both variables these limits were constructed by bootstrapping (Efron and Tibshirani 1993) because both have integral time scales of ~4 days, and neither are normally distributed.) Typical monthly transport amplitudes are ~0.5 Sv, ~2.5 times the record length mean.

In addition to month-to-month variability, there is considerable interannual variability. For example, downcanyon transport predominated from November 2010 – March 2011, while upcanyon transport dominated over the same period in 2012. Although the seasonal variability is largely masked by month-to-month variations, the mean monthly transports of Figure D5 describe an annual cycle (Figure D6a). The mean summer (May – September) transport was 0.45 Sv downcanyon, with the annual maximum of ~0.7 Sv occurring in July, whereas the mean transport from October through April was not significantly different from zero.

Seasonal transport variability is also reflected in the higher order statistics, as summarized in the summer and combined fall and winter probability density functions (pdfs; Figure D7; fall and winter were combined because their pdfs are similar.) For example, the summer variance (~0.29 Sv<sup>2</sup>) is about half the fall/winter variance (~0.54 Sv<sup>2</sup>). In both seasons the transport pdfs are negatively skewed; extreme flow events are primarily upcanyon. Skewness is more negative in summer than in fall/winter even though upcanyon flows are more frequent and stronger in fall and winter (i.e., 21% of all fall/winter transports are ≤-0.6 Sv, but only ~7% of summer upcanyon transports are ≤-0.6 Sv). The seasonal skewness differences reflect seasonal changes in the kurtosis. The summer pdfs are leptokurtic; ~76% of all mean daily transports are within one standard deviation of the mean, implying that summer transport changes are small. The fall/winter (and record length) pdfs are platykurtic, consistent with upcanyon flow events being intermittent but more frequent and larger than those of summer. Neither pdf is normally distributed; each fails the Kolmogorov-Smirnov goodness of fit test at the 95% confidence level.

Variability in the along-canyon transport is largely wind-forced (Figure D4). The maximum correlation accounts for ~47% of the transport variance, using the wind-component projected along 67°T and leading the transport by ~1 day. This result is similar to that found by Itoh et al. (2013) at the mouth of the canyon and by Gong and Pickart (2015) from an assemblage of synoptic cross-canyon velocity sections. The lagged response of the transport may reflect the spin-up time ( $h/r$ ) for the bottom boundary layer; where  $h$  is the water depth (~45 m) and  $r$  the linear resistance coefficient. For a frictional time scale of 1 day,  $r$  is ~  $5 \times 10^{-4} \text{ m s}^{-1}$ , consistent with estimates from other continental shelves (Brink 1998).

Although the local winds explain nearly half the transport variance, there are prominent deviations from this relationship. For example, there is a distinct annual transport cycle (Figure D6a), but the mean monthly along-canyon winds for the 2011 – 2015 period showed no seasonality (Figure D6b). Moreover, from June through August 2011 the mean flow was ~0.5 Sv downcanyon while the winds averaged ~3 m s<sup>-1</sup> upcanyon (Figure D5). In contrast, the average transport was upcanyon at 0.5 Sv from November 2012 through March 2013 when the mean winds were upcanyon at ~4 m s<sup>-1</sup>. Such large transport differences cannot be ascribed to the small changes in local winds.

One clue to the differential transport responses to the winds is apparent in comparing the regional wind and sea level pressure maps for June, July, August, and September 2011 (Figures D8a – d), December 2012, and January, February, and March 2013 (Figures D8e – h). From June through September 2011, winds over the northeastern Chukchi shelf were easterly or northeasterly at 3 – 6 m s<sup>-1</sup>. In all months except September, the flow was downcanyon at rates of 0.2 to 0.7 Sv. Only in September did the flow

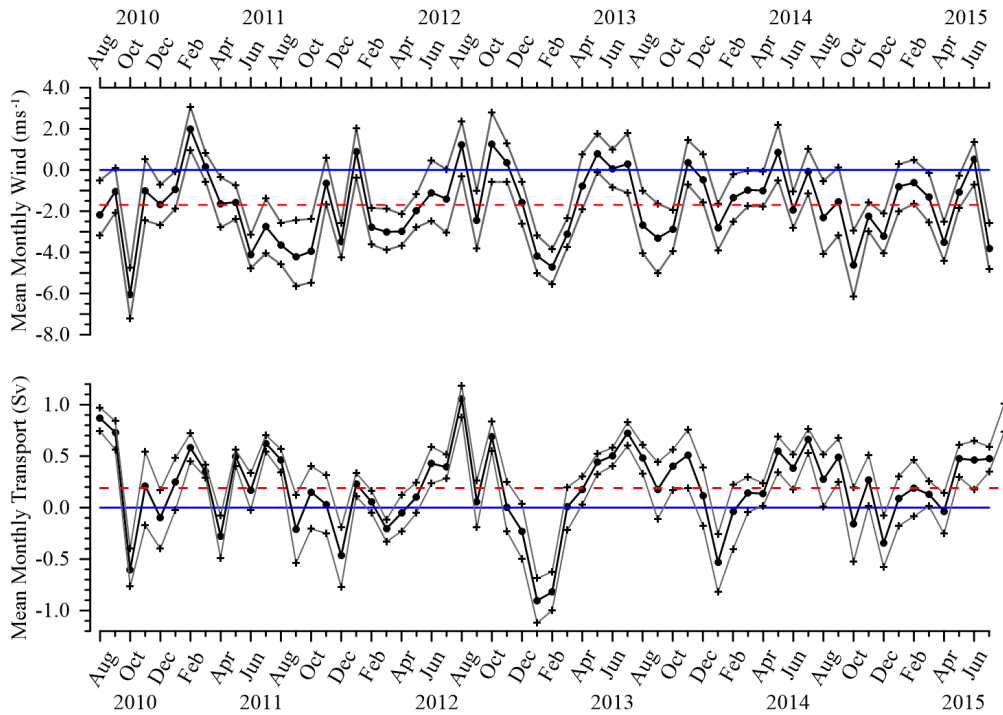


**Figure D5.** Mean monthly along-canyon winds (top) and transport (bottom) are denoted by black lines and dots. Crosses and gray lines delineate the 95% confidence limits. Dashed red lines on show the record-length means in transport ( $0.19 \text{ Sv}$ ) and along-canyon wind velocity ( $1.7 \text{ m s}^{-1}$ ).

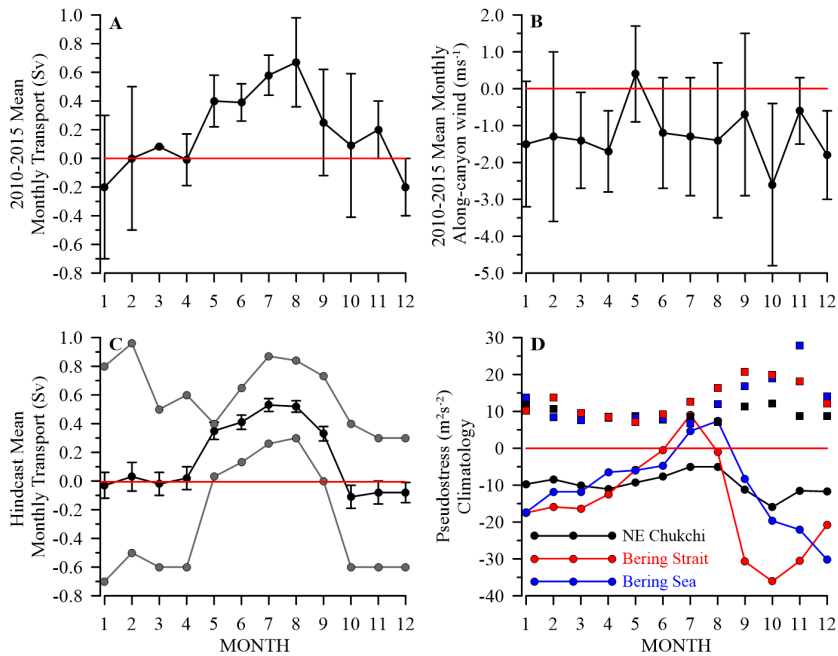


**Figure D6.** Panels A and B are the means (filled circles) and standard deviations (error bars) of the monthly transport and along-canyon wind velocity, respectively, for 2010 – 2015. Panel C is the mean monthly transport (black line and circles) and 95% confidence limits (error bars) based on the January 1979 – July 2015 GLM hindcast. The gray lines and circles indicate the maximum and minimum values in each month. Panel D displays the monthly means (circles) and standard deviations (squares) of the pseudostress for the January 1979 – July 2015 period at the three locations used in the GLM.

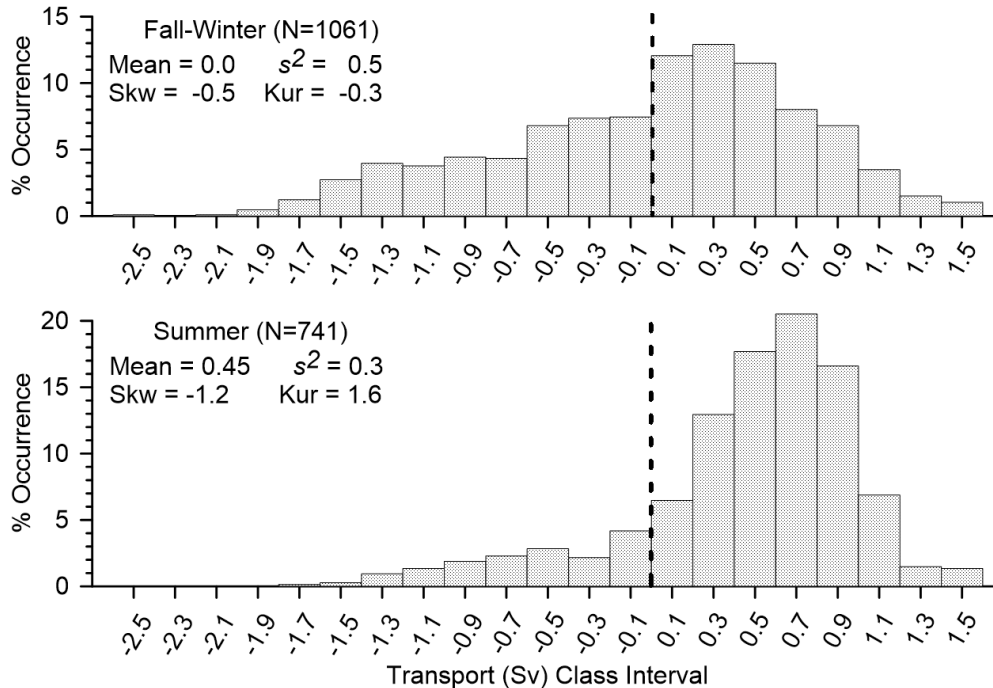


**Figure D7.** Probability density functions of the mean daily transport in Barrow Canyon for winter (October – April; top) and summer (May – September; bottom). Each panel includes the value of the mean, sample variance ( $s^2$ ), and the skewness (Skw) and kurtosis (Kur) coefficients, computed per King and Julstrom (1982). The vertical dashed line delineates the upcanyon from the downcanyon class intervals.

become upcanyon, coincident with the onset of strong northeasterly winds over the northeastern Chukchi shelf *and* northerly winds over the northern Bering Sea. The transport was upcanyon at  $\sim -0.2$  Sv in December 2012 when the along-canyon winds were northeasterly at  $\sim 2$  m  $s^{-1}$ , but the winds over the northern Bering shelf were northerly at  $5 - 7$  m  $s^{-1}$ . Upcanyon transports of  $\sim -1$  Sv occurred in January and February 2013 as well, when strong northeasterly (northerly) winds of  $4 - 6$  m  $s^{-1}$  blew over the northeastern Chukchi (Bering Strait). The mean transport was nil in March when winds over the northern Bering Sea collapsed, although moderate northeasterly winds of  $3 - 4$  m  $s^{-1}$  persisted over the northeastern Chukchi. These results recall those of Danielson et al. (2014), who showed that circulation variability in the eastern Chukchi Sea was mediated by northward propagating, down- and/or upwelling, long, continental shelf waves generated on the Bering Sea shelf. In addition, other adjustments in the shelf wide pressure field arise from coastal convergences and divergences over the entire Chukchi (Winsor and Chapman 2004; Spall 2007) and northern Bering shelves (Danielson et al. 2014).

### D.3.3 Transport: Hindcast and Climatology

Based on the preceding results and following Danielson et al. (2014), we applied general linearized models (GLM) in an effort to improve transport predictability in Barrow Canyon. This approach recognizes that it is the along-shore integral of the shelf winds upstream of the point of interest that affects the local circulation (e.g., Gill and Schumann 1974). Our GLM uses NARR winds at locations listed in Table D1 in Barrow Canyon (BC2), Bering Strait (A3), and the northern Bering Sea shelf (C40). We proceeded by first finding the highest correlation for both the rotation angle and time lag by regressing the transport against each of the six individual wind components over the entire transport record and then applying these lags and angles to the GLM regression (and given in Table D2). Separate regressions were made for summer (May – September) and fall/winter (October – April).

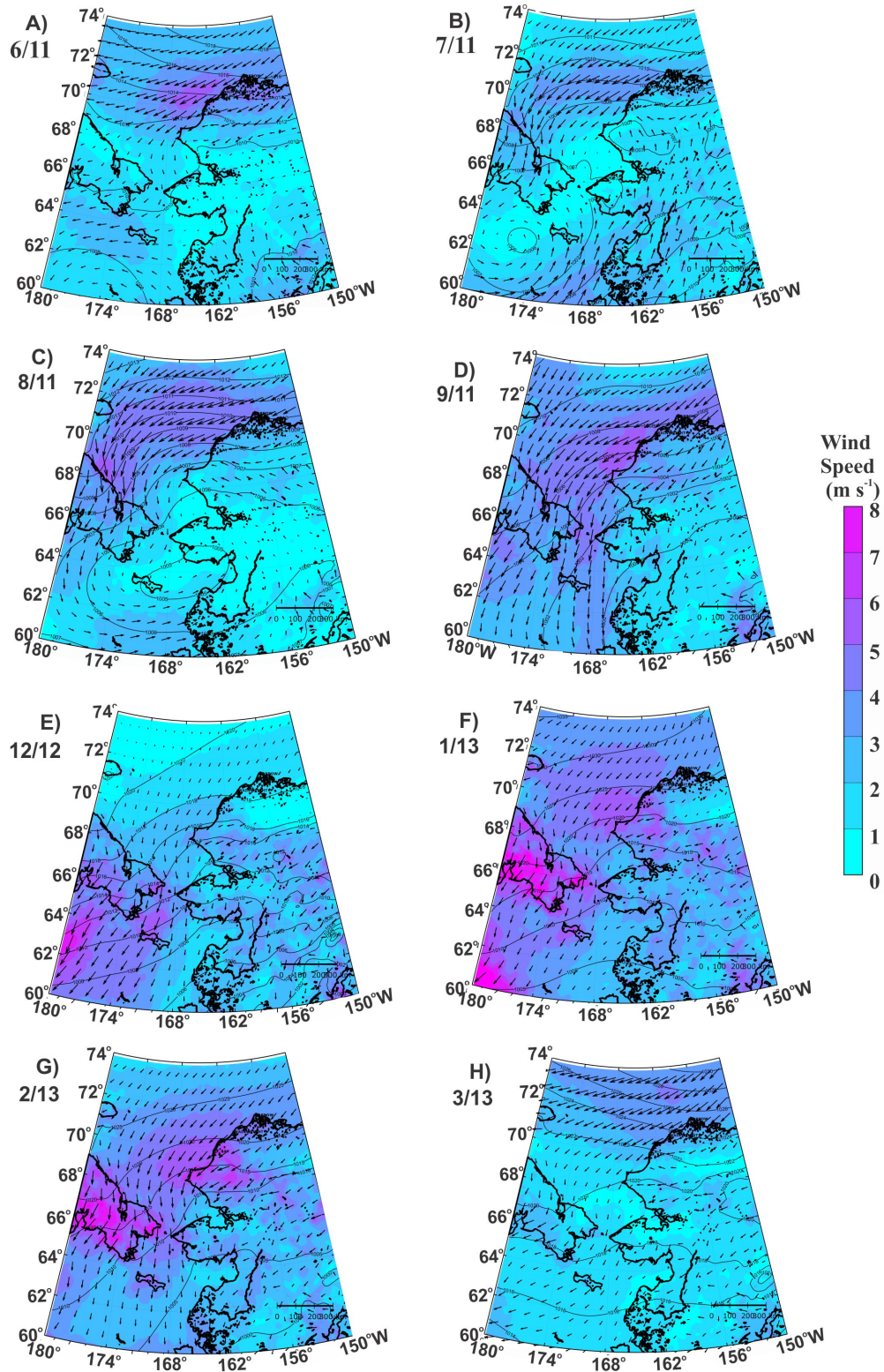


**Figure D8.** Mean monthly maps of sea level pressure (contours), wind speed (color), and direction (arrows) over the northern Bering and Chukchi seas. The 2011 maps are for: A) June, B) July, C) August, and D) September and the 2012 – 2013 maps are for: E) December, F) January, G) February, and H) March.

The summer and fall/winter regressions (rows 2 and 3 of Table D2) explain 55 and 59%, respectively, of the transport variance. Although these seasonal differences are not substantially different from one another, the GLM results are a significant improvement over models using only Barrow Canyon winds by explaining ~10% or more of the variance. All but the C40 (Bering shelf) model coefficients differ significantly from their seasonal counterparts. For example, the summer intercept is almost 30% larger than the winter intercept, and both seasons' intercepts are positive and consistent with downcanyon transport being maintained by an along-shore pressure gradient in the absence of wind-forcing. In contrast, the magnitudes of all the winter wind coefficients (except C40) are significantly larger than the summer coefficients.

We applied the GLM to hindcast mean daily Barrow Canyon transports using NARR winds from January 1979 through July 2015 and then formed monthly means to construct a climatological annual transport cycle (along with 95% confidence limits and the range in mean monthly transports, Figure D6c). The climatology suggests that three seasons comprise the annual transport cycle: 1) winter (January – April), when the net transport is zero; 2) summer (May –September), when the net transport is ~-0.45 Sv downcanyon; and 3) fall (October – December), when the net transport is ~-0.1 Sv upcanyon. The ranges for summer months imply that individual monthly transports are always downcanyon, whereas the fall/winter ranges indicate that individual monthly transports can be upcanyon or downcanyon. The hindcast cycle is similar in phasing to the annual cycle computed from the five years of measurements (Figure D6a), and the 95% confidence limits on the observed monthly means overlap those of the hindcast values.

As a further illustration of the seasonality in wind forcing over the Bering and Chukchi seas, we show the seasonal variation in the along-shore pseudostress (the product of wind speed and the along-shore wind component) from the northern Bering Sea, Bering Strait, and Barrow Canyon derived from the 37-year NARR record (Figure D6d). Although the annual pseudostress cycles at each location are nearly in-phase everywhere, the annual amplitudes of the pseudostress at the Bering locations are ~30 – 45  $\text{m}^2 \text{s}^{-2}$  while that for Barrow Canyon is ~5  $\text{m}^2 \text{s}^{-2}$ . The monthly standard deviations are nearly equal at all locations from December through July, and over Barrow Canyon they are virtually constant throughout the whole year. At the Bering locations pseudostress variability from September through November is 2 – 3 times greater in comparison to other months and/or to Barrow Canyon. These differences suggest that the influence of remote winds on Barrow Canyon transports should vary considerably from year-to-year, especially in autumn.

Variability in the entire monthly hindcast record (not shown) is dominated by the annual signal, which oscillates about a long-term mean value of 0.16 Sv. Monthly transport anomalies derived from the hindcast climatology cycle (Figure D9) show that the anomaly magnitudes are large and exceed 0.2 Sv in about one-third of the months. Fall and winter anomaly magnitudes are ~0.2 Sv on average, twice those of summer. The maximum mean monthly transport is ~1.0 Sv (February 1989), and the minimum is ~-0.7 Sv (January 2001). Month-to-month changes in anomaly sign show little persistence, although upon smoothing with a 13-month running mean, there is a suggestion of anomaly magnitudes of ~0.1 Sv persisting for 3 to 10 years. For example, transports between 1979 – 1988 and 1999 – 2006 were ~0.1 Sv below the long-term average, while those from 1989 – 1998 and since 2006 were above the mean by a similar amount.

As discussed later, monthly transports that are either up- or downcanyon in fall or winter likely have a profound influence on the circulation and water masses on the northeastern Chukchi Sea. We thus consider the larger-scale atmospheric patterns associated with monthly transport anomalies. Figure D10 shows maps of atmospheric pressures and surface winds composited using all March and October months (representative of the winter and fall, respectively) for which the transport anomalies exceed one standard deviation from the climatological monthly mean. The maps in the top row indicate that abnormally large

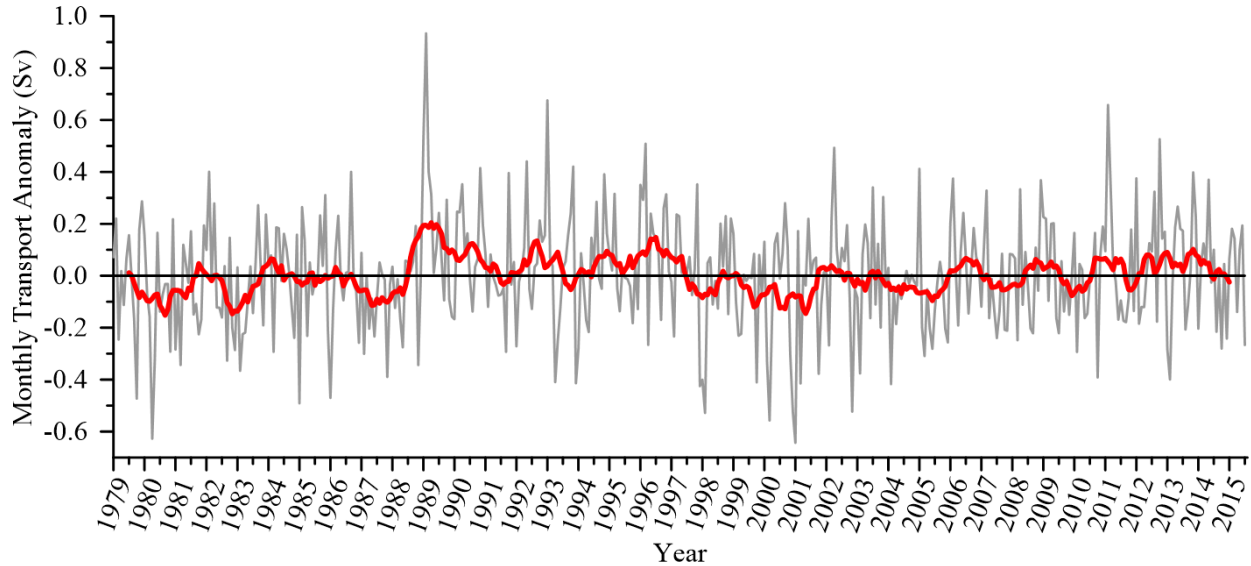


**Figure D9.** Monthly transport anomalies (gray) for the 1979 – 2015 period based on the GLM hindcast. The thick red curve is the 13-month running mean of the anomalies.

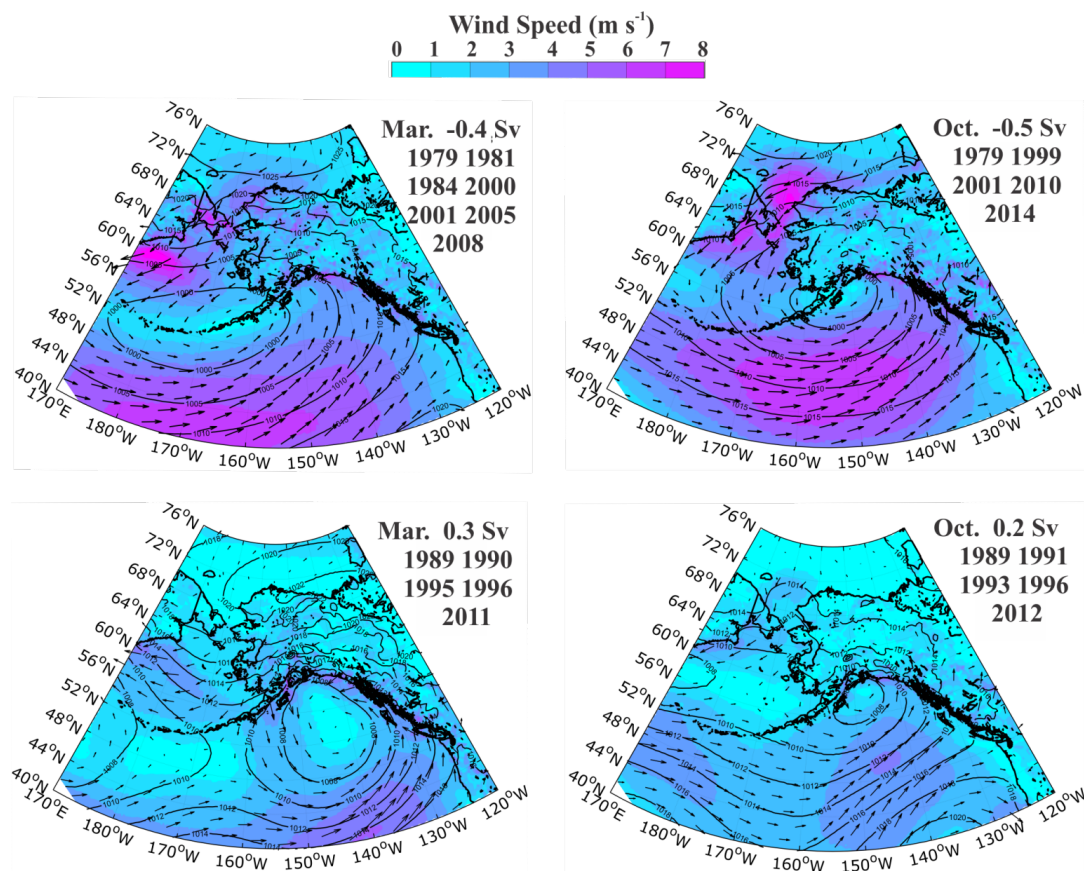


**Figure D10.** Sea level pressure (contours), surface wind vectors (arrows), and wind speeds (colors) for Marches (left) and Octobers (right) in which there was anomalously large upcanyon (top row; contour interval of 5 mb) and downcanyon transports (bottom row; contour interval of 2 mb). The maps are composites based on the month and years shown to the right of each map, which includes the mean monthly transport for those years.

winter and fall upcanyon transports are associated with a deep Aleutian Low, centered along 52°N between 150°W and 170°W, and a strong Beaufort High. The juxtaposition of these pressure systems impels northeasterly (northerly) winds over the Chukchi (Bering) shelves. For months when the downcanyon transport is anomalously large, winds are feeble, the Aleutian Low is weak and displaced into the Gulf of Alaska, and the meridional pressure gradients over northern Alaska are diminished.

The observed transport pdfs indicated large seasonal differences in the kurtosis, which we further explore using the mean daily hindcast transports to compute cumulative probabilities of flow event duration and the total number of events for each season for both the up- and downcanyon cases (Figures D11a and b, respectively). (Transport events that extend across seasons were assigned to the season in which most of the event occurred.)

From the climatological perspective, there are nearly equal probabilities of up- and downcanyon events within any given season. Consequently, seasonal differences in kurtosis are associated with seasonal differences in event durations and/or transport magnitudes. Differences in event durations are most striking in summer, when 75% of upcanyon events are  $\leq 2$  days, and only 10% are 4 – 10 days in length (with 10 days being the maximum length). By contrast, only  $\sim 20\%$  of summer downcanyon events are  $\leq 2$  days duration, and more than 40% exceed 10 days (with the maximum duration being 120 days). Short ( $\leq 2$  days) duration events have smaller mean daily transport magnitudes than events  $> 2$  days. Hence in summer, the magnitude of the mean daily downcanyon transport is  $\sim 2.5$  times larger than that for the upcanyon transport. Differences in event durations are smaller in fall and winter, when  $\sim 75\%$  of up- and downcanyon event durations are  $\leq 5 - 6$  days, and mean daily transport magnitudes for each event are more equal.

### D.3.4 Thermohaline Variability

Our description of temperature and salinity variations at the head of the canyon is based on near-bottom measurements (within  $\sim 4$  m of the seabed). Although these may not be representative of the water column, they provide a sense of the spatial and temporal scales in water mass variability. We first address these scales by examining the potential temperature ( $\theta$ ) and salinity (S) records from moorings BC1, BC2, and BC5 for the August 2010 – August 2012 period (Figure D12; we omit the other records to enhance clarity). BC5 data are representative of  $\theta$  and S at BC4 and BC6. The BC3  $\theta$  and S records are similar to those at BC1 and BC2, but the magnitude of the variations at BC3 is smaller.

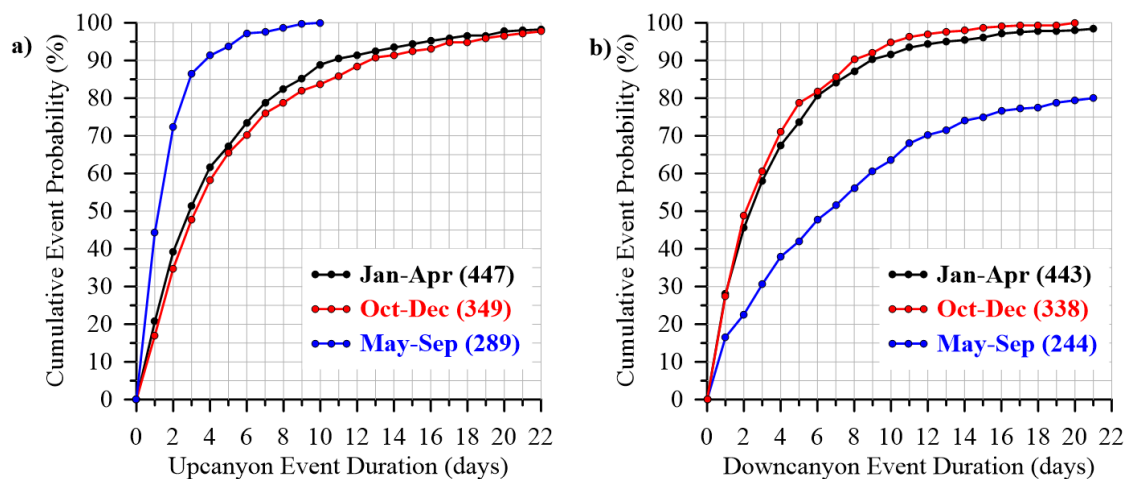


**Figure D11.** The seasonal cumulative probabilities for a) upcanyon and b) downcanyon events based on the hindcast transport record. The numbers associated with the seasons in the legend on each graph refer to the number of events over the 37-year record.

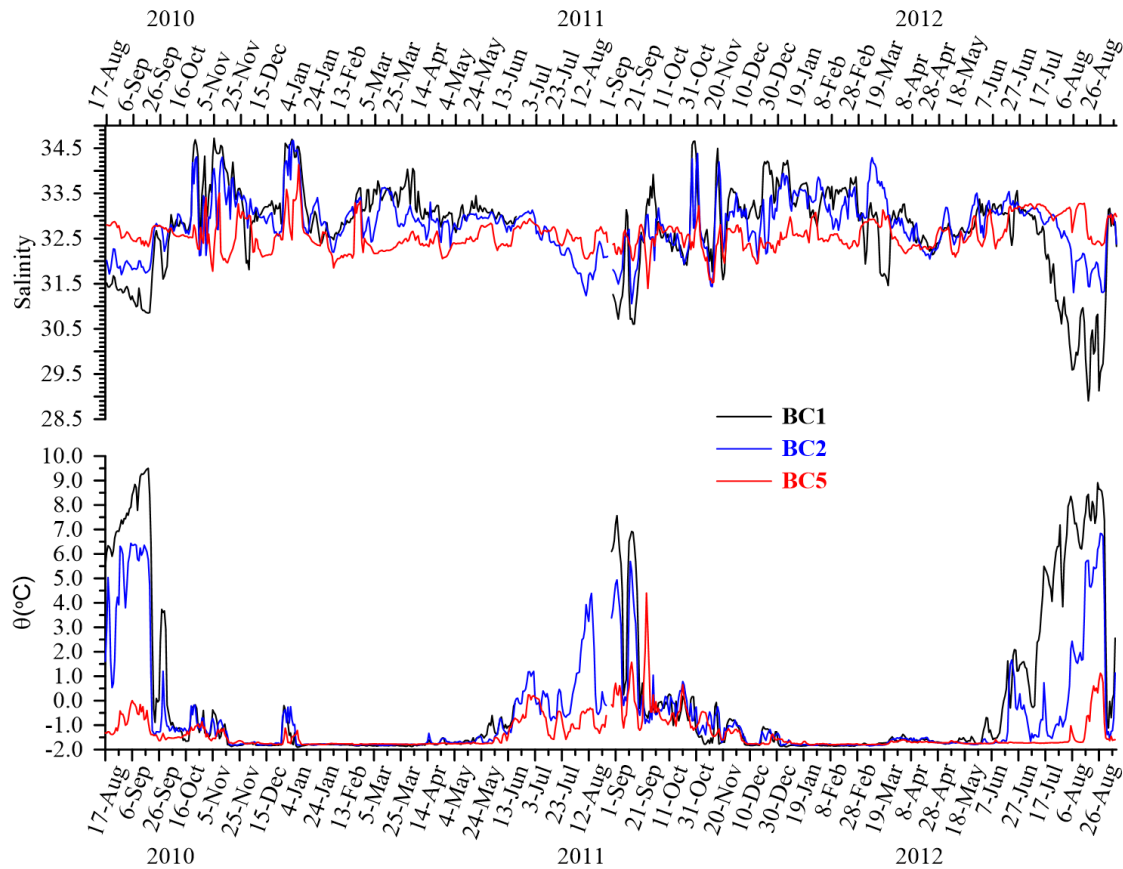


**Figure D12.** Time series of salinity (top) and potential temperature,  $\theta$ , (bottom) at moorings BC1 (black), BC2 (blue), and BC5 (red) for the August 2010 – August 2012 period.

There is little seasonal variability in salinity at BC5 where the average and standard deviation of  $S = 32.6 \pm 0.3$ . BC5 temperatures are  $\theta = -1.4 \pm 0.7^\circ\text{C}$ , with  $q$  near-freezing in all months except between June and November. In contrast BC1 and BC2 have distinct seasonal variations. From late November/early December through April/early May,  $\theta$  is at or near the freezing point, and the salinity average and standard deviation are  $\sim 33$  and  $0.5$ , respectively. Consequently, the density of near-bottom waters in winter decreases moving offshore. At all locations, but most noticeably at BC1 and BC2, there are episodes of warm ( $-1.5^\circ\text{C} < \theta < \sim 0^\circ\text{C}$ ), salty ( $\geq 33.1$ ) intrusions in fall and winter, which are associated with upcanyon flows of slope waters (discussed later). There were also periods when very salty ( $> \sim 33$ ), near-freezing waters were present at BC1 and BC2 (and BC3) but not at BC5, e.g., February – March 2011 and January – February 2012. In fact, the saltiest fractions occur more frequently at BC1 than at BC2, in spite of BC1 measuring at a shallower depth. These are cold, salty, recently formed winter waters, most likely produced in the latent heat polynyas along Alaska’s northwestern coast (Cavaliere and Martin 1994). They are subsequently transported into the head of the canyon (Weingartner et al. 1998) where, as expected, they are trapped to the coast by the sloping topography (Chapman 2000).

The cross-shore density gradient reverses sign from June through September, when, in general, salinity (and density) increases and temperature decreases moving offshore. This reversal has little to do with changes in water properties at BC5 but is instead due to the impressive changes in temperature and salinity at BC1 and BC2. Warming and freshening begins in May and proceeds gradually via a series of pulses coincident with energetic downcanyon transport events. In 2012 (and perhaps 2010), these pulses

gave way to a sustained period of warm ( $8^{\circ}\text{C}$ ), fresh ( $29 - 30$ ) ACW, which persisted at BC1 through August and September. The salinity records imply that the cross-shore salinity gradients within the canyon attain their maximum values in these months. In August and September 2010, the mean density difference between BC1 and BC3 was  $\sim 1.4 \text{ kg m}^{-3}$  implying a vertical shear in the along-canyon velocity of  $\sim 5 \times 10^{-3} \text{ s}^{-1}$ , assuming thermal wind balance and that the gradient holds over the entire water column. Under these assumptions the velocity difference over the uppermost 30 m of the water column between BC1 and BC3 would be  $\sim 20 \text{ cm s}^{-1}$ . If we further assume that this shear was typical for August and September 2010, the baroclinic geostrophic contribution to the total along-canyon transport was  $\sim 0.15 \text{ Sv}$ , which is in line with the synoptic observations of Münchow and Carmack (1997), Pickart et al. (2005), Gong and Pickart (2015), and the model results of Signorini et al. (1997). By comparison, the measured transport for this period was  $\sim 0.8 \text{ Sv}$ , suggesting the barotropic component accounted for  $\sim 80\%$  of the canyon transport.

Figure D13 shows the 5-year BC2 temperature and salinity time series along with the mean daily transport. Clearly the inferences drawn from the two years shown in Figure D12 regarding the seasonal variability in temperature and salinity at BC2 hold over the entire record. The longer record underscores

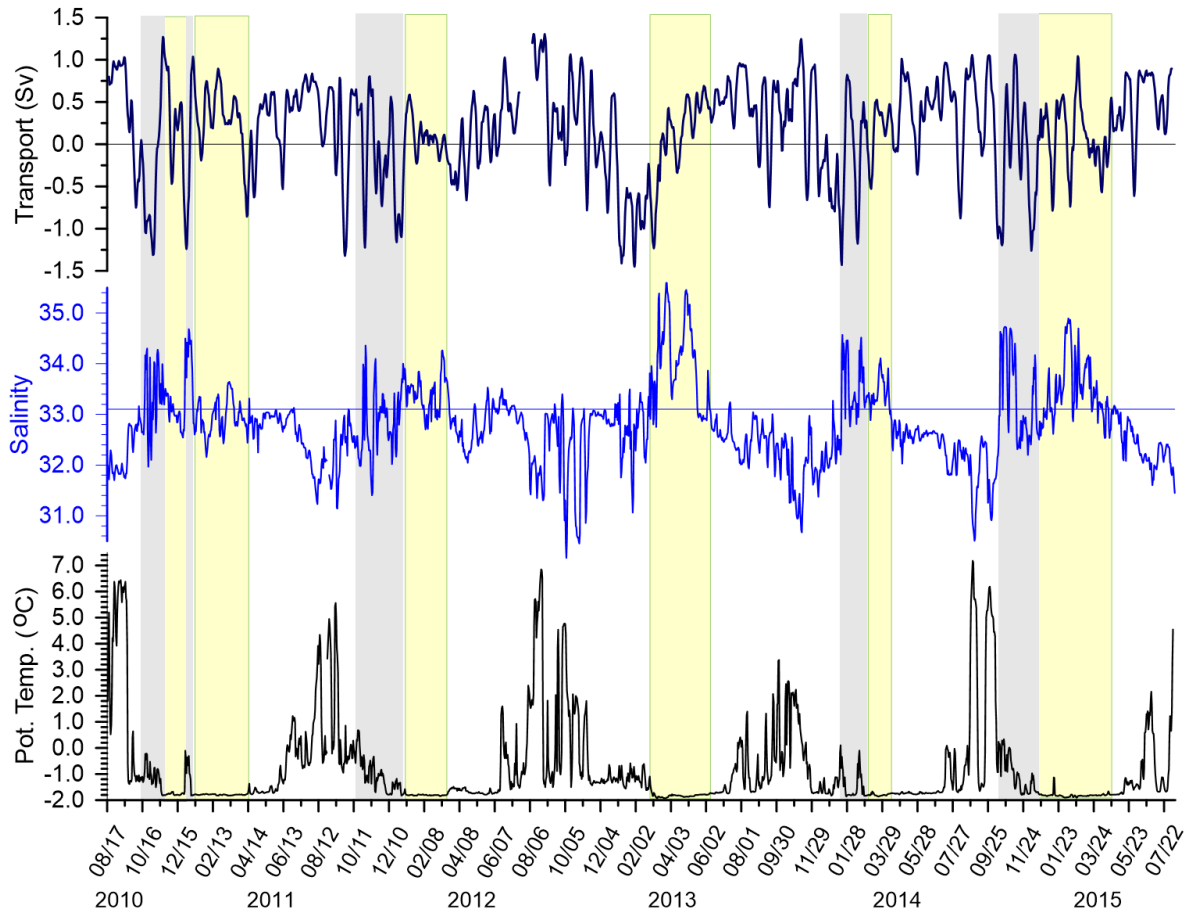


**Figure D13.** Time series of temperature (bottom) and salinity (middle) from mooring BC2 and the along-canyon transport (smoothed with a 7-day running mean; top). The horizontal line on the salinity plot delineates the 33.1 value. The light grey shading encompasses the periods of upcanyon transports that contained lower halocline and Atlantic Water signatures (e.g.,  $S > 33.1$  and  $\theta > -1.6^{\circ}\text{C}$ ). The light yellow shading captures periods of dense water ( $S > 33.1$  and  $\theta = \text{freezing point}$ ).

the tremendous interannual variability in water mass properties. For example, the maximum water temperature in summer and fall 2013 was  $\sim 3 - 4^{\circ}\text{C}$  cooler than in the other years, and while winter bottom temperatures were always close to the freezing point, winter-to-winter variations were primarily associated with upcanyon incursions of warmer slope waters. There is also variability in the timing of the spring and/or summer arrival of above-freezing temperatures. We assessed this by examining the dates when BC2 temperatures first reached  $0$  and  $2^{\circ}\text{C}$ . (The arrival of water of  $-1^{\circ}\text{C}$  is followed within a few days by water at  $0^{\circ}\text{C}$ , and the  $1.5$  and  $2^{\circ}\text{C}$  arrival dates are similarly close). The “early” summers of 2011, 2012, and 2015 all detected  $0^{\circ}\text{C}$  between 20<sup>th</sup> and 22<sup>nd</sup> of June, with temperatures rising quite rapidly afterwards. In 2011 and 2012,  $2^{\circ}\text{C}$  water occurred during the first week of August, and in 2015 it arrived a full month earlier. In the “late” summers of 2013 and 2014,  $0^{\circ}\text{C}$  water appeared on the 29<sup>th</sup> and 18<sup>th</sup> of July, respectively. In 2013, temperatures reached  $2^{\circ}\text{C}$  in late September, and in 2014 this benchmark occurred in late August. Variations in the spring/summer arrival of warm bottom waters are not obviously related to the spring or early summer transports. The average transports from April – June in the “late” summers of 2013 and 2014 were  $\sim 0.38$  Sv and more than double the corresponding averages for the “early” summers. Nor did we find a compelling relationship between the May and June ice extent over the Chukchi Sea shelf and the timing of warm water arrival. Such a relationship would suggest that solar penetration and heating of sub-surface waters was responsible for the difference in arrival times. The lack of convincing connections between the timing of the summer arrival of “warm” water and summer transport magnitudes or ice extent suggest that the summer warm water signature is established by conditions well south of Barrow Canyon and most likely on the Bering Sea shelf.

The fresh, warm waters of late summer/fall routinely terminate with the upcanyon transport of salty ( $>33.1$ ) water with  $\theta$  between  $-1.6^{\circ}\text{C}$  and  $0.5^{\circ}\text{C}$ . Waters with these characteristics are found over the continental slope within the lower halocline (140 – 180 m depth) and/or even deeper ( $\sim 200$  m) within the Atlantic Layer (Shimada et al. 2005). The grey shaded regions in Figure D13 highlight the more prominent packets of upcanyon events, in which lower halocline or Atlantic Water was transported to the head of the canyon. Most of these (indeed four of the five highlighted events) occur in the October – December period. Following these events, temperatures at the head of the canyon decreased to  $\leq -1^{\circ}\text{C}$ .

Interestingly, the depth of the slope water source (based on the  $\theta/S$  characteristics described earlier) does not appear to be a function of the magnitude or duration of the upcanyon flow events as suggested by Signorini et al. (1997). The most obvious example of this was the prolonged and strong upcanyon flows that occurred between December 2012 and February 2013. Throughout this time the upcanyon transport had salinities  $< 33.1$  and  $\theta \leq -1^{\circ}\text{C}$ . In contrast, the warmest ( $\theta \sim 1^{\circ}\text{C}$ ) and most saline ( $\sim 34.5$ ) waters occurred during the sequence of up- and downcanyon flows of October 2014. Hence, the magnitude and persistence of upcanyon flow events do not solely determine the source depth of slope waters fluxed into the canyon. Other mechanisms, likely occurring over the shelfbreak and slope, must be important in this regard.

## D.4 Discussion

### D.4.1 Transport Comparisons

Our average transport estimate of  $\sim 0.2$  Sv at the head of Barrow Canyon is in reasonable agreement with the modeled mean transport of Spall (2007) of  $\sim 0.25$  Sv, but it is  $\sim 50\%$  smaller than the  $\sim 0.45$  Sv average of Itoh et al. (2013) determined at the mouth of the canyon. We examine the possibility that these differences are a result of sampling bias and/or unaccounted transports into the canyon between its head and mouth. We first address these possibilities using vertically-averaged means and variances from various moorings located in Barrow Canyon and over the northeastern shelf for the 2010 – 2011, 2011 – 2012, and 2012 – 2013 periods shown in Figures D14a, b, and c, respectively. (The plot contains two

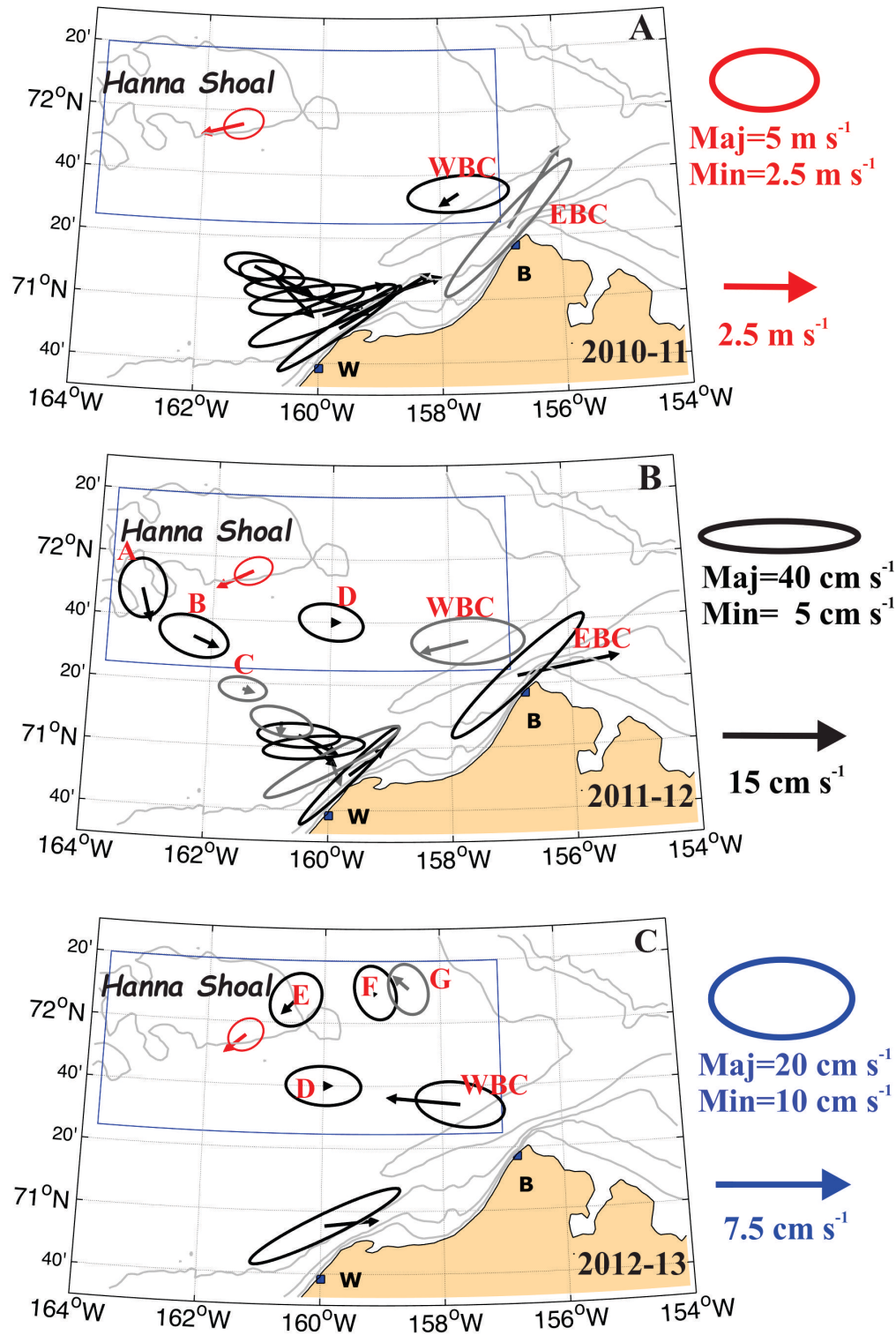


**Figure D14.** Vertically-averaged mean velocity vectors and variance ellipses for currents and winds in A) 2010 – 2011, B) 2011 – 2012, and C) 2012 – 2013. Red symbols and text are for winds, black are for currents outside of the blue box, and blue are for currents within the blue boxes. Gray (black) vectors and ellipses in each figure denote record lengths of from 6 to 10 (11 to 12) months duration.

different scales for the currents; scales within the blue box are one-half those outside of the box to enhance viewing the smaller currents farther from the canyon axis.)

Our array may be biased if there is substantial flow moving northeastward between the offshore end of the BC mooring array and the southeast side of Hanna Shoal. This undetected flow would enter the canyon north of the BC array. We examine this possibility using results from moorings A, B, and C (Figure D14b) that extend northwestward from the end of the BC array to the southern side of Hanna Shoal. The means and standard deviations of these records were  $\sim 2 \text{ cm s}^{-1}$  and  $\sim 10 \text{ cm s}^{-1}$ , respectively. The vectors and the ellipses are oriented toward the head of Barrow Canyon (similar to the statistics from moorings BC4 and BC5) at A and C, although the flow direction at B suggests that some of this flow might enter the canyon north of the BC array.

At each mooring the mean flow along the minor axis was  $< 1 \text{ cm s}^{-1}$  southwestward but not significantly different from zero at the 95% confidence level. This finding is consistent with that of Pickart et al. (2016), who observed southeastward flow along the south side of Hanna Shoal from synoptic summer velocity and hydrographic sections. Collectively these results suggest that: 1) flow over the northeastern Chukchi Sea shelf south of Hanna Shoal was funneled toward the head of the canyon (consistent with inferences by Weingartner et al. 2005) and 2) that there was little northeastward transport from the central Chukchi to the shelf between Hanna Shoal and Barrow Canyon. Both findings comport with the model results of Winsor and Chapman (2004) and Spall (2007).

We next examine current data for the shelf east and northeast of Hanna Shoal. At mooring D (Figures D14b and c) the mean vertically-averaged flow was not statistically different from zero. There appears to be negligible flow over the weakly sloping shelf between the 40 and 55 m isobaths as measured by moorings E, F, and G northeast of the Shoal in both 2012 – 2013 (Figure D14c) and in 2013 – 2014 (not shown). Although somewhat ambiguous, these results suggest that this portion of the shelf is not a major feed for Barrow Canyon. There is the possibility, however, of net eastward transport between the 55 m isobath and the shelfbreak.

A second potential source of bias is in the mooring array at the mouth of the canyon. Recall that Itoh et al.'s (2013) transport estimates derive from 3 moorings, deployed at 10 km intervals, from east to west, on the 80, 250, and 150 m isobaths, respectively (Figure D15). The gap between their westernmost mooring and the 70 m isobath on the west side of the canyon is  $\sim 30 \text{ km}$  ( $\sim 5$  times the baroclinic radius of deformation). This gap is wide enough to permit the  $\sim 15 \text{ km}$  wide, subsurface, eastward flowing Chukchi shelfbreak current carrying winter waters (Corlett and Pickart 2017) to enter the western side of the canyon. (Their estimate is tentative insofar as it is based on a compilation of synoptic sections collected between the months of May and October in different years.) We expect that the eastward shelfbreak flow follows the isobaths around the western lip of Barrow Canyon and continues upcanyon along the western wall. Proceeding upcanyon, this transport should diminish as it becomes entrained into the prevailing downcanyon flow along the eastern wall. This additional mass transport would be captured by the mooring array at the mouth of the canyon, but not the array at the head of the canyon. This interpretation is reflected in Shroyer's (2012) synoptic sections and in the vertically-averaged current statistics from two moorings deployed west of Barrow on the 70 m isobath on the eastern (EBC) and western (WBC) sides of the canyon (Figures D14a, b, and c). In all 3 years, the vertically-averaged flow at WBC was statistically significant and southwestward (or westward in 2012 – 2013) at  $\sim 1 - 3 \text{ cm s}^{-1}$ . By contrast, along the eastern wall of the canyon the mean flow was  $\sim 15 \text{ cm s}^{-1}$  northeastward and statistically significant.

Another potential mass source is associated with westward flow over the Beaufort shelf. As seen in Figure D15, the HFR-averaged surface currents for September – October 2013 between the coast and the 40 m isobath ( $\sim 50 \text{ km}$  offshore) was  $\sim 7 \text{ cm s}^{-1}$ . If this estimate is comparable to the vertically and annually-averaged currents, then the western Beaufort shelf contributes  $\sim 0.07 \text{ Sv}$  into Barrow Canyon

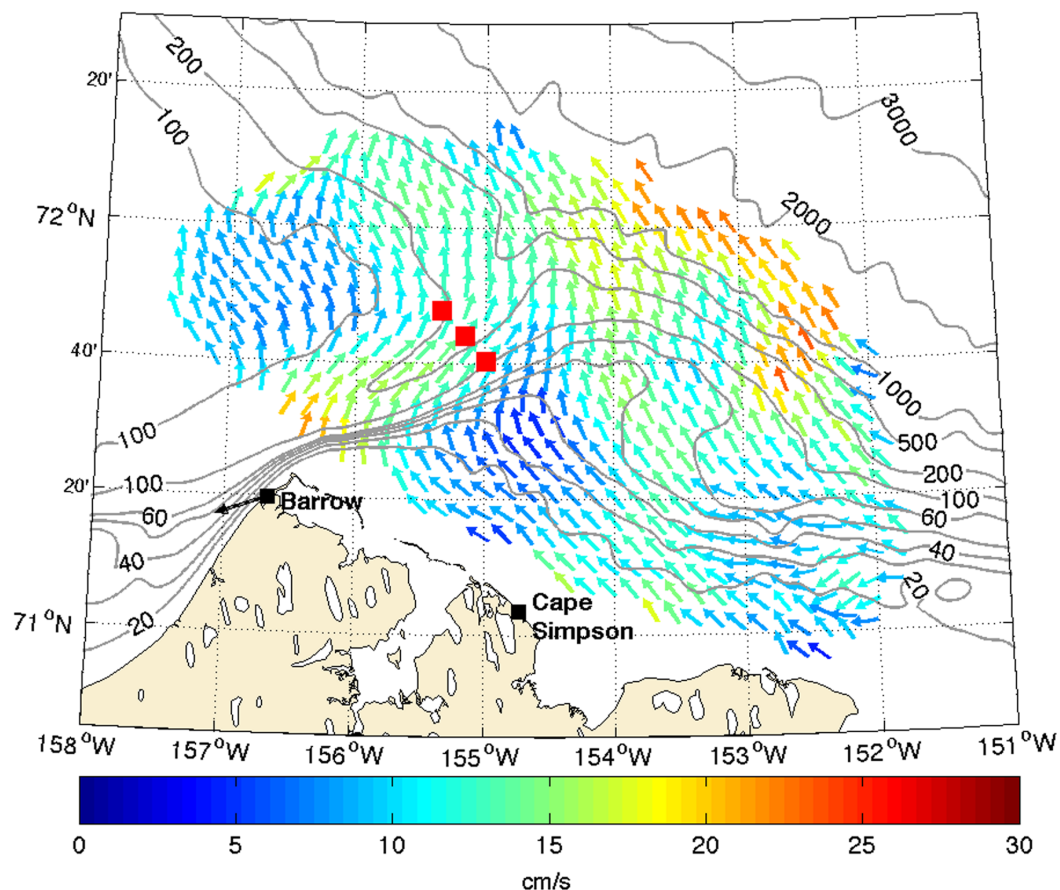


**Figure D15.** Mean September – October 2013 surface current map of the western Beaufort Sea shelf and the northern end of Barrow Canyon. The mean winds at Barrow were from the east-northeast (as indicated by the arrow) at  $3 \text{ m s}^{-1}$ . The red squares at the mouth of Barrow Canyon are the locations of the moorings discussed by Itoh et al. (2013).

upstream of the canyon mouth. The mean winds on the Beaufort Sea shelf are westward year-round suggesting that this shelf transports water into the canyon.

Taken together the subsurface eastward flow along the Chukchi shelfbreak and the westward flow from the Beaufort shelf may add  $\sim 0.15 \text{ Sv}$  to the  $\sim 0.2 \text{ Sv}$  canyon outflow we measured. If correct, these contributions substantially reduce the  $0.25 \text{ Sv}$  transport deficit between the head and the mouth of the canyon. We emphasize, however, that the estimates of the additional mass sources are tentative at best and await better resolution.

#### D.4.2 Consequences of Transport Seasonality

When compared to the transport climatology in Bering Strait (Woodgate et al. 2005b), we find that, on average in summer,  $\sim 40\%$  of the Bering Strait summer transport is carried into the head of Barrow Canyon, but none of the Strait's transport enters the canyon in fall and winter. This finding implies fall/winter flow convergence over the shelf south of Barrow Canyon because the net northward Strait transport must be diverted elsewhere, with the Central Channel, Herald Valley, and Long Strait being the likely avenues of egress. Although diversion has been inferred to happen in some winters (e.g.,

Weingartner et al. 1998) and in numerical models subject to synoptic wind events (Winsor and Chapman 2004; Spall 2007), our results imply that it is an annual occurrence. If so, seasonal switching of the points of entry into the Arctic Ocean of Pacific waters should affect the shelfbreak circulation structure and the seasonality of slope/basin exchange. We next consider other implications of this annual cycle.

#### **D.4.3 Hydrographic Implications**

The downcanyon advection of warm waters characteristic of summer effectively concludes with the upcanyon transport of colder waters in fall. The duration and intensity of these upcanyon flow events may be critical in initiating freeze-up on the northeastern Chukchi shelf because the oceanic heat flux convergences associated with these events can be substantially greater than the heat loss to the atmosphere (Weingartner et al. 2013a). The interplay between up- and downcanyon transports in fall may also affect the properties of dense winter waters produced on the shelf. Large volumes of dense water can be produced in the extensive latent heat polynyas along the northwest coast of Alaska, which are most prominent in December and January (Cavaliere and Martin 1994; Weingartner et al. 1998; Ladd et al. 2016). The initial polynya salinity depends upon advection from either the south (low to moderately saline Bering waters) or from the north (MW and WW) and is a key ingredient in establishing the properties of the dense water formed (Winsor and Chapman 2002). Winter circulation can also affect dense water production. If the along-shelf flow collapses, dense water residence time in the polynyas can be prolonged and thus become denser over the duration of the polynya event. In addition, the absence of an along-shelf flow implies that a greater fraction of the dense water is carried cross-shelf by eddies (Gawarkiewicz and Chapman 1995) rather than into the canyon by the along-shelf flow. Finally, negligible winter canyon transport implies sluggish flow over the northeastern Chukchi shelf, thus expanding the time for exchanges between the seabed and bottom waters. Each of these processes affects the properties of the dense winter water that ultimately enters the Arctic Ocean.

#### **D.4.4 Shelf Response to Wind-Forcing**

Transport variations are largely controlled by local and remote winds. The latter includes Bering Sea shelf winds, where the seasonal variations in wind stress are much larger than over the northeastern Chukchi Sea. The summer and fall/winter wind-transport regression coefficients were significantly different from each other with the summer intercept being ~30% greater than the winter intercept. One reason for this difference might be due to the baroclinic contribution to the downcanyon transport, which amounted to ~20% of the total August and September transport. The baroclinic tendency should weaken through fall, and in winter it should either vanish entirely or reverse, as suggested by our observations.

Seasonal differences in regression coefficients may arise from oceanic processes that mediate vertical stress divergence in the along-shore momentum balance. Chapman and Lentz (2005) demonstrated that for stratified shelves the frictional stress exerted by the bottom boundary layer (bbl) is diminished compared to the unstratified case so that stratification enhances the along-shore transport forced by an along-shore pressure gradient. The response depends upon the magnitude of the slope Burger number ( $Bu = \alpha N/f$ , where  $N$  is the buoyancy frequency and  $\alpha$  is the bottom slope). Bottom slopes are  $\sim 5 \times 10^{-4}$  over the Bering and Chukchi shelves (and  $\sim 10^{-3}$  in Barrow Canyon).  $N$  varies from  $\sim 0.1 \text{ s}^{-1}$  in spring and early summer due to heavy stratification associated with ice melt (Weingartner et al. 2013b) and/or runoff over portions of the Bering Sea shelf (Danielson et al. 2012) to  $\sim 0 \text{ s}^{-1}$  in winter (Aagaard et al. 1981; Aagaard et al. 1985). As a result,  $Bu$  may be  $\geq 0.2$  in summer, and  $Bu \sim 0$  in winter on the shelf. Complete bbl shutdown occurs for  $Bu > 1$  (MacCready and Rhines 1993), but Chapman and Lentz (2005) find an appreciable increase in the along-shore transport for  $Bu \geq 0.2$ . Spatial variations in  $Bu$  render comparisons with theory difficult, but the seasonal differences in  $Bu$  are consistent with the summer intercept being larger than that of winter.

Chapman and Lentz's (2005) arguments imply that the summer wind coefficients should be greater than those of winter, but instead the winter coefficients are  $\sim 1.5$  times greater than those of summer. Three possible reasons, operating alone or in concert, may account for this difference. First, fall and winter wind along-shore pseudostresses over the Bering Sea are greater than those of summer, and so the differences may simply reflect our choice of seasons in constructing the statistical model. Second, mobile sea ice covers all or portions of these shelves in fall and winter, and the ice-ocean drag should enhance the transfer of momentum from the atmosphere to the ocean (Lu et al. 2011; Schulze and Pickart 2012). Third, the winds force rapidly propagating, long continental shelf waves in fall/winter when the stratification is weak. In summer, a greater fraction of the wave energy should be carried by smaller, more slowly propagating coastal-trapped waves. These are more susceptible to coastline scattering as they propagate northward, reducing the response of the transport to the winds.

#### D.4.5 Transport Intermittency

The intermittent nature of upcanyon and downcanyon transport events is an important feature of the flow. Intermittency is seasonally-modulated, as reflected in the seasonal pdfs (Figure D7) and in the seasonal flow event duration pdfs (Figure D11). The differences, which arise because summer downcanyon (upcanyon) events are of greater (shorter) duration than those of fall and winter, may have consequences for shelf-basin exchange.

Upcanyon transport events have a maximum velocity scale of  $\sim 0.4 \text{ m s}^{-1}$  (Figure D3e), suggesting that the advective time scale for a parcel to travel from the mouth to the head of the canyon is  $\sim 6$  days. In summer,  $\sim 5\%$  of upcanyon flow events are  $\geq 6$  days, whereas in winter and fall, nearly 20% of upcanyon flows exceed 6 days. Thus, the transport of basin waters onto the shallower reaches of the Chukchi shelf is relatively rare and largely confined to fall and winter. Based on a comparison of the temperature and salinity records from moorings BC2 and EBC (where EBC is  $\sim 110$  km northeast of BC2, Figures D15a and b), we find that only  $\sim 1/3$  of the upcanyon events that transport slope waters as far as Barrow carry them to the head of the canyon.

Intermittency in downcanyon transports may have consequences on the formation of Arctic Ocean eddies. Nof (1991) argues that intermittent outflows can lead to unbalanced fluid patches that eventually break up into anticyclonic lenses. This mechanism is independent of the stability properties that evolve from quasi-geostrophic flows, such as that modeled by Spall et al. (2008) for a steady eastward shelfbreak current over the Chukchi/Beaufort slope. Presumably, short duration outflows from Barrow Canyon are more prone to generating eddies through imbalance, whereas longer, steadier duration outflows preferentially lead to quasi-geostrophic instabilities. Given the marked seasonal asymmetry in downcanyon event duration, Nof's arguments would suggest that current instabilities predominate in summer, and unbalanced motions prevail in fall and winter. Conceivably eddy generation sites might also change seasonally; unbalanced motions predominate at the canyon mouth while instabilities occur farther eastward along the Beaufort shelfbreak. As a final point, the halocline cold-core anticyclones generated along the Beaufort shelfbreak contain  $\sim 5 \times 10^{10} \text{ m}^3$  Pacific-derived waters (based on a diameter of  $\sim 20$  km and a thickness of  $\sim 150$  m (Zhao et al. 2014)). A similar volume is transported during fall/winter downcanyon events of  $\sim 2$  days duration, which have a mean daily transport of  $\sim 0.3 \text{ Sv}$ . This agreement may be fortuitous but it suggests consideration be given to the connection between intermittency and basin eddies containing Pacific-derived waters.

As noted by Itoh et al. (2014) the summer downcanyon transport is a significant source of heat and freshwater to the Arctic basin by feeding the shelfbreak currents that flow eastward along the Beaufort shelfbreak and, within the upper ocean, westward along the Chukchi slope (Corlett and Pickart 2017). Upwelling and reversals from east to west of the Beaufort shelfbreak flow depend upon the magnitude of the easterly along-shelf winds (Schulze and Pickart 2012); however, these winds may not cause a

simultaneous reversal in the canyon transport. For example, in July 2011 strong northeasterly winds (Figure D8b) resulted in westward flow and upwelling along the entire Chukchi and Beaufort shelfbreak (Spall et al. 2014). The Barrow Canyon transport in July 2011 was downcanyon (Figures D4 and D5), so the warm, fresh outflow was presumably carried westward along the Chukchi shelfbreak. Similarly, the mean westward surface flow (Figure D15) at the mouth of Barrow Canyon and over the Chukchi and Beaufort shelves and shelfbreaks was westward in September and October 2013 when mean winds were from the east-northeast at  $\sim 3 \text{ m s}^{-1}$  (Figure D14). These winds likely caused weak shelfbreak upwelling but not a complete reversal of the subsurface eastward shelfbreak jet (Schulze and Pickart 2012). However, the winds were not strong enough to reverse the transport at the mouth (Figure D15) or head of the canyon (Figure D5). Schulze and Pickart (2012) find that  $>65\%$  of all westward wind events having wind speeds of  $4 - 7 \text{ m s}^{-1}$  result in significant Beaufort shelfbreak upwelling. Using the hindcast record we computed the probability of a downcanyon event versus easterly wind speed over the Beaufort slope (at the NARR gridpoint located at  $\sim 72^\circ\text{N}$ ,  $152^\circ\text{W}$ ). We find that  $\sim 35\%$  of all downcanyon transports occur under easterly winds when these wind speeds are within the  $4 - 7 \text{ m s}^{-1}$  range.

The confluence of the westward-flowing shelfbreak current and the downcanyon flow at the mouth of the canyon is presumably complicated. The PV structures of these flows differ; the shelfbreak flow has an upwelled frontal structure whereas the downcanyon flow is in the downwelled configuration. Upon converging at the mouth of the canyon, the different PV fields of both currents must adjust to one another. How this adjustment evolves remains to be determined but may involve intense mixing and a variety of sub-mesoscale motions. In both the numerical model of Watanabe (2011) and Nof's (1988) inviscid, analytical model the fate of the outflow is sensitive to the PV structure of both the outflow and the ambient current field. Interestingly, Nof finds that the outflow could be deflected to the east or to the west or even switch back and forth depending on PV structures.

## D.5 Summary

We used a 5-year time series of transport, temperature, and salinity measurements obtained at the head of Barrow Canyon to describe the seasonality of these variables and to construct a 37-year hindcast of the mean daily transport. The annual cycle is in-phase with that in Bering Strait insofar as the maximum occurs in summer and the minimum in winter. The climatological Bering Strait transport is northward year-round (Woodgate et al. 2005b), but this is not the case in Barrow Canyon. Here the annual transport cycle consists of three seasons: a) the May through September or “summer” season in which the transport is downcanyon (northeastward and into the Arctic Ocean) and averages  $0.45 \text{ Sv}$ , b) the October through December or “fall” season in which the average transport is upcanyon (southwestward and onto the Chukchi Shelf) at  $0.1 \text{ Sv}$  and; c) the January through April or “winter” season when the along-canyon transport is not significantly different from zero.

## E. A Quasi-Lagrangian Perspective on the Surface Circulation of the Chukchi Sea

### E.1 Introduction

This section of the report builds on a number of satellite-tracked drifter studies undertaken in collaboration with BOEM and included as a part of this project. These studies were initiated in 2011 under a Coastal Marine Institute program in partnership with Shell, and from 2012 – 2014 in partnership with the North Slope Borough-Shell Baseline Studies Program. The 2011 – 2013 work and analysis details were summarized by Weingartner et al. (2015). Additional deployments were made in 2014 by the North Slope Borough-Shell Baseline Studies Program with the analysis conducted in partnership with this BOEM program and through BSEE.

The 2014 deployments complement the previous efforts in several ways. First, the 2014 deployments provide a unique perspective of a broad-scale coastal upwelling event along the west coast of Alaska. Such events are likely common in the Chukchi Sea, especially in fall and winter when there are few surface current observations.

Second, the drifters were deployed in large clusters (similar to the deployments made in 2012 and 2013), which allows us to improve climatological estimates of relative dispersion during the open water season on the Chukchi shelf. Dispersion measures how a patch of fluid containing suspended and/or dissolved tracers (such as pollutants, chemicals, plankton, and sediments) evolves; i.e., where the “tracer cloud” goes and how these particles are mixed into the environment. Relative dispersion quantifies the spread of particles about the center of mass of the “patch” (or cluster in our case). This measure, which depends upon the initial size of the patch, is due to sub-mesoscale (defined here as being  $<1$  baroclinic radius of deformation,  $R_{bc}$ , which is  $\sim 6$  km in the Chukchi Sea in summer and fall), mesoscale ( $1 - 4 R_{bc}$ ) and larger scale processes (LaCasce 2008). Although in general we may not be able to identify specific processes associated with dispersive “events”, the climatological construct allows a quantifiable estimate of these processes. These estimates may then be compared with estimates derived from numerical models, which require some parameterization of sub-grid scale processes.

Third, the clustered sampling approach also allows us to examine key kinematical and dynamical aspects of the surface circulation. The former includes velocity gradients and the terms comprising the deformation tensor. Our dynamical exploration focuses on the relative roles of surface gravity waves, winds, and horizontal pressure gradients in driving the near-surface circulation. Understanding the relative importance of these three influences should help guide the development of oil spill and/or ecosystem models that examine how particles and/or pollutants are advected. The dynamical examination is of particular importance in the Chukchi Sea where the geostrophic flow is controlled by both the mean pressure gradient between the Pacific and Arctic oceans (Woodgate et al. 2006) and more rapidly varying pressure gradients associated with wind-forced coastal convergences/divergences (Weingartner et al. 2013a). The surface circulation results from the interaction of these pressure gradients, the local Ekman balance, and the wave field, none of which have been separately quantified to our knowledge. The individual contributions may be quite important and may conflict with conclusions drawn from simple two-dimensional wind-driven models of continental shelf circulation. These models find that at distances  $>1$  barotropic radius of deformation ( $R_{bt}$ ,  $\sim 150$  km in the Chukchi Sea) the surface circulation is controlled solely by Ekman dynamics (Csanady 1982). The momentum balance estimates made by Weingartner et al. (2013a) indicate that this is not the case in the Chukchi Sea where the horizontal pressure gradients, which appear to be largely barotropic, may be quite large at distances  $>1 R_{bt}$ .

This section will also address two important questions pertinent to understanding mesoscale circulation phenomena in the lower reaches of Barrow Canyon (e.g., north of Point Barrow). The first question we ask bears on the fate of the outflow from Barrow Canyon. As evident in the drifter records of Weingartner et al. (2015) and those shown herein, some of the drifters turn east and some turn west at the mouth or in the lower portion of the canyon. In general, the drifters that turn at the mouth of the canyon then move along the shelfbreak of either the Beaufort or the Chukchi seas, whereas the others are generally confined to the shelf. We hypothesize that winds play a central role in this turning process, which in turn governs the fate of the outflow from Barrow Canyon; mesoscale processes such as current instability or current separation from curving isobaths could also be involved. Our second question asks if there are differences in the level of mesoscale (eddy) energy between the mouth of Barrow Canyon and that of the continental slope to the east and west of the canyon. This question is motivated by the fact that the shelf topography and width changes moving eastward from the Chukchi Sea, across Barrow Canyon, and onto the Beaufort shelf. To the west of the canyon, the shelf is very broad, whereas the Beaufort shelf to the east of the canyon is substantially narrower. These transitions in shelfbreak width, coupled with the abrupt topographic transition associated with the canyon itself, suggest that eastward-propagating continental shelf or coastally-trapped waves may be scattered by these abrupt topographic changes. Although the scattering mechanisms are complex (Yankovsky and Chapman 1995; Yankovsky and Chapman 1996), they effectively transfer incoming wave energy into other waves, some of which have considerably smaller scales than the incident wave. Shorter waves are associated with current variations at similarly small scales and this variability may be reflected in the drifter statistics. The lower magnitude group velocity of short waves means that these waves are unlikely to propagate far from the canyon's mouth before dissipating. Wave scattering and its attendant mesoscale motions may be one source of the enhanced vertical mixing observed at the mouth of Barrow Canyon (Shroyer 2012). We emphasize that our data cannot resolve waves or wave-related processes, but spatial differences in current variability would be consistent with wave-scattering. The large number of drifter observations collected in the vicinity of Barrow Canyon over the several years of this program, provides the ability to address these questions.

## **E.2 Methods**

### **E.2.1 Drifter Deployments**

The satellite-tracked drifters were CODE-type drifters (Pacific Gyre Microstar) that measure currents in the upper 1 m of the water column. Three of 2014's clusters were deployed in nearshore waters by NSB residents from local villages, including a cluster of 27 drifters deployed offshore of Point Hope on 23 July, a cluster of 23 drifters deployed offshore of Point Lay on 26 July, and a cluster of 27 drifters deployed offshore of Wainwright on 29 July (Figure E1). Additionally, a cluster of 28 drifters was deployed on 15 September 2012 near the Burger prospect. Most of these drifters entered Barrow Canyon and contributed to the canyon analyses described below. Data processing procedures of all drifters follow the procedure described by Weingartner et al. (2015). The drifters in each cluster were deployed rapidly so that all were within a few 10s of meters of one another initially. These clusters are used to update the relative dispersion relationships for the Chukchi Sea shelf given in Weingartner et al. (2015). In evaluating the surface dynamics, we use these clusters in addition to the 2013 deployments made offshore of Point Lay and to the northeast and northwest of Hanna Shoal. We note that a limited number of drifters deployed over the lifetime of this program included sensors that detected when the drogue separated from the surface float. We find that this occurred on a limited number of drifters 60 days after deployment. Consequently, calculations are limited to within 60 days of deployment.

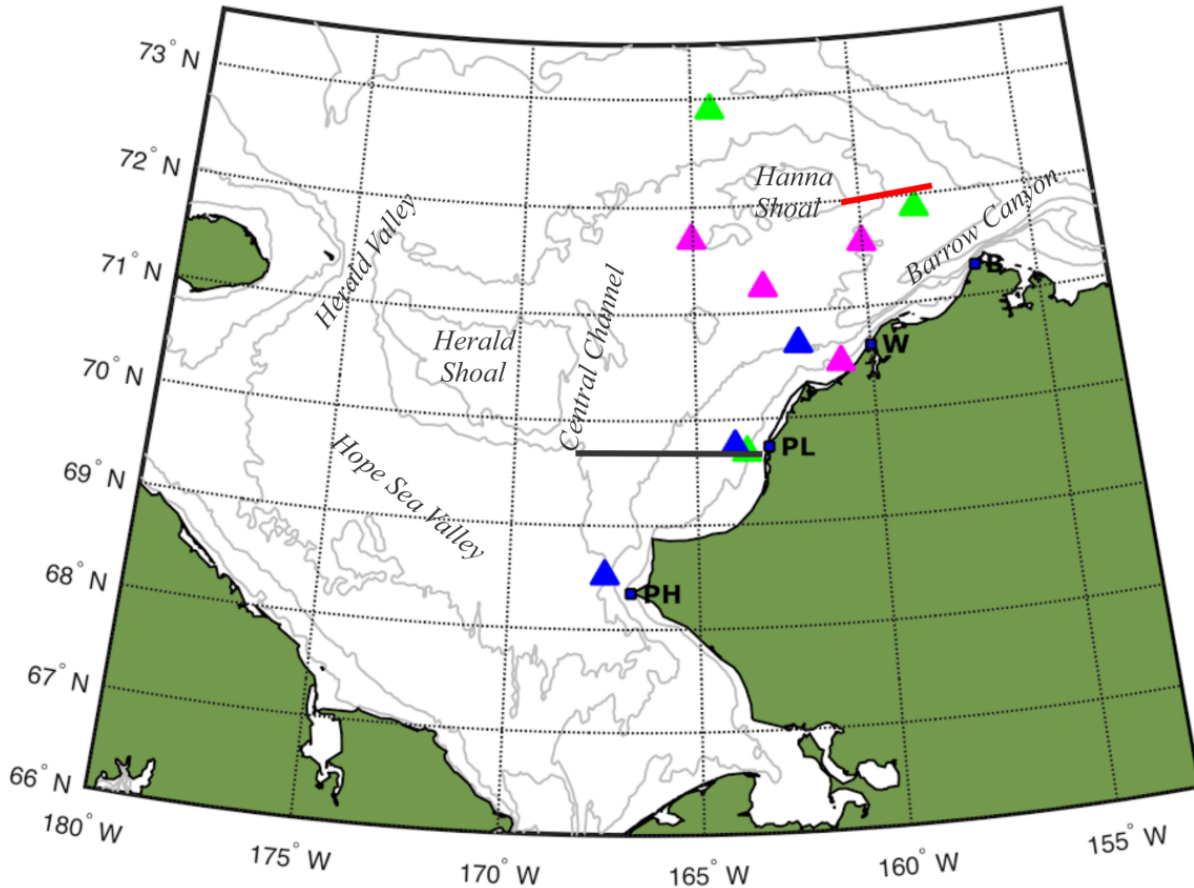


**Figure E1.** Bathymetric map of the Chukchi Sea showing the drifter deployment locations (triangles) in 2012 (magenta), 2013 (green), and 2014 (blue). The 2014 and 2013 deployments are used in evaluating the momentum balances and the 2014 deployments were used to update relative dispersion estimates presented by Weingartner et al. (2015). The villages of Point Hope (PH), Point Lay (PL), Wainwright (W), and Barrow (B) are indicated. The black horizontal line offshore of Point Lay shows the August 2013 trajectory of a glider and the red horizontal line shows the September 2013 location of the Acrobat CTD section northeast of Hanna Shoal.

## E.2.2 Momentum Balance Terms

The currents that displace an individual drifter arise due to the linear combination of the Stokes' drift (due to waves), the local Ekman response due to winds, and the geostrophic motion associated with pressure gradients:  $\overline{u'} - \overline{u_{ST}} = \overline{u_E} + \overline{u_G}$ , where the overbar indicates a vector and the subscripts "ST" signifies the Stokes' drift, "E" is the Ekman current, and "G" is the geostrophic contribution. The velocity vector is comprised of the zonal ( $u$ ) and meridional ( $v$ ) components. After low-pass filtering the velocity data from each drifter, we estimate the Stokes' drift current components based on the significant wave height predictions of the NOAA Wavewatch forecast models. These estimates are made by interpolating the model results (made every 3 hours and with a grid mesh of 35 km intervals) to the location of the drifter at each time step. The Stokes' velocity vector,  $\overline{u_{ST}}(z)$ , at a given depth,  $z$ , was estimated from the significant wave height ( $H_S$ ) and the corresponding significant wave period ( $T_S$ ) and wavelength ( $\lambda_S$ ):

$$\vec{u}_{st}(z=1m) = \frac{H_S^2 \omega k \cosh[2k(z+h)]}{16 \sinh^2[kh]} \vec{k}$$

where:  $\omega$  = wave frequency ( $\omega = 2\pi/T_S$ ),  $k$  = wavenumber ( $k = 2\pi/\lambda_S$ ), and  $\vec{k}$  = unit wave number vector, and  $h$  = water depth ( $h > 0$ ).

Comparisons between the Wavewatch-derived Stokes' drift with those based on the measurements from the oil industry's meteorological buoy in Klondike indicates that the two estimates are significantly correlated with one another ( $r^2 \sim 0.8$ ). Estimates of  $u_{ST}$  were removed from the drifter velocity data at each time step, i.e.,  $\vec{u}' - \vec{u}_{ST} = \vec{u}_E + \vec{u}_G$ . The adjusted velocities,  $u$ , were then used in evaluating the following momentum balances:

$$\frac{\partial u}{\partial t} - f(v_G + v_E) = -\frac{1}{\rho_0} \frac{\partial p}{\partial x} + \frac{1}{\rho_0} \frac{\partial \tau^x}{\partial z} \quad (\text{zonal momentum balance})$$

$$\frac{\partial v}{\partial t} + f(u_G + u_E) = -\frac{1}{\rho_0} \frac{\partial p}{\partial y} + \frac{1}{\rho_0} \frac{\partial \tau^y}{\partial z} \quad (\text{meridional momentum balance})$$

In these equations, the variables  $x$  and  $y$  are the zonal and meridional directions, respectively, and  $t$  is time. The reference density,  $\rho_0$ , is equal to  $1,024 \text{ kg m}^{-3}$ . The first term on the left-hand side of each equation is the local acceleration, which we estimated by central differencing of the drifter velocity record. The second term is the Coriolis acceleration, which depends upon the Coriolis parameter,  $f$ , evaluated at the latitude of the drifter at each time step. The Coriolis terms are typically an order of magnitude larger than the local acceleration terms and so we give no further consideration to the local accelerations. On the right hand side of each equation, the first term represents the horizontal pressure ( $p$ ) gradient and the second term describes accelerations arising from vertical divergence of the zonal and meridional stresses,  $\tau^x$  and  $\tau^y$ , respectively. We assume that the vertical gradient of horizontal stresses are due to the surface wind stress only (e.g., the Ekman assumption).

We solve the momentum equations for the Ekman and geostrophic velocities as follows. We first estimate the Ekman velocity at a depth of one meter using the Rutgers Ocean Model System (ROMS). We do this by running the model for several days (until steady-state is reached) at the range of wind velocities encountered by the drifters. The model was run using both unstratified and stratified conditions. Our estimates of the stratification derived from Acrobat and/or glider CTD surveys taken near in space and time to the drifter trajectories. Specifically, we used a glider section taken in August 2013 offshore of Point Lay and from two Acrobat (towed-CTD) sections from across the center and on the northeast and northwest sides of Hanna Shoal in 2013. The locations of all of these transects will be shown in Section E3.1 below. The differences between the stratified and unstratified model-predicted  $u_E$  and  $v_E$  at 1 m depth are small (generally only a few percent) and not considered significant. At each time step, we then remove the Coriolis acceleration associated with the "stratified-model" Ekman velocity estimate at 1 m. Our assumed momentum balance means that the residual velocities are the geostrophic velocities,  $u_G$  and  $v_G$ , which can then be used to estimate the horizontal pressure gradients.

Our wind stress estimates are based on the wind forecasts from either the NARR (Mesinger et al. 2006) or NOAA Wavewatch III models and formulated following Large and Pond (1981). The skill in wind prediction from both forecast models is  $\sim 0.95$  when compared with meteorological buoy observations from the central Chukchi Sea and the root mean square error between the model and observed winds is  $1.5 - 2.0 \text{ m s}^{-1}$  (Weingartner et al. 2015). We used a  $2 \text{ m s}^{-1}$  wind speed uncertainty in order to estimate

the error in our residual velocities. For winds speeds  $<10 \text{ m s}^{-1}$  the uncertainty in the residual velocity is  $3 \text{ cm s}^{-1}$  and at greater winds speeds the uncertainty increases to  $\sim 5 \text{ cm s}^{-1}$ . We emphasize that we are not precisely calculating the contribution due to various sources of motion. Instead, our calculations are meant to provide a qualitative sense of the importance of one source of motion relative to another over the course of the cluster's trajectory.

### E.2.3 Wind and Current Variability

To examine the influence of the winds on the waters moving through Barrow Canyon, the downcanyon (northeastward) trajectories were visually inspected and classified into 5 groups based on the location where the trajectory diverged from its initial downcanyon path (Figure E2). We selected a point of interest (POI) along the east side of the mouth of the canyon on the 100 m isobath and located at  $71.75^\circ\text{N}$ ,  $154^\circ\text{W}$ . This point was chosen because it is the northernmost location of the 100 m isobath as it bends from trending northeastward along the canyon to the southeast along the Beaufort shelfbreak. Group I consists of trajectories that turn to the west or northwest after passing north of this point. Group II trajectories are those that move east of  $154^\circ\text{W}$  after passing to the north of the POI at  $71.75^\circ\text{N}$ . Group III trajectories are those that exit the east side of the canyon south of the POI and remain on the Beaufort shelf for 24 hours or more before returning to the canyon (if they do). Group IV turns westward or northwestward before reaching  $71.75^\circ\text{N}$ . Finally, Group V consists of drifters that turn around and return up-canyon. In order for a drifter to be considered in this classification, it must cross the "Start Line" (Figure E2), which extends westward across the canyon from Point Barrow. Only drifters that move from the southwest to the northeast are considered. A drifter that meets these criteria on more than one occasion is considered a valid candidate for the analysis. Approximate dates of the turns made by these drifters (or the dates of passing the POI in the case of Group II) are recorded; winds interpolated to each drifter track on those dates are used to determine the mean and standard deviation of the wind velocity at the time of the turn for each group.

We compared the current variability at the mouth of the canyon to current variations over the shelfbreak to the east and west of the canyon by dividing the region into three geographic boxes. The mouth of the canyon is defined to be between  $157^\circ$  and  $153^\circ\text{W}$  and from  $71.5^\circ\text{N}$  northward to the 3,000 m isobath

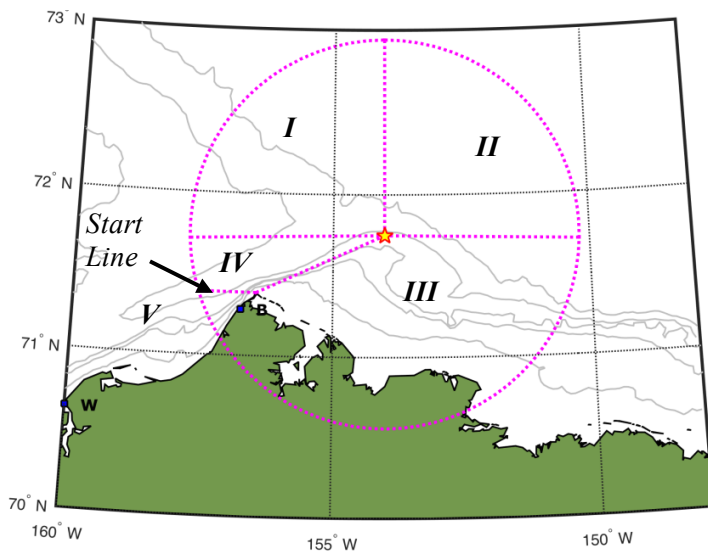


**Figure E2.** Delineation of the five different classification groups used to examine the fates of drifters moving northeastward through Barrow Canyon. A drifter must pass northeastward across the "Start Line" in order to be considered in the analysis. The yellow star indicates the location of the point of interest (POI) on the 100 m isobath.

(green, Figure E3). The Chukchi slope is defined as between 157° and 162°W and between the 100 and 3,000 m isobaths (blue, Figure E3). The Beaufort slope is defined as between 153° and 145°W and between the 100 and 3,000 m isobaths (yellow, Figure E3). In this analysis, multiple reentries by a drifter into the same box are included in the analyses. Drifter and wind velocities were recorded at each time step and assigned to one of the three appropriate boxes. We computed the drifter and wind Mean Kinetic Energy (MKE) and Eddy Kinetic Energy (EKE) as:

$$\text{MKE} = 0.5[U_i^2 + V_i^2] \text{ and } \text{EKE} = 0.5[u_i^2 + v_i^2],$$

where  $U_i, V_i$  are the zonal and meridional velocity component means, respectively, in the “*ith*” box. The variables  $u_i, v_i$  are the corresponding zonal and meridional deviations from the “*ith*” box mean. The Barrow Canyon analyses also included a number of 10 m drogued SVP drifters that were deployed in 2011. These were analyzed separately from the 1 m drogued drifters.

## E.3 Results

### E.3.1 Hydrographic Background

We begin with a brief description of the hydrography from 2013, because this illustrates the different types of stratification likely encountered by the drifters. Figure E4 shows a vertical section orthogonal to the coast occupied by glider 191, which transited ~120 km eastward from the Central Channel toward the Alaskan coast along 70.5°N between 11 and 14 August 2013.

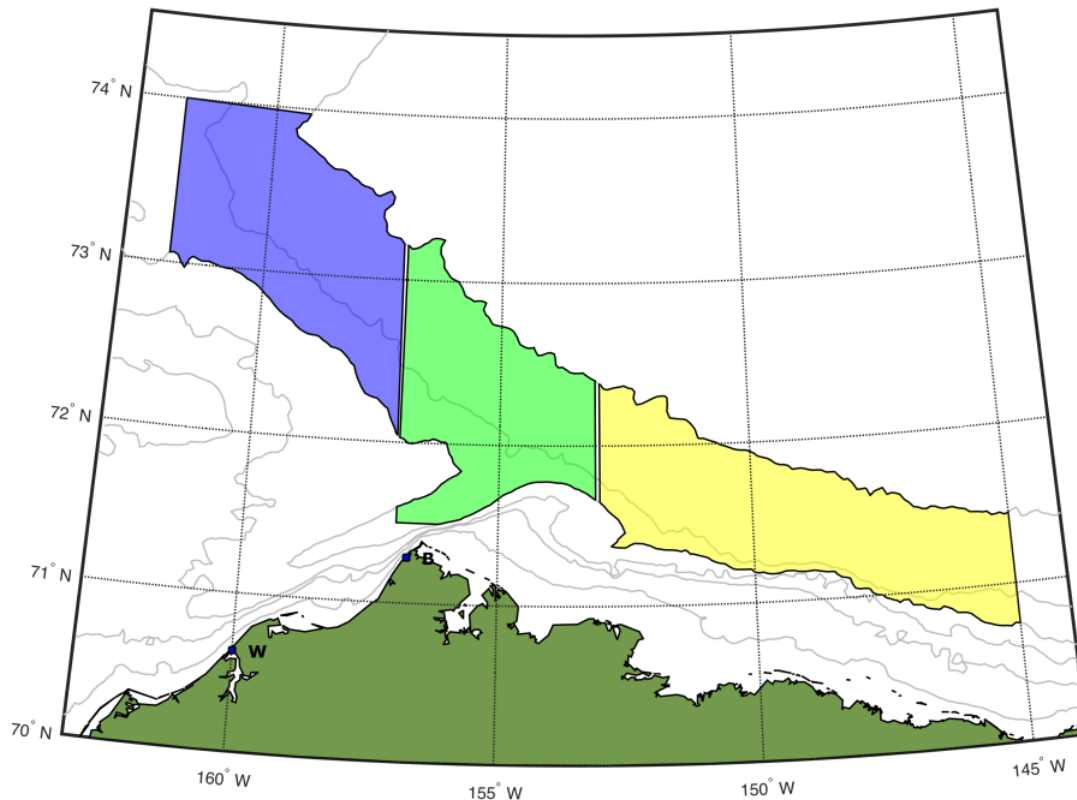


**Figure E3.** Map showing the shelfbreak and slope “boxes” used to evaluate mean and eddy kinetic energies. These regions are the Chukchi (blue), Barrow Canyon (green), and Beaufort (yellow).

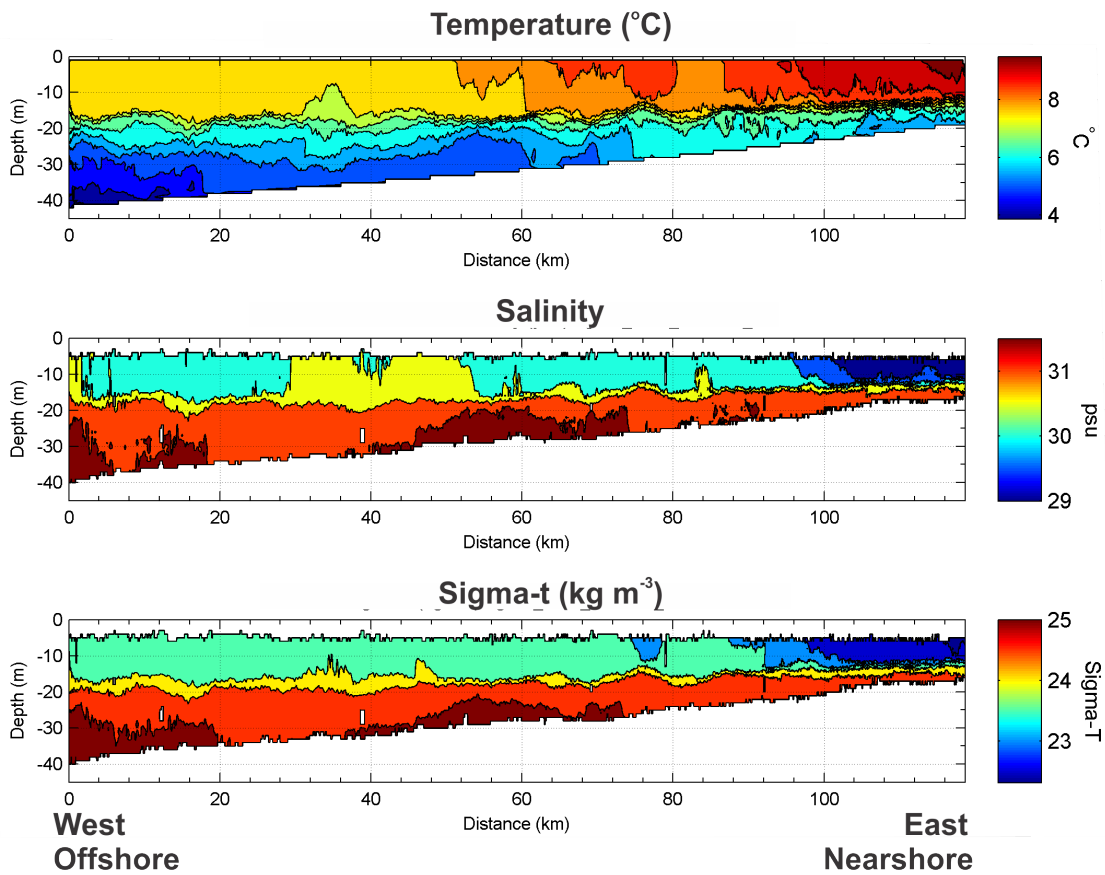
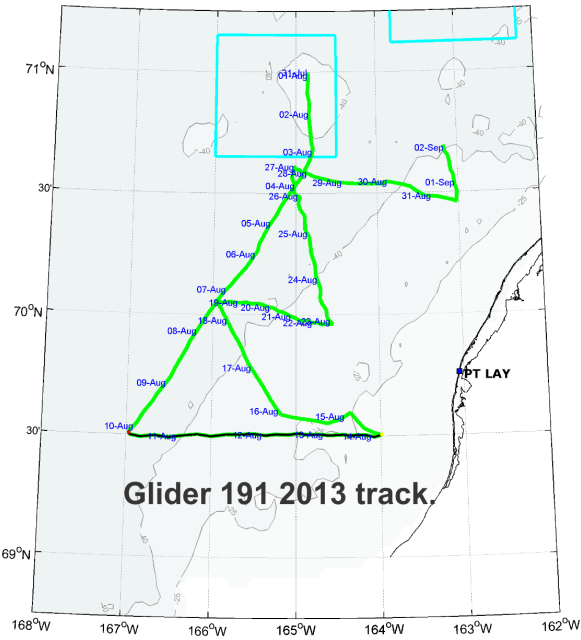


**Figure E4.** Top panel: map showing location (indicated by red line) of the west-to-east transect of glider 191 from 10 to 14 August 2013. The bottom three panels are the vertical sections of temperature (top), salinity (middle), and density (expressed as sigma-t; bottom) along the transect. The westernmost end of the transect is on the left of the figure.

For reasons pertaining to glider navigability, it did not enter very shallow waters, but only came within ~40 km of the coast. Close to the coast (between 100 – 120 km), the waters were warm (8 – 9°C), fresh (<29.5) Alaskan Coastal Water in the uppermost 20 m. Beneath this layer, the waters were cooler (~4°C) and saltier (31). A surface front, located at km 100, separated the nearshore surface waters from cooler (7 – 8°C), saltier (>~30) water. The offshore waters below 20 m depth had temperatures of 5 – 6°C and salinities of ~31. The stratification across the section was moderately strong, with the strongest stratification inshore. The pycnocline was thin ~10 m and centered at ~20 m depth. Our Ekman calculations for the region of the Chukchi shelf south of 70.5°N used a stratification that was similar to the offshore region sampled by glider 191.

Figures E5 – E7 show sections taken from transects to the northeast, over the top of, and to the northwest side of Hanna Shoal. All sections indicate a strongly stratified water column, which is a consequence of fresh, cold meltwaters (MW) in the upper 15 m and saline, near-freezing winter waters below 25 m depth. The strong stratification is prevalent throughout this region even across the top of the Shoal (Figure E6).

There are two other noteworthy features of these sections. The first is the suggestion of small-scale variability in temperature and salinity within the surface layer. These variations occur over a variety of spatial scales and range in size from a few to 10 km or so. They may be MW fronts and/or small eddies confined to the mixed layer and are thus capable of affecting the surface circulation. The other

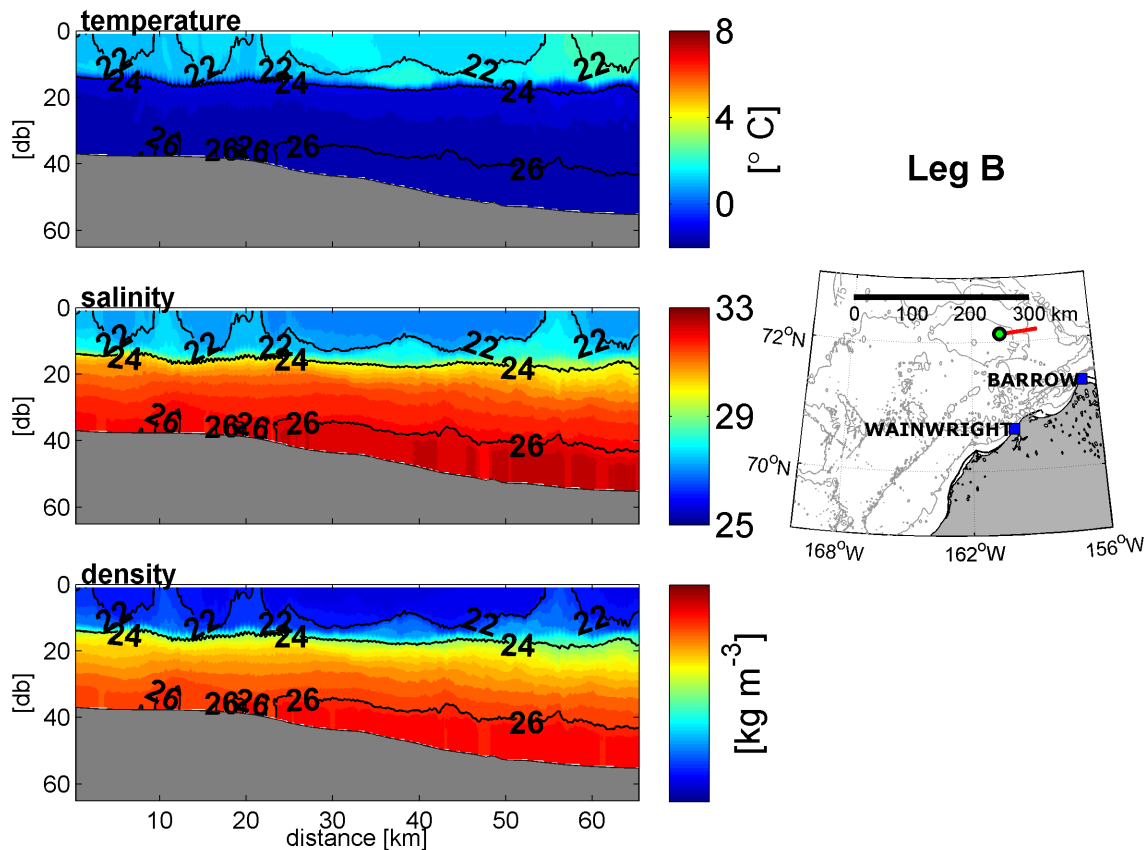


**Figure E5.** Vertical sections of temperature, salinity, and  $\sigma_t$  from an Acrobat transect along the northeastern side of Hanna Shoal on 11 September 2013. The western part of the section is on the left-hand side of the figure.

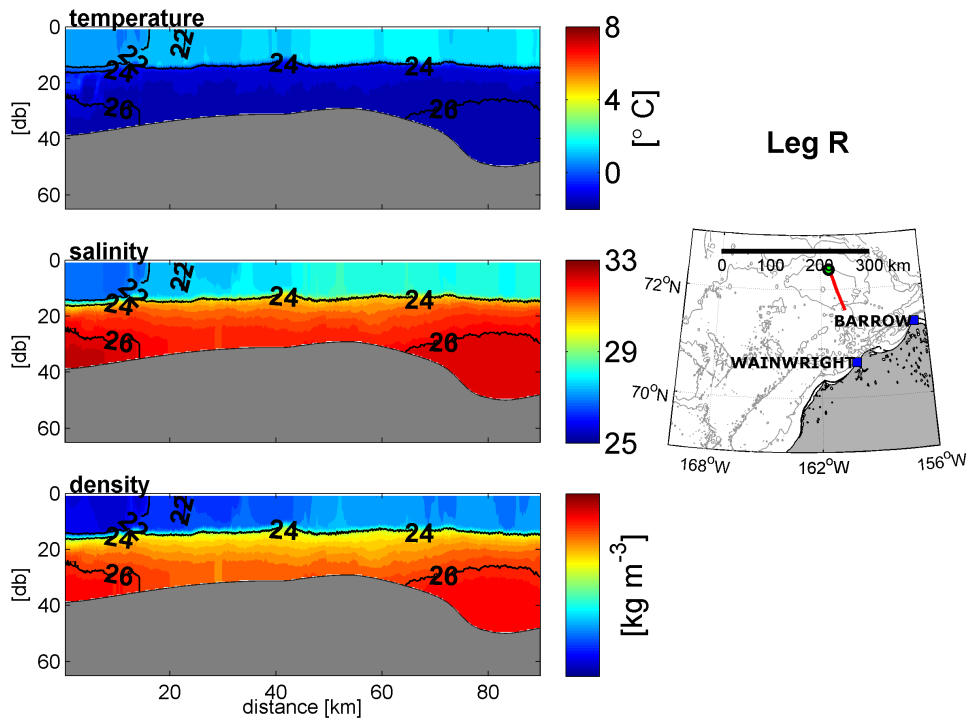


**Figure E6.** Vertical sections of temperature, salinity, and  $\sigma_t$  from an Acrobat transect across the top of Hanna Shoal on 10 September 2013. The northern part of the section is on the left-hand side of the figure.

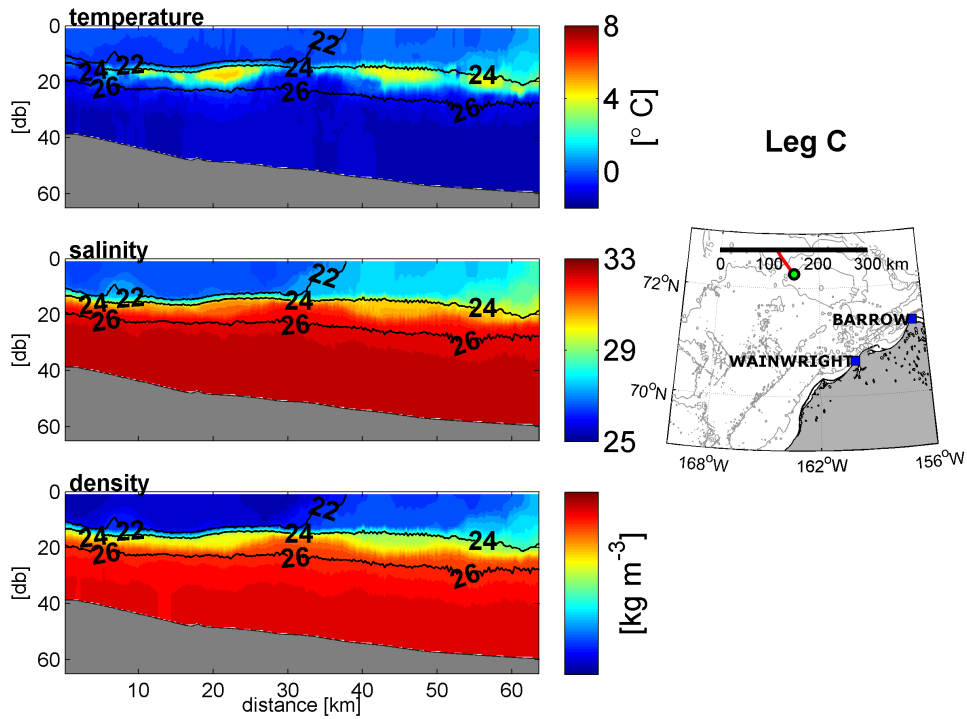


**Figure E7.** Vertical sections of temperature, salinity, and  $\sigma_t$  from an Acrobat transect on the northwest side of Hanna Shoal on 10 September 2013. The southeast end of the section is on the left-hand side of the figure.

feature of note is that the isopycnals on the northeast and northwest sides of Hanna Shoal (Figures E5 and E7, respectively) slope downward away from the Shoal. These slopes are indications of baroclinic pressure gradients, which would tend to accelerate the currents counterclockwise around the Shoal and opposite to the barotropic pressure gradients that tend to accelerate the flow clockwise around Hanna Shoal (Winsor and Chapman 2004; Spall 2007). The model results and the observations suggest that these pressure gradients act in opposition to one another as discussed in Section H.

### E.3.2 Surface Circulation

We begin this section by examining the cluster of drifters deployed ~20 km offshore of Point Lay on 19 August 2013. Figure E8 shows the trajectory of the cluster centroid and the individual drifters along with time series of the centroid and wind velocities and the mean sea surface temperature. Figure E9 consists of time series of the zonal and meridional components of the velocities. Labels along the track and associated with the time series in both Figures E8 and E9 refer to distinct events that are discussed. After deployment (Period A) the cluster moved to the southwest offshore under the influence of northeasterly winds until 25 August. Note that as the drifter began moving offshore, SSTs increased from 6 to 8°C. Recall that ~5 days earlier the inshore glider data indicated 6°C water near the bottom and >8°C at the surface. One interpretation of the drifter SST measurements is that the near-bottom waters of the previous week had upwelled to the surface and the warmer surface water was spreading offshore. Throughout this initial movement to the southwest, the net motion was governed by Ekman dynamics zonally and geostrophic meridionally. Typical velocities for both of these components were ~10 – 20 cm s<sup>-1</sup>. The winds shifted and became more variable through the end of August. The circulation response included a rapid reversal to the northeast due primarily to geostrophy. This response is consistent with the northeastward flowing Alaskan Coastal Current (ACC) in this region. The motive force for this flow is the Pacific-Arctic pressure gradient and the zonal density gradient evident in Figure E4. During Period B (9/1 – 9/6), the winds were northeasterly at 5 – 10 m s<sup>-1</sup> and the cluster drifted ~120 km rapidly westward and entered the Central Channel southeast of Herald Shoal. The zonal Ekman drift, at 10 – 30 cm s<sup>-1</sup>, was principally responsible for this westward transit. Note that the meridional geostrophic component remained northward throughout this period, and was slightly larger in magnitude and tended to cancel the southward Ekman component. Once in the Central Channel, the cluster was subjected to weak and variable winds. During Periods CC1 (9/7 – 9/15) and CC3 (9/22 – 10/6), northward geostrophic motion dominated. The zonal motion was eastward and geostrophic during CC1 while both Ekman and geostrophic dynamics governed motion during CC3. Strong (~10 m s<sup>-1</sup>) northeasterly winds prevailed during Periods CC2 (9/16 – 9/21) and CC4 (10/7 – 10/10). During CC2, the net southwestward zonal motion was dominated by Ekman dynamics; however, the geostrophic motion was northeastward and thus tended to offset the Ekman displacement. In Period CC4, the net westward displacement was due to both Ekman and geostrophic dynamics. Over all periods, the Ekman and geostrophic velocity components have the largest magnitudes with most falling within the 5 – 20 cm s<sup>-1</sup> range. In contrast, the Stokes' current speeds are ≤5 cm s<sup>-1</sup>. Although these speeds are comparatively small, the Stokes' drift, when integrated over time can lead to substantial displacements. For example, during Period B, the cluster moved ~120 km westward in 6 days. The Stokes' drift accounted for ~20% of this westward displacement.

We next consider the drift of the cluster of the drifter cluster deployed offshore of Point Lay on 28 July 2014. Figure E10 shows the trajectory of the cluster centroid and the individual drifters along with time series of the centroid and wind velocities and the mean sea surface temperature. Figure E11 contains the time series of the zonal and meridional components of the velocities. The initial stages of this drift are quite similar to the 2013 Point Lay deployment insofar as this includes upwelling-favorable winds that moved the cluster offshore to the Central Channel followed by northward displacement in the Channel. Unlike 2013, the cluster turned eastward toward the coast upon reaching 71°N in the Channel. The other

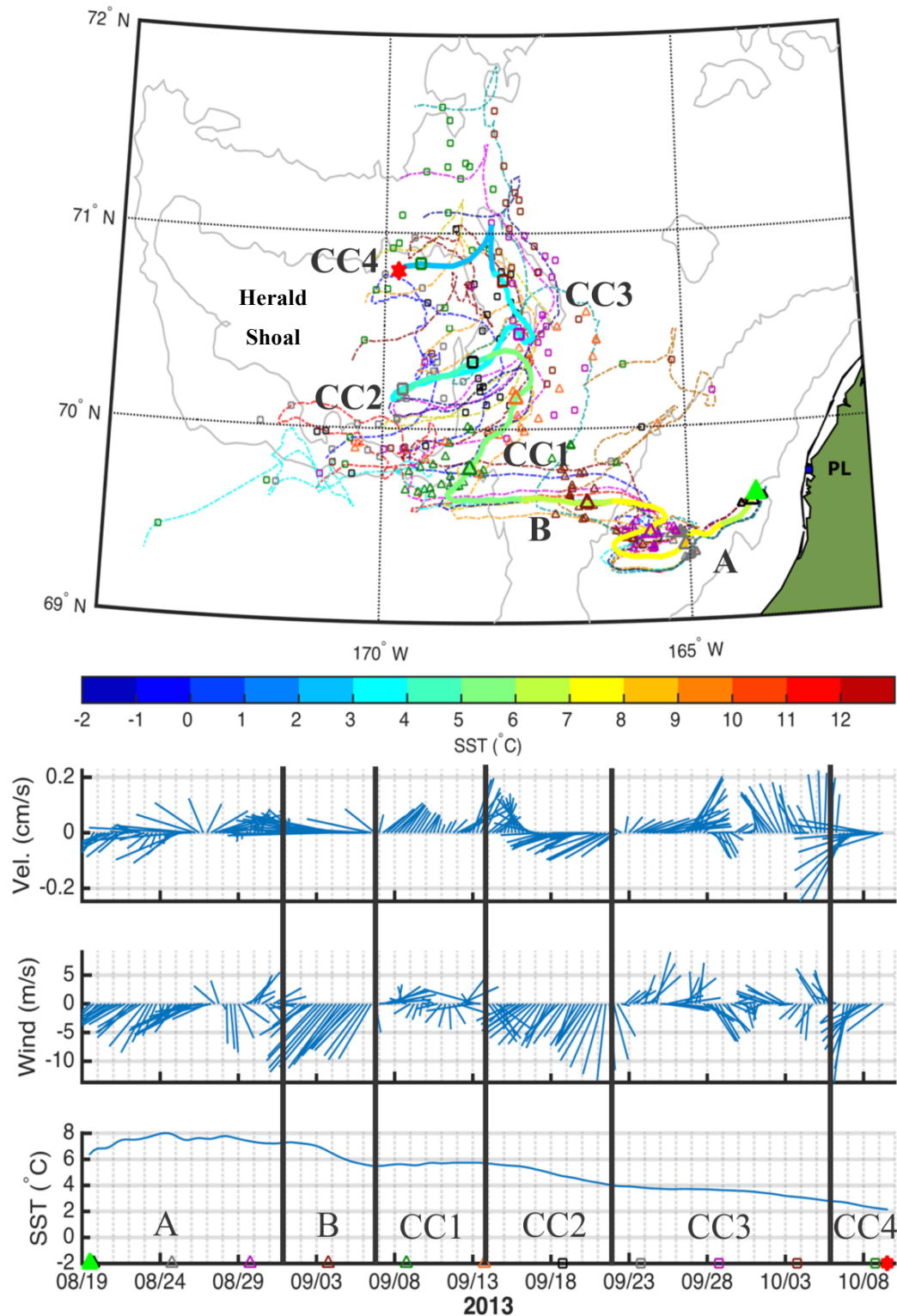


**Figure E8.** Trajectory of the Point Lay 2013 cluster centroid (color-coded by SST) and the 13 individual drifters within this cluster (top panel). Additional plots are the time series of the centroid (2<sup>nd</sup> from top) and wind (3<sup>rd</sup> from top) velocities and SST (bottom). The colored symbols along each trajectory are at 5-day intervals and correspond to the date axis on the SST time series plot. Events A, B, and CC1 – 4 are discussed in the text.

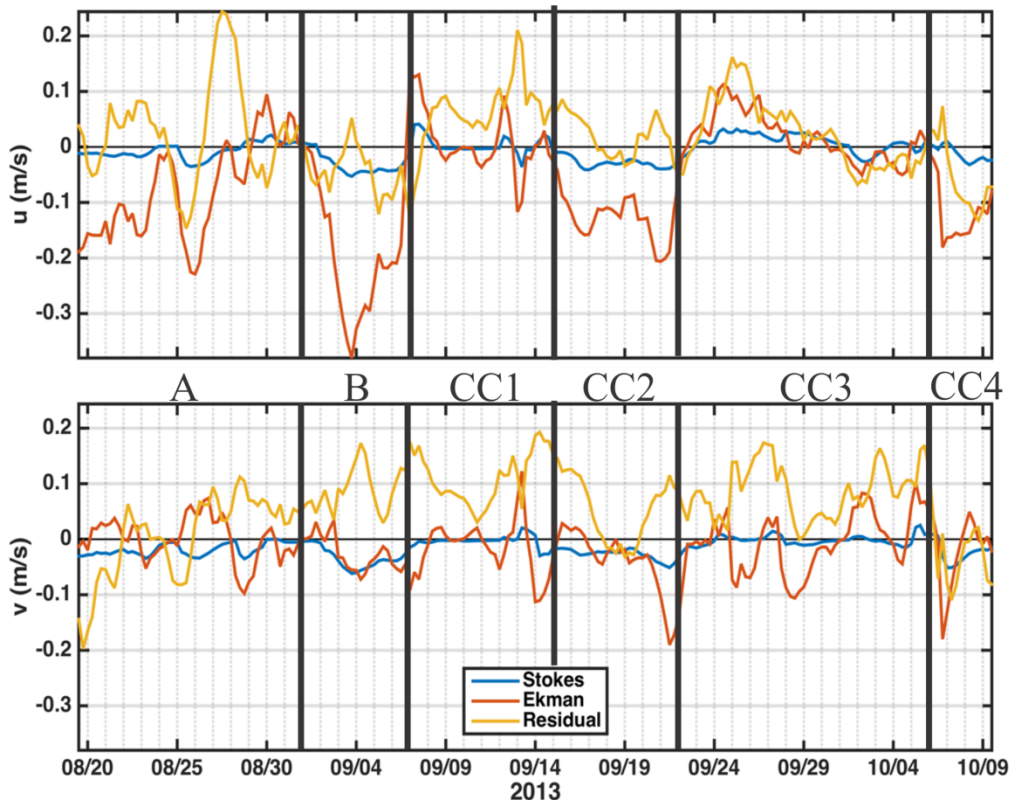


**Figure E9.** Time series of the zonal (top) and meridional (bottom) velocity components associated with the Stokes (blue), Ekman (red), and geostrophic (yellow) contributions to the surface velocity. The letters and vertical lines correspond to the periods in Figure E8 and discussed in the text.

obvious difference between these two clusters is the remarkable degree to which the 2014 cluster remained intact compared to the much larger dispersal in 2013.

The cluster headed northeastward at  $\sim 10 \text{ cm s}^{-1}$  for the first week following deployment with winds being both up- and downwelling-favorable but at speeds of  $\sim 5 \text{ m s}^{-1}$ . This drift was primarily geostrophic; the meridional Ekman currents were weak and the zonal Ekman currents opposed geostrophy initially, but then enhanced it during the latter half of the week. The Stokes drift was negligible. Strong northeasterly winds of  $\sim 10 \text{ m s}^{-1}$  prevailed throughout Period D (8/3 – 8/15) when the cluster moved  $\sim 200 \text{ km}$  westward in 12 days. The net westward motion was due to a mean Ekman drift of  $\sim 20 \text{ cm s}^{-1}$ . In contrast, the zonal geostrophic flow was eastward at  $5 - 10 \text{ cm s}^{-1}$ . In the meridional direction, the northward Ekman component was largely compensated for by the southward geostrophic component. The Stokes' drift averaged  $\sim 4 \text{ cm s}^{-1}$  and was consistently southwestward throughout Period D. Given that the Ekman and geostrophic components tend to buffer one another, the Stokes' drift alone can result in substantial displacement of the surface waters over a prolonged wind event.

The westward motion halted on 15 August as the cluster reached the east side of Herald Shoal and the winds veered to being southerly at  $\sim 6 \text{ m s}^{-1}$  over the next 3 days. The cluster moved eastward over these 3 days and then it moved  $\sim 100 \text{ km}$  northward in the Central Channel throughout the 6-day long Period E (8/18 – 8/24). Geostrophy dominated during this period with the geostrophic currents being  $\sim 15 - 20 \text{ cm s}^{-1}$ . When the drifters reached  $71^\circ\text{N}$  on 24 August, the winds switched and became west-northwesterly at  $\sim 5 \text{ m s}^{-1}$ . During Period F (8/26 – 9/5) the cluster moved eastward towards Barrow Canyon and eventually

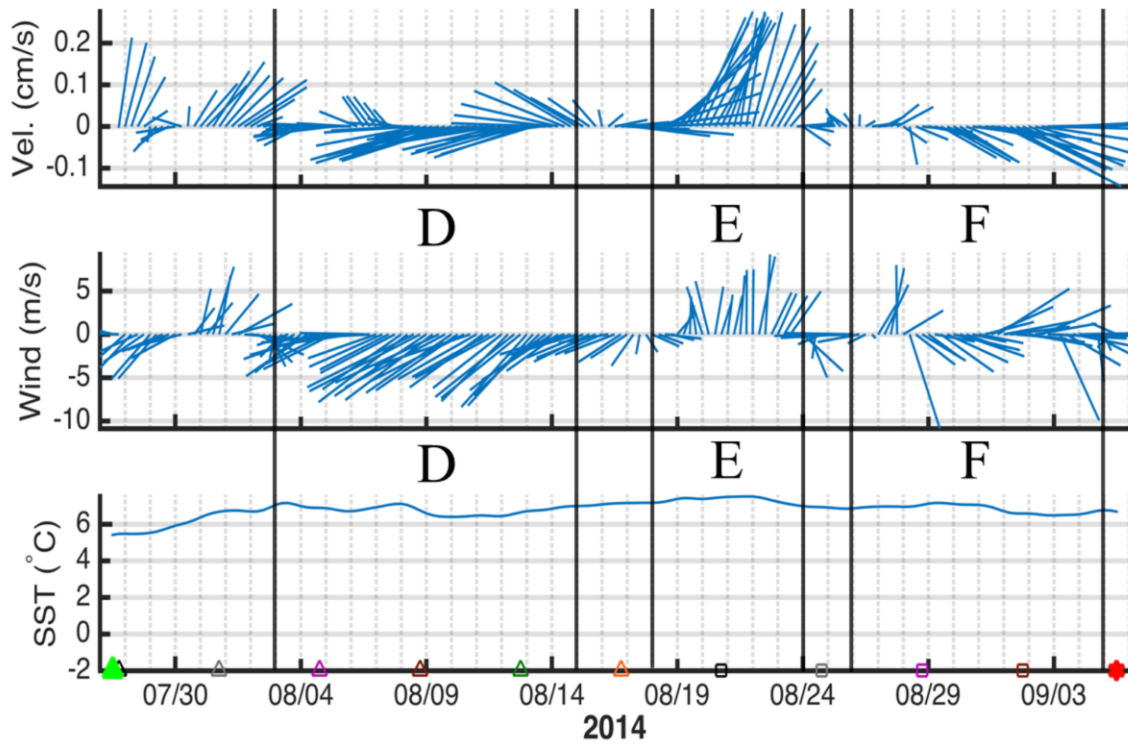
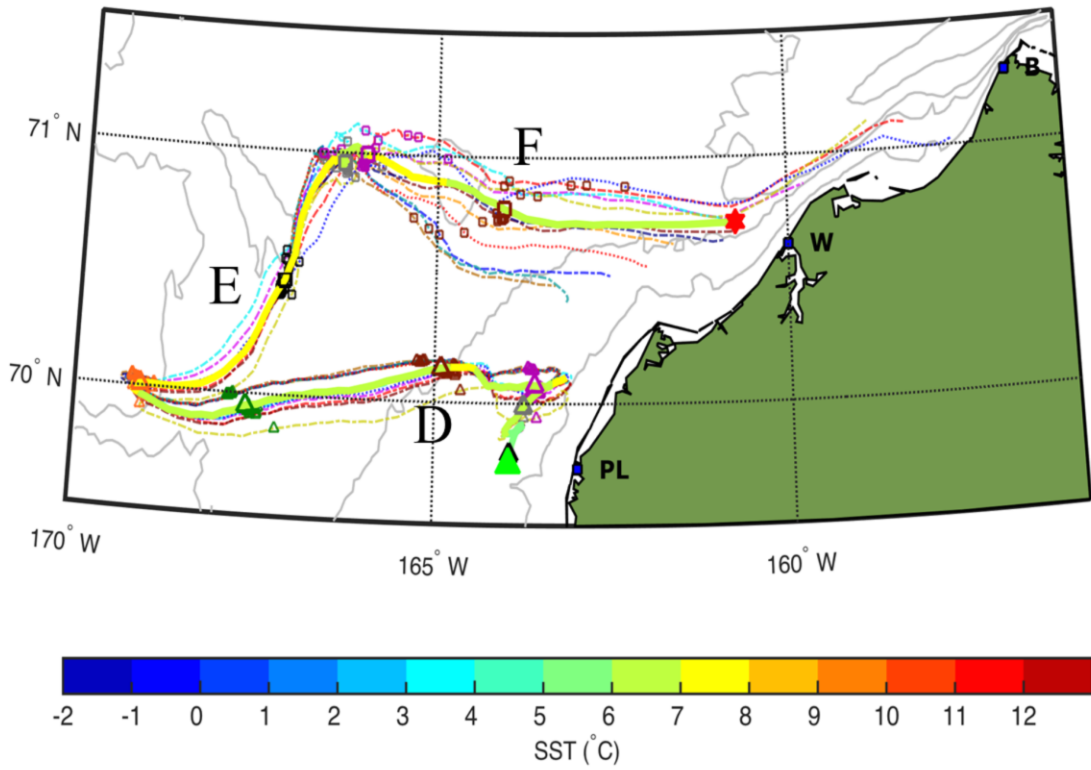


**Figure E10.** As in Figure E8 but for the Point Lay 2014 cluster. Segments D, E, and F are discussed in the text.

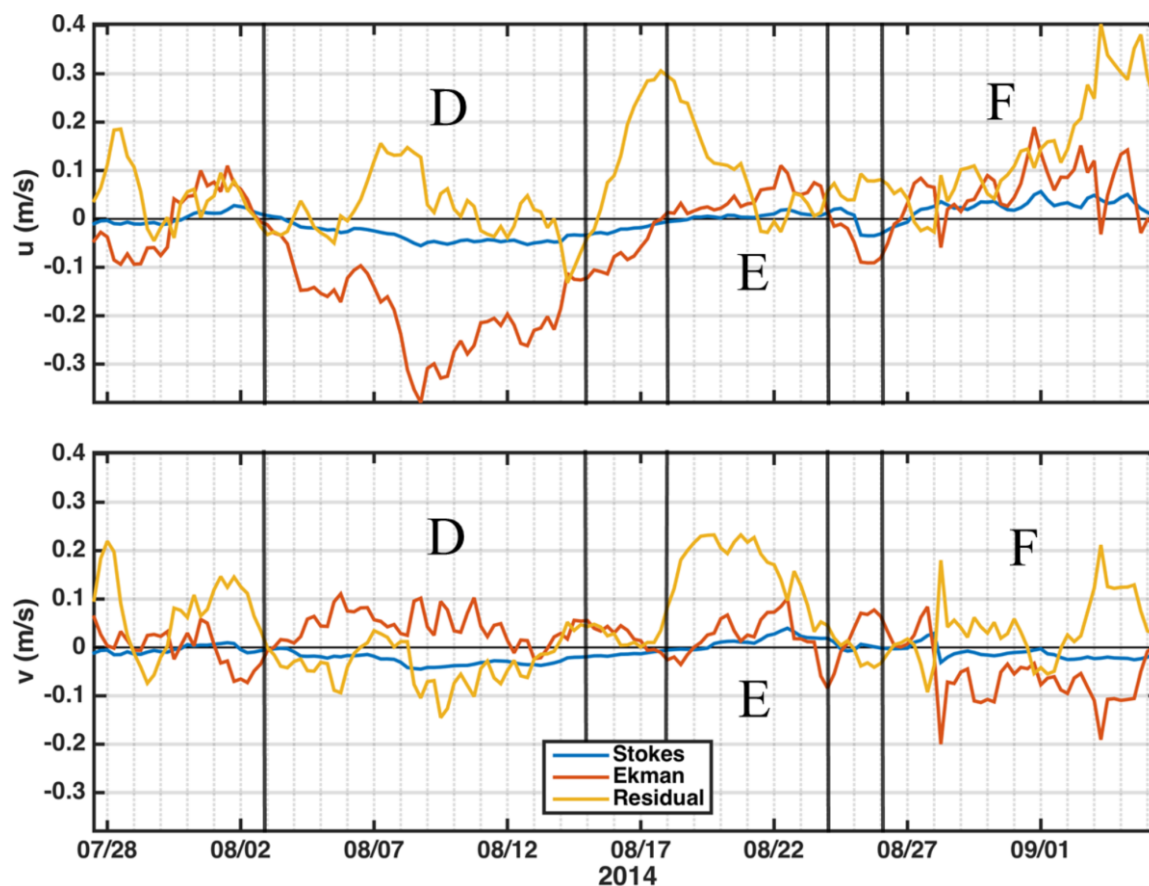


**Figure E11.** Time series of the zonal (top) and meridional (bottom) velocity components associated with the Stokes (blue), Ekman (red), and geostrophic (yellow) contributions to the surface velocity for the Point Lay 2014 deployment. The letters and vertical lines correspond to the periods in Figure E10 and are discussed in the text.

through the canyon (not shown here). During this transit from the Central Channel to Barrow Canyon, the Ekman and geostrophic components were both eastward and contributed to the zonal velocity. In contrast, the meridional Ekman and geostrophic components were equal in magnitude but opposite in direction, with the geostrophic velocity being northward. After 1 September, the cluster approached Barrow Canyon and the zonal, meridional geostrophic components rapidly increased in magnitude, and the cluster began to disperse.

In another deployment, a cluster of 27 drifters was deployed a few kilometers offshore of Point Hope on 24 July 2014. All the drifters began heading to the northwest but within about 5 days, the cluster split. All of the drifters continued west, but about half took a northerly route across Hope Sea Valley and proceeded westward along the south side of Herald Shoal (Figure E12). The other half took a more southerly route and drifted westward across Hope Sea Valley (Figure E13). Because of this bifurcation, we shall analyze the momentum balances of these two “sub-clusters” separately. Before proceeding with that analysis though, we consider some of the kinematic aspects of each cluster. The two groups separated from one another at about  $68.8^{\circ}\text{N}$ ,  $169^{\circ}\text{W}$ . We applied the approach developed by Okubo and Ebbsmeyer (1976) and used by Weingartner et al. (2015) for clusters from previous years to compute the terms in the

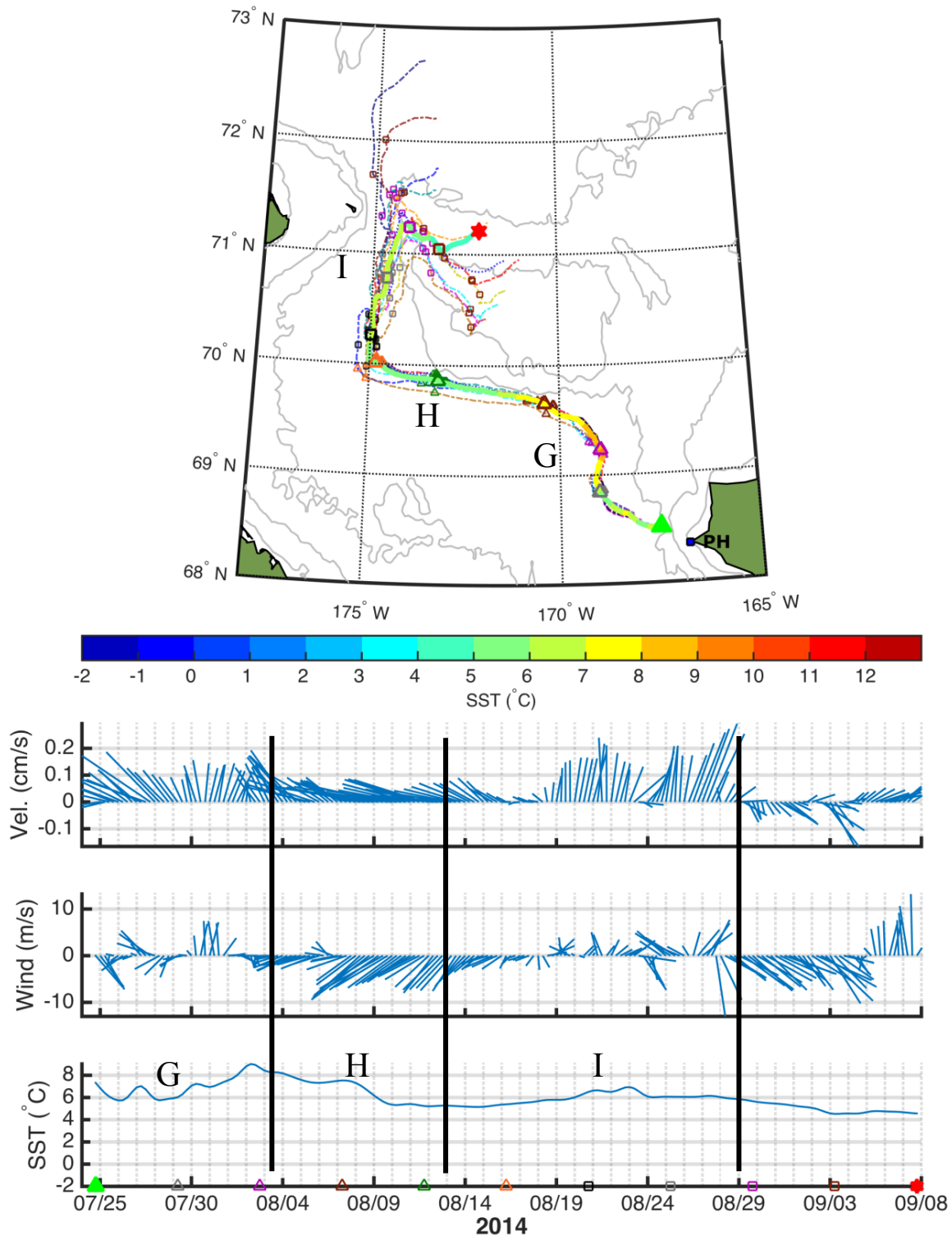


**Figure E12.** As in Figure E8 but for the Point Hope 2014 northerly cluster. Segments G, H, and I are discussed in the text.

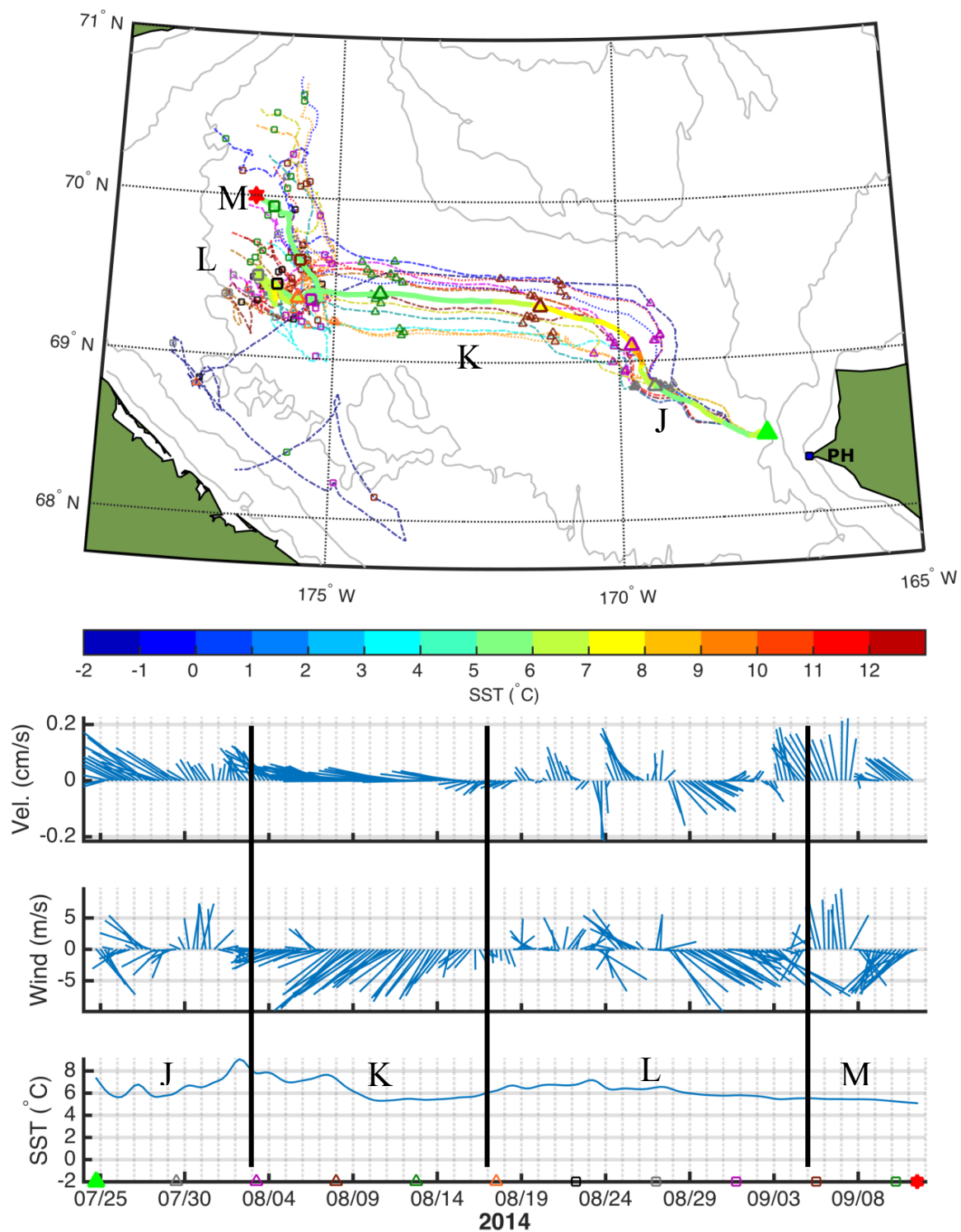


**Figure E13.** As in Figure E8 but for the Point Hope 2014 southerly cluster. Segments J, K, L, and M are discussed in the text.

deformation stress tensor for each of the Point Hope sub-clusters. Time series of these terms are shown in Figure E14 for each cluster. Our experience is that these terms are generally large immediately after deployment, but rapidly decay shortly thereafter. What is striking in these time series, is that the magnitudes of the relative vorticity ( $\zeta$ ) and shearing deformation ( $\xi$ ) terms are quite large, especially for the northern cluster from 27 to 29 July, when the two groups began breaking up. At this time  $\zeta$  was  $\sim 0.5f$ , indicating that the velocity field contained a substantial amount of anticyclonic vorticity.

We also found that  $\partial u/\partial y \gg \partial v/\partial x$  so that the meridional gradient of zonal velocity was the primary contributor to  $\zeta$  and  $\xi$ . Collectively, these results suggest that as the drifters moved northwestward from Point Hope, they encountered an eddy, front, or some other mesoscale feature (which type cannot be determined with the data at hand). Most likely, this feature was associated with the buoyancy-influenced Alaskan Coastal Current (ACC) that flows northwestward along the Alaskan coast southeast of Point Hope. The ACC's offshore boundary consists of a strong haline front (Coachman et al. 1975; Weingartner et al. 1999), which could be a region of considerable anticyclonic  $\zeta$ . Alternatively, as the ACC rounds the sharp bend associated with Point Hope, it may shed eddies. As a further consideration, the time rate of change of a fluid parcel's absolute vorticity ( $\zeta+f$ ) is given by:

$$\underbrace{\frac{d}{dt}(\zeta + f)}_{\substack{\text{rate of change} \\ \text{of absolute vorticity}}} + \underbrace{(\zeta + f)\gamma}_{\text{stretching vorticity}} = \text{sources and sinks for } (\zeta + f).$$

where the horizontal divergence is  $\gamma = \left(\frac{\partial u}{\partial x} + \frac{\partial v}{\partial y}\right)$ . The first term on the right describes the rate of change of the absolute vorticity and the second term is vortex tube stretching due to convergence or divergence within the fluid. Vorticity sources or sinks arise from torques associated with the surface wind or bottom stresses, or from baroclinic torques associated with the density field. Our data allow us to evaluate the terms on the left hand side only. If there are no vorticity sources or sinks then the left hand side should sum to zero. As shown in Figure E15 this balance is non-zero shortly after deployment of the Point Hope clusters. This is not unexpected since vorticity adjustments can be very large at the small horizontal scales captured early in the clusters' evolution. More noteworthy is that the stretching vorticity becomes very large in the northern cluster on 29 – 30 July, precisely as it separates from the southern cluster. The stretching is not compensated for by the local rate of change in absolute vorticity, so absolute vorticity production is occurring. We doubt that frictional torques (essentially arising from the curl of the wind or bottom stresses) occur on these small horizontal scales. The only likely source of vorticity production would be baroclinic torques associated with frontal processes. After the clusters separate from one another, the terms in the deformation tensor remain small (e.g.,  $\leq 1 \times 10^{-5} \text{ s}^{-1}$ ; Figure E14), the absolute vorticity is constant through time, and the stretching vorticity term is negligible (Figure E15).

Regardless of the mechanism responsible for the cluster separation, the result profoundly affected the fate of the water parcels initially tagged by the drifters. The northern cluster moved westward to 175°W and then made a 90° turn to the north and entered Herald Canyon. As the cluster turned northward, all of the terms in the deformation tensor remained  $\leq 0.1f$ . Thereafter this cluster began dispersing. The dispersal comes about because the northward flow in the valley is horizontally sheared (Pickart et al. 2010); the drifters entering along the eastern side of the valley (and adjacent to Herald Shoal) move northward more slowly than those closer to the center of the trough. The drifters making up the southern cluster milled about the western end of Hope Sea Valley. About half of these died in this region, while the other half either entered the East Siberian Sea or ran aground on Wrangel Island or the Chukotkan coast. The other

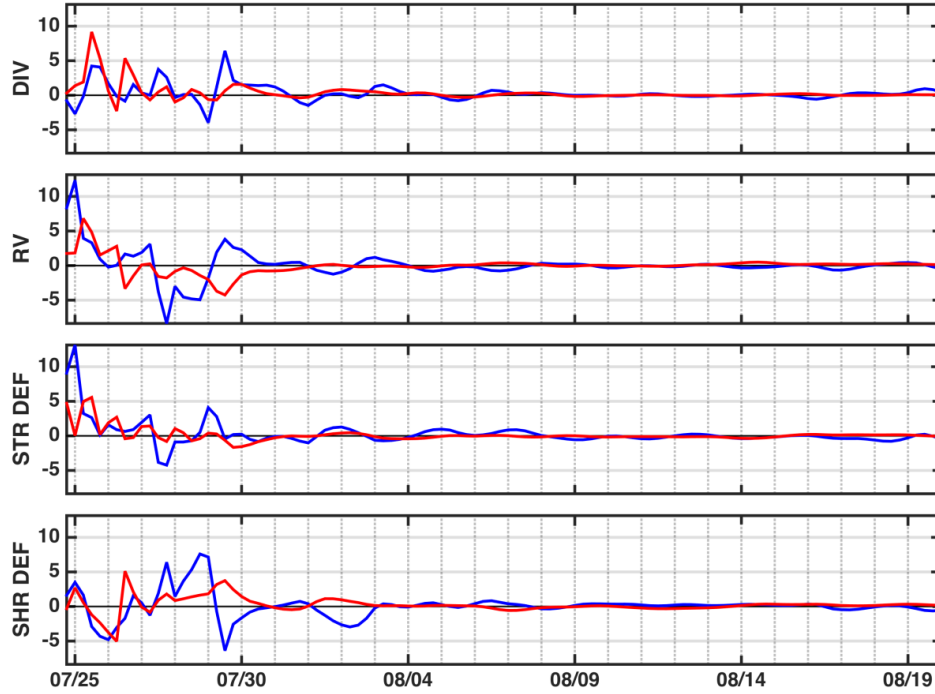


**Figure E14.** Time series of the four terms comprising the deformation tensor (div = divergence, RV = relative vorticity, STR DEF = stretching deformation, and SHR DEF = shearing deformation). The Point Hope North cluster terms are in blue and those for the Point Hope South cluster are red. Units are  $10^{-5} \text{ s}^{-1}$ .

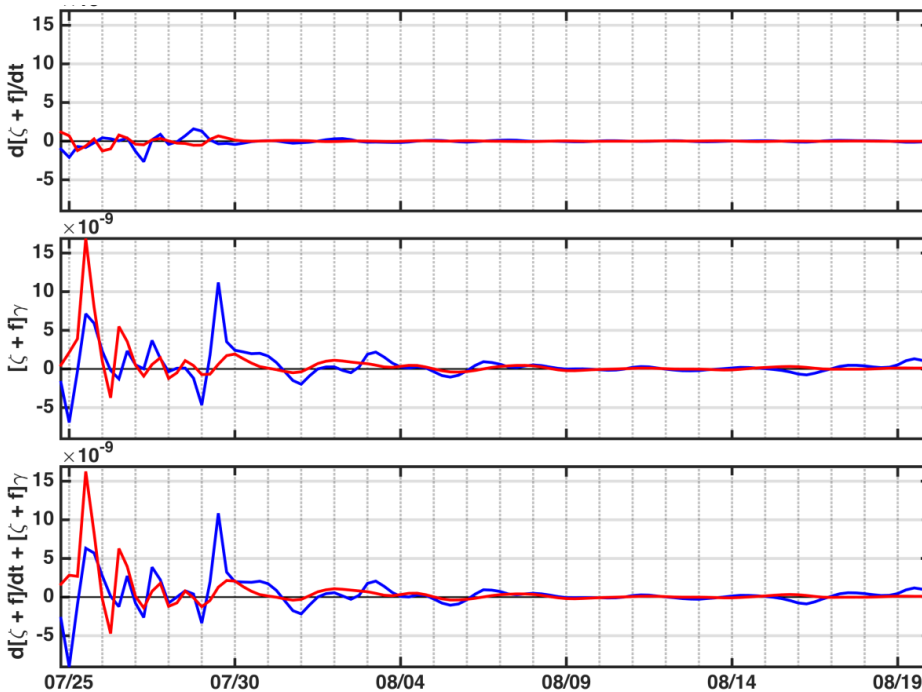


**Figure E15.** Time series of the terms comprising the absolute vorticity tendencies for the Point Hope North (blue) and Point Hope South (red) clusters. From top to bottom these are the rate of change of absolute vorticity, stretching vorticity, and the sum of the first two terms. Units are  $10^{-9} \text{ s}^{-2}$ .

feature of interest shared by both clusters is that the SSTs remained remarkably uniform throughout the ~45 day record. For the most part SSTs were ~6°C. The most prominent temperature changes occurred early in the records and towards the end. The first major change occurred after the two clusters separated on 29 July, when the SST increased from 6 to 8°C for several days and then decreased to 6°C again as the clusters moved westward across Hope Sea Valley. Temperatures also decreased noticeably in the northern cluster as it moved northward through Herald Canyon.

The momentum balance for the Point Hope North cluster is shown in Figure E16. Initially, geostrophy dominates the northwestward drift of ~10 – 15 cm s<sup>-1</sup> during Period G (7/25 – 8/3). The flow continued to the northwest during Period H (8/4 – 8/13) with the surface Ekman drift dominating the balance from 6 – 13 August when strong northeasterlies prevailed. The geostrophic currents were also northwestward at this time, although substantially smaller than the zonal Ekman flow. These winds abated on 16 August and during Period I (8/13 – 8/29), the meridional geostrophic flow moved the cluster northward into Herald Canyon; by 29 August, the cluster began dispersing rapidly. The dominant balances for the Point Hope South cluster (Figure E17) also included geostrophic flow initially (Period J; 7/25 – 8/3) followed by westward Ekman drift during Period K (8/3 – 8/17). During Period L (8/17 – 9/5), the cluster remained largely in place, with the geostrophic and Ekman terms variable and largely balancing. On approximately 9/3, the winds relaxed and the geostrophic flow carried the cluster northward. Period M (9/5 – 9/12) was dominated by the northward geostrophic flow.

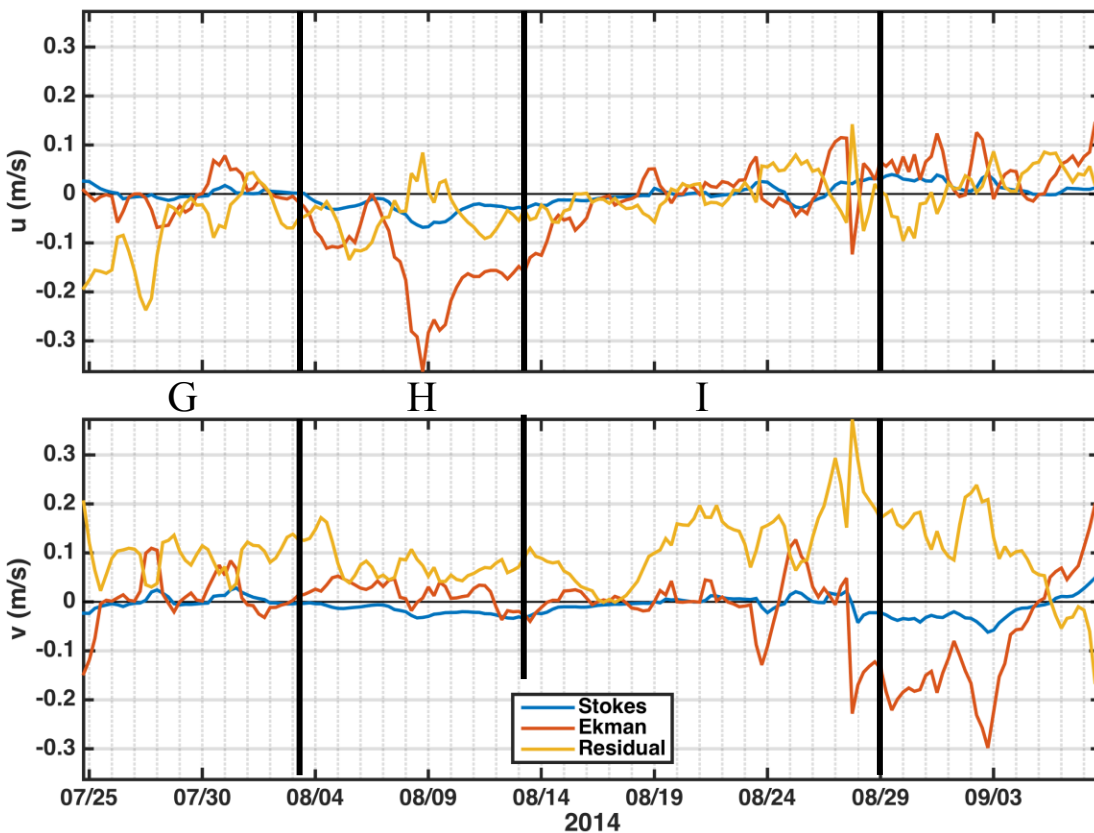


**Figure E16.** Time series of the zonal (top) and meridional (bottom) velocity components associated with the Stokes (blue), Ekman (red), and geostrophic (yellow) contributions to the surface velocity for the Point Hope North deployment. The letters and vertical lines correspond to the periods in Figure E12 and are discussed in the text.

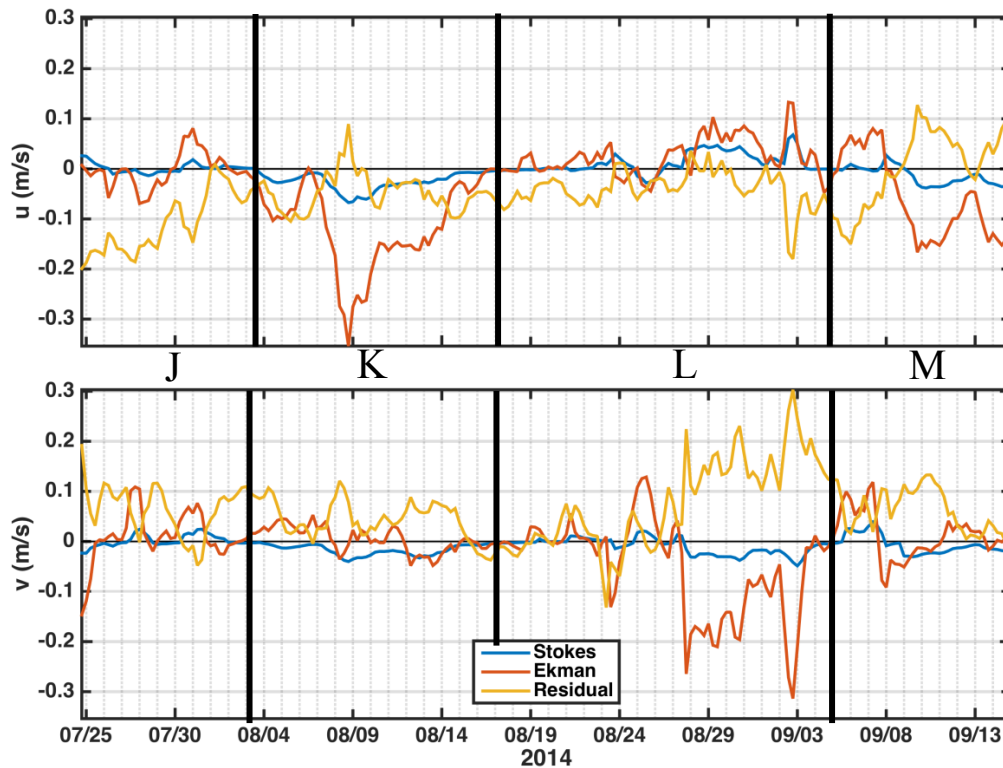


**Figure E17.** Time series of the zonal (top) and meridional (bottom) velocity components associated with the Stokes (blue), Ekman (red), and geostrophic (yellow) contributions to the surface velocity for the Point Hope South deployment. The letters and vertical lines correspond to the periods in Figure E13 and are discussed in the text.

Each of the previous clusters discussed evinced impressive coastal upwelling events in which warm, dilute nearshore Alaskan Coastal Water was transported substantial distances across the shelf. In the case of the Point Lay clusters, this water was brought as far west as the Central Channel; the Point Hope cluster suggests that these waters were carried to the western extreme of the Chukchi Sea and into Herald Canyon. We next consider the two Hanna Shoal clusters, which were deployed at the northern end of the shelf and far from the coast.

The NE Hanna Shoal cluster of 12 drifters was deployed  $\sim 50$  km east of Hanna Shoal on 10 September 2013. The trajectory and inferred dynamic balances are shown in Figures E18 and E19, respectively. Winds were variable but mainly westward at  $5 \text{ m s}^{-1}$  over the first few days as the drifters moved northward at  $5 - 10 \text{ cm s}^{-1}$  driven by Ekman drift. Period N (9/14 – 10/13) encompasses the time when the cluster first began moving onto Hanna Shoal and when it eventually moved off. The movement onto the Shoal occurred primarily via the zonal component of the Ekman drift from 9/14 – 9/23, when the winds were northeasterly and strong ( $7 - 10 \text{ m s}^{-1}$ ). As the cluster moved onto the Shoal, the SST decreased by  $\sim 2^\circ\text{C}$ , a change consistent with the temperature section shown in Figure E5. From 9/24 – 10/14, the winds were weaker, and more variable. The cluster meandered around the top of the Shoal but slowly drifted westward. The circulation dynamics over the Shoal are complicated. Over most of this portion of the record, the meridional balance indicates weak and opposing Ekman and geostrophic contributions. In the zonal direction, Ekman forcing was the dominant cause of the westward motion, whereas the zonal geostrophic tendency was weak and variable and generally opposed this drift. The eastward geostrophic tendency is consistent with the mean clockwise flow around the Shoal associated with barotropic forcing

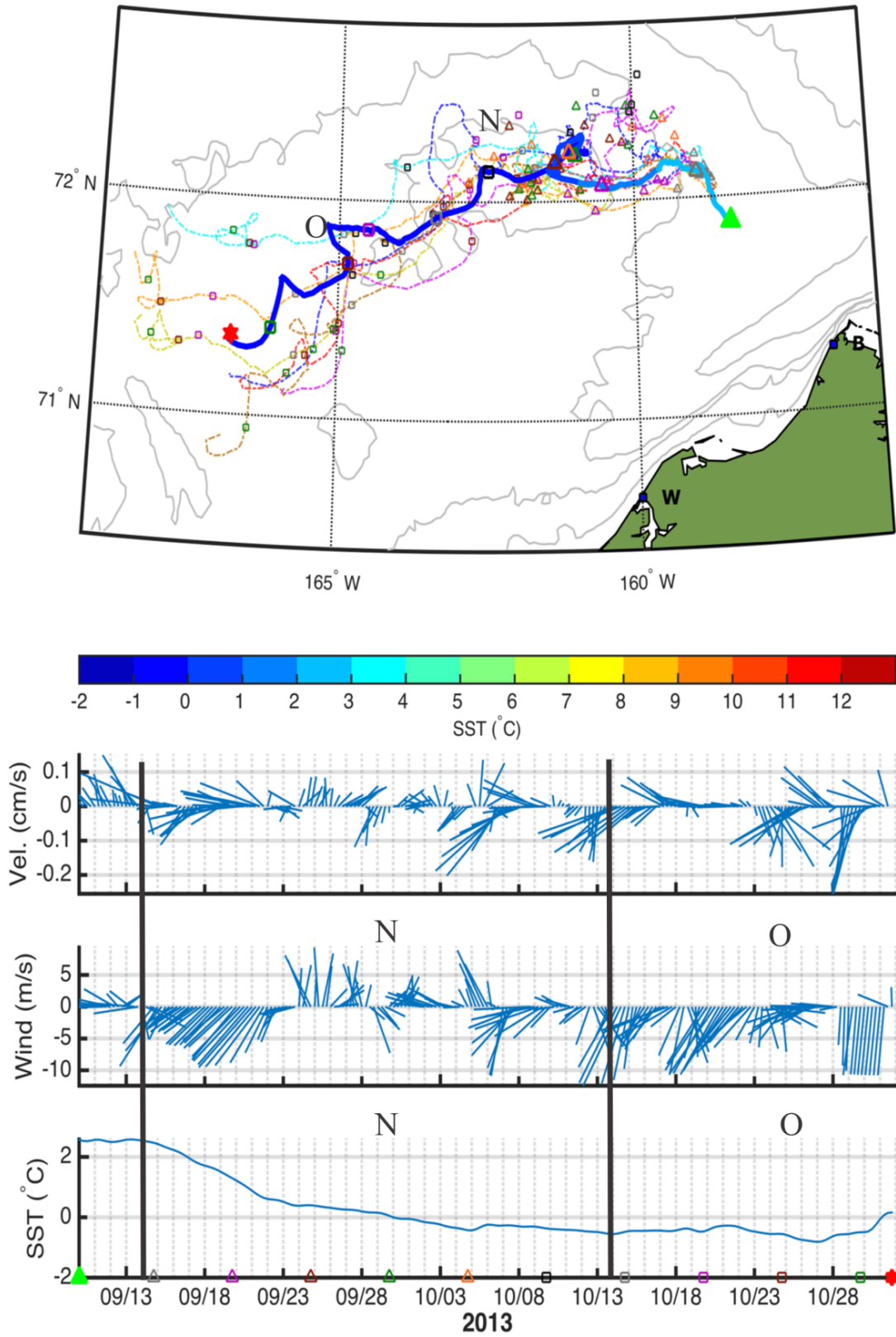


**Figure E18.** As in Figure E8 but for the NE Hanna Shoal cluster. Segments N and O are discussed in the text.

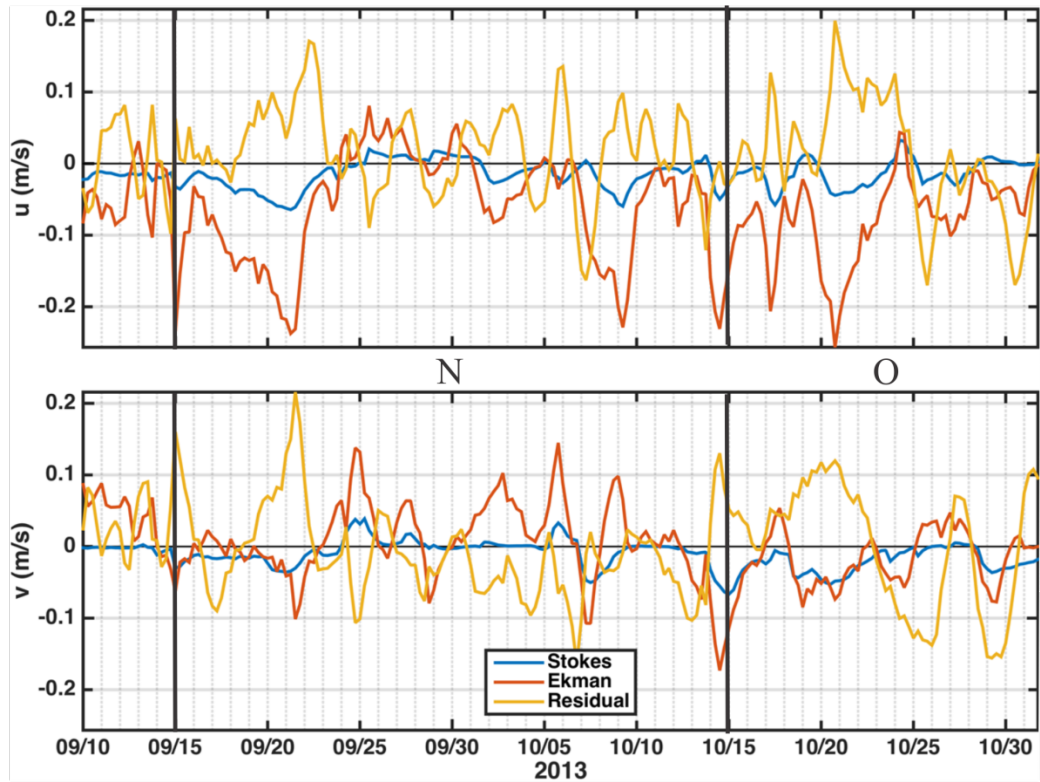


**Figure E19.** Time series of the zonal (top) and meridional (bottom) velocity components associated with the Stokes (blue), Ekman (red), and geostrophic (yellow) contributions to the surface velocity for the NE Hanna Shoal deployment. The letters and vertical lines correspond to the periods in Figure E18 and are discussed in the text.

(e.g., Spall 2007; Fang et al. in prep) even though this forcing should be very weak atop the Shoal. Clearly, there are baroclinic pressure gradients associated with the numerous, shallow frontal features that range in horizontal size from the mesoscale ( $\sim 20$  km) to the sub-mesoscale ( $\sim 1$  km). These features are evident in the various CTD sections (Figures E5 – E7) around the Shoal and are also documented by Timmermans and Winsor (2013) elsewhere in this region of the Chukchi Sea. These shallow fronts are expected to respond very quickly to changes in the wind field and some of the noise in our data may reflect these variations. By 14 October, the cluster had drifted to the southwest corner of Hanna Shoal. Period O (10/15 – 11/1) consists of a generally southwestward drift into the Central Channel, during which winds were primarily from the northeast at speeds ranging from  $8 - 12 \text{ m s}^{-1}$ . That movement was largely accomplished by both the Ekman and Stokes drifts. From 10/15 – 10/23, the geostrophic tendency was northeastward and afterwards it was southwestward.

The NW Hanna Shoal cluster, deployed 11 September 2013 is the final cluster examined; these results are displayed in Figures E20 and E21. During Period P (9/11 – 9/25), the winds were northeasterly from  $5$  to  $10 \text{ m s}^{-1}$ , and the cluster moved to the west-northwest with the zonal motion primarily due to Ekman forcing and the meridional motion due to geostrophy. Beginning on 23 September and continuing through 13 October, the winds were weak and variable in direction. For the most part, the cluster continued moving westward at speeds of  $\sim 10 \text{ cm s}^{-1}$ , with this motion being primarily geostrophic. There was a particularly strong west-southwest geostrophic flow of  $\sim 25 \text{ cm s}^{-1}$  centered around 26 September. The coincidence of this event with a rapid change in SST suggests that the cluster may have been entrained in a mesoscale feature, perhaps associated with a front. Overall, the meridional displacement during Period

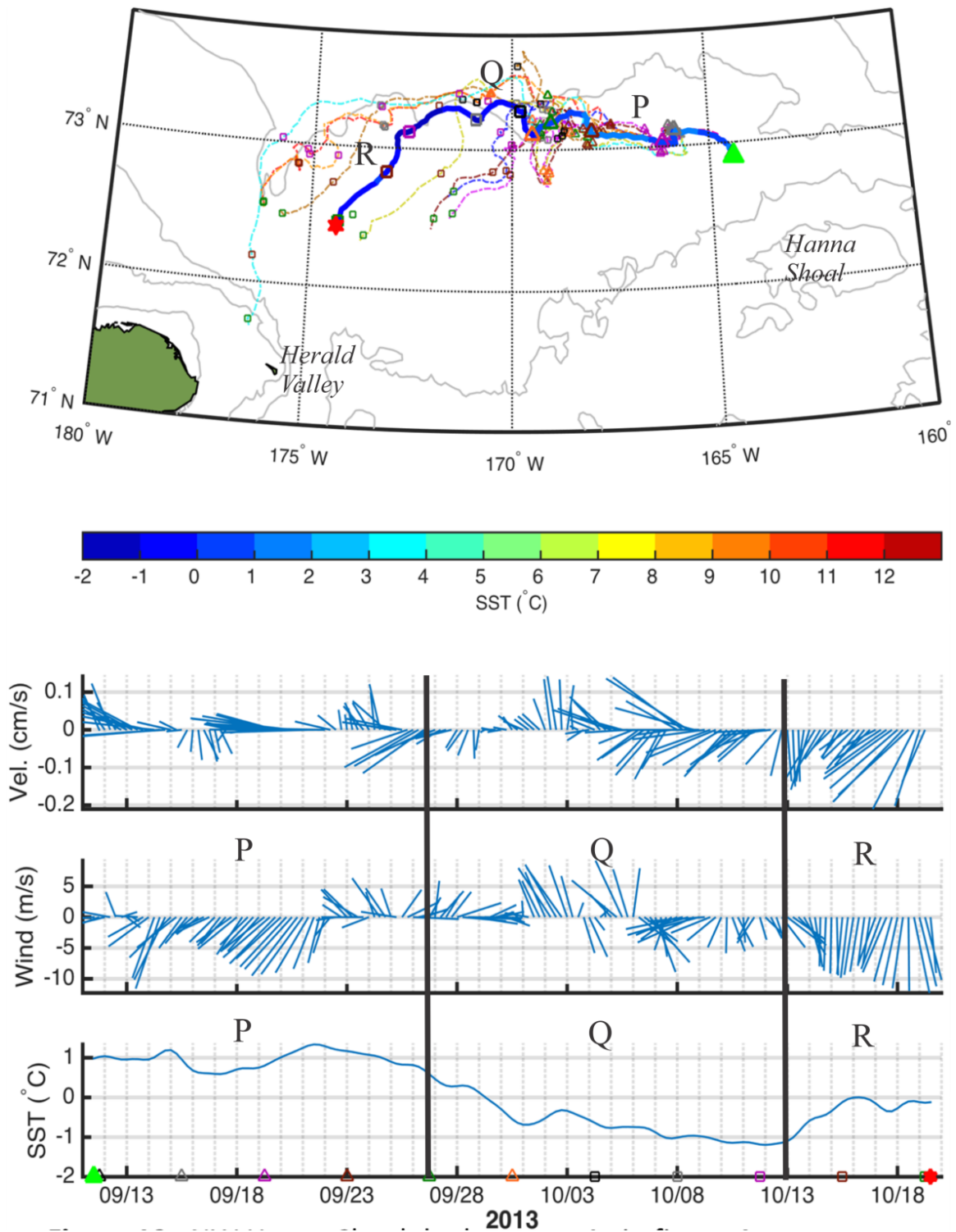


**Figure E20.** As in Figure E8 but for the NW Hanna Shoal cluster. Segments P, Q, and R are discussed in the text.

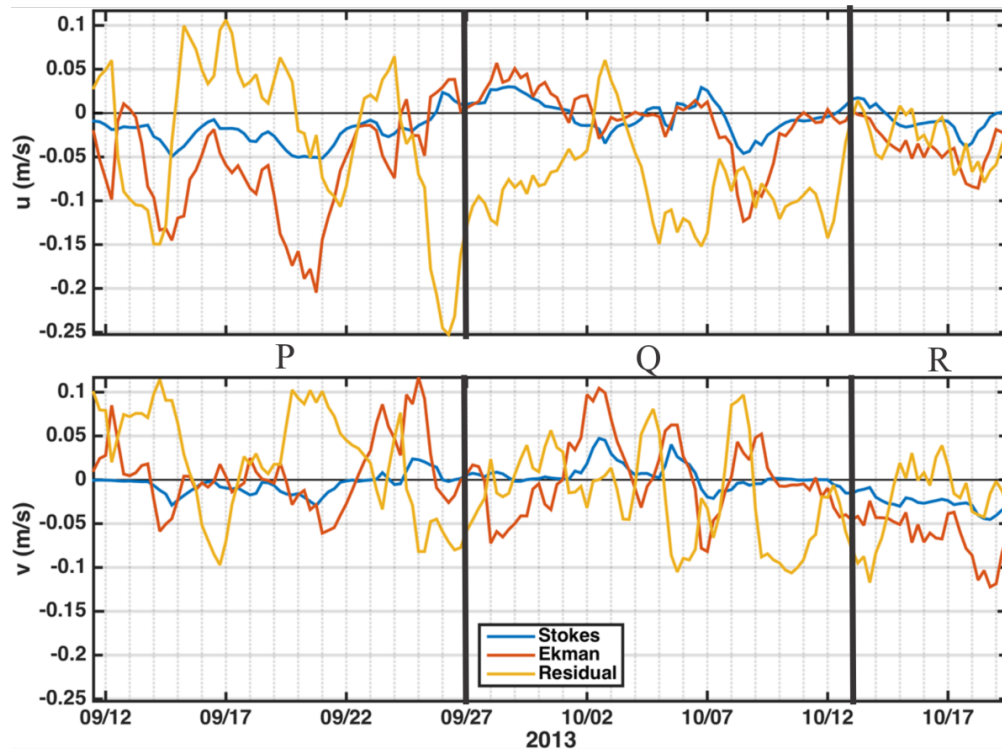


**Figure E21.** Time series of the zonal (top) and meridional (bottom) velocity components associated with the Stokes (blue), Ekman (red), and geostrophic (yellow) contributions to the surface velocity for the NW Hanna Shoal 2013 deployment. The letters and vertical lines correspond to the periods in Figure E20 and are discussed in the text.

P was small and governed primarily by both northward and southward geostrophic motion. During Period Q (9/27 – 10/12), the wind speeds ranged from 5 to 7 m s<sup>-1</sup> and directions were variable. Over the first half of the period, the net drift was toward the northwest at a comparatively sluggish rate. From 3 – 13 October, the cluster moved rapidly (10 – 15 cm s<sup>-1</sup>) westward along 73.33°N and over the 100 m isobath. Over most of this period, the motion was primarily geostrophic. We offer two possible sources for the pressure gradient driving this geostrophic flow. The first is an ice-edge front. Satellite-imagery indicates that the ice-edge was zonally oriented in this region, advancing southward and within 50 km of the cluster. The other possibility is that the westward flow was part of the southern limb of the clockwise-flowing Beaufort Gyre. Strong northeasterly winds of 10 m s<sup>-1</sup> dominated during Period R (10/13 – 10/19) and the cluster moved southwestward and ultimately entered Herald Canyon. The Stokes, Ekman, and geostrophic zonal contributions were all westward and of comparable magnitude. In the meridional direction, the Stokes and Ekman contributions were dominant and southward.

### E.3.3 Dispersion

Following Weingartner et al. (2015), the relative dispersion results are presented in terms of the zonal ( $D_x^2$ ), meridional ( $D_y^2$ ), cross-product or cross-correlation ( $D_{xy}$ ) and total horizontal dispersion ( $D^2$ ). The results for the Point Lay 2014 cluster (Figure E22) are remarkable insofar as the dispersion variables are all small until late August, after the cluster had moved northward through the Central Channel and begun moving eastward toward the coast. Zonal dispersion was the dominant term and accounted for ~80% of the total horizontal dispersion.

Before examining the dispersion properties for the entire Point Hope deployment, we first compare the dispersion characteristics of the northern (Figure E23) and southern (Figure E24) clusters. For the

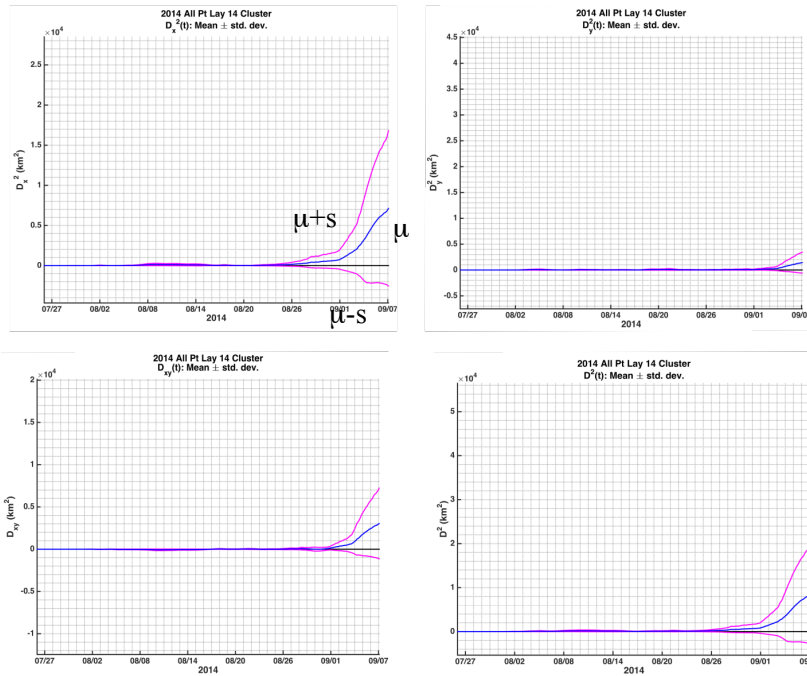


**Figure E22.** Time series of relative zonal ( $D_x^2$ ; top left) and meridional ( $D_y^2$ ; top right) dispersion, the cross-correlation term ( $D_{xy}$ ; bottom left), and the relative dispersion ( $D^2$ ; bottom right) for the Point Lay 2014 cluster. As indicated in the upper left, each panel includes the mean ( $\mu$ ) value and the mean value  $\pm$  one standard deviation ( $s$ ).

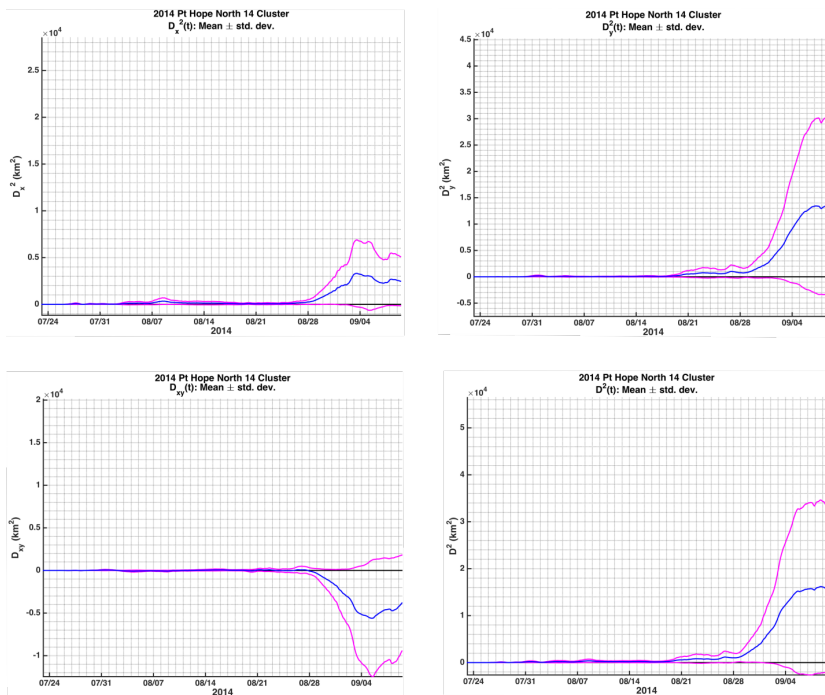


**Figure E23.** Time series of relative zonal ( $D_x^2$ ; top left) and meridional ( $D_y^2$ ; top right) dispersion, the cross-correlation term ( $D_{xy}$ ; bottom left), and the relative dispersion ( $D^2$ ; bottom right) for the Point Hope northern cluster. Each panel includes the mean ( $\mu$ ) value and the mean value  $\pm$  one standard deviation ( $s$ ) per Figure E22.

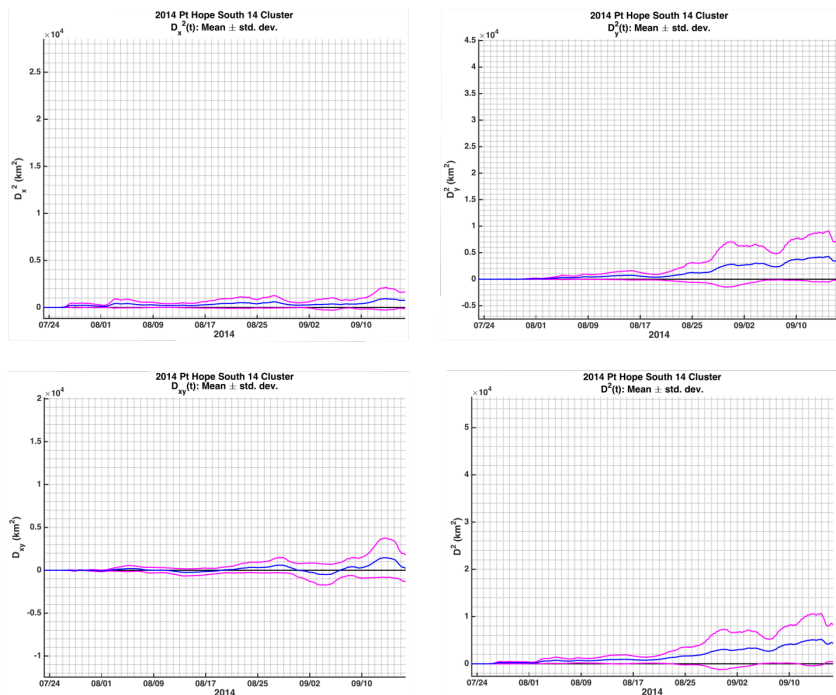


**Figure E24.** Time series of relative zonal ( $D_x^2$ ; top left) and meridional ( $D_y^2$ ; top right) dispersion, the cross-correlation term ( $D_{xy}$ ; bottom left), and the relative dispersion ( $D^2$ ; bottom right) for the Point Hope southern cluster. Each panel includes the mean ( $\mu$ ) value and the mean value  $\pm$  one standard deviation ( $\sigma$ ) per Figure E22.

northern cluster, all components of the dispersion are very small ( $\leq 1,000 \text{ km}^2$ ) until 28 August, which was after the cluster had entered Herald Canyon. The dispersion accelerated as part of the cluster continued northward in the Valley and the other drifters turned anticyclonically around the north side of Herald Shoal. Dispersion accelerated rapidly through 4 September and then reached a plateau of  $\sim 15,000 \text{ km}^2$  over the last few days of the record. Very little dispersion occurred for the southern cluster, with the zonal component being  $< 1,000 \text{ km}^2$  throughout the record and the meridional component being  $\sim 3,000 \text{ km}^2$  at a maximum. The cross-correlation term is effectively zero as there was no major eddying or turning motions associated with this cluster.

The dispersion calculation for the entire Point Hope deployment (Figure E25) indicates that all the dispersion terms began to increase rapidly on 20 August, i.e., when the northern cluster began its northward turn into Herald Canyon. What is remarkable about the entire Point Hope cluster is that there were only two key transitions in its entire  $\sim 45$  day life history. The first event was its breakup into two sub-clusters as it rounded Point Hope. The dispersion characteristics of the sub-clusters were then very similar over the next month. The next major transition was when the northern cluster turned into Herald Canyon on 20 August. It is noteworthy that the duration of each of these events was only a couple of days and that both events occurred under comparatively mild wind conditions!

### E.3.4 Barrow Canyon Mesoscale Analyses

One of our stated goals is to determine if there is a discernible difference in EKE, effectively a measure of mesoscale current variance, over the shelfbreak and slope at the mouth of Barrow Canyon compared to the EKE levels along the Chukchi and Beaufort slopes and shelfbreaks. The results for the 1 m drogued

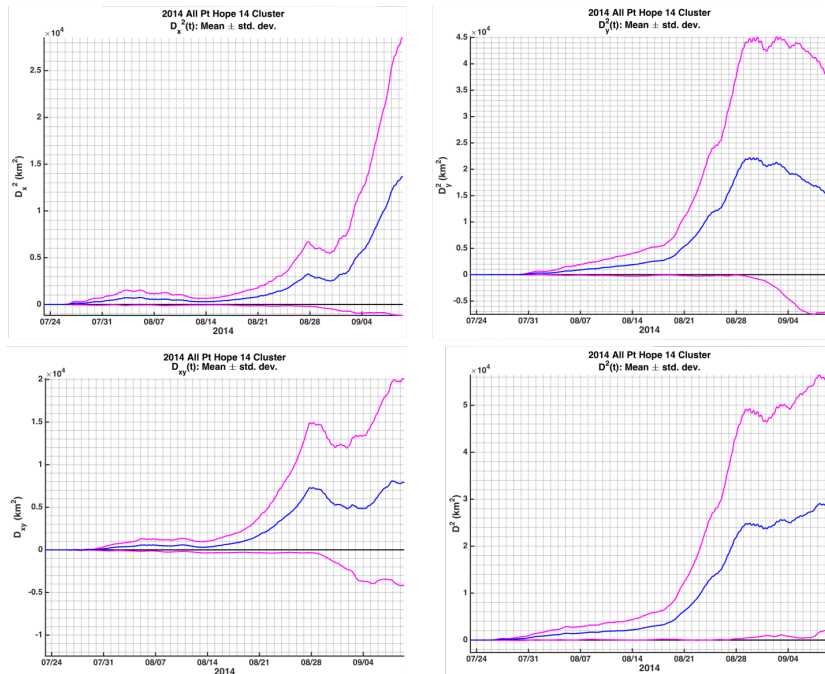


**Figure E25.** Time series of relative zonal ( $D_x^2$ ; top left) and meridional ( $D_y^2$ ; top right) dispersion, the cross-correlation term ( $D_{xy}$ ; bottom left), and the relative dispersion ( $D^2$ ; bottom right) for the entire Point Hope cluster. Each panel includes the mean ( $\mu$ ) value and the mean value  $\pm$  one standard deviation ( $\sigma$ ) per Figure E22.

Microstar drifters and the 10 m drogued SVP drifters are listed in Tables E1 and E2, respectively. The tables also contain the EKE and MKE values for the winds based on simultaneous observations of the drifter velocities and the ratio of the ocean EKE to the wind EKE. Before discussing the results, it is worth noting that the number of observations in the Barrow Canyon and Chukchi shelfbreak boxes is more than twice that for the Beaufort shelfbreak. Also note that the wind MKE levels over all regions are quite dissimilar. There is no physical reason why these wind MKE levels should differ and we conclude that our Beaufort and Chukchi sample sizes are probably too small or weighted heavily towards a particular year or set of events. Bearing this in mind, we find that the current MKE levels are smallest at the mouth of Barrow Canyon, four times larger over the Chukchi region, but only twice as large for the Beaufort shelfbreak. The EKE levels are quite similar across all locations and differ only by a factor of  $\sim 1.5$  at most. The EKE/MKE ratio at the mouth of Barrow Canyon is 1.5 – 5 times greater than at the other locations. Although these differences are suggestive, the ratio of the ocean EKE to the wind EKE is virtually identical at all locations. We would expect that if the oceanic EKE was generated by spatially-varying internal processes, then these ratio might vary spatially as well. The SVP results (Table E2) also show no compelling differences between the three regions with respect to MKE and EKE levels. Note, however, that the sample sizes for the SVP analyses are nearly an order of magnitude smaller than for the Microstar drifters so the results are likely biased by the small sample size.

In summary, we find suggestions, but no compelling evidence, that the EKE levels are higher at the mouth of Barrow Canyon than elsewhere along the Chukchi and Beaufort slopes and shelfbreaks. We emphasize that our analysis has concentrated on surface measurements and that these may not be representative of mesoscale variances at greater depths. It would not be surprising if the amplitudes of mesoscale currents were much higher at depth than at the surface. This would be expected if, as

**Table E1.** Mean and Eddy Kinetic Energy comparisons for 1 m drogued Microstar drifters.

Analysis Location	Currents			Winds			$\frac{EKE_{Ocean}}{EKE_{Wind}}$	Number of Points
	$MKE$ ( $m^2 s^{-2}$ )	$EKE$ ( $m^2 s^{-2}$ )	$EKE / MKE$ ( $\times 10^4$ )	$MKE$ ( $m^2 s^{-2}$ )	$EKE$ ( $m^2 s^{-2}$ )	$EKE / MKE$		
Barrow Canyon	0.004	139	3.6	1	12	13	11	3824
Chukchi Slope	0.016	115	0.7	0.3	12	45	9.5	2435
Beaufort Slope	0.008	179	2.2	5	15	3	12	1476

**Table E2.** Mean and Eddy Kinetic Energy comparisons for 10 m drogued SVP drifters.

Analysis Location	Currents			Winds			$\frac{EKE_{Ocean}}{EKE_{Wind}}$	Number of Points
	$MKE$ ( $m^2 s^{-2}$ )	$EKE$ ( $m^2 s^{-2}$ )	$EKE / MKE$ ( $\times 10^4$ )	$MKE$ ( $m^2 s^{-2}$ )	$EKE$ ( $m^2 s^{-2}$ )	$EKE / MKE$		
Barrow Canyon	0.006	202	3.1	2	13	6	15	442
Chukchi Slope	0.012	173	1.4	0.6	12	19	14	339
Beaufort Slope	0.006	206	3.3	3	9	3	23	258

postulated earlier, the source of the mesoscale variability is associated with baroclinic waves, in which case the waves' amplitudes will be larger beneath the upper layers of the ocean.

Figure E26 summarizes our analysis of the turning of surface water outflow from Barrow Canyon. Recall that the turning criteria were based on where a drifter turned with respect to a point of interest (POI), which we established at 71.75°N, 154°W, the point where the 100 m isobaths angles southward (Figure E2). We find that ~80% of all of the drifters initially turned eastward crossing the meridian of the POI. Group III (turning eastward to pass the south of the POI) contained 46% of all observations and Group II (turning eastward after passing the POI on the north) contained 33% of the observations. Of the remaining drifters, 11% passed the POI on the west and then continued westward (Group I), 4% turned westward before the POI (Group IV), and 6% reversed their motion and were swept upcanyon (Group V). The numbers in this analysis are small and it seems quite likely that these percentages would change considerably with a larger sample size that included deployments in different years and throughout the fall when the flow in Barrow Canyon is often reversed. Nevertheless, there are two intriguing aspects of the results. The first is that even though most of the drifters initially turned eastward and passed the POI, they subsequently reversed direction and were transported westward along the Chukchi slope. The other point of interest is that Groups II and III segregated according to the magnitude of the zonal component of the wind. Group II turns occurred under mild easterly winds ( $-2.4 m s^{-1}$ ), whereas Group III turns occurred under westerlies of  $\sim 2 m s^{-1}$ . Groups I and IV turned westward under easterly winds of  $4 m s^{-1}$  or greater. The meridional wind component was weak in all of these cases and appears to have little influence on turning. Group V turned under strong northeasterly winds of  $9 m s^{-1}$ . With the possible

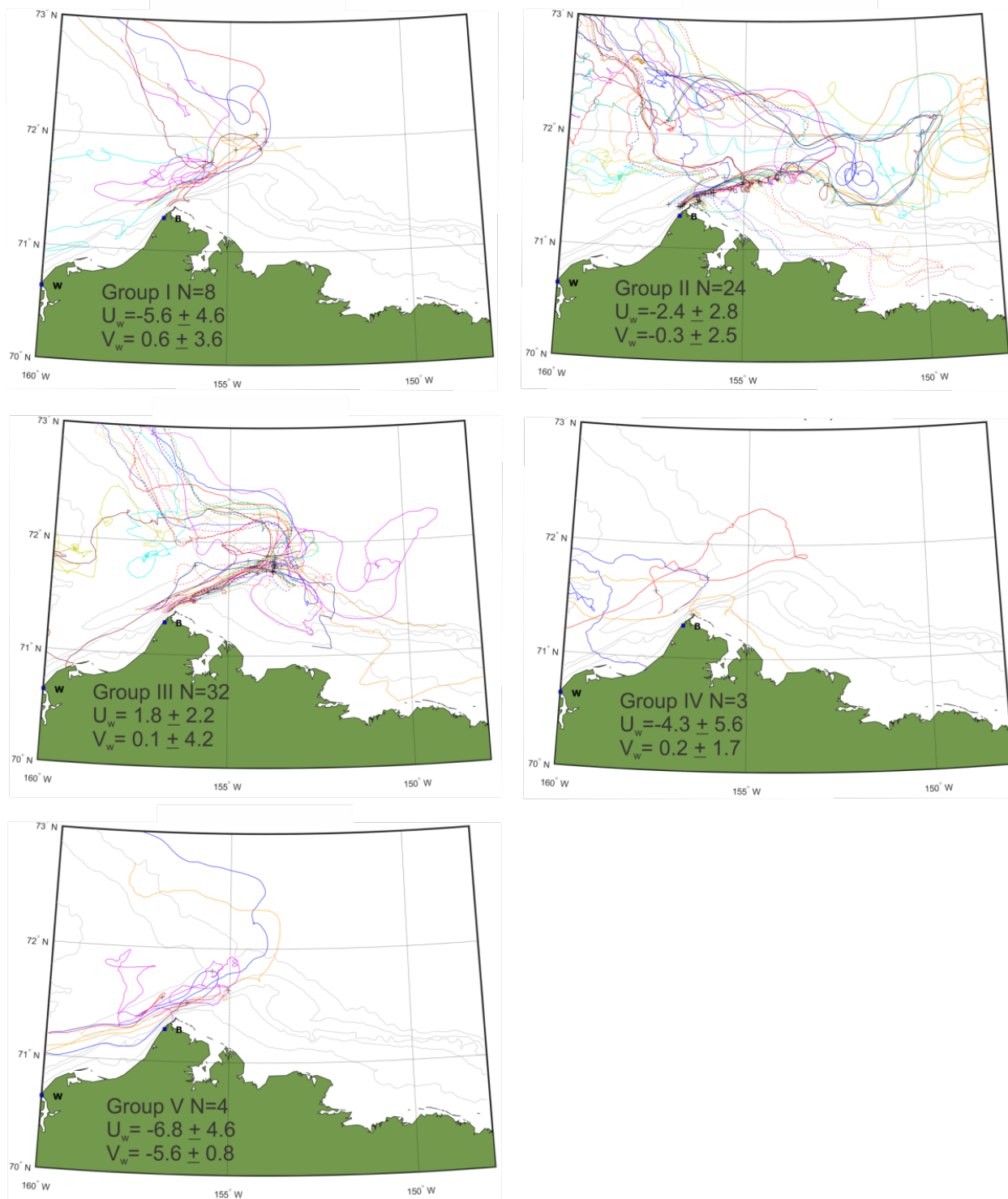


**Figure E26.** Trajectories and summary statistics for all 1 m drogued drifters according to their turning classification.

exception of Groups II and III, the mean wind vectors cited here should not be used as a turning criterion because they derive from a very small set of measurements.

## E.4 Discussion and Summary

The addition of the 2014 clusters and re-analysis of some of the earlier Chukchi clusters have revealed aspects of the surface circulation dynamics expressed in terms of the relative importance of the Ekman, geostrophic, and Stokes' drift contributions to the velocity field. In general, the Stokes' drift was always the smallest contributor to the surface velocities, although we believe that it cannot be regarded as negligible in terms of its potential in transporting pollutants and/or other dissolved and suspended materials in the upper meter of the Chukchi Sea. For example, the Point Lay and Point Hope 2014 Stokes' drift estimates suggests that this term alone would have caused a westward drift of 30 – 50 km between 3 and 15 August. That drift is ~20% of the estimated drift due to the Ekman current at 1 m depth.

Our dynamical analysis provides some insight on why the linear regressions we have applied to the drifters in the past have yielded uneven results (Weingartner et al. 2015) including varying from one cluster to another or, more specifically, from one portion of the shelf to another. To some degree the uneven results are a consequence of spatially varying geostrophic flows. There are several examples of these in our data set. For example, in the Central Channel and Herald Canyon the geostrophic flows are strong and northward on average (Weingartner et al. 2005; Woodgate et al. 2005; Pickart et al. 2010; Weingartner et al. 2013a) and likely include a cross-channel velocity shear. We suggested that sub-mesoscale and mesoscale geostrophic variability might be associated with the patchy remnants of MW fronts over Hanna Shoal. Similarly, the divergence of the Point Hope cluster shortly after deployment was probably associated with mesoscale geostrophic variability such as an eddy or front to the west of Point Hope. In the western Chukchi Sea, we noted that the disparate behaviors in the southern and northern Point Hope clusters had to be associated with spatial variations in the geostrophic flow. And finally, we ascribe the swift westward flow observed along 73°N and over the 100 m isobath as being associated with a portion of the Beaufort Gyre. In addition to the spatially-varying pressure gradients, the shelf-wide geostrophic field will change in response to local and remote wind forcing (Winsor and Chapman 2004; Spall 2007; Danielson et al. 2014). Consequently, these background geostrophic motions, which are neither constant in time or space, can be as large as the Ekman drift and lead to degradation of statistical relationships between the local currents and the winds.

Mesoscale variability may also affect the relative dispersion characteristics. For example, the total relative dispersion of the NE Hanna Shoal cluster reported by Weingartner et al. (2015) reaches 1,000 km<sup>2</sup> and 2,000 km<sup>2</sup> by 7 and 9 days, respectively, after deployment. For the clusters reported here and the others examined by Weingartner et al. (2015), the 1,000 km<sup>2</sup> dispersion value was attained 14 – 31 days after deployment, while the 2,000 km<sup>2</sup> limit was reached 17 – 36 days after deployment. These differences cannot be attributed to the wind variability, as this was similar in all of the cases. Instead, we hypothesize that these differences are a function of the sub-mesoscale and mesoscale structure at the ocean surface. Although our hydrographic data is limited, it suggests that this variability is greater over Hanna Shoal than over the Chukchi shelf south of ~71°N. We will explore this hypothesis in the future by examining the spatial variability in sea surface temperature and salinity data collected by underway shipboard systems and in the Acrobat and glider CTD data.

The Point Hope and Point Lay 2014 drifter deployments have yielded more than 2,000 drifter days of data from the Chukchi Sea, which allows us to upgrade the relative dispersion climatology presented by Weingartner et al. (2015). The new climatology, based on clustered deployments from 2012, 2013, and 2014, is summarized in Figure E27 on log-log plots of the relative meridional, zonal and horizontal dispersion. The improved climatology suggests that the dispersion is isotropic insofar as both the zonal

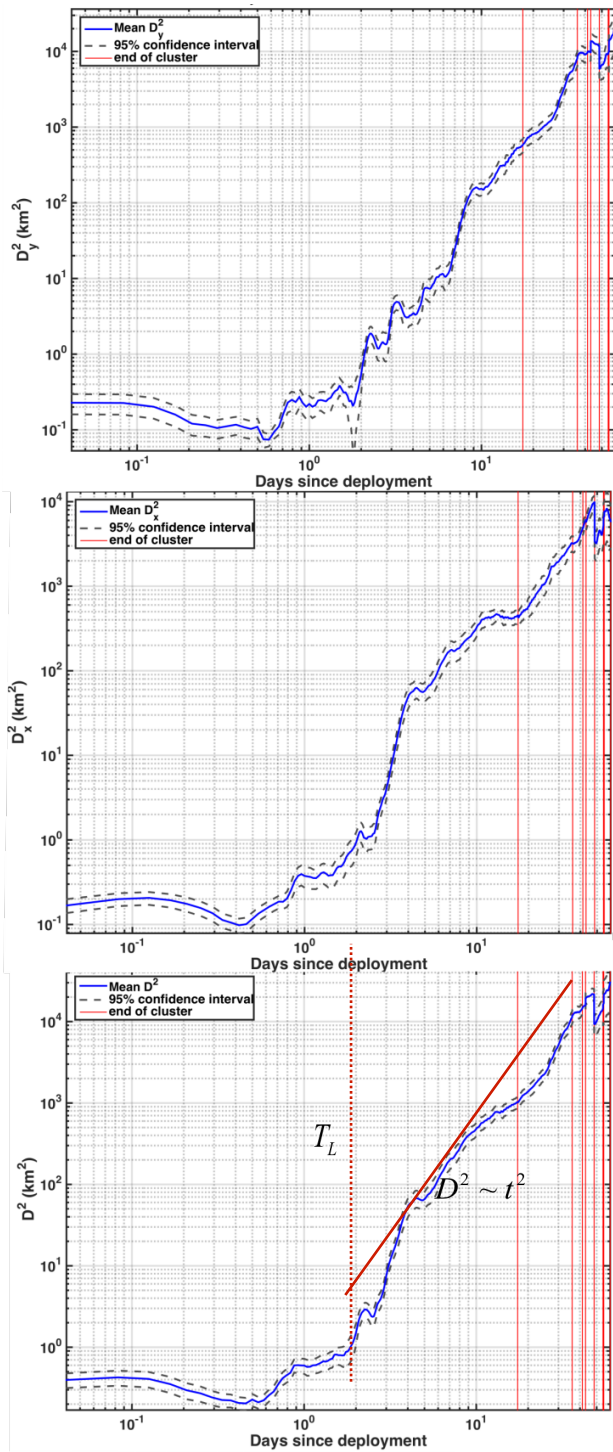


**Figure E27.** Log-log plots of the relative meridional ( $D_y^2$ ; top), zonal ( $D_x^2$ ; middle), and horizontal ( $D^2$ ; bottom) dispersion based on the 2012, 2013, and 2014 clusters. The black dashed lines are the 95% confidence interval on the mean (blue curve). On the bottom plot, the Lagrangian time scale ( $T_L$ ) is  $\leq 2$  days and denoted by the red, dotted line and the red solid line denotes a dispersion growth rate proportional to  $t^2$ .

and meridional dispersion values are  $\sim 10,000 \text{ km}^2$  by day 40. The zonal relative diffusivity is given by  $K_{xx} = 0.5[dD_x^2 / dt]$  (similar to the meridional relative diffusivity). Our new estimates are based on values between day 2 and 40, where 2 days is the approximate Lagrangian decorrelation time scale ( $T_L$ ) for the drifters. The results suggest relative diffusivities of  $\sim 3,300 \text{ m}^2 \text{ s}^{-1}$  over these time scales. The new climatology suggests that all components of dispersion grow at a rate proportional to the square of time (again after  $\sim 2$  days) implying that the area occupied by a dissolved or suspended substance is doubling roughly every 1.5 days.

We examined the drifter data at the mouth of Barrow Canyon to test the hypotheses that current variance here may be higher than elsewhere along the Chukchi and Beaufort slopes due to internal oceanic processes rather than the winds. The results did not support this hypothesis, although this test may have failed for two reasons related to sample design. First, mesoscale current variances may have larger amplitudes at depth, not at the surface where our measurements were made. Second, our drifter deployments were performed in clusters. This “clumped” sampling approach is probably not ideal for undertaking the type of hypothesis test that we conducted. A sampling approach that was more broadly distributed in time may have been better suited to detecting different levels of mesoscale variability in this region.

Finally, we examined the conditions under which surface drifters turned east or west at the mouth of Barrow Canyon. We found that the vast majority (80%) of the drifters initially turned eastward upon exiting the canyon, although virtually all of these eventually drifted westward. Under westerly winds, the drifters turned eastward onto the Beaufort Sea shelf south of the 100 m isobath. Under mild easterly winds, the drifters turn eastward north of the 100 m isobath. Future work will examine the wind conditions that force the drifters to reverse their eastward motion.

## **F. The Summer Hydrographic Structure of the Hanna Shoal Region on the Northeastern Chukchi Sea Shelf: 2011 – 2013**

### **Abstract**

We used shipboard and towed CTD, current meter, and satellite-tracked drifter data to examine the hydrographic structure in the northeastern Chukchi Sea in August – September of 2011, 2012, and 2013. In all years the densest winter water was around and east of Hanna Shoal. In 2012 and 2013, a ~15 m deep layer of cold, dilute meltwater overlaid the dense water north of the shelf region between ~71.2 and ~71.5°N. A front extends from the southwest side of Hanna Shoal toward the head of Barrow Canyon, separated meltwaters from warmer, saltier Bering Sea Summer Waters to the south. Stratification was stronger and the surface density variances in the meso- and sub-mesoscale range were higher north of the front than to the south. No meltwater or surface fronts were present in 2011 due to a very early ice retreat. Differences in summer ice cover may be due to differences in the amount of grounded ice atop Hanna Shoal associated with the previous winter's regional ice drift.

Along the north side of Hanna Shoal the model-predicted clockwise barotropic flow carrying waters from the western side of the Shoal appears to converge with a counterclockwise, baroclinic flow on the northeast side. The baroclinic tendency is confined to the upper 30 m and can include waters transported from the shelfbreak. The inferred zonal convergence implies that north of the Shoal: a) near-surface waters are a mixture of waters from the western and eastern Chukchi Sea and b) the cross-isobath pressure gradient collapses thereby facilitating leakage of upper layer waters northward across the shelf.

### **F.1 Introduction**

Pacific waters flowing northward through Bering Strait and across the Chukchi Sea spread poleward across three principal bathymetric depressions: Herald Valley in the west, the Central Channel in mid-shelf, and Barrow Canyon along the Alaskan coast (Figure F1a). Hanna Shoal lies between the latter two features (Figure F1b). Its western side abuts the northern end of the Central Channel, while its eastern flank yields to an 80 km wide bench along the western wall of Barrow Canyon. The Shoal is a west-east oriented oval ~150 km long and ~55 km wide (based on the 40 m isobath). The shelfbreak (~100 m isobath) lies 75 km to the north, and the broad, gently sloping central shelf of 40 – 45 m depth is to the south. Minimum depths atop the Shoal are ~20 m and shallow enough to ground sea ice with deep keels, as evidenced by the heavily scoured gravelly seabed (Grantz and Eitrem 1979).

Circulation models (Winsor and Chapman 2004; Spall 2007) depict the average flow as northward in the Central Channel and Herald Valley (Figure F1a), with the outflows from both proceeding eastward over the outer shelf and shelfbreak. Some of this eastward flow is predicted to continue clockwise around the southeast side of Hanna Shoal before retroflecting eastward. Upon retroflecting, this flow merges at the head of Barrow Canyon with eastward flow over the central shelf and northeastward flow along the coast (Figure F1a) (Weingartner et al. 2017a; Fang et al. in prep). The models suggest that southward flow on the east side and over Hanna Shoal is weaker than the flow along its northern and southern flanks, which is consistent with the spreading of the isobaths between the western and eastern sides of the Shoal. Martin and Drucker (1997) attributed the weak flow over the Shoal to Taylor column formation and suggested that this feature was one reason why ice persists here well after it has retreated elsewhere on the shelf. The summertime persistence of sea ice over Hanna Shoal is of considerable ecological importance as the area supports a large number of ice-obligate and ice-associated species (Moore and Huntington 2008; Moore et al. 2016). These species are sustained by the high benthic biomass found throughout the

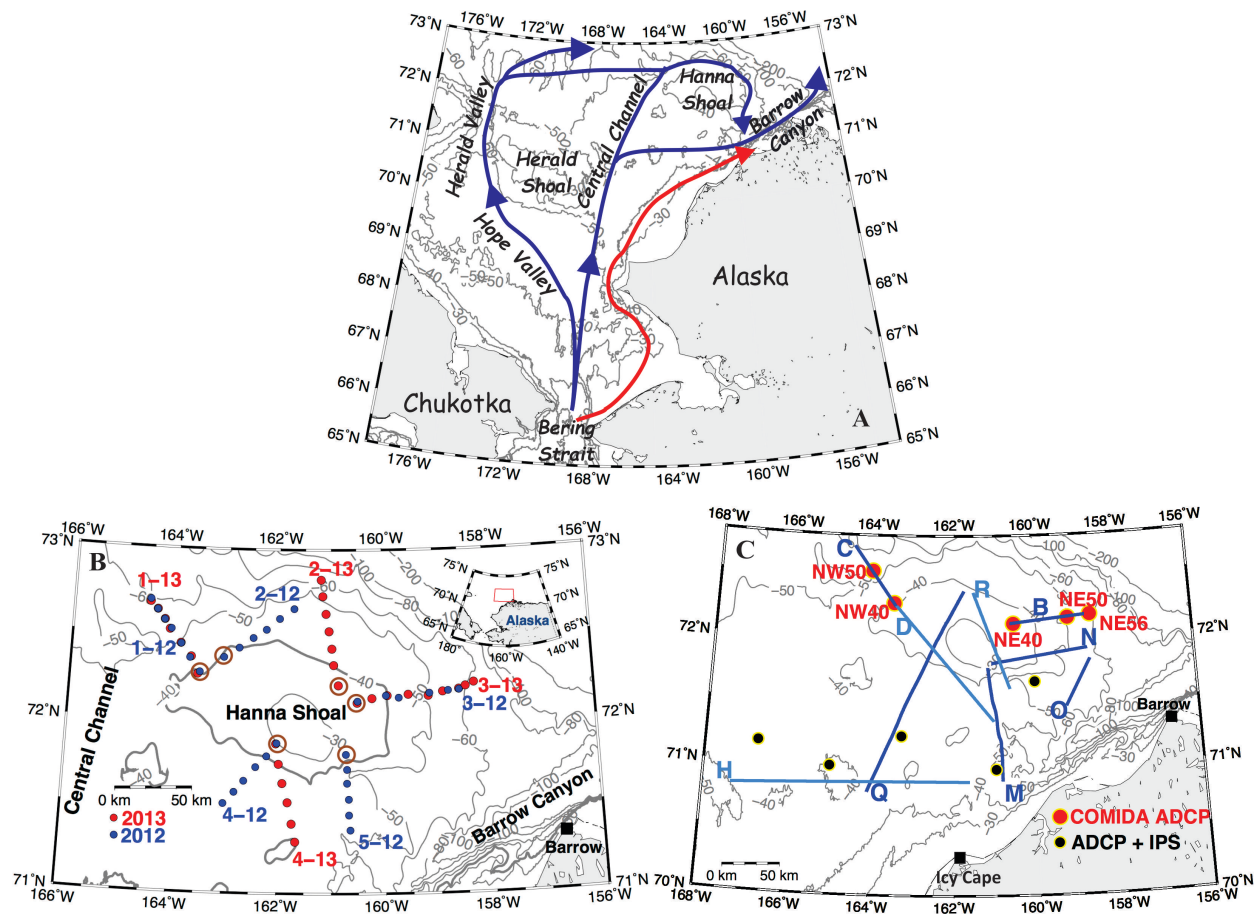


**Figure F1.** A) Bathymetric map of the Chukchi Sea showing principal flow pathways northward from Bering Strait. The pathway denoted by the red arrow denotes the Alaskan Coastal Current, which carries the freshest and warmest fraction of the Bering Strait outflow and the blue arrows denote the pathways for the cooler and saltier fractions. B) Map of Hanna Shoal and the surrounding shelf showing locations of 2012 (blue) and 2013 (red) CTD stations. C) Location of various current meter and ice profiling sonar (IPS) moorings (symbols) and Acrobat towed-CTD transects (blue lines).

region, with particularly large numbers of benthic organisms found on the southeast side of the Shoal (Blanchard et al. 2013).

This study was motivated by the need to provide observations for evaluating ocean circulation models in a region of the Chukchi shelf susceptible to potential impacts from offshore oil development. Moreover, Pacific-derived waters undergo substantial modification while crossing this shelf and not all the flow pathways and modification sites are understood. In particular, the region around Hanna Shoal has received limited attention because heavy ice has often impeded sampling here. We describe interannual variations in the regional hydrographic structure of the northeastern shelf in summer (August – September) and examine the connectivity in the circulation between the west and east sides of the Shoal. Section F2 outlines the data sets used, which span the years from 2011 – 2013. In Section F3.1, we summarize the summer wind and ice conditions in these years. We next provide an overview of the hydrography of the central shelf and Hanna Shoal region with an emphasis on differences between summers with light and heavy ice concentration (Section F3.2). Section F3.3 examines in greater detail the differences in hydrographic and circulation structure between the western and eastern sides of the

Shoal. Section F4 discusses the results and suggests reasons for the marked differences in summer ice concentrations between 2011 and the later years.

## **F.2 Data and Methods**

### **F.2.1 Hydrography**

Three different hydrographic data sets, each averaged into 1 db vertical bins, are used. The first consists of shipboard CTDs collected during the Chukchi Offshore Monitoring in Drilling Area (COMIDA) program from the USCGC *Healy* in 2012 and 2013 (Figure F1b). The station spacing varied but was typically ~10 km. Time constraints prevented us from conducting extensive CTD surveys south of Hanna Shoal during both COMIDA cruises. To place the COMIDA CTD data in a broader spatial and temporal context, we use CTD data collected on separate cruises under the auspices of the Chukchi Sea Environmental Studies Program (CSESP; sponsored by the oil industry) in August and September of 2011, 2012, and 2013. The August cruises were confined to small study areas over the shelf south of Hanna Shoal, whereas the September cruises enabled broader surveys that extended to the north and east of Hanna Shoal. CTD processing followed the procedures of Weingartner et al. (2013a). The August and September cruises occurred at identical times in each year, with the sampling progressing from south to north across the domain. Although not synoptic, the data underscore the large interannual differences in the seasonal hydrography of this region. The third data set consists of several high-resolution (~250 m) Acrobat towed CTD and fluorometric sections (Figure F1c) supported by the Bureau of Ocean Energy Management (BOEM) and processed per Martini et al. (2016). The sensors were calibrated at the factory prior to the cruise and the chlorophyll values are estimated based on this calibration because no chlorophyll samples were collected on these cruises. The chlorophyll *a* concentrations are to be regarded as relative, not absolute, values.

### **F.2.2 Meteorology; Sea Ice Concentration, Drift, and Thickness; and Satellite-Tracked Drifters**

We used winds and sea level pressures forecast at 3-hour intervals from NOAA's North American Regional Reanalysis (NARR) models (Mesinger et al. 2006). Sea ice concentration maps for June and July, from 2011 to 2013, were constructed from data obtained by the Advanced Microwave Scanning Radiometer (AMSR-E), Special Sensor Microwave Imager (SSM/I) satellite sensor, and the Advanced Microwave Scanning Radiometer-2 (AMSR2), respectively and processed according to Spreen et al. (2008). More detailed maps of the ice edge for the August – September periods of each year were prepared based on National Ice Center (NIC) analyses. Through CSESP, the oil industry supported paired ice-profiling sonar (IPS) and ADCP moorings to measure ice thickness and drift respectively during the winters of 2011 – 2013 at several locations south of Hanna Shoals (Figure F1c). The IPS processing follows Melling et al. (1995), and a detailed description of the processing procedures for the IPS and ADCP data is given by Mudge et al. (2015). In Section F4 we use the mean ice keel values computed over the upper 25% of the keel depth frequency distribution. Following Melling et al. (1995), the latter were formed from 50 km long sections based on the ice drift. We then computed monthly means based on these values assigning segments that spanned across months to the month in which the majority of the segment occurred. The COMIDA program also included current data from five moored ADCPs positioned on the northwest and northeast sides of Hanna Shoal, 2012 – 2014 (Figure F1c). We use subsets of these data coincident in time with the COMIDA CTD sections. A more in-depth analysis of these and the CSESP moorings will be the focus of a future paper.

In addition, we show trajectories from a subset of 13 satellite-tracked Microstar drifters (manufactured by Pacific Gyre) equipped with a CODE-type drogue (Davis 1985) at 1 m depth. The drifters were deployed

concurrently near Icy Cape (Figure F1c) and within ~15 km of the Alaskan coast on 12 August 2012. Processing details and additional descriptions are given by Weingartner et al. (2015).

### F.3 Results

#### F.3.1 Sea Ice Conditions

Figure F2 shows maps of the shelf-wide distribution of sea-ice concentrations in mid-June and mid-July of 2011 – 2013 and time series of the mean daily winds for June and July. In 2011, the ice retreat occurred early insofar as the Chukchi shelf south of 71°N was largely ice-free by mid-June (Figure F2a). The remainder of the Chukchi shelf and the western Beaufort Sea were ice free by mid-July (Figure F2b). Northeasterly winds prevailed in both months (Figure F2c). In 2012, winds varied from northeasterly to southwesterly but were from the southeast on average (Figure F2f). By mid-June 2012, the western Chukchi had heavy ice concentrations, but a broad swath of the northeast shelf was ice-free (Figure 2d).

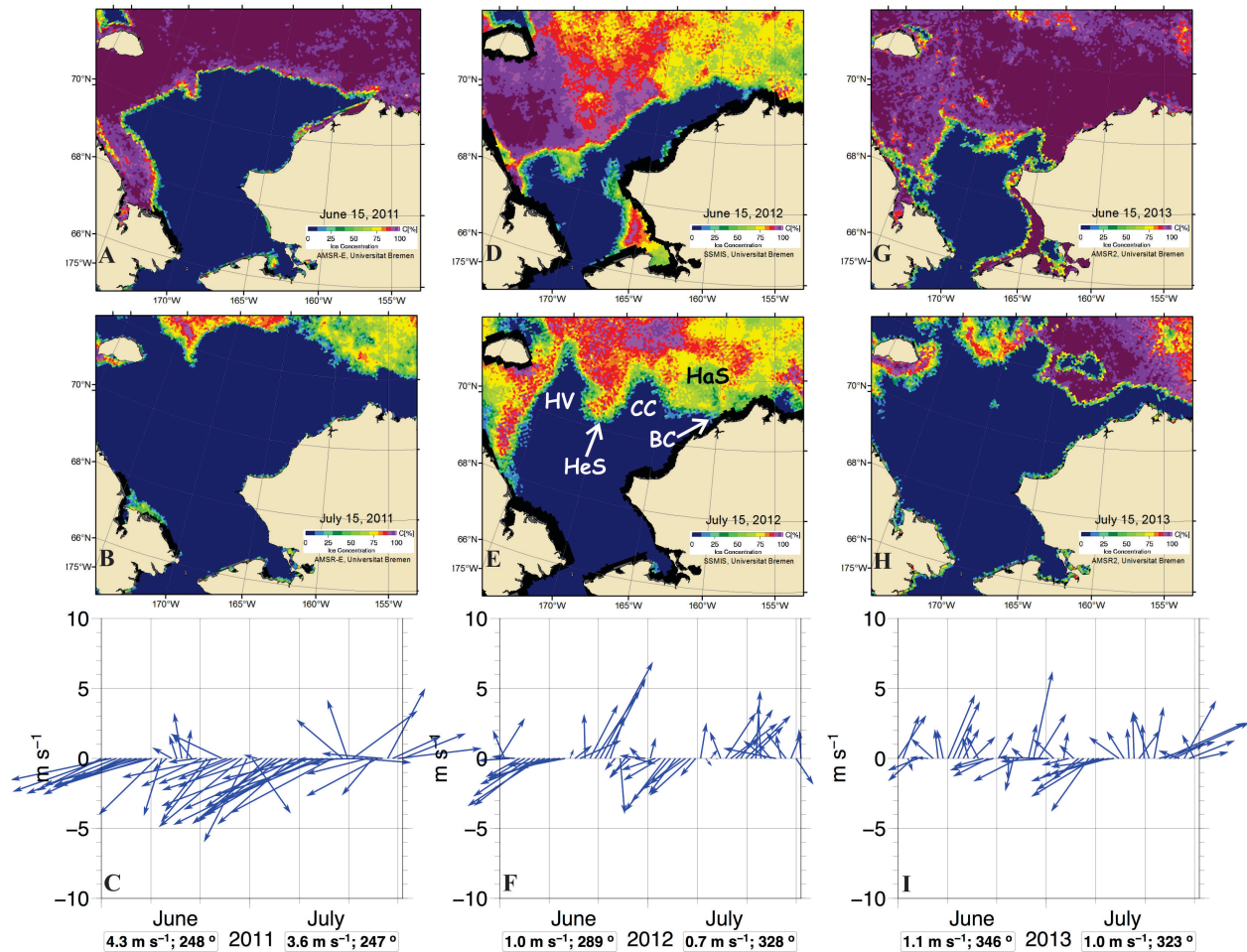


**Figure F2.** Sea ice concentration maps on 15 June (top) 15 July (middle) and mean daily wind vectors (bottom). Panels a, b and c are for 2011, d, e, and f are for 2012, and g, h, and i are for 2013. The features labeled in map E are: Herald Valley (HV), Herald Shoal (HeS), Central Channel (CC), Hanna Shoal (HaS), and Barrow Canyon (BC). Wind vector plots include mean monthly wind velocity and wind speed in parentheses.

By mid-July, the ice had retreated northward over the western shelf but advanced southward over portions of the northeast shelf (Figure F2e). In addition, distinct embayments formed in Herald Valley, the Central Channel, and Barrow Canyon with the ice edge oriented from west to east between the Channel and the Canyon along  $\sim 71^\circ\text{N}$ . The embayments, discussed by Paquette and Bourke (1981) and Martin and Drucker (1997), correspond to the principal flow pathways along which warm Bering Sea Summer Waters (BSSW) cross the shelf. These indentations are annually recurring features and were well-known to 19<sup>th</sup> century whalers (Bockstoce 1986). They vary in extent from year-to-year and are separated from one another by heavier ice concentrations over Herald and Hanna Shoals (Figure F2e). In mid-June 2013 (Fig 2g), the ice-edge had retreated to  $\sim 70^\circ\text{N}$  over the central shelf, but heavy concentrations remained elsewhere. By mid-July 2013 (Figure F2h), the western Chukchi was largely ice-free with open water present at the northern end of the Central Channel (along  $73^\circ\text{N}$ , between  $165^\circ$  and  $170^\circ\text{W}$ ) and over Barrow Canyon, although heavy ice concentrations remained over Hanna Shoal. In both months winds were variable but primarily southerly (Figure F2i).

The subsequent evolution of ice concentrations in the Hanna Shoal region is given by biweekly maps of the 15% ice concentration isopleth (as estimated by NIC) for the August-September period of each year along with the corresponding mean daily NARR winds for the same period (Figure F3). In 2011, the region was virtually ice-free and remained so through September. In 2012, ice remained over Hanna Shoal through mid-September. The same basic pattern persisted in 2013, although the ice rapidly retreated from south of Hanna Shoal on 1 September to the northwest of the Shoal by mid-September. The ice conditions of Figure F3 were not obviously related to the concurrent winds. For example, in both 2011 (ice-free year) and 2013 (moderate to heavy ice year) the winds were persistently from the northeast and moderately strong ( $\sim 5 - 10 \text{ m s}^{-1}$ ). In contrast, in 2012 (heavy ice year) the winds were from the south through August and then northeasterly through most of September. During the 2012 and 2013, COMIDA cruises observations from the *Healy* bridge suggested extensive grounding of very thick ice atop Hanna Shoal, which limited sampling here. Possible causes for these interannual variations in the Hanna Shoal ice cover will be considered in Section F4.

### F.3.2 Hydrography: Broad-Scale Perspective

We begin by examining plan views of the vertically-averaged upper and bottom 10 m of the water column in both August and September 2012 (Figure F4) because we believe that these conditions are typical of the Hanna Shoal region (Weingartner et al. 2013a). There are several water mass classifications for the Chukchi Sea shelf (e.g., Coachman et al. 1975; Gong and Pickart 2015). For our purposes we define BSSW as consisting of a warm ( $\geq 4^\circ\text{C}$ ) and dilute ( $\sim 31 - 32$ ) fraction and a colder ( $2 - 4^\circ\text{C}$ ) and saltier ( $32 - 32.5$ ) fraction. The warmer waters are typically carried northward in the Alaskan Coastal Current (red arrow in Figure F1a), while the cooler and saltier fraction is transported through the Central Channel and Herald Valley. In addition, the shelf contains ice meltwaters (MW), which are cold ( $\leq 2^\circ\text{C}$ ) and fresh ( $24 - \sim 30$ ) and winter waters (WW), which are  $\leq -1.0^\circ\text{C}$  and salty ( $> 32.5$ ). WW is near freezing when produced in winter on the Bering and Chukchi shelves as a result of ice formation and can warm slightly in summer months (Gong and Pickart 2015). The disposition of these water masses varies seasonally. WW is pervasive in winter but is gradually displaced northward with the springtime increase in transport through Bering Strait (Weingartner et al. 2005; Woodgate et al. 2005) and by late summer occurs over the northern half of the shelf underlying MW and/or BSSW (Weingartner et al. 2013a; Pickart et al. 2016).

In August, the surface waters from  $\sim 70.5^\circ$  to  $71^\circ\text{N}$  and between  $164^\circ$  and  $165^\circ\text{W}$  were warm ( $\sim 6^\circ\text{C}$ ) and moderately salty ( $31 - 32$ ). Bottom waters were slightly colder with both water masses consistent with BSSW advected northward from Bering Strait in summer. North of this location and south of Hanna Shoal, surface waters were cool ( $2 - 4^\circ\text{C}$ ) and fresh ( $\sim 30$ ), suggestive of MW, perhaps warmed by solar radiation and/or mixed with BSSW. North of  $\sim 71.25^\circ\text{N}$  bottom waters were the very cold ( $\leq -1^\circ\text{C}$ ) and salty ( $\geq 32.8$ ) WW. The more complete coverage of September 2012 illustrates the enormous spatial

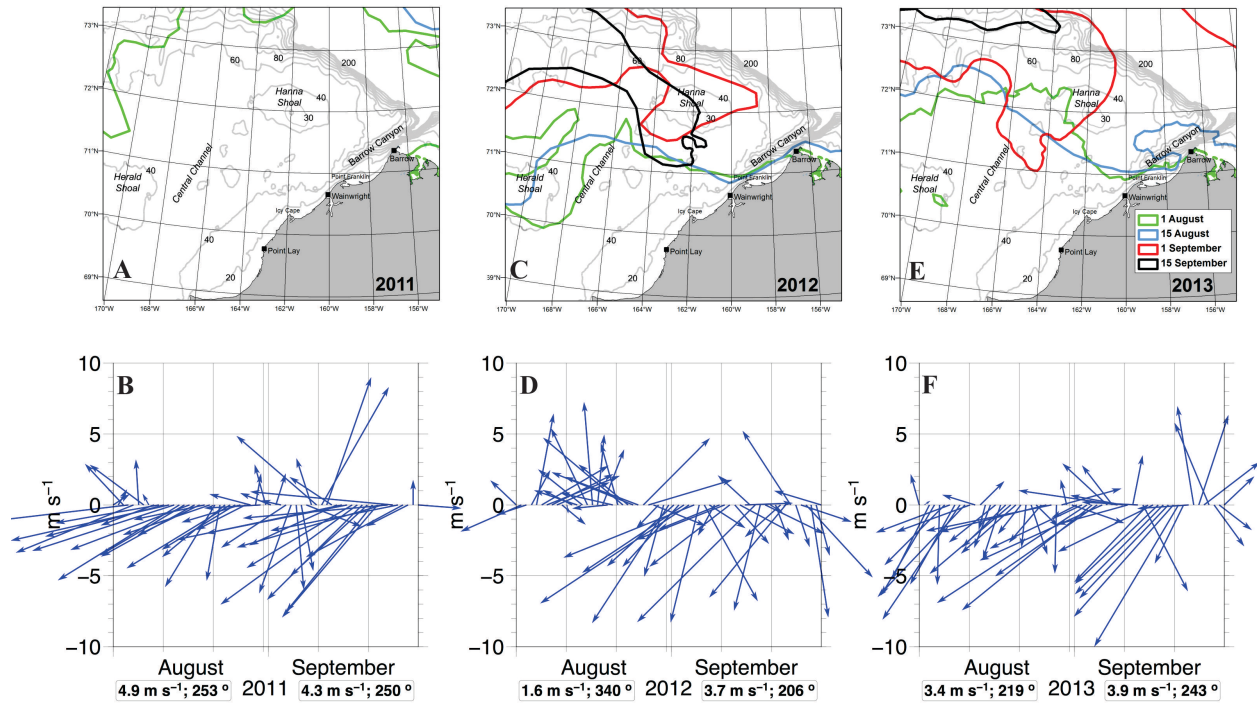


**Figure F3.** Maps of the 15% ice concentration isopleth at biweekly intervals for the August – September period (top row) and mean daily wind vectors (bottom row). Panels a and b are for 2011, c and d are for 2012, and e and f are for 2013. The mean monthly wind velocity and wind speed (in parentheses) are listed below the x-axis for each year.

extent of the surface MW, which occupied the entire region north of  $\sim 71.5^\circ\text{N}$ . South of this latitude, the shelf contained BSSW, with this water mass extending northward in the Central Channel along  $166^\circ\text{W}$  as well as eastward toward the coast near Wainwright. Overall these data suggest a front which extends southward from  $72^\circ\text{N}$ ,  $166^\circ\text{W}$  (approximately parallel to the Central Channel) and then trending eastward along  $71.5^\circ\text{N}$  towards Barrow Canyon. Very likely this MW front is part of the same frontal system that extends along the length of Barrow Canyon (Pickart et al. 2005; Gong and Pickart 2015). The spatial distribution of WW along the bottom in September was similar in extent to the surface MW, although WW extended farther inshore than MW. Note also that the coldest WW formed an arc along the southern and eastern sides of Hanna Shoal. The 2013 CESP hydrography (Weingartner et al. 2014) was broadly similar to that of 2012 in terms of the areal distributions of the major water masses and location of the MW/BSSW frontal system along  $\sim 71.5^\circ\text{N}$ . The major difference was that bottom salinities were slightly fresher (32.5 – 32.8) compared to 2012.

Water mass distributions in 2011 were quite different in several important respects (Figure F5). Most obvious was the complete absence of MW, which is not surprising given the early retreat of sea ice in 2011 (Figures F2 and F3). The surface layer in both August and September consisted entirely of BSSW, was nearly homogeneous in salinity, lacked surface fronts, and had only weak meridional thermal gradients. In August 2011, the bottom waters between  $70^\circ - 71^\circ\text{N}$  and  $164^\circ - 165^\circ\text{W}$  were BSSW, while WW occupied the shelf north of this location and along the southern side of Hanna Shoal. In September, BSSW was prominent at the surface and bottom in the Central Channel, over the shelf south of  $\sim 71^\circ\text{N}$ , and was even found over the shallowest portions of Hanna Shoal, although the low salinities here could have been a remnant of MW that had either mixed with the BSSW or had warmed. Except as noted with respect to the Central Channel, WW surrounded most of Hanna Shoal. It extended as far south as  $71^\circ\text{N}$

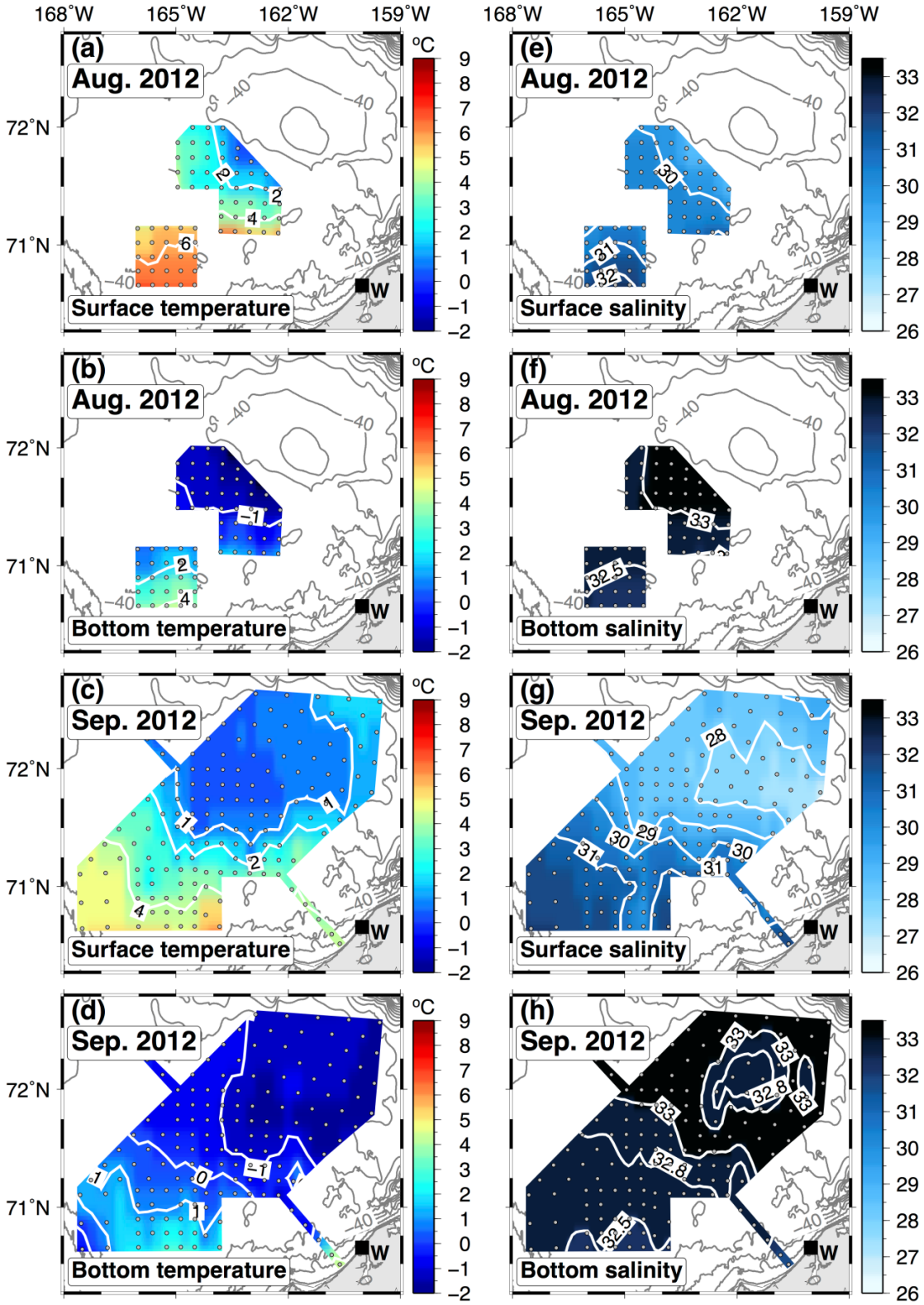


**Figure F4.** Plan views of temperature (left) and salinity (right) in August and September of 2012 based on averages of the upper and bottom 10 m of the water column. The village of Wainwright is designated with a "W". Filled circles show CTD station locations.

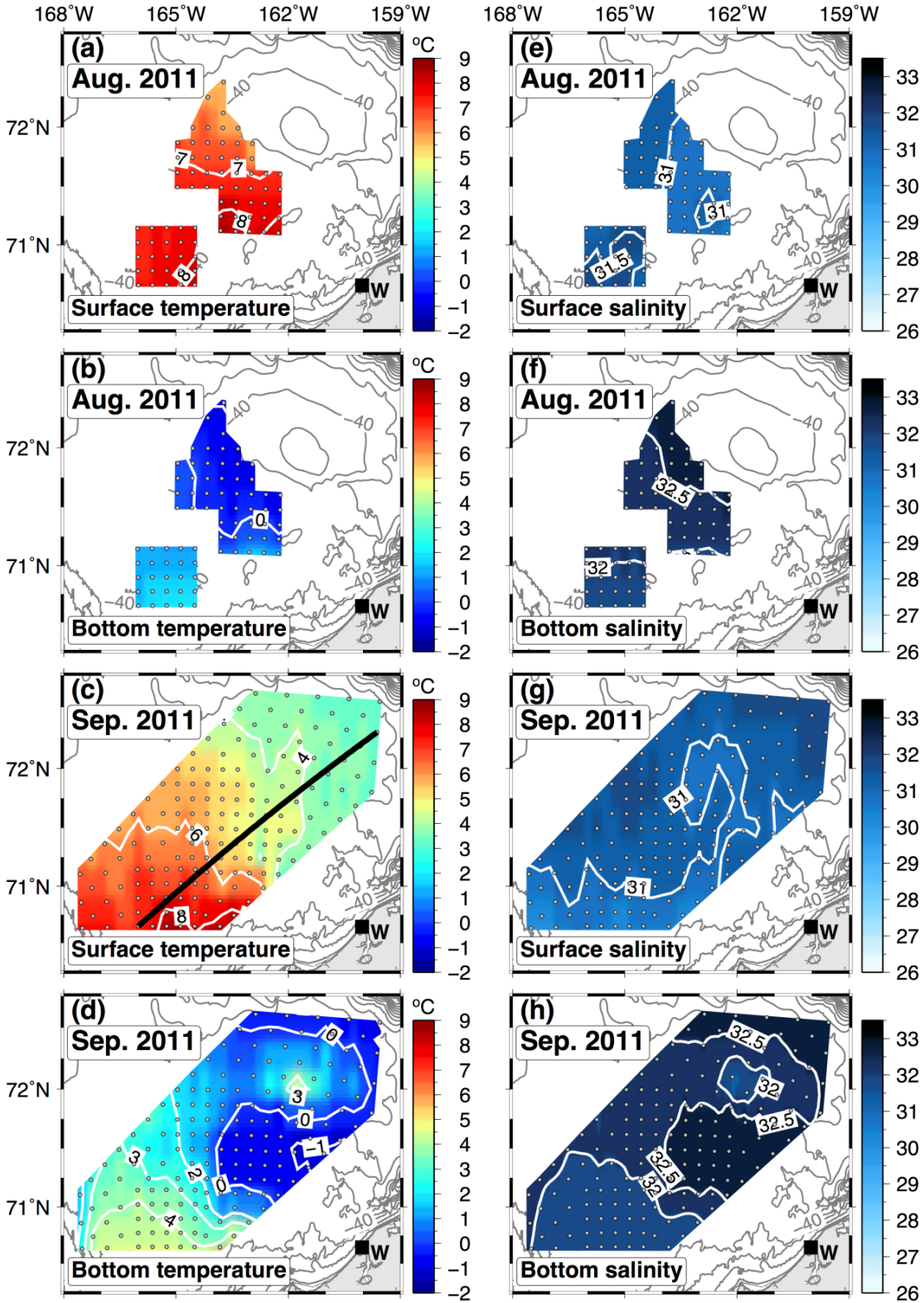


**Figure F5.** Plan views of temperature (left) and salinity (right) from August and September 2011 based on averages of the upper and bottom 10 m of the water column. The village of Wainwright is designated with a “W”. Filled circles show CTD station locations. The black line in panel c shows the location of the vertical sections from 2011 and 2102 shown in Figure F6.

with the coldest waters forming a prominent lobe on the southern side of Hanna Shoal. A thermohaline bottom front separated this WW from the adjacent BSSW. The WW properties in 2011 were fresher ( $\sim 32.5$ ) than the corresponding WW salinities  $\geq 32.8$  of 2012 (Figure F4h).

An alternative perspective of the contrasting thermohaline structure between these two years is given by Figure F6, which consists of two, 300 km long vertical sections occupied in September 2011 and 2012. The transect (shown in Figure F5c) extended from the southwest ( $\sim 70.5^\circ\text{N}$ ,  $166^\circ\text{W}$ ) to the northeast ( $\sim 72.5^\circ\text{N}$ ,  $160^\circ\text{W}$ ) with the northern portion of the transect along the eastern side of Hanna Shoal. In 2011, warm, moderately salty BSSW entirely encompassed the upper 20 m of the water column and along the bottom over the first 100 km. WW was present below  $\sim 20$  m on the northern and southern sides of Hanna Shoal and was separated from BSSW in the south by a bottom temperature front. In contrast, the 2012 section consisted of a strong frontal system associated with MW and BSSW at km 140, in addition to weaker MW fronts at km 175 and km 200. The sections also differ with respect to the vertical stratification, which in both years was dominated by the vertical salinity gradient. The stratification in 2012 (and 2013) was nearly twice as strong as in 2011, with these differences primarily due to the absence of MW in 2011 and its presence in 2012 (and 2013).

Another notable feature in the 2012 section was the presence, at km 225, of a “lens” of warm ( $\sim 2^\circ\text{C}$ ) water, signified by an upward distension of the 29 isohaline above the lens and a less prominent, downward-bowing of the 32 isohaline below. This feature is likely an anticyclonic, intrapycnocline eddy

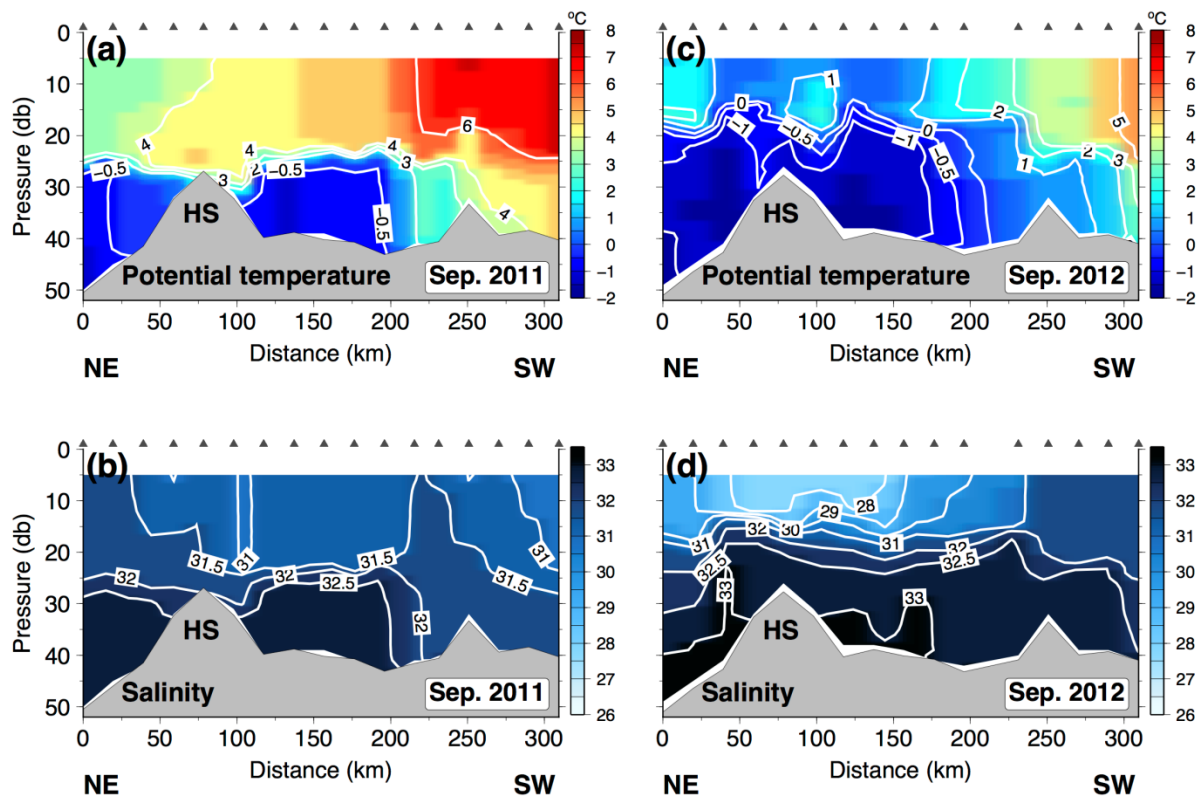


**Figure F6.** Vertical sections of potential temperature (top row) and salinity (bottom row) collected from early to late of September 2011 (a, b) and 2012 (c, d), respectively. The location of both sections is shown in Figure F5c. Hanna Shoal is denoted as “HS”. Inverted triangles indicate station locations.

formed via a baroclinic instability of the MW/BSSW front. These features are often observed when MW/BSSW fronts are present and are probably important agents for lateral mixing (Lu et al. 2015).

The coarse resolution of the CESP CTD sampling did not permit adequate horizontal resolution of the MW/BSSW fronts but Acrobat sections collected in September 2013 along Legs Q and M (Figure F1b) resolve the frontal width scale. In both cases, the front was  $\sim 10$  km wide and located at  $\sim 71.5^\circ\text{N}$  on Leg Q and  $71.2^\circ\text{N}$  on Leg M (Figure F7a, b, c, and d). We examined the stability of these fronts using the balanced Richardson number criterion (Thomas et al. 2016) and found that portions of the MW/BSSW front (including some sections not presented here) met the necessary conditions for symmetric instability, whereas other segments did not. The results are equivocal and, at best, suggest that there was spatio-temporal variability along the front with respect to this criterion.

The chlorophyll distributions (Figure F7e, f) along these sections are interesting in two regards. First, the densest chlorophyll concentrations occur in the highly-stratified region north of the front on the  $26 \sigma_t$  isopycnals at  $\sim 25$  m depth, and below the pycnocline. Second, the chlorophyll distribution appears very patchy with the patch scales ranging from  $\sim 1$  to  $\sim 20$  km based upon visual inspection. Nutrient concentrations, reported by Codispoti et al. (2005), Questel et al. (2013), and Danielson et al. (2016) indicate that WW bottom waters have sufficiently high nutrient levels to sustain primary production, while MW is nutrient deficient. Although high in nutrients upon leaving Bering Strait, BSSW nutrient levels are depleted by the time these waters reach the northeastern Chukchi shelf in August and September. Consequently, neither the absence of chlorophyll in the surface waters or the sub-surface chlorophyll maxima in the heavily stratified MW/WW is surprising. There is, however, no indication of chlorophyll patchiness or of well-defined sub-surface chlorophyll maximum in the less-stratified regions south of the front where BSSW overlies WW.

These (and other) Acrobat sections suggest that the surface layer containing BSSW south of the front is horizontally homogenous in contrast to the more heterogeneous surface layer north of the front. Indeed, Figure F7 suggests that north of the main front, there were weaker and equally shallow fronts composed solely of MW of varying salinities and temperatures. We quantified these differences by computing

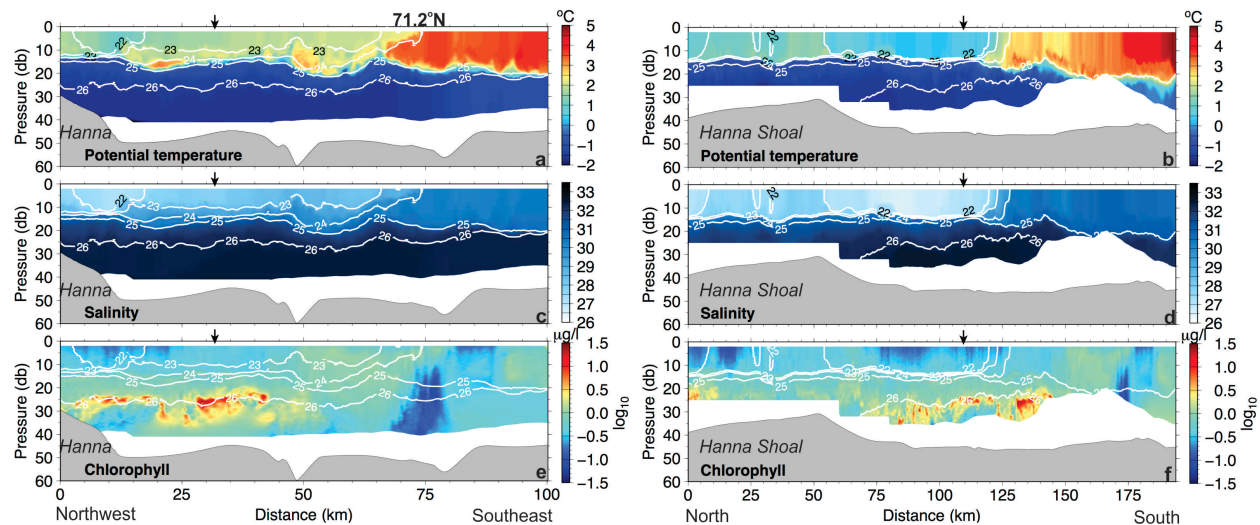


**Figure F7.** Vertical sections of potential temperature (a, b), salinity (c, d), and fluorescence expressed as  $\mu\text{g l}^{-1}$  of chlorophyll a (e, f) in September 2012 along Leg M (left) and Leg Q (right). The white contours indicate  $\sigma_t$  isolines. The arrows at the top of each figure indicate latitude  $71.5^\circ\text{N}$ . The locations of these transects are shown in Figure F1c. The front along Leg M is located at  $71.2^\circ\text{N}$  as indicated.

the wavenumber spectra of density at 10 m depth (similar to Timmermans and Winsor, 2012). The spectra were computed north and south of the front from different Acrobat sections (Figure F1b) but not across the front. We then integrated the spectra over three different spatial bands (1 – 5 km, 5 – 10 km, and 10 – 20 km) and compared the variance in each band. Regionally the baroclinic radius of deformation is  $\sim 5$  km, so we define the mesoscale portion of the spectrum as having length scales of  $>5$  km and the sub-mesoscale range  $<5$  km. The computations were done separately using sections north and south of the front and the results summarized in Figure F8. South of the front, the variance was uniformly low across the entire spectral range, with typical values being  $1 - 2 \text{ kg}^2 \text{ m}^{-6}$ . North of the front, the variances increase, although not consistently across all the sections. In general, the variances north of the front were a factor of 2 to 5 times greater in these bands than the variances south of the front. Quite possibly this greater spatial variability includes vertical motions over similar spatial scales that contribute to the patchiness in the chlorophyll distributions.

### F.3.3 Hydrography: Hanna Shoal

In this section we examine the temperature and salinity structure around the Shoal based on CTD sections occupied during the 2012 and 2013 mid-August COMIDA cruises. In both years heavy ice and other time constraints limited the spatial coverage. We occupied five sections in 2012 and four sections in 2013 (Figure F1b), with each section radiating outward from the Shoal. The 2012 sections included three sections (1-12, 2-12, and 3-12) arrayed from west to east on the northern side of the Shoal (Figure F9) where ice concentrations were 60 – 80%, except along the inner portion of section 1-12 where concentrations were  $\sim 30\%$ . Winds during the 2012 sampling were southerly at  $\sim 4 \text{ m s}^{-1}$ . Under these conditions the flow over the shelf south of the front was likely eastward at  $5 - 10 \text{ cm s}^{-1}$ , veering northeastward and becoming swifter along the coast (Weingartner et al. 2013a) while the surface currents east of Hanna Shoal were weakly eastward at  $2 - 5 \text{ cm s}^{-1}$  (Weingartner et al. 2017a; Fang et al. in prep). Similar sections were occupied in 2013 (Figure F10, but note that section 2-13 differs in location from section 2-12, Figure F1a). Winds during the 2013 sampling were northeasterly at  $\sim 4 \text{ m s}^{-1}$ , in which

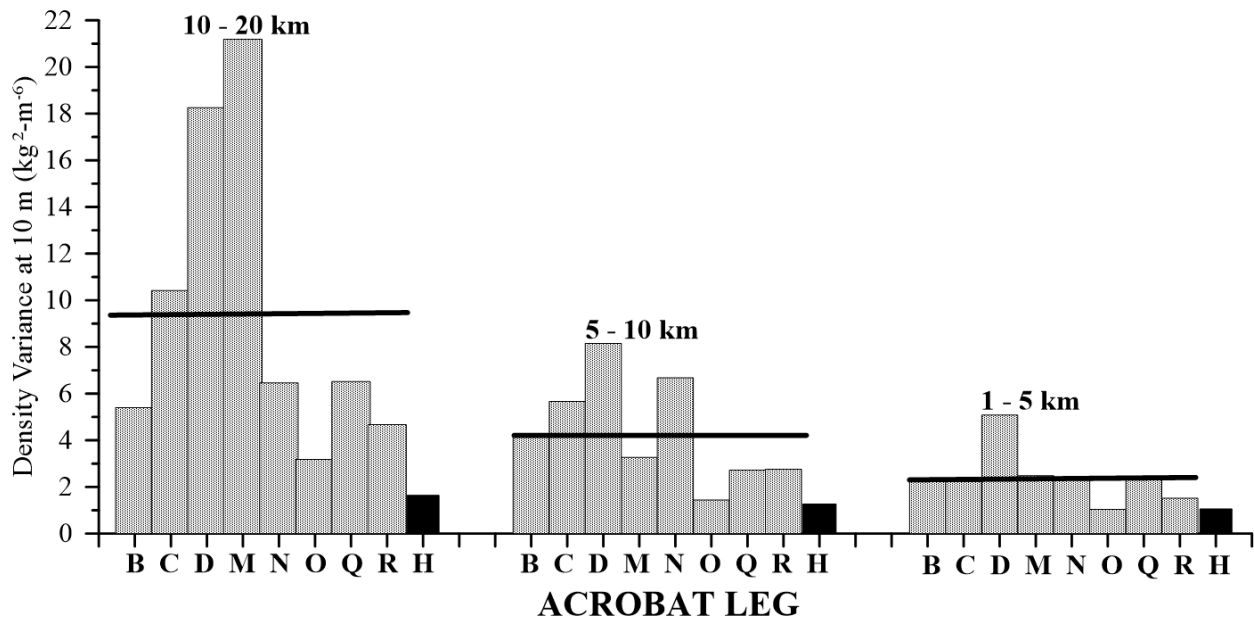


**Figure F8.** Histograms of density variance at 10 m depth as a function of horizontal length scale based on 2013 Acrobat CTD tows collected north of the front (gray stippled bars) and south (black bars) of the front. The horizontal bars denote the mean density variance in each band for the gray bars.

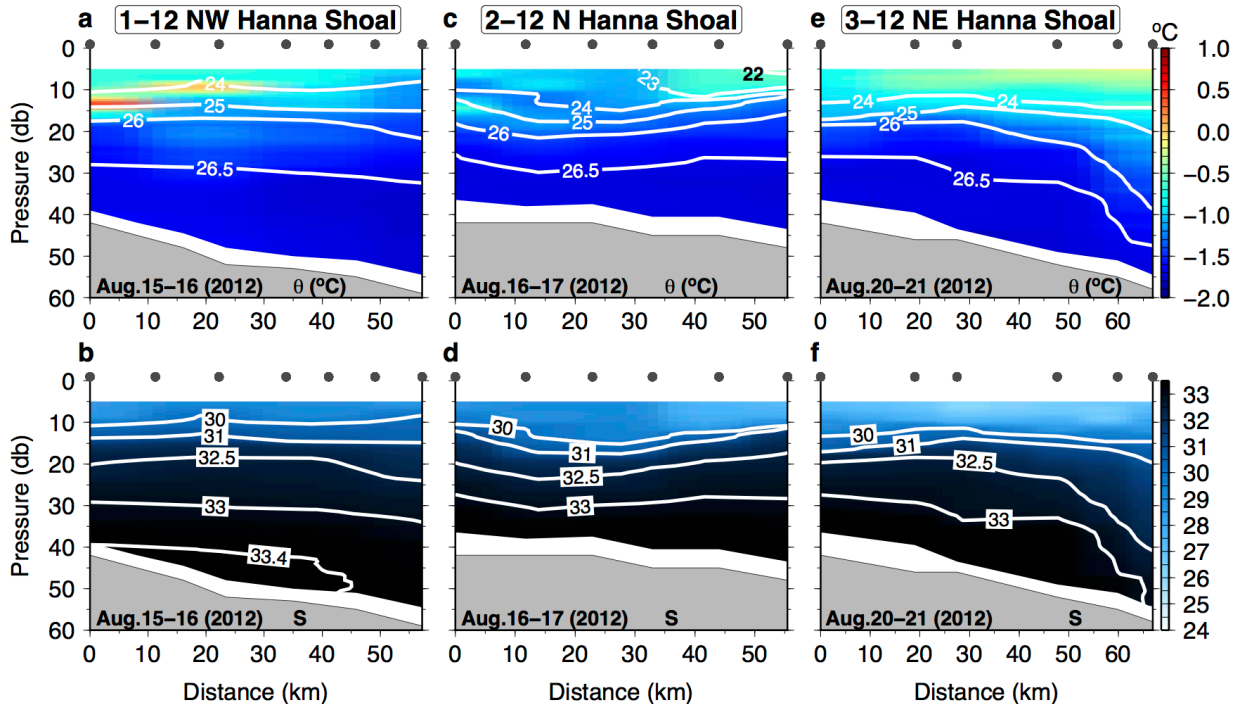


**Figure F9.** Vertical sections of potential temperature ( $\theta$ ; top) and salinity (S; bottom) along transects 1-12 (a, b), 2-12 (c, d), and 3-12 (e, f) on the northwestern, northern, and northeastern sides of Hanna Shoal, respectively. Figure F1 shows transect locations. Hanna Shoal is on the left of each panel.

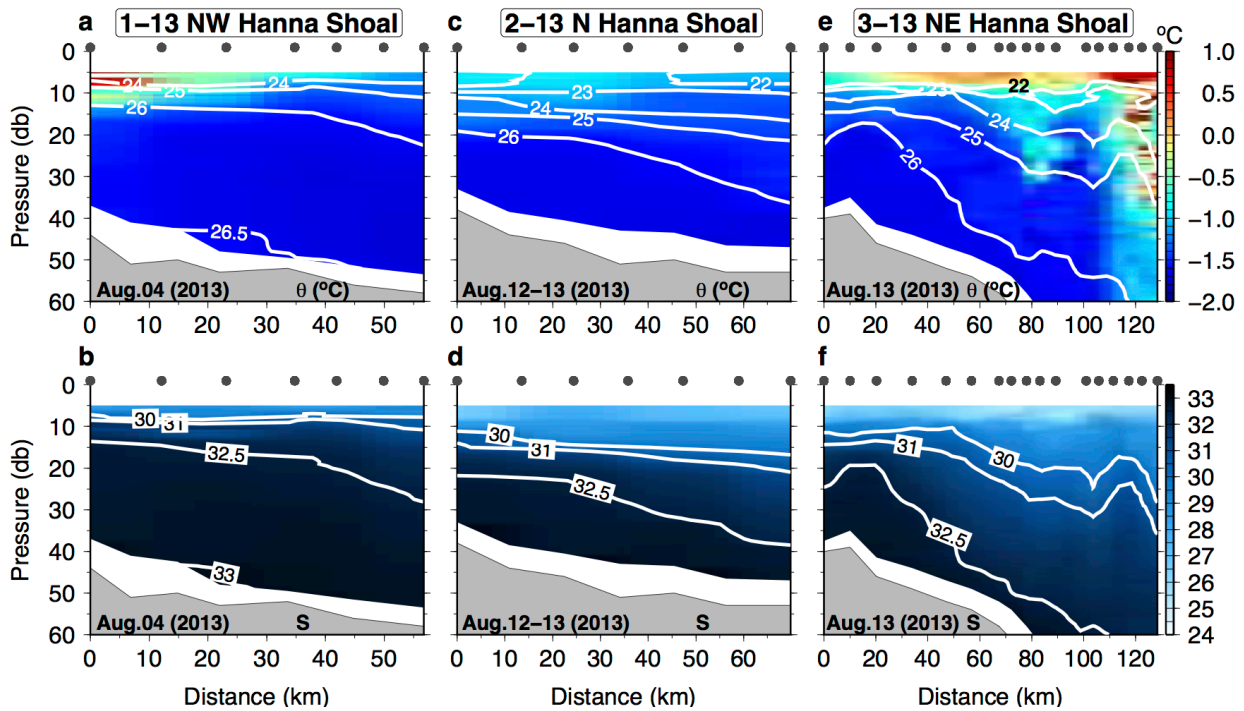


**Figure F10.** As in Figure F9 but for transects 1-13 (a, b), 2-13 (c, d), and 3-13 (e, f) on the northwestern, northern, and northeastern sides of Hanna Shoal, respectively. Figure F1 shows transect locations. Hanna Shoal is on the left of each panel.

currents should also be eastward south of the front at  $\sim 5 \text{ cm s}^{-1}$  (Weingartner et al. 2013a), but westward at  $\sim 5 \text{ cm s}^{-1}$  at the surface east of Hanna Shoal (Fang et al. in prep). Thus we feel that in both years the sections were sampled synoptically during the occupation of the COMIDA transects. Ice concentrations along these sections were similar to those of 2012, except the concentrations were generally 0 – 30% along section 1-13. Figure F11 shows sections (4-12, 5-12, and 4-13) on the southern side of the Shoal, where there was heavy ice along the northern part of each section.

Several features are common to all sections. First, below  $\sim 20 \text{ m}$  depth the water column consists entirely of WW with salinities  $>32.5$  and temperatures  $\leq -1.6^\circ\text{C}$ . In 2012, salinities within 10 – 15 m of the bottom exceeded 33, with maximum salinities ( $>33.4$ ) near the bottom on section 1-12 (Figure F9b). Bottom salinities rarely exceeded 33 in 2013. Second, in general the surface layer consisted of MW with low salinities ( $<30$ ) and temperatures between  $-0.5^\circ\text{C}$  and  $0.5^\circ\text{C}$ . Third, along the northern side of the Shoal and proceeding from west to east, the salinities in the upper 10 m decreased by  $\sim 2$ . Fourth, the 2-layer stratification of the water column was set by a strong halocline centered between 10 and 15 m depth. There are a number of exceptions to these general features. First, warmer ( $1 - 2^\circ\text{C}$ ), near surface waters were observed south of Hanna Shoal at the southern end of sections 4-12, 5-12, and 4-13 (Figure F11). Each of these sections extended as far south as  $\sim 71.5^\circ\text{N}$ , suggesting that the warm water source was BSSW intruding across the front (Figure F4).

Second, warm ( $\geq 0^\circ\text{C}$ ) surface or near surface waters were found within the first 35 km of sections 1-12 (Figure F9a) and 1-13 (Figure F10a) along stations nearest to the Shoal. In both cases, the warmest water was in a subsurface temperature maximum embedded in the pycnocline. These warm waters were likely BSSW, albeit modified by MW, which had flowed northward through the Central Channel and had

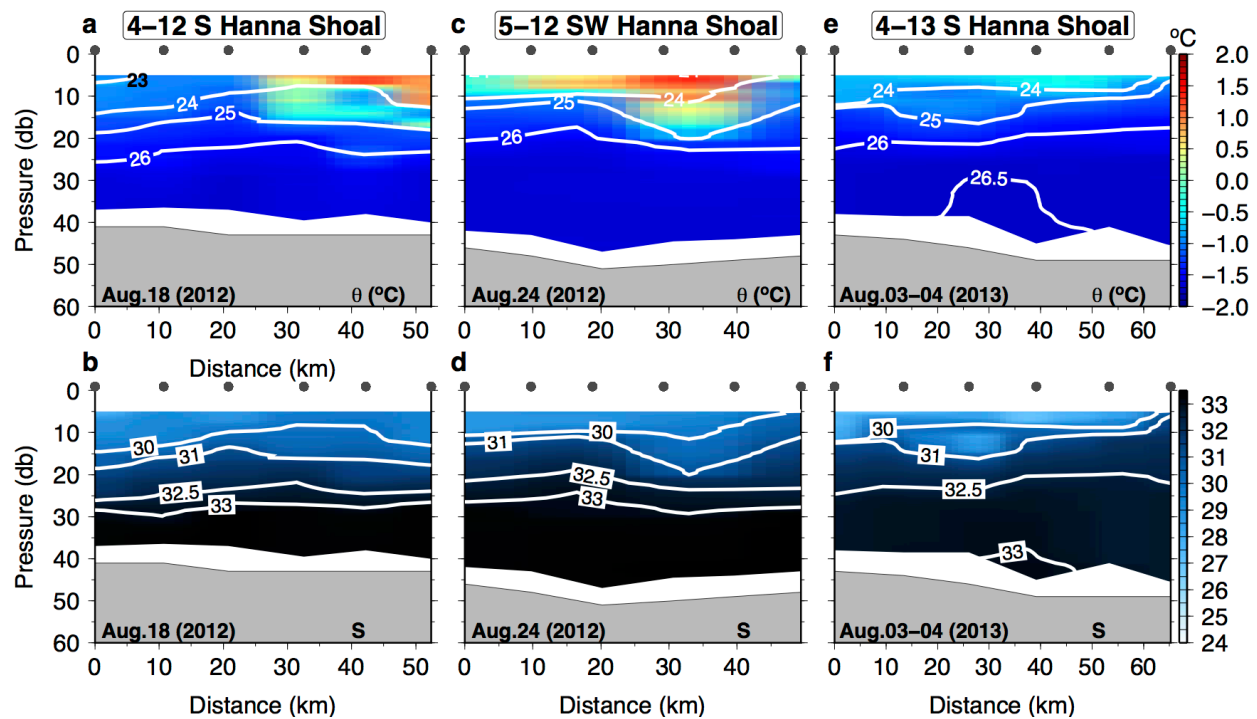


**Figure F11.** As in Figure F9 but for transects 4-12 (a, b), 5-12 (c, d), and 4-13 (e, f). Panels a, b, e, and f are on the southern side of Hanna Shoal, and panels c and d are on the southeastern side. Figure F1 shows transect locations. Hanna Shoal is on the left of each panel. Note the temperature scale differs from that of Figures F9 and F10.

begun to flow clockwise around the northern side of the Shoal. This interpretation is consistent with velocities at moorings HSNW-40 and -50 in 2012 where the mean flow was  $\sim 7 \text{ cm s}^{-1}$  toward the east-northeast during the time that sections 1-12 to 3-12 were occupied. In 2013, this flow averaged  $\sim 5 \text{ cm s}^{-1}$  eastward over the time required to occupy sections 1-13 to 3-13. (In both years the flow was largely barotropic insofar as the velocity shears were small; the differences between the near-surface and near-bottom ADCP bins were  $\sim 3 \text{ cm s}^{-1}$ .) However, subsurface temperature maxima were absent along the sections further east. In 2012 the warmest waters along 2-12 (Figure F9c) were at the distal end of the section, whereas on 2-13 the warmest water was adjacent to the Shoal. We argue later that these warm signals are likely a mixture of the waters from the western and northeastern sides of the Shoal.

Third, surface waters over the outer parts of sections 3-12 and 3-13 were also warm and fresh, suggesting that these were either MW that had warmed by solar radiation or were derived from the Alaska Coastal Current emanating from Barrow Canyon. Corlett and Pickart (2017) reported the presence of coastal waters flowing westward in the Chukchi Slope Current. Here we show that the coastal waters can, at least occasionally, be transported from the Chukchi Slope Current onto the shelf northeast of Hanna Shoal and thence continue westward on the shelf and/or southward over the Shoal. Figure F12 shows the sea surface temperature (SST) color-coded trajectories for 6 of the 13 total drifters between 12 August 2012 (when they were deployed in the Alaskan Coastal Current near Icy Cape) and 30 September, along with the winds for the same time period. Upon deployment, the winds were southerly and the drifters moved rapidly through Barrow Canyon. At the mouth of the canyon, all but one eventually moved westward in the slope current. Six of the drifters (those shown in Figure F12) crossed back onto the shelf northeast of Hanna Shoal after the winds became northeasterly on  $\sim 31$  August, while the remaining six continued westward along the slope. SSTs decreased from  $\sim 10^\circ\text{C}$  at deployment to  $2 - 3^\circ\text{C}$  by mid-September on the shelf north and east of Hanna Shoal. For those drifters that continued farther south, the SST decreased to  $\sim 0^\circ\text{C}$  by month's end. The cooling was most likely due to mixing between the coastal water and MW along the drifter path and, beginning mid-September, due to heat loss to the atmosphere.

The final noteworthy difference among the COMIDA CTD sections is that the slopes of the subsurface isopycnals differ around the Shoal. On the south side of the Shoal the isopycnal slopes were nearly flat indicating very little baroclinicity. On the north side and below the pycnocline, the isopycnals on sections 1-12, 3-12, 1-13, 2-13, and 3-13 slope downward away from the Shoal. The largest slopes were below the pycnocline along sections 3-12 and 3-13, both on the northeast side of Hanna Shoal. As shown below these slopes imply a baroclinic velocity field that likely plays an important role in the circulation north of Hanna Shoal.

### **F.3.4 The North Side of Hanna Shoal**

In this section we seek to understand the source of the warm surface waters on the north side of the Shoal, specifically along sections 2-12 and 2-13. Recall that these waters are cooler than those on either the northwest or northeast sides of the Shoal. We first consider the possibility that these waters simply resulted from the cooling of warm waters from the Central Channel flowing around the northwest side of the Shoal across sections 1-12 and 1-13. We examine this possibility by computing the horizontal heat flux divergence of the warm water band over the upper 15 m and over a horizontal width of 30 km (essentially the width of the warm water flowing from the Central Channel) and assume only vertical heat exchanges occur, to either the ice or to the water column below 15 m. The calculation uses the velocity averages given previously and also assumes the warm water at the outer end of section 2-12 entirely captured the remnants of the warm waters flowing through section 1-12. In 2012, the heat flux calculations imply a heat loss to the ice of  $\sim 20 \text{ W m}^{-2}$ , for an ice melt rate of  $0.6 \text{ cm day}^{-1}$ . The advective time scale between sections 1-12 and 2-12 is  $\sim 10$  days, which would result in the addition of 6 cm of MW to the upper 15 m. Assuming a sea ice salinity of 5; this MW flux would reduce the salinity by 0.1 between the two sections, which is far less than the observed salinity decrease of  $\sim 0.8$ .

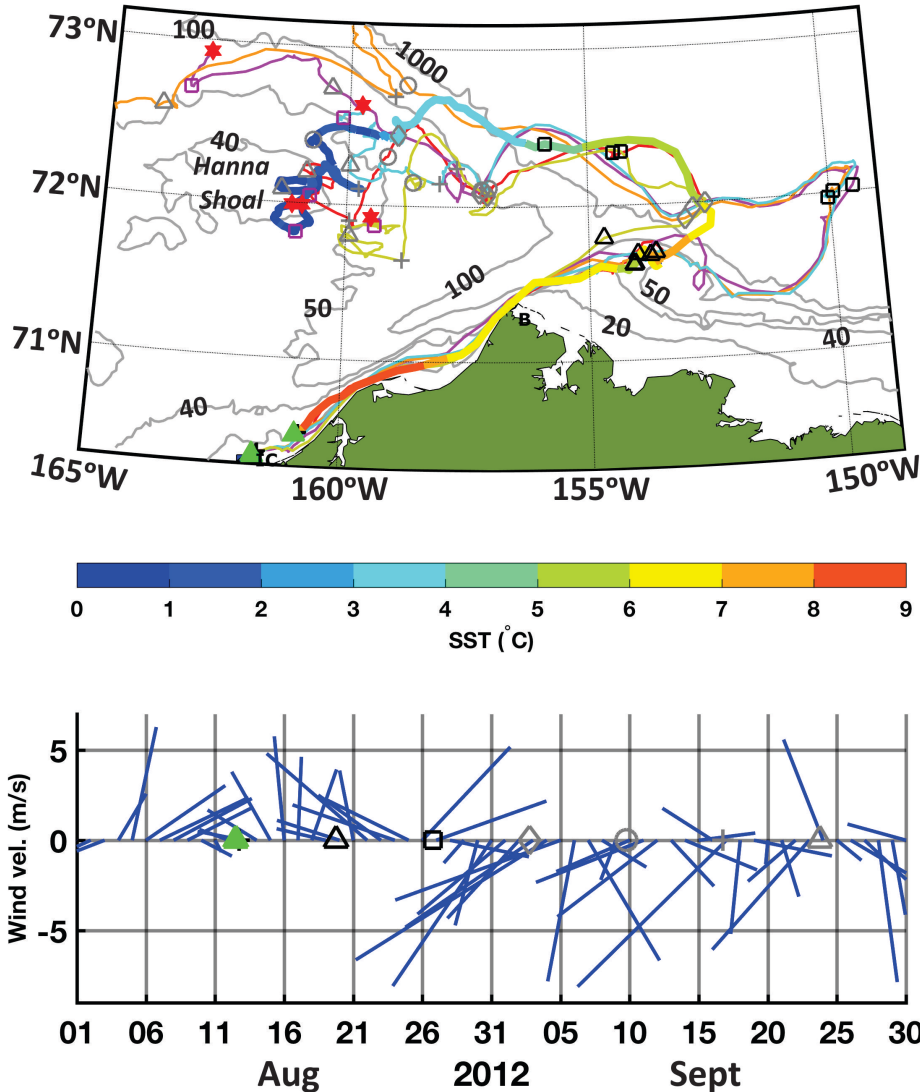


**Figure F12.** The trajectories of 6 satellite-tracked drifters (1 m drogue depth) deployed offshore of Icy Cape on 12 August 2012. One of the trajectories is color-coded according to measured SST. The various symbols along each trajectory are at 7-day intervals with the dates given on the wind vector time series (bottom plot). The 20, 40, 50, 100, and 1,000 m isobaths are labeled. Green triangles signify the deployment position and red stars the last good transmission from each drifter.

Moreover, the additional ice melt influx required to satisfy the salinity change implies an atmospheric heating rate of  $\sim 185 \text{ W m}^{-2}$ . For a surface ice albedo of 0.6, the required solar radiative influx amounts to  $\sim 300 \text{ W m}^{-2}$ . These values seem unrealistically high even in the absence of the dense fog present in the area at the time. For example, on a monthly basis, Maykut (1986) estimates that the net radiation balance in mid-summer is  $\sim 100 \text{ W m}^{-2}$ . The same calculation for the 2013 data yields a similar conclusion, e.g., the solar radiative influx is much greater than feasible. We conclude the salinity imbalance implies an advective contribution of MW from elsewhere, most likely from the northeast side of the Shoal.

There are two lines of evidence to support this contention. The first follows from the  $\theta/S$  diagrams compiled from sections 1, 2, and 3 from each year (Figure F13) over the upper 30 m of the water column.

Included in this figure are the average  $\theta/S$  values in the upper 15 m encompassing the warm waters along each section. Clearly the surface water properties along section 2-12 could be obtained by cooling and mixing of the surface waters from the eastern and western sides of the Shoal. In 2013, the warm band along section 2-13 was  $\sim 0.3^\circ\text{C}$  cooler than that on the northeast side of the Shoal, and the salinities were identical at  $\sim 28.7$ . In contrast the salinity on the northwest side of the Shoal was, at  $\sim 30.8$ , much greater. The second line of evidence follows from the baroclinic geostrophic tendencies along sections 3-12, 2-13, and 3-13 (Figure F14). (Baroclinicity along section 2-12 is weak and variable and, thus, not shown.) In 2012, the baroclinic tendency was northwestward along section 3-12, and, over the outer half of the section, averaged  $\sim 5 \text{ cm s}^{-1}$  in the upper 20 m. Along the 40 m isobath, the tendency was southeastward at

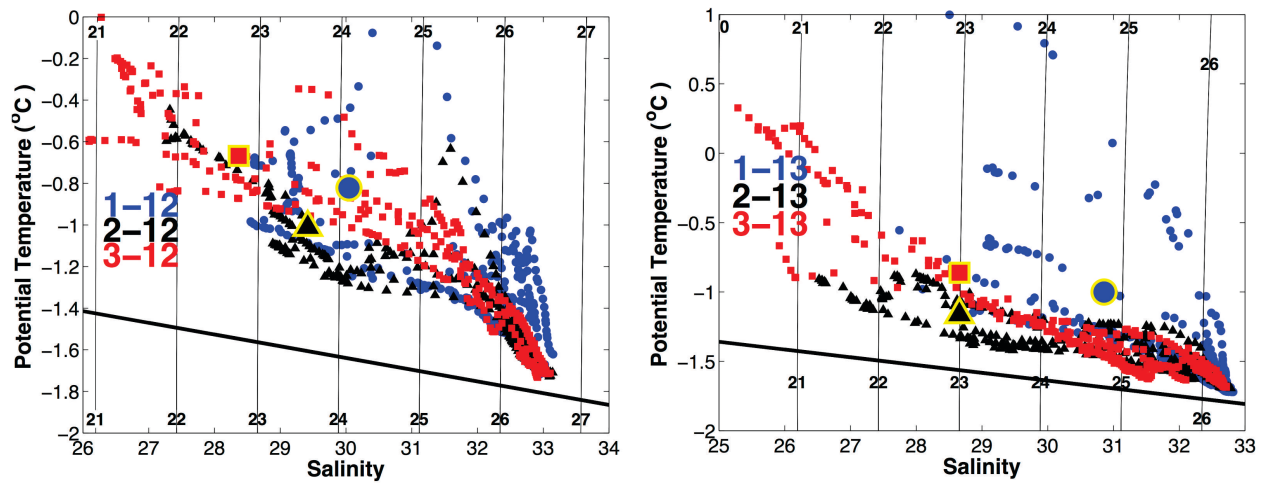


**Figure F13.** Scatterplots of potential temperature versus salinity over the upper 30 m of the water column for sections 1, 2, and 3 in 2012 (left) and 2013 (right). Only stations along the first 65 km of the transect are included. Note the scales change between 2012 and 2013. The black slanted line denotes the freezing point curve. The larger symbols outlined in yellow depict the mean values along each section in the upper 15 m.

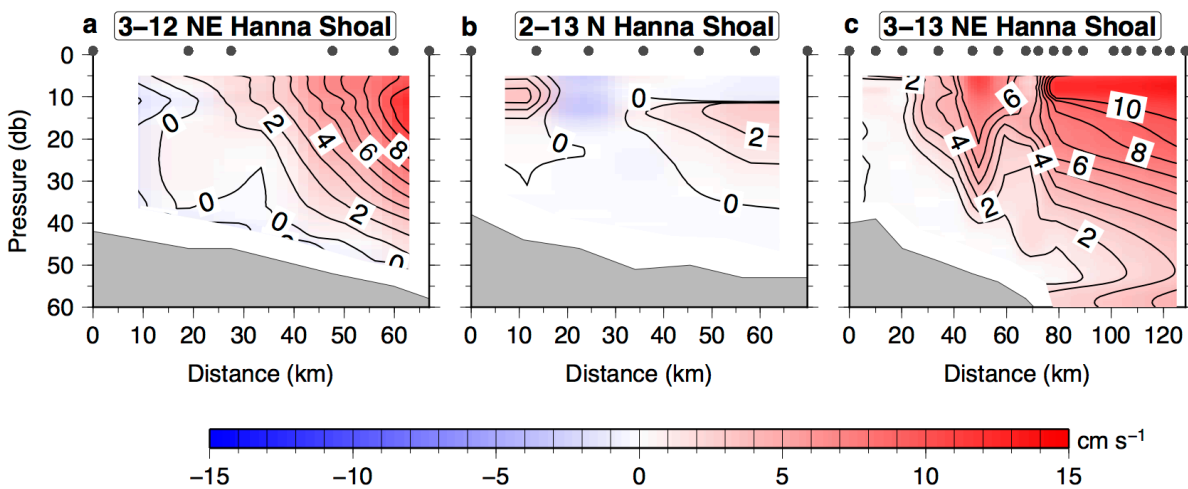


**Figure F14.** Baroclinic, geostrophic velocity field for transects a) 3-12, b) 2-13, and c) 3-13. The corresponding temperature and salinity sections are shown in Figures F9 e, f; F10 b, d; and F10 e, f, respectively. Positive velocities are north-northwestward and negative values are south-southeastward.

$\sim 5 \text{ cm s}^{-1}$ . These values are in good agreement with currents measured by the moorings deployed during occupation of the section. During the first three days after deployment, the currents in the upper 20 m were west-northwest currents at 6 and 13  $\text{cm s}^{-1}$  over the 50 and 56 m isobaths, respectively. There was similar agreement between the computed and measured velocity shears as well. The velocity difference over the 25 m between 20 and 45 m depth at the two moorings were  $\sim 10 \text{ cm s}^{-1}$  compared to  $\sim 6 \text{ cm s}^{-1}$  based on the thermal wind estimates. The mooring deployed on the 40 m isobath recorded 3  $\text{cm s}^{-1}$  toward the west- southwest. In 2013, the geostrophic computations yielded results similar to those of 2012 between the 40 and 60 m isobaths. The calculations also indicate that the baroclinic tendency increased to  $\sim 10 \text{ cm s}^{-1}$  over the deeper part of the section. The moored measurements averaged over the upper 25 m of the water column during the transit of this section in 2013 section were  $\sim 5 \text{ cm s}^{-1}$  to the southwest over the 40 m isobath and  $\sim 10 \text{ cm s}^{-1}$  northwestward on the 50 m isobath (the ADCP moored on the 56 m isobath died a month earlier). The baroclinic contribution was weaker along section 2-13 (north of Hanna Shoal) although still westward. In summary our results suggest that there was zonal convergence, at least along the 50 m isobath and over the upper portion of the water column, north of Hanna Shoal in August of both 2012 and 2013.

## F.4 Discussion

Our analyses clearly highlight the importance of sea ice, MW, and dense water to the hydrographic structure of the northeastern Chukchi Sea, particularly in the Hanna Shoal region. MW was absent in 2011, consistent with early ice retreat and the absence of ice over the Shoal in August. The heavy and persistent ice concentrations over Hanna Shoal in 2012 and 2013 resulted in a  $\sim 15 \text{ m}$  thick cap of dilute MW sitting above much denser winter water over most of the shelf north of  $\sim 71.5^\circ\text{N}$ . As a consequence the shelf stratification was substantially greater in 2012 and 2013 than in 2011. A front extending from the southwest side of Hanna Shoal (along  $\sim 71.5^\circ\text{N}$ ) eastward to Barrow Canyon separated the MW region from BSSW to the south. The MW pool north of the front supported substantially more mesoscale and sub-mesoscale surface layer density variations than the waters south of the front. In the absence of MW in 2011, we presume that surface density variability was comparatively small during that summer.

We suggest that the enhanced variability in the MW region in 2012 and 2013 may be a result of two distinct causes. The first is due to instability of the MW/BSSW front (Lu et al. 2015), which is expected to enhance the variance at the longer length scales and subsequently, through forward cascade (McWilliams 2008), to smaller length scales. The second may arise as a consequence of the ice floe size distribution, which changes seasonally. Winter floes tend to be large and consolidated, whereas in summer, floe consolidation decreases, and floe areas and thicknesses span a broader range (Perovich and Jones 2014). Spatial heterogeneity in the ice thickness distribution implies variations on similar spatial scales in the ice-ocean drag and melt rates. In August of 2012 and 2013, Hanna Shoal was covered by consolidated and grounded ice spanning 10s of  $\text{km}^2$ , as well as regions containing smaller, unconsolidated floes interspersed with leads. The buoyant MW plumes formed should vary in size accordingly, thus contribute to the surface density variance wavenumber spectrum. Different plume sizes are subject to different dynamical constraints; those within the mesoscale range are subject to rotation while ageostrophic dynamics are important over the sub-mesoscale portion of the spectrum (Yankovsky and Yashayaev 2014).

What caused the differences in Hanna Shoal summer ice conditions across the 2011 – 2013 period? While we cannot provide a definitive answer, we offer several possibilities. First we note that the northward heat transport through Bering Strait was substantially greater in 2011 than in 2012 and 2013 (Woodgate et al. 2012; Woodgate et al. 2015), which suggests that the ocean heat flux to the ice was greater in 2011. Indeed, the 2011 heat flux through Bering Strait was as large as that in 2007, when ice retreat across the Chukchi Sea shelf was also unusually early (Woodgate et al. 2010). Persistent northeasterly winds

observed in summer 2011 favors the westward drift of ice (Spall 2007). These winds would also force a westward drift (Pisareva et al. 2015) of newly exposed surface waters heated by solar radiation and an ever-increasing fetch over which waves would be generated. Both factors would enhance ice-edge retreat. We have also examined solar radiation differences amongst these summers and find that this variable alone cannot account for the differences among years. For example, NARR incoming solar radiation estimates from Bering Strait and the southern and northeastern Chukchi shelf indicate that the mean daily June and July values in 2012 exceeded that of the other years by  $\sim 40 \text{ W m}^{-2}$ , and yet ice concentrations were quite high that summer.

While northeasterly winds in the early part of summer 2011 may have played a role in ice retreat, the heavy ice concentrations over Hanna Shoal in 2012 and 2013 do not appear to be related to the August winds. In August 2012, mean winds were southerly at  $1 \text{ m s}^{-1}$ , whereas in 2013, the mean August winds were northeasterly at  $2 \text{ m s}^{-1}$  (Figure F2c – f). Additionally ice conditions on Hanna Shoal do not correspond to ice concentrations in the Arctic basin. According to the NIC, the heavy ice concentrations in summer 2012 occurred when the arctic-wide sea ice extent was the third lowest over the 1979 to 2013 period, with only the summers of 2007 and 2011 having lower ice concentrations. Indeed, in 2012, the entire Beaufort Sea shelf and slope were ice-free while Hanna Shoal was covered by thick ice at high concentrations.

Another factor affecting Hanna Shoal summer ice conditions may be processes that occurred the previous winter. In both August 2012 and 2013 thick ice was grounded atop Hanna Shoal. According to A. Mahoney (pers. comm.), grounding was evident over Hanna Shoal in late winter of both years. Eicken and Mahoney (2015) maintain that the source of this grounded ice is westward-drifting, heavily deformed ice from the eastern Beaufort (corroborated by Babb et al. (2013) who deployed ice beacons in 2011) and/or from a heavily-ridged ice arch that often protrudes north of Point Barrow. Ice keels must be  $\sim 20 \text{ m}$  in order to ground on the shallower portions of the Shoal. Sufficiently thick and deformed ice does not typically occur in the Beaufort Sea until January, at the earliest (H. Eicken pers. comm.). Once firmly grounded ice is established over Hanna Shoal, additional ice, even if thin, may collide and adhere on the windward side of the grounding zone. In this scenario the initial grounding subsequently promotes consolidation and additional ice deformation, which leads to heavy concentrations of thick ice that persist through summer.

There is indirect support for this hypothesis based on the mean January through April winds and ice drift derived from moored ADCP and IPS data (Figure F15). Figures F15b, d, and f show the mean winds and sea level pressure over the northern Bering and Chukchi Seas from January through April of 2011, 2012, and 2013. In 2011, the mean winds were weak ( $< 1 \text{ m s}^{-1}$ ) and southerly. In contrast, the mean winds in 2012 were north-northeasterly at  $2 - 3 \text{ m s}^{-1}$ , and in 2013 they were northeasterly at  $3 - 5 \text{ m s}^{-1}$ . These differences are reflected in the mean monthly ice velocity and variance ellipses for January through April of each year (Figure F15a, c, and e). In the winter of 2011, the ice drift was northeastward in accordance with mean currents in these areas (Weingartner et al. 2005). Although the drift east and north of Hanna Shoal may have been different, the mean winds were clearly unfavorable for ice advection from the Beaufort Sea. In contrast the ice drift in the winter of 2012 was southwesterly at  $\sim 5 \text{ cm s}^{-1}$  at all sites and in 2013 the drift was westerly at  $\sim 5 - 10 \text{ cm s}^{-1}$ . Although the interannual differences in drifts corroborate this hypothesis, the results based on the mean keel depths using only the upper 25% of the ice keel distributions are less supportive. In each year the largest of these means occurred in March and April and there was generally little spatial variability amongst sites. In 2011 and 2013 the values were  $14.5 \text{ m}$  and in 2012 they were  $21 \text{ m}$ . On this basis, it appears that 2012 was more favorable for ice grounding on the Shoal than in the other years.

Our measurements indicate that in all three years the densest winter water surrounded the Shoal. The source of this dense water is somewhat uncertain, however. One conceivable source is local formation

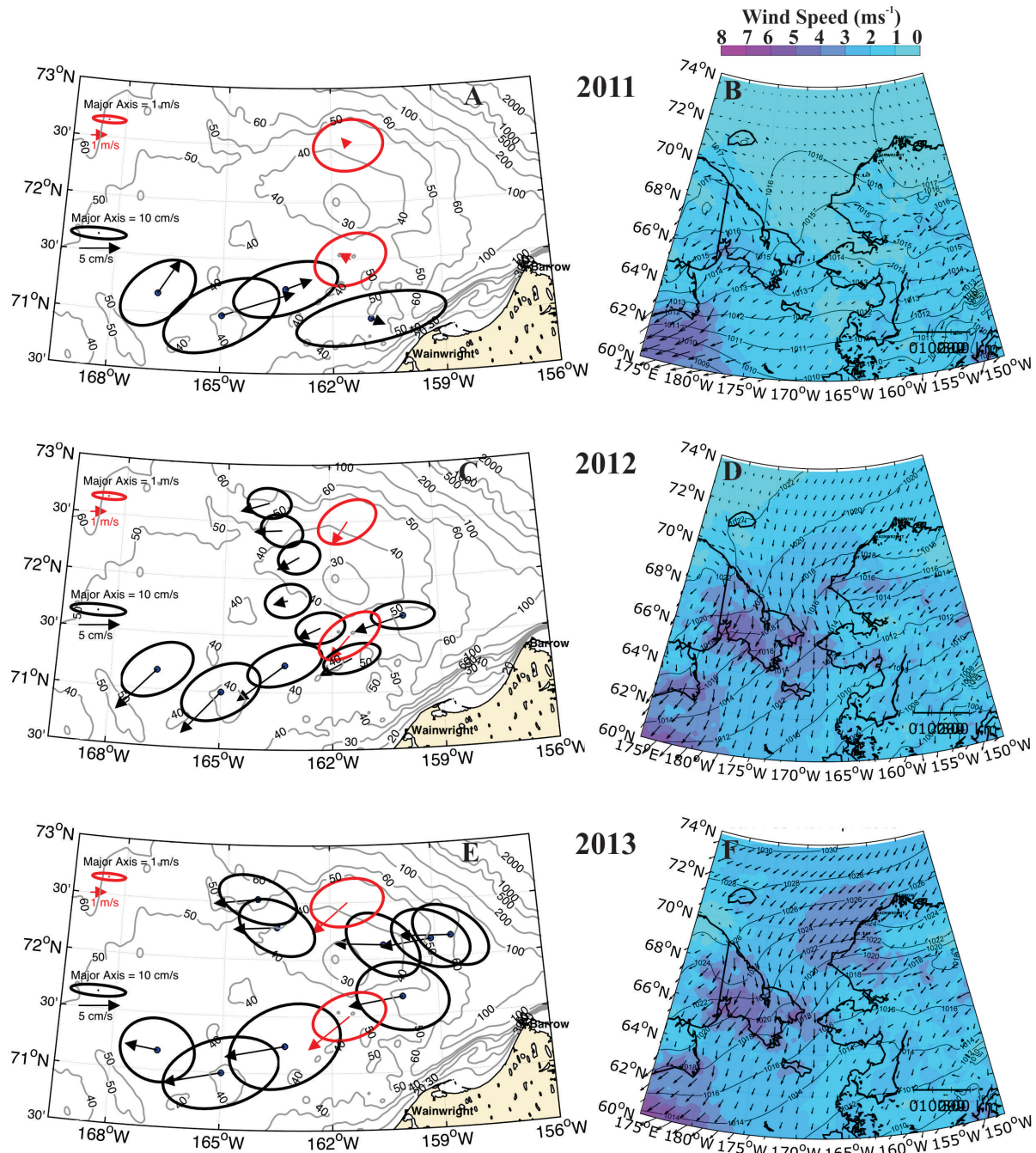


**Figure F15.** Each row shows the mean January – March ice and wind velocities (left panels) and regional wind vectors and sea level pressure (right side) over the northern Bering and Chukchi seas for 2011 (top row), 2012 (middle row), and 2013 (bottom row). Black arrows and ellipses denote the mean ice velocity and the corresponding velocity variance ellipses, while the red arrows and ellipses are for the winds.

over the Shoal during the preceding winter, as polynyas can form in the lee of grounded ice (Mahoney et al. 2012). Alternatively, brine repulsion from leads over the shallow Shoal would enhance local dense water formation. Under either circumstance, the dense water would be trapped to the Shoal and, in the absence of additional forcing, circulate anticyclonically around the Shoal (Spall 2013). However, the

summer synoptic shipboard measurements of Pickart et al. (2016) and the annually averaged measurements from moorings in 2011 (Weingartner et al. 2017a) along the south side of the Shoal suggest a mean flow of  $\sim 2 \text{ cm s}^{-1}$  to the southeast, which would transport the dense water toward Barrow Canyon. On the northwest side of the Shoal, the mean annual flow is northeastward at  $\sim 5 \text{ cm s}^{-1}$  (unpublished data). Although the vertically-averaged flow on the northeast side of the Shoal is not significantly different from zero (Weingartner et al. 2017a), the mean bottom flow is southward at  $\sim 2 \text{ cm s}^{-1}$  (unpublished data). The smaller of these values implies an advective time scale of 75 days for the movement of bottom waters from the west to the east side of the Shoal. If all of this dense water resulted solely from local ice formation processes, this time scale implies that the dense water surrounding the Shoal should have been absent by August assuming freezing ends in mid-May as suggested by climatology (Maykut 1986). The presence of dense water well into September suggests another advective source that transports dense waters toward the Shoal from either the Central Channel and/or Herald Valley (Pickart et al. 2010). Regardless of the source, there were considerable interannual differences in dense water salinities with the saltiest ( $\sim 33$ ) water observed in 2012 and the least salty ( $\sim 32.5$ ) in 2011. These differences may affect the vertical stratification in the following summer and perhaps the strength of the baroclinic flow on the northeast side of the Shoal.

## F.5 Conclusion

Hydrographic data from the northeastern Chukchi shelf collected in August and September of 2011 – 2013 showed large interannual variations in the hydrographic properties surrounding Hanna Shoal. These differences primarily relate to the salinities of the bottom waters and to the presence or absence of surface MW. The latter is tied to processes that govern summer ice retreat and, as hypothesized here, to the previous winter's history of ice advection, which may control grounding on the Shoal. We also found a northwestward baroclinic flow on the northeast side of the Shoal, which opposed the model-predicted clockwise barotropic motion around the northwest side of the Shoal. These opposing flow tendencies suggest zonal flow convergence on the north side of the Shoal, which implies that the vertically-integrated meridional pressure gradient must vanish or otherwise adjust to these opposing tendencies. If convergence is a persistent feature of the circulation here then the region north of Hanna Shoal may be a site of enhanced cross-shelf transport.

## **G. Circulation of the Chukchi Sea Shelfbreak and Slope from Moored Timeseries**

### **Abstract**

Data from a year-long mooring array, deployed across the shelfbreak and slope of the Chukchi Sea 160 km to the west of Barrow Canyon, are used to describe and quantify the circulation and water masses of the region. Two currents are identified: an eastward-flowing shelfbreak jet and a westward-flowing current over the continental slope. While both of these features have been noted previously in the literature, the timeseries presented here demonstrate their year-round existence. In the mean the Chukchi slope current is estimated to transport  $0.45 \pm 0.03\text{Sv}$  of Pacific water westward, while the shelfbreak jet transports  $0.049 \pm 0.004\text{Sv}$  eastward towards Barrow Canyon. The slope current is surface-intensified in summer and fall, but in winter and spring it becomes middepth-intensified, moves shoreward, and weakens. Using composite averages, we investigate the two extreme states of the circulation: (i) a strong slope current coincident with a reversed (westward-flowing) shelfbreak, and (ii) a strong (eastward-flowing) shelfbreak jet coincident with a weak slope current. Both states occur under varied wind conditions, but the wind stress curl patterns are consistent with the anomalous circulation in each case. In state (i) the wind stress curl field implies a sea surface height gradient across the Chukchi shelf-slope that drives enhanced flow to the west via geostrophic set up, while the opposite is true for state (ii). Upwelling at the shelfbreak occurs throughout the year, but these events are not always associated with easterly winds as is the case in the Beaufort Sea. Finally, the observed signals and timing of the cold winter water within Barrow Canyon and within the Chukchi slope current are consistent with the notion that the current is fed by the Pacific water outflow from the canyon.

### **G.1 Introduction**

The Pacific inflow through Bering Strait, driven by the large-scale sea level gradient between the Pacific and Arctic Oceans (Coachman and Aagaard 1988), plays a key role in the regional ecosystem of the Chukchi Sea and Canada Basin (Aagaard and Carmack 1989; Walsh 1995; Steele et al. 2004; Shimada et al. 2006). The Pacific-origin water carries nutrients, heat, and freshwater into the Chukchi Sea which, among other things, impacts the circulation and stratification of the shelf, the growth of phytoplankton, and the distribution of sea ice (Weingartner et al. 2005; Hill et al. 2005; Yang 2006; Woodgate et al. 2010; Spall et al. 2013). After some degree of modification on the Chukchi shelf, the water is then fluxed into the Canada Basin via different mechanisms of shelf-basin exchange, where it has a profound effect on the chemical and physical properties of the interior halocline (Pickart et al. 2005; Spall et al. 2008; Toole et al. 2010).

It is generally believed that there are three main, topographically steered pathways by which Pacific water flows poleward through the Chukchi Sea (Figure G1) (Weingartner et al. 2005). The western pathway progresses through Herald Canyon between Wrangel Island and Herald Shoal; the central pathway flows through the Central Channel between Herald and Hanna Shoals; and the eastern pathway parallels the Alaskan coast from Cape Lisburne to Barrow Canyon. In summertime this branch is known as the Alaskan coastal current (ACC; Paquette and Bourke 1974). Recent work has suggested that the central branch forms a number of smaller filaments as it flows towards Hanna Shoal (Figure G1) (Pickart et al. 2016). The precise partitioning of transport between the three branches remains uncertain. Woodgate et al. (2005) suggest that, averaged over the year, the division of transport is roughly equal. However, their study was based on a limited number of moorings. On the other hand, various studies have suggested that,

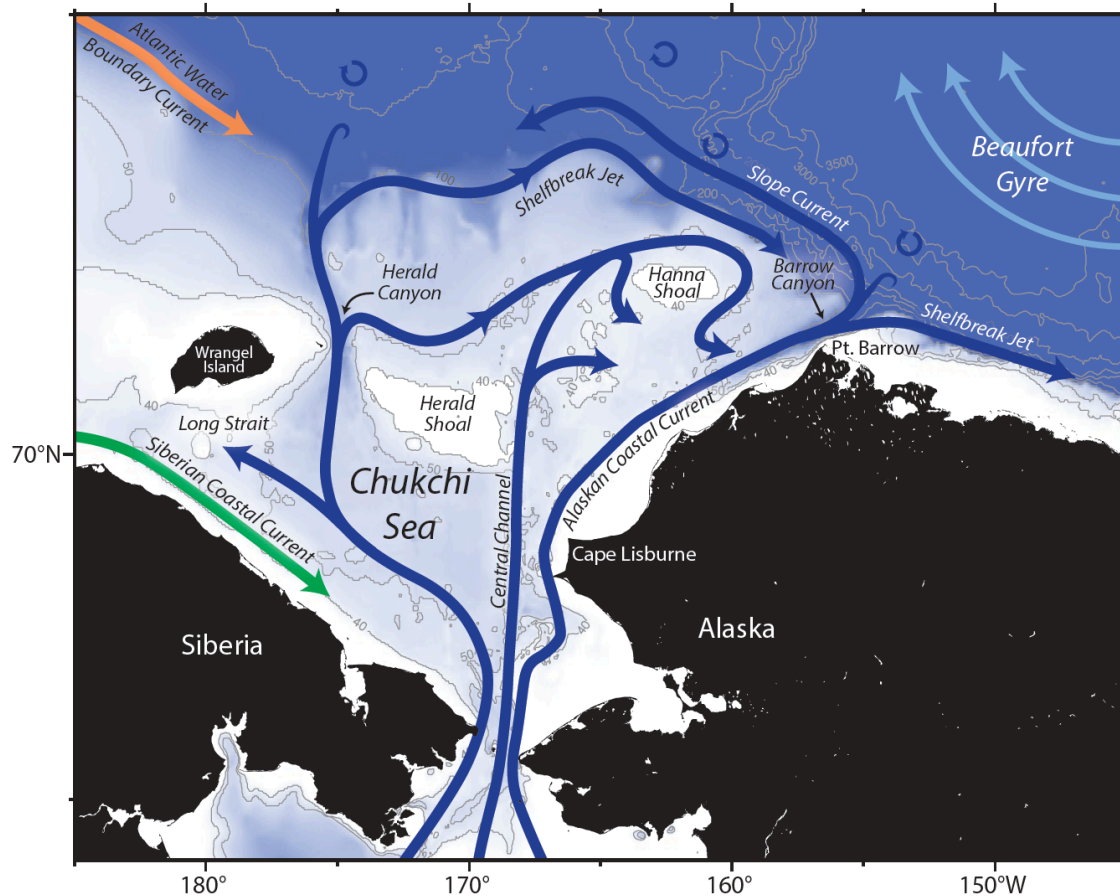


**Figure G1.** Schematic circulation in the Chukchi Sea (from Corlett and Pickart 2017), showing the three pathways by which Pacific water flows poleward through the Chukchi Sea.

at least during the summer months, much of the Pacific water flowing through Bering Strait is eventually channeled into Barrow Canyon (Itoh et al. 2013; Gong and Pickart 2015; Pickart et al. 2016).

There is also uncertainty as to how and where the Pacific water exits the Chukchi shelf into the Canada Basin. A portion of the outflow from Barrow Canyon turns eastward along the edge of Beaufort Sea to form the Beaufort shelfbreak jet (Pickart 2004; Nikolopoulos et al. 2009). Using data from a high-resolution mooring array, the year-long mean transport of the jet from summer 2002 to summer 2003 was estimated to be  $0.13 \pm 0.08\text{Sv}$  (Nikolopoulos et al. 2009). However, Brugler et al. (2014) demonstrated that this transport dropped by more than 80% later in the decade, suggesting that the Beaufort shelfbreak jet can only account for a small fraction of the Bering Strait inflow. Some of the Pacific water also exits the Chukchi shelf through Herald Canyon and forms an eastward-flowing shelfbreak jet along the edge of the Chukchi Sea (Mathis et al. 2007; Pickart et al. 2010; Linders et al. 2017). A portion of the water also appears to enter the East Siberian Sea through Long Strait (Woodgate et al. 2005), although this has not yet been established as a permanent pathway. Recently, Timmermans et al. (2017) argued that some of the Pacific water is fluxed into the Canada Basin via subduction along the entire edge of the Chukchi shelf.

The long-term mean northward transport of Pacific water at the mouth of Barrow Canyon has been estimated to be  $0.44\text{ Sv}$  (Itoh et al. 2013), which is far greater than the eastward transport of the Beaufort

shelfbreak jet. The obvious question then is: where does the bulk of the Pacific water go upon exiting the canyon? A new study has documented the existence of a westward-flowing current along the continental slope of the Chukchi Sea. Using hydrographic and velocity data from 46 shipboard transects across the shelfbreak/slope of the Chukchi Sea between 2002 and 2014, Corlett and Pickart (2017) revealed the presence of the current during the summer months (July – October), which is surface-intensified and order 50 km wide. The strongest flow occurs within 25 km of the shelfbreak. Corlett and Pickart (2017) named the current the Chukchi slope current, and estimated the transport of Pacific water to be  $0.50 \pm 0.07$  Sv. It was argued that the current is formed from the outflow from Barrow Canyon, and, using these new data together with historical measurements, Corlett and Pickart (2017) constructed a mass budget of the Chukchi shelf where the inflows and outflows balance each other within the estimated errors.

In addition to the westward-flowing Chukchi slope current, Corlett and Pickart (2017) also quantified the presence of the eastward-flowing Chukchi Shelfbreak Jet (Figure G1), whose existence was implied previously from anecdotal evidence only. Using the large number shipboard transects, Corlett and Pickart (2017) estimated the jet's mean summertime transport to be  $0.10 \pm 0.03$  Sv. Notably, the flow at the shelfbreak can at times be westward. It is thought that the jet gets entrained into the Chukchi slope current at the mouth of Barrow Canyon (Figure G1).

One of the dominant mechanisms of shelf-basin exchange across the edge of the Beaufort Sea is wind-driven upwelling (Pickart et al. 2009; Pickart et al. 2011; Lin et al. 2018). Easterly winds, arising from the intensification of the Beaufort High and/or passing Aleutian Lows to the south, readily reverse the Beaufort shelfbreak jet and drive water from the slope onto the shelf. This occurs during all seasons of the year and under different ice conditions (Schulze and Pickart 2012). Evidence of upwelling on the Chukchi slope is far less conclusive. Llinás et al. (2009) suggested the occurrence of upwelling based on a single shipboard transect north of Hanna Shoal, characterized by the presence of Atlantic water on the upper slope as well as surface-intensified westward flow, which they interpreted as a reversed shelfbreak jet. Using observations and a simplified numerical model, Spall et al. (2014) argued that upwelling of nutrients from the halocline to the outer shelf north of Central Channel contributed to the massive under-ice phytoplankton bloom reported by Arrigo et al. (2014). Recently, Corlett and Pickart (2017) presented evidence that the westward-flowing Chukchi slope current is intensified under enhanced easterly winds. However, more extensive measurements are necessary to robustly establish the occurrence of upwelling along the Chukchi slope and its forcing mechanisms.

This study presents results from a mooring array that was deployed across the shelfbreak and slope of Chukchi Sea from October 2013 to September 2014 to the northeast of Hanna Shoal. It is the first set of high spatial resolution timeseries obtained from the region. The primary aim of the study is to elucidate the structure and transport of both the Chukchi shelfbreak jet and Chukchi slope current, and to identify the nature and causes of the variability of the two currents. We begin with a presentation of the different sources of data used in the study in Section G2, followed in Section G3 by an investigation of the mean structure and seasonality of the circulation and hydrography. In Section G4 the volume transport of the shelfbreak jet and slope current, as well as their correlation, are addressed. In Section G5 we consider extreme states of the two currents using a composite analysis. The occurrence of upwelling is then investigated in Section G6, followed by consideration of the propagation of water mass signals from Barrow Canyon into the slope current in Section G7.

## **G.2 Data and Methods**

The data used in this study were collected as part of a year-long field program funded by the Bureau of Ocean and Energy Management (BOEM) entitled “Characterization of the Circulation on the Continental Shelf Areas of the Northeast Chukchi and Western Beaufort Seas”. The program employed moorings,

gliders, drifters, and included multiple shipboard surveys. The present analysis uses primarily the mooring data, along with various ancillary data sets.

### G.2.1 Mooring Data

From October 2013 to September 2014, six moorings (CS1-5 and FM1) were deployed across the shelfbreak and slope of the Chukchi Sea (Figure G2). All of the moorings were equipped with an upward-facing acoustic Doppler current profiler (ADCP, 300 KHz or 75 KHz) near the bottom, which provided hourly velocity profiles with a vertical resolution of 5 – 10 m. Hydrographic properties were measured by MicroCATs situated next to the ADCPs, and with two types of conductivity-temperature-depth (CTD) profilers: Coastal Winched Profilers (CWPs) at CS1 and FM1, and Coastal Moored Profilers (CMPs) at every site except CS1. The CMPs provided vertical traces of temperature and salinity nominally four times per day with a vertical resolution of 2 m, while the CWPs produced profiles once per day with a resolution of 1m. A detailed summary of the mooring components is contained in Table G1.

All of the ADCPs and MicroCATs returned high quality year-long records, with the exception of the ADCP at mooring CS1 which experienced compass problems. Consequently, this record was not used in the analysis (this has no bearing on our results since CS1 and FM1 were essentially at the same location).

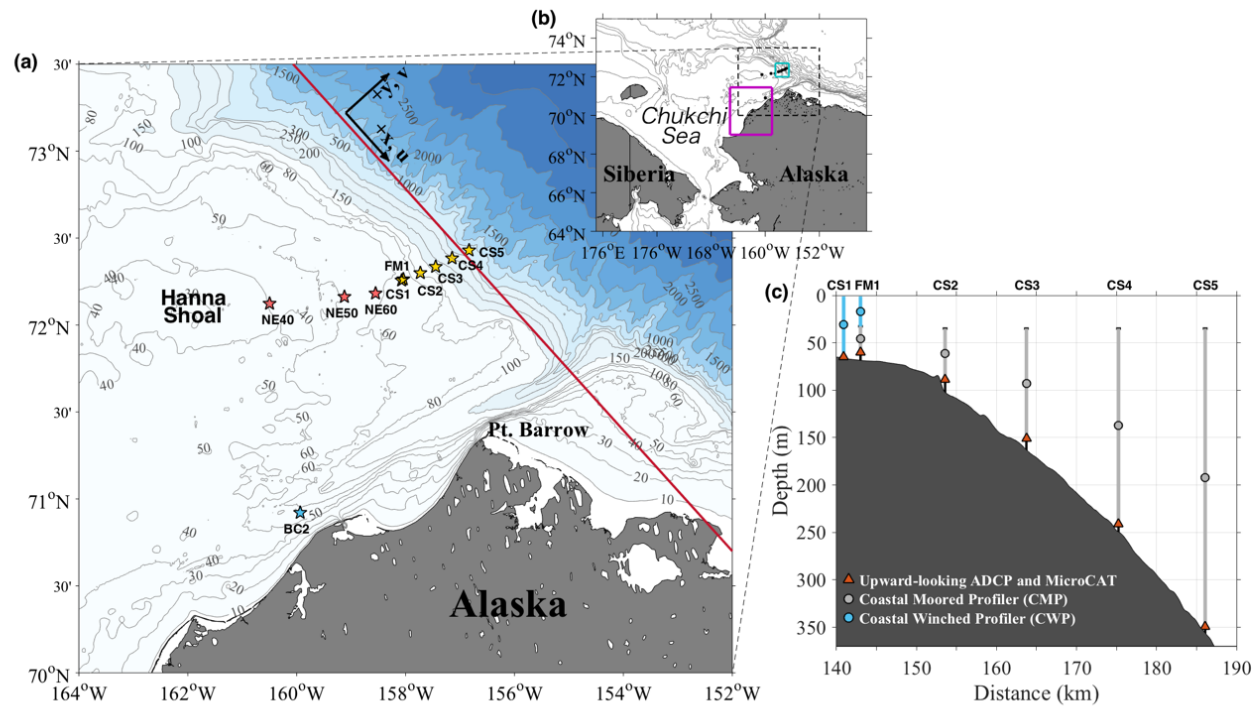


**Figure G2.** (a) Bathymetric map of the northeastern Chukchi Sea showing mooring locations used in the study. The six moorings comprising the shelfbreak/slope array are shown by the yellow stars. The three additional moorings east of Hanna Shoal and the mooring at the head of Barrow Canyon are shown by the red and blue stars, respectively. The red line and black coordinate frame indicate the rotated coordinate system. The bathymetry is from IBCAO v3. (b) Large-scale map showing the entire Chukchi Sea. The region in (a) is indicated by the dashed box. The magenta and cyan boxes delineate the domain over which the ice concentration is calculated for the shelfbreak/slope array and for the coastal polynya region south of Barrow Canyon, respectively. The mooring sites are shown by the black dots. (c) Configuration of shelfbreak/slope moorings in the vertical plane. The origin of the x-axis is Hanna Shoal.

**Table G1.** Mooring information

Mooring ID	Latitude	Longitude	Water Depth (m)	Instrument	Duration	Instrument Depth (m)	Range Depth (m)	Sample Interval (h)	Vertical resolution (m)
CS1	72°15.37'N	158°04.26'W	66	CWP	10/16/2013-11/15/2013	-	1-65	24	1
				MicroCAT	10/15/2013-09/21/2014	65	-	0.25	-
FM1	72°15.81'N	158°02.46'W	67	ADCP	10/25/2013-09/21/2014	60	8-53	1	5
				MicroCAT	10/25/2013-09/21/2014	60	-	0.25	-
CS2	72°18.02'N	157°43.52'W	102	ADCP	10/12/2013-09/22/2014	89	11-81	1	5
				MicroCAT	10/12/2013-09/22/2014	89	-	0.25	-
CS3	72°20.18'N	157°26.89'W	163	CMP	10/14/2013-09/21/2014*	-	39-146	6	2
				ADCP	10/13/2013-09/22/2014	151	22-132	1	10
				MicroCAT	10/12/2013-09/22/2014	151	-	0.25	-
CS4	72°23.10'N	157°8.76'W	249	CMP	10/15/2013-09/21/2014	-	50-235	6	2
				ADCP	10/13/2013-09/22/2014	241	22-222	1	10
				MicroCAT	10/12/2013-09/22/2014	241	-	0.25	-
CS5	72°25.82'N	156°50.37'W	356	CMP	10/15/2013-06/21/2014	-	42-340	6	2
				ADCP	10/13/2013-09/22/2014	349	31-331	1	10
				MicroCAT	10/13/2013-09/22/2014	349	-	0.25	-
NE40	72°7.35'N	160°29.68'W	41	ADCP	09/09/2013-09/18/2014	40	3-37	0.5	1
NE50	72°9.73'N	159°7.52'W	50	ADCP	09/09/2013-09/18/2014	49	4-46	0.5	1
NE60	72°10.89'N	158°33.07'W	57	ADCP	09/09/2013-09/18/2014	56	5-53	0.5	1

\*CMP at CS3 got stuck near the top of the mooring on December 9, 2013.

Unfortunately, the moored profiler coverage was generally poor. The CWP at CS1 collected data for about one month and then stopped abruptly, while the CWP at FM1 failed immediately. Of the CMPs, only the one at CS4 profiled for the entire duration of the deployment. The instrument at CS5 profiled for eight months, the one at CS3 for two months, and the one at FM1 not at all. In the latter two instances, however, the CTD sensor on the profiler remained operational at a fixed depth, acting as a de facto MicroCAT. The CMP at CS2 failed entirely. Details regarding the mooring instrumentation and data coverage are found in Table G1

Three additional moorings (NE40, NE50, NE60) were maintained from September 2013 to September 2014 on the eastern side of Hanna Shoal at roughly the 40 m, 50 m, and 60 m isobaths (Figure G2). Together, the two sets of moorings comprise an array extending from the edge of Hanna Shoal across the shelfbreak to the upper slope. The shelf moorings were equipped with ADCPs and MicroCATs at the bottom, recording velocity twice per hour and hydrographic data four times per hour. The vertical resolution of the ADCPs was 1 m. Velocity with same resolution and daily-averaged hydrographic data from a mooring at the head of Barrow Canyon (BC2, Figure G2) were also used for part of the analysis. The reader should consult Weingartner et al. (2017a) for details about the configuration of this mooring.

All of the velocity data were de-tided using the T\_Tide harmonic analysis toolbox (Pawlowicz et al. 2002). This revealed that there was low tidal energy level across the array: the maximum amplitude of the eight dominant tidal constituents was found to be less than  $2.2 \text{ cm s}^{-1}$ , which is considerably smaller than the sub-tidal signals of interest. The inertial signal was also found to be generally insignificant. A rotated coordinate system was used in the analysis. The alongstream direction was determined by averaging the year-long mean, depth-integrated velocity vectors at the five outer moorings. The positive  $x$  (alongstream) direction is defined as southeastward ( $138^\circ\text{T}$ ) and the positive  $y$  (cross-stream) direction is northeastward ( $48^\circ\text{T}$ , Figure G2a). The associated velocities are referred to as  $u$  and  $v$ , respectively. Vertical sections of the two components of velocity were constructed at each time step using Laplacian-spline interpolation, with a horizontal grid spacing of 2 km and vertical grid spacing of 15 m. The domain of the vertical sections is limited to the five outer moorings, i.e., the region of the shelfbreak and slope, which is the main focus of the paper.

### **G.2.2 Wind Data**

Wind timeseries from the Barrow, AK meteorological station are used in the study. This site is roughly 120 km to the southeast of the array. The data were obtained from the National Oceanographic Data Center (NODC) of the National Oceanic and Atmospheric Administration (NOAA) and have been quality controlled and interpolated to an hourly time base. The reader is referred to Pickart et al. (2013) for details.

### **G.2.3 Atmospheric Reanalysis Fields**

To assess the effect of the broad-scale atmospheric forcing, we used reanalysis data from the North American Regional Reanalysis (NARR) (Mesinger et al. 2006). This includes sea level pressure (SLP) and 10 m wind fields with a lateral resolution of 32 km and time resolution of 6 hours. The NARR product represents an improvement on the global National Centers for Environmental Prediction (NCEP) reanalysis dataset in this region in both accuracy and resolution. The correlation between the Barrow wind timeseries and the NARR wind record in the vicinity of moorings is 0.8, at a confidence level of 95%.

### **G.2.4 Ice Concentration Data**

The ice concentration data used in the study are the blended Advanced Very High Resolution Radiometer (AVHRR) and the Advanced Microwave Scanning Radiometer (AMSR) product from NODC, NOAA. The spatial and temporal resolution of the data are  $0.25^\circ$  and once per day. We constructed a timeseries of ice concentration for the location of the array by averaging the data within the cyan box in Figure G2b. To assess the polynya activity south of Barrow Canyon we averaged the data within the magenta box in Figure G2b.

### G.3 Mean and Seasonality of the Circulation and Hydrography of the Shelfbreak and Slope

The year-long, depth-mean vectors (Figure G3) indicate that there is persistent flow to the northwest along the Chukchi slope. This confirms that the Chukchi slope current is a year-round feature, i.e., it is not only present during the summer months as reported in Corlett and Pickart (2017). Notably, the depth-integrated flow at mooring CS2 is much weaker than at the other sites; in fact, it is not significantly different than zero. This can be explained by considering the mean vertical section of alongstream velocity (Figure G4a), which reveals the presence of the Chukchi shelfbreak jet at this location. The mean velocity section shown here is remarkably consistent with that presented in Corlett and Pickart (2017) using the summertime shipboard data (their Figure G4b). In particular, both sections (using independent data) indicate a bottom-intensified, eastward-flowing shelfbreak jet inshore of the surface-intensified, westward-flowing slope current. Furthermore, both data sets show that there is an eastward-flow of Atlantic water at depth on the mid-slope. Unfortunately, the mooring array did not extend far enough offshore to completely bracket the slope current. The hydrographic data from the mooring array indicates that, percentage-wise, the most common water types sampled were remnant winter water and Atlantic water (Figure G4b).

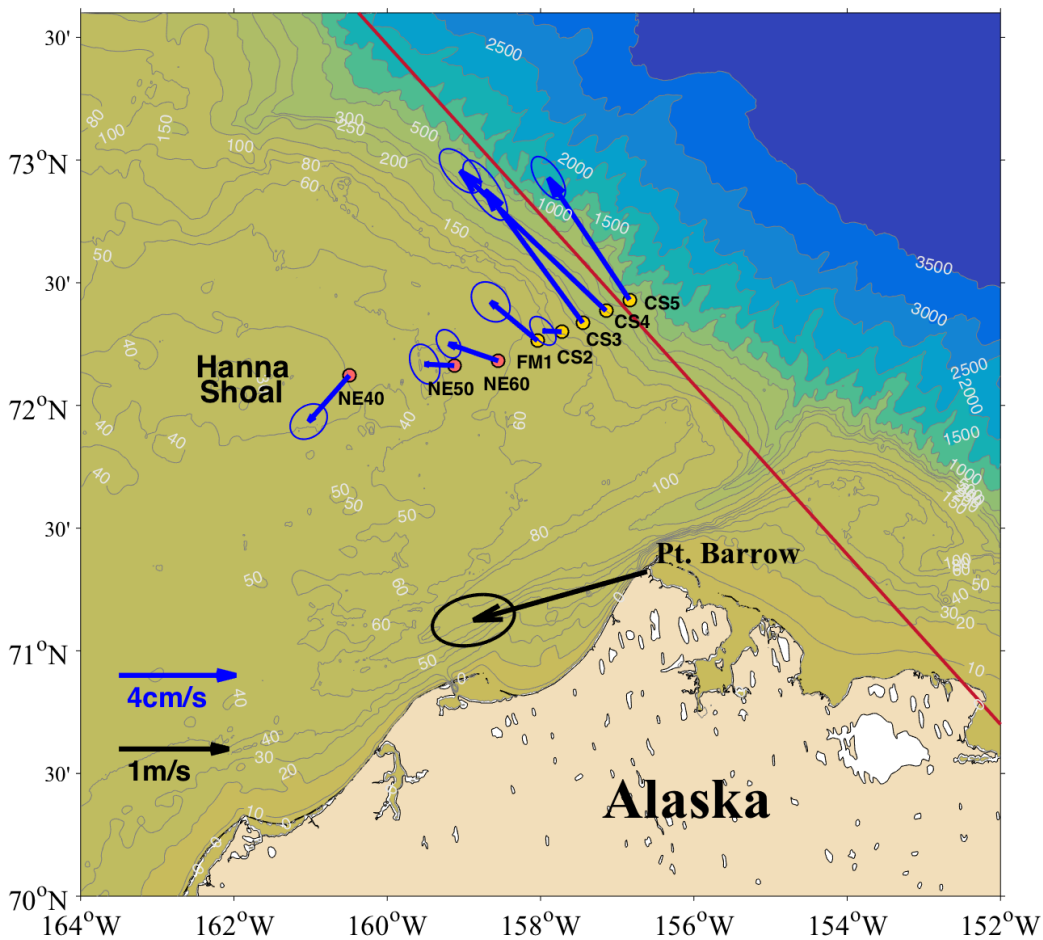


**Figure G3.** Year-long, depth-mean velocity vectors (blue) at the mooring sites and mean 10 m wind vector (black) at the Barrow, AK meteorological station. The standard error ellipses are shown (see the scales at the lower left). The red line indicates the along-stream direction (see Figure G2).

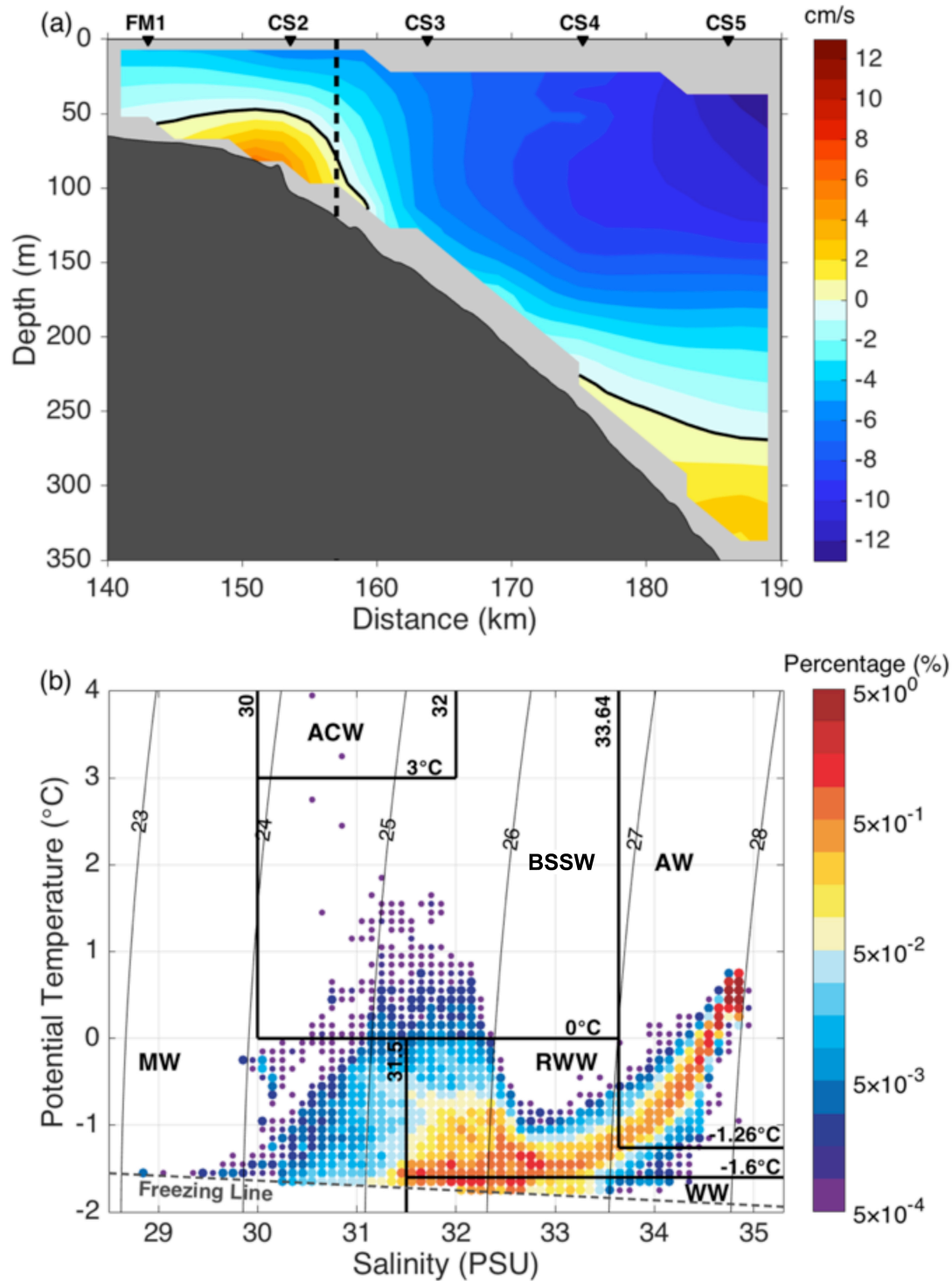


**Figure G4.** (a) Year-long mean along-stream velocity section (positive is southeastward). The thick black line is the zero velocity contour. The dashed black line shows the boundary of shelfbreak and slope. The grey shading denotes regions of no data coverage. The mooring sites are shown at the top. (b) Potential temperature-Salinity diagram for all of the hydrographic data. The color represents the percentage of data within a 0.1°C by 0.1°C grid. The black lines delimit the different water masses: MW = meltwater; ACW = Alaskan Coastal Water; BSSW = Bering Sea Summer Water; RWW = Remnant Winter Water; WW = newly-ventilated Winter Water; AW = Atlantic Water.

There is pronounced seasonality of the slope current (Figure G5). It is surface-intensified in summer and autumn, and middepth-intensified in winter and spring. Furthermore, it migrates onshore during the winter and spring. By contrast, there is little seasonal variation of the shelfbreak jet: it is always bottom-intensified, although it appears to be a bit stronger in fall and weaker in spring. The hydrographic timeseries of temperature and salinity in the slope current (Figure G6) reveal the presence of newly-ventilated winter water starting in late-April, lasting until the end of August (although its presence is intermittent). There is also evidence of local convection during the winter months. In particular, there are numerous instances of newly-ventilated winter water appearing in the upper 50 – 75 m. This is likely the signature of convective overturning driven by brine rejection as a result of re-freezing polynyas. The nature and frequency of these ventilation events warrants further investigation.

The mean wind measured by the Barrow meteorological station during 2013 – 2014 was out of the east/northeast at  $1.6 \text{ m s}^{-1}$  (Figure G3). The wind rose shown in Figure G7 reveals that, while occasionally there were strong southwesterly/westerly winds, these occurred much less frequently. The seasonal cycle of winds and ice concentration are shown in Figure G8. Overall the winds were strongest during the fall and early winter, and weakest during the spring (Figure G8a). Freeze-up at the array site occurred in late November, and the ice cover remained between 90 – 100% until early July (Figure G8b). We also show the ice concentration in the region south of Barrow Canyon, where the northeast Chukchi Sea polynya is known to form. One sees that the polynya opened up three times during the year – in early-January, late-January/early-February, and again in late-April/early-May. These periods are marked in Figure G8b. Interestingly, the ice cover also decreased over the mooring array during these times. Comparing the wind record to the ice concentration timeseries, it is seen that in each case the winds were blowing out of the northeast prior to the ice opening up.

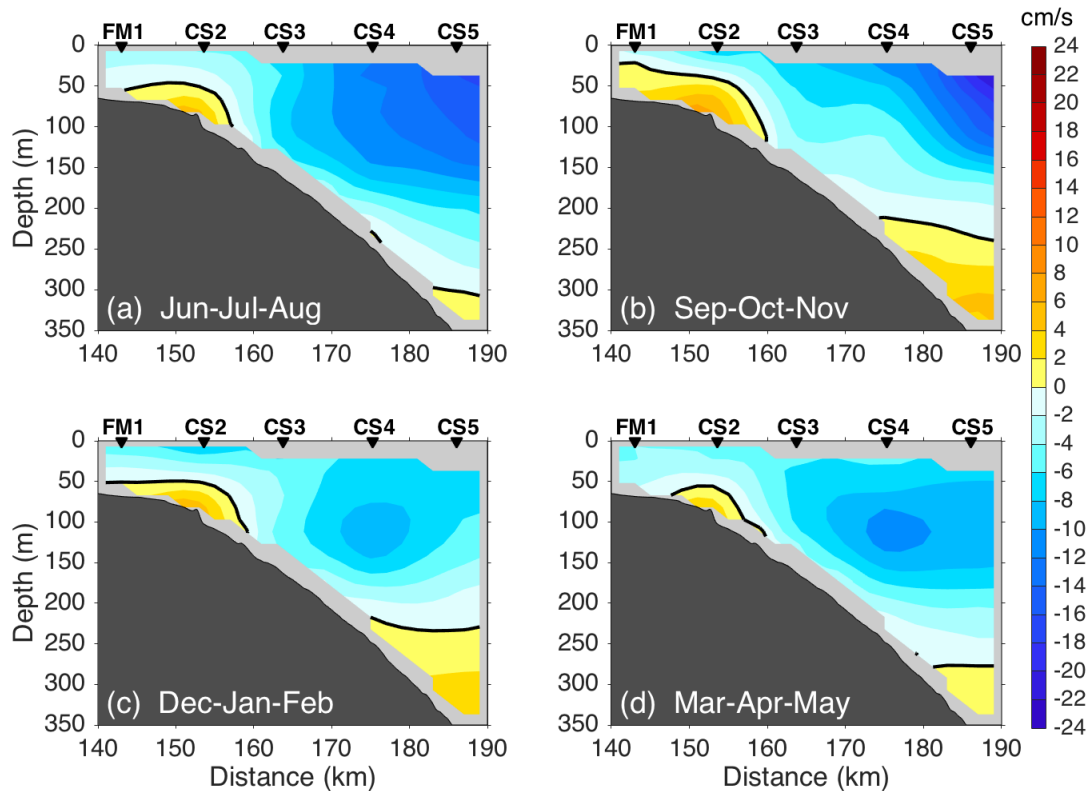


**Figure G5.** Vertical sections of the seasonally averaged along-stream velocity. The presentation is the same as in Figure G4a.

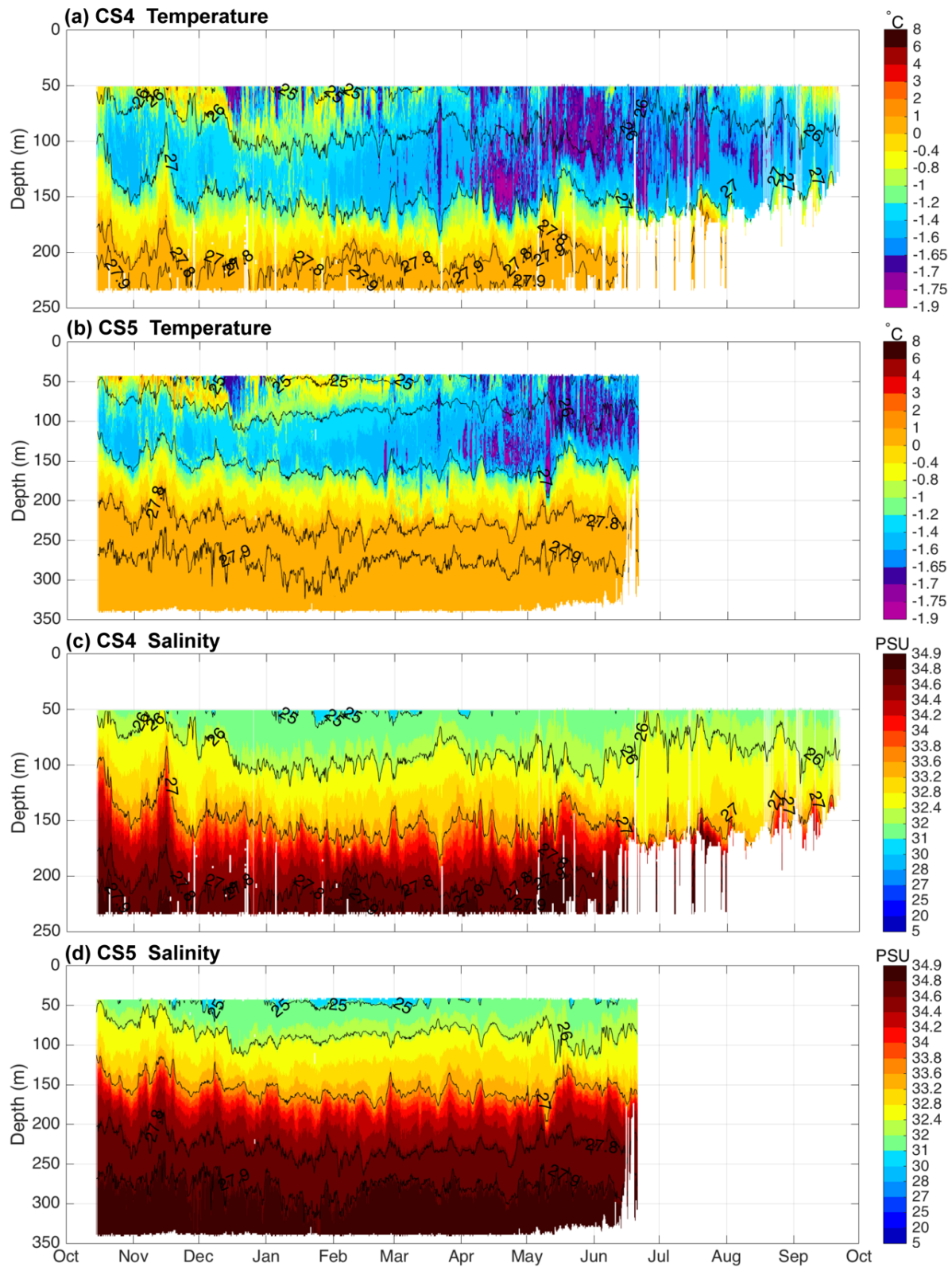


**Figure G6.** Depth-time plot of potential temperature and salinity at CS4 (a, c) and CS5 (b, d), overlain by potential density (contours).

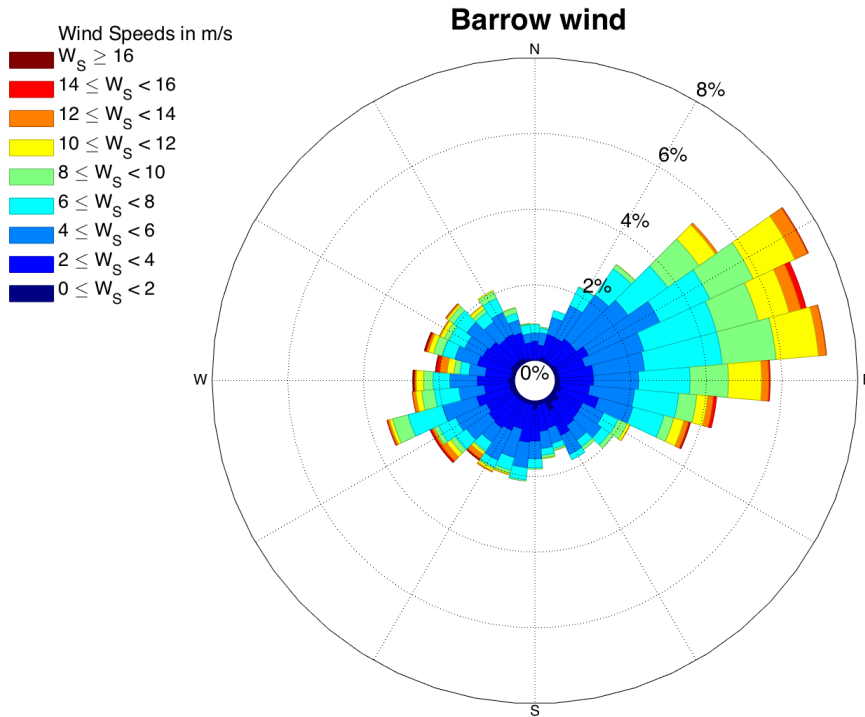


**Figure G7.** Wind rose showing wind speed and direction at Barrow for the duration of the deployment.

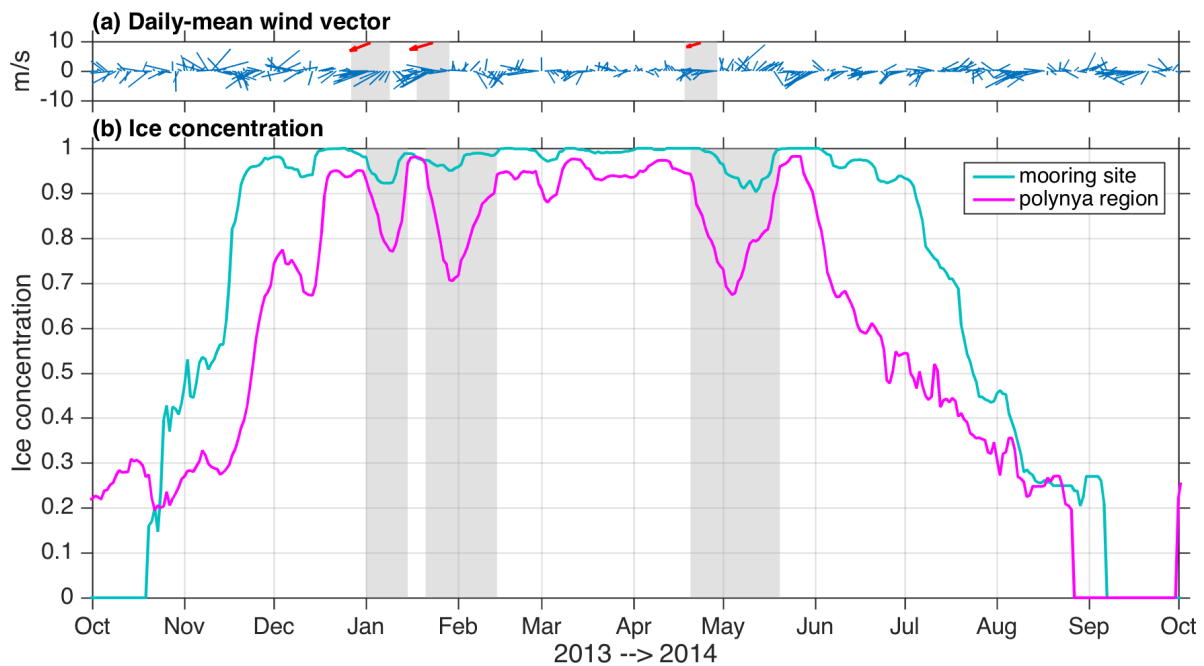


**Figure G8.** (a) Daily-mean wind velocity at the Barrow meteorological station (blue vectors). The gray shading and red vectors denote periods of northeasterly wind, and the corresponding mean wind velocity, preceding the three major occurrences of reduced ice cover at the mooring array site and south of Barrow Canyon. (b) Ice concentration timeseries at the array site (cyan curve) and at the location of the polynya south of Barrow Canyon (magenta curve). The gray shading indicates the three periods of reduced ice concentration.

## G.4 Volume Transport of the Slope Current and Shelfbreak Jet

In the volume transport calculations below, we used the value of  $x = 156$  km as the dividing line between the shelfbreak jet and slope current (see Figure G4a). In particular, the transport between  $140 \text{ km} < x < 156 \text{ km}$  is taken to be that of the shelfbreak jet, which can be positive (eastward) or negative (westward), while the negative (westward) transport seaward of  $x = 156$  km is considered to be the slope current. As noted above, the array did not always bracket the slope current, so we invoked a “mirroring” technique to estimate the missing transport. Specifically, in instances when the velocity core of the current was close to or beyond the edge of the grid, we took the offshore part of the current to be the mirror image of the inshore part. This was only done using information within 10 km of the edge of the grid, and was also limited vertically to the upper 150 m of the water column. This was an attempt to boost the transport estimate to be closer to the true value, although this extrapolated estimate is still clearly an underestimate.

The year-long mean westward transport of the slope current is  $-0.57 \pm 0.04$  Sv. Using the potential vorticity constraint developed by Nikolopoulos et al. (2009) to identify the boundary between the Pacific water and Atlantic water, we find that the transport of Pacific water is  $-0.45 \pm 0.03$  Sv. We stress that this is an underestimate since the array did not fully capture the current. However, the mean absolute geostrophic velocity section of Corlett and Pickart (2017) did bracket the flow, and they found a mean Pacific water transport of  $-0.50 \pm 0.07$  Sv for the months of July – October, which is fairly close to the value computed here (our value for July – October is  $-0.57 \pm 0.05$  Sv). Using the mooring data, the year-long mean transport in the vicinity of the shelfbreak is also westward,  $-0.014 \pm 0.006$  Sv. However, as seen in Figure G4a, the eastward-flowing shelfbreak jet is bottom intensified; isolating this eastward flow gives a transport of  $0.049 \pm 0.004$  Sv. This value is somewhat larger than the transport of the Beaufort shelfbreak jet in recent years (mean of  $0.023 \pm 0.018$  Sv from 2008 – 2014; P. Lin pers. comm., 2017).

The transport of the slope current varies substantially on a variety of time scales, ranging from a value of zero to 2 Sv (Figure G9a). The monthly mean timeseries implies that the transport is larger in summer, with a peak value in September (Figure G9c). We note that this is at odds with the results of Corlett and Pickart (2017) who found that the slope water transport was largest in October. The flow at the shelfbreak fluctuates between positive and negative throughout the year (Figure G9b), with range of approximately 0.2 to -0.2 Sv. The monthly mean values are westward from December through June, with eastward flow in late-summer and fall (except for September). Notably, removing the high-frequency fluctuations by applying a 5-day low-pass filter indicates that the transport of the slope current and that of the shelfbreak jet are significantly correlated ( $r = 0.6$ , 95% confidence). Possible reasons for this are addressed below.

## G.5 Extreme States of the Slope Current and Shelfbreak Jet

Using an extensive collection of shipboard data, Corlett and Pickart (2017) found that the westward flow of the Chukchi slope current was enhanced under strong easterly winds. They demonstrated this by constructing a composite mean vertical section of absolute geostrophic velocity for calm wind conditions, and comparing this to the composite section when the easterly wind exceeded  $4 \text{ m s}^{-1}$ . In this case easterly was taken to be the component of wind directed out of the southeast parallel to the shelfbreak. Their result is reproduced in Figure G10 (left hand column). One sees that when the winds are weak there is a stronger eastward-flowing shelfbreak jet (and stronger eastward flow of Atlantic water at depth), and when the winds are strong the slope current is stronger and wider. When we compute the analogous composite sections – using the mooring data for the same seasonal period as Corlett and Pickart (2017) (July – October) – we obtain a similar result (Figure G10, right hand column). In an effort to shed more light on the influence of the wind on both the slope current and the shelfbreak jet, we considered the extreme states of the two currents. Specifically, we isolated those times when the slope current was strong while the shelfbreak jet was simultaneously reversed to the west, and those times when the shelfbreak jet was

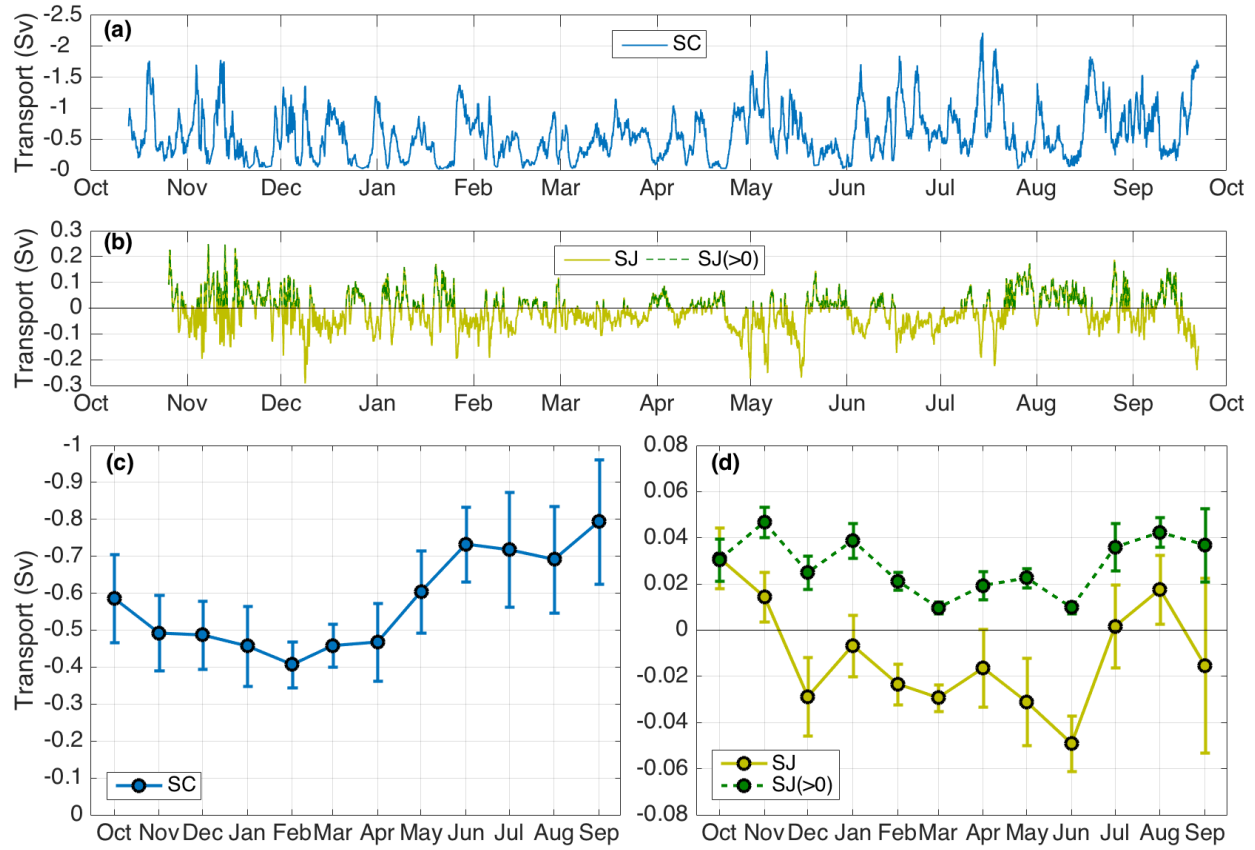


**Figure G9.** Volume transport timeseries of (a) the Chukchi slope current (blue curve), and (b) the Chukchi shelfbreak jet (yellow curve is the full transport and green dashed curve is the positive transport). (c) Monthly-averaged slope current transport with standard errors. (d) Monthly-averaged transport and standard errors for the full shelfbreak jet (yellow curve) and for times when the jet transport is positive (green dashed curve).

flowing strongly to the east while the slope current was weak. We developed objective criteria for identifying these two states of the circulation.

### G.5.1 Strong Slope Current and Reversed Shelfbreak Jet

The criteria used for first type of event was that the slope current transport be at least 0.3 standard deviations greater than the mean, while the flow at the shelfbreak be at least 0.3 standard deviations weaker than the mean (recall that the average flow at the shelfbreak is westward). These conditions were met approximately 25% of the time over the course of the year (Table G2). Based on the results of Corlett and Pickart (2017), one might expect these conditions to always correspond to an easterly wind (i.e., with a component of the wind paralleling the shelfbreak from the southeast). Surprisingly, however, this extreme state occurred under various wind conditions, with the wind blowing out of all four quadrants depending on the event (Table G2). Here we show the composite fields for the two wind conditions that resulted in the most days with a strong slope current and reversed shelfbreak jet.

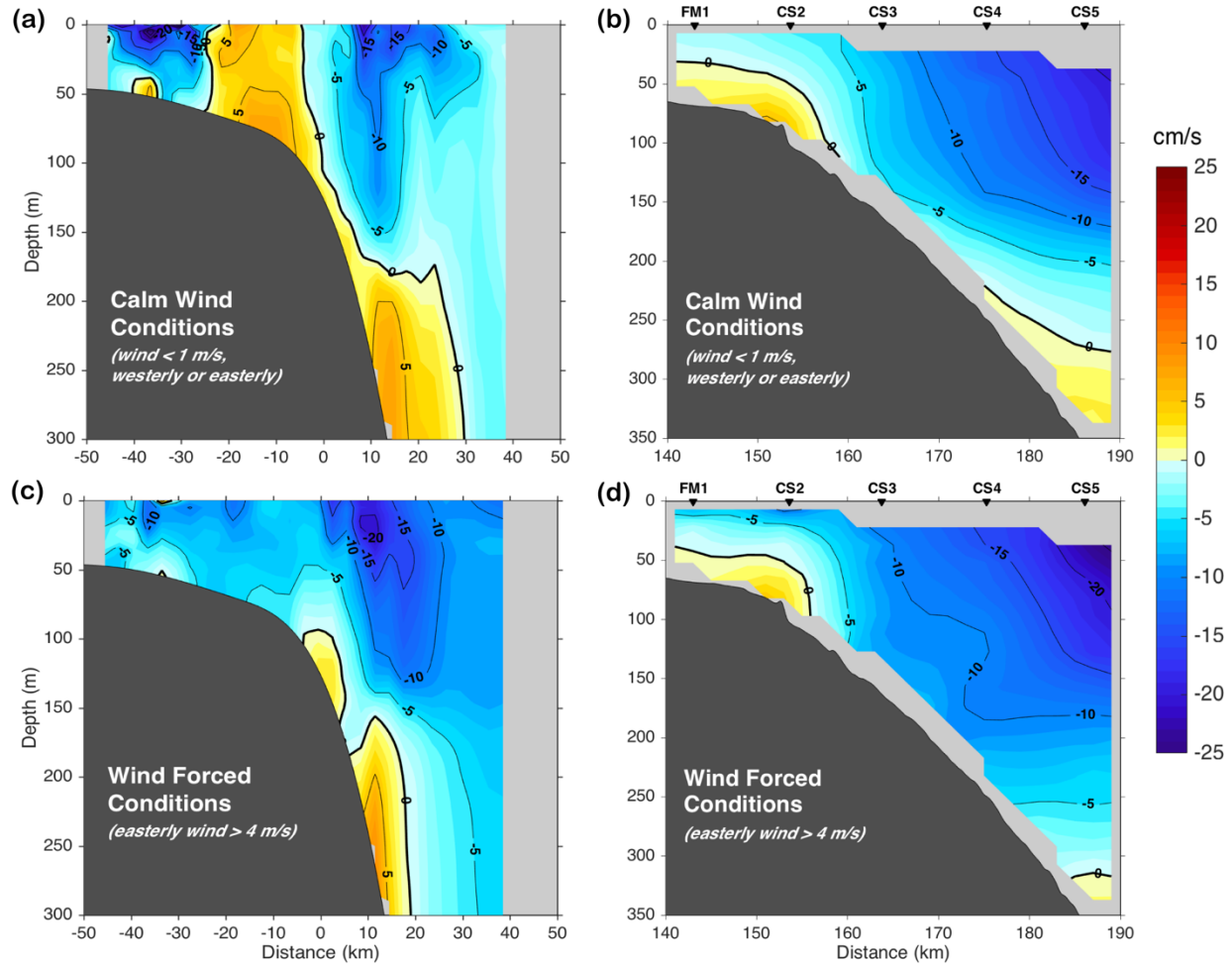


**Figure G10.** Composite velocity sections during (a, b) calm wind conditions and (c, d) times when the easterly winds exceeded  $4 \text{ m s}^{-1}$  for the months of July – October. (a) and (c) are reconstructed sections of absolute geostrophic velocities (color) from Corlett and Pickart (2017). (b) and (d) are velocity sections (color) from mooring data. The thin black lines are velocity contours.

### G.5.1.1 Winds from the Southwest

There were 11 instances, totaling 46 days, in which the slope current was anomalously strong and the shelfbreak jet was reversed while the wind was out of the southwest. The composite average vertical section of alongstream velocity (Figure G11a) shows that there was westward flow throughout the array, with the slope current  $5 - 10 \text{ cm s}^{-1}$  stronger than normal (Figure G11b). The atmospheric conditions corresponded to low SLP north of the Chukchi Sea and associated cyclonic winds (Figure G11c). The wind stress curl was strongly positive over the northern part of the Chukchi shelf, but weakly positive offshore of the array on the Chukchi slope and basin (Figure G11d). This implies that there would be a larger drop in sea surface height on the shelf than offshore, which would set up a geostrophic response of enhanced flow to the west, consistent with the mooring observations.

**Table G2.** Statistics for the two types of extreme events considered in the text: (i) strong slope current and reversed shelfbreak jet; (ii) strong shelfbreak jet and weak slope current. The first column indicates the quadrant from which the wind was blowing. The percentage in parentheses means the fraction of the event length relative to the total length in the last row. The underlined percentages represent the fraction of total length relative to the entire year-long duration of the record.

	Strong Slope Current & Reversed Shelfbreak Jet			Strong Shelfbreak Jet & Weak Slope Current		
	Number of events	Total length in days	Mean event length in days (range)	Number of events	Total length in days	Mean event length in days (range)
SW-wind	11	46 (51.7%)	4.1 (0.5-17.1)	7	8 (8.3%)	1.1 (0.6-2.1)
NE-wind	7	17 (19.1%)	2.4 (0.6-5.2)	16	66 (68.8%)	4.1 (0.7-12.3)
SE-wind	5	13 (14.6%)	2.6 (1.0-4.4)	6	12 (12.5%)	2.0 (0.7-6.0)
NW-wind	8	13 (14.6%)	1.6 (0.6-4.0)	5	10 (10.4%)	2.0 (0.6-4.6)
Total	31	89 (25.6%)		34	96 (27.8%)	

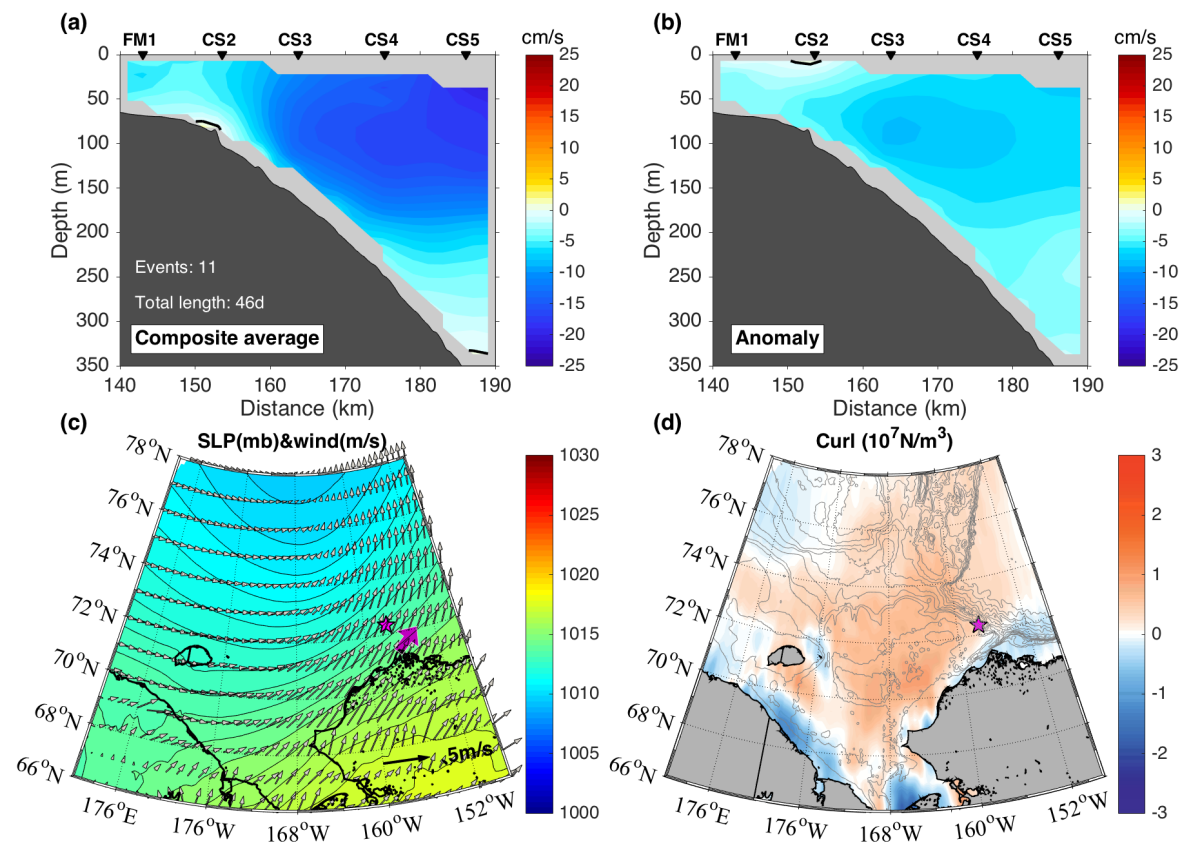


**Figure G11.** Composite average fields for the strong slope current and reversed shelfbreak jet events with southwesterly wind. (a) Vertical section of alongstream velocity. The number of events and their total duration is marked on the lower left. (b) Vertical section of alongstream velocity anomaly (composite minus the year-long mean). (c) Sea level pressure (color) and 10 m wind vectors from NARR, along with the measured wind from the Barrow meteorological station (purple vector). The location of the shelfbreak/slope mooring array is indicated by the purple star. (d) Wind stress curl (color).

### G.5.1.2 Winds from the Northeast

The second largest segment of time for this circulation state corresponded to winds out of the northeast over the mooring site (17 days, Table G2). Again the alongstream flow was westward everywhere, with anomalous velocities in the slope current between  $10 - 15 \text{ cm s}^{-1}$  (the largest increase was at depth, Figure G12a, b). In contrast to the previous case, low SLP was present to the southeast of the Chukchi Sea, with higher SLP over the basin (Figure G12c). The wind stress curl field was again conducive for increased flow to the northwest along the slope via geostrophic set up, with positive curl on the shelf (lowered sea surface height) and negative curl offshore of the array (raised sea surface height, Figure G12d).

### G.5.2 Strong Shelfbreak Jet and Weak Slope Current

The other extreme state, that of strong eastward flow along the shelfbreak and a weakened slope current, occurred approximately 28% of the time during the year (Table G2). The criteria employed here was that the shelfbreak jet be at least 0.3 standard deviations larger than the mean, while the slope current be at least 0.3 standard deviations weaker than the mean. In this case there was one dominant scenario in which the wind blew from the northeast (totaling 66 days, Table G2). The composite vertical sections show eastward flow from the outer shelf to the mid-slope, with a clear signature of the shelfbreak jet centered at mooring CS2 and enhanced flow of Atlantic water at depth (Figure G13a, b). The slope current is confined to the upper right-hand part of the section. The strongest anomalous flow is between  $5 - 10 \text{ cm s}^{-1}$ .

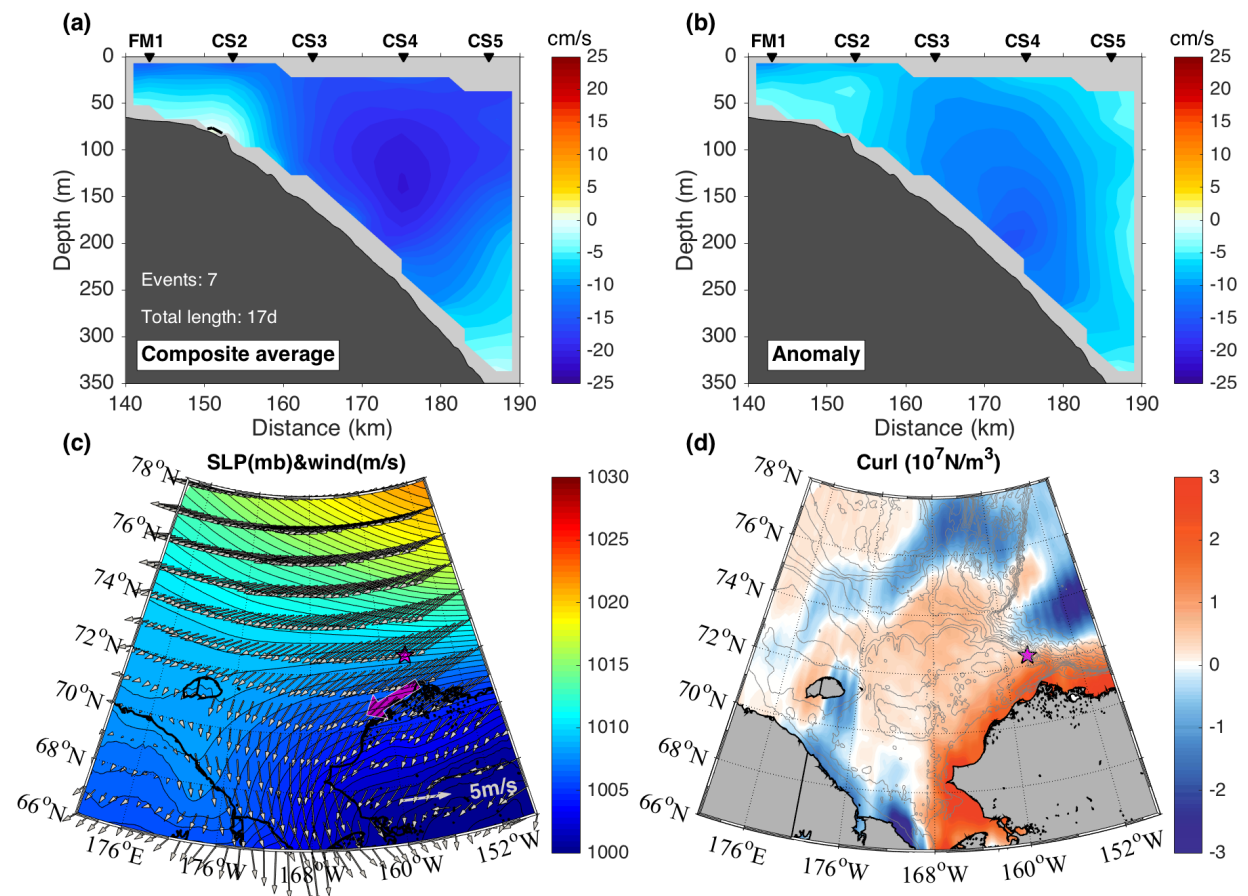


**Figure G12.** Same as Figure G11, except the strong slope current and reversed shelfbreak jet events with northeasterly wind.

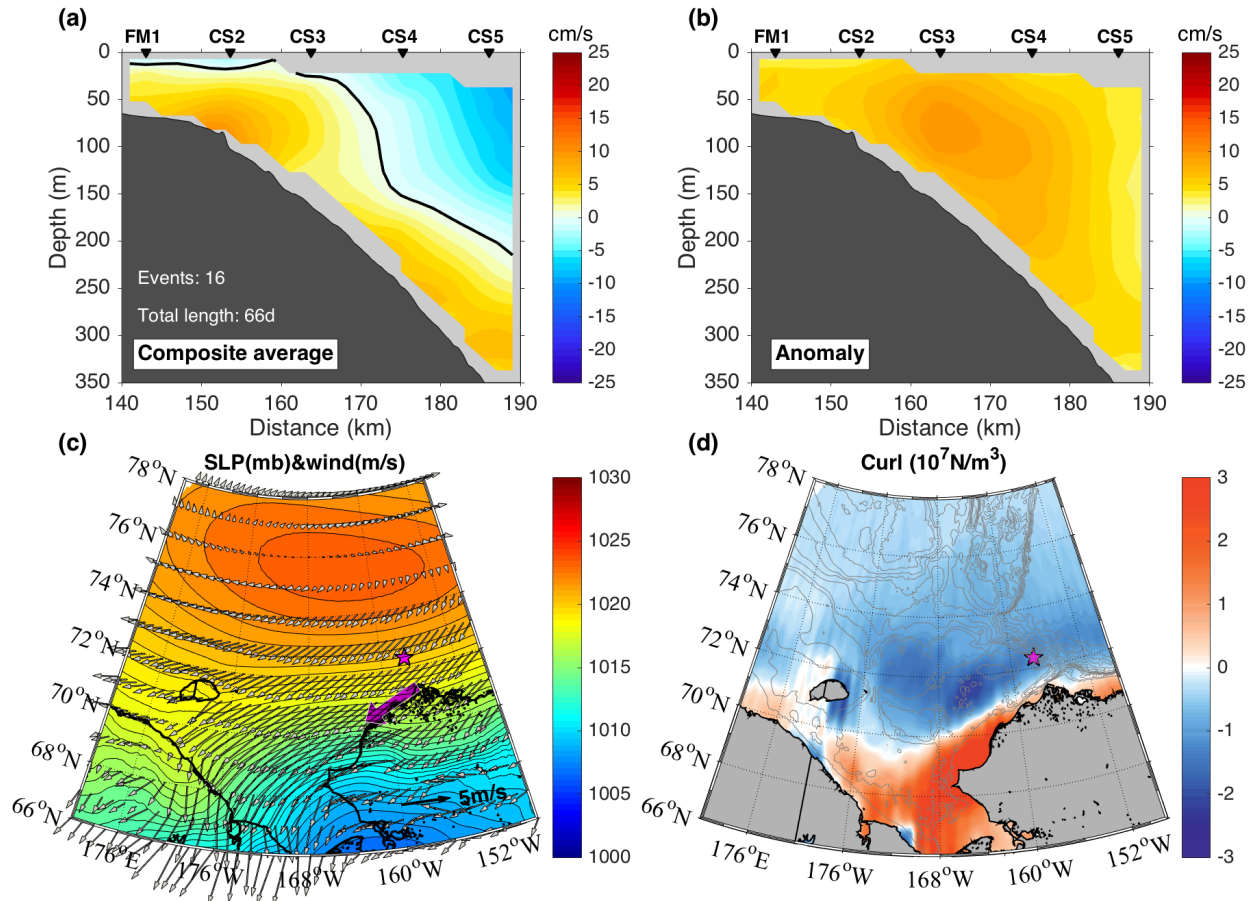


**Figure G13.** Same as Figure G11, except the strong shelfbreak jet and weak slope current events with northeasterly wind.

The atmospheric pattern associated with this state corresponds to a strong Beaufort High north of the Chukchi Sea and the presence of an Aleutian Low near the southern end of the domain (Figure G13c). These conditions typically lead to a reversed (westward-flowing) shelfbreak jet in the Beaufort Sea and concomitant upwelling, yet our Chukchi slope array shows a strengthened (eastward-flowing) shelfbreak jet. This can be explained by the wind stress curl pattern (Figure G13d). The curl is strongly negative on the northeast Chukchi shelf, while offshore of the array it is less negative. The resulting sea level gradient (higher sea level on the shelf, lower sea level northeast of the moorings) would promote stronger geostrophic flow to the southeast. By contrast, the positive curl on the Beaufort shelf, in conjunction with the negative curl offshore, would lead to enhanced westward flow along the Beaufort shelfbreak (i.e., a reversed shelfbreak jet). This is the same situation that was studied by Pickart et al. (2011) using in-situ data and a numerical model. They showed that, during an upwelling event in the Beaufort Sea, the eastward flow along the Chukchi shelfbreak/slope became stronger as a result of a sea level increase on the Chukchi shelf.

## G.6 Upwelling

Wind-driven upwelling has been well studied on the Beaufort slope, and is associated with enhanced easterly winds and a reversed shelfbreak jet (e.g., Pickart et al. 2009; Pickart et al. 2011; Lin et al. 2018).

Following Lin et al. (2018), we used the near-bottom potential density anomaly in the vicinity of the Chukchi shelfbreak/upper-slope to identify the presence of upwelled water from the basin. In particular, we low-passed the deep MicroCAT potential density records at moorings FM1 (shelfbreak) and CS2 (upper slope) using a filter width of 20 days, and computed the difference between these smoothed values and the instantaneous values. Upwelling was deemed to occur when the density anomaly was positive at both sites for more than a day. The purpose of the low-pass was to remove the influence of more slowly-varying hydrographic properties of the shelfbreak jet due to alongstream advection. Lin et al. (2018) carried out a similar procedure using monthly averages.

Using this criterion, 15 upwelling events were identified over the course of the year, ranging in length from 1.3 to 6.2 days (Table G3). By comparison, Lin et al. (2018) reported an average of 19 events per year on the Beaufort slope over a 6-year period. As a measure of the strength of the upwelling, we followed Lin et al. (2018) and defined an upwelling index, UI, as the time integral of the potential density anomaly (at CS2) over the duration of the event. This takes into account both the magnitude and duration of the density signal. The average value of UI was  $5.9 \text{ kg m}^{-3} \text{ h}$ , with a range of  $1.1 - 26.7 \text{ kg m}^{-3} \text{ h}$  (Table G3). On the Beaufort slope Lin et al. (2018) reported an average UI of  $49.9 \text{ kg m}^{-3} \text{ h}$  with a range of  $0.9 - 222.1 \text{ kg m}^{-3} \text{ h}$ . Hence, overall, the upwelling on the Beaufort slope appears to be more intense than that on the Chukchi slope.

Here we diagnose the strongest occurrence of upwelling (event #9 in Table G3), which took place in May 2014. Figures G14 – 16 show composite averages for before, during, and after the event. The timeseries of potential density anomaly at the two mooring sites is shown in panel (c) of each figure for reference. Prior to the event (Figure G14) the slope current was well established, and the shelfbreak jet was reversed. The cross-stream flow varied in magnitude and direction across the array, which can be seen in Figure G14 e, f (note that positive cross-stream flow is directed offshore). During the event (Figure G15) the westward-flowing shelfbreak jet and the slope current both became stronger and veered shoreward, which is especially evident in the vector plot of Figure G15f. The onshore flow extended throughout the water column and was especially strong at the shelfbreak (Figure G15e). After the event (Figure G16) the slope current became markedly weaker and the shelfbreak jet re-established itself to the east (Figure G16b), although there was still weak onshore flow from the mid-slope to the outer-shelf near the bottom (Figure G16e).

**Table G3.** Statistics of all upwelling events. The rows show the event number, length (in days) of each event, value of the upwelling index (UI, unit:  $\text{kg m}^{-3} \text{ h}$ ), mean wind direction, and sign of the mean wind stress curl condition (+ and – mean positive and negative curl, respectively) in the vicinity of mooring array (cyan box in Figure G2b) for the day before each event.

Event	1	2	3	4	5	6	7	8	9	10	11	12	13	14	15	Mean
Length (d)	1.7	2.5	1.9	6	2.2	6.2	3.3	2	4.5	2.4	1.3	3.6	4.5	5.1	4.6	3.5
UI	3.8	1.8	5.5	11.1	1.1	9.0	6.4	2.4	26.7	2.0	3.5	7.8	1.5	2.4	3.4	5.9
Wind direction	NE	SE	SW	NE	NW	W	NW	SE	SW	SE	NW	SW	NE	SW	SW	SW
Wind stress curl	-	-	+	+	-	+	+	-	+	+	+	+	-	-	+	-

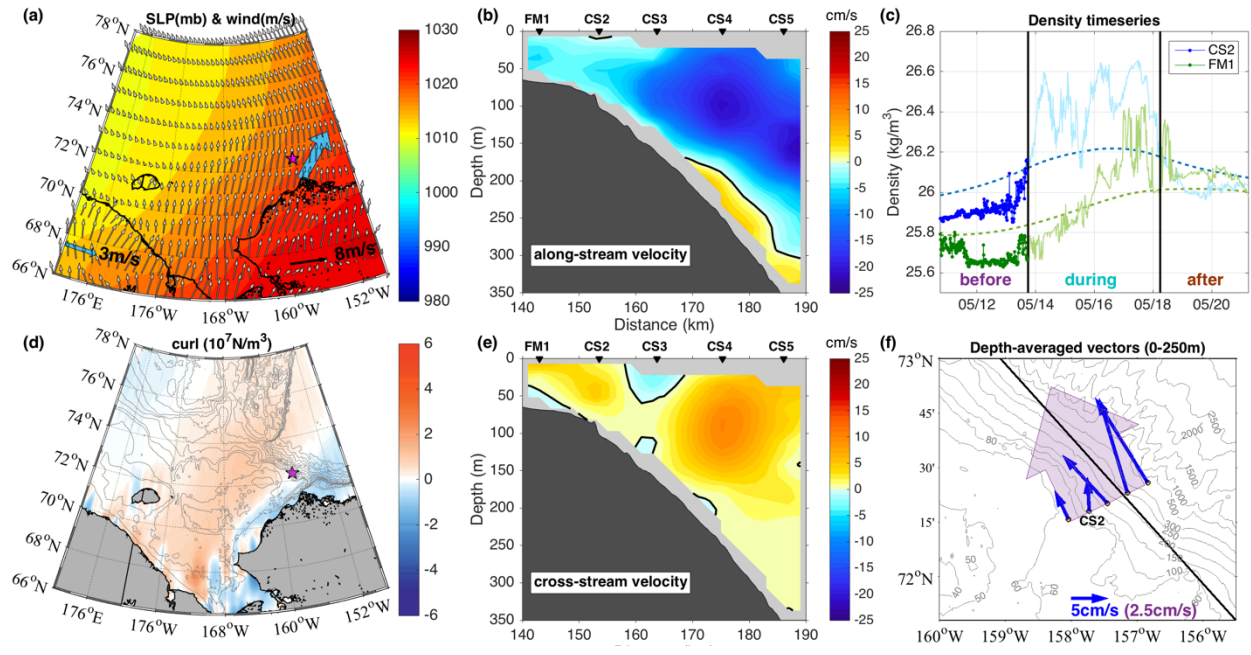


**Figure G14.** Composite average fields prior to the strongest upwelling event (event 9, May 2014). (a) Sea level pressure (color) and 10 m wind vectors from NARR, along with the measured wind from the Barrow meteorological station (blue vector). The location of the shelfbreak/slope mooring array is indicated by the purple star. (b) Along-stream velocity section. (c) Density timeseries at mooring CS2 and FM1 from 3 days before the event to 3 days after the event, where the bold indicates the time period before the upwelling. The dashed lines are the 20-day low-passed curves. (d) Wind stress curl (color). (e) Cross-stream velocity section (positive is northeastward). (f) Depth-averaged (0 – 250 m) velocity vectors at the mooring sites (blue arrows) and the mean velocity vector of all moorings (large arrow).

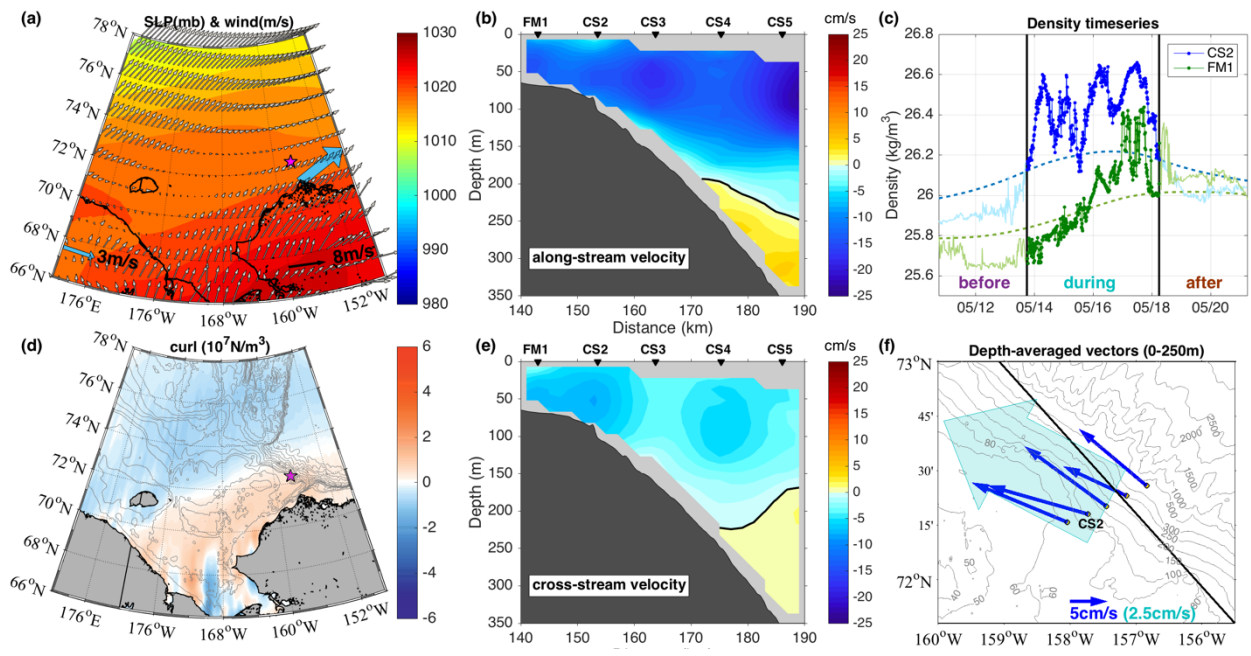


**Figure G15.** Same as Figure G14, except for the time period during the upwelling.

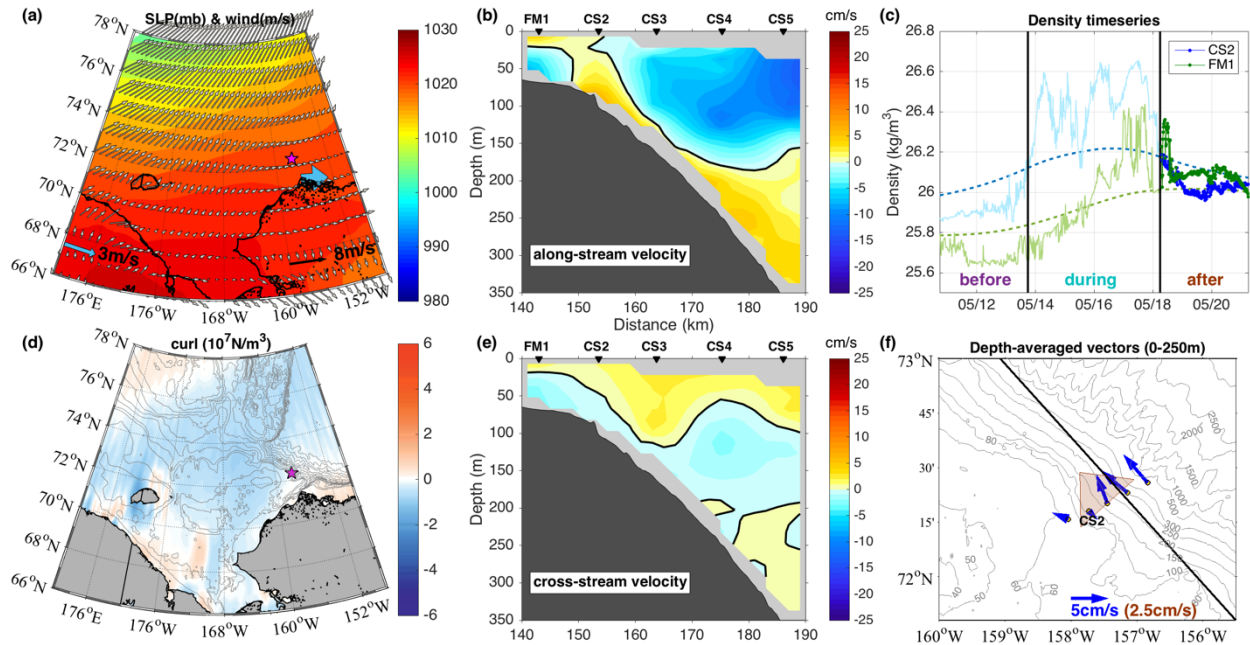


**Figure G16.** Same as Figure G14, except for the time period after the upwelling.

The nature of the upwelling event in May – indeed for all of the upwelling events – remains unclear. It is certain, however, that the process is different on the Chukchi slope than on the Beaufort slope. In the Beaufort Sea enhanced easterly/northeasterly winds consistently drive coastal upwelling (Lin et al. 2018). By contrast, upwelling in the Chukchi Sea seems to occur for all wind directions and for both positive and negative local wind stress curl (Table G3). In the example shown, the strength of the wind was comparable before and during the event, although the wind direction was more out of the west during the upwelling (compare Figures G14a and G15a). This in turn caused a wind stress curl pattern that would lead to enhanced westward flow at the array site due to geostrophic set up (Figure G15d). This is reminiscent of the extreme state described above in Section G5.1.1 – i.e., a strong slope current and reversed shelfbreak jet under southwesterly winds. However, it remains to be determined what caused the flow to veer onshore. A more thorough investigation of upwelling, perhaps in conjunction with a numerical model, is needed.

## G.7 Propagation of Water Mass Signals from Barrow Canyon to the Chukchi Slope

Using the definitions of the different water types in Figure G4b, we constructed timeseries of the water masses measured throughout the year at three locations: the head of Barrow Canyon (mooring BC2); in the Chukchi slope current (mooring CS4), and in the Chukchi shelfbreak jet (mooring CS2, Figure G17). The most common water mass passing through the head of Barrow Canyon was newly ventilated winter water (WW, keeping in mind that the MicroCAT was located near the bottom). This cold water mass was present almost exclusively in the canyon from around the beginning of February to early-July (marked by the black triangles in Figure G17a). Comparing this to the site of the Chukchi mooring array, one sees that the bulk of the WW appeared in the slope current from early-April to early-September (marked by the black triangles in Figure G17b). Hence, the water was present at both locations for roughly five months, with an offset on the order of two months. This supports the notion put forth by Corlett and Pickart (2017) that the outflow from Barrow Canyon feeds the slope current.

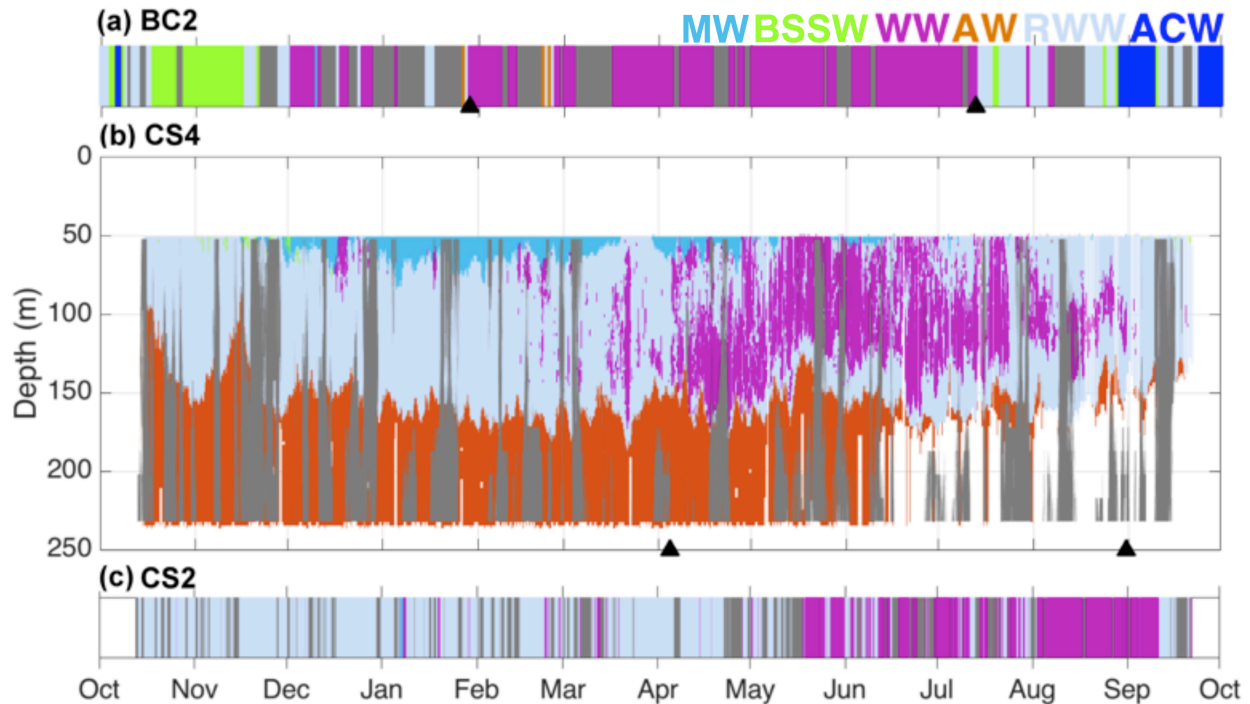


**Figure G17.** Timeseries of water mass occurrence at the Chukchi shelfbreak/slope moorings (CS2, CS4) and the mooring at the head of Barrow Canyon (BC2). See Figures G2 and G3 for mooring locations. Note that there is no depth scale for moorings CS2 and BC2 since these sites have a single sensor near the bottom. The gray shading indicates times when the flow is in the opposite direction of the predominant current (southwestward, southeastward, and northwestward in the three panels, respectively). The black triangles denote the time periods when the bulk of Winter Water was present.

To investigate this further, we examined the variation in potential temperature of the WW at the two locations (Figure G18). The first thing to note is that the water is systematically warmer on the Chukchi slope than in Barrow Canyon, by approximately  $0.07^{\circ}\text{C}$ . This makes sense in that lateral mixing would warm the water as it exits Barrow Canyon and then flows westward in the slope current. Furthermore, at both sites there is a clear moderation of the WW to warmer temperatures as the season progresses. We vertically averaged the moored profiler record at CS4 and compared this to the record at BC2. The maximum correlation between the two timeseries ( $r = 0.6$ , significant at the 95% confidence level) was found for a lag of 60 days (BC2 leading CS4). This is consistent with the offset noted above in the arrival times of the WW at the two sites.

The geographical distance from the head of Barrow Canyon to its mouth, plus the distance to the Chukchi slope array, is approximately 300 km. For a time lag of 60 days, this implies a mean advective speed of  $5.6 \text{ cm s}^{-1}$ . The mean velocity at BC2 during the WW period was  $17.9 \text{ cm s}^{-1}$ , which is considerably larger than this. However, it is probably more appropriate to use the velocity at the array site for this comparison. This is because the flow at head of the Barrow Canyon is locally convergent and the velocity there is stronger than farther down the canyon (Pickart et al. 2005). The velocity at CS4 averaged over the depth of the WW layer for the appropriate period is  $9.3 \text{ cm s}^{-1}$ , which is closer to the above estimate deduced from the water mass signals.

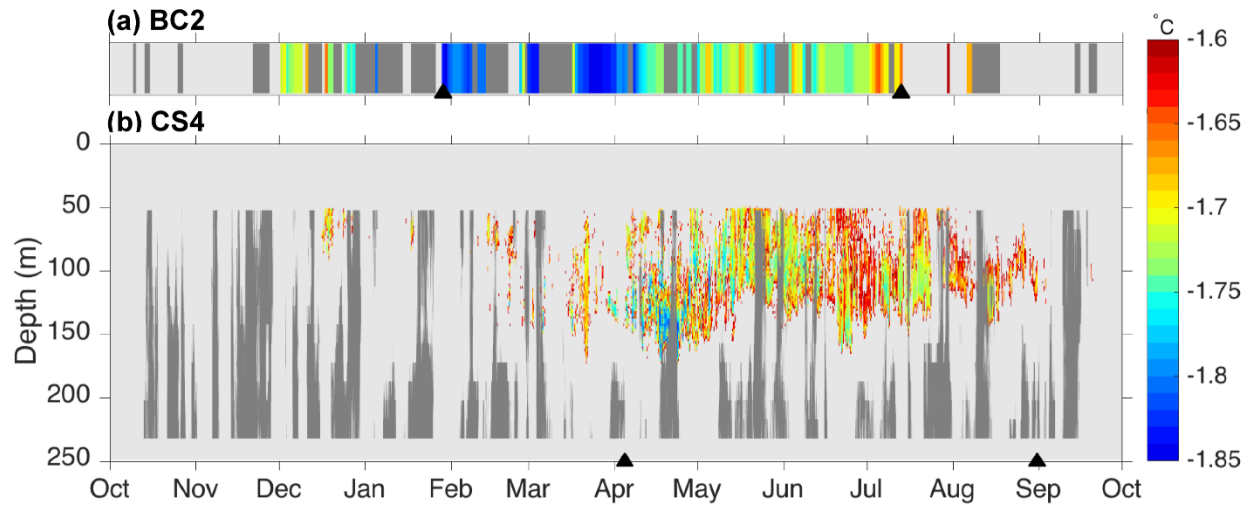


**Figure G18.** Potential temperature of the Winter Water at (a) mooring BC2 at head of Barrow Canyon (near the bottom) and CS4 on the Chukchi slope. The light gray shading means that there is no WW present. The dark gray shading indicates when the flow is in the opposite direction of the primary current (southwestward and southeastward in (a) and (b), respectively). The black triangles denote the time periods when the bulk of WW appeared.

The WW signal in the Chukchi shelfbreak jet (at mooring CS2) appears in late-May and lasts until mid-September (Figure G17c). The origin of the water in this current is likely the outflow from Herald Canyon. Observations suggest that the Pacific-origin water exiting the canyon turns to the right and forms a shelfbreak jet along the northern edge of the Chukchi Sea (Pickart et al. 2010; Linders et al. 2017). Models also indicate this (Winsor and Chapman 2004; Spall 2007). The mean velocity at the bottom of mooring CS2 (near the MicroCAT) was  $4.8 \text{ cm s}^{-1}$ . Using the distance along the shelfbreak from the mouth of Herald Canyon to the array site, this gives an advective time of approximately 6 months for the WW to reach the array. This would seem to imply that the cold water finished flushing through Herald Canyon in mid-March. Based on the limited observations to date in the canyon, this seems unlikely (Woodgate et al. 2005; Pickart et al. 2010; Linders et al. 2017). However, considering the large distance between the two sites (order 750 km), it could be that the WW leaving the canyon later in the season warms and becomes remnant winter water by the time it reaches the array. Notably, Corlett and Pickart (2017) also found that the presence of WW in this region decreased markedly after September.

## **H. Physical Oceanography of the Northeastern Chukchi Sea: A Synthesis**

### **H.1 Introduction**

The overall goal of this program is to provide an improved understanding of the physical oceanography of the northeastern Chukchi shelf, as well as exchanges between the Chukchi/Beaufort shelves and the adjacent basin. In previous sections, we addressed specific objectives of our program in detail. In this section, we will attempt to integrate the findings from those previous sections with other data sets, including a variety of ice profiling sonar (IPS) and ADCP data sets collected by the oil industry as part of the CSESP, the Barrow Canyon and COMIDA Hanna Shoal mooring arrays, NSF-supported moorings provided by S. Okkonen and C. Ashjian, and the NSF-sponsored Arctic Observing Network (AON) mooring deployed along the Beaufort Sea shelfbreak at 152°W (previously discussed by Nikoloupolus et al. 2000).

Assimilating these further datasets allows us to provide a general overview of our emerging understanding of the northeastern Chukchi Sea shelf and shelfbreak. We begin with a discussion of the seasonal ice cover because ice formation and retreat has a major influence on the hydrography throughout the year. We add additional hydrographic data (collected in summer and fall) to that previously discussed to underscore how sea ice meltwater (MW) isolates Hanna Shoal from the remainder of the shelf. The section concludes with an overview of the circulation connections (or lack thereof) among various portions of the northeastern Chukchi Sea shelf and highlights connections with prominent hydrographic features. Figure H1 shows the location of moorings used in this section of the report.

### **H.2 Sea Ice**

Our description of sea ice variability on the Chukchi Shelf begins with an overview of 1979 – 2013 and then focuses on the northeastern Chukchi Sea shelf for the years 2011 – 2013. We focus on these years for two reasons. First, these years illustrate extremes in the interannual variability in summer ice conditions. Second, our most comprehensive set of hydrographic data comes from these years, and thus can serve as an introduction to how extreme ice conditions affect ocean physics.

Sea ice generally begins forming in the northern Chukchi Sea in late October and effectively covers the entire shelf, including Bering Strait, by late December. Ice retreat commences in late April or early May. Using satellite data from Scanning Multichannel Microwave Radiometer (SMMR), Special Sensor Microwave/Imager (SSM/I), and Special Sensor Microwave Imager/Sounder (SSMIS) acquired from the National Snow and Ice Data Center we examined spatial patterns of ice retreat by computing Empirical Orthogonal Functions (EOF) of May through August 1979 – 2013 sea ice concentrations. (We performed this calculation using both mean daily and monthly ice concentration maps and found virtually identical results.)

As a first attempt at understanding the relationship of these patterns to the atmosphere, we correlated the EOF time amplitude functions with wind velocity and wind speed over Bering Strait and the Chukchi Sea shelf. Winds for all analyses were obtained from the North American Regional Reanalysis (NARR) products produced by NOAA's National Center for Environmental Prediction (NCEP). The NARR forecasts are provided at 3-hourly intervals on a 35 km grid (Mesinger et al. 2006).

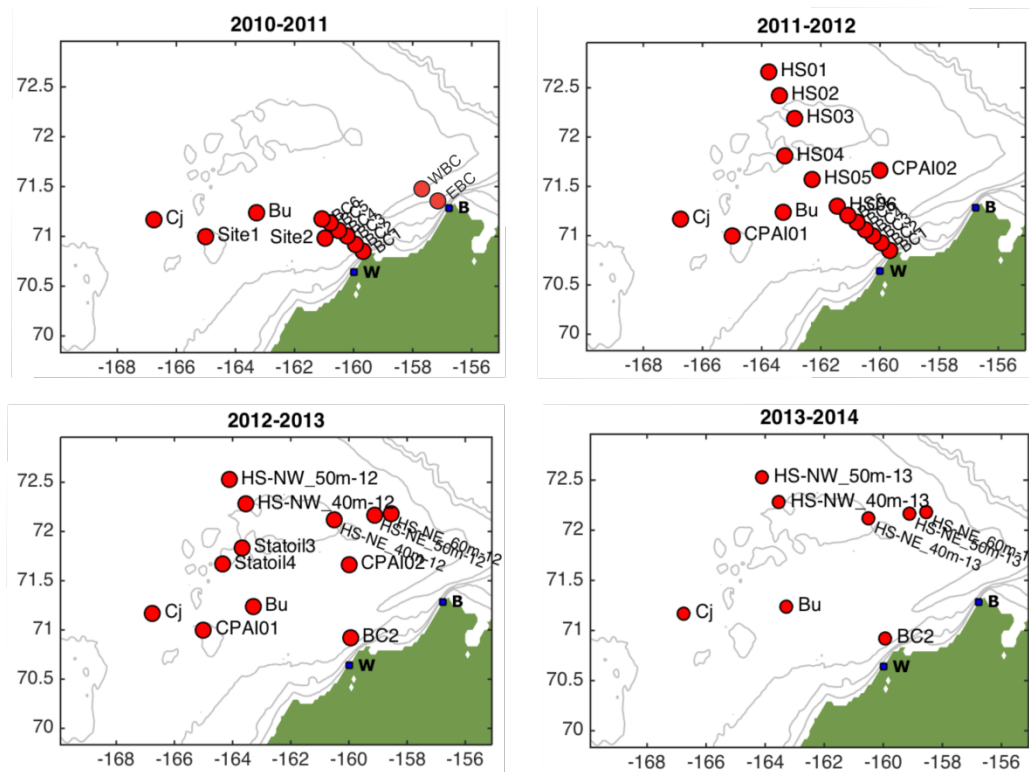


**Figure H1.** Map showing the locations of moorings used in this section of the report as a function of year. Moorings Cj (Crackerjack), Bu (Burger), Site1 & 2, CPAI 01 & 02, Statoi 3 & 4, and HS 01-06 were all deployed and processed under industry support. HSNE and HSNW moorings were supported by the BOEM-COMIDA program. WBC and EBC were supported by NSF. Barrow Canyon moorings (BC 1 – 6) were supported by BOEM Study 2012-079, and BC2 from 2012 – 2016 was supported by this project.

There are two statistically significant EOF modes of ice-retreat in May (Figure H2). The dominant mode (EOF1) accounts for 46% of the variance in ice concentration and corresponds to ice retreat and/or ice melt proceeding northward from Bering Strait. The second mode (EOF2) accounts for 27% of the variance and describes a pattern in which changes in ice concentration along the northwestern coast of Alaska are out-of-phase with changes in concentration along the northern coast of Chukotka. Correlations between the May EOFs and the monthly wind velocity component anomalies indicate that EOF1 is positively correlated with both the east–west (correlation coefficient,  $r = 0.43$ ) and north–south ( $r = 0.44$ ) wind components in Bering Strait (and also over the central Bering shelf, where the correlation coefficients are smaller, but nevertheless still significant). The signs of these correlations are consistent with the hypothesis that wind-induced forcing in the Strait and over the Bering shelf affects northward transport (and the northward heat flux) through the Strait (Danielson et al. 2014). EOF2 is significantly correlated with winds over the northeastern Chukchi Sea, with winds from the east (west) and or south (north) leading to reduced (increased) ice concentrations along the northwest Alaskan coast. The correlation coefficients are  $r = 0.68$  and  $r = 0.64$  for the zonal and meridional wind components, respectively. Although not explored further here, a possibly important consequence of EOF2, when it results in open water along the northwest Alaskan coast, is that it exposes the underlying water to more intense solar radiation much earlier than would otherwise occur. The increase in solar radiation should then lead to earlier pelagic phytoplankton blooms and earlier warming of coastal waters. The structure and evolution of EOF2 is analogous to the behavior of a polynya in the absence of freezing air temperatures (and an infinitely wide ocean). Under such conditions there is no limit on polynya width as long as the winds continue blowing offshore (Pease 1987).

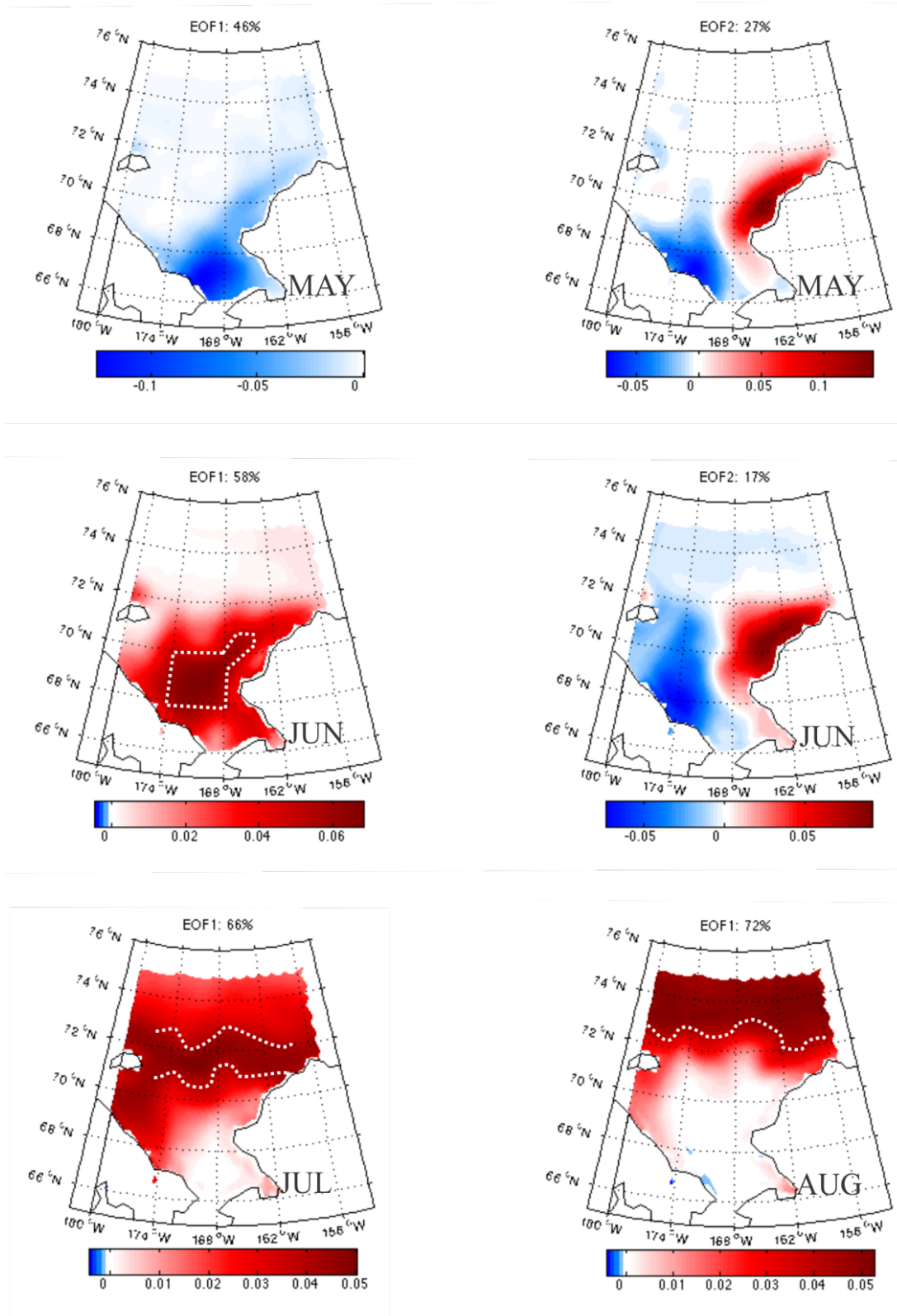


**Figure H2.** The spatial structure of the most significant EOFs of ice concentration for May (top row), June (middle row), July (bottom left), and August (bottom right). Where sketched, the white dotted lines outline the region of maximum spatial variability in EOF1.

The June EOFs (Figure H2) have patterns similar to those of May. The June EOF1 describes variability in northward ice retreat and accounts for 58% of the variance in ice concentration. The modal weights indicate that maximal variability occurs in the area outlined by the dotted white lines (i.e., over Hope Sea Valley, with an extension to the northeast in the Central Channel). The spatial structure of EOF1 shows that the patterns of ice retreat are beginning to outline the principal flow pathways (in Herald Canyon, the Central Channel, and the west coast of Alaska). EOF1 is uncorrelated with the winds over the Bering shelf and in Bering Strait, but it is significantly correlated with the zonal and meridional winds in the Chukchi Sea ( $r = 0.37$  and  $r = 0.24$ , respectively). The decrease in these correlations from May suggests that other atmospheric influences (solar radiation) and/or ocean-based processes (heat advection and/or mixing) exert more influence on this mode's variability. EOF2 for June accounts for 17% of the variance, and its structure is similar also to the May EOF2, in that it has an anti-phase relationship between the eastern and western Chukchi Sea. June EOF2 again shows significant correlations with the zonal and meridional components of the wind ( $r = 0.42$  and  $r = 0.54$ , respectively) over the Chukchi Sea.

Only the first EOF is statistically significant in July (Figure H2). It accounts for 66% of the variance in ice concentration, and the pattern describes meridional variability in ice concentrations. The region of maximal variability occupies a zonal belt between  $70.5^{\circ}\text{N}$  and  $72^{\circ}\text{N}$  (outlined by dotted white lines) all along the northern perimeter of the Chukchi shelf. There is no significant correlation between EOF1 and wind velocities; however, it is significantly correlated ( $r = 0.43$ ) with wind speed over the Chukchi Sea, with the sign implying that a reduction in ice concentration is associated with an increase in wind speed. This correlation could arise in two ways. First, mechanical break-up of the ice and the production of smaller floes may be enhanced under higher wind speeds. Smaller floes will have higher surface area-to-volume ratios than bigger floes and so melt more rapidly. Second, a significant amount of heat is contained in the Pacific-derived waters advected across the Chukchi shelf in June and July (Woodgate et al. 2012). Because these waters are generally more dense than the surface waters formed from melting ice (Coachman et al. 1975), they reside below the MW layer that surrounds the marginal ice zone and lies beneath the melting ice (Paquette and Bourke 1981). Higher wind speeds should enhance turbulent mixing, promote the upward flux of oceanic heat from the Pacific waters to the underside of the ice, and increase the rate of ice melt.

EOF1 is the only significant mode in August as well (Figure H2), and it accounts for 72% of the variance in ice concentration. The region of maximum variability includes Hanna Shoal and lies north of  $\sim 72$  and  $73^{\circ}\text{N}$  with north-south meanders that approximately align with the principal flow pathways. The only significant correlation ( $r = 0.42$ ) between this mode and wind velocity is with the east-west component of wind over the northeastern Chukchi Sea shelf. The sign of the correlation is such that eastward winds are associated with a decrease in ice cover. This would be consistent with an Ekman response of the ice; its drift would include a southward component that would make the ice-edge more diffuse and advect floes southward toward warmer water. There also is a positive correlation ( $r = 0.56$ ) between EOF1 and wind speed.

Although we have identified a number of significant correlations between EOF modes and the winds, the relationships do not account for a large fraction of the ice concentration variance. Indeed the largest correlation coefficients were those between EOF2 and the wind velocity components in May and July (which account for  $\sim 35\%$  of the variance in that mode at most) and the wind speed in August. As mentioned, these low correlations may indicate that other physical processes associated with either the atmosphere or the ocean are as important, if not more so, than the winds, or it may imply that the wind's effects are manifested in non-linear ways. Bear in mind, however, that our analysis has not been exhaustive, and by concentrating on EOF modes as bulk measures of sea ice concentration patterns, our statistical approach may have masked the importance of winds in affecting variations in the seasonal retreat of sea ice. The results do remind us that ice retreat on this shelf is a complicated process and that the role of winds, currents, and air-sea heat exchange play in this retreat have not been adequately

addressed. As discussed in section F and explored further later, the absence or persistence of sea ice critically influences the hydrographic structure of the Chukchi Sea shelf.

### H.3 Winter Sea Ice Statistical Properties

Prior to discussing statistical properties of the ice as determined from IPS sensors, we examine some of the broader scale aspects of the onset of ice over the northeastern Chukchi Sea for autumn 2011, 2012, and 2013. Recall that the main difference among these years was that warm Bering Sea Summer Waters pervaded the entire surface layer of the northeastern Chukchi in summer and fall 2011, whereas in 2012 and 2013 cold MW was present over the Hanna Shoal region between the Central Channel and Barrow Canyon. In each year, the Chukchi shelf was ice-free through the end of October, according to SSMIS and Advanced Microwave Scanning Radiometer 2 (AMSR2) imagery (Figure H3) (Spren et al. 2008). In 2012, the ice advanced rapidly southward with much of the shelf being partially ice-covered by mid-November and completely ice-covered by the end of the month. By contrast, the ice advanced slowly southward through mid-November in 2011 and 2013. A direct relationship between wind velocity and the rate of advance of sea ice is not readily apparent. For example, moderately strong northeasterly winds prevailed through mid-November 2011, while weak and variable winds occurred over the same period in 2012. One might have expected that the winds in 2011 would have promoted more rapid cooling and freezing than in 2012, yet ice developed more rapidly in 2012 than in 2011. Regardless of the exact causes, the rate of ice advance in these years increased rapidly after mid-November, although substantial areas of open water or low concentrations remained, especially in the western Chukchi Sea, through to the end of November in 2011 and 2013. The signatures of the principal current pathways across the shelf are also evident in the 15 November ice concentration maps as embayment-like features occurred in all three years. Although these embayments have been noted frequently with respect to summer ice retreat, they appear to be a regular fall feature of the shelf as well and are an indication of the influence of the northward flow from Bering Strait on patterns of ice advance.

Through our partnership with the oil industry, we were provided with the processed IPS data sets from Crackerjack, Klondike (Site 1), Burger, CPAI02, Statoil03, and Statoil04 (Figure H1). The processing followed the procedure of Melling et al. (1995) and is given in detail by Mudge et al. (2015). Here we highlight just a few examples of the types of statistical information available from these data, as the analyses are ongoing. The statistical properties discussed here were formed (again following Melling et al. 1995) from 50 km long sections of ice drift recorded by ADCP moorings that accompanied each IPS mooring. In this procedure, we compute ice displacement as a function of time and record the date midway along each segment. (The displacement diagrams are identical to progressive vector diagrams often used in descriptive oceanography. The diagrams are qualitatively useful in providing a picture of movement, but they should not be interpreted as a Lagrangian measurement. Figure H4 shows displacement maps derived from the 2010 – 2013 Burger deployments.) All statistics are then designated by this date. Note that the time lapse between dates can be quite variable, with some segments spanning only a day while others may span 2 weeks. In most cases the duration of a segment was only a few days. These different time lapses simply reflect the fact that ice motion is more rapid during some periods than others. As noted by Melling et al. (1995) the reason for adopting this “sampling-through-distance” as opposed to “sampling-through-time” is that if the ice does not move then one is effectively sampling the same piece of ice repeatedly and generating biased statistics. Although the IPS records keel depth, we converted these to thickness by multiplying the keel depth by 1.1 (Bourke and Paquette 1989). For each segment we computed the mean thickness (including open water), the first and second modes, and examples of ice thickness histograms or probability density functions (pdfs). We show a subset of these data and offer general descriptive statements which hold across time and for different sites.

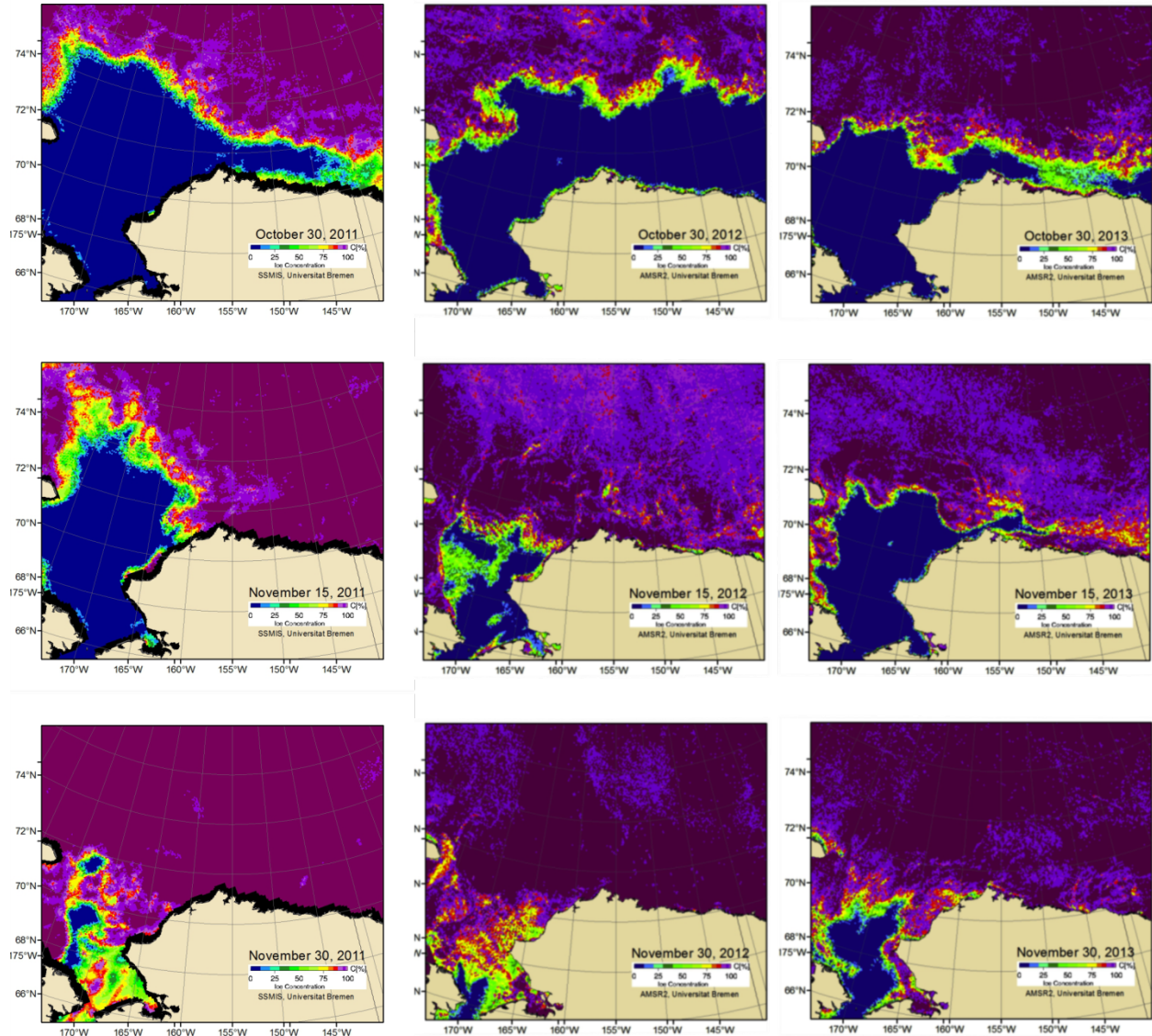


**Figure H3.** The evolution of sea ice concentrations as seen on 30 October (top row), 15 November (middle row), and 30 November (bottom row) for 2011 (left column), 2012 (middle column), and 2013 (right column).

The displacement figures provide a qualitative sense of the dynamic nature of the ice drift over the Chukchi Sea shelf (Figure H4). For example, during January and February 2013 the suggested displacement was  $\sim 500$  km at a mean speed of  $\sim 10$  cm  $s^{-1}$ . In each year, the drifts were southwestward beginning in late fall. In early 2011 the drift reversed and was northeastward from January through April and weak thereafter. For the 2011 – 2012 and 2012 – 2013 records the drifts were primarily toward the southwest. By late spring the ice motion was weak, and the drift was variable in direction.

Figure H5 shows the mean ice thickness for each drift segment from the Burger 2010 – 2013 IPS records, determined from the 50 km segments of Figure H4. Note that each plot begins on the common date October 30, although ice was not always recorded at that time. The last date plotted corresponds to the last date in which a 50 km segment was obtained. We have also fitted these data with a power law and

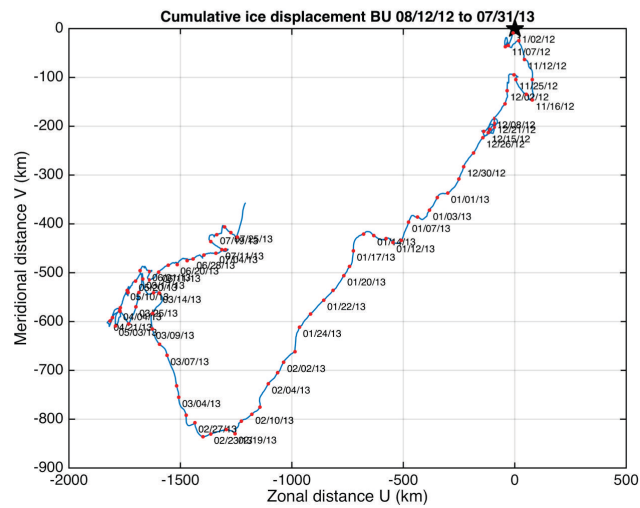
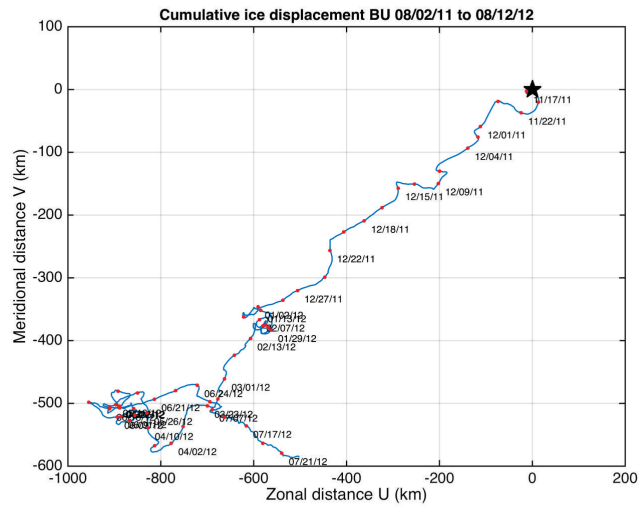
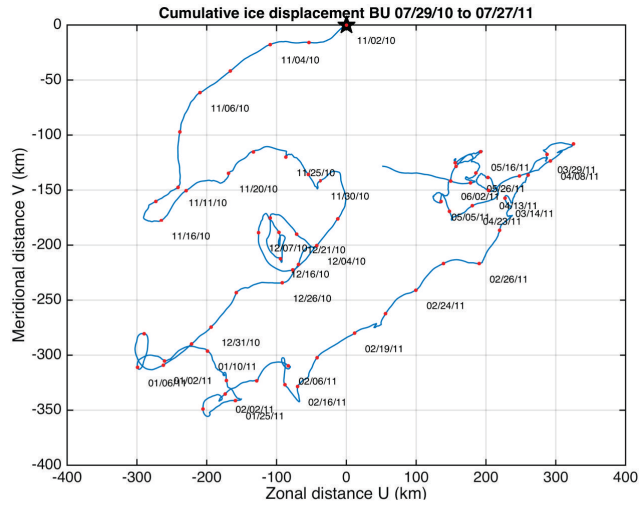


**Figure H4.** Ice displacement as a function of time for the Burger deployments from 2010 – 2011 (top), 2011 – 2012 (middle), and 2012 – 2013 IPS and ADCP deployments. The stars indicate the starting position and correspond to the first 50 km segment in which any ice was recorded. Red dots indicate the mid-point of each 50 km segment and every other segment is labeled by date.

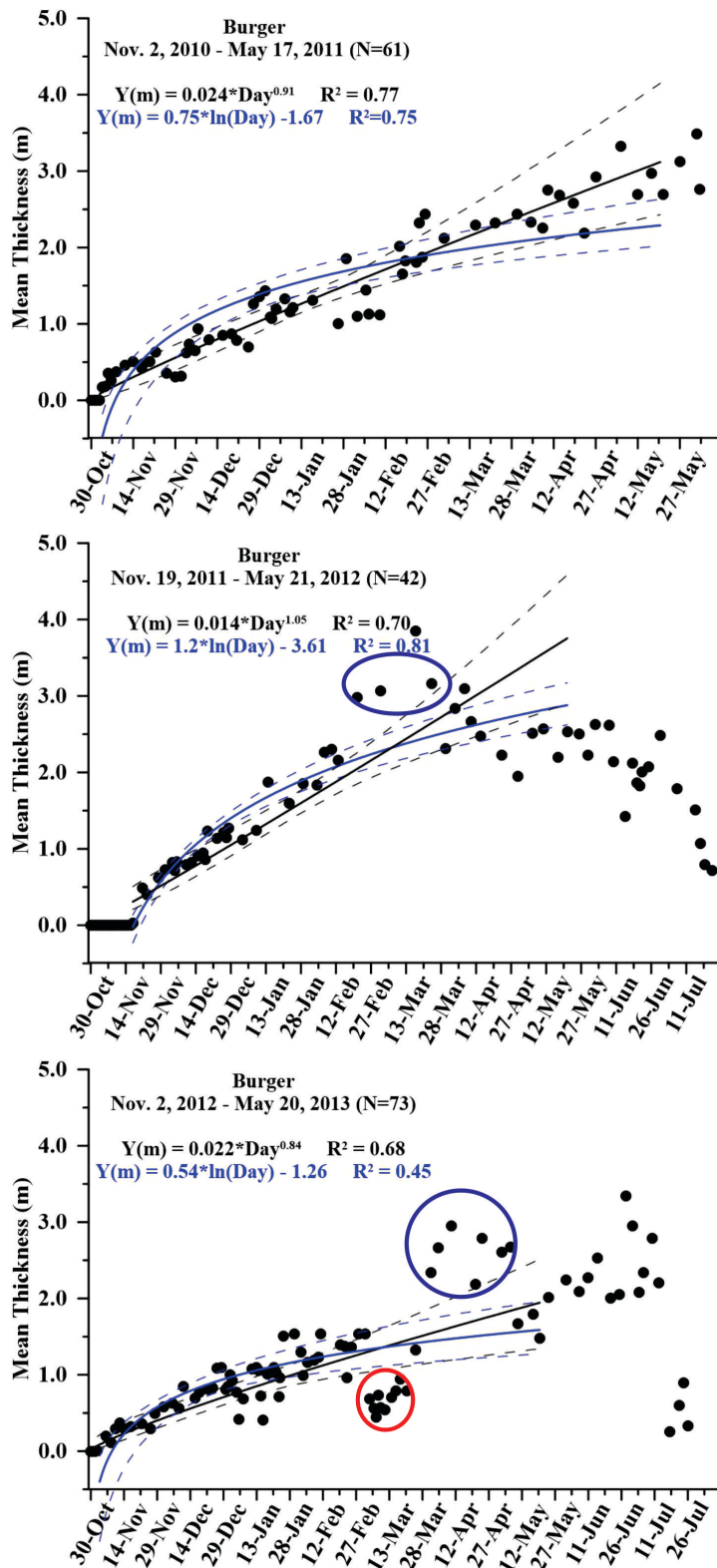


**Figure H5.** Mean ice thickness and statistical fits as a function of time (50 km segment) for the Burger deployments from 2010 – 2011 (top), 2011 – 2012 (middle), and 2012 – 2013 (bottom). Means encircled by a red ellipse suggest periods of new, thinner ice formation, and those with a blue ellipse suggest periods when thicker ice was advected over the site.

logarithmic fit between the first date ice was recorded and about the 20<sup>th</sup> of May. Inspection of these and other plots indicated that after this date the mean thickness begins to decrease. Overall, the power law and/or logarithmic fits perform equally well (including other years not shown). We ascribe deviations from these fits to major advective events in which thicker ice was advected past the mooring site, or numerous leads formed in which new and thinner ice developed. In general the mean thickness increases to about 2 m by late May and then rapidly declines thereafter due to melting.

Figure H6 shows the seasonal evolution of ice thickness based on subsets of the pdfs of ice thickness as a function of selected dates from Burger for the 2010 – 2013 period. These are plotted separately for three trimesters: 1) November through mid-January, 2) late January through late March, and 3) from April – June (or July). To facilitate comparison we prepared the figure by choosing segment dates from each year as close to one another as possible. Several features emerge upon inspection. First, the pdfs evolve most rapidly (toward progressively thicker ice) during the first trimester as ice first develops. Initially, ice thickness increases and the pdfs consist of a single mode which thickens through time. Soon afterwards, additional modes develop, as new ice forms and/or thicker ice deforms. However, by mid-January most of the ice thicknesses were  $\leq 1$  m. During the second trimester, the ice pdfs become more regular and generally contain 2 modes, one at  $> \sim 1$  m and the second being thinner. These thinner modes presumably represent new ice forming in leads. In most years the ice was  $\sim 1.5$  m thick by late March, although in 2011 the primary mode was  $\leq 1$  m. The thick mode at 3 m on 17 March 2012 is unlikely a result of local thermodynamic processes based on the theoretical estimate provided by Maykut (1986). In using his formulation we assumed a seasonal average of 3,000 freezing degree-days based upon a freezing season of 150 days in length and 20°C as the average difference between the air temperature and freezing point of seawater. If we assume a snow cover of 10 cm, then the ice thickness at the end of the freezing season would be  $\sim 0.8$  m. (A thicker snow cover yields thinner ice and vice versa.) Repeating the calculation for a temperature difference of 30°C results in a thickness of 1 m of ice at the end of March.

By the third trimester two modes generally occur with the dominant one being at  $\sim 1.5$  m and the secondary mode at  $\sim 0.5$  m. Figure H6 summarizes the seasonal evolution of the primary and secondary modes for each year. These time series are based on all 50 km segments from each deployment and thus not sub-sampled as in Figure H5. The overall impression from these pdfs is that the seasonal evolution of ice involves the development of numerous ice thickness classes, with a general thickening proceeding throughout the season. However, modes can form and disappear rapidly, with ice thickness classes arising and disappearing over relatively short time intervals. This conclusion is corroborated in Figure H7, which shows the seasonal evolution of the primary (blue) and secondary (red) modes based on all 50 km segments in each year. As with the means, we restrict the least squares fits to the period spanning from the first detection of ice in the fall through the latter part of May. Although the thickness of both modes increases throughout the season the progression is far from regular and includes episodes of rapid thinning and/or thickening, which yields poor fits to the data.

The episodic nature of mode evolution is a consequence of advection in which thicker or thinner floes are brought past the site or local convergence or divergence. As floes converge they deform and thicken and as they diverge leads develop and new ice forms. New ice formation is critical to the formation of dense water that forms across the shelf throughout winter. Upon formation the dense water is at the freezing point and is enriched in salinity due to brine repulsion from the forming sea ice. Ice, and in particular, the thick floes formed by deformation processes, is a source of cold, dilute surface when they melt the following summer.

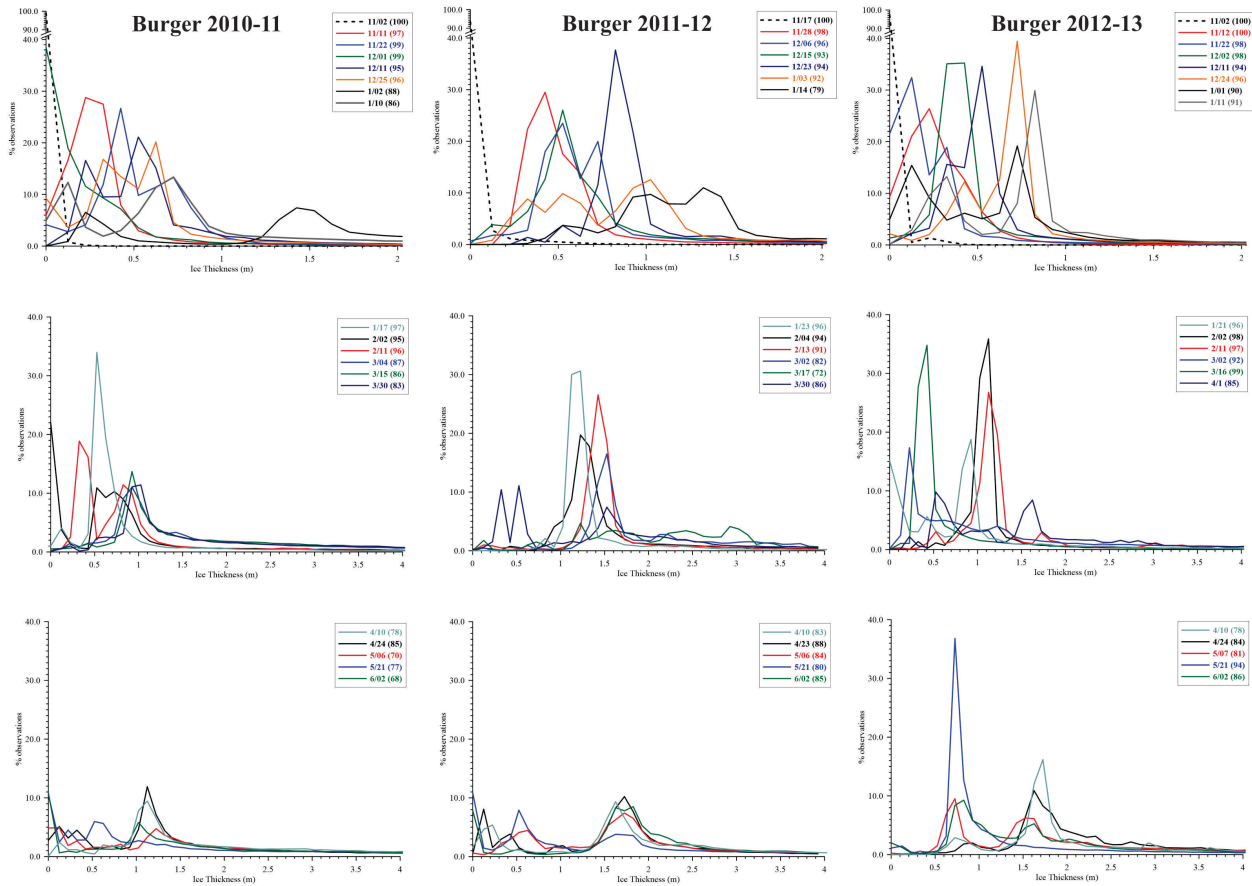


**Figure H6.** Probability density functions (pdfs) for selected dates from the Burger 2010 – 2011 (left), Burger 2011 – 2012 (middle), and Burger 2012 – 2013 (right) IPS deployments. The y-axes represent the percentage of time a particular ice thickness interval (x-axis) occurred over the 50 km long sampling interval. Numbers in parentheses in legend indicate the percentage of all observations less than or equal to the maximum value of the ice thickness on the x-axis. Note that the x-axis maximum is 2 m for the top row and 4 m for the bottom two rows.

## H.4 Hydrography

Summer and fall water masses on the Chukchi Sea shelf consist of an amalgam of different water masses. As a prelude to this section we first review these with the aid of the potential temperature-salinity ( $\theta/S$ ) diagram in Figure H8. These water masses consist of cold ( $<4^{\circ}\text{C}$ ), dilute ( $<30$ ) MW layer, warmer and saltier Bering Sea Summer Water (BSSW) waters that have entered the Chukchi Sea through Bering Strait during the summer months. BSSW waters include Alaskan Coastal Water (ACW) and Bering Sea Water (BSW), where the former is fresher and warmer than the latter. Large portions of the shelf also include near-freezing, salty (and dense) bottom winter waters (WW) formed the previous winter on both the Chukchi and Bering shelves. This water mass is gradually displaced northward throughout the summer. WW can be warmed at depth by penetrating solar radiation, such that it has the very high salinities characteristic of WW, but with temperatures elevated above the freezing point. Gong and Pickart (2015) termed this water mass Chukchi Summer Water (CSW). As evident in the figure, these water masses are not discrete, but instead blend together and tend to overlap in property space as a consequence of vertical and horizontal mixing and/or heating by solar radiation. (Finer-scale discrimination of water masses is possible based on nutrient and  $\delta\text{O}^{18}$  data, which were not collected as part of this program.)

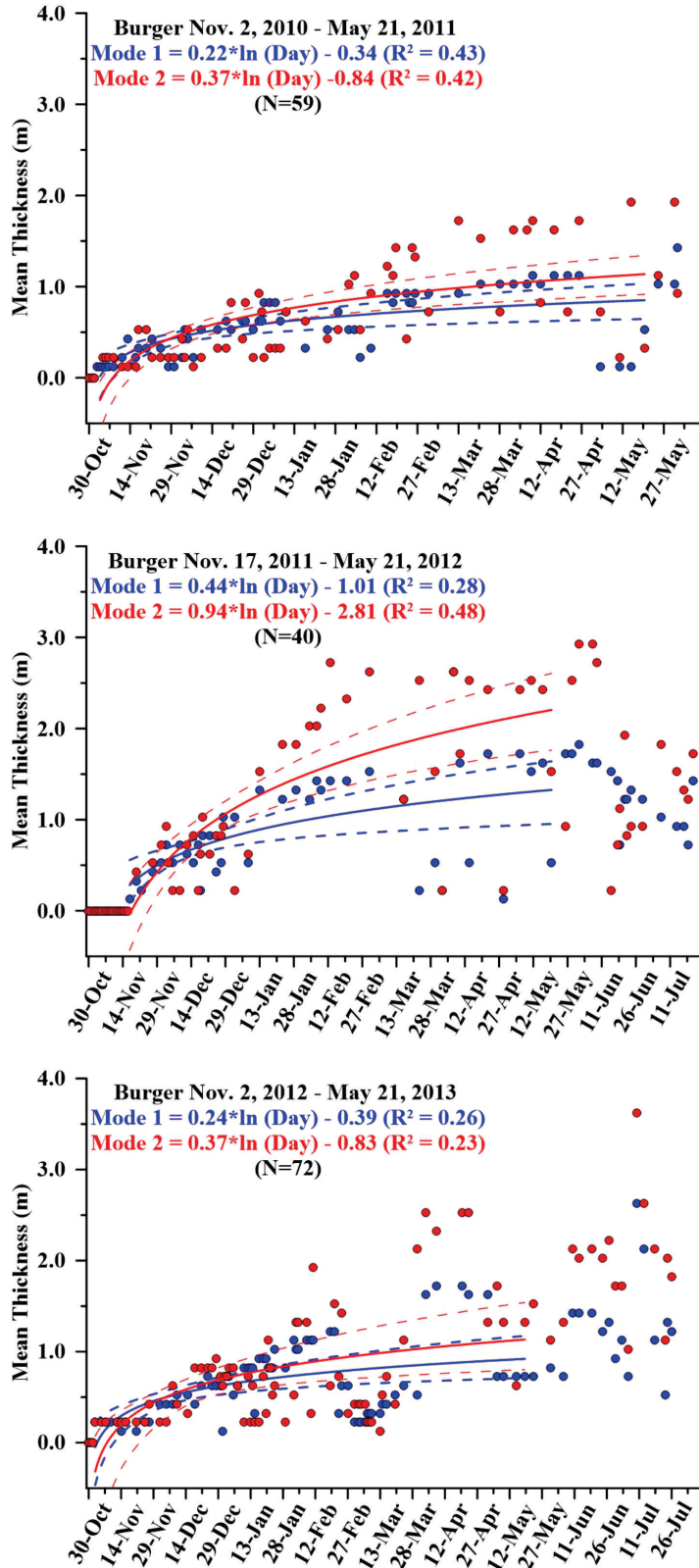


**Figure H7.** Time series of the primary (blue) and secondary (red) mode ice thickness modes along with logarithmic statistical through time. The modes are determined from each 50 km segment for the Burger deployments from 2010 – 2011 (top), 2011 – 2012 (middle), and 2012 – 2013 (bottom).

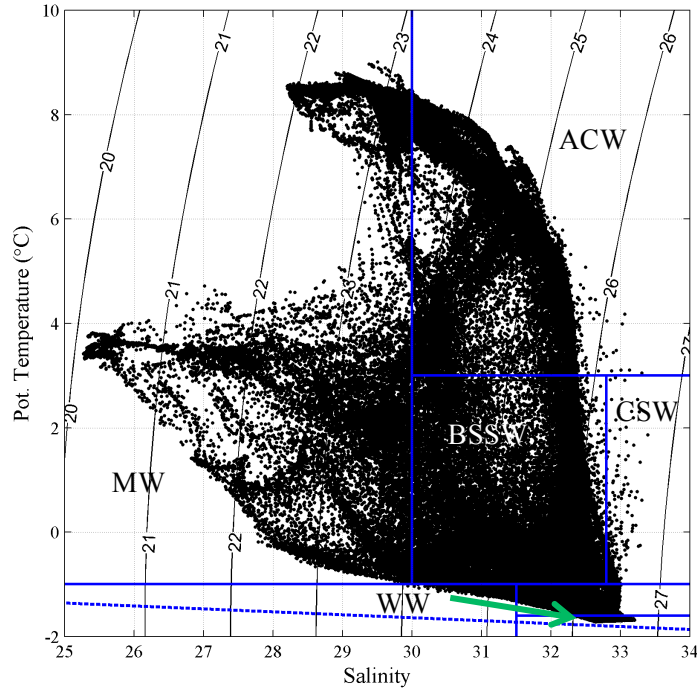


**Figure H8.** Potential temperature-salinity ( $\theta/S$ ) diagram illustrating various water masses found on the northeastern Chukchi Sea shelf in summer and early fall.

As discussed in section F, the rate of disappearance of ice over Hanna Shoal appears to be a controlling influence on vertical stratification and the formation of upper ocean fronts on the northeastern Chukchi Sea shelf. When large volumes of MW are present, the stratification is strong and shallow, with the pycnocline centered between 10 and 15 m depth. The MW region extends to the south of Hanna Shoal and is separated by a strong front from warmer and saltier BSSW waters over the shelf to the south and west. The western edge of this front appears to extend from the southwest corner of Hanna Shoal southward to  $\sim 71.5^\circ\text{N}$  and thence southeastward to  $\sim 71.2^\circ\text{N}$  toward the head of Barrow Canyon. Here we show that this MW layer extends eastward from Hanna Shoal to Barrow Canyon and that the front, on approaching the head of Barrow Canyon, curves northeastward along the length of the canyon. This conclusion is based on Figures H9 – H14, which are a sequence of Acrobat-towed CTD legs collected in 2012 that extend from near the head of the canyon (Leg Y; Figure H9) to the mouth of the canyon (Leg U; Figure H14). The figures are arranged such that the viewer is looking upcanyon toward the southwest, with the coast to the left in the figure and consist of separate vertical sections for potential temperature, salinity, and chlorophyll, a map showing the location of the transect, and a  $\theta/S$  diagram.

On each section ACW occurred closest to the coast and occupied the entire depth of the water column. BSW and/or WW was below the ACW along the canyon floor. MW was a consistent feature of the upper water column to the west of the ACW with these water masses separated by a strong front, and WW occurred beneath the MW. There were indications of horizontal mixing processes evident in sections E, Q, S, and U (Figures H10, H12, H13, and H14, respectively) where lenses of warmer ACW and/or BSW infiltrated below the MW layer on the west side of the canyon. When present, the chlorophyll distribution tended to be dense, but horizontally patchy, and clustered within and/or just below the pycnocline separating MW from WW. The reason for this is that WW contains high nutrient concentrations, whereas MW and ACW are always nutrient-poor, and the nutrients in BSW are exhausted by the time this water mass reaches the northeastern shelf in late summer.

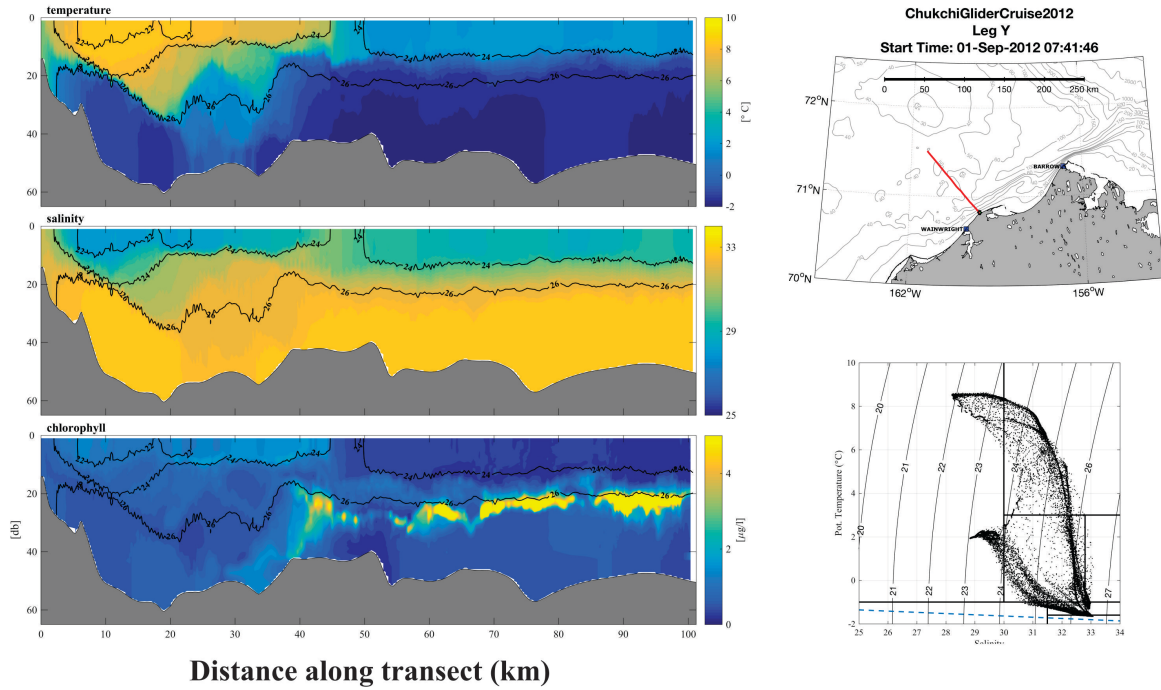


**Figure H9.** Summary figures for Acrobat Leg Y. The left hand side consists of vertical sections of temperature (top), salinity (middle), and chlorophyll (bottom). The black contours on each section are isolines of potential density plotted at a contour interval of 2. The right hand sides of each figure contain a transect location map (top right) and a  $\theta/S$  plot based on the data from that section. The view is toward the southwest with land to the left of each panel.

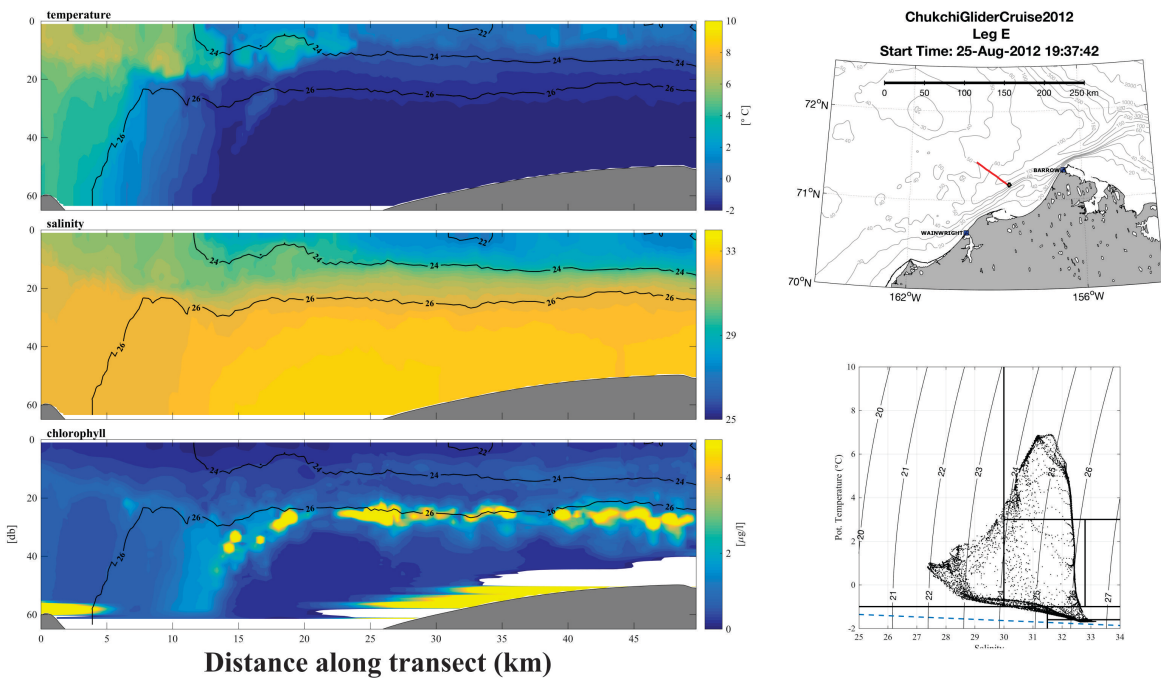


**Figure H10.** As in Figure H6 but for Acrobat Leg E.

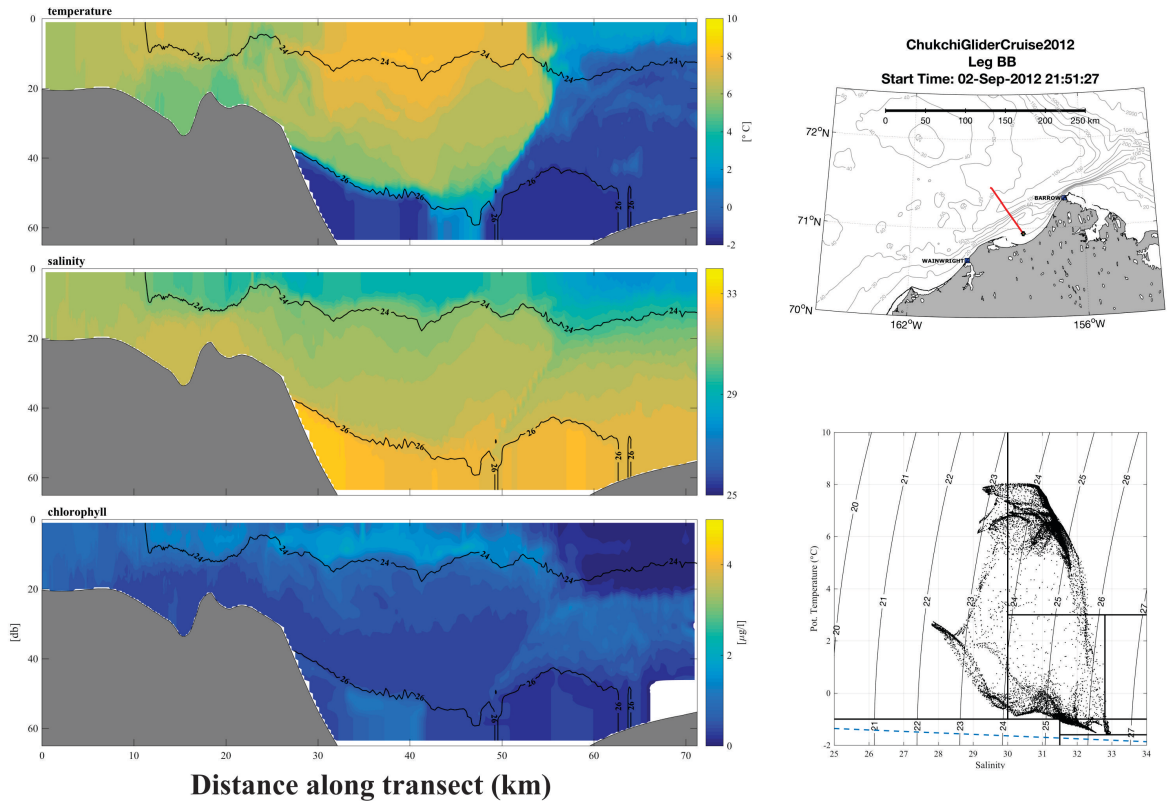


Figure H11. As in Figure H6 but for Acrobat Leg BB.

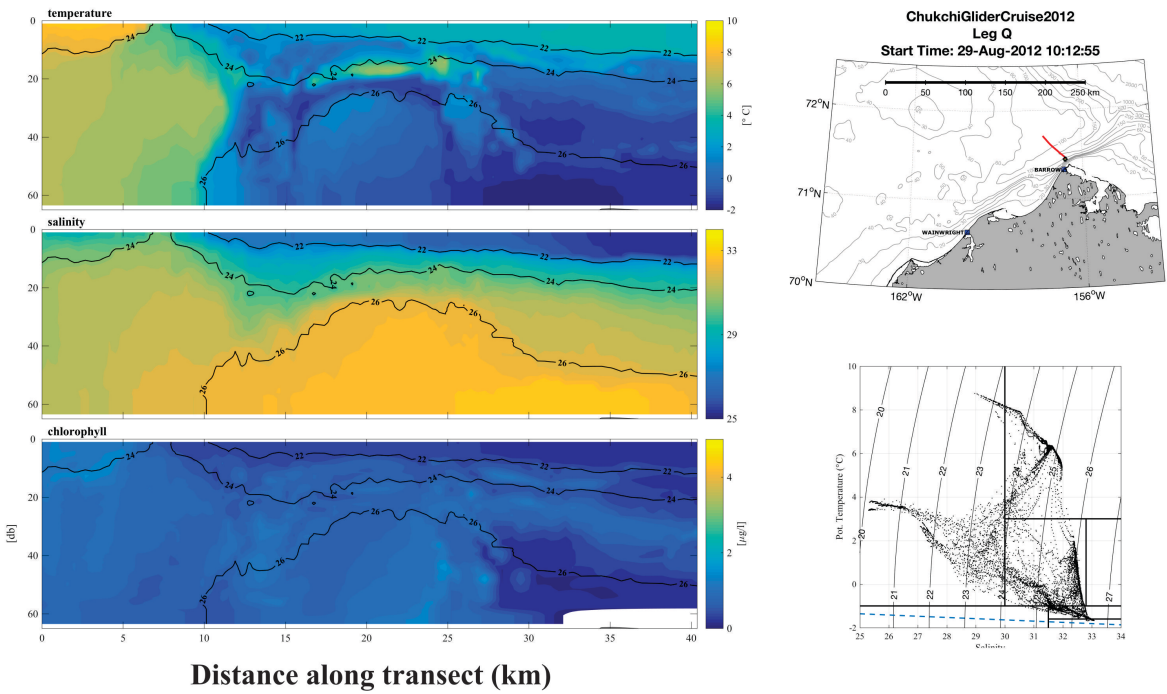


Figure H12. As in Figure H6 but for Acrobat Leg Q.

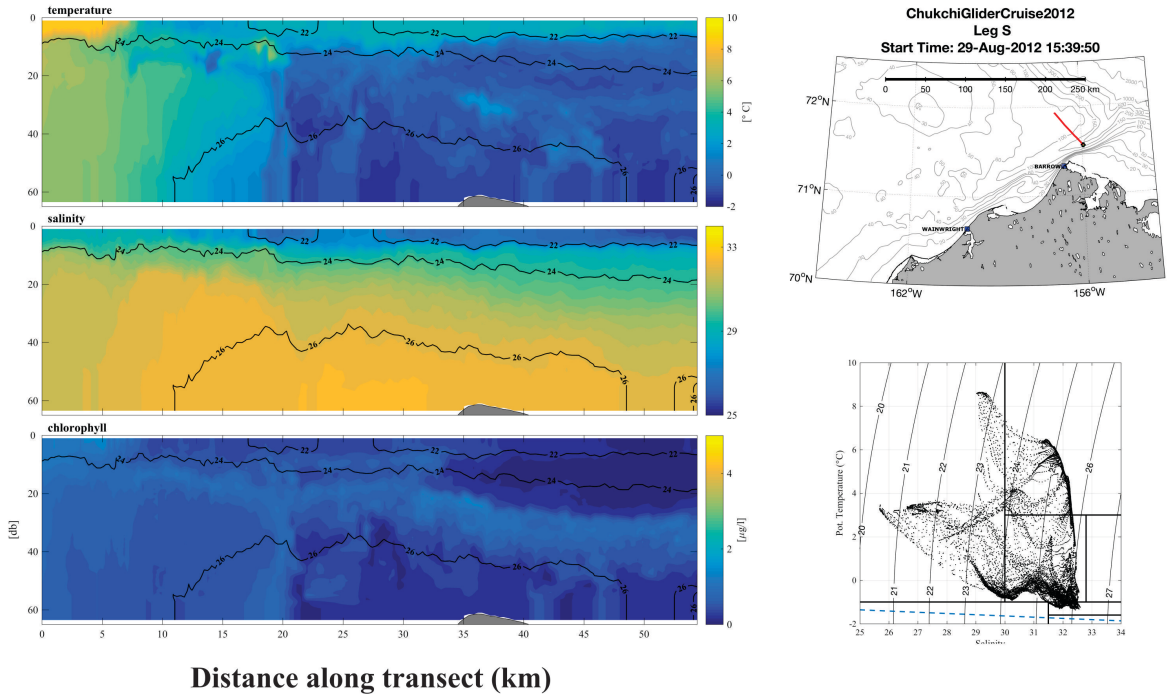


Figure H13. As in Figure H6 but for Acrobat Leg S.

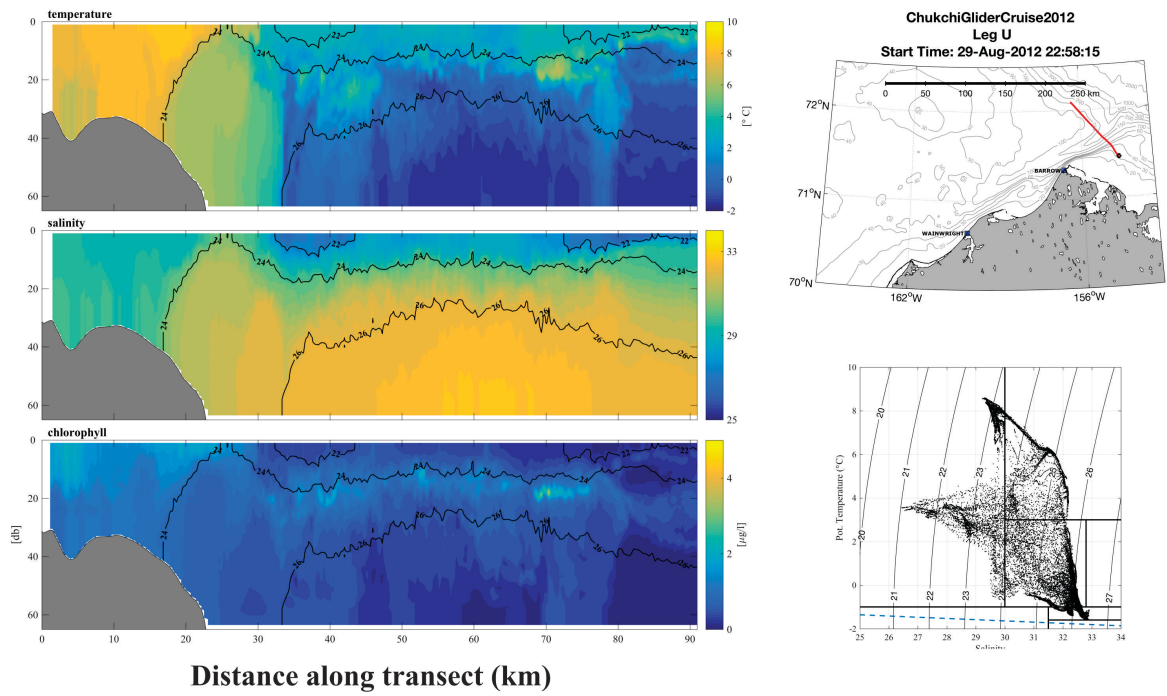
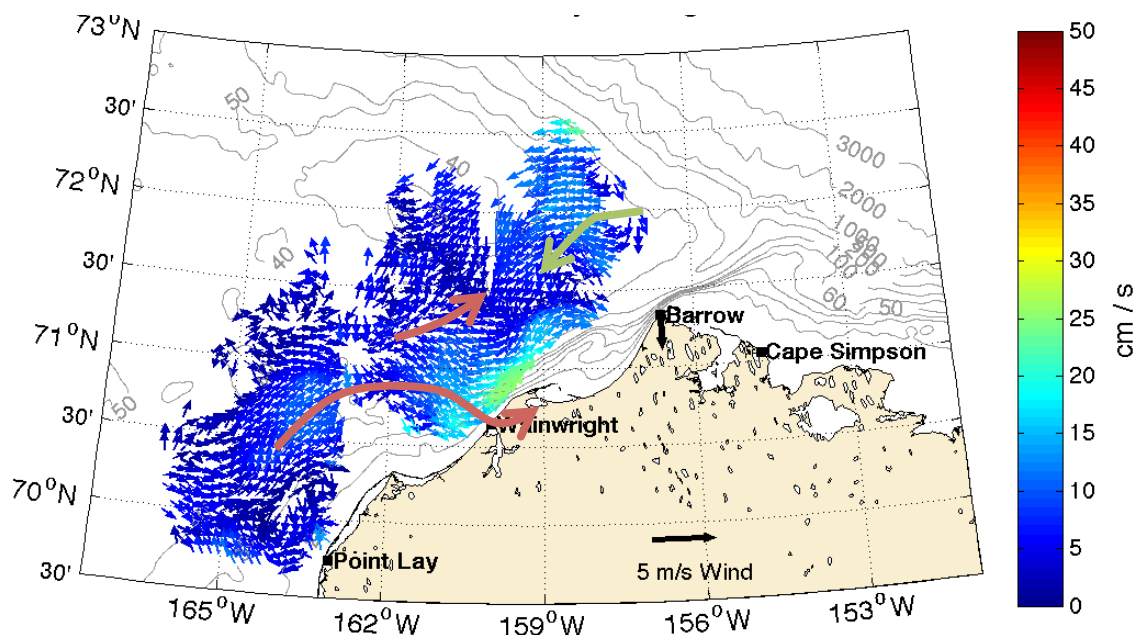


Figure H14. As in Figure H6 but for Acrobat Leg U.

Based on the results of Section F and the Acrobat sections presented here, we conclude that when ice remains over Hanna Shoal late in summer a front separating MW from BSSW forms an arc extending from the southwest side of Hanna Shoal, eastward to Barrow Canyon and thence along the western side of the canyon to at least the shelfbreak, circumscribing a distance of ~450 km. Beneath the MW layer, the shelf largely consists of WW. Along the south side of Hanna Shoal there is a bottom front separating the WW from BSSW, although this front is not necessarily collocated with the surface front. As discussed by Lu et al. (2015), these fronts are potentially unstable, resulting in horizontal mixing. In Section C, we noted that the within the MW region, the surface circulation tends to be weak and largely a result of Ekman dynamics forced by the winds. South of the front the circulation is primarily zonal and forced by a combination of geostrophy and Ekman dynamics, while within the canyon the flow is primarily geostrophic. In each case the geostrophic pressure field is established by a combination of the wind-forced sea level setups and the mean pressure gradient between the Pacific and Arctic Oceans.

The MW/BSSW fronts affect the circulation field in several ways. The cross-frontal density gradient forces an along-front jet having the same width as the front and velocities of  $10 - 20 \text{ cm s}^{-1}$  (the direction of flow is such that the MW is to the right of a viewer looking downstream along the jet's axis). The jets are baroclinically unstable and generate energetic meanders and eddies, which are fundamentally important in mixing (Thomas 2008; Thomas et al. 2008). The MW/BSSW front involves horizontal flow convergence exemplified by surface current vector maps derived from HFRs averaged during the week of 5 September 2012 from radars in Barrow, Wainwright, and Point Lay (Figure H15). The vector distribution suggests a convergence zone extending from west to east along about  $71.5^\circ\text{N}$ . North of this zone, but near the front, the surface flow is southward (and downwind based on the mean wind vector at Barrow during this time). South of the zone, the flow is northeastward and typical of the shelf flow offshore of Wainwright and south of Hanna Shoal under mild wind conditions. The convergence is roughly aligned with the position of the fronts discussed above and signatures of it appear to extend eastward to Barrow Canyon. Surface current vector maps obtained in August and September 2011 showed no such features, which is consistent with the hydrography from that year. As might be expected the presence of mesoscale motions should



**Figure H15.** Mean surface current vectors for the week of 5 September 2012, as estimated from HFRs.

yield differences in surface current variability. In 2011, the variance in both the zonal and meridional velocity components across the radar mask was half that for the same velocity components in 2012. These differences cannot be attributed to differences in the wind energy between these two years for the variances in both wind vector components were identical in both years.

As a second example, we show the trajectory of a 10 m drogued, SVP satellite-tracked drifter that was released from the USCG *Healy* on 13 August 2012 (Figure H16) southwest of Hanna Shoal. Over its first 45 days, the drifter's trajectory included a number of meanders and large excursions in sea surface temperature (SST), few of which were associated with changes in winds. The drifter's trajectory is especially convoluted in the vicinity of 71.3°N, 163.5°W where the SST variations are large and vary from ~5°C south of this latitude to ~2°C north of it. This temperature range brackets temperatures typical of MW and BSSW. The variations in SST and the drifter's trajectory path are suggestive (but not conclusive) that the drifter was entrained into mesoscale motions associated with frontal instability. The unstable motions give rise to current fluctuations across both the sub-mesoscale (<6 km) and the mesoscale (6 – 18 km) spatial scales. Such motions should enhance the dispersion of dissolved and suspended material.

The strong stratification found over the shelf north of 71.5°N is a perennial feature due to MW and/or BSSW in the upper 15 – 20 m and WW at depth. The preceding results indicate that the stratification northeast of Hanna Shoal is stronger than that to the northwest of the Shoal. In part this difference is because the upper layer salinities west of the Shoal are influenced by the moderately salty BSW flowing northward in the Central Channel. East of the Shoal, the BSW influence is very limited and here the surface layers may receive contributions from the more dilute ACW. With the onset of freezing and increased wind-mixing, the stratification over the shelf should break down. Such a transition appears to occur annually on the south of Hanna Shoal (Weingartner et al. 1998; Weingartner et al. 2005).

We next examine the seasonal variations in stratification on the northwest and northeast sides of Hanna Shoal by comparing the seasonal changes in vertically-averaged currents and temperature and salinity at moorings HSNW50-12 (Figure H17) and HSNE50-12 (Figure H18). The latter figure includes the time

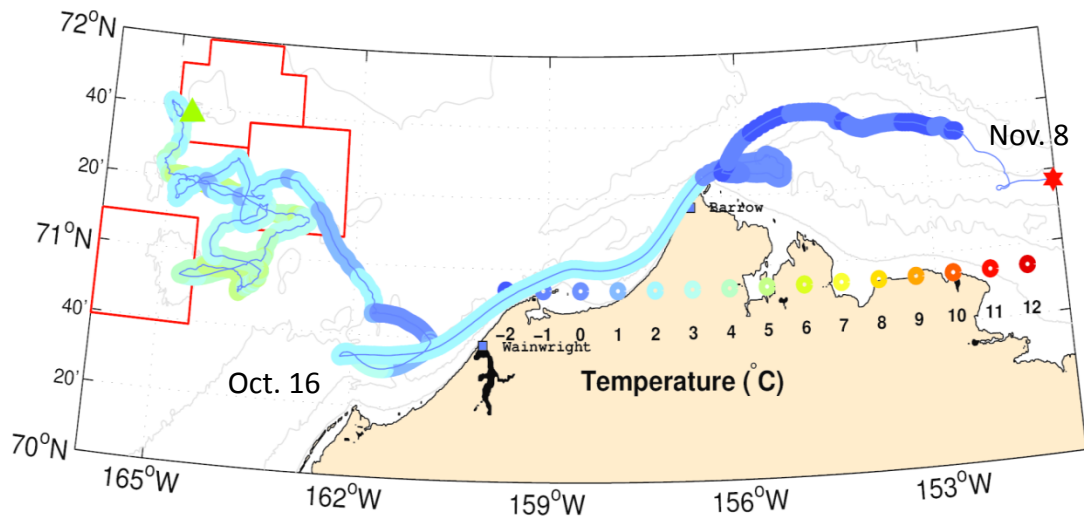


**Figure H16.** Color-coded (by SST) trajectory of a satellite-tracked drifter released at the location of the green triangle on 13 August 2012. The drifter's last reported position was on 15 November 2012 at the location of the red star.

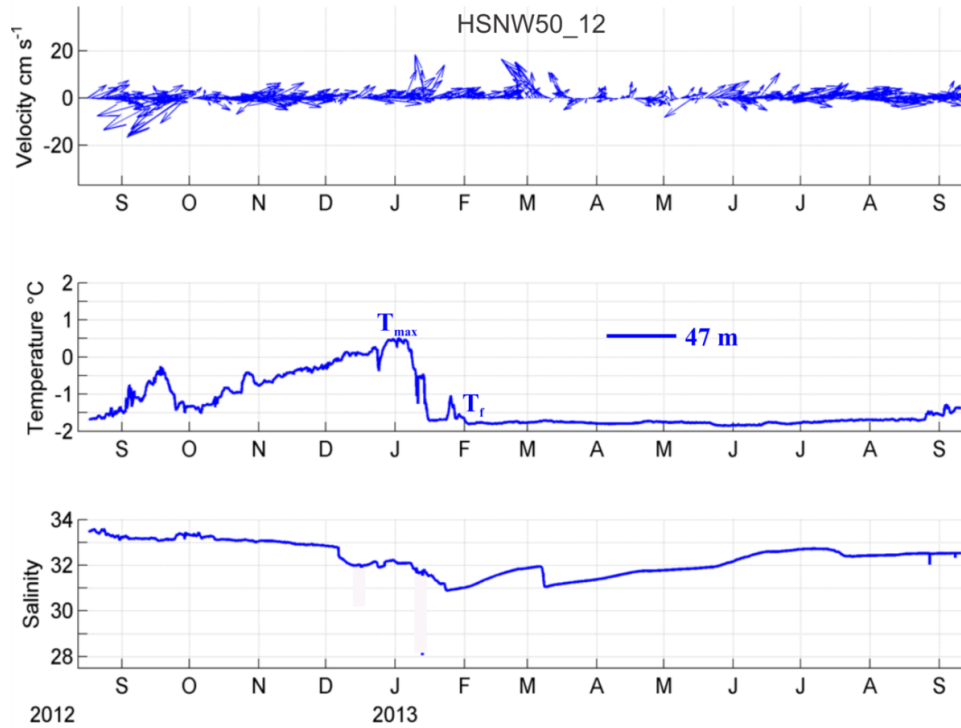


**Figure H17.** Time series of vertically averaged current vectors (top), temperature (middle) and salinity (bottom) at 47 m depth from mooring HSNW50-12. The timing of the temperature maximum ( $T_{max}$ ) and the descent to the freezing point ( $T_f$ ) are noted.

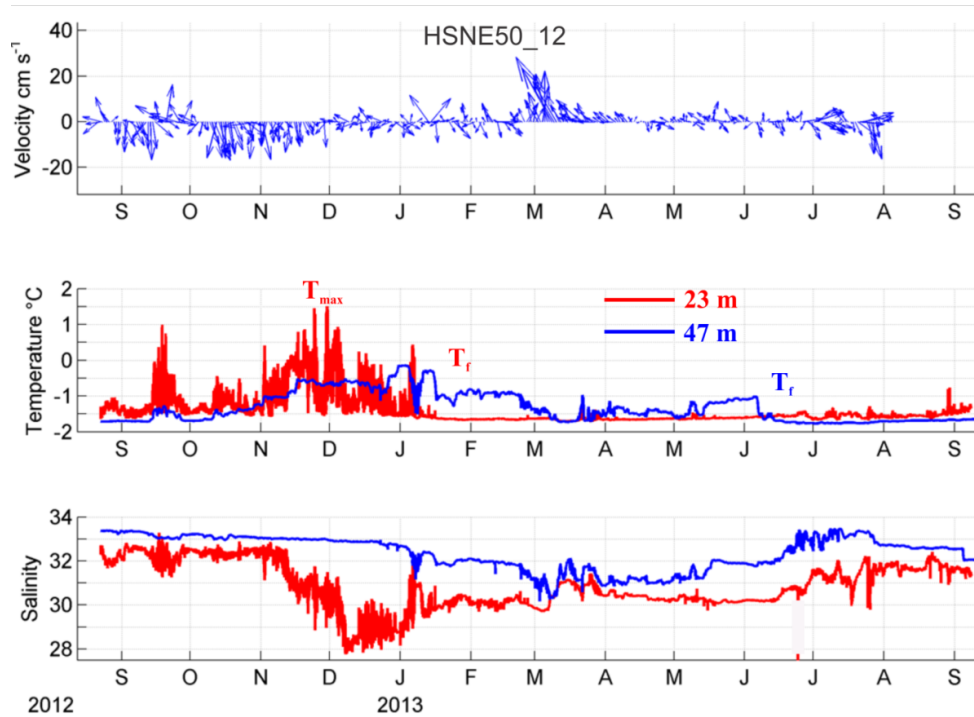


**Figure H18.** Time series of vertically averaged current vectors (top), temperature (middle) and salinity (bottom) at 23 m (red) and 47 m (blue) depth from mooring HSNE50-12. The timing of the temperature maximum ( $T_{max}$ ) and the descent to the freezing point ( $T_f$ ) are noted.

series of temperature and salinity from a CTD moored at 23 m below the surface and another moored at 43 m depth. Except for a southwestward flow reversal in September 2012 and a burst of northward flow in March 2013, the vertically-averaged flow at HSNW50-12 was steadily eastward with a mean speed of  $\sim 7 \text{ cm s}^{-1}$ . At the beginning of the record in August 2012, the bottom temperatures were near freezing ( $\sim -1.8^\circ\text{C}$ ), and aside from some shorter period excursions through fall, bottom temperatures increased steadily to a maximum of  $\sim 0.5^\circ\text{C}$  by late December. In January the temperature decreased and reached the freezing point in early February. Salinities were  $\sim 33.5$  in September but gradually decreased to a minimum of  $\sim 31$  in mid-January. Over the remainder of the record, the salinity increased gradually and reached  $\sim 32.5$  by September 2013. The gradual fall transition from cold, salty water to warmer, fresher conditions reflects advective replacement of WW by BSW. Almost certainly, the stratification eroded through fall as well and complete breakdown occurred in January as near-freezing, dilute waters in the upper portion of the water column mixed with the warmer, saltier bottom waters. We assume that the collapse of bottom temperatures to the freezing point signifies the complete breakdown in stratification.

A very different transition occurred on the shelf east of Hanna Shoal. At mooring HSNE50-12 the vertically-averaged velocity was variable throughout the year and not statistically different from zero. In fall, the flow was primarily south-southeastward and this was accompanied by a gradual increase in temperature and decrease in salinity at the bottom (similar to the trend on the northwest side of Hanna Shoal). The velocity record and these trends suggest that bottom waters were being advected from the west to the east side of Hanna Shoal through fall. From December through August; however, the flow on the east side of the Shoal was weak and variable, and bottom temperatures and salinities evolved quite differently from those on the west. Bottom temperatures were  $\sim 0.5 - 1^\circ\text{C}$  above freezing until mid-June when they reached the freezing point and salinities increased. These changes heralded the arrival of WW. This WW was advected into the area because it arrived about two months after the onset of melt. Its source was probably the west side of Hanna Shoal because the velocity record shows an increase in the number of southeastward flow events beginning in April, with these events increasing in frequency and strength through July.

The salinity records at 23 and 47 m provide insight on the vertical stratification changes (because of the density dependence upon salinity). In fall, the vertical salinity difference between the two depths was  $\sim 1$ , and this difference increased to  $\sim 5$  by mid-December. These salinity differences are comparable to the values observed over the water column in the fall and reflect the gradual deepening of the pycnocline through the fall. (Recall that the fall CTD sections suggested that the pycnocline was  $\sim 5$  m thick and centered at  $\sim 15$  m depth.) The late fall change in the salinity difference was primarily due to freshening at 23 m even though the bottom salinity had also decreased slightly through fall! The freshening at 23 m was accompanied by increasing temperatures, which reached a maximum of  $\sim 1.5^\circ\text{C}$  in late November before decreasing into January. By mid-January temperatures reached freezing and salinities increased at 23 m. All of these changes suggest a deepening and weakening of the pycnocline by vertical mixing. What is remarkable about this record is that the vertical salinity difference reached a minimum of  $<1$  for only a brief period in March but otherwise remained strong throughout the year. The March weakening in stratification coincided with northward flow and, at both measurement depths, an increase in salinity and temperatures near the freezing point. These changes came about due to advection of a weakly stratified water column from the south.

Although these records indicate that vertical stratification over this portion of the Chukchi Sea shelf remains strong and intact throughout the year, local vertical mixing does occur and is important. For example, the decrease in mid-depth temperature from its maximum in late November to the freezing point in early January was almost certainly due to local freezing processes and penetrative convection, which was insufficient to entirely erode the pycnocline.

There are two other aspects of the mid-depth temperature and salinity records worth noting. First, mid-depth temperatures remained at the freezing point through early June but began to increase at about the same time that the bottom temperatures collapsed to the freezing point. We speculate that these changes are unrelated to each other and that the mid-depth temperature increase was due to warming by solar radiation as sea ice began breaking up and meltponds allowed solar radiation to penetrate through the ice and into the water column (Light et al. 2008). Second, the 23 m instrument captured the signature of very high-frequency oscillations that were most prominent from November through early January. These large-amplitude fluctuations are manifestations of internal waves, evident because the CTD was near the middle of the thin, but strong pycnocline.

The bottom temperature and salinity records from the 2013 – 2014 HSNE deployments (Figure H19) show the same basic seasonal evolution in temperature and salinity as observed in 2012 – 2013. However, the seasonal evolution was quite different at the HSNW moorings. The annual maximum in temperature occurred in mid-November 2013, nearly two months earlier than in the previous year. Temperatures then dropped to the freezing point in early December and remained there into July. We tentatively ascribe these differences to differences in fall ice concentration, as detected by the moored ADCPs, between 2102 and fall 2013. In 2012, the ADCP records indicated nearly 100% ice coverage over the shelf around Hanna Shoal by mid-November, consistent with the satellite estimates of ice coverage shown in Figure H3. In 2013, the attainment of the 100% ice cover occurred later and included episodic advances and retreats. Moreover, complete ice cover developed earlier on the east side of the Shoal than in the Central Channel and northwest side of the Shoal (Figure H3). These differences in ice cover (in conjunction with the assumed differences in stratification) on either side of the Shoal would lead to earlier cooling at the HSNW moorings compared to the HSNE moorings.

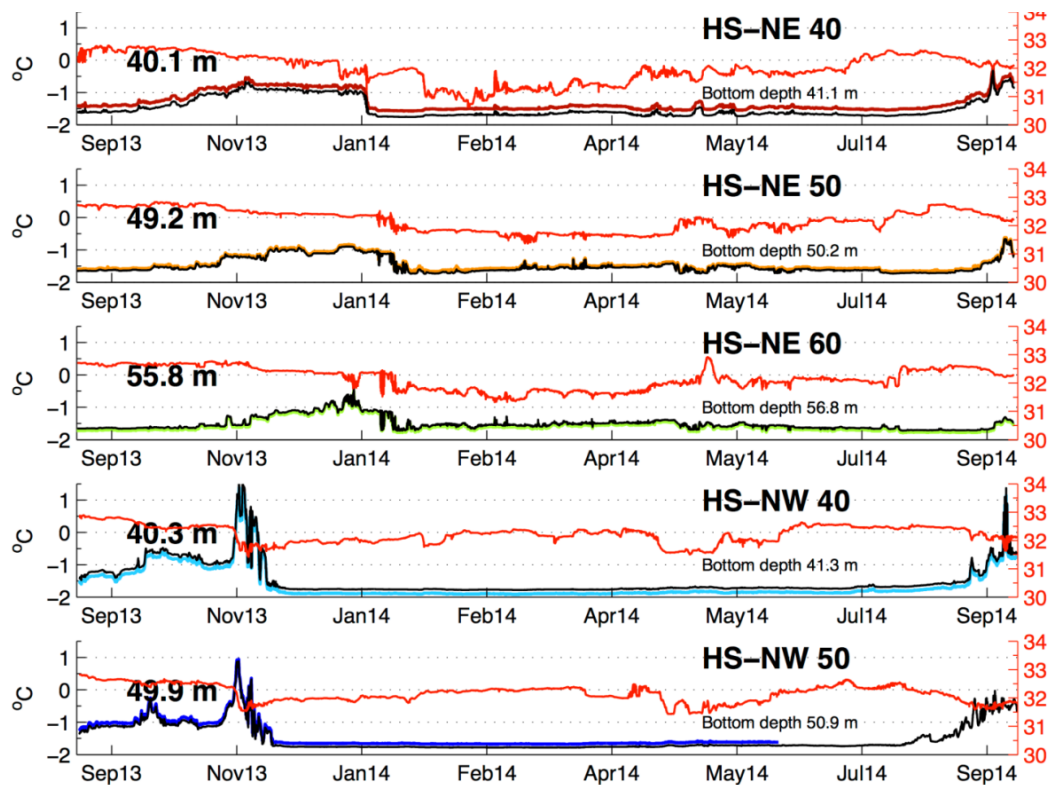


**Figure H19.** Time series of bottom temperature and salinity from the COMIDA 2013 – 2014 mooring array.

## H.5 Circulation Connections

### H.5.1 Chukchi Sea Shelf

Our description of the circulation field over the northeastern Chukchi Sea is based primarily on the mean vectors and variance ellipses of vertically-averaged velocities, and those from the topmost, mid-depth, and bottommost ADCP bins. (Typically the topmost bin represents data from  $\sim 7$  m depth, although deeper velocities are used if the ice thickness extends below this depth.) Maps of these quantities are shown for the mooring years 2010 – 2011, 2011 – 2012, 2012 – 2013, and 2013 – 2014 (Figures H20 – H23, respectively). We selected each of these years for discussion because: 1) they contain the largest numbers of moorings deployed, 2) the mooring locations changed somewhat from year-to-year, and 3) not all moorings yielded full-length records.

The 2010 – 2011 records (Figure H20) indicate that the mean flow within the Central Channel is north-northeastward at  $\sim 5 \text{ cm s}^{-1}$ , and over the shelf south of Hanna Shoal the flow is eastward at similar speeds. At these locations, the standard deviations are 3 – 4 times the magnitude of the means, and the ellipses are aligned in approximately the same direction as the means. The eastward flow transports waters from the Central Channel to the coast and accelerates upon nearing Barrow Canyon, where, as discussed in section D, it turns northeastward into the canyon within about 40 km of the coast. The vertical current shears in the Central Channel, at the head of Barrow Canyon, and over the central shelf are weak. The lack of shear over the central shelf is noteworthy given that the flow is comparatively weak and nearly opposite the surface wind stress. The only locations where there was substantial vertical shear were the two moorings about midway down Barrow Canyon and west of Point Barrow (WBC and EBC; Figure H1). Here the

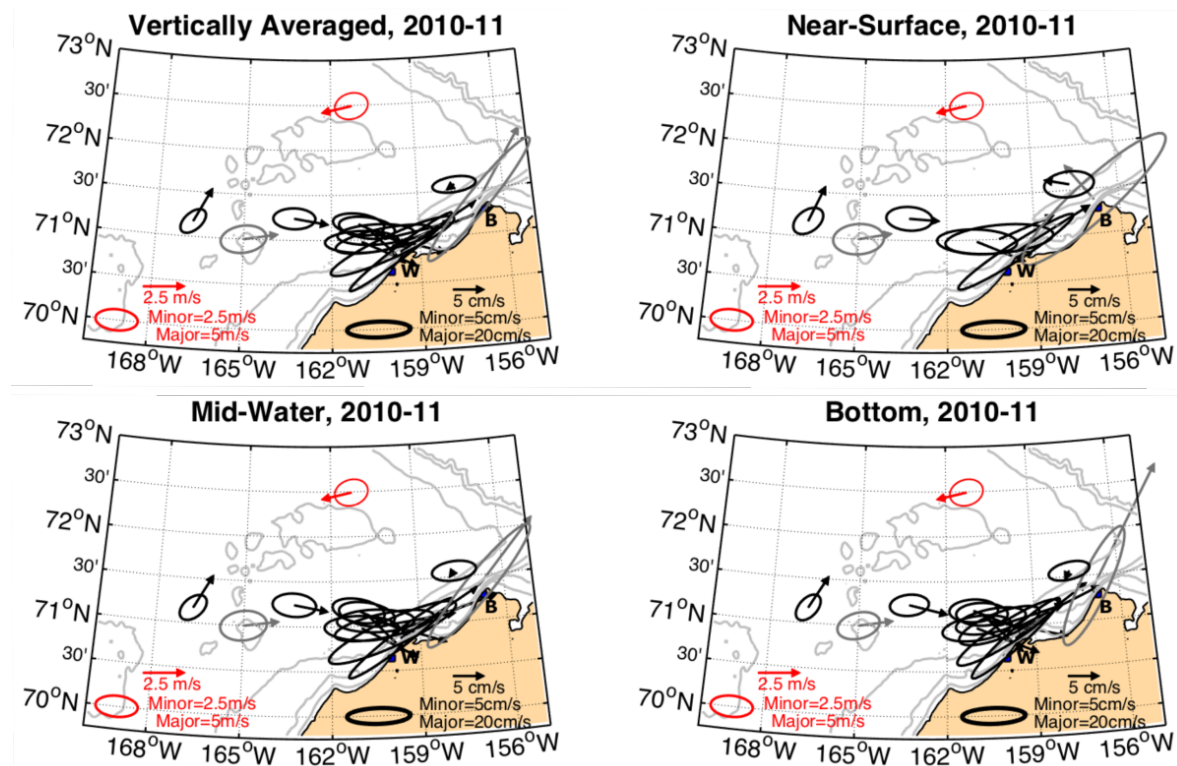


**Figure H20.** Mean vectors and variance ellipses for the 2010 – 2011 moorings. Full-length records are in black, partial-length records are in gray, and NARR wind records are in red.

surface flow was westward. Closest to the coast, the vertically-averaged and deeper velocity vectors were northeastward, or downcanyon, and over the western side of the canyon the vertically-averaged and deeper velocity vectors were weak and oriented upcanyon. The westward drift at the surface at these locations implies the advection of fresh surface waters onto the shelf east of Hanna Shoal. This advective flux would have carried ACW onto the shelf east of Hanna Shoal and thus contributed to the warm waters observed there in 2011.

The shelf circulation portrayed by the 2011 – 2012 moored array (Figure H21) was similar to that described above insofar as the flow was north-northeastward in the Central Channel, eastward over the shelf south of Hanna Shoal, and northeastward at the head of Barrow Canyon and near Point Barrow. This deployment included three moorings along the northwest side of Hanna Shoal (HS01 – HS03; Figure H1). Closest to the Shoal, the mean flow was negligible at all depths. The two northernmost moorings measured a mean drift to the northeast of 5 – 10 cm s<sup>-1</sup> and detected little vertical shear. There were three other moorings along the south and southeast side of the Shoal (HS04 – HS06), which connected to the western end of the Barrow Canyon array (BC1 – BC6). The flow at each of these three moorings was southeastward and similar in direction to the flow at the outer end of the Barrow Canyon array. This is the same southeastward flow that Pickart et al. (2016) identified from synoptic sections in summer, and the moorings indicate that this is a persistent feature of the central shelf's circulation field. It further substantiates previous suggestions that waters from the Central Channel leak eastward along the entire length of the Channel (Weingartner et al. 2013a). The data from these three moorings and from the outer three moorings of the Barrow Canyon array demonstrate that there is no mean flow orthogonal to this mooring line. This implies that waters on the shelf east of Hanna Shoal do not communicate directly with waters to the south of the Shoal. The one other mooring deployed in this year was in ~40 meters water depth and east of Hanna Shoal at ~71.7°N, 161°W (CPAI02; Figure H1). The flow there was negligible at

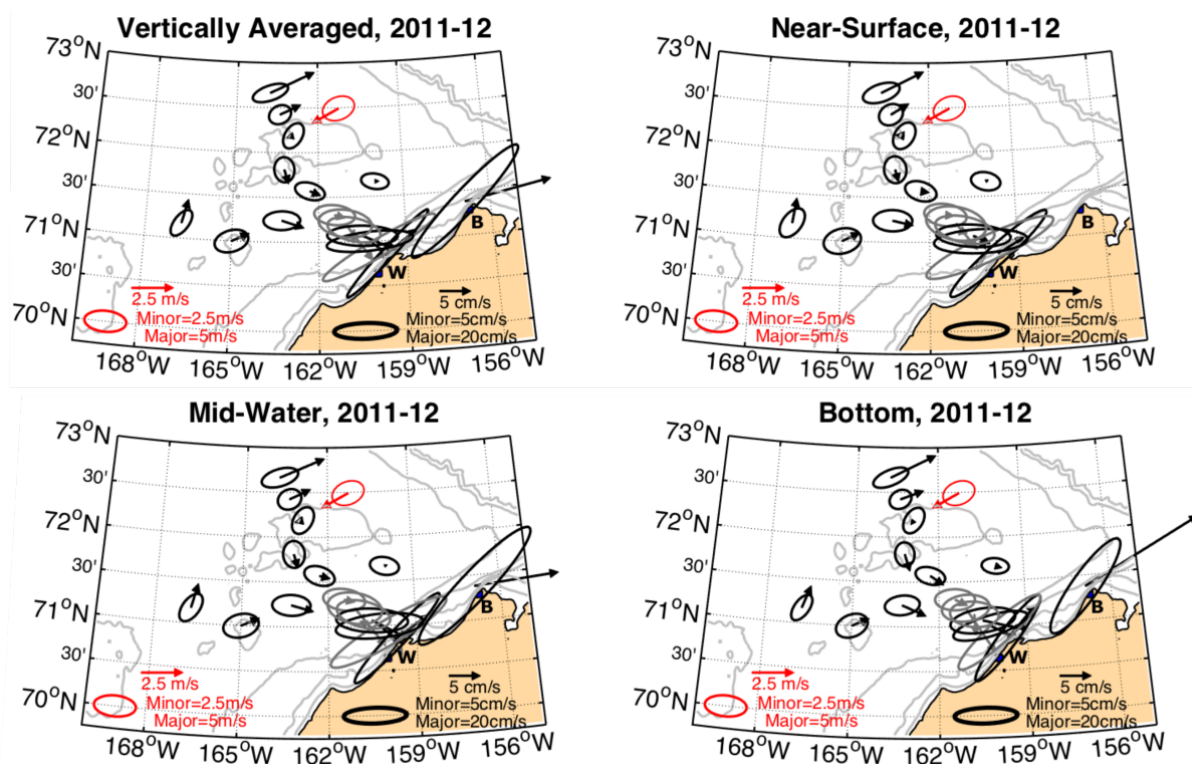


**Figure H21.** Mean vectors and variance ellipses for the 2011 – 2012 moorings. Full-length records are in black, partial-length records are in gray, and NARR wind records are in red.

all depths, except at the bottom where it was  $\sim 1 \text{ cm s}^{-1}$  southeastward, i.e., directed toward Barrow Canyon.

The 2012 – 2013 and 2013 – 2014 deployments (Figures H22 and H23) also showed that the flow was north-northeastward in the Central Channel, eastward over the shelf south of Hanna Shoal, and northeastward at the head of Barrow Canyon. For both deployments, the vertically-averaged flow northwest of Hanna Shoal at  $72.5^\circ\text{N}$  (in 50 m water depth) was northeastward at  $\sim 5 \text{ cm s}^{-1}$ , and the vertical shear was small. Nearer to the Shoal and in shallower water, the vertically-averaged flow was weakly east-southeastward and sheared, with the flow strongest at the bottom. Northeast of Hanna Shoal, the vertically-averaged flow was negligible in the mean, although the surface flow was northwestward, and the bottom flow was southeastward. Finally, the mooring east of Hanna Shoal (deployed only in 2012 – 2013) had westward surface flow, eastward bottom flow, and negligible vertically-averaged flow.

Based on these reviews of hydrography and the mooring deployments made throughout the years, we tentatively offer the following description of the mean flow over the northeastern Chukchi Sea shelf. It includes a remarkably consistent north-northeastward flow in Central Channel. West of  $162^\circ\text{W}$ , a portion of the Central Channel flow is carried eastward between  $71 - 72^\circ\text{N}$  (south of Hanna Shoal) across the central shelf. In late summer, this flow typically carries BSW, ACW, and WW, and possibly MW. There appears to be no net flow between the central shelf and the shelf east of Hanna Shoal. Instead the central shelf flow converges on approaching the Alaskan coast, accelerates to the northeast, and enters Barrow Canyon within 40 km of the coast offshore of Wainwright. Another portion of the northward flow in the Central Channel continues eastward around the northwestern flank of Hanna Shoal. Here it likely merges with an eastward-flowing waters derived from Herald Canyon. This description is consistent with results from the ocean circulation models of Winsor and Chapman (2004) and Spall (2007).

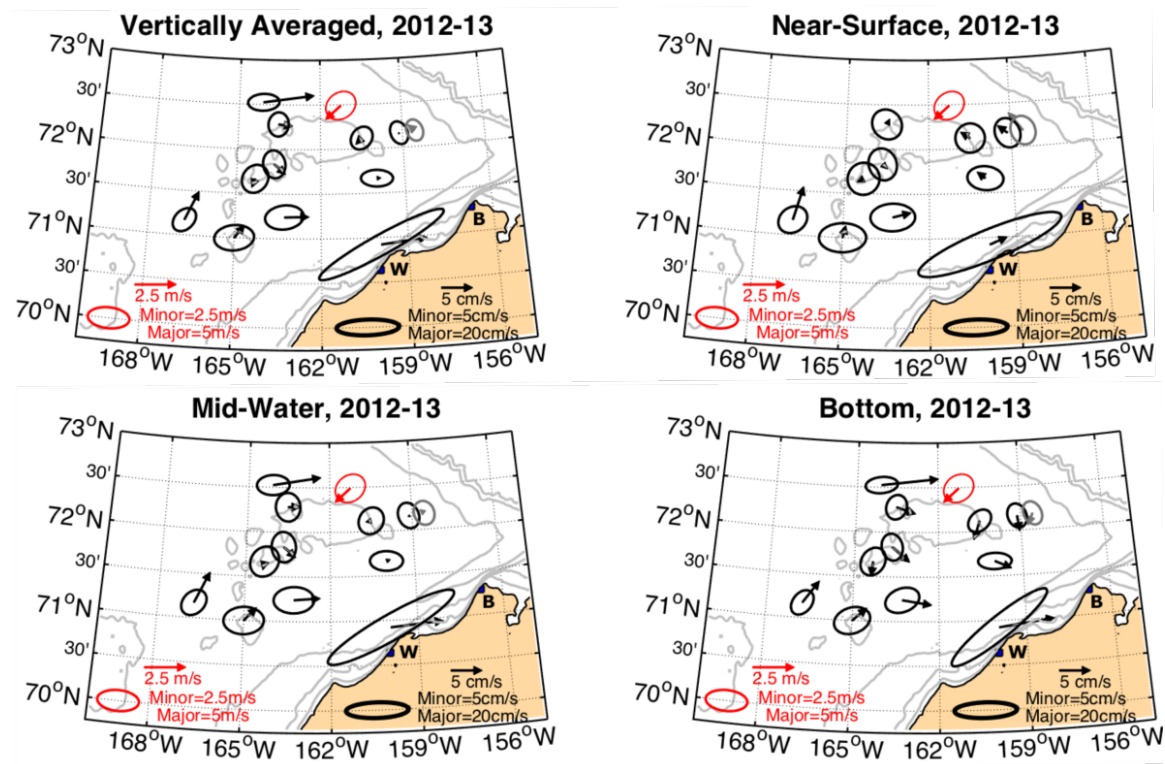


**Figure H22.** Mean vectors and variance ellipses for the 2012 – 2013 moorings. Full-length records are in black, partial-length records are in gray, and NARR wind records are in red.

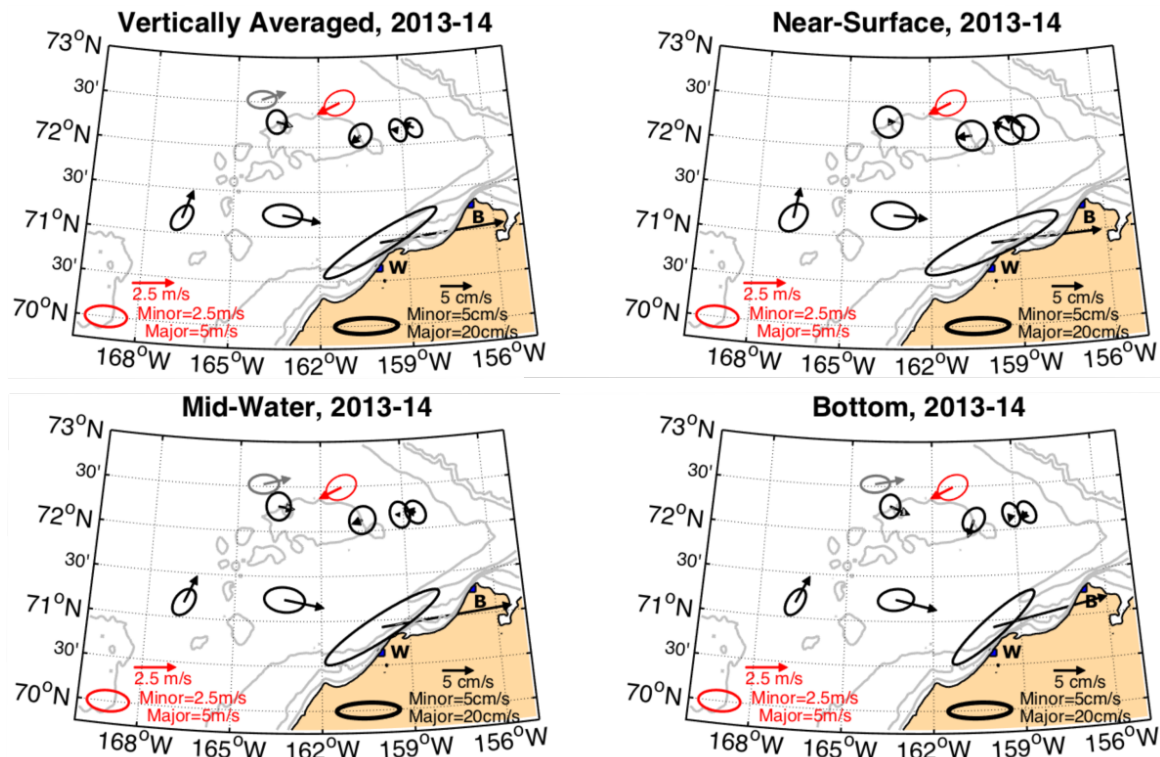


**Figure H23.** Mean vectors and variance ellipses for the 2013 – 2014 moorings. Full-length records are in black, partial-length records are in gray, and NARR wind records are in red.

The flow over the shelf between the eastern side of Hanna Shoal and the western wall of Barrow Canyon is extremely weak on vertical average. However, the surface waters (and ice) drift to the west or northwest, while the bottom waters flow east or southeast. These results imply that the flow field north of Hanna Shoal is convergent, at least within the surface layer (Section F) but quite possibly over much of the water column. The converging fluid presumably moves northward toward the shelfbreak, where, depending upon its density, it will either feed the dilute waters of the westward, surface-flowing Chukchi Slope Current or the deeper and denser waters engaged in the eastward-flowing shelfbreak flow discussed in Section B. It seems very likely that some of this eastward shelfbreak flow enters Barrow Canyon on the west side of the canyon. As it proceeds upcanyon, this flow weakens by losing mass to the much larger and swifter downcanyon transport exiting the Chukchi shelf.

The observed flow over the shelf east of Hanna Shoal is not in complete agreement with the models that predict a mean clockwise flow around the south side of Hanna Shoal which then retroreflects to merge with the eastward flow over the central shelf and enter Barrow Canyon. Our observations suggest that the bottom flow is clockwise around the Shoal but that it does not continue south of Hanna Shoal. It appears, instead, that the bottom waters flow eastward and spill into the canyon. Quite possibly this spillage occurs over the entire western side of Barrow Canyon, although this cannot be determined from the observations.

The discrepancy between the models and observations pertains to the surface and vertically-averaged circulation on the east side of Hanna Shoal. The counterclockwise circulation in the surface layer northeast of Hanna Shoal is a consequence of the west to east divergence of the isobaths and the baroclinic pressure gradients over the shelf east of the Shoal. As the isobaths diverge the eastward geostrophic flow and the barotropic pressure gradient that forces this flow must weaken. We suggest that the weaker barotropic pressure gradient is opposed, and likely overwhelmed, in the upper ocean by baroclinic pressure gradients. These gradients arise because ocean densities decrease radially outward

from Hanna Shoal, as shown in hydrographic sections in Section F. The baroclinic pressure (and density) gradients are larger to the east of the Shoal than to its west because dilute surface waters are fed onto the eastern shelf occasionally. As noted, this fresher water may be surface waters from the shelfbreak, or it may be transported via the mean westward Ekman transport of dilute waters from Barrow Canyon and/or the Beaufort Sea shelf displayed in the drifter analysis (Section E). The latter mechanism is also illustrated by the mean monthly surface velocities for May, June, July, and August 2011 (Figure H24). Recall that in 2011, MW appeared absent in August and September from the shelf around Hanna Shoal. The data indicate that the surface flow along the western side of the canyon (mooring WBC indicated by the orange box) was westward while the other moorings in the canyon measured northeastward flow and the moorings over the central shelf indicated eastward flow toward Barrow Canyon. The surface waters advected westward from the canyon in 2011 were ACW (for the most part) and so were much fresher than the BSW waters transported through the Central Channel, which bathe the west side of Hanna Shoal in summer.

As a final note, the baroclinic pressure gradients weaken with depth and nearly vanish within the bottom layer of WW, so that the circulation below the pycnocline is primarily due to the barotropic pressure field and thus clockwise. The opposing barotropic and baroclinic pressure gradients are the reason why the flow field east of Hanna Shoal is vertically-sheared. The disposition of the barotropic pressure field around Hanna Shoal precludes transport between the central shelf and the shelf east of Hanna Shoal. In Spall's (2007) model this blockage occurs south of Hanna Shoal. Our data suggests that it occurs farther north and to the east, not to the south of the Shoal. Regardless of location, it effectively isolates the shelf east of Hanna Shoal from the central shelf. Our results also imply that the bottom waters on the shelf east of Hanna Shoal are renewed slowly. We estimate that the area between the 40 and 50 m isobaths on the

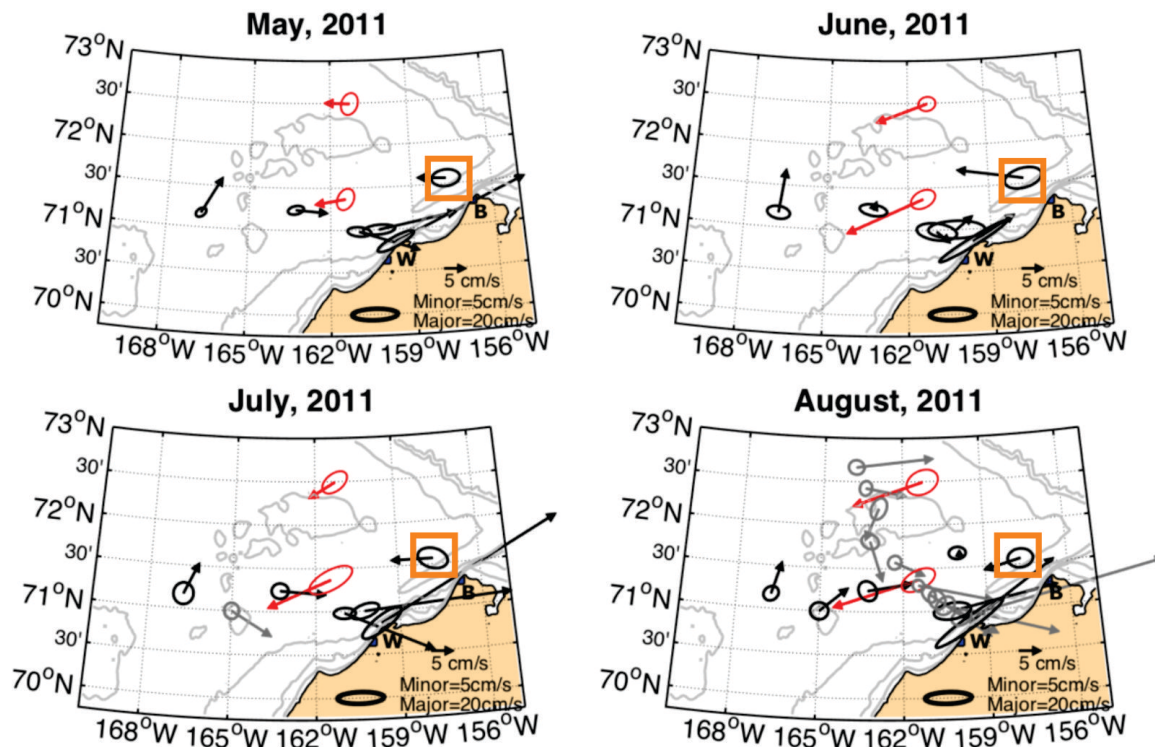


**Figure H24.** Mean monthly vectors and current ellipses (black) in the topmost ADCP bin (~7 m depth) for the months of May, June, July, and August 2011. Comparable quantities are shown for the winds in red. Mooring WBC is highlighted by the orange box in each figure. Gray ellipses and vectors indicate less than a full month's worth of data was available.

east side of the Shoal is  $\sim 10^{10} \text{ m}^2$ , and we assume that the mean thickness of the WW layer in this region is 20 m. The distance between moorings HSNE40 and HSNE50 is  $\sim 50 \text{ km}$ , and the mean bottom flow is  $\sim 1 \text{ cm s}^{-1}$ , which implies that the time scale for renewal of the deep water east of Hanna Shoal is  $\sim 8$  months. This is somewhat longer than Spall's (2007) estimate of 6 months for the time it takes water to flow from Bering Strait to the Chukchi shelfbreak.

We have examined the coherence scales associated with the circulation over the northeastern shelf by calculating the EOFs of the vertically-averaged velocity projected along the principal axis of variance at each mooring. We computed annual EOFs for three deployments: 2011 – 2012, 2012 – 2013, and 2013 – 2014. We chose these three years because they have reasonably good coverage around Hanna Shoal, the Central Channel, the central shelf, and Barrow Canyon. We have not used all the moorings in each year because EOFs are dependent upon the choice of inputs, in that the results can be biased by groups of similar moorings that are not present in all years. Interannual comparisons across years are made difficult if the sampling sites are not reasonably consistent from year-to-year. For this reason, we have eliminated all but one of the Barrow Canyon moorings and all of the industry moorings that extend westward from the Barrow Canyon array. We also eliminated the shallower moorings on the east and west sides of Hanna Shoal. Because of the irregular shape of the variance ellipses, EOF results at these moorings sites tend to be too noisy to add to our results. We conducted the EOF calculations at all depths and locations and find that the results are in basic agreement with the following depiction. Figures H25 – H27 show maps of the eigenvectors and the amplitude time series for the first three EOFs (which are statistically significant). Note that the length of the vector on each map is proportional to the eigenvector's weight at that location, and the direction is that of the major principal axis.

Vertically Averaged Currents, Rotated to Major Axis, 08/01/11 - 08/01/12

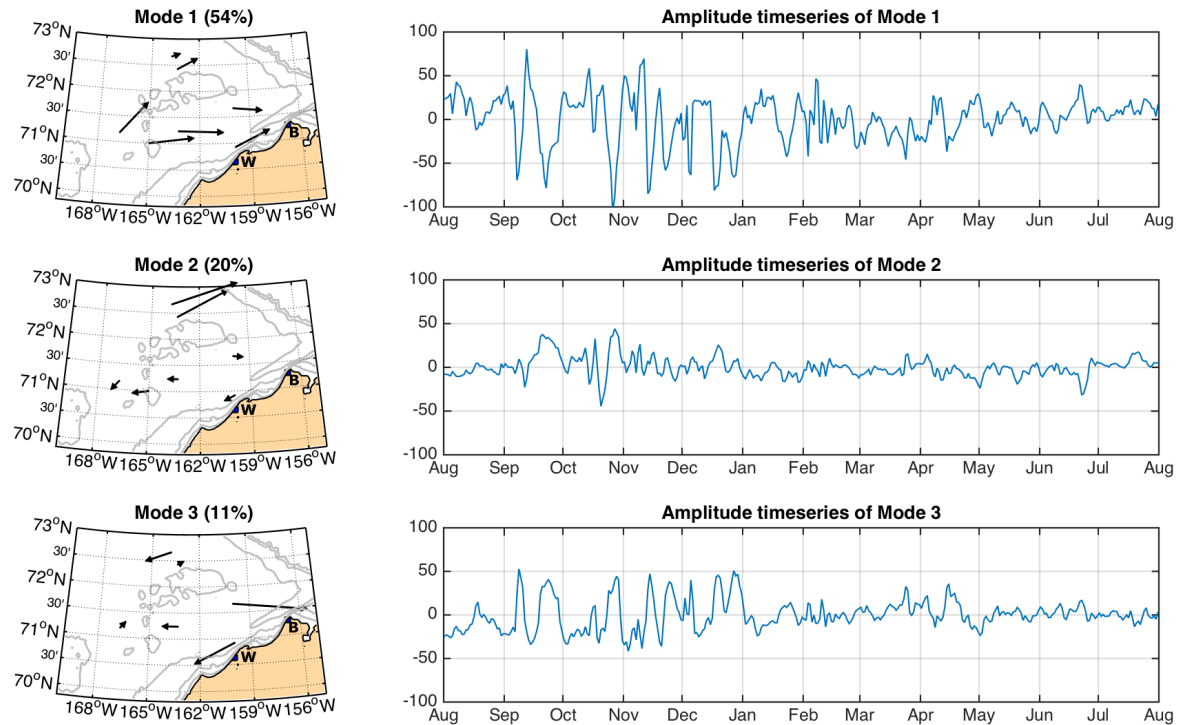


**Figure H25.** The first three EOF modes of the principal axis velocity component for the 2011 – 2012 mooring array.

Vertically Averaged Currents, Rotated to Major Axis, 08/01/12 - 08/01/13

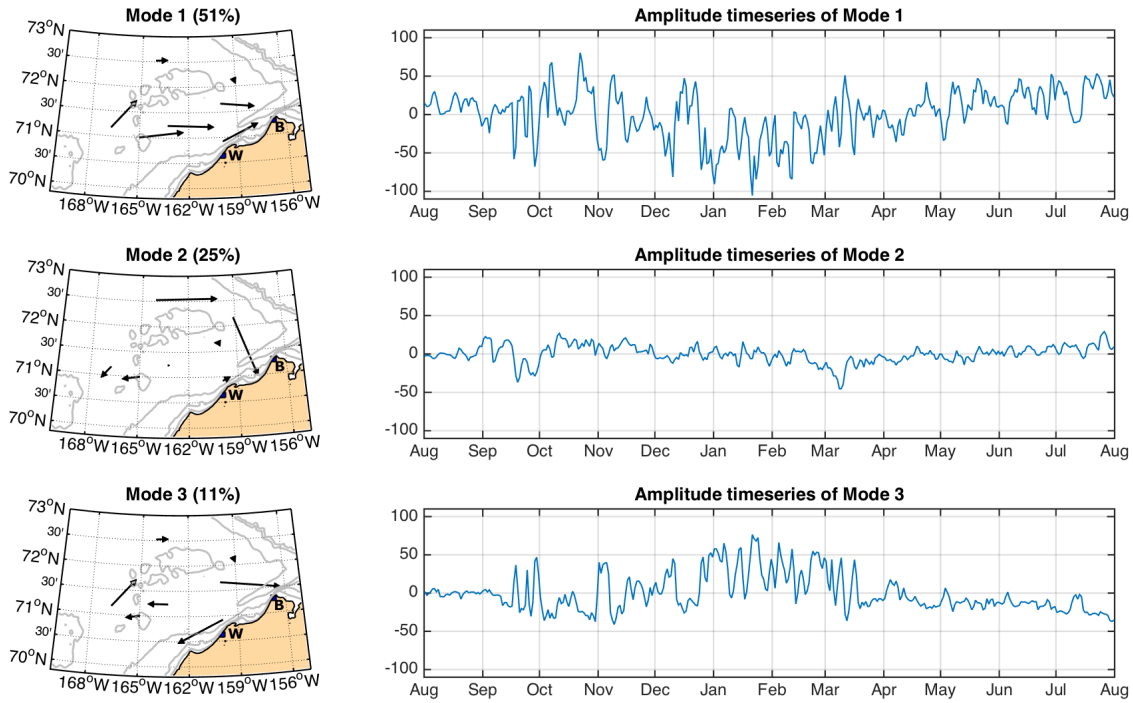


**Figure H26.** The first three EOF modes of the principal axis velocity component for the 2012 – 2013 mooring array.

Vertically Averaged Currents, Rotated to Major Axis, 08/01/13 - 08/01/14

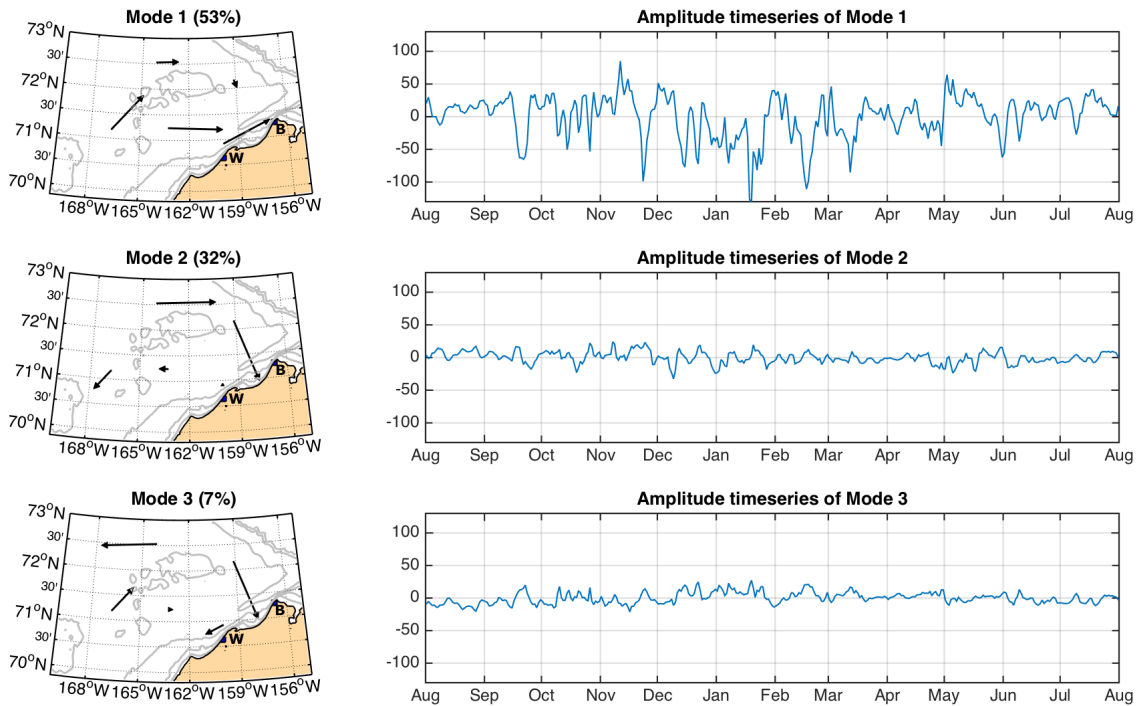


**Figure H27.** The first three EOF modes of the principal axis velocity component for the 2013 – 2014 mooring array.

In all years, the first mode explains 50 – 55% of the variance. The velocity fluctuations are coherent and in-phase everywhere except on the northeast side of Hanna Shoal. The eigenvector weights are largest south of Hanna Shoal, e.g., in the Central Channel, central shelf, and Barrow Canyon. The second mode explains 20 – 30 % of the variance. It captures out-of-phase motions between the north and south sides of Hanna Shoal, and its weights are largest on the northwest and northeast sides of Hanna Shoal. Interestingly, the eigenvector weight for the mooring directly east of Hanna Shoal (CPAI02) is small for this mode. Mode 3 captures ~10% of the variance. Current fluctuations between the central shelf and Barrow Canyon are in-phase with one another but out-of-phase with those in the Central Channel. The relationship between these fluctuations and those around Hanna Shoal are a bit confusing, although it appears that the fluctuations on the shelf east of Hanna Shoal are also out-of-phase with those over the central shelf and Barrow Canyon.

The corresponding modal amplitude time series indicate that the largest fluctuations are in the fall and winter months. As it turns out, all modes are significantly correlated with the along-canyon component of the winds discussed in Section D with respect to the transport in Barrow Canyon. The correlation coefficients range from 0.51 (2011 – 2012) to 0.64 (2013 – 2014) between this wind component and Mode 1. The most straightforward explanation for this relationship is that the currents south of Hanna Shoal fluctuate in response to variations in the strength of northeasterly winds, while there is a more limited response to these winds around Hanna Shoal. For Mode 3, the correlation coefficients are all negative and range from -0.37 (2013 – 2014) to -0.58 (2012 – 2013). We suspect that this relationship indicates that there are periods when the winds reverse the currents in Barrow Canyon and the central shelf but not those within the Central Channel. We do not have satisfactory explanations for the Mode 3 response around Hanna Shoal to the winds. The wind Mode 2 correlations were quite variable: -0.38 (2011 – 2012), +0.18 (2012 – 2013), and -0.30 (2013 – 2014). We cannot provide a satisfactory explanation for this correlation but note that it explains less than 20% of the variance in Mode 2.

We have also extended the EOF analyses to include data from Bering Strait collected by R. Woodgate (U. Washington) between 2011 and 2014. These results are shown in Figures H28 – H30 and summarized as follows. In all years, Mode 1 explains about 50% of the current variance and suggests coherence and in-phase fluctuations in Bering Strait, the Central Channel, Barrow Canyon, and the northwest side of Hanna Shoal. The structure of Mode 1 is very similar to that of Mode 1 using only the moorings in the northeast Chukchi Sea and is significantly correlated with the winds over the northeast Chukchi Sea. The correlations range from 0.4 (2011 – 2012) to 0.6 (2012 – 2013) and thus explain from 16 to 36% of the total flow variance. Mode 2 explains from 18 – 27% of the variance, and its structure is very similar to that using only the moorings over the northeast shelf. In fact, it appears to be confined to the northeastern shelf insofar as the modal weights in Bering Strait are very small. Mode 2 correlations with the winds are nearly identical to the Mode 2 results using only the northeastern Chukchi moorings. Finally Mode 3 explains from 10 – 12% of the total variance. The modal structure varies from year-to-year, but generally shows, weak northward or strong southward flow in Bering Strait and the Central Channel and either out-of-phase or in-phase flow regimes in Barrow Canyon and the northwest side of Hanna Shoal. The correlations with the winds vary from year-to-year and are 0 – 0.4 in 2011 – 2012, and 0.46 and 0.4 in 2012 – 2013 and 2013 – 2014, respectively.

Figures H31 to H33 explore in more detail the correlations between the northward currents in Bering Strait and flow along the principal axes in the Central Channel (using the Crackerjack mooring), Burger, and in Barrow Canyon, respectively. The correlations are expressed via the coherence and phase spectra, which quantify the strength of the correlation and phase differences as a function of period. Currents in Bering Strait are generally coherent at all periods with those in the Central Channel (Figure H31), with the coherence generally stronger at longer periods (>10 days) than shorter periods. Coherence is generally stronger in the October – April (winter) period than for the (May – September) (summer) period. At

Vertically Averaged Currents, Rotated to Major Axis, 08/01/11 - 08/01/12, Daily

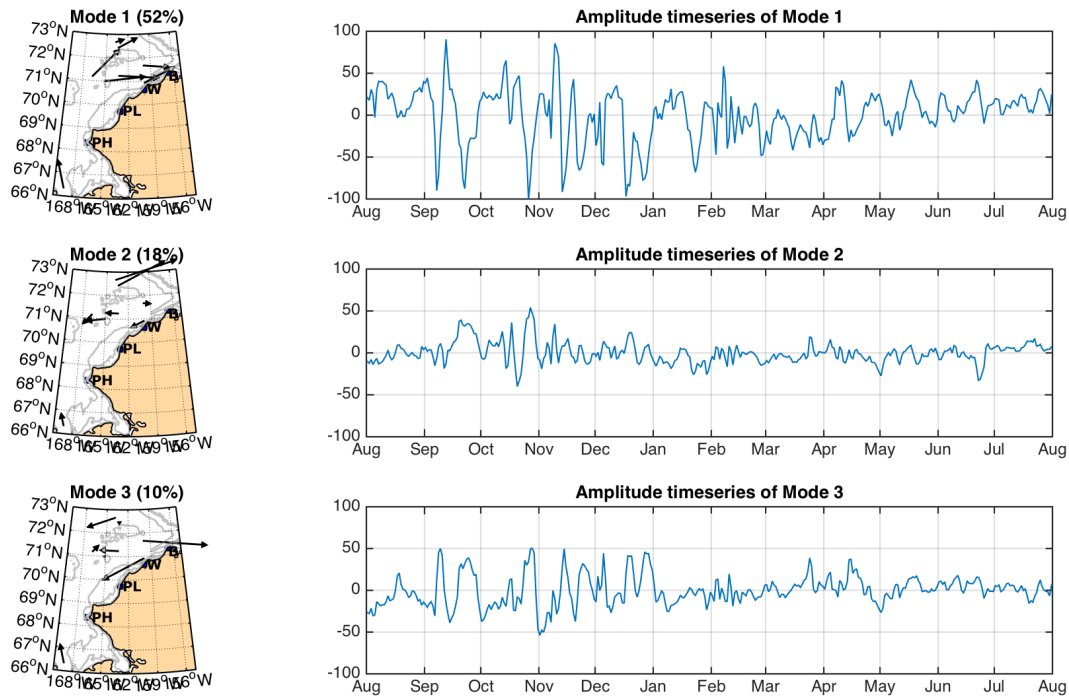


**Figure H28.** The first three EOF modes of the principal axis velocity component for the 2011 – 2012 mooring array, which includes Bering Strait.

Vertically Averaged Currents, Rotated to Major Axis, 08/01/12 - 08/01/13, Daily

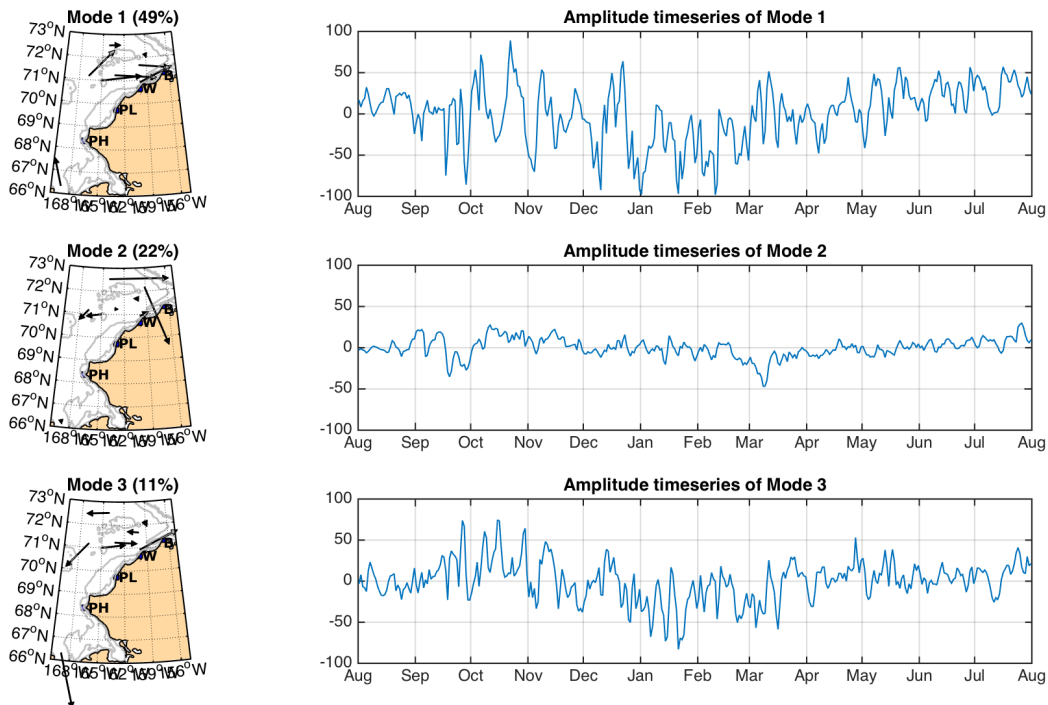


**Figure H29.** The first three EOF modes of the principal axis velocity component for the 2012 – 2013 mooring array, which includes Bering Strait.

Vertically Averaged Currents, Rotated to Major Axis, 08/01/13 - 08/01/14, Daily

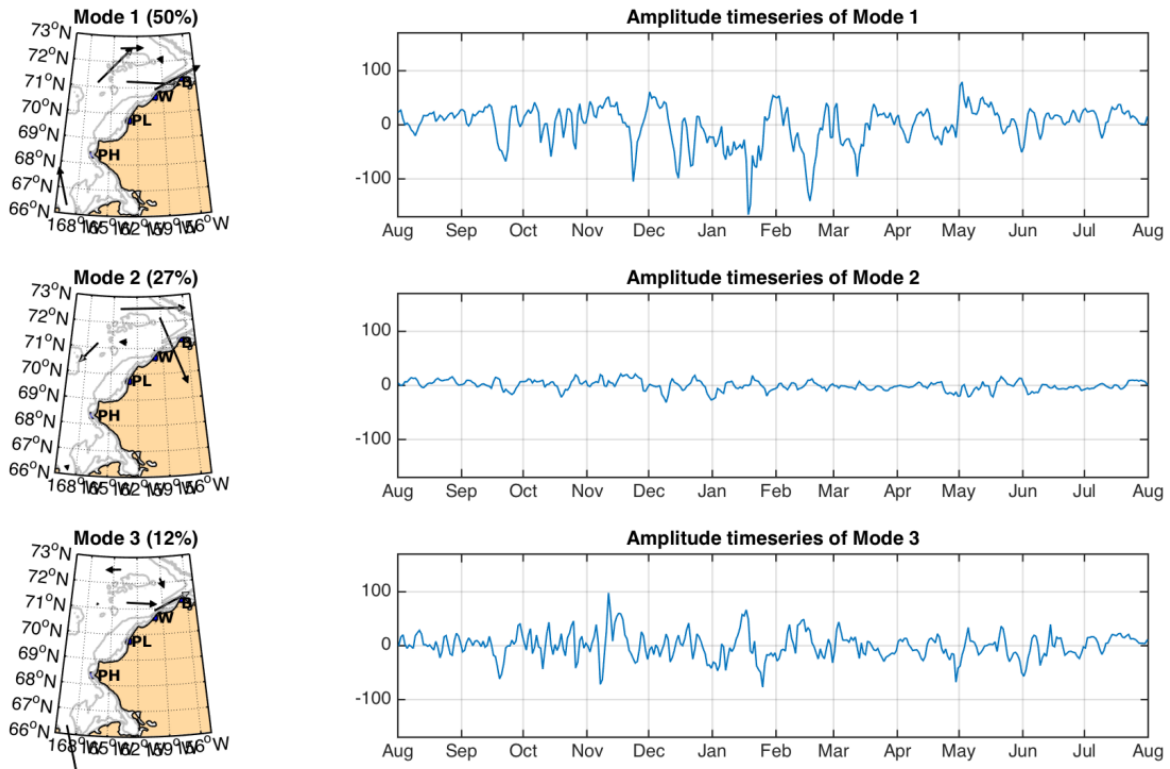


**Figure H30.** The first three EOF modes of the principal axis velocity component for the 2013 – 2014 mooring array, which includes Bering Strait.

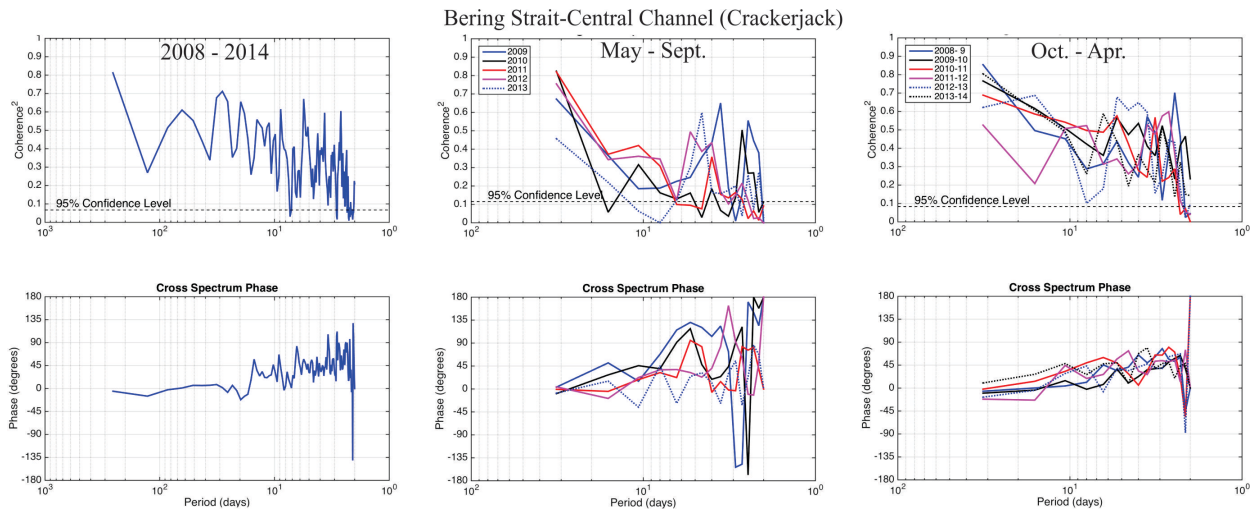


**Figure H31.** Cross-spectral results between vertically averaged currents in Bering Strait and the Central Channel for the entire 2008 – 2014 record (left), the individual May – September periods (middle), and the October – April periods (right). Top panel is coherence-squared and bottom panel is the phase.

longer periods the currents are in-phase, whereas at shorter periods, Bering Strait leads the Central Channel by about 1 day. Similar results were obtained for the Bering Strait and Burger records (Figure H32), although coherences between Burger and Bering Strait are slightly lower overall. Among these mooring pairs the strongest coherence was between Bering Strait and Barrow Canyon at all periods >2 days, with the coherence stronger in winter than summer. We attribute the stronger coherence between the Bering Strait and Barrow Canyon pair compared to the other pairs to shelf wave dynamics associated with the coastal waveguide. Burger and the Central Channel are outside or at best, at the edge of the waveguide, whereas the moorings in both Bering Strait and Barrow Canyon are well within one barotropic radius of deformation. The coherence results for Bering Strait and Barrow Canyon are very consistent with the conclusions of Section D regarding the influence of continental shelf waves propagating northward from the Bering Sea and influencing transport fluctuations in Barrow Canyon.

All the coherence spectra indicate that there is considerable interannual variability in the coherence structure of the shelf circulation field. For example, for the May – September period in 2013, current fluctuations in Bering Strait at ~10 day periods were incoherent with those in the Central Channel, while in 2011 the currents were significantly coherent with one another for this period. The reasons for this are not apparent and would take additional effort to understand. Most likely they are associated with the interplay amongst atmospheric forcing, ice patterns, and stratification.

We have sufficiently long and concurrent data at Barrow Canyon, Crackerjack, and the two central shelf sites CPAI01 (and Site 1) and Burger (Bu) to construct a tentative climatological annual cycle based on the monthly means (Figure H34). The figure contains the annual cycle in transport based on the 2010 – 2015 data from Barrow Canyon discussed in Section D and, from the 2010 – 2014 period, the mean monthly velocities projected along the principal axes at the remaining sites. Each site manifests an annual cycle. At Barrow Canyon and the central shelf sites (CPAI01 and Burger), the maximum is on July and August and the minimum is December and January. These minima are negative, implying a reversal in the direction of the flow. The Central Channel differs from these sites in two important ways. First, its annual maximum occurs from May through July, and its minimum occurs from September through December. Consequently, the annual cycle at all sites except Crackerjack is in-phase with the annual cycle in Bering Strait transport (where the monthly averages are all northward). Second, the mean flow in each month is positive (e.g., toward the north-northeast) so that the mean monthly flow never reverses, similar to Bering

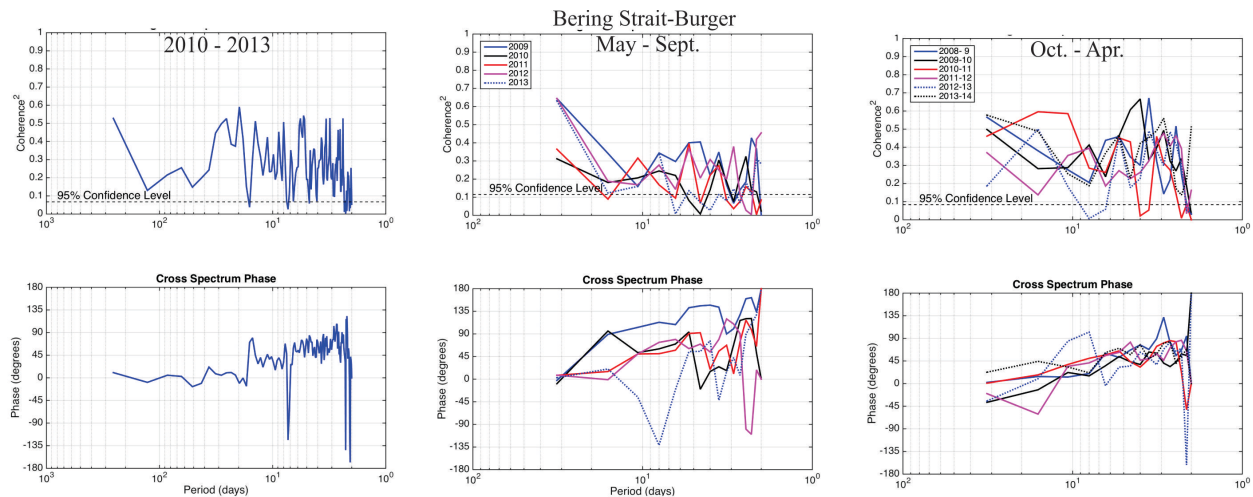


**Figure H32.** Cross-spectral results between vertically averaged currents in Bering Strait and the Burger for the entire 2010 – 2013 record (left), the individual May – September periods (middle), and the October – April periods (right). Top panel is coherence-squared and bottom panel is the phase.

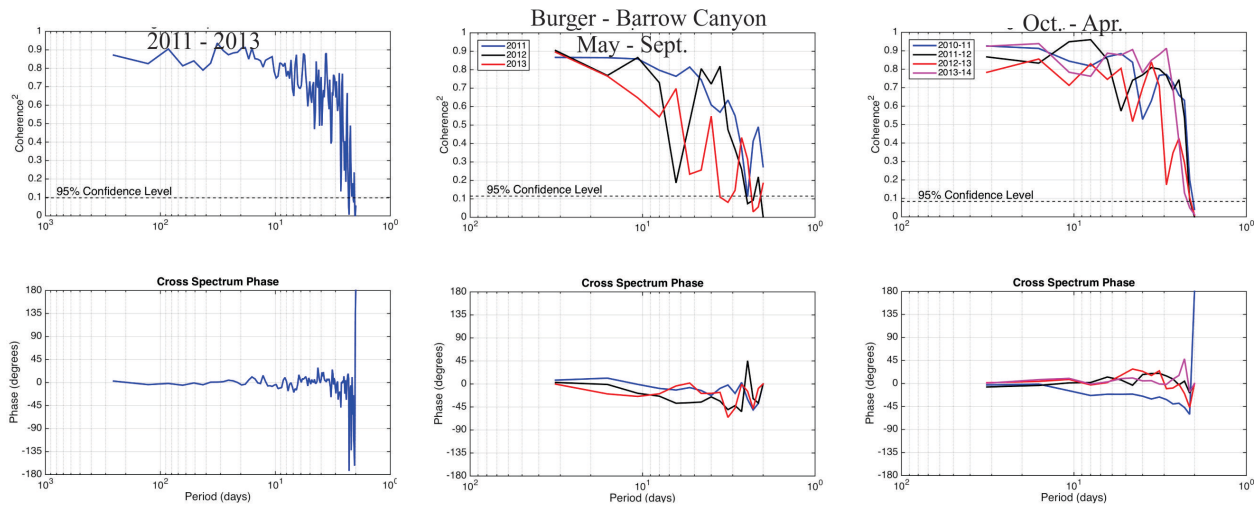


**Figure H33.** Cross-spectral results between vertically averaged currents in Bering Strait and Barrow Canyon for the entire 2011 – 2013 record (left), the individual May – September periods (middle), and the October – April periods (right). Top panel is coherence-squared and bottom panel is the phase.

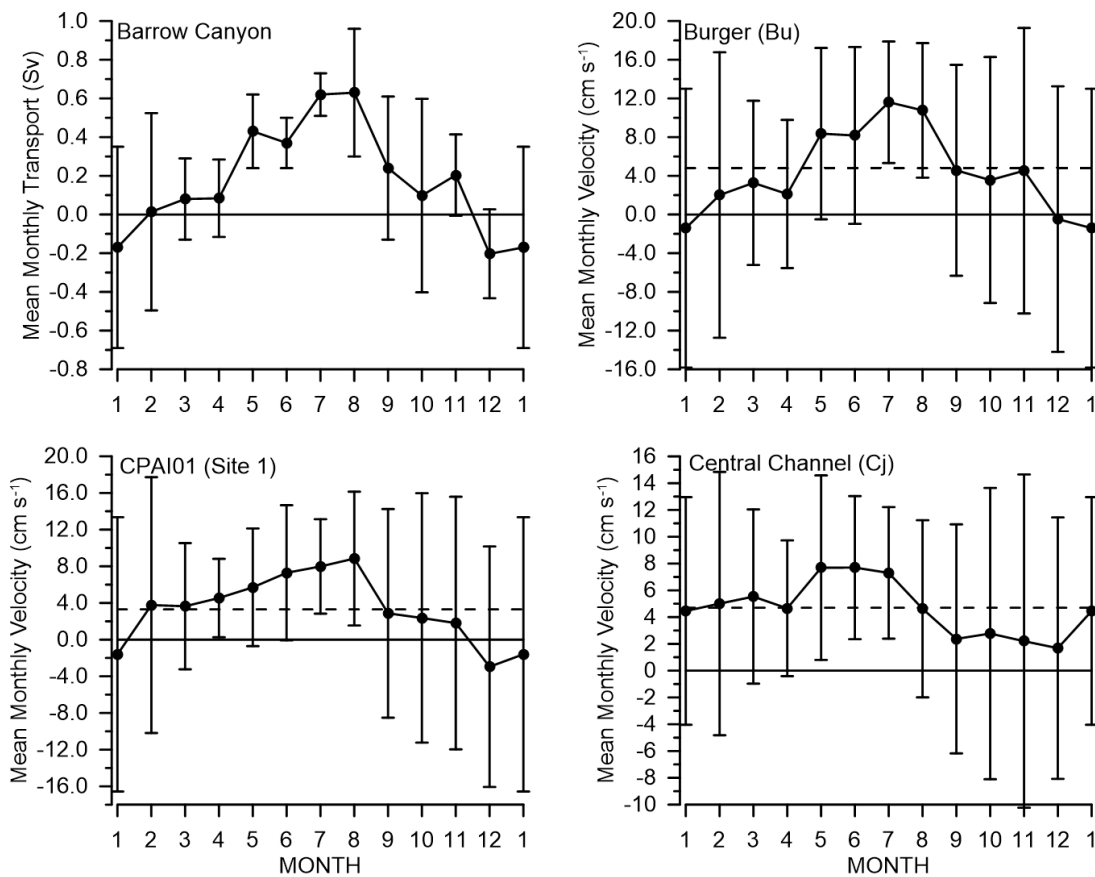


**Figure H34.** Climatological annual cycle based on mean monthly values of Barrow Canyon transport (top left) and vertically-averaged velocities projected along the principal axis at moorings over the central shelf: Burger (Bu), CPAI01 (previously called Site 1), and in the Central Channel at mooring Crackerjack (Cj). Dotted horizontal lines on the velocity figures denote the annual mean.

Strait but unlike the other sites. This implies that the entire Chukchi shelf transport must reorganize itself seasonally. Reversals in Barrow Canyon imply westward flow over the central shelf and, based on HFR measurements, southwestward flow along the Alaskan coast. Because the transport remains northward in Bering Strait, reversals in Barrow Canyon and the central shelf imply that this water must escape the Chukchi Sea through either the Central Channel and/or Herald Canyon. In a climatological sense, these seasonal events must mirror the shorter-lived and massive coastal upwelling events documented in Section E based on surface drifters in August 2013 and 2014 (and in Section D based on Barrow Canyon transports). During those events, nearshore waters were transported into the Central Channel and/or into the western Chukchi Sea and ultimately Herald Canyon.

## H.5.2 Chukchi Sea Shelf and Alaskan Beaufort Sea Shelfbreak

In this section we examine the connection between Barrow Canyon transport as determined from BC2 with the long-term mooring supported by NSF’s Arctic Observing Network Program at 152°W (mooring BS3) on the Beaufort Sea shelfbreak (Nikolopoulos et al. 2009). Data from the latter are available from 2008 – 2014 and from the former from 2010 – 2015. Thus the datasets overlap from August 2010 through August 2014. Figure H35 shows the mean monthly transports from both moorings are correlated with one another.

The coherence and phase spectra (Figure H36) show that BC2 and BS3 are significantly coherent, especially at periods from 2 to 35 days. Overall transport fluctuations in Barrow Canyon explain ~65% of the transport variance at BS3 for periods of 2 to 30 days, with BC2 fluctuations leading those at BS3 by <0.5 day. As found for the shelf sites, the coherence is poorer in summer than in winter, and there is interannual variability in the coherence spectra.

The coherence calculations suggest that BS3 transports can be predicted from the Barrow Canyon transport as illustrated by the linear regressions of the transport between BS3 and BC2 on both a monthly (Figure H37) and daily (Figure H38) basis. As expected the predictability is better in winter than in summer and when using the mean monthly values. The regression using the monthly means is significant at the 95% confidence level with BC2 explaining ~66% of the transport variance at BS3 (Figure H1). Note also that BC2 transports are, on average ~5 times greater than the BS3 transports. The regression intercept indicates that the transport at BS3 is weakly westward when there is no transport in the canyon. The fits are noisier, although still significant, when using the daily values. Seasonally the regressions are better in the fall and winter months than for the May – September period. These differences are consistent

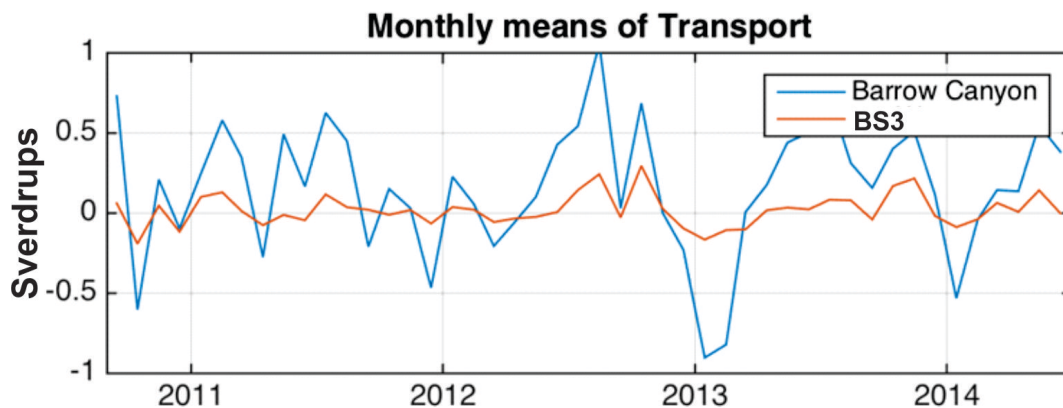
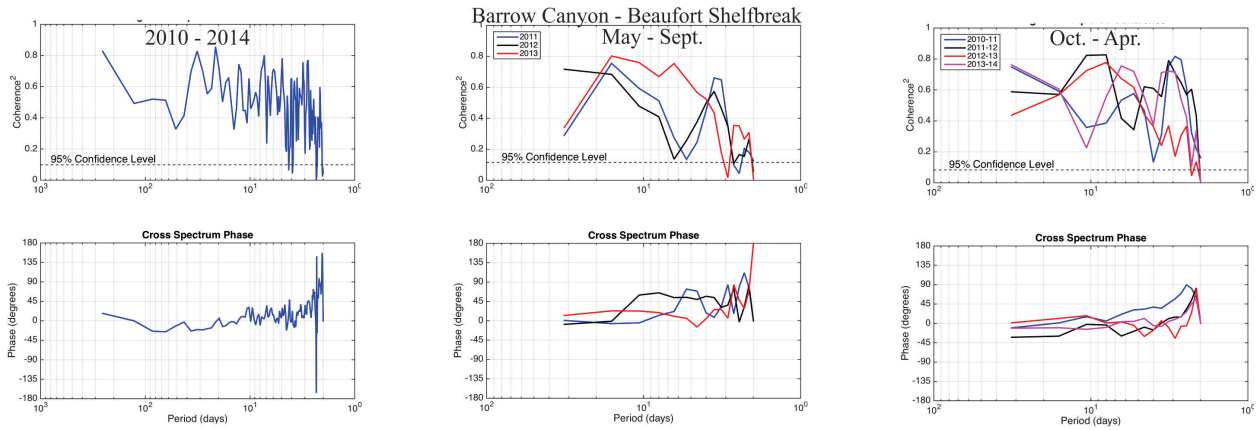
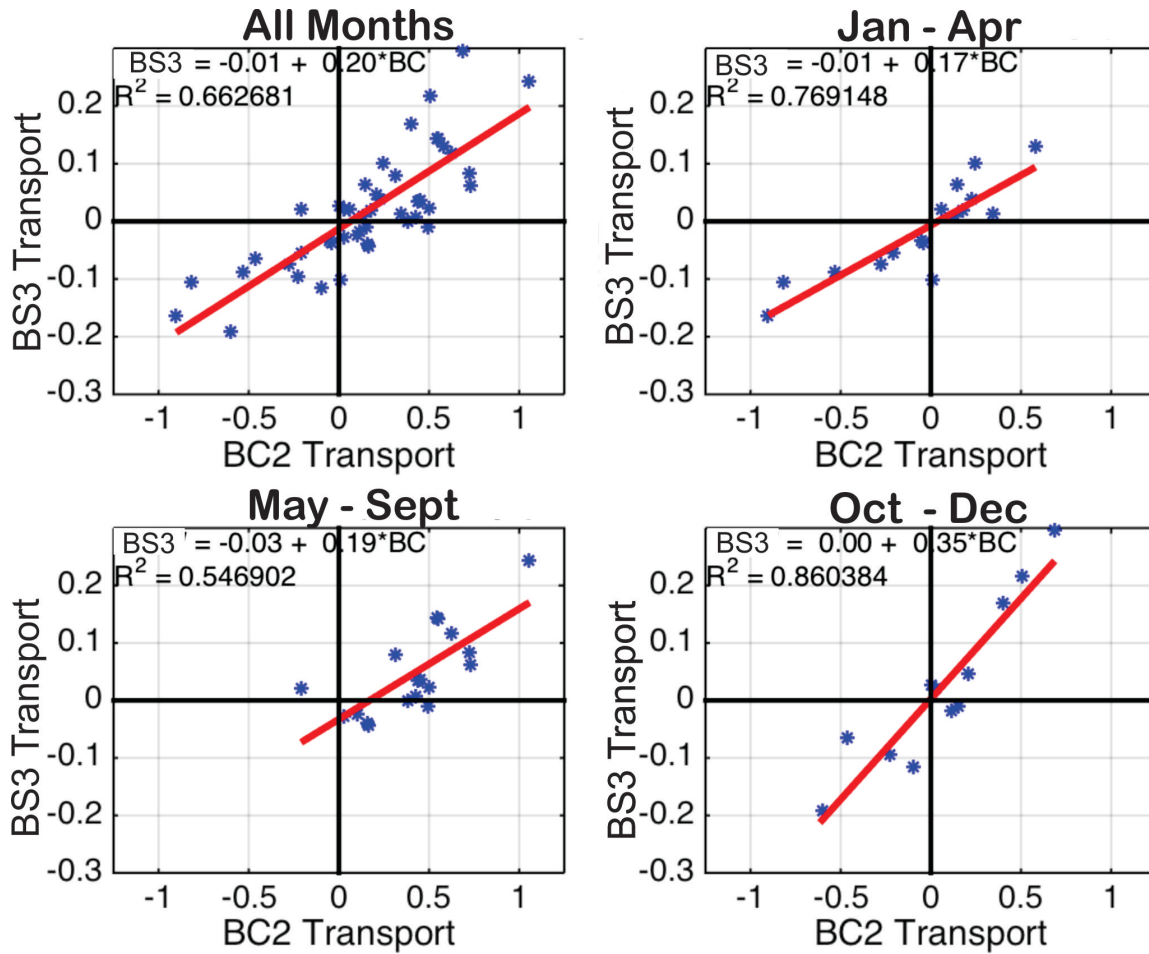


Figure H35. Mean monthly transports at BC2 (blue) and BS3 (red) in Sverdrups.



**Figure H36.** Coherence squared and phase spectra of mean daily transports at Barrow Canyon and along the Beaufort shelfbreak for the entire record (left), May – September (middle) and October – April (right).



**Figure H37.** Linear regressions of BS3 against BC2 mean monthly transports for all months (upper left), January – April (upper right), May – September (lower left), and October –December (lower right).

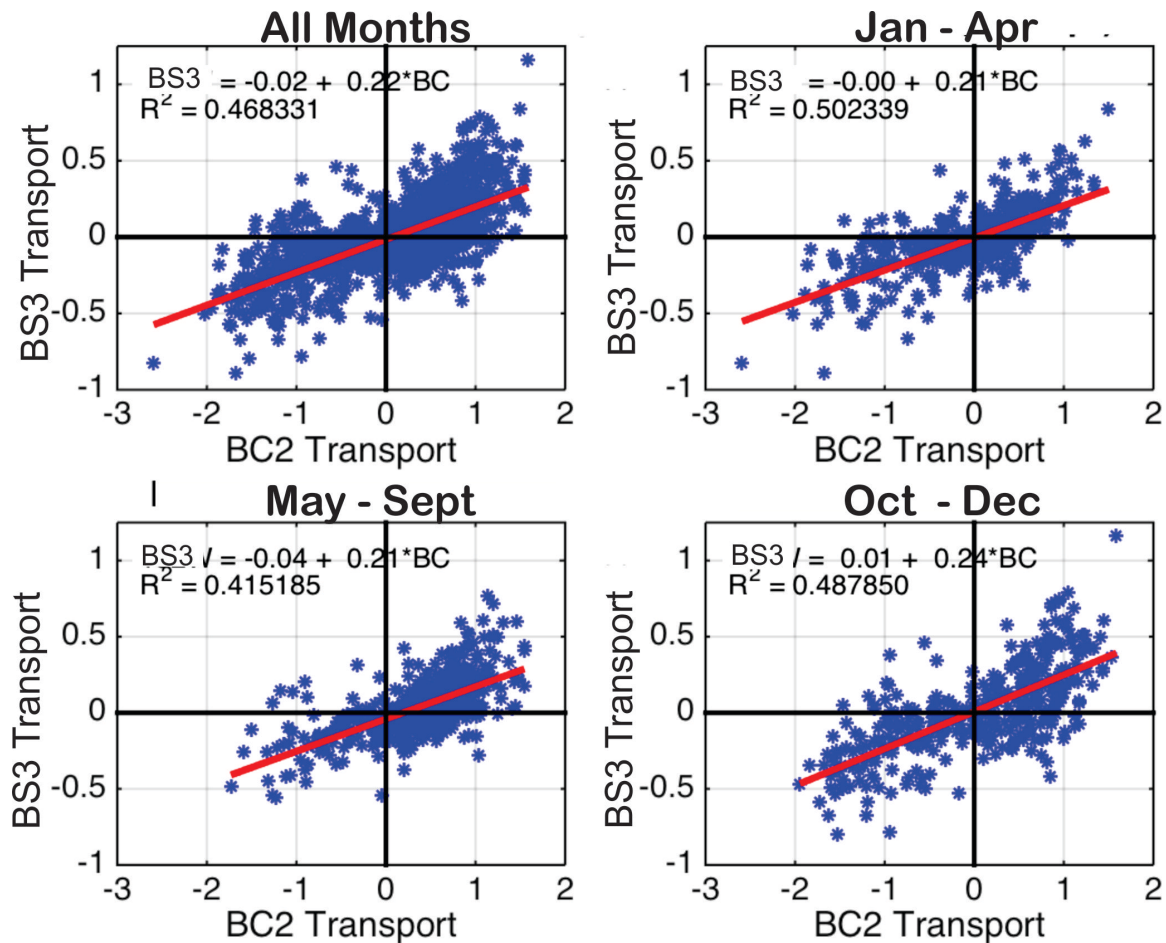


**Figure H38.** Linear regressions of BS3 against BC2 daily mean transport for all months (upper left), January – April (upper right), May – September (lower left), and October – December (lower right).

with Weingartner et al. (2017a) who found that wind-Barrow Canyon transport regressions are better in fall and winter than in summer. Weingartner et al. (2017a) argued that the seasonal differences are likely associated with the more complicated dynamics associated with enhanced stratification in the summer months.

We have also quantified the frequency distribution of four different flow configurations, or regimes. These are defined as follows based on the mean daily transports at each site:

1. Regime 1, northeastward (or downcanyon) at BC2 and eastward at BC3;
2. Regime 2, northeastward at BC2 and westward at BS3;
3. Regime 3, southwestward (upcanyon) at BC2 and westward at BS3;
4. Regime 4, southwestward at BC2 and eastward at BS3.

The results, summarized in Table H1, indicate that about half of the time Regime 1 holds, e.g., downcanyon flow coincides with eastward transport along the Beaufort shelfbreak. However, nearly 20% of the time the flow along the Beaufort shelfbreak is westward while the flow is northeastward in the canyon. This implies a convergence in transports at the mouth of the canyon. Regime 3 occurs 27% of the time and suggests some degree of continuity in the transport with Beaufort shelf waters possibly feeding

**Table H1.** Number of days observed and the frequency of occurrence of different flow regimes in Barrow Canyon (BC2) and the Beaufort shelfbreak (BS3).

Regime	BC2	BS3	Days	Percent
1	Northeastward	Eastward	666	47%
2	Northeastward	Westward	297	21%
3	Southwestward	Westward	390	27%
4	Southwestward	Eastward	69	5%

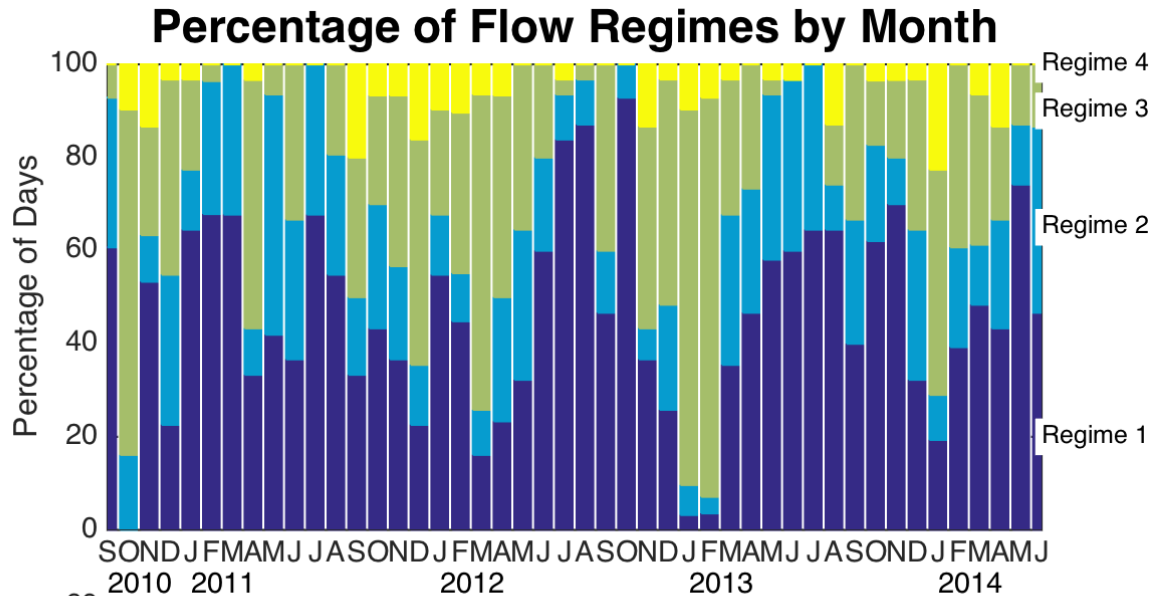
upcanyon flows. Regime 4 occurs only 5% of the time and implies discontinuous or divergent flow between the canyon and Beaufort shelfbreak.

The frequency of occurrence of the flow regimes varies from month-to-month and interannually as shown in Figure H39. The figure suggests that Regime 1 dominates in summer months and occurs less frequently in the winter months when Regimes 2 and 3 are more abundant. There is considerable variability from month-to-month in the regime occurrences. There are several months when the transport is almost entirely positive at both locations (Regime 1: June, July, and October 2012) or entirely negative at both (Regime 3: October 2010 and January and February 2013). Regime occurrence can vary by >50% from month-to-month.

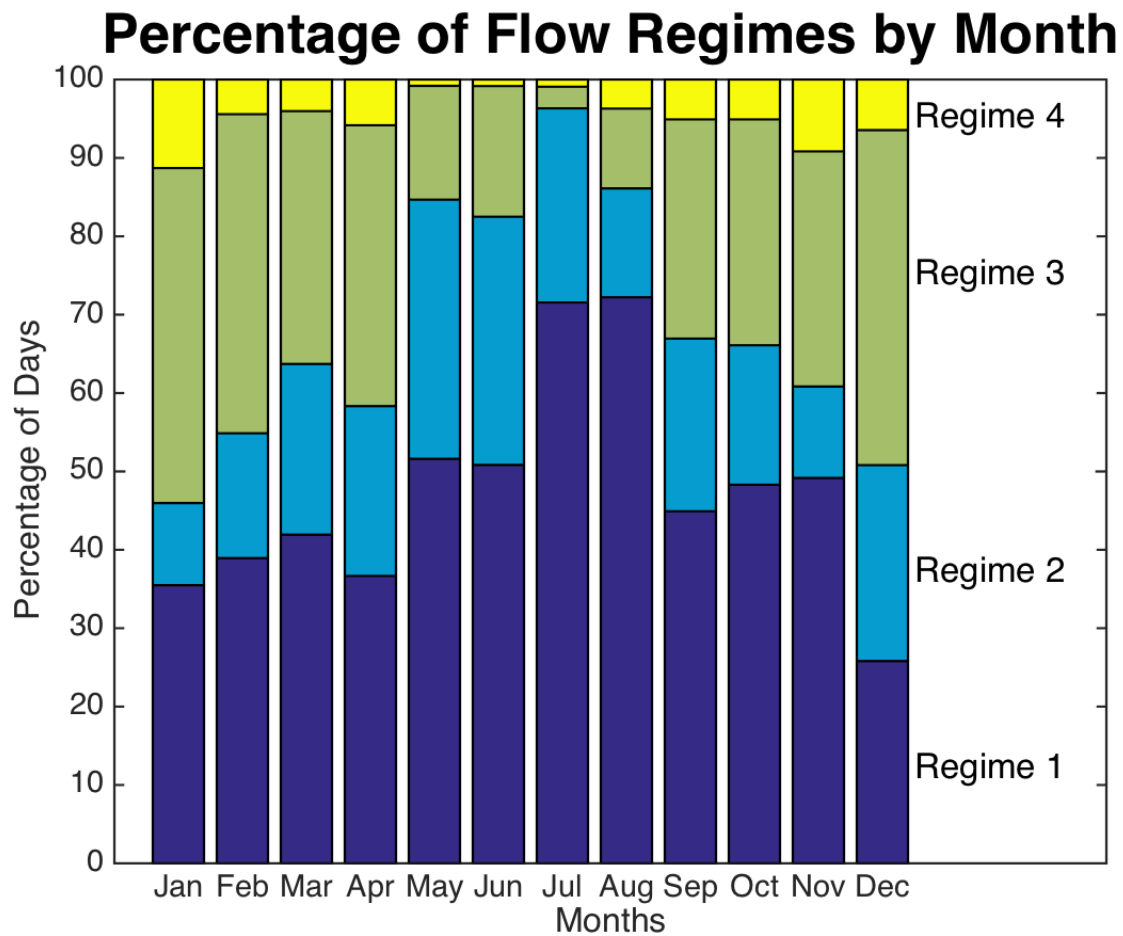
We investigated the annual cycle in regime occurrences by preparing bar charts that summarize the percentage of days that each regime occurs in each month for the whole record and then combine these into mean monthly histograms to form a climatology (Figure H40). Regime 1 dominates during the May – September period, and Regimes 3 and 4 occur most frequently in the winter months, while Regime 2 is more equitably distributed throughout the year.

Figure H41 shows the frequency of occurrence of regimes as a function of the direction *toward* which the wind is blowing at the National Weather station in Barrow (PABR). Regime 1 occurs more than 50% of the time when winds are blowing from the southern sectors. Regime 2 can occur under any wind direction but mostly when the winds are blowing toward the west. Regime 3 dominates when the winds are from the north and northeast. A similar exercise was conducted for 2013 HFR surface currents (Figure H42). The surface flow was found to be westward nearshore for nearly all wind directions, other than when winds were from the southwest, when the nearshore surface flow was generally eastward.

Our results indicate that only a fraction of the mean transport of 0.2 Sv flowing downcanyon in Barrow Canyon feeds the eastward shelfbreak current. Indeed the mean transport computed at BS3 over these years was ~0.025 Sv eastward or <15% of the mean canyon transport. (The transport along the Beaufort shelfbreak has apparently decreased substantially since 2003 due to an increase in easterly winds over the Beaufort Sea (Brugler et al. 2014)). This result is surprising insofar as geostrophic dynamics require that the canyon transport should exit the canyon and proceed eastward along the shelfbreak in its entirety. Our results imply that other dynamics are dominating, which prevent the canyon outflow from proceeding eastward. These dynamics must cause the canyon outflow to either turn westward or to enter the basin shortly after exiting the canyon, before the outflow reaches 152°W. We cannot address the fate of the canyon outflow with existing data, but Nof (1988, 1991) and Watanabe et al. (2011) showed that the fate of the outflow can be quite variable and is dependent upon the potential vorticity structures of the outflow, the receiving basin, and the continental slope. The PV structures within each region most certainly change on synoptic and seasonal time scales in response to the winds and in conjunction with the vertical and horizontal density structures in each region.



**Figure H39.** Monthly distribution of flow regimes.



**Figure H40.** Annual cycle of the four flow regimes characterizing transports in Barrow Canyon and the Beaufort shelfbreak.

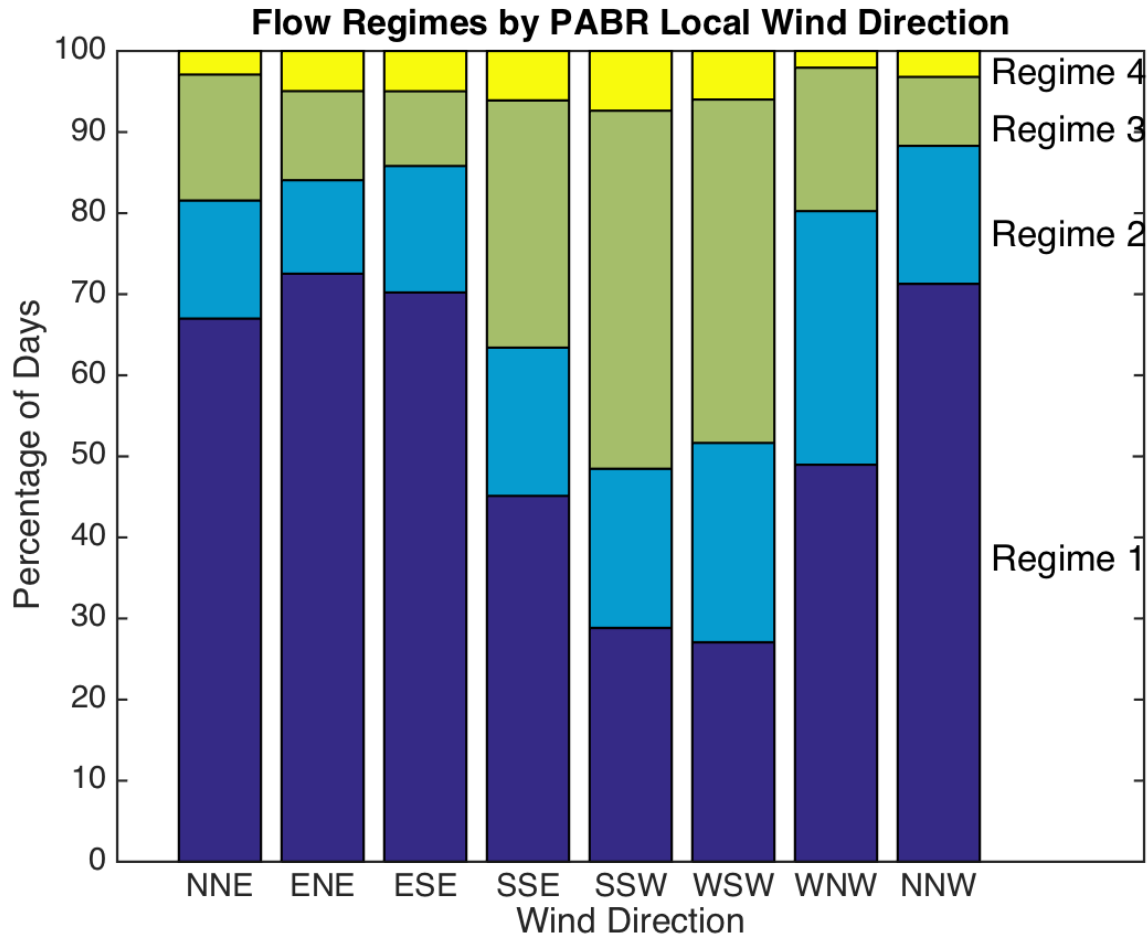


**Figure H41.** Frequency of occurrence of regimes as a function of the direction toward which the wind at Barrow (PABR) is blowing.

The coherence calculations between Bering Strait and Barrow Canyon and between Barrow Canyon and the Beaufort shelfbreak suggest that Bering Strait and the Beaufort shelfbreak might also reflect coherent motions. Dynamically, we expect that wavelike motions excited in the Bering Sea or Bering Strait should propagate along the shelfbreak as well. Consequently, we computed the coherence and phase spectra between Bering Strait and the Beaufort shelfbreak (Figure H43). These spectra indicate that there is some coherence between these two regions at periods less than 30 days, with fluctuations in Bering Strait leading those along the Beaufort shelfbreak by ~0.5 days. As with the other pairwise coherence tests the results vary seasonally, with coherence being better in the fall and winter months than in summer. There is also considerable interannual variability evident in the results. Understanding this variability will require additional analyses using models.

We conclude this section by briefly characterizing the tides over the Chukchi Sea shelf. We computed the tidal ellipse properties and phases of four semidiurnal ( $M_2$ ,  $S_2$ ,  $N_2$ , and  $K_2$ ) and four diurnal ( $O_1$ ,  $K_1$ ,  $P_1$ , and  $Q_1$ ) tidal constituents following Foreman (1978). The results are listed in Appendix B, which includes the number of deployments used in the estimations. Figure H44 displays a map of the tidal ellipses. In some locations the constituents were unresolvable because either the record length or the signal to noise ratio was too small to yield reliable results.

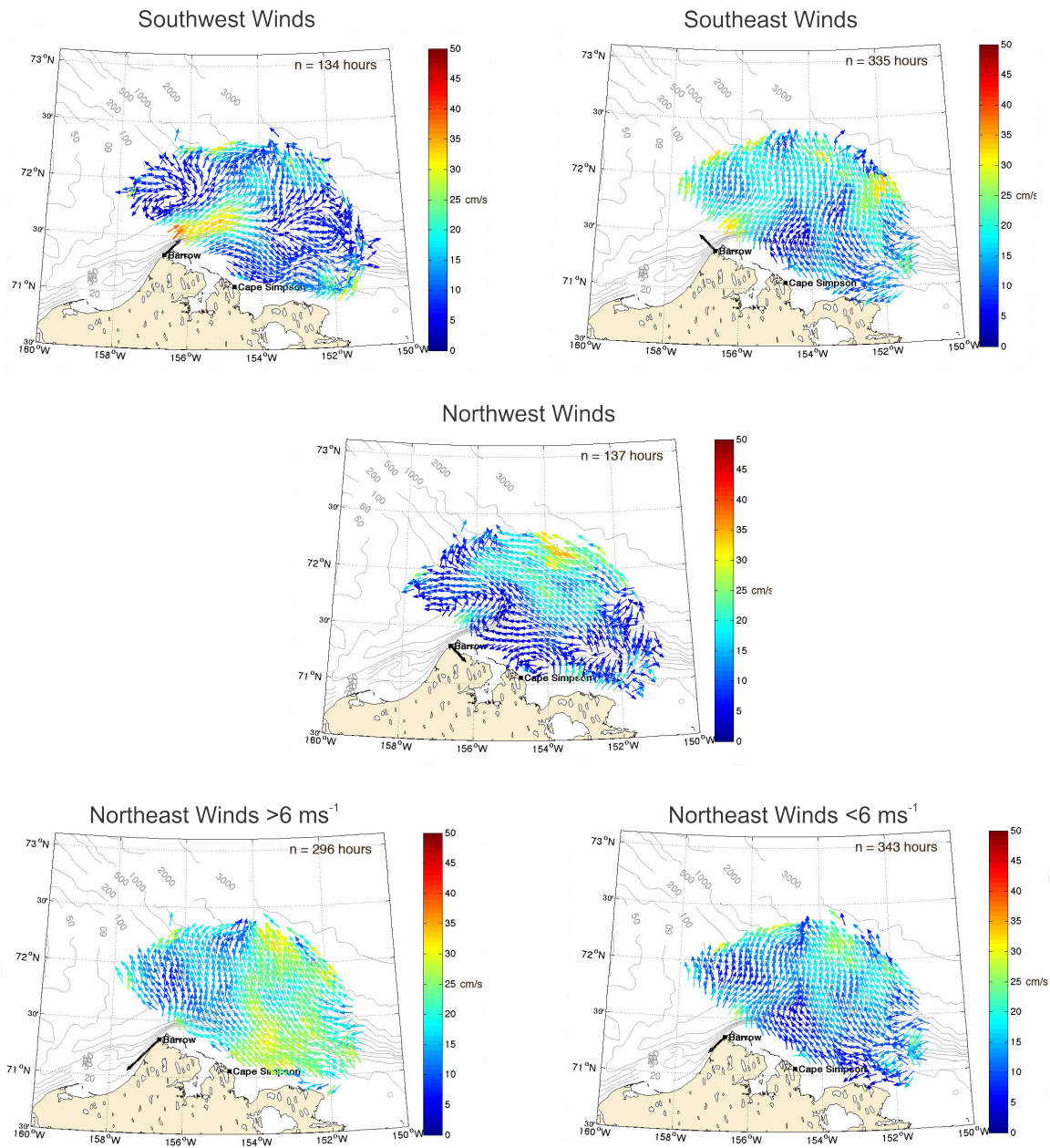


**Figure H42.** Mean surface currents estimated from the Point Barrow and Cape Simpson HFR system under different wind conditions in 2013. The number of hours under which a given wind condition prevailed is indicated in the upper right hand corner of each map.

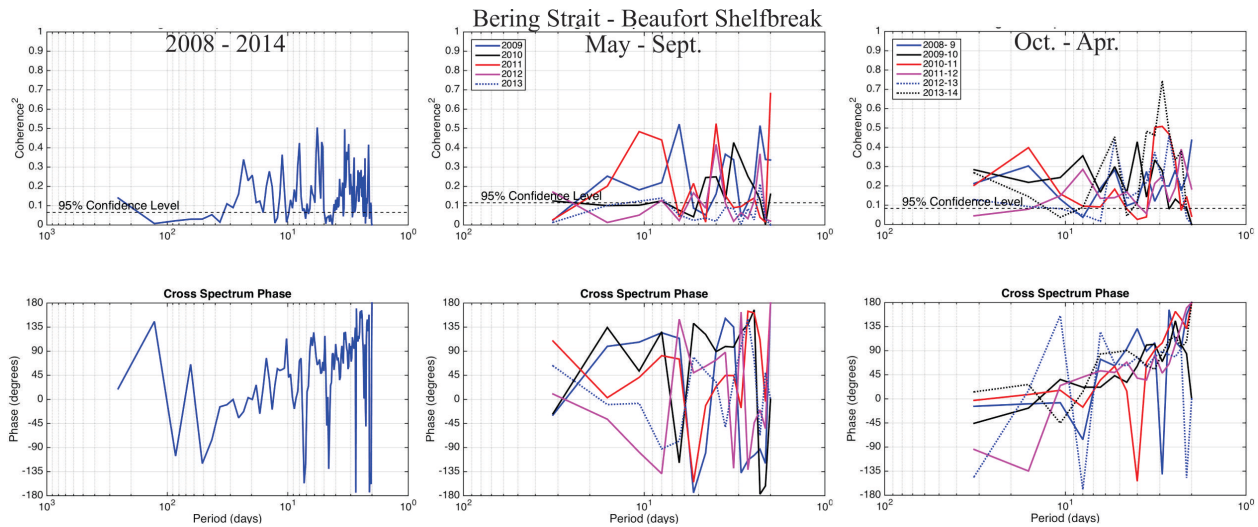


**Figure H43.** Coherence squared and phase spectra of mean daily transports at Bering Strait and along the Beaufort shelfbreak for the entire record (left), May – September (middle), and October – April (right).

The  $M_2$  tide was the dominant tidal constituent over most of the shelf, although the associated currents were small ( $\leq 4 \text{ cm s}^{-1}$ ).  $M_2$  current magnitudes were largest west and south of Hanna Shoal and diminished to  $\sim 1 \text{ cm s}^{-1}$  or less in Barrow Canyon. The  $S_2$  currents were  $\leq 2 \text{ cm s}^{-1}$ ; however, this constituent was largest on the shelf northeast of Hanna Shoal and, in fact, was larger than the  $M_2$  currents in this location. The reason for this is unclear but it may be related to resonant interaction of the sub-inertial  $S_2$  wave with the sloping bottom in the vicinity of the shelfbreak as found, for example, by Pnyushkov and Polyakov (2012) in the Laptev Sea. The  $O_1$  tide is the dominant diurnal constituent, but again, its magnitudes were small ( $\leq 1 \text{ cm s}^{-1}$ ) and largest on the shelf northeast of Hanna Shoal.

## H.6 Summary

This program utilized a wide variety of observations obtained from moored oceanographic instruments, satellite-tracked drifters, hydrography (both recent from autonomous underwater vehicles and towed- and shipboard CTD, as well as historical shipboard measurements), high-frequency radars, meteorological buoys, and satellite imagery to develop an improved understanding of the physical oceanography of the northeastern Chukchi shelf, as well as exchanges between the Chukchi/Beaufort shelves and the adjacent basin. Our measurements spanned the shelf region from Point Hope northward to the Chukchi and Beaufort continental slopes and from the Alaskan coast to the US-Russian Convention Line. Our primary focus area was the shelf and shelfbreak region between the Central Channel and the western Beaufort Sea and north to the shelfbreak. This is an enormous data set that will continue to be analyzed in the future. In this section we summarize our conclusions using Figure H45, which is based largely on the moorings discussed herein and from data published by Itoh et al. (2014) for the mouth of Barrow Canyon, as a guide.

The figure shows two surface fronts: the MW/BSSW front (denoted by the blue line), which surrounds most of Hanna Shoal, and the ACW front (red line) that parallels the Alaskan coast from south of Bering Strait to over the Beaufort Sea shelfbreak. This front is primarily a summer and fall phenomenon, as it is much weaker or even absent in winter and early spring. We are less certain about the seasonality of the MW/BSSW front, although we believe that it persists to some degree along the southeast of Hanna Shoal year-round except in those years (such as 2011), when MW is absent from the Hanna Shoal region.

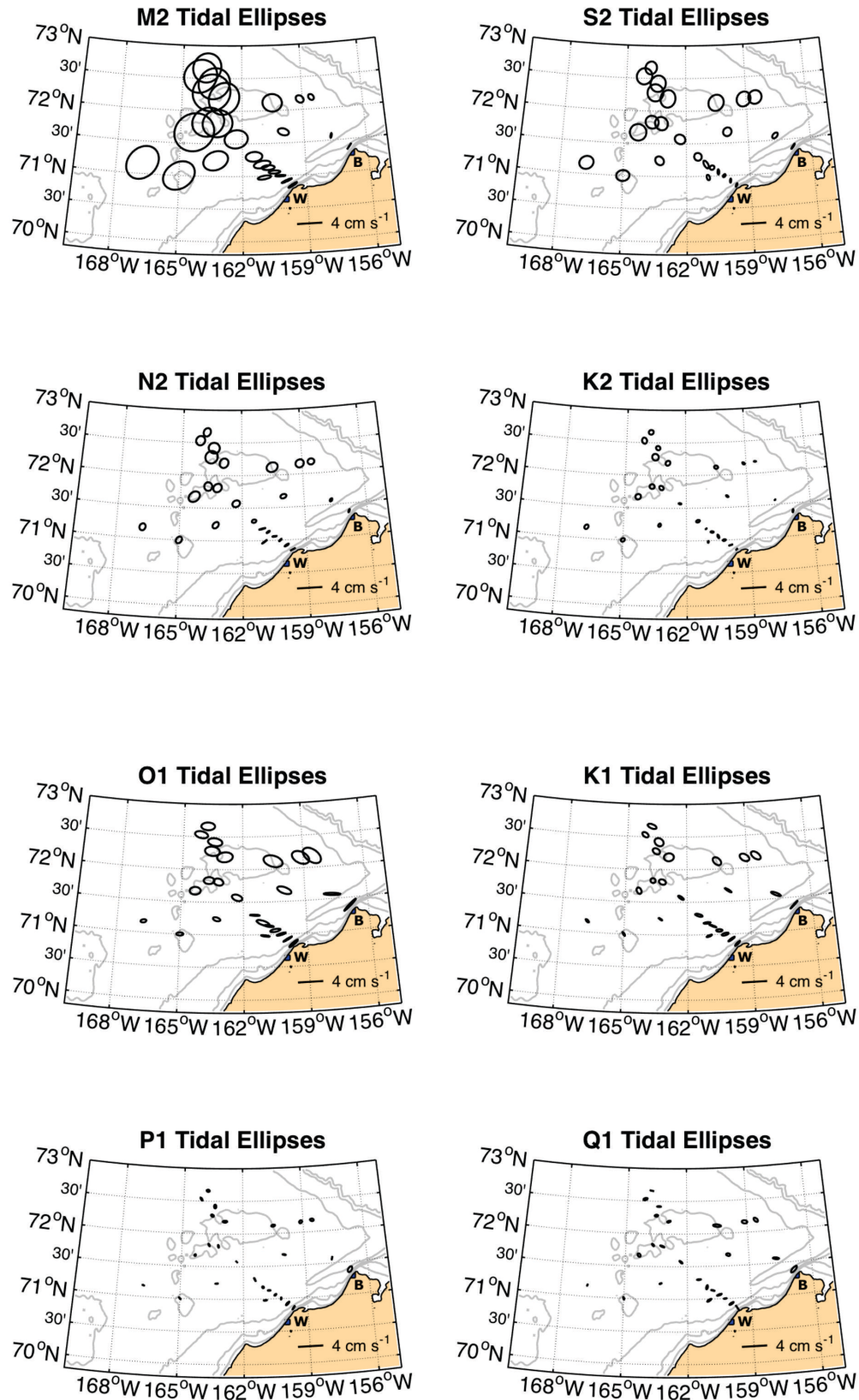


**Figure H44.** Tidal ellipses for the principal semi-diurnal (upper four panels) and diurnal tides on the Chukchi Sea shelf.

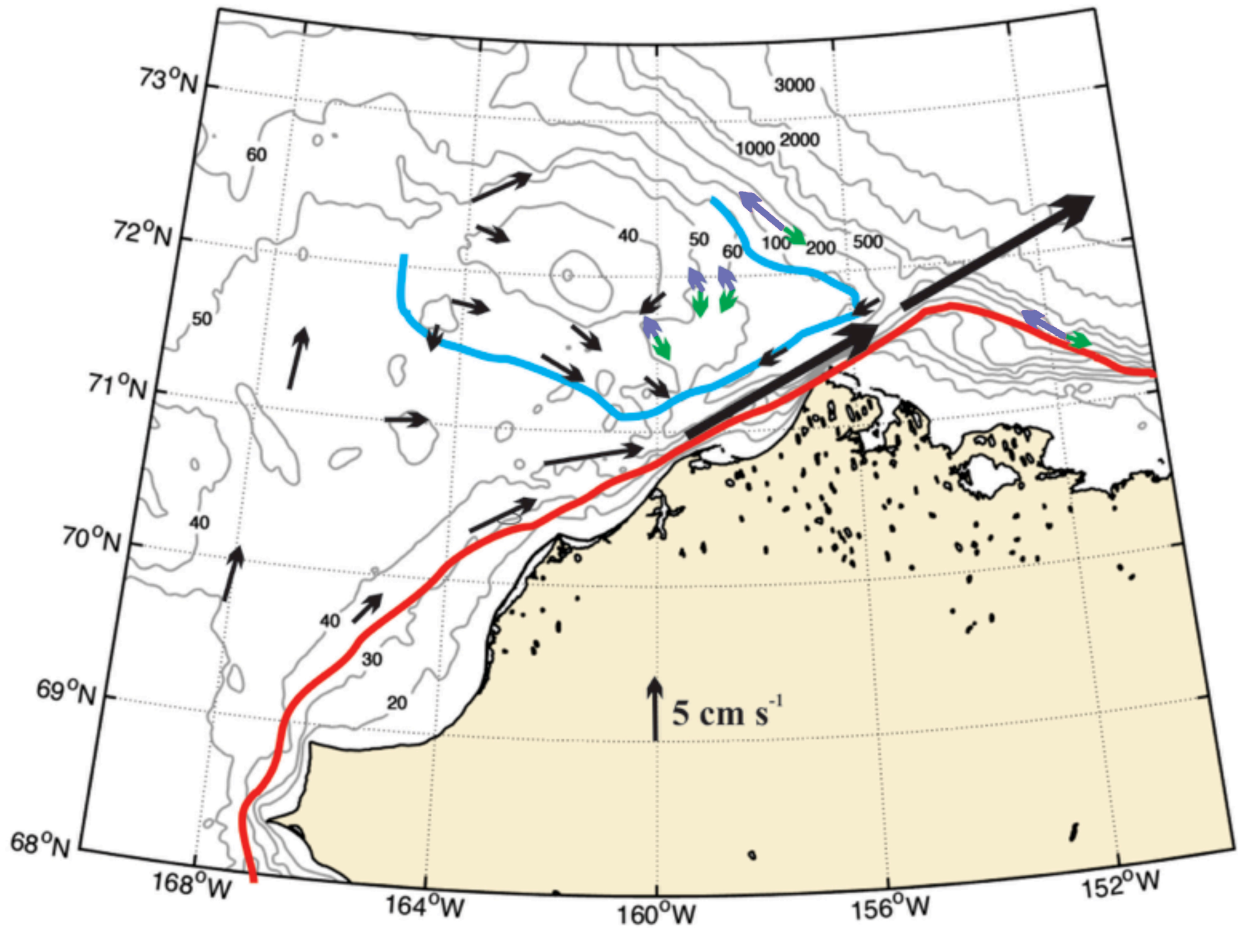


**Figure H45.** Schematic of the mean circulation of the northeastern Chukchi Sea. The red line denotes the Alaskan Coastal Water (ACW) front bordering the offshore side of the Alaskan Coastal Current. The blue line indicates the meltwater/Bering Sea Summer Water (MW/BSSW) front surrounding Hanna Shoal. Black arrows indicate regions where the surface and sub-surface currents are similar in direction and magnitude. Green arrows indicate near-bottom currents, and purple arrows indicate near-surface currents.

Throughout the year and over most of the shelf south of 71.5°N, including within the Central Channel and along the northwest side of Hanna Shoal (as far north as the 50 m isobath), the flow is weakly sheared vertically, with surface and sub-surface flows being within ~30 degrees of one another and all having similar magnitudes. Exceptions to this may involve large shears between drifting ice and the sub-surface flow and/or large shears during the melt season. During melt, the near-surface stratification is very strong (similar to the stratification found on the shelf east of Hanna Shoal), such that the sub-surface and surface circulations may be uncoupled from one another. This is the situation encountered on the East Hanna Shoal Shelf (EHSS) where vertical shears are large year-round. Other regions of strong vertical shear include the Beaufort and Chukchi shelfbreaks and slopes and portions of Barrow Canyon in summer and fall.

We have examined the strength, persistence, and variability of the model-predicted clockwise circulation around Hanna Shoal, including southwestward flow over the shelf between the Barrow Canyon and Hanna Shoal. Substantial elements of the models are largely correct, but there are important differences

between the models and observations. We found that the component of the clockwise circulation on the northwest side of Hanna Shoal extends through the water column as predicted by the models and includes cold Bering Sea Water (BSW) and Winter Water (WW) along the bottom. Both of these water masses are transported from the Central Channel and Herald Canyon. However, on the EHSS, only the bottom waters, consisting of BSW and WW, engage in the clockwise circulation. The upper layer flows westward and/or northwestward over the EHSS. This flow is a consequence of horizontal density gradients that extend northeastward and eastward from Hanna Shoal, which drive a counterclockwise baroclinic, geostrophic circulation in the upper layer that transports MW and/or modified ACW. The latter is transported onto the EHSS via Ekman transport from Barrow Canyon and/or by onshelf transport from the Chukchi shelfbreak. The different flow regimes on either side of Hanna Shoal have two effects. First, these result in a zonal exchange of water masses that maintains strong stratification year-round on the EHSS. Second, we infer that the shelf north of Hanna Shoal is a region of zonal flow convergence, wherein waters must be transported toward the shelfbreak. This transport, which certainly involves the surface layers and possibly the bottom waters, should effect the magnitude and structure of the flow over the Chukchi shelfbreak.

Models also suggest that the clockwise flow around Hanna Shoal extends south of Hanna Shoal in the form of a southwestward drift that eventually turns eastward across the central shelf and continues toward the head of Barrow Canyon. The observations indicate that this is not the case. Indeed, we found that there was no net transport between the EHSS and the central shelf. Instead there is a southeastward flow along the south side of Hanna Shoal that transports water (usually WW) toward the head of Barrow Canyon. This flow essentially represents a dynamic boundary that blocks communication between the EHSS and the central shelf. As a consequence of this boundary and the weak mean flow on the northern side of the Shoal, the residence time of bottom waters on the shelf east of the Shoal is  $\sim 9$  months, much longer than elsewhere in the Chukchi Sea.

As noted, the inferred zonal convergence north of the Shoal provides a possible mechanism for shelf/slope exchange in which MW, WW, and BSW are transported offshelf in this area. There are however other mechanisms that foster exchange. Our retrospective analysis of hydrographic data from the Chukchi shelfbreak indicates that this consists of a surface flow that carries Chukchi Sea water masses (the Pacific-derived summer waters, WW, and MW) westward and an eastward sub-surface flow that is confined to the shelfbreak and which transports WW eastward. The waters flowing westward are largely derived from the Barrow Canyon outflow. The WW that comprises the eastward subsurface flow is mainly derived from northward flows through the Central Channel and Herald Canyon, although some probably forms in winter around the periphery of Hanna Shoal. The potential vorticity structure of the shelfbreak circulation satisfies the conditions for baroclinic instability, which should lead to eddy-driven exchanges between the shelfbreak and basin as is known to occur frequently along the Beaufort Sea shelfbreak.

Our results suggest that most of the Chukchi shelf water masses that enter the head of Barrow Canyon are drawn from the shelf south of Hanna Shoal. Of the 0.2 Sv average transport we estimate to be flowing into the head of the canyon, at least  $\sim 0.1$  Sv flows eastward across the central shelf from the Central Channel. The remainder presumably flows northeastward along the coast. Although we are unable to estimate the transports involved, we infer that additional waters enter the canyon along its length (downcanyon from the head) due to spillage of bottom waters from the EHSS or from westward-flowing waters from the Beaufort Sea. There also appears to be, on average, an upcanyon flow along the west side of the canyon. This flow probably transports waters from the subsurface shelfbreak current flowing eastward along the Chukchi slope. Most likely this inflow proceeds only part way up the canyon because it continuously loses mass to the downcanyon transport along the east side of the canyon. The WW comprise the bulk of the water masses spilling into the canyon and/or transported upcanyon from the shelfbreak.

The circulation and transports in the Central Channel, across the central shelf, and in Barrow Canyon vary annually and are (mostly) in-phase with the annual transport cycle in Bering Strait. For the 2010 – 2015 period, we found that the downcanyon transport is large (0.4 – 0.6 Sv) from May through August, weak ( $\leq 0.2$  Sv) from September through November and from February through April, and reversed (e.g., upcanyon at  $\sim 0.1$  Sv) in December and January. The annual cycle over the central shelf is in-phase with that in Barrow Canyon and includes a reversed (westward) flow in December and January. In contrast, the flow in the Central Channel is northward in all months. These results suggest that in early winter the circulation over the northeastern Chukchi Sea shelf undergoes a major reorganization: waters transported upcanyon may extend onto the central shelf, and nearshore waters are transported westward into the Central Channel and even the western Chukchi Sea. Once in the Central Channel, these nearshore waters would be transported northward. This reorganization provides a means by which WW, formed in the latent heat polynyas along the northwest coast of Alaska in December and January, can be carried far offshore and eventually to Hanna Shoal.

This seasonal reorganization of the flow was likely reflected during synoptic coastal upwelling events such as the one captured by satellite-tracked drifters August 2014. During that event, the cross-shelf transport of surface coastal waters was a response to various competing mechanisms including the geostrophic transport associated with the mean Pacific-Arctic pressure gradient and in response to the winds, surface Ekman drift, shelf-wide pressure gradient adjustments, and Stokes' drift, which although small is not negligible. The drifter observations showed that surface nearshore waters can be transported from the coast to either the Central Channel and/or the head of Herald Canyon in less than a month. Similarly, self-organized mapping analysis applied to the HFR observations clearly indicate that waters transported up Barrow Canyon can easily be carried westward onto the central shelf and/or southward along the Alaskan coast. In fall, the coastal upwelling events and Barrow Canyon reversals likely lead to cooling of nearshore waters and, thus, enhance ice formation.

The shelf circulation also includes a complex variety of mesoscale circulations. One example (observed about 10% of the time) is the “divergent” mode, which occurs during transitions from northeasterly to southeasterly winds. In such events, a pair of counter-rotating vortices form in which the eastward onshore flow from the central shelf splits upon approaching the coast; some water enters a cyclonic vortex to the north of Wainwright and some enters an anticyclonic vortex offshore of Point Lay. The water entering the anticyclonic vortex recirculates over the central shelf. Two other examples are the inferred shedding or generation of eddies as the Alaskan Coastal Current rounds Point Hope and the collision of the westward-flowing Beaufort shelf waters with the along-canyon flow in Barrow Canyon. There are also numerous MW fronts that occur on this shelf, which we suggest are of two types (at least). The first type consists of what appears to be numerous small sub-mesoscale ( $\leq 6$  km) fronts that are shallow (10 – 15 m thick) and found over Hanna Shoal and the EHSS. There is another, more prominent, type of mesoscale front, which in August and September extends from the western end of Hanna Shoal eastward to the head of Barrow Canyon along the south side of the Shoal and then northward along the western half of Barrow Canyon. These fronts separate moderately-stratified BSW to the south (and east in Barrow Canyon) from the strongly-stratified, two-layered MW/WW structure to the north. The fronts are  $\sim 15$  km wide, baroclinically unstable, and generate both anticyclonic and cyclonic eddies at the surface and anticyclonic eddies primarily within the pycnocline north of the front.

These mesoscale and sub-mesoscale motions play an important role in the lateral and vertical mixing of water masses and in the dispersion of dissolved and suspended materials. To a large degree, the mesoscale phenomena that we have identified on the shelf are linked to the distribution of MW. Over the northeastern shelf, the summer MW pool is tied to ice conditions over Hanna Shoal, which can vary considerably from year-to-year. We suggest that the rate of ice retreat over the Shoal in summer may depend upon a number of variables. In summer, early ice retreat seems to be favored when winds are strong and persistent from the northeast. However, the degree to which ice retreats over the Shoal depends

upon the ice thickness distribution, in particular, the presence or absence of thick, grounded ice. We suggest that the summer thickness distribution on the Shoal is likely a consequence of ice advection onto the Shoal during the previous winter. If the advected ice is thick enough to ground on the Shoal in winter then it may encourage additional deformation and accretion of ice throughout the winter and early spring.

## I. Recommendations for Future Study

1. There is a strong eastward flow along the northwest side of Hanna Shoal, which likely extends farther to the northwest than the 60 m isobath. This flow includes waters emanating from both the Central Channel and Herald Canyon farther to the west. Information is needed on the circulation between Herald Canyon and Hanna Shoal as this transport has an important influence on the northeastern Chukchi Sea. This can be determined by deploying an array of moorings from south to north slightly east of the Russian-US Convention Line. We recommend that a meridional array of moorings be deployed between the 50 and 100 m isobaths to assess this transport.
2. An effort should be made to quantify the transport in the Central Channel. We believe that this could be done by deploying 2 – 3 moorings at the southern end of the Channel and 2 – 3 at the northern end to the west of Hanna Shoal. The moorings in recommendation 1 and 2 should include T/C/P recorders at multiple depths in order to assess seasonality in stratification.
3. We hypothesized that flow convergence occurs over the shelf to the north of Hanna Shoal. This hypothesis should be explored by conducting a zonal sequence of cross-isobath synoptic sections to examine water properties and the circulation here. This survey should include VMADCP data and consideration should be given to deploying shallow- and deep-drogued (i.e., 10 and 30 m) satellite tracked drifters to assess the surface and deep circulation on the north side of the Shoal.
4. Two surprising and related observations were the year-round presence of heavy stratification and the inferred year-round counterclockwise baroclinic pressure tendency on the shelf east of Hanna Shoal. The baroclinic pressure field is largest in the upper half of the water column where it opposes the barotropic pressure field. These competing pressure fields are critical in establishing the inferred convergence north of the Shoal and the weak circulation and water properties east of the Shoal. Verification of this baroclinicity and its seasonality can be accomplished with a few moorings using ISCATs (used successfully in COMIDA) and/or a string of T/C/Ps in conjunction with bottom pressure sensors. This deployment could be done in conjunction with the Chukchi Environmental Observatory (Danielson pers comm.).
5. The persistence of sea ice (or lack thereof) in summer on Hanna Shoal has a profound influence on the regional circulation and hydrography. In addition, it also affects the regional biology through control of stratification and as habitat for walrus and other marine mammals. It may also play a key role in governing sources and sinks of carbon and the structure of the benthos. A prudent area of investigation would be to determine the sources of ice on Hanna Shoal, the mechanisms controlling these sources, and those that affect its persistence or its ablation.
6. A systematic effort is required to determine the relative roles of winds, air-sea heat exchange and ocean heat flux convergences, on the seasonal retreat and advance of sea ice on the Chukchi Sea shelf. Such a study will require careful experimental work that addresses horizontal advection and vertical and horizontal mixing processes.
7. It is becoming increasingly clear that not all flow field fluctuations are forced locally over the Chukchi shelf and that some but not all northeastern Chukchi shelf variations are subsequently transmitted to the Beaufort shelf. We recommend studies that will reveal the role of remote processes impacting advection of ice and water locally. Such fluctuations may be important for certain landfast ice breakout events and synoptic-scale flow field variations. Ocean-atmosphere couplings and oceanic transmissions may vary seasonally so investigations would need to assess

the roles of landfast ice, river plumes, and stratification, and their interactions with the seafloor topography.

8. The accuracy of satellite-derived ice motions using the ADCP bottom-track data should be assessed. Comparisons from other sites around the Arctic suggest that derived ice motion products perform reasonably well at some locations and some times of year but the performance of these products have not been well evaluated in the study region.

The outcomes of each of these recommended studies are relevant to an understanding of ecosystem processes as well as providing an understanding of, and an ability to predict, the fate of pollutants.

## J. References

- Aagaard K, Weingartner TJ, Danielson SL, Woodgate RA, Johnson GC, Whitley TE. 2006. Some controls on flow and salinity in Bering Strait. *Geophys Res Lett.* 33(L19602). doi:10.1029/2006GL026612.
- Aagaard K, Roach AT. 1990. Arctic ocean-shelf exchange: Measurements in Barrow Canyon. *J Geophys Res.* 95(C10):18163-18175. doi:10.1029/JC095iC10p18163.
- Aagaard K, Carmack EC. 1989. The Role of Sea Ice and Other Fresh Water in the Arctic Circulation. *J Geophys Res.* 94(C10):14485-14498. doi:10.1029/jc094ic10p14485.
- Aagaard K, 1988. Current, CTD, and pressure measurements in possible dispersal regions of the Chukchi Sea. Outer Continental Shelf Environmental Research Program. Final Rep 57:255-333. Dept. of Commerce/Dept. of Interior. Anchorage, AK.
- Aagaard K, Swift JH, Carmack EC. 1985. Thermohaline Circulation in the Arctic Mediterranean Seas. *J Geophys Res.* 90(C3):4833-4846.
- Aagaard K, Coachman LK, Carmack E. 1981. On the halocline of the Arctic Ocean. *Deep-Sea Res.* 28:529-545.
- Aksenov Y, Ivanov VV, Nurser AJG, Bacon S, Polyakov IV, Coward AC, Naveira-Garabato AC, Beszczynska-Moeller A. 2011. The Arctic Circumpolar Boundary Current, *J. Geophys. Res. Oceans*, 116, doi:10.1029/2010JC006637.
- Allen JS. 1973. Upwelling and Coastal Jets in a Continuously Stratified Ocean. *J Phys Oceanogr.* 3:245-257. doi:10.1175/1520-0485(1973)003<0245:UACJIA>2.0.CO;2.
- Allen SE, Durrieu de Madron X. 2009. A review of the role of submarine canyons in deep-ocean exchange with the shelf. *Ocean Sci.* 5:607-620. doi:10.5194/os-5-607-2009.
- Appen W-J von, Pickart RS. 2012. Two Configurations of the Western Arctic Shelfbreak Current in Summer. *J Phys Oceanogr.* 42: 329-351. doi:10.1175/jpo-d-11-026.1.
- Arrigo, KR, [van Dijken GL](#). 2015. Continued increases in Arctic Ocean primary production. *Prog Oceanogr.* 136:60-70. <http://dx.doi.org/10.1016/j.pcean.2015.05.002>.
- Arrigo KR, Perovich DK, Pickart RS, Brown ZW, van Dijken GL, Lowry KE, Mills MM, Palmer MA, Balch WM, Bates NR, et al. 2014. Phytoplankton blooms beneath the sea ice in the Chukchi Sea. *Deep-Sea Res II.* 105:1-16. doi:10.1016/j.dsr2.2014.03.018.
- Babb DG, Galley RJ, Asplin MG, Lukovich JV, Barber, DG. 2013. Multiyear sea ice export through the Bering Strait during winter 2011–2012. *J Geophys Res Oceans.* 118:2489-5503. doi:10.1002/jgrc.20383.
- Barrick DE, Lipa BJ. 1986. Correcting for Distorted Antenna Patterns in CODAR Ocean Surface Measurements. *IEEE J of Oceanic Engr.* OE-11(2):304-309.
- Barrick DE. 1978. HF Radio Oceanography – A Review. *Boundary Layer Meteorol.* 13:22-43. doi:10.1007/BF00913860.

- Beckers JM, Rixen M. 2003. EOF Calculations and Data Filling from Incomplete Oceanographic Datasets. *J Atmos Oceanic Technol.* 20(12):1839-1856. doi:10.1175/1520-0426(2003)020<1839:ECADFF>2.0.CO;2.
- Blanchard AL, Parris CL, Knowlton AL, Wade NR. 2013. Benthic ecology of the northeastern Chukchi Sea. Part II. Spatial variation of megafaunal community structure, 2009 – 2010. *Cont Shelf Res.* 67:67-76. doi:10.1016/j.csr.2013.04.031.
- Bockstoce JR. Whales, Ice, and Men: The History of Whaling in the Western Arctic. Seattle (WA): University of Washington Press; 1986.
- Bourke RH, Paquette RG. 1989. Estimating the thickness of sea ice. *J Geophys Res.* 94:919-923.
- Brink KH. 1998. Wind-driven currents over the continental shelf. *The Sea.* 10:3-20.
- Brugler ET, Pickart RS, Moore GWK, Roberts S, Weingartner TJ, Statscewich H. 2014. Seasonal to Interannual Variability of the Pacific Water Boundary Current in the Beaufort Sea. *Prog Oceanogr.* 127:1-20. doi:10.1016/j.pocean.2014.05.002.
- Cavaliere D, Martin S. 1994. The contribution of Alaska, Siberian, and Canadian coastal polynyas to the cold halocline layer of the Arctic Ocean. *J Geophys Res.* 99(C9):18343-18362. doi:10.1029/94JC01169.
- Chapman DC, Lentz SJ. 2005. Acceleration of a Stratified Current over a Sloping Bottom, Driven by an Alongshelf Pressure Gradient. *J Phys Oceanogr.* 35:1305-1317. doi:10.1175/JPO2744.1.
- Chapman DC. 2000. The influence of an alongshelf current on the formation and offshore transport of dense water from a coastal polynya. *J Geophys Res.* 105(C10):24007-24019. doi:10.1029/2000JC000296.
- Chavanne C, Janeković I, Flament P, Poulain P-M, Kuzmić M, Gurgel K-W. 2007. Tidal currents in the northwestern Adriatic: High-frequency radio observations and numerical model predictions. *J Geophys Res.* 112(C03S21). doi:10.1029/2006JC003523.
- Citta JJ, Quakenbush LT, Okkonen SR, Druckenmiller ML, Maslowski W, Clement-Kinney J, George JC, Brower H, Small RJ, Ashjian CJ, et al. 2015. Ecological characteristics of core-use areas used by Bering–Chukchi–Beaufort (BCB) bowhead whales, 2006–2012. *Prog Oceanogr.* 136:210-220. doi:10.1016/j.pocean.2014.08.012.
- Coachman LK, Aagaard K. 1988. Transports through Bering Strait: Annual and interannual variability. *J Geophys Res.* 93(C12):15535-15539. doi:10.1029/JC093iC12p15535.
- Coachman LK, Aagaard K, Tripp RB. Bering Strait: The Regional Physical Oceanography. Seattle (WA): University of Washington Press; 1975.
- Codispoti LA, Flagg C, Kully V, Swift JH. 2005. Hydrographic conditions during the 2002 SBI process experiments. *Deep-Sea Res II.* 52:3199-3226. doi:10.1016/j.dsr2.2005.10.007.
- Corlett WB, Pickart RS. 2017. The Chukchi Slope Current. *Prog. Oceanogr.* 153:50-65. doi:10.1016/j.pocean.2017.04.005.
- Csanady G. Circulation in the coastal ocean. Netherlands: Springer; 1982.

- Davis RE. 1985. Drifter observations of coastal surface currents during CODE: The method and descriptive view. *J Geophys Res.* 90(C3):4741-4755. doi:10.1029/JC090iC03p04741.
- Day RH, Weingartner TJ, Hopcroft RR, Aerts LAM, Blanchard AL, Gall AE, Gallaway BJ, Hannay DE, Holladay BA, Mathis JT, et al. 2013. The Offshore Northeastern Chukchi Sea, Alaska: A Complex High-Latitude Ecosystem. *Cont Shelf Res.* 67:147-165. doi:10.1016/j.csr.2013.02.002.
- Danielson SL, Eisner L, Ladd C, Mordy C, Sousa L, Weingartner TJ. 2016. A comparison between late summer 2012 and 2013 water masses, macronutrients, and phytoplankton standing crops in the northern Bering and Chukchi Seas. *Deep-Sea Res II.* 135:7-26. doi:10.1016/j.dsr2.2016.05.024.
- Danielson SL, Weingartner TJ, Hedstrom KS, Aagaard K, Woodgate R, Curchitser E, Stabeno PJ. 2014. Coupled wind-forced controls of the Bering-Chukchi shelf circulation and the Bering Strait throughflow: Ekman transport, continental shelf waves, and variations of the Pacific-Arctic sea surface height gradient. *Prog Oceanogr.* 125:40-61. doi:10.1016/j.pocean.2014.04.006.
- Danielson S, Curchitser E, Hedstrom K, Weingartner T, Stabeno P. 2012. On ocean and sea ice modes of variability in the Bering Sea. *J Geophys Res.* 116(C12034). doi:10.1029/2011JC007389.
- Dunton KH, Grebmeier JM, Trefry JH. 2014. The Benthic Ecosystem of the Northeastern Chukchi Sea: An Overview of Its unique Biogeochemical and Biological Characteristics. *Deep-Sea Res II.* 102:1-8. doi:10.1016/j.dsr2.2014.01.001.
- Dzwonkowski B, Park K, Jiang L. 2011. Subtidal across-shelf velocity structure and surface transport effectiveness on the Alabama shelf of the northeastern Gulf of Mexico. *J Geophys Res.* 116(C10012). doi:10.1029/2011JC007188.
- Efron B, Tibshirani RJ. *An Introduction to the Bootstrap.* New York: Chapman & Hall; 1994.
- Eicken H, Mahoney AR. 2015. Sea Ice: Hazards, Risks, and Implications for Disasters. In: *Sea and Ocean Hazards, Risks, and Disasters.* Oxford (UK): Elsevier; p. 381-401. doi:10.1016/B978-0-12-396483-0.00013-3.
- Fang Y-C, Weingartner TJ, Potter RA, Stoudt C, Dobbins EL. The Circulation Structure Around Hanna Shoal on the Northeastern Chukchi Sea Shelf. Forthcoming 2018.
- Fang Y-C, Potter RA, Statscewich H, Weingartner TJ, Winsor P, Irving BK. 2017. Surface Current Patterns in the Northeastern Chukchi Sea and Their Response to Wind Forcing. *J Geophys. Res. Oceans.* 122. doi:10.1002/2017JC013121.1.
- Fang Y-C, Weingartner TJ, Potter RA, Winsor PR, Statscewich H. 2015. Quality Assessment of HF Radar-Derived Surface Currents Using Optimal Interpolation. *J Atmos Oceanic Technol.* 32:282-296. doi:10.1175/JTECH-D-14-00109.1.
- Fang Y-C, Weingartner TJ, Potter RA, Statscewich H, Winsor P, Danielson S. Mapping the Northeastern Chukchi Sea Surface Currents and Their Dynamical Response Under Different Environmental Conditions. Poster session presented at Ocean Sciences Meeting; 2014 February 23-28; Honolulu, HI.
- Foreman MG. Manual for tidal currents analysis and prediction. Pacific Marine Science Report 78-6. Sidney (BC): Institute of Ocean Sciences; 1978.
- Fissel DB, Mudge TD, Borg K, Kulan N, Sadowy D, Budd K, Lawrence J, Marko JR, Kanwar A, Cowen D, Bard A. 2011. Analysis of ice and metocean measurements, Chukchi Sea, 2009-2010. 131 p.

- Fredj E, Roarty H, Kohut J, Smith M, Glenn S. 2016. Gap Filling of the Coastal Ocean Surface Currents from HFR Data: Application to the Mid-Atlantic Bight HFR Network. *J Atmos Oceanic Technol.* 33:1097-1111. doi:10.1175/JTECH-D-15-0056.1.
- Gawarkiewicz G, Chapman DC. 1995. A numerical study of dense water formation and transport on a shallow, sloping continental shelf. *J Geophys Res.* 100(C3):4489-4507. doi:10.1029/94JC01742.
- Geoffroy M, Majewski A, LeBlanc M, Gauthier S, Walkusz W, Reist JD, Fortier L. 2016. Vertical segregation of age-0 and age-1+ polar cod (*Boreogadus saida*) over the annual cycle in the Canadian Beaufort Sea. *Polar Biol.* 39:1023-1037. doi:10.1007/s00300-015-1811-z.
- Gill AE, Schumann EH. 1974. The generation of long shelf waves by the wind. *J Phys Oceanogr.* 4:83-90.
- Gong D, Pickart RS. 2016. Early Summer Water Mass Transformation in the Eastern Chukchi Sea. *Deep-Sea Res II.* 103:43-55. doi:10.1016/j.dsr2.2016.04.015.
- Gong D, Pickart RS. 2015. Summertime circulation in the eastern Chukchi sea. *Deep-Sea Res II.* 118:18-31. doi:10.1016/j.dsr2.2015.02.006.
- Grantz A, Eittreim S. 1979. Geology and Physiography of the Continental Margin North of Alaska and Implications for the Origin of the Canada Basin. U.S. Geological Survey, Open-File Report 79-288, 61 p.
- Grebmeier JM, McRoy CP. 1989. Pelagic-benthic coupling on the shelf of the northern Bering and Chukchi Seas. III. Benthic food supply and carbon cycling. *Mar Ecol Prog Ser.* 53:79-91.
- Hansell D, Whitley TE, Georing JJ. 1993. Patterns of nitrate utilization and new production over the Bering-Chukchi shelf. *Cont Shelf Res.* 13:601-627.
- Hill VJ, Cota GF. 2005. Spatial patterns of primary production on the shelf, slope, and basin of the western Arctic in 2002. *Deep-Sea Res II.* 52:3344-3354. doi:10.1016/j.dsr2.2005.10.001.
- Hill V, Cota G, Stockwell D. 2005. Spring and Summer Phytoplankton Communities in the Chukchi and Eastern Beaufort Seas. *Deep-Sea Res II.* 52(24-26):3369-3385. doi:10.1016/j.dsr2.2005.10.010.
- Hirano D, Fukamachi Y, Watanabe E, Ohshima KI, Iwamoto K, Mahoney AR, Eicken H, Simizu D, Tamura T. 2016. A wind-driven, hybrid latent and sensible heat coastal polynya off Barrow, Alaska. *J Geophys Res Oceans.* 121:980-997. doi:10.1002/2015JC011318.
- Itoh M, Nishino S, Kawaguchi Y, Kikuchi T. 2013. Barrow Canyon volume, heat, and freshwater fluxes revealed by long-term mooring observations between 2000 and 2008. *J Geophys Res Oceans.* 118:4363-4379. doi:10.1002/jgrc.20290.
- Itoh M, Shimada K, Kamoshida T, McLaughlin F, Carmack E, Nishino S. 2012. Interannual Variability of Pacific Winter Water Inflow Through Barrow Canyon from 2000 to 2006. *J Oceanogr.* 68:575-592. doi:10.1007/s10872-012-0120-1.
- Johnson WR. 1989. Current Response to Wind in the Chukchi Sea: A Regional Coastal Upwelling Event. *J Geophys Res.* 94(C2):2057-2064. doi:10.1029/JC094iC02p02057.
- Kaihatu JM, Handler RA, Marmorino GO, Shay LK. 1998. Empirical Orthogonal Function Analysis of Ocean Surface Currents Using Complex and Real-Vector Methods. *J Atmos Oceanic Technol.* 15(4):927-941. doi:10.1175/1520-0426(1998)015<0927:EOFAOO>2.0.CO;2.

- Kaplan DM, Halle D, Paduan J, Largier JL. 2009. Surface currents during anomalous upwelling seasons off central California. *J Geophys Res Ocean*. 114(C12026). doi:10.1029/2009JC005382.
- Kaplan DM, Lekien F. 2007. Spatial interpolation and filtering of surface current data based on open-boundary modal analysis. *J Geophys Res*. 112(C12007). doi:10.1029/2006JC003984.
- Kim SY, Cornuelle BD, Terrill EJ. 2010. Decomposing observations of high-frequency radar-derived surface currents by their forcing mechanisms: Decomposition techniques and spatial structures of decomposed surface currents. *J. Geophys Res*. 115(C12007). doi:10.1029/2010JC006222.
- Kim SY, Cornuelle BD, Terrill EJ. 2009. Anisotropic Response of Surface Currents to the Wind in a Coastal Region. *J Phys Oceanogr*. 39(6):1512-1533. doi:10.1175/2009JPO4013.1.
- Kim SY, Terrill EJ, Cornuelle BD. 2008. Mapping surface currents from HF radar radial velocity measurements using optimal interpolation. *J Geophys Res*. 113(C10023). doi:10.1029/2007JC004244.
- Kim SY, Terrill E, Cornuelle B. 2007. Objectively mapping HF radar-derived surface current data using measured and idealized data covariance matrices. *J Geophys Res*. 112(C06021). doi:10.1029/2006JC003756.
- King RS, Julstrom B. *Applied Statistics Using the Computer*. Sherman Oaks (CA): Alfred Publishing Co.; 1982.
- Kohonen T. *Self-Organizing Maps*. 3rd ed. New York (NY): Springer-Verlag; 2001.
- Kohut JT, Glenn S. 2003. Improving HF radar surface current measurements with measured antenna beam patterns. *J Atmos and Ocean Tech*. 20:2303-1316.
- Kundu PK, Allen JS. 1976. Some Three-Dimensional Characteristics of Low-Frequency Current Fluctuations near the Oregon Coast. *J Phys Oceanogr*. 6:181-199. doi:10.1175/1520-0485(1976)006<0181:STDCOL>2.0.CO;2.
- LaCasce JH. 2008. Statistics from Lagrangian observations. *Prog Oceanogr*. 77:1-29.
- Ladd C, Mordy CW, Salo SA, Stabeno PJ. 2016. Winter Water Properties and the Chukchi Polynya. *J Geophys Res Oceans*. 121:5516-5534. doi:10.1002/2016JC011918.
- Large WG, Pond S. 1981. Open ocean momentum flux measurements in moderate to strong winds. *J Phys Oceanogr*. 11:324-481.
- Li Y, Wang W, Liu T, Ren L, Zhou Y, Yu C, Qu X, Hu Y. 2015. Source analysis of P3a and P3b components to investigate interaction of depression and anxiety in attentional systems. 17138. doi:10.1038/srep17138.
- Light B, Grenfell TC, Perovich DK. 2008. Transmission and absorption of solar radiation by Arctic sea ice during the melt season. *J Geophys Res*. 113(C03023). doi:10.1029/2006JC003977.
- Lin P, Pickart RS, Moore K, Spall M, Hu J. 2018. Characteristics and Dynamics of wind-driven upwelling in the Alaskan Beaufort Sea based on six years of mooring data. *Deep-Sea Res II*.
- Lin P, Pickart RS, Stafford KM, Moore GWK, Torres DJ, Bahr F, Hu J. 2016. Seasonal Variation of the Beaufort Shelfbreak Jet and Its Relationship to Arctic Cetacean Occurrence. *J Geophys Res Ocean*. 121:8434-8354. doi:10.1002/2016JC011890.

- Linders J, Pickart RS, Björk G, Moore GWK. 2017. On the Nature and Origin of Water Masses in Herald Canyon, Chukchi Sea: Synoptic Surveys in Summer 2004, 2008, and 2009. *Prog Oceanogr.* 159:99-114. doi:10.1016/j.pocean.2017.09.005.
- Liu Y, Weisberg RH, Shay LK. 2007. Current Patterns on the West Florida Shelf from Joint Self-Organizing Map Analyses of HF Radar and ADCP Data. *J Atmos Oceanic Technol.* 24:702-712. doi:10.1175/JTECH1999.1.
- Liu Y, Weisberg RH, Mooers CNK. 2006. Performance evaluation of the self-organizing map for feature extraction. *J Geophys Res.* 111(C05018). doi:10.1029/2005JC003117.
- Liu Y, Weisberg RH. 2005. Patterns of ocean current variability on the West Florida Shelf using the self-organizing map. *J Geophys Res.* 110(C06003). doi:10.1029/2004JC002786.
- Llinás L, Pickart RS, Mathis JT, Smith SL. 2009. Zooplankton inside an Arctic Ocean cold-core eddy: Probable origin and fate. *Deep-Sea Res II.* 56:1290-1304. doi:10.1016/j.dsr2.2008.10.020.
- Lowry KE, Pickart RS, Mills MM, Brown ZW, van Dijken GL, Bates NR, Arrigo KR. 2015. The Influence of Winter Water on Phytoplankton Blooms in the Chukchi Sea. *Deep-Sea Res II.* 118:53-72. doi:10.1016/j.dsr2.2015.06.006.
- Lu K, Weingartner T, Danielson S, Winsor P, Dobbins E, Martini K, Statscewich H. 2015. Lateral mixing across ice meltwater fronts of the Chukchi Sea shelf. *Geophys Res Lett.* 42:6754-6761. doi:10.1002/2015GL064967.
- Lu P, Li Z, Cheng B, Leppäranta M. 2011. A parameterization of the ice-ocean drag coefficient. *J Geophys Res.* 116(C07019). doi:10.1029/2010JC006878.
- MacCready P, Rhines PB. 1993. Slippery Bottom Boundary Layers on a Slope. *J Phys Oceanogr.* 23:5-22.
- Mahoney AR, Eicken H, Shapiro LH, Gens R, Heinrichs T, Meyer F, Graves J, Gaylord A. 2012. Mapping and Characterization of Recurring Spring Leads and Landfast Ice in the Beaufort and Chukchi Seas. U.S. Dept. of the Interior, Bureau of Ocean Energy Management, Alaska Region, Anchorage, AK. OCS Study BOEM 2012-067. 179 p.
- Martin S, Drucker R. 1997. The effect of possible Taylor columns on the summer sea ice in the Chukchi Sea. *J Geophys Res.* 102(C5):10473-10482. doi:10.1029/97JC00145.
- Martini KI, Stabeno PJ, Ladd C, Winsor P, Weingartner TW, Mordy CW, Eisner LB. 2016. Dependence of subsurface chlorophyll on seasonal water masses in the Chukchi Sea. *J Geophys Res Oceans.* 121:1755-1770. doi:10.1002/2015JC011359.
- Mathis JT, Bates NR, Hansell DA, Babila T. 2009. Net community production in the northeastern Chukchi Sea. *Deep-Sea Res II.* 56(17):1213-1222.
- Mathis JT, Pickart RS, Hansell DA, Kadko D, Bates NR. 2007. Eddy transport of organic carbon and nutrients from the Chukchi Shelf: Impact of the upper halocline of the western Arctic Ocean. *J Geophys Res.* 112(C05011). doi:10.1029/2006JC003899.
- Mau J-C, Wang D-P, Ullman DS, Codiga DL. 2007. Characterizing Long Island Sound outflows from HF radar using self-organizing maps. *Estuar Coast Shelf Sci.* 74. doi:10.1016/j.ecss.2007.04.007.

- Maykut GA. 1986. The surface mass and heat balance. In: *The Geophysics of Sea Ice*. New York (NY): Plenum Press; p. 395-463.
- McWilliams JC. 2008. Fluid dynamics at the margin of rotational control. *Environ Fluid Mech.* 8:441-449. doi:10.1007/s10652-008-9081-8.
- Melling H, Johnston PH, Riedel DA. 1995. Measurement of the Underside Topography of Sea Ice by Moored Subsea Sonar. *J Atmos Oceanic Technol.* 12:589-602. doi:10.1175/1520-0426(1995)012<0589:MOTUTO>2.0.CO%3B2.
- Mesinger F, DiMego G, Kalnay E, Mitchell K, Shafran PC, Ebisuzaki W, Jovic D, Woollen J, Rogers E, Berbery EH, et al. 2006. North American Regional Reanalysis. *Bull Amer Meteor Soc.* 87(3):343–360. doi:10.1175/BAMS-87-3-343.
- Mihanović H, Cosoli S, Vilibić I, Ivanković D, Dadić V, Gačić M. 2011. Surface current patterns in the northern Adriatic extracted from high-frequency radar data using self-organizing map analysis. *J Geophys Res.* 116. doi:10.1029/2011JC007104.
- Mizobata K, Watanabe E, Kimura N. 2016. Wintertime variability of the Beaufort Gyre in the Arctic Ocean derived from CryoSat-2/SIRAL observations. *J Geophys Res Oceans.* 121:1685-1699. doi:10.1002/2015JC011218.
- Moore SE, Stabeno PJ, Grebmeier JM, Okkonen SR. 2016. The Arctic Marine Pulses Model: Linking annual oceanographic processes to contiguous ecological domains in the Pacific Arctic, *Deep-Sea Res. II*, doi:10.1016/j.dsr2.2016.10.011.
- Moore SE, Huntington HP. 2008. Arctic marine mammals and climate change: impacts and resilience. *Ecol Appl.* 18:157-165.
- Mountain DG, Coachman LK, Aagaard K. 1976. On the Flow Through Barrow Canyon. *J Phys Oceanogr.* 6:461-470. doi:10.1175/1520-0485(1976)006<0461:OTFTBC>2.0.CO;2.
- Mudge TD, Fissel DB, Sadowy D, Borg K, Billenness D, Knox K, Slonimer A, Batistuzzo H, Milutinovic N, Clouston R, et al. 2015. Analysis of Ice and Metocean Measurements, Chukchi Sea 2013-2014, for Shell. Project Report for Shell International Exploration and Production Inc., Houston, Texas by ASL Environmental Sciences Inc., Victoria, B.C. Canada, 108 p.
- Muench RD, Schumacher JD, Salo SA. 1988. Winter Currents and Hydrographic Conditions on the Northern Central Bering Sea Shelf. *J Geophys Res.* 93:516-526. doi:10.1029/JC093iC01p00516.
- Münchow A, Carmack EC, Huntley DA. 2000. Synoptic density and velocity observations of slope waters in the Chukchi and East Siberian Seas. *J Geophys Res.* 105:14103-14119.
- Münchow A, Carmack EC. 1997. Synoptic Flow and Density Observations near an Arctic Shelf Break. *J Phys Oceanogr.* 27:1402-1419. doi:10.1175/1520-0485(1997)027<1402:SFADON>2.0.CO;2.
- Nikolopoulos A, Pickart RS, Fratantoni PS, Shimada K, Torres DJ, Jones EP. 2009. The western Arctic boundary current at 152°W: Structure, variability, and transport. *Deep-Sea Res II.* 56:1164-1181. doi:10.1016/j.dsr2.2008.10.014.
- Nishino S, Kikuchi T, Yamamoto-Kawai M, Kawaguchi Y, Hirawake T, Itoh M. 2011. Enhancement/reduction of biological pump depends on ocean circulation in the sea-ice reduction regions of the Arctic Ocean. *J Oceanogr.* 67:305-314. doi:10.1007/s10872-011-0030-7.

- Nof D. 1991. Lenses generated by intermittent currents. *Deep-Sea Res.* 38(3):325-345.
- Nof D. 1988. Outflows Dynamics. *Geophys Astrophys Fluid Dynamics.* 40:165-193.
- North GR, Bell TL, Cahalan RF, Moeng FJ. 1982. Sampling Errors in the Estimation of Empirical Orthogonal Functions. *Mon Wea Rev.* 110:699-706. doi:10.1175/1520-0493(1982)110<0699:SEITO>2.0.CO;2.
- Okkonen SR, Ashjian CJ, Campbell RG, Maslowski W, Clement-Kinney JL, Potter R. 2009. Intrusion of warm Bering/Chukchi waters onto the shelf in the western Beaufort Sea. *J Geophys Res.* 114(C00A11). doi:10.1029/2008JC004870.
- Okubo A, Ebbesmeyer CC. 1976. Determination of vorticity, divergence, and deformation rates from analysis of drogoue observations. *Deep-Sea Res II.* 23:349-352.
- Pacini A, Pickart RS, Moore GWK, Nobre C, Bahr F, Vage K, Arrigo KA. submitted 2017. Characteristics and Transformation of Pacific Winter Water on the Chukchi Shelf in Late Spring. *Deep-Sea Res II.*
- Paduan JD, Washburn L. 2013. High-Frequency Radar Observations of Ocean Surface Currents. *Ann Rev Mar Sci.* 5:115-1136. doi:10.1146/annurev-marine-121211-172315.
- Paquette RG, Bourke RH. 1981. Ocean circulation and fronts as related to ice melt-back in the Chukchi Sea. *J Geophys Res.* 86(C5):4215-4230. doi:10.1029/JC086iC05p04215.
- Paquette RG, Bourke RH. 1974. Observations on the Coastal Current of Arctic Alaska. *J Mar Res.* 32:195-207.
- Pawlowicz R, Beardsley B, Lentz S. 2002. Classical tidal harmonic analysis including error estimates in MALAB using T\_TIDE. *Computers and Geosciences.* 28:929-937.
- Pease CH. 1987. The size of wind-driven coastal polynyas. *J Geophys Res.* 92(C7):7049-7059. doi:10.1029/JC092iC07p07049.
- Perovich DK, Jones KF. 2014. The seasonal evolution of sea ice floe size distribution. *J Geophys Res Oceans.* 119:8767-8777. doi:10.1002/2014JC010136.
- Pickart RS, Moore GWK, Mao C, Bahr F, Nobre C, Weingartner TJ. 2016. Circulation of winter water on the Chukchi shelf in early Summer. *Deep-Sea Res II.* **130**:56-75. doi:10.1016/j.dsr2.2016.05.001.
- Pickart RS, Schulze LM, Moore GWK, Charette MA, Arrigo KR, van Dijken G, Danielson SL. 2013. Long-term trends of upwelling and impacts on primary productivity in the Alaskan Beaufort Sea. *Deep-Sea Res I.* 79:106-121. doi:10.1016/j.dsr.2013.05.003.
- Pickart RS, Spall MA, Mathis JT. 2013. Dynamics of upwelling in the Alaskan Beaufort Sea and associated shelf-basin fluxes. *Deep-Sea Res I.* 76:35-51. doi:10.1016/j.dsr.2013.01.007.
- Pickart RS, Spall MA, Moore GWK, Weingartner TJ, Woodgate RA, Aagaard K, Shimada K. 2011. Upwelling in the Alaskan Beaufort Sea: Atmospheric forcing and local versus non-local response. *Prog Oceanogr.* **88**:78-100. doi:10.1016/j.pcean.2010.11.005.
- Pickart RS, Pratt LJ, Torres DJ, Whitledge TE, Proshutinsky AY, Aagaard K, Agnew TA, Moore GWK, Dail HJ. 2010. Evolution and dynamics of the flow through Herald Canyon in the western Chukchi Sea. *Deep-Sea Res II.* 57:5-26. doi:10.1016/j.dsr2.2009.08.002.

- Pickart RS, Moore GWK, Torres DJ, Fratantoni PS, Goldsmith RA, Yang J. 2009. Upwelling on the continental slope of the Alaskan Beaufort Sea: Storms, ice, and oceanographic response. *J Geophys Res.* 114(C00A13). doi:10.1029/2008JC005009.
- Pickart RS, Weingartner T, Pratt LJ, Zimmermann S, Torres DJ. 2005. Flow of winter-transformed Pacific water into the Western Arctic. *Deep-Sea Res II.* 52:3175-3198. doi:10.1016/j.dsr2.2005.10.009.
- Pickart RS. 2004. Shelfbreak circulation in the Alaskan Beaufort Sea: Mean structure and variability. *J Geophys Res.* 109(C04024). doi:10.1029/2003JC001912.
- Pisareva MN, Pickart RS, Spall MA, Nobre C, Torres DJ, Moore GWK, Whitledge TE. 2015. Flow of Pacific water in the western Chukchi Sea: Results from the 2009 RUSALCA expedition. *Deep-Sea Res I.* 105:53-73. doi:10.1016/j.dsr.2015.08.011.
- Pnyushkov AV, Polyakov IV. 2012. Observations of Tidally Induced Currents over the Continental Slope of the Laptev Sea, Arctic Ocean. *J Phys Oceanogr.* 49. doi:10.1175/JPO-D-11-064.1.
- Potter RA, Fang Y-C, Statscewich H, Weingartner TJ, Winsor P. Surface Currents on the Northeastern Chukchi and Western Beaufort Sea Shelves as Detected by High Frequency Radars. Poster session presented at Ocean Sciences Meeting; 2016 February 21-26; New Orleans, LA.
- Questel JM, Clarke C, Hopcroft RR. 2013. Seasonal and interannual variation in the planktonic communities of the northeastern Chukchi Sea during the summer and early fall. *Cont Shelf Res.* 67:23-41. doi:10.1016/j.csr.2012.11.003.
- Richardson AJ, Risien C, Shillington FA. 2003. Using self-organizing maps to identify patterns in satellite imagery. *Prog Oceanogr.* 59:223-239. doi:10.1016/j.pocean.2003.07.006.
- Roach AT, Aagaard K, Pease CH, Salo SA, Weingartner T, Pavlov V, Kulakov M. 1995. Direct measurements of transport and water properties through the Bering Strait. *J Geophys Res.* 100(C9)18443-18457. doi:10.1029/95jc01673.
- Rudels B. 2012. Arctic ocean circulation and variability – advection and external forcing encounter constraints and local processes. *Ocean Science.* 8(2):261–286.
- Rudels B, Jones EP, Anderson LG, Kattner G. 1994. The Polar Oceans and Their Role in Shaping the Global Environment. In: Johannessen, OM, Muench RD, Overland JE, editors. *On the Intermediate Depth Waters of the Arctic Ocean.* Washington DC: American Geophysical Union. p. 33-46. doi:10.1029/GM085p0033.
- Schulze LM, Pickart RS. 2012. Seasonal Variation of upwelling in the Alaskan Beaufort Sea: Impact of sea ice cover. *J Geophys Res.* 117(C06022). doi:10.1029/2012JC007985.
- Serreze MC, Barrett AP, Slater AG, Woodgate RA, Aagaard K, Lammers RB, Steele M, Moritz R, Meredith M, Lee CM. 2006. The large-scale freshwater cycle of the Arctic. *J. Geophys Res.* 111(C11010). doi:10.1029/2005JC003424.
- Shimada K, Kamoshida T, Itoh M, Nishino S, Carmack E, McLaughlin F, Zimmermann S, Proshutinsky A. 2006. Pacific Ocean inflow: Influence on catastrophic reduction of sea ice cover in the Arctic Ocean. *Geophys Res Lett.* 33(L08605). doi:10.1029/2005GL025624.
- Shimada K, Itoh M, Nishino S, McLaughlin F, Carmack E, Proshutinsky A. 2005. Halocline structure in the Canada Basin of the Arctic Ocean. *Geophys Res Lett.* 32(L03605). doi:10.1029/2004GL021358.

- Shroyer EL. 2012. Turbulent Kinetic Energy Dissipation in Barrow Canyon. *J Phys Oceanogr.* 42:1012-1021. doi:10.1175/JPO-D-11-0184.1.
- Shroyer EL, Plueddemann AJ. 2012. Wind-driven modification of the Alaskan coastal current. *J Geophys Res.* 117(C03031). doi:10.1029/2011JC007650.
- Signorini SR, Münchow A, Haidvogel D. 1997. Flow dynamics of a wide Arctic canyon. *J Geophys Res.* 102(C8):18661-18680. doi:10.1029/97JC00739.
- Smith W, Wessel P. 1990. Gridding with continuous curvature splines in tension. *Geophysics.* 55(3):293-305.
- Spall MA, Pickart RS, Brugler ET, Moore GWK, Thomas L, Arrigo K. 2014. Role of shelfbreak upwelling in the formation of a massive under-ice bloom in the Chukchi Sea. *Deep-Sea Res II.* 105:17-29. doi:10.1016/j.dsr2.2014.03.017.
- Spall MA. 2013. On the circulation of Atlantic Water in the Arctic Ocean. *J Phys Oceanogr.* 43:2352-2371. doi:10.1175/JPO-D-13-079.1.
- Spall MA, Pickart RS, Fratantoni PS, Plueddemann AJ. 2008. Western Arctic Shelfbreak Eddies: Formation and Transport. *J Phys Oceanogr.* 38:1644-1668. doi:10.1175/2007JPO3829.1.
- Spall MA. 2007. Circulation and water mass transformation in a model of the Chukchi Sea. *J Geophys Res.* 112(C05025). doi:10.1029/2005JC003364.
- Spren G, Kaleschke L, Heygster G. 2008. Sea ice remote sensing using AMSR-E 89 GHz channels. *J Geophys Res.* 113(C02S03). doi:10.1029/2005JC003384.
- Springer AM, McRoy CP. 1993. The paradox of pelagic food webs in the northern Bering Sea—iii. Patterns of primary production. *Cont Shelf Res.* 135-6:575–599.
- Statscewich H, Weingartner T, Danielson S, Grunau B, Egan G, Timm T. 2011. A High-Latitude Modular Autonomous Power, Control, and Communication System for Application to High-Frequency Surface Current Mapping Radars. *Mar Technol Soc J.* 453:59-68. doi:10.4031/MTSJ.45.3.7.
- Steele M, Zhang J, Ermold W. 2010. Mechanisms of summertime upper Arctic Ocean warming and the effect on sea ice melt. *J Geophys Res.* 115(C11004). doi:10.1029/2009JC005849.
- Steele M, Ermold W, Zhang J. 2008. Arctic Ocean surface warming trends over the past 100 years. *Geophys Res Lett.* 35(L02614). doi:10.1029/2007GL031651.
- Steele M, Morison J, Ermold W, Rigor I, Ortmeyer M, Shimada K. 2004. Circulation of summer Pacific halocline water in the Arctic Ocean. *J Geophys Res.* 109(C02027). doi:10.1029/2003JC002009.
- Stewart RH, Joy JW. 1974. HF radio measurements of surface currents. *Deep-Sea Res.* 21:1039–1049.
- Stigebrandt A, 1984. The North Pacific: A Global-Scale Estuary. *J Phys Oceanogr.* 14:464–470. doi:10.1175/1520-0485(1984)014<0464:TNPAGS>2.0.CO;2.
- Taylor MH, Losch M, Wenzel M, Schröter J. 2013. On the Sensitivity of Field Reconstruction and Prediction Using Empirical Orthogonal Functions Derived from Gappy Data. *J Clim.* 26(22):9194–9205. doi:10.1175/JCLI-D-13-00089.1.

- Teague C. 2001. Ionospheric effects on coastal radar systems, *Radiowave Oceanography: The First International Workshop*. Graber HC, Paduan JD, editors. University of Miami. p. 56–61.
- Thomas LN, Taylor JR, Ferrari R, Joyce TM. 2016. Symmetric instability in the Gulf Stream. *Deep-Sea Res II*. 91:96-110. doi:10.1016/j.dsr2.2013.02.025.
- Timmermans M-L, Marshall J, Proshutinsky A, Scott J. 2017. Seasonally derived components of the Canada Basin halocline. *Geophys Res Lett*. 44:5008-5015. doi:10.1002/2017GL073042.
- Timmermans M-L, Proshutinsky A, Golubeva E, Jackson JM, Krishfield R, McCall M, Platov G, Toole J, Williams W, Kikuchi T, Nishino S. 2014. Mechanisms of Pacific Summer Water variability in the Arctic's Central Canada Basin. *J Geophys Res Oceans*. 119:7523-7548. doi:10.1002/2014JC010273.
- Timmermans M-L, Winsor P. 2013. Scales of horizontal density structure in the Chukchi Sea surface layer. *Cont Shelf Res*. 52:39-45. doi:10.1016/j.csr.2012.10.015.
- Thomas LN. 2008. Formation of intrathermocline eddies at ocean fronts by wind-driven destruction of potential vorticity. *Dyn Atmos Ocean*. 45(3-4):252-273. doi:10.1016/j.dynatmoce.2008.02.002.
- Thomas LN, Tandon A, Mahadevan A. 2008. Sub-mesoscale processes and dynamics. In: Hecht MW, Hasumi H, editors. *Ocean Modeling in an Eddying Regime*, Geophysical Monograph Series. 177. Washington DC, American Geophysical Union. p. 17-38.
- Toole JM, Timmermans M-L, Perovich DK, Krishfield RA, Proshutinsky A, Richter-Menge JA. 2010. Influences on the ocean surface mixed layer and thermohaline stratification on Arctic sea ice in the central Canada Basin. *J Geophys Res Oceans*. 115(C10018). doi:10.1029/2009JC005660.
- Vilibić I, Kalinić H, Mihanović H, Cosoli S, Tudor M, Žagar N, Jesenko B. 2016. Sensitivity of HF radar-derived surface current self-organizing maps to various processing procedures and mesoscale wind forcing. *Comput Geosci*. 20(1):115-131. doi: 10.1007/s10596-015-9550-3.
- Walsh JJ. 1995. DOC storage in Arctic seas: the role of continental shelves. In: Smith, Jr. WO, Grebmeier JM, editors. *Arctic Oceanography: Marginal Ice Zones and Continental Shelves*. Washington DC, American Geophysical Union. p. 203-230.
- Walsh JJ, McRoy CP, Coachman LK, Goering JJ, Nihoul JJ, Whitledge TE, Blackburn TH, Parker PL, Wirick CD, Shuert PG, et al. 1989. Carbon and nitrogen cycling within the Bering/Chukchi seas: Source regions for organic matter affecting AOU demands of the Arctic Ocean. *Prog Oceanogr*. 22:277-359. doi:10.1016/0079-6611(89)90006-2.
- Watanabe E. 2011. Beaufort shelf break eddies and shelf-basin exchange of Pacific summer water in the western Arctic Ocean detected by satellite and modeling analyses. *J Geophys Res*. 116(C08034). doi:10.1029/2010JC006259.
- Watanabe E, Hasumi H. 2009. Pacific Water Transport in the Western Arctic Ocean Simulated by an Eddy-Resolving Coupled Sea Ice-Ocean Model. *J Phys Oceanogr*. 39:2194-2211. doi: 10.1175/2009JPO4010.1.
- Weingartner TJ, Fang Y-C, Winsor P, Dobbins E, Potter R, Statscewich H, Mudge T, Irving B, Soursa L, Borg K. 2017b. The Summer Hydrographic Structure of the Hanna Shoal Region on the Northeastern Chukchi Sea Shelf: 2011 – 2013. *Deep-Sea Res II*. 144:6-20. doi: 10.1016/j.dsr2.2017.08.006.

- Weingartner TJ, Potter RA, Stoudt CA, Dobbins EL, Statsceiwch H, Winsor PR, Mudge TD, Borg K. 2017a. Transport and Thermohaline Variability in Barrow Canyon on the Northeastern Chukchi Sea Shelf. *J Geophys Res Oceans*. 122(5):3565-3585. doi:10.1002/2016JC012636.
- Weingartner TJ, Irvine CB, Dobbins EL, Danielson S, Desousa L, Adams B, Suydam R, Neakok W. 2015. Satellite-tracked Drifter Measurements in the Chukchi and Beaufort Seas. US Dept Inter Alaska Outer Cont Shelf Reg; OCS Study BOEM 2015-022. 171 p. (Available online <https://www.boem.gov/BOEM-2015-022/>).
- Weingartner T, Danielson S, Dobbins L, Potter R. 2014. Physical oceanographic measurements in the Northeastern Chukchi Sea: 2013. Technical report prepared for ConocoPhillips, Inc., Shell Exploration & Production Company, and Statoil USA E&P, Inc. 52 p.
- Weingartner T, Dobbins E, Danielson S, Winsor P, Potter R, Statsceiwch H. 2013a. Hydrographic variability over the northeastern Chukchi Sea shelf in summer-fall 2008–2010. *Cont Shelf Res*. 67:5-22. doi:10.1016/j.csr.2013.03.012.
- Weingartner TJ, Winsor P, Potter RA, Statsceiwch H, Dobbins EL. 2013b. Application of High Frequency Radar to Potential Hydrocarbon Development Areas in the Northeast Chukchi Sea. US Dept Inter Alaska Outer Cont. Shelf Reg; Contract M09AC15207; OCS Study BOEM 2012- 079. 162 p. (Available online <https://www.boem.gov/BOEM-2012-079/>).
- Weingartner T, Aagaard K, Woodgate R, Danielson S, Sasaki Y, Cavalieri D. 2005. Circulation on the north central Chukchi Sea Shelf. *Deep-Sea Res II*. 52:3150-3174. doi:10.1016/j.dsr2.2005.10.015.
- Weingartner TJ, Danielson S, Sasaki Y, Pavlov V, Kulakov M. 1999. The Siberian Coastal Current: a wind and buoyancy-forced arctic coastal current. *J Geophys Res*. 104:29697-29713.
- Weingartner TJ, Cavalieri DJ, Aagaard K, Sasaki Y. 1998. Circulation, dense water formation, and outflow on the northeast Chukchi shelf. *J Geophys Res*. 103(C4):7647-7661. doi:10.1029/98JC00374.
- Weisberg RH, Petrafesa LJ. 1983. Kinematics and correlation of the surface wind field in the South Atlantic Bight. *J Geophys Res*. 88(C8):4593-4610. doi:10.1029/JC088iC08p04593.
- Winsor P, Chapman DC. 2004. Pathways of Pacific Water across the Chukchi Sea: A numerical model study. *J Geophys Res*. 109(C03002). doi:10.1029/2003JC001962.
- Winsor P, Chapman DC. 2002. Distribution and interannual variability of dense water production from coastal polynyas on the Chukchi Shelf. *J Geophys Res*. 107(C7). doi:10.1029/2001JC000984.
- Wood KR, Bond NA, Danielson SL, Overland JE, Salo SA, Stabeno PJ, Whitefield J. 2015. A decade of environmental change in the Pacific Arctic Region. *Prog Oceanogr*. 136:12-31. doi:10.1016/j.pcean.2015.05.005.
- Woodgate RA, Stafford KM, Prahlg FG. 2015. A Synthesis of Year-Round Interdisciplinary Mooring Measurements in the Bering Strait (1990-2014) and the RUSALCA years (2004-2011). *Oceanography*. 28(3):46-67. doi:10.5670/oceanog.2015.57.
- Woodgate RA, Weingartner TJ, Lindsay R. 2012. Observed increases in Bering Strait oceanic fluxes from the Pacific to the Arctic from 2001 to 2011 and their impacts on the Arctic Ocean water column. *Geophys Res Lett*. 39(L24603). doi:10.1029/2012GL054092.

- Woodgate RA, Weingartner TJ, Lindsay R. 2010. The 2007 Bering Strait oceanic heat flux and anomalous Arctic sea-ice retreat. *Geophys Res Lett.* 37(L01602). doi:10.1029/2009GL041621.
- Woodgate RA, Aagaard K, Weingartner TJ. 2006. Interannual changes in the Bering Strait fluxes of volume, heat and freshwater between 1991 and 2004. *Geophys Res Lett.* 33(L15609). doi:10.1029/2006GL026931.
- Woodgate RA, Aagaard K, Weingartner TJ. 2005. A year in the physical oceanography of the Chukchi Sea: Moored measurements from autumn 1990–1991. *Deep-Sea Res II.* 52:3116-3149. doi:10.1016/j.dsr2.2005.10.016.
- Woodgate RA, Aagaard K, Weingartner TJ. 2005. Monthly temperature, salinity, and transport variability of the Bering Strait through flow. *Geophys Res Lett.* 32(L04601). doi:10.1029/2004GL021880.
- Wyllie-Echeverria T, Barber WE, Wyllie-Echeverria S. 1992. Water masses and transport of Age-0 Arctic Cod and age-0 Bering Flounder into the northeastern Chukchi Sea. In: Reynolds JB, editor. *Fish Ecology in Arctic North America.* American Fisheries Society. p. 60-68.
- Yamamoto-Kawai M, McLaughlin FA, Carmack EC, Nishino S, Shimada K. 2008. Freshwater budget of the Canada Basin, Arctic Ocean, from salinity,  $d^{18}O$ , and nutrients. *J Geophys Res.* 113(C01007). doi:10.1029/2006JC003858.
- Yang J. 2006. The Seasonal Variability of the Arctic Ocean Ekman Transport and Its Role in the Mixed Layer Heat and Salt Fluxes. *J Climate.* 19:5366-5387. doi:10.1175/JCLI3892.1.
- Yankovsky AE, Yashayaev I. 2014. Surface buoyant plumes from melting icebergs in the Labrador Sea. *Deep-Sea Res I.* 91(1–9). doi:10.1016/j.dsr.2014.05.014.
- Yankovsky AE, Chapman DC. 1996. Scattering of shelf waves by a spatially varying mean current. *J Geophys Res.* 101:3479-3487.
- Yankovsky AE, Chapman DC. 1995. Generation of mesoscale flows over the shelf and slope by shelf wave scattering in the presence of a stable, sheared mean current. *J Geophys Res.* 100(C4):6725-6742.
- Zhang J, Steele M, Runciman K, Dewey S, Morison J, Lee C, Rainville L, Cole S, Krishfield R, Timmermans M-L, Toole J. 2016. The Beaufort Gyre intensification and stabilization: A model-observation synthesis. *J Geophys Res Oceans.* 121:7933-7952. doi: 10.1002/2016JC012196.
- Zhao M, Timmermans M-L, Cole S, Krishfield R, Proshutinsky A, Toole J. 2014. Characterizing the eddy field in the Arctic Ocean halocline. *J Geophys Res Oceans.* 119:8800-8817. doi:10.1002/2014JC010488.

# Appendix A: Surface Current Patterns in the Northeastern Chukchi Sea and Their Response to Wind Forcing

## A.1 Introduction

SOM derived surface current and wind patterns from 2012 were used to define circulation features in the northeastern Chukchi Sea. Generating 12 patterns allowed us to isolate data gaps and unique circulation features; however, it also derived many patterns that were similar to one another. To simplify presented results in the main manuscript, similar patterns were grouped together (Table A-1). We provide all 12 original patterns here for those interested in more detail. Figure A-1 corresponds to the simplified Figures C2a-d, while Figure A-2 corresponds to Figure C4.

Please note that the number of the pattern is not a ranking, but rather an arbitrarily assigned identification number. This should be evident from the percentage of occurrence recorded in each figure.

## A.2 SOM Grouping Explained

Figures A-1a and A-1b were grouped together as the reversal regime (Figure C2b) as these patterns both depict overall flow in the domain to the southwest/west under northeasterly winds. Figures A-1c and A-1f are classified as the northwesterly wind regime (Figure C2c). Figure A-1d stands alone as the divergent mode (Figure C2d). Figure A-1e represents Pattern G, indicative of times when data returns were sparse.

Figures A-1g through A-1l were grouped together as the northeastward-flowing regime (Figure C2a). All of these patterns contained predominantly northeastward-flowing currents along the coastline. The main differences result from winds and data gap distributions. Patterns 7 (Figure A-1g) and 10 (Figure A-1j) depict discontinuities between the northern and southern masks, with sparse, variable currents in the

**Table A-1.** A summary of the original SOM patterns and how they are grouped as circulation regimes in the main manuscript.

SOM Pattern Number	Regime Grouping
1	Reversal
2	Reversal
3	Northwesterly Wind
4	Divergent Mode
5	Data Gap
6	Northwesterly Wind
7	Northeastward-Flowing
8	Northeastward-Flowing
9	Northeastward-Flowing
10	Northeastward-Flowing
11	Northeastward-Flowing
12	Northeastward-Flowing

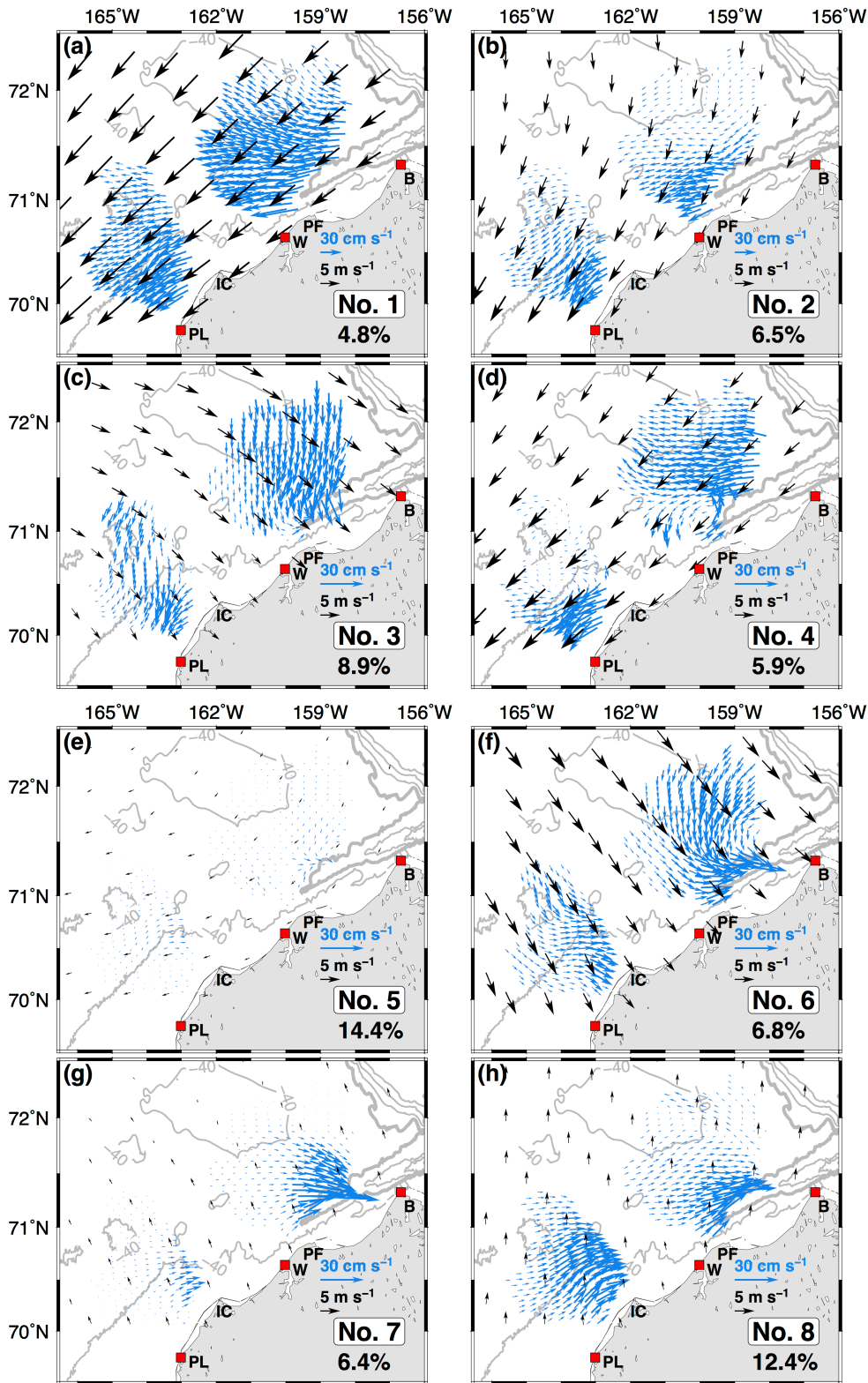


**Figure A-1.** (a)-(h), SOM-derived patterns No. 1–8 of surface currents (blue vectors) and paired winds (black vectors) for 2012 data. Pattern number and its relative frequency of occurrence are shown in the lower right corner. The 80 m isobath is thicker to define Barrow Canyon. Note that the scales of current vectors in Patterns No. 3–8 are different.

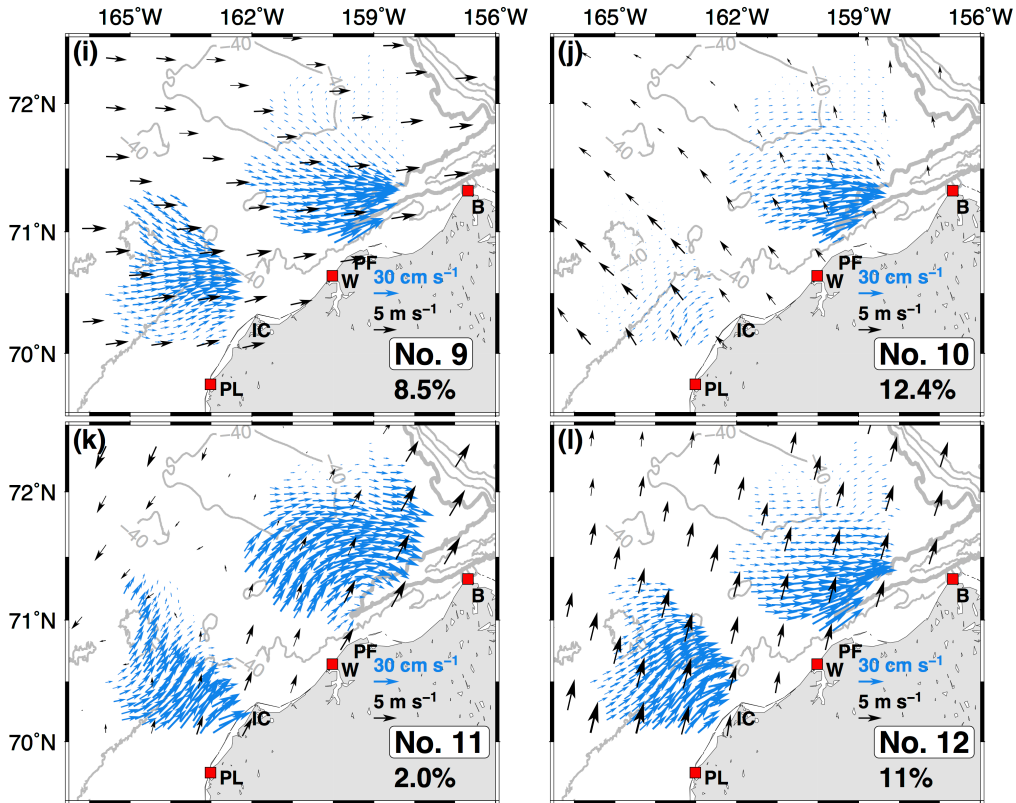


**Figure A-1.** (continued) (i)-(l), SOM-derived patterns No. 9–12 of surface currents (blue vectors) and paired winds (black vectors) for 2012 data.

southern region near Point Lay and Icy Cape. A review of the data confirmed that the Point Lay HFR was experiencing maintenance issues in August 2012, when patterns 7 and 10 occurred most often. Given that the northern region of currents is derived from the Wainwright and Barrow HFR, which were operational, it follows that the currents in the northern region are accurate while the currents in the southern region are not. Therefore it is still appropriate to categorize patterns 7 and 10 as the northeastward-flowing regime, although they depict currents when only the northern mask is operational.

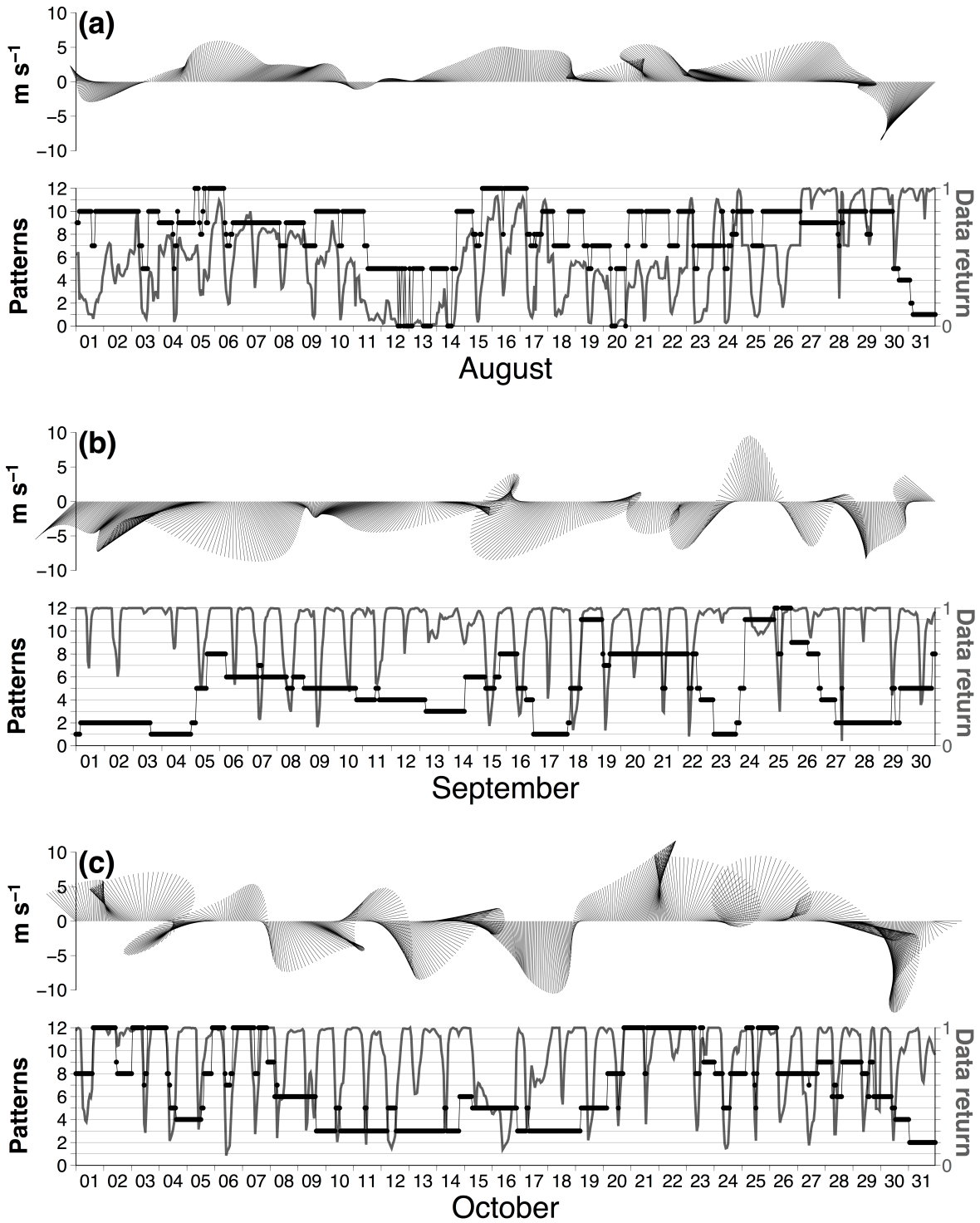


**Figure A-2.** (a) Upper panel: time series of wind vectors in August 2012. The vector direction follows oceanographic convention. Lower panel: SOM-derived patterns (black dots) in August 2012 and normalized data returns (gray line). Pattern numbers correspond to Figure A-1. Pattern 0 denotes times when data return is zero. (b) As in (a), but for September 2012. (c) As in (a), but for October 2012.

## Appendix B: Tidal Ellipse Properties for the Chukchi Sea Shelf

Table B-1. M2 Tidal Ellipse Parameters

Mooring Id	Major Axis (cm/s)	Minor Axis (cm/s)	Rotation Direction	Inclination (°)	Greenwich Phase (°)	$\frac{Minor}{Major}$	# of years
BC1	$0.8 \pm 0.2$	$0.1 \pm 0.2$	CCW	$30 \pm 13$	$-155 \pm 15$	0.19	2
BC2	$0.9 \pm 0.2$	$0.1 \pm 0.2$		$22 \pm 15$	$-152 \pm 18$	0.15	5
BC3	$0.8 \pm 0.1$	$0.1 \pm 0.1$	CW	$1 \pm 11$	$-87 \pm 12$	0.14	2
BC4	$0.9 \pm 0.1$	$0.3 \pm 0.1$	CW	$2 \pm 10$	$176 \pm 9$	0.28	2
BC5	$1.0 \pm 0.2$	$0.4 \pm 0.1$	CW	$2 \pm 11$	$73 \pm 12$	0.38	2
BC6	$1.4 \pm 0.3$	$0.6 \pm 0.3$	CW	$11 \pm 16$	$165 \pm 13$	0.42	2
Bu	$2.1 \pm 0.1$	$1.5 \pm 0.1$	CW	$23 \pm 9$	$136 \pm 8$	0.71	6
CPAI01	$2.8 \pm 0.1$	$2.1 \pm 0.2$	CW	$35 \pm 9$	$125 \pm 9$	0.76	5
CPAI02	$0.9 \pm 0.1$	$0.6 \pm 0.1$	CW	$163 \pm 18$	$-15 \pm 16$	0.59	2
Cj	$3.0 \pm 0.1$	$2.3 \pm 0.1$	CW	$50 \pm 9$	$111 \pm 8$	0.78	6
EBC	$0.5 \pm 0.2$	$0.0 \pm 0.2$	CW	$51 \pm 31$	$-28 \pm 29$	0.04	3
HS01	$2.4 \pm 0.1$	$2.2 \pm 0.1$	CW	$59 \pm 31$	$103 \pm 32$	0.92	1
HS02	$2.7 \pm 0.2$	$2.4 \pm 0.2$	CW	$43 \pm 30$	$104 \pm 30$	0.92	1
HS03	$2.7 \pm 0.1$	$2.4 \pm 0.1$	CW	$59 \pm 25$	$109 \pm 25$	0.9	1
HS04	$2.5 \pm 0.1$	$2.2 \pm 0.1$	CW	$14 \pm 28$	$138 \pm 27$	0.91	1
HS05	$1.9 \pm 0.1$	$1.5 \pm 0.1$	CW	$9 \pm 12$	$147 \pm 11$	0.77	1
HS06	$1.4 \pm 0.1$	$0.8 \pm 0.1$	CW	$4 \pm 9$	$155 \pm 9$	0.58	1
HSNE40	$1.6 \pm 0.2$	$1.4 \pm 0.2$	CW	$-8 \pm 55$	$72 \pm 56$	0.91	2
HSNE50	$0.7 \pm 0.2$	$0.5 \pm 0.2$	CW	$139 \pm 57$	$0 \pm 59$	0.78	2
HSNE60	$0.5 \pm 0.2$	$0.4 \pm 0.2$	CW	$130 \pm 60$	$-15 \pm 57$	0.7	2
HSNW40	$3.1 \pm 0.2$	$3.0 \pm 0.2$	CW	$32 \pm 43$	$129 \pm 44$	0.95	2
HSNW50	$2.8 \pm 0.2$	$2.6 \pm 0.2$	CW	$47 \pm 36$	$115 \pm 35$	0.91	2
Site2	$1.1 \pm 0.2$	$0.3 \pm 0.3$	CW	$10 \pm 17$	$170 \pm 15$	0.28	4
Statoil3	$2.7 \pm 0.1$	$2.3 \pm 0.1$	CW	$24 \pm 18$	$138 \pm 18$	0.88	1
Statoil4	$3.3 \pm 0.1$	$3.0 \pm 0.1$	CW	$34 \pm 19$	$125 \pm 20$	0.91	1
WBC	$0.4 \pm 0.2$	$0.1 \pm 0.2$	CW	$76 \pm 38$	$-38 \pm 30$	0.26	3

**Table B-2. S2 Tidal Ellipse Parameters**

<b>Mooring Id</b>	<b>Major Axis (cm/s)</b>	<b>Minor Axis (cm/s)</b>	<b>Rotation Direction</b>	<b>Inclination (°)</b>	<b>Greenwich Phase (°)</b>	$\frac{\text{Minor}}{\text{Major}}$	<b># of Months</b>
BC1	0.3 ± 0.2	0.1 ± 0.2		64 ± 46	70 ± 39	0.26	2
BC2	0.3 ± 0.2	0.1 ± 0.2	CW	83 ± 52	83 ± 47	0.27	5
BC3	0.3 ± 0.1	0.2 ± 0.1	CW	53 ± 59	104 ± 52	0.58	2
BC4	0.4 ± 0.1	0.1 ± 0.1	CW	89 ± 24	74 ± 25	0.33	2
BC5	0.4 ± 0.1	0.3 ± 0.1	CW	28 ± 90	138 ± 90	0.87	2
BC6	0.7 ± 0.3	0.3 ± 0.3	CW	118 ± 38	60 ± 35	0.49	2
Bu	0.8 ± 0.1	0.6 ± 0.1	CW	134 ± 40	41 ± 41	0.82	6
CPAI01	1.1 ± 0.1	0.9 ± 0.1	CW	10 ± 31	51 ± 31	0.82	5
CPAI02	0.7 ± 0.1	0.7 ± 0.1	CW	52 ± 74	97 ± 75	0.91	2
Cj	1.2 ± 0.1	1.0 ± 0.1	CW	29 ± 41	169 ± 40	0.87	6
EBC	0.5 ± 0.2	0.1 ± 0.3	CW	51 ± 33	104 ± 33	0.16	3
HS01	1.1 ± 0.1	0.9 ± 0.1	CW	75 ± 43	103 ± 44	0.88	1
HS02	1.4 ± 0.1	1.2 ± 0.2	CW	70 ± 58	92 ± 57	0.91	1
HS03	1.4 ± 0.1	1.2 ± 0.1	CW	79 ± 31	102 ± 31	0.85	1
HS04	1.1 ± 0.1	1.0 ± 0.1	CW	123 ± 49	49 ± 51	0.91	1
HS05	0.9 ± 0.1	0.8 ± 0.1	CW	154 ± 44	12 ± 42	0.86	1
HS06	0.6 ± 0.1	0.6 ± 0.1	CW	116 ± 98	47 ± 104	0.95	1
HSNE40	1.4 ± 0.2	1.2 ± 0.2	CW	58 ± 55	84 ± 56	0.88	2
HSNE50	1.3 ± 0.2	1.1 ± 0.2	CW	58 ± 59	80 ± 59	0.87	2
HSNE60	1.1 ± 0.2	1.1 ± 0.2	CW	52 ± 87	77 ± 85	0.93	2
HSNW40	1.4 ± 0.2	1.3 ± 0.2	CW	87 ± 63	83 ± 64	0.92	2
HSNW50	1.3 ± 0.2	1.2 ± 0.2	CW	67 ± 69	114 ± 68	0.93	2
Site2	0.4 ± 0.2	0.2 ± 0.2	CW	107 ± 53	35 ± 49	0.57	4
Statoil3	1.1 ± 0.1	1.0 ± 0.1	CW	145 ± 74	32 ± 74	0.94	1
Statoil4	1.4 ± 0.1	1.3 ± 0.1	CW	120 ± 109	60 ± 111	0.99	1
WBC	0.6 ± 0.2	0.3 ± 0.2	CW	44 ± 36	90 ± 37	0.6	3

**Table B-3. N2 Tidal Ellipse Parameters**

<b>Mooring Id</b>	<b>Major Axis (cm/s)</b>	<b>Minor Axis (cm/s)</b>	<b>Rotation Direction</b>	<b>Inclination (°)</b>	<b>Greenwich Phase (°)</b>	$\frac{\text{Minor}}{\text{Major}}$	<b># of Months</b>
BC1	0.4 ± 0.2	0.0 ± 0.2		25 ± 23	97 ± 32	0.04	2
BC2	0.4 ± 0.2	0.1 ± 0.2		30 ± 40	140 ± 41	0.27	5
BC3	0.3 ± 0.1	0.1 ± 0.1		42 ± 36	99 ± 39	0.21	2
BC4	0.3 ± 0.1	0.1 ± 0.1	CW	6 ± 25	17 ± 26	0.15	2
BC5	0.3 ± 0.2	0.1 ± 0.2	CW	33 ± 42	104 ± 47	0.26	2
BC6	0.5 ± 0.2	0.1 ± 0.3	CW	13 ± 36	86 ± 35	0.15	2
Bu	0.6 ± 0.1	0.4 ± 0.1	CW	48 ± 31	75 ± 32	0.71	6
CPAI01	0.6 ± 0.1	0.4 ± 0.1	CW	56 ± 43	64 ± 46	0.75	5
CPAI02	0.5 ± 0.1	0.3 ± 0.1	CW	19 ± 39	111 ± 37	0.65	2
Cj	0.6 ± 0.1	0.5 ± 0.1	CW	66 ± 61	55 ± 61	0.83	6
EBC	0.3 ± 0.2	0.1 ± 0.2		64 ± 78	-176 ± 80	0.39	3
HS01	0.7 ± 0.1	0.6 ± 0.2	CW	65 ± 45	57 ± 42	0.79	1
HS02	0.9 ± 0.1	0.9 ± 0.1	CW	164 ± 124	319 ± 129	0.95	1
HS03	0.8 ± 0.1	0.7 ± 0.1	CW	59 ± 52	85 ± 53	0.86	1
HS04	0.8 ± 0.1	0.6 ± 0.1	CW	43 ± 38	72 ± 38	0.84	1
HS05	0.7 ± 0.1	0.5 ± 0.1	CW	27 ± 40	98 ± 36	0.8	1
HS06	0.4 ± 0.1	0.3 ± 0.1	CW	15 ± 47	104 ± 43	0.7	1
HSNE40	0.9 ± 0.2	0.8 ± 0.2	CW	26 ± 43	114 ± 45	0.81	2
HSNE50	0.7 ± 0.2	0.6 ± 0.2	CW	38 ± 95	120 ± 89	0.91	2
HSNE60	0.5 ± 0.2	0.5 ± 0.2	CW	15 ± 91	145 ± 94	0.89	2
HSNW40	1.0 ± 0.2	1.0 ± 0.1	CW	50 ± 90	80 ± 89	0.93	2
HSNW50	0.8 ± 0.2	0.7 ± 0.2	CW	56 ± 86	51 ± 84	0.91	2
Site2	0.5 ± 0.2	0.0 ± 0.3	CW	35 ± 32	98 ± 31	0.11	4
Statoil3	0.7 ± 0.1	0.7 ± 0.1	CW	93 ± 72	46 ± 72	0.93	1
Statoil4	1.0 ± 0.1	0.8 ± 0.1	CW	40 ± 24	88 ± 24	0.75	1
WBC	0.3 ± 0.1	0.2 ± 0.2	CW	53 ± 75	140 ± 76	0.66	3

**Table B-4. K2 Tidal Ellipse Parameters**

<b>Mooring Id</b>	<b>Major Axis (cm/s)</b>	<b>Minor Axis (cm/s)</b>	<b>Rotation Direction</b>	<b>Inclination (°)</b>	<b>Greenwich Phase (°)</b>	$\frac{\text{Minor}}{\text{Major}}$	<b># of Months</b>
BC1	0.1 ± 0.2	0.0 ± 0.1	CW	41 ± 81	162 ± 99	0.11	2
BC2	0.3 ± 0.2	0.0 ± 0.2	CW	16 ± 60	171 ± 66	0.09	5
BC3	0.2 ± 0.1	0.1 ± 0.1	CW	9 ± 55	-140 ± 49	0.5	2
BC4	0.3 ± 0.1	0.1 ± 0.1	CW	109 ± 38	101 ± 38	0.36	2
BC5	0.2 ± 0.2	0.1 ± 0.1	CW	-5 ± 56	125 ± 61	0.49	2
BC6	0.1 ± 0.1	0.0 ± 0.1	CW	40 ± 102	210 ± 112	0.2	1
Bu	0.3 ± 0.1	0.2 ± 0.1	CW	63 ± 66	128 ± 66	0.74	6
CPAI01	0.3 ± 0.1	0.3 ± 0.1	CW	34 ± 77	165 ± 78	0.81	5
CPAI02	0.2 ± 0.1	0.1 ± 0.1	CW	143 ± 72	30 ± 99	0.31	2
Cj	0.4 ± 0.1	0.3 ± 0.1	CW	55 ± 64	148 ± 65	0.76	6
EBC	0.2 ± 0.2	0.1 ± 0.2		77 ± 77	124 ± 81	0.33	3
HS01	0.4 ± 0.1	0.4 ± 0.1	CW	29 ± 98	164 ± 101	0.92	1
HS02	0.4 ± 0.2	0.3 ± 0.2	CW	144 ± 110	35 ± 98	0.92	1
HS03	0.4 ± 0.1	0.3 ± 0.1	CW	50 ± 93	130 ± 90	0.83	1
HS04	0.4 ± 0.1	0.3 ± 0.1	CW	132 ± 68	54 ± 70	0.79	1
HS05	0.2 ± 0.1	0.1 ± 0.1	CW	170 ± 52	19 ± 50	0.48	1
HS06	0.3 ± 0.1	0.2 ± 0.1	CW	18 ± 61	155 ± 54	0.63	1
HSNE40	0.3 ± 0.2	0.3 ± 0.2	CW	-18 ± 103	132 ± 108	0.85	2
HSNE50	0.2 ± 0.2	0.1 ± 0.2	CW	138 ± 105	59 ± 113	0.48	2
HSNE60	0.2 ± 0.2	0.1 ± 0.2	CW	-8 ± 101	99 ± 106	0.44	2
HSNW40	0.6 ± 0.2	0.5 ± 0.2	CW	126 ± 112	78 ± 117	0.95	2
HSNW50	0.5 ± 0.2	0.4 ± 0.2	CW	106 ± 80	123 ± 77	0.79	2
Site2	0.1 ± 0.1	0.1 ± 0.1		73 ± 88	128 ± 84	0.49	2
Statoil3	0.4 ± 0.1	0.4 ± 0.1	CW	170 ± 92	21 ± 92	0.93	1
Statoil4	0.5 ± 0.1	0.4 ± 0.1	CW	36 ± 97	163 ± 93	0.93	1
WBC	0.1 ± 0.1	0.0 ± 0.1		38 ± 112	-50 ± 137	0.22	2

**Table B-5. O1 Tidal Ellipse Parameters**

<b>Mooring Id</b>	<b>Major Axis (cm/s)</b>	<b>Minor Axis (cm/s)</b>	<b>Rotation Direction</b>	<b>Inclination (°)</b>	<b>Greenwich Phase (°)</b>	$\frac{\text{Minor}}{\text{Major}}$	<b># of Months</b>
BC1	0.9 ± 0.4	0.2 ± 0.3	CCW	38 ± 32	49 ± 31	0.24	2
BC2	0.8 ± 0.5	0.1 ± 0.4		29 ± 32	42 ± 40	0.12	5
BC3	0.8 ± 0.3	0.1 ± 0.2	CW	15 ± 19	54 ± 28	0.18	2
BC4	0.8 ± 0.3	0.2 ± 0.2	CW	10 ± 20	55 ± 22	0.27	2
BC5	0.8 ± 0.3	0.1 ± 0.2	CW	171 ± 16	-131 ± 24	0.16	2
BC6	1.1 ± 0.4	0.3 ± 0.5	CW	160 ± 33	-136 ± 27	0.33	2
Bu	0.6 ± 0.2	0.3 ± 0.2	CW	-17 ± 27	-144 ± 30	0.49	6
CPAI01	0.6 ± 0.2	0.3 ± 0.2	CW	2 ± 33	-32 ± 31	0.48	5
CPAI02	1.2 ± 0.2	0.5 ± 0.2	CW	158 ± 14	-138 ± 16	0.42	2
Cj	0.5 ± 0.1	0.3 ± 0.1	CW	12 ± 38	-51 ± 39	0.57	6
EBC	1.4 ± 0.6	0.1 ± 0.6		41 ± 27	69 ± 30	0.1	3
HS01	1.1 ± 0.2	0.6 ± 0.2	CW	179 ± 18	200 ± 17	0.56	1
HS02	1.2 ± 0.2	0.6 ± 0.2	CW	171 ± 14	181 ± 13	0.53	1
HS03	1.3 ± 0.2	0.8 ± 0.1	CW	7 ± 14	5 ± 17	0.63	1
HS04	0.8 ± 0.1	0.6 ± 0.1	CW	163 ± 24	195 ± 22	0.68	1
HS05	0.9 ± 0.2	0.5 ± 0.1	CW	161 ± 15	211 ± 17	0.55	1
HS06	0.8 ± 0.3	0.1 ± 0.2	CW	177 ± 15	218 ± 18	0.12	1
HSNE40	1.6 ± 0.3	0.9 ± 0.2	CW	162 ± 12	-172 ± 14	0.56	2
HSNE50	1.5 ± 0.2	0.9 ± 0.2	CW	151 ± 17	-169 ± 19	0.61	2
HSNE60	1.7 ± 0.3	1.0 ± 0.3	CW	141 ± 17	-171 ± 17	0.59	2
HSNW40	1.2 ± 0.2	0.8 ± 0.2	CW	-7 ± 14	-85 ± 15	0.62	2
HSNW50	1.1 ± 0.3	0.6 ± 0.2	CW	168 ± 17	-167 ± 19	0.51	2
Site2	0.7 ± 0.4	0.1 ± 0.4		-9 ± 33	-144 ± 36	0.13	4
Statoil3	0.9 ± 0.2	0.6 ± 0.2	CW	1 ± 27	3 ± 29	0.64	1
Statoil4	0.9 ± 0.2	0.6 ± 0.2	CW	1 ± 32	351 ± 32	0.7	1
WBC	1.3 ± 0.7	0.2 ± 0.5	CW	-5 ± 22	37 ± 29	0.15	3

**Table B-6. P1 Tidal Ellipse Parameters**

<b>Mooring Id</b>	<b>Major Axis (cm/s)</b>	<b>Minor Axis (cm/s)</b>	<b>Rotation Direction</b>	<b>Inclination (°)</b>	<b>Greenwich Phase (°)</b>	$\frac{\text{Minor}}{\text{Major}}$	<b># of Months</b>
BC1	0.3 ± 0.3	0.0 ± 0.3	CW	53 ± 69	107 ± 75	0.15	2
BC2	0.4 ± 0.3	0.1 ± 0.3		45 ± 83	115 ± 82	0.29	5
BC3	0.2 ± 0.2	0.0 ± 0.2	CW	81 ± 92	74 ± 111	0.3	2
BC4	0.2 ± 0.2	0.1 ± 0.2		38 ± 96	74 ± 107	0.46	2
BC5	0.2 ± 0.2	0.1 ± 0.2		0 ± 64	-27 ± 100	0.28	2
BC6	0.1 ± 0.1	0.1 ± 0.2	CW	134 ± 119	270 ± 120	0.87	1
Bu	0.2 ± 0.2	0.0 ± 0.1		3 ± 59	-167 ± 72	0.19	6
CPAI01	0.2 ± 0.2	0.0 ± 0.2		132 ± 70	-168 ± 75	0.2	5
CPAI02	0.3 ± 0.2	0.1 ± 0.2	CW	166 ± 48	-132 ± 68	0.27	2
Cj	0.1 ± 0.1	0.0 ± 0.1		160 ± 79	-137 ± 91	0.17	6
EBC	0.5 ± 0.5	0.3 ± 0.4		55 ± 89	145 ± 88	0.54	3
HS01	0.2 ± 0.1	0.2 ± 0.1	CW	165 ± 82	219 ± 81	0.75	1
HS02	0.3 ± 0.1	0.2 ± 0.1	CW	91 ± 70	230 ± 61	0.62	1
HS03	0.3 ± 0.2	0.1 ± 0.1	CW	1 ± 29	18 ± 39	0.43	1
HS04	0.2 ± 0.1	0.1 ± 0.1	CW	102 ± 49	231 ± 49	0.38	1
HS05	0.2 ± 0.1	0.0 ± 0.1		135 ± 51	224 ± 51	0	1
HS06	0.3 ± 0.2	0.0 ± 0.2	CW	116 ± 51	245 ± 50	0.15	1
HSNE40	0.3 ± 0.2	0.2 ± 0.2	CW	11 ± 54	-108 ± 62	0.52	2
HSNE50	0.3 ± 0.2	0.2 ± 0.2	CW	44 ± 89	-63 ± 105	0.81	2
HSNE60	0.3 ± 0.2	0.2 ± 0.2	CW	168 ± 90	156 ± 106	0.71	2
HSNW40	0.2 ± 0.1	0.2 ± 0.1	CW	148 ± 70	-153 ± 71	0.68	2
HSNW50	0.3 ± 0.2	0.1 ± 0.2	CW	122 ± 58	-138 ± 53	0.36	2
Site2	0.3 ± 0.2	0.1 ± 0.2		5 ± 77	18 ± 95	0.22	2
Statoil3	0.2 ± 0.2	0.1 ± 0.2	CW	116 ± 54	233 ± 55	0.3	1
Statoil4	0.1 ± 0.2	0.1 ± 0.2	CW	49 ± 119	269 ± 119	0.86	1
WBC	0.2 ± 0.3	0.0 ± 0.2	CCW	74 ± 76	124 ± 107	0.08	2

**Table B-7. K1 Tidal Ellipse Parameters**

<b>Mooring Id</b>	<b>Major Axis (cm/s)</b>	<b>Minor Axis (cm/s)</b>	<b>Rotation Direction</b>	<b>Inclination (°)</b>	<b>Greenwich Phase (°)</b>	$\frac{\text{Minor}}{\text{Major}}$	<b># of Months</b>
BC1	0.6 ± 0.3	0.1 ± 0.3	CCW	42 ± 40	125 ± 43	0.19	2
BC2	0.6 ± 0.4	0.1 ± 0.4	CCW	33 ± 43	70 ± 62	0.22	5
BC3	0.6 ± 0.3	0.2 ± 0.2	CCW	13 ± 38	175 ± 36	0.36	2
BC4	0.5 ± 0.3	0.2 ± 0.2	CCW	-1 ± 40	174 ± 48	0.42	2
BC5	0.6 ± 0.3	0.1 ± 0.2		158 ± 22	-114 ± 31	0.13	2
BC6	0.6 ± 0.4	0.1 ± 0.4	CW	5 ± 64	-164 ± 50	0.18	2
Bu	0.3 ± 0.2	0.1 ± 0.2		146 ± 43	-145 ± 46	0.22	6
CPAI01	0.4 ± 0.2	0.1 ± 0.2		123 ± 48	-140 ± 47	0.31	5
CPAI02	0.6 ± 0.2	0.1 ± 0.2	CW	146 ± 22	-150 ± 24	0.2	2
Cj	0.3 ± 0.1	0.1 ± 0.1	CW	138 ± 38	-155 ± 36	0.42	6
EBC	0.8 ± 0.5	0.1 ± 0.5	CCW	42 ± 46	91 ± 47	0.08	3
HS01	0.8 ± 0.2	0.3 ± 0.2	CW	159 ± 20	187 ± 18	0.45	1
HS02	0.8 ± 0.1	0.6 ± 0.1	CW	148 ± 36	186 ± 37	0.78	1
HS03	0.8 ± 0.2	0.7 ± 0.1	CW	4 ± 37	351 ± 39	0.8	1
HS04	0.6 ± 0.1	0.4 ± 0.1	CW	157 ± 32	189 ± 31	0.69	1
HS05	0.5 ± 0.2	0.2 ± 0.1	CW	145 ± 20	205 ± 19	0.32	1
HS06	0.6 ± 0.2	0.2 ± 0.2	CW	164 ± 22	228 ± 24	0.31	1
HSNE40	0.8 ± 0.2	0.5 ± 0.2	CW	137 ± 31	-163 ± 34	0.64	2
HSNE50	0.8 ± 0.2	0.5 ± 0.2	CW	148 ± 28	-170 ± 29	0.61	2
HSNE60	0.9 ± 0.2	0.5 ± 0.2	CW	141 ± 26	-173 ± 27	0.52	2
HSNW40	0.6 ± 0.2	0.4 ± 0.1	CW	149 ± 35	-175 ± 35	0.69	2
HSNW50	0.6 ± 0.2	0.3 ± 0.2	CW	146 ± 45	-173 ± 46	0.6	2
Site2	0.5 ± 0.3	0.1 ± 0.4		20 ± 55	28 ± 74	0.34	4
Statoil3	0.4 ± 0.1	0.4 ± 0.1	CW	146 ± 108	191 ± 107	0.93	1
Statoil4	0.6 ± 0.2	0.4 ± 0.2	CW	113 ± 51	216 ± 45	0.67	1
WBC	0.8 ± 0.5	0.2 ± 0.5		-25 ± 38	160 ± 42	0.24	3

**Table B-8. Q1 Tidal Ellipse Parameters**

<b>Mooring Id</b>	<b>Major Axis (cm/s)</b>	<b>Minor Axis (cm/s)</b>	<b>Rotation Direction</b>	<b>Inclination (°)</b>	<b>Greenwich Phase (°)</b>	$\frac{\text{Minor}}{\text{Major}}$	<b># of Months</b>
BC1	0.4 ± 0.4	0.0 ± 0.3	CW	121 ± 50	156 ± 62	0.03	2
BC2	0.4 ± 0.4	0.1 ± 0.4		31 ± 76	9 ± 93	0.35	5
BC3	0.2 ± 0.2	0.0 ± 0.2	CCW	8 ± 67	-53 ± 100	0.2	2
BC4	0.4 ± 0.3	0.1 ± 0.2		18 ± 45	-76 ± 50	0.24	2
BC5	0.3 ± 0.3	0.0 ± 0.2	CW	165 ± 53	-140 ± 74	0.23	2
BC6	0.3 ± 0.4	0.1 ± 0.3		75 ± 64	-98 ± 109	0.34	2
Bu	0.2 ± 0.2	0.1 ± 0.2		19 ± 68	-93 ± 91	0.35	6
CPAI01	0.2 ± 0.2	0.1 ± 0.2		106 ± 71	-126 ± 69	0.29	5
CPAI02	0.3 ± 0.2	0.2 ± 0.2	CW	166 ± 71	-160 ± 82	0.63	2
Cj	0.1 ± 0.1	0.0 ± 0.1		70 ± 80	-70 ± 96	0.21	6
EBC	0.7 ± 0.6	0.2 ± 0.5		44 ± 61	57 ± 64	0.38	3
HS01	0.3 ± 0.2	0.0 ± 0.2	CW	168 ± 39	160 ± 45	0.04	1
HS02	0.3 ± 0.2	0.1 ± 0.1	CCW	178 ± 41	150 ± 36	0.2	1
HS03	0.3 ± 0.2	0.1 ± 0.2	CW	19 ± 47	3 ± 56	0.46	1
HS04	0.3 ± 0.1	0.1 ± 0.1	CW	156 ± 26	188 ± 27	0.23	1
HS05	0.3 ± 0.1	0.1 ± 0.2	CW	138 ± 38	215 ± 39	0.3	1
HS06	0.3 ± 0.2	0.1 ± 0.2	CCW	2 ± 43	43 ± 57	0.19	1
HSNE40	0.6 ± 0.2	0.2 ± 0.2	CW	-7 ± 24	69 ± 28	0.32	2
HSNE50	0.4 ± 0.2	0.3 ± 0.2	CW	-8 ± 57	57 ± 68	0.59	2
HSNE60	0.4 ± 0.2	0.2 ± 0.2	CW	133 ± 58	173 ± 61	0.57	2
HSNW40	0.3 ± 0.2	0.2 ± 0.1	CW	7 ± 62	-30 ± 75	0.58	2
HSNW50	0.3 ± 0.2	0.2 ± 0.2	CW	17 ± 57	-133 ± 66	0.48	2
Site2	0.4 ± 0.3	0.1 ± 0.3		32 ± 64	-68 ± 74	0.26	4
Statoil3	0.2 ± 0.2	0.1 ± 0.2	CW	128 ± 66	195 ± 62	0.42	1
Statoil4	0.3 ± 0.2	0.2 ± 0.2	CW	125 ± 88	207 ± 93	0.7	1
WBC	0.5 ± 0.5	0.1 ± 0.4	CW	-9 ± 50	-172 ± 91	0.26	3



### **Department of the Interior (DOI)**

The Department of the Interior protects and manages the Nation's natural resources and cultural heritage; provides scientific and other information about those resources; and honors the Nation's trust responsibilities or special commitments to American Indians, Alaska Natives, and affiliated island communities.



### **Bureau of Ocean Energy Management (BOEM)**

The mission of the Bureau of Ocean Energy Management is to manage development of U.S. Outer Continental Shelf energy and mineral resources in an environmentally and economically responsible way.

### **BOEM Environmental Studies Program**

The mission of the Environmental Studies Program is to provide the information needed to predict, assess, and manage impacts from offshore energy and marine mineral exploration, development, and production activities on human, marine, and coastal environments. The proposal, selection, research, review, collaboration, production, and dissemination of each of BOEM's Environmental Studies follows the DOI Code of Scientific and Scholarly Conduct, in support of a culture of scientific and professional integrity, as set out in the DOI Departmental Manual (305 DM 3).